Electrostatic effects in soft matter

René Messina

Institut für Theoretische Physik II
Heinrich-Heine-Universität Düsseldorf
Universitätsstr. 1
D-40225 Düsseldorf
Germany

E-mail: *messina@thphy.uni-duesseldorf.de*

Habilitationsschrift
vorgelegt der Mathematisch-Naturwissenschaftlichen Fakultät
der Heinrich-Heine-Universität Düsseldorf

February 1, 2007

Abstract

The influence of electrostatic effects in various model systems of the soft matter is presented. Computer simulations (Monte Carlo and molecular dynamics) as well as numerical and analytical theories are developed to understand the role of the Coulomb interaction in those systems. In particular, phenomena such as anomalous counterion distribution (overcharging), polyelectrolyte adsorption and multilayering, image forces, and charged colloids in bulk and in strong confinement are investigated and discussed.

Übersicht

Diese Habilitationsschrift fasst meine Forschungsarbeit im Gebiet der geladenen weichen Materie. Eigentlich sind alle Materialien mehr oder weniger an der mesoskopischen Skala geladen, dies hängt vom Grad der Polarizabilität des Lösungsmittels (oder Matrix) und der gelösten Partikel (z. B. kolloidale Partikel, Polymere, Membranen. etc.) ab. Das meiste weithin bekannte Beispiel des polaren Lösungsmittels ist zweifellos Wasser, welches eine entscheidende Rolle im Leben, in biologischen Prozessen sowie bei Industrieanwendungen spielt. Wenn die gelösten Partikel auch polar sind, können sie sich dann in geladene Teilchen (Makroionen) und (mikroskopische) Gegenionen trennen. Die Gegenion-Verteilung in der Nähe der Makroionen erweist sich für die Oberflächeneigenschaften als entscheidend.

Historisch wurden mittleres Feld (mean-field) Theorien erstmals eingeführt und verwendet um geladene soft-matter-systeme zu charakterisieren. Die Pionierarbeiten von Gouy und Chapman [Gou10, Cha13] wurden vor fast einem Jahrhundert realisiert. Sie haben die Gegenion-Verteilung in der Nähe von einer flachen geladenen Grenzfläche analysiert. Die heute genannte Poisson-Boltzmann Theorie anwendend, demonstrierten sie, dass die Gegenion-Verteilungsprofile algebraisch als eine Funktion der Trennung von der Wand mit einer charakteristischen Länge abfallen. Diese ist umgekehrt proportional zur Oberflächenladungsdichte der Grenzfläche. Zehn Jahre später vollendeten Debye und Hückel [DH23] einen grundlegenden Fortschritt zum Verständnis der Abschirmung. Diese Theorie wurde ursprünglich für Elektrolyte entwickelt (d.h. eine Lösung der mikroskopischen Kationen und der Anionen, z.B. NaCl) und basierte auf der Linearisation der Poisson-Boltzmann Gleichung. Diese wird heute weitgehend im Plasma und in der Festkörperphysik benutzt.[1]

Aufgrund ihrer intuitiven und klaren physikalischen Grundlage, sind mittleres Feld Theorien attraktive Werkzeuge. Es sind robuste Theorien, solange die *elektrostatischen Korrelationen* nicht zu gross sind. In vielen praxisnahenn Situationen (Chro-

[1] Man beachte, dass ein ähnliches Potential der Wechselwirkung (sogenanntes Yukawa Potential) an der subatomistichen Skala entsteht, um die Kohäsion der nuklearen Materie zu beschreiben. Nichtsdestoweniger ist die Interpretation dieses Potentials hinsichtlich der Abschirmung in diesem Fall weniger direkt.

matin, Polyelektrolytvielschichte, geladene kolloidale Suspension) sind elektrostatische Korrelationen stark genug, um diese Theorien zu entkräften sogar auf einem qualitativen Niveau. Zwei auffallend und natürliche Konsequenzen der elektrostatischen Korrelationen, die sich nicht mittels mittler Feld Theorien erkären lassen können, sind Ladung-Umkehrung (auch benannt Überladung) und "Anziehung gleicher Ladungen": (i) Überladung betrifft die Situation, in der ein Makroion durch eine Wolke von Gegenionen bedeckt wird, deren globale Ladung die des Makroions überkompensiert. Folglich ändert die Nettoladung (oder effektive Ladung) ihr Zeichen. (ii) Anziehung gleicher Ladungen ist die gegenintuitive Anziehung zwischen zwei Makroionen, die das gleiche Ladungszeichen tragen.

Andere ebenso interessante und noch komplexere Systeme werden von der Kombination unterschiedlicher Sorten hoch geladener Körper angeboten. Die Adsorption geladener sphärischer kolloidaler Teilchen auf einen gegesätzlich geladenes Substrat oder die Anordnung von Polyelektrolyt-multilayers (Mischung von Polykationen und Polyanionen) sind typische Beispiele deren volles Verständnis auch Methoden erfordert, die weit über die mittleres Feld Konzepte hinausragen.

Die vorliegende Arbeit untersucht das Problem elektrostatischer Korrelationen, die in Systeme der weichen Materie auftretten. Dabei werden Computersimulationen und einfachen theoretischen Modellen benutzt. Kapitel 2 behandelt die Rolle der Gegenionen-Korrlationen. Das Verhalten komplexerer Systeme wie Kolloid-Polyelektrolyt Komplexbildung, die Polyelektrolyte in der Nähe einer geladenen Wand oder die Polyelektrolytvielschichte werden im Kapitel 3 diskutiert. Geladene kolloidale Suspensionen in der starken Raum-Beschränkung werden in Kapitel 4 präsentiert. Einige ausgewählte entsprechende Publikationen befinden sich im Anhang.

Contents

Acknowledgments

I would like to express my thanks to:

- Kurt Kremer, who made me discover the fascinating domain of soft matter and welcomed me in his "Theory Group" as a post-doc at the Max-Planck-Institut für Polymerforschung in Mainz. Very frequent discussions and exchanges of ideas with him and Christian Holm were a great benefit to my research work.
- Hartmut Löwen, who is another important scientific mentor in my career. Thanks to his continuous support and encouragement, but also very enlightening discussions, he has been considerably contributing to my research work.
- Marcelo Lozada-Cassou, for his hospitality at the Instituto Mexicano del Petroleo in Mexico-City. I learned there many fundamental aspects on charged soft matter.
- Ladislas Kubin, who was my PhD supervisor in Paris. Thanks to his wide-open approach to material science, he could perfectly and competently supervise my research works combining experiments, theory and computer simulation.
- The following people, for the valuable time spent with them allowing me to deepen my knowledge and understanding of many physical problems in (charged) soft matter: Elshad Allahyarov, Marcia Barbosa, Ronald Blaak, Markus Deserno, Burkard Dünweg, Felipe Jimenez, Albert Johner, Christos Likos, Thomas Palberg, Helmut Schiessel, Boris Shklovskii, Matthias Schmidt.

PART I:

SUMMARY OF SCIENTIFIC WORK

Chapter 1

INTRODUCTION

THIS thesis outlines my research work in the field of charged soft matter. Virtually all materials are more or less charged at the mesoscopic scale, depending on the degree of the polarizability of the embedding solvent (or matrix) and the solute particles (e. g., colloidal particles, polymers, membranes. etc.). The most well known example of polar solvent is evidently water which plays a crucial role in life, biological processes as well as industrial applications. When the solute particles are polar too, they can then dissociate into charged particles (also called macroions) and (microscopic) counterions. The counterion distribution near macroions turns out to be decisive for the surface properties of the latter.

Historically, mean-field theories were first introduced and applied to characterize charged soft-matter-systems. The pioneering works of Gouy and Chapmann [Gou10, Cha13], realized almost one century ago, concerns the counterion distribution near a planar charged interface. Applying the nowadays called Poisson-Boltzmann theory, they demonstrated that the counterion distribution profiles decays algebraically as a function of the separation from the wall with a characteristic length that is inversely proportional to the surface charge density of wall. Ten years later, Debye and Hückel [DH23] accomplished a fundamental advance towards the understanding of screening. This theory originally developed for electrolytes (i.e. a solution of microscopic cations and anions, e.g. NaCl) and based on the linearization of the Poisson-Boltzmann equation is now widely used in plasma and solid state physics.[1]

Mean-field theories are appealing tools due to their intuitive and clear physical basis, and are robust theories as long as *electrostatic correlations* are not too important.

[1] Note that a similar potential of interaction (so-called Yukawa potential) arises at the subatomistic scale to describe the cohesion of the nuclear matter. Nonetheless, the interpretation of this potential in terms of screening is less straightforward in that case.

In many practical situations (chromatin, polyelectrolyte multilayering, charged colloidal suspension) electrostatic correlations are strong enough to make mean-field theories fail even on a qualitative level. Two striking and natural consequences of electrostatic correlations, that can not be explained by mean-field theories, are charge reversal (also called overcharging) and like charge attraction: (i) Overcharging concerns the situation where a macroion is locally covered by a cloud of counterions whose global charge overcompensates that of the macroion so that the net charge (or effective charge) changes its sign. (ii) Like charge attraction is the counterintuitive effective attraction between two macroions carrying the same electric charge sign.

Other equally interesting and more complex systems are offered by the combination of different species of highly charged bodies. For instance the adsorption of charged spherical colloidal particles onto an oppositely charged planar substrate, or the formation of polyelectrolyte multilayers (i.e., a "stratified" mixing of polycations and polyanions) are typical examples whose full understanding necessitates also approaches that go far beyond mean-field concepts.

The present work examines the problem of electrostatic correlations setting in soft matter systems using computer simulations and simple theoretical models. The role of the counterion correlations is addressed in chapter 2. The behavior of more complex systems such as colloid-polyelectrolyte complexation, polyelectrolytes near a charged wall, or polyelectrolyte multilayers are discussed in chapter 3. Charged colloidal dispersions in strong confinement are presented in chapter 4. Some selected corresponding reprinted publications can be found in the appendix.

Chapter 2

ELECTROSTATIC CORRELATIONS IN SOFT MATTER

Most of the materials in soft matter are made up of water solvent embedding solute bodies (macroscopic/mesoscopic particles). When those solute particles are polar, they can dissociate into charged macroions and counterions.

The first theoretical determination of counterion distribution for an inhomogeneous fluid was realized by Gouy [Gou10] and Chapman [Cha13] independently almost one century ago. They applied the so-called Poisson-Boltzmann (PB) theory to predict the distribution of monovalent ions near a uniformly charged interface. The basis of the PB theory is the classical Poisson equation, $\Delta\phi(\vec{r}) = -\rho(\vec{r})/\varepsilon$, relating the second derivative of the (mean) electrostatic potential, $\phi(\vec{r})$, to the source of charges, $\rho(\vec{r})$, within the solution assuming a Boltzmann distribution $\rho(\vec{r}) \propto \exp[-\beta e\phi(\vec{r})]$. It is precisely this latter approximation (i.e., the potential of mean force [HM90] is replaced by the mean electrostatic potential in the Boltzmann factor) that makes the PB theory a *mean-field* one. To be more precise, lateral ion-ion correlations are ignored in the same spirit of the Curie-Weiss theory of magnetism. A nice feature of this mean-field theory is that the PB equation can be solved analytically for some cases, and the numerical procedure is rather simple compared to other more sophisticated existing theories. Furthermore, as long as the Coulomb coupling between ions is "fairly" moderate (which is the case for monovalent ions in aqueous solution), the PB theory describes astonishingly well the ion distribution when compared to computer simulations [JWH80, BDHM04, EML06] and even experiments [BVT06]. Nonetheless, as soon as ion-ion correlations get relevant, mean field theories such as the Poisson-Boltzmann one or its linearized version (so called Debye-Hückel theory) can not explain effects (experimentally observed) such as like-charge attraction [GC97, BS98] or overcharging [RVMW00, LGB04]. A large part of my work de-

scribed in this chapter is devoted to the understanding of the effect of ion correlations and especially overcharging occurring in charged colloidal suspensions.

2.1 Overcharging and like-charge attraction

One of the most curious and spectacular effect in the soft condensed matter community is the appearance, under specific circumstances, of an effective attraction between-like charged colloids. At the beginning of the 21$^{\text{th}}$ century [MHK00b, MHK00a, MHK01b], we discovered a possible mechanism explaining a *long-ranged* attraction between like-charged spheres. The underlying physical mechanism is based on the overcharging. The latter corresponds to an excess charge of the counterions in the vicinity of the macroion so that the net charge of the macroion changes its sign (also called *charge inversion*). Naively, one could think that the stable configuration corresponds to an exact neutralization of macroion by the counterions. This intuition is only correct for the case where the counterions are uniformly smeared out over the surface of the colloid. Indeed a simple calculation shows that the energy of interaction, between a central charge $Z_m e < 0$ (representing the macroion charge) and the shell of the counterions of radius a and charge $Z_c e > 0$ (with e being the elementary charge), is given by $E = \frac{Z_m Z_c e^2}{a} + \frac{Z_c^2 e^2}{2a}$. The criterion of stability is provided by $\frac{\partial E}{\partial Z_c} = 0$ leading to neutrality, i.e. $Z_c = -Z_m$. In reality, the counterions are discrete, and when electrostatically bound to the macroion's surface, they will maximize their separation such as to minimize the counterion-counterion repulsion. This problem turns out to be exactly the one that was addressed one century ago by Thomson [Tho04] (also called the Thomson sphere or Thomson problem) who studied the ground state energy and structure of n (classical) electrons confined on a sphere (model of a classical atom). The Thompson problem has only (exact) analytical solutions for $n \leq 5$ and possibly for some magic numbers (e.g., $n = 72$ corresponding to the fullerene structure). Nonetheless, based on Wigner crystal ideas [BM77, Shk99a, GNS02], we have developed a model that (nearly) quantitatively accounts for the energy gain upon adsorbing overcharging counterions [1] [MHK00b, MHK01b]. Our simple approach to the understanding of the overcharging via the Thomson problem, Wigner crystal concept and computer simulations has triggered a new interest in the community [Lev02, LA02, PPK03, MSB03] for the Thomson problem applied to soft matter.

We now consider the problem of a pair of macroions. In our paper [MHK00b], we show that two equally charged spheres are likely to be overcharged and under-

[1] To achieve overcharging in nature one should normally add salt to the system to ensure global electroneurality. For the sake of simplicity, however, we will consider non-neutral systems because they can on a very simple basis explain why colloids prefer to be overcharged.

charged in the strong Coulomb coupling regime leading to a metastable *ionized state* that yields a strong long-ranged attraction due to a *monopolar* contribution. (All the mechanisms, so far reported in the literature, can only explain *short-ranged* like-charge attraction [GJBP98, ADL98, LL99, NO99, SR90, LLP00, GJMBG97, HL97, Shk99b, KL99, ASL99, NAHN04, OJLC06] .) To further rationalize this phenomenon and the stability of ionized states [MHK00a, MHK01b], we have considered two charged spheres (of same radius a) carrying the same electric sign of charge but characterized by a charge ratio ρ_Z such that $0 < \rho_Z \equiv Z_B/Z_A \leq 1$. Starting from a macroion pair where each macroion is neutralized by its counterions, we investigate the process where a counterion is transfered from macroion B (low bare charge) to macroion A (high bare charge). Having demonstrated that the ability of a macroion to get overcharged increases with growing (bare) surface charge density (or the bare charge at fixed radius), it is clear that this counterion-transfer process will be energetically favorable below a certain value of ρ_Z. Our theoretical prediction shows that the criterion for stable ionized states (latter also called by other authors auto-ionization) is governed by the value of $\sqrt{Z_A} - \sqrt{Z_B}$, which reflects the correlation-hole energy difference between the two macroions. In particular, it was demonstrated that the higher the charge-asymmetry (i.e., ρ_Z) the more stable the ionized state and concomitantly the higher the degree of ionization.

Our main findings related to this work [MHK00b, MHK00a, MHK01b], (see also Appendices A, B, C) can be summarized as follows:

- The ground state of a charged sphere is always overcharged due to counterion correlations.
- At finite temperature and in the strong Coulomb regime (accessible with multivalent *aqueous* ions), colloids having different bare surface charge density auto-ionize due to counterion correlations.

2.2 Discretely charged surfaces

The structural (i.e., bare) charge of spherical macroions is usually modeled by a *central* charge, which, by virtue of the Gauss' law, is equivalent to a *uniformly* charged macroion's surface as far as the electrostatic field (or potential) *outside* the sphere is concerned. However, in nature the charges on the colloidal surface are *discrete* (exactly as the counterions are) and localized. Thus, a natural question that comes up is: *Why* and *how* does the strength of overcharging and more generally counterion-counterion correlations depend on the way the macroion structural charge is represented (i.e., uniformly charged or discrete charges on its surface)? It is precisely this problem that was addressed in our publications [MHK01a, Mes02b].

Why is the counterion distribution sensitive to the choice of the representation of the macroion charge (discrete vs. uniform)? This question can be best answered by looking at and comparing the (intrinsic) electrostatic potentials generated by discretely and uniformly charged macroions (without counterions) [MHK01a]. It was demonstrated in Ref. [MHK01a] that the electrostatic potential at a reduced distance r/a from the sphere (where a stands for the distance of closest approach between an external unit test-charge and the macroion surface) may be significantly different according to the nature of the macroion charge. In particular we show that the higher the bare surface charge (i.e., the closer we get from a uniform charge distribution) the shorter the correlation length (typically $r_c \sim \sqrt{1/\sigma_0}$, with σ_0 being the macroion's surface charge density) between the discrete surface charges, as intuitively expected. Besides, at contact $r = a$, the difference of the calculated electrostatic potentials between discrete and uniform charge distributions is considerable. To be more specific, the contact potential is sensitive to the localization of the discrete charges, leading to pronounced depth in their vicinity. All those features, solely based on the spatial behavior of the electrostatic potential stemming from the bare macroion, indicate that the counterion distribution should be much more complicated for a discrete macroion's surface charge distribution than for the uniform case.

We now come to the other important question: *How* is the counterion distribution modified when introducing the more realistic discrete macroion's surface charge distribution? This point is thoroughly addressed in [Mes02b], where two regimes are considered: Ground state ($T = 0$) and finite temperatures. The corresponding relevant findings (see also Appendices D, E) can be summed up as follows:

- At zero temperature, the counterion (surface) structure is the more ordered the higher σ_0 and/or counterion valence Z_c.
- When overcharging comes into play several scenarios occur: (i) At large σ_0, the overcharging is quasi the same as that obtained at a uniformly charged macroion's surface. (ii) At low σ_0 and for *monovalent* counterions, overcharging is always weaker for discrete macroion charge distribution, due to the ion-pairing frustration for the overcharging counterions. (iii) At low σ_0 and for *highly multivalent* counterions, overcharging can even be stronger in the discrete case due to ion-pairing.
- At finite temperature (in aqueous solutions), the volume counterion distribution is only affected for low σ_0 and multivalent counterions.

The effect of surface charge discretization was later examined for similar systems by several groups [MN02, LSLP02, ALHL03, HSPP04, TSYT05, QL05].

2.3 The crucial role of excluded volume

So far, we have a pretty good understanding of the overcharging caused by counterion correlations in the regime of strong Coulomb coupling in *salt-free* (or low salt content) where excluded volume effects are irrelevant. The situation becomes much more complicated at finite salt-concentration in aqueous solutions (i.e., water at room temperature), where the Coulomb coupling is (rather) weak especially for monovalent ions. Thereby, a direct application of Wigner crystal ideas is not straightforward to account for the unexpected overcharging at *weak* Coulomb coupling that was reported (by integral-equation and simulation [GTLCH85, DJAHLC01]), but unexplained, for *monovalent* salt-ions of large size.

In our Letter [MGLCH02] (see Appendix F), we perform molecular dynamics computer simulations as well as use integral-equation theory to *identify the mechanisms* that govern overcharging in this weak Coulomb coupling regime. Those mechanisms are as follows:

- Increasing the electrolyte particle *size* (at given salt concentration) decreases the available volume of the fluid (or equivalently its entropy) which *favors ion-ion correlations*.
- The interface provided by the macroion causes an increase of the ion density close to it, and concomitantly enhances the *lateral ordering* (similar to the prefreezing phenomenon in *neutral* inhomogeneous fluids).
- Surface lateral ordering and weak Coulomb coupling lead to overcharging.

2.4 Image charges in spherical geometry

In a typical experimental setup, the dielectric constant of a macroion is rather low ($\varepsilon_m \approx 2-5$) which is much smaller than that of its embedding solvent (e. g., for water $\varepsilon_w \approx 80$) leading to a *high dielectric contrast*, $\Delta_\varepsilon \equiv \frac{\varepsilon_w - \varepsilon_m}{\varepsilon_w + \varepsilon_m}$, at the interface. The (practical) consequence of this dielectric discontinuity is that a solute ion will then induce surface polarization charges whose strength and sign are dictated by the value of Δ_ε. Hence the electrostatic interactions for an electrolyte at finite Δ_ε is much more complicated compared to the case where $\Delta_\varepsilon = 0$, since now the contribution of the induced surface charges (whose distribution may be very complicated) at the interface must be taken into account. It turns out that for perfect *planar* substrates (that can be seen as a colloid of vanishing curvature), there is an elegant analytical solution: The electric field generated by the induced surface charge at the interface

positioned at $z = 0$ (due to the presence of a point-like ion of charge q located at $z = b$) can be exactly obtained by a "fictive" point-like charge $q_{im} = \Delta_\varepsilon q$ located at $z = -b$ [Jac75]. This technique corresponds to the so-called method of *image charges*. The inclusion of such image forces for the case of an electrolyte close to a planar dielectric interface was studied in the past by computer simulations [TVP82, TVO84, BJW86, MN02], integral equation formalisms [KM84, KM85], mean-field [OB83, Net99, vGM00] and strong-coupling theories [MN02].

The problem of image forces in *spherical* geometry is, already at the level of a single ion, more complex. If we want to think in terms of image charges, one would need in that case an *infinite* number of image charges making the use of the image charge method much less attractive than in the planar case. Due to this difficulty, the problem of image charges in spherical geometry is sparsely studied in soft matter. Nonetheless, twenty years ago, Linse studied the counterion distribution with image forces around spherical charged micelles by means of Monte Carlo simulations [Lin86]. In his work [Lin86], he used a *two-image* charge approximation instead of the full continuous image charge distribution. The conclusions of his study remain qualitatively correct.

In my work [Mes02a] (see Appendix G), I study analytically and exactly the electrostatics of an ion interacting with a dielectric sphere. Furthermore, I performed Monte Carlo simulations to elucidate the behavior of an electrolyte near a spherical macroion at finite dielectric contrast, where image forces are properly taken into account. My main results are as follows:

- *Single ion*: A compact and exact analytical expression has been derived for the polar profile of the induced surface charge. The *strength* as well as the *range* of image forces in spherical geometry are considerably smaller than at vanishing curvature, due to the *auto-screening*.
- *Electrolyte*: For monovalent ions the (effective) image force is basically equal to the *self-image* one. However, when dealing with multivalent counterions, the *lateral* image-counterions correlations can significantly affect the (local) counterion density and, as a major effect, they *screen* the self-image repulsion. Upon adding salt, it was shown that the strength of the image forces induced by the *coions* is marginal. Besides, overcharging is robust against image forces.

Chapter 3

POLYELECTROLYTE ADSORPTION AND MULTILAYERS

Polyelectrolytes (PEs) are polymers containing a variable (usually large) amount of ionizable monomer along the chemical backbone. Once dissolved in a suitable polar solvent such as water, the ion pairs dissociate by creating a charged chain with floating counterions. PEs represent a broad and interesting class of materials that attract an increasing attention in the scientific community. PEs have applications in modern technology as well as biology, since virtually all proteins, as well as DNA, are charged. The adsorption of PEs onto surfaces is an important process, since they modify the physico-chemical properties of the surface. From a theoretical point of view, charged polymers (in bulk or adsorbed) are much less understood [BJ96, Joa01] than neutral ones [dG79]. One of the main difficulties is the addition of new length scales set by the tremendous long-ranged Coulomb interaction. Hence, the study of adsorption of PEs is motivated by fundamental aspects as well as practical ones.

Over the last years, I have studied PE adsorption essentially by means of computer simulations. Probably, one of the most exciting research work that I performed in this field concerns the study of PE multilayers [MHK03, Mes03, Mes04b]. We wrote a short overview [MHK04] (see Appendix H) on "*Polyelectrolyte Adsorption and Multilayering on Charged Colloidal Particles*" emphasizing theoretical and computer simulation results. I now briefly describe my contribution to this research area.

3.1 Polyelectrolyte-colloid complexation

The complexation of flexible PEs with oppositely charged macroions is a relevant process in biology [Sch03]. For instance a nucleosome can be seen as an electrostatic binding between DNA and histone proteins. The latter can be visioned as charged spheres. We are aware that this assumption is at best a caricature of a real system (provided that non-specific interactions are dominant). Nonetheless, from an electrostatic viewpoint, we think that the qualitative features should be captured. Whereas many studies were devoted for the case of chain-sphere complexation where the two charged bodies are oppositely charged (see [Sch03] and references therein), much less is known concerning the problem of *like-charge sphere-PE complexation*.

In [MHK02a, MHK02b], we discuss the complexation between a sphere and a long flexible PE (*both negatively charged*). Whereas like-charge attraction in the strong coupling limit is expected (and therefore complexation too), new and rather unexpected chain conformations are reported. Different coupling regimes as well as the influence of the linear charge density, f, of the PE chain were considered in [MHK02b] (see Appendix I). The relevant conclusions are as follows:

- At strong coupling the PE chain is always adsorbed in a *flat* structure, whose conformation strongly depends on f. At high f, the conformation consists of a densely packed monomers following a Hamiltonian-walk. Upon reducing f the chain tends to spread more and more over the particle surface. Those findings could have some relevance for organic solutions.
- Under *aqueous* conditions, complexation can be obtained with multivalent counterions and for high enough values of f. In contrast to the strong coupling case, the formation of *loops* is reported.

3.2 Polyelectrolyte adsorption at planar surfaces

The adsorption of highly charged polyelectrolytes onto oppositely charged *planar* surfaces in a salt-free environment was investigated by means of Monte Carlo simulations. Flexible [Mes04a, Mes06b] (see Appendix J) as well as rod-like [Mes06a] (i. e., rigid - see Appendix K) PEs are considered. Having well understood and analyzed the problem of image charges in spherical geometry [Mes02a], I decided to elucidate the problem of dielectric discontinuity to the case of PE adsorption onto planar surfaces.

3.2.1 Flexible chains

When *no* image forces are present (i.e., $\Delta_\varepsilon = 0$), it was found that the monomer density profile, $n(z)$, decays monotonically for very short chains even near contact. Longer chains experience a short-ranged repulsion in the vicinity of the charged wall ($z \lesssim a$, with a denoting the diameter of a monomer) due to *chain-entropy* effects. In all investigated cases, the density-contact-value seems to be nearly independent of the chain length N_m and it is surprisingly close to the (exact) value obtained for systems containing only counterions of the charged interface [$n(z = a/2) = 2\pi l_B \sigma_0^2$, with l_B representing the Bjerrum length, i.e., the distance at which two monovalent ions feel a repulsion of magnitude $k_B T$]. This feature can be qualitatively understood by saying that near the interface, (nearly) all the little counterions were replaced by the monomers and the entropy of the latter is similar to that of the free surface counterions.

When *image forces* come into play, (partial) monomer desorption sets in, whose strength increases with growing chain length N_m. This feature is due to the repulsive image-chain force that scales like N_m^2, whereas the attractive chain-interface one scales like N_m.

The fraction of charge $\sigma^*(z)$ of the fluid as a function of monomer-wall separation, z, is another interesting quantity to characterize the adsorption behavior. At $\Delta_\varepsilon = 0$, overcharging [as signaled by $\sigma^*(z) > 1$] occurs as soon as chains are longer than dimers. In the presence of image forces, the strength of the overcharging is presently nearly identical to that obtained without image forces at $\Delta_\varepsilon = 0$. Thereby, the main effect of image charges is (i) to decrease the fraction of charge $\sigma^*(z)$ near contact ($z \lesssim 1.2a$) upon growing N_m and (ii) to (slightly) shift the position of the maximum of $\sigma^*(z)$ to larger z.

3.2.2 Rigid chains

Dimers exhibit a monotonic behavior for $n(z)$ that is similar to point-like ions. For longer chains there exits a small monomer depletion near the charged wall for an *intermediate* regime of N_m. At high enough N_m, $n(z)$ reveals again a monotonic behavior. This interesting effect is the result of two antagonistic *entropy*-driving forces, namely, (i) chain-entropy and (ii) counterion release. Electrostatic chain-chain correlations, whose strength grows in a non-trivial way with N_m, favor also chain adsorption. A comparison to the case of flexible chains [Mes04a] shows that the adsorption of rigid PEs is much stronger than that of flexible ones.

Upon polarizing the interface, it is found that the degree of adsorption is considerably reduced. Nonetheless, a comparison with the flexible case [Mes06b] shows that the values at contact at finite Δ_ε are quite similar.

3.2.3 Summary

The adsorption behavior of *flexible* and *rigid* PEs was addressed using computer Monte Carlo simulations. The influence of chain length and repulsive image forces were systematically investigated. My main findings can be summarized as follows:

- Without dielectric discontinuity ($\Delta_\varepsilon = 0$), *flexible* PE chains experience short-ranged repulsion near the charged substrate due to chain-entropy effects. In contrast, *rigid* PE chains are more strongly adsorbed (due to a weaker loss of chain-entropy) and, when long enough, experience a purely effective attraction.
- Image forces lower the degree of adsorption for flexible and rigid PE chains. However, the overcharging of the substrate by the PEs is robust (irrespectively to the chain flexibility) against image forces.

3.3 Polyelectrolyte multilayers at planar and spherical substrates

PE multilayer thin films are often obtained using a so-called layer-by-layer deposition technique [DHS92, Dec97]: A (say negatively) charged substrate is alternatively exposed to a polycation (PC) solution and a polyion (PA) one. This method and the resulting materials have a fantastic potential of application in technology, e. g., biosensing [CFA$^+$98], catalysis [OAK99], nonlinear optical devices [WYLR99], nanoparticle coating [CCM98], etc.

From the theoretical side the literature is rather poor. However, a few analytical works about PE multilayers on charged planar surfaces based on different levels of approximation are available [SdlC99, NJ99, CJ00]. Solis and Olvera de la Cruz considered the conditions under which the spontaneous formation of polyelectrolyte layered structures can be induced by a charged wall [SdlC99]. Based on Debye-Hückel approximations for the electrostatic interactions, but including some lateral correlations by the consideration of given adsorbed PE structures, Netz and Joanny[NJ99]

found a remarkable stability of the (semi-flexible) PE multilayers supported by scaling laws. For weakly charged flexible polyelectrolytes at high ionic strength qualitative agreements between theory [CJ00], also based on scaling laws, and experimental observations [LSV$^+$00] (such as the predicted thickness and net charge of the PE multilayer) were achieved.

A tremendous difficulty in PE multilayer is the strong electrostatic correlations between PCs and PAs, which are hard to be satisfactorily taken into account in (modified) mean-field theories. In this respect, computer simulations are of great help. In my work I have addressed those PE multilayer structures by means of Monte Carlo computer simulations [MHK03, Mes03, Mes04b]. I hereby outline our findings for spherical [MHK03] and planar substrates [Mes04b].

3.3.1 Spherical substrates

From this study [MHK03] (see Appendix L) that concerns substrates with finite radii (i. e., charged spheres), we have learned that *non-electrostatic* forces are required to obtain (true) PE multilayers. More precisely, by introducing a (additional) *short-range* van der Waals-like attraction (whose strength is characterized by its value at contact, χ_{vdw}, in units of k_BT) between the substrate's surface and the (monomers of the) oppositely charged chains. The PE structure results then from a complicated interplay between: (i) PC-PA strong attraction (favoring a collapse into a compact globular state) (ii) PE-substrate correlations (favoring *flat* adsorption and *wrapping* [1] around the sphere). Briefly, our findings are as follows:

- Flat *bilayer*-structures, involving two long oppositely charged chains, set in only for large enough χ_{vdw}. At low χ_{vdw}, the strong driving PA-PC force leads to PE globular structures.
- Stable and flat multilayers are only obtainable at large enough χ_{vdw}. In a purely electrostatic regime ($\chi_{vdw} = 0$) PE globules are formed preventing a uniform coverage of the surface.
- Short chains are not suitable candidates for PE multilayers, due to the weaker chain-substrate correlations.

[1] Note that the wrapping from the chain(s) around the colloid is peculiar to spherical substrates. Besides it should be reminded that wrapping is also governed by the repulsive interaction between the turns of a chain [GNS02].

3.3.2 Planar substrates

PE multilayering onto planar substrates were investigated in [Mes04b] (see Appendix M). The zero-curvature case differs qualitatively from the spherical one. First the intrinsic electric field is higher in the former case[2]. Secondly the chain-wrapping is no-longer present at zero curvature. Consequently at given surface charge density, we expect a stronger PE-layering. The important results can be formulated as follows:

- Like for spherical substrates, the relevance of short-ranged non-electrostatic forces was also demonstrated here. Flat multilayers can not be achieved with solely electrostatic forces.
- The formation of islands (i.e., clusters of PC-PA chains) onto the substrate are reported and qualitatively confirm the experimental observations in the early stage of PE deposition (one or two bilayers) [MJCP03, HB00].

[2] At zero curvature we have $V \sim r$ in contrast to finite curvature where $V \sim 1/r$

Chapter 4

CONFINED CHARGED COLLOIDS

It is well known from solid state studies that strongly confined (i.e., quasi two-dimensional) systems exhibit properties and a phase behavior that may drastically differ from those in the bulk. This feature is also vivid in colloidal systems and those materials represent ideal model systems to analyze (experimentally as well as theoretically) and understand confinement effects on a mesoscopic scale corresponding to the interparticle distance. Using external fields, a colloidal system can be prepared in a controlled way into prescribed equilibrium and non-equilibrium states [Löw01]. For instance, in equilibrium, solidification near interfaces (provided by a substrate or a large "impurity") can occur under thermodynamic conditions where the bulk is still fluid (so-called prefreezing). In non-equilibrium, a wall may act as a center of heterogeneous nucleation (favored by the excess surface-energy already offered by the wall/nucleus interface) and initiate crystal growth. Most of our experimental knowledge of freezing in confining slit-like geometry is based on real-space measurements of mesoscopic model systems such as charged colloidal suspensions between glass plates [MSW90, NBLP97].

The effective interaction between these mesoscopic macroions is neither hard-sphere like nor purely Coulombic, but it is rather described by an intermediate screened Coulomb [also called Yukawa or DLVO (Derjaguin-Landau-Verwey-Overbeek) [DL41, VO48]] due to the screening mediated by the additional microions present in the system. The screening strength can be tuned by varying the microion concentration: For colloidal systems, salt ions can be conveniently added to the aqueous suspension; The complex plasma, on the other hand, consists of electrons and impurity ions.

Recently, we have investigated crystalline colloidal bilayers at equilibrium [ML03, BSK$^+$05] and out of equilibrium under shear [ML06, LMH$^+$05]. Our research achievement in this field is outlined below.

4.1 Phase diagram of crystalline colloidal bilayers

The *equilibrium* phase diagram at zero temperature of crystalline bilayers was investigated theoretically in [ML03] (see Appendix N). The constitutive particles interact via a Yukawa pair potential of the form $V(r) = V_0 \frac{\exp(-\kappa r)}{\kappa r}$, where κ represents the screening strength and V_0 sets the energy scale.[1] The choice of this potential is motivated by the experimental model systems described above. The crystalline bilayer consists of two (identical) layers containing in total N particles in the (x,y) plane. The corresponding (total) surface density ρ is then given by N/A, with A being the the (macroscopic) layer area. The distance D, separating the two layers. in the z-direction is prescribed by an external confining the system.

The zero-temperature phase behavior is fully determined by two dimensionless parameters, namely the reduced layer density, $\eta = \rho D^2/2$, and the reduced screening strength, $\lambda = \kappa D$. Using a straightforward lattice sum technique, the phase diagram was calculated for arbitrary λ and η.[2] Our most interesting findings [ML03] are as follows:

- Whereas the two known extreme limits of zero [SSP99b, SSP99a, GP98] and infinite [PSP83, SL96, SL97] screening strength λ are recovered by our calculations, it is demonstrated that, at intermediate λ, the phase behavior is strikingly different from a simple interpolation between these two limits. First, there is a first-order coexistence between two different staggered rhombic lattices differing in their relative shift of the two unit cells. Second, one of these staggered rhombic phases exhibits a novel reentrant effect for fixed density and varied screening length. Depending on the density, the reentrant transition can proceed via a staggered square or a staggered triangular solid including even a *double reentrant transition* of the rhombic phase.

- In a joint publication [BSK$^+$05] with the Group of Palberg at Mainz, a comparative study on the phase behavior of highly charged colloidal spheres in a confined wedge geometry reveals semi-quantitative agreement between theory and experiment.

[1] Note that in the ground state, i.e. at rigorously zero temperature, the value of V_0 is irrelevant. Nonetheless in experimental situations, the energy amplitude $V_0 = Z^2 \frac{\exp(2\kappa R)}{\varepsilon(1+\kappa R)^2}$ scales like the square of the charge Z of the particles with a physical hard core radius R reduced by the dielectric constant ε of the solvent ($\varepsilon = 1$ for the dusty plasma). For a charged colloids, Z is typically of the order of $100 - 100\,000$ elementary charges such that $V(r = d)$ can be much larger than $k_B T$ at interparticle distance (d), justifying formally our zero-temperature calculations.

[2] Note that η must have an upper bound, such as to prevent the onset of *multi*layers.

4.2 Crystalline colloidal bilayers under shear flow

The *non-equilibrium* case[3] at finite temperature as driven by a linear shear flow has been addressed in [ML06, LMH$^+$05] (see also Appendix O). The steady state developed under shear as well as the relaxation back to equilibrium after cessation of shear were analyzed with the help of non-equilibrium Brownian dynamics. The pertinent results are:

- For increasing shear rates, the following steady states are reported: First, up to a threshold of the shear rate, there is a static solid which is elastically sheared. Then, at higher shear rates the crystalline bilayer melts, and even higher shear rates lead to a reentrant solid stratified in the shear direction.
- After instantaneous cessation of shear, a nonmonotonic behavior of the typical relaxation time is found. In particular, application of high shear rates accelerates the relaxation back to equilibrium since shear-induced ordering facilitates the growth of the equilibrium crystal.
- The orientation of a crystalline bilayer can be tuned at wish upon applying a (strong) shear rate in the desired direction and subsequently letting the system relax.

[3] The starting unsheared configuration corresponds to a staggered square lattice with a reduced surface particle density $\eta = 0.24$ and a reduced screening strength $\lambda = 2.5$. Two walls are present to ensure the confinement. To this end, screened Coulomb and short-ranged (of the Lennard-Jones type) repulsive potentials were tested, and it was found that our results are marginally sensitive to the choice of the repulsive wall-particle interaction.

Chapter 5

CONCLUSIONS

In this thesis, I have presented my humble point of view and understanding of electrostatic effects in soft matter. Charged systems are fascinating because they simultaneously involve short-ranged excluded volume effects (as soon as the latter are properly taken into account) already present in neutral systems, and additionally the long-ranged Coulomb interaction. The latter constitutes a formidable theoretical challenge.

In terms of similarities with classical solid state physics and (elementary) quantum chemistry, I noticed two striking analogies: (i) The overcharging occurring at a sphere is (rigorously) equivalent to the old Thomson's problem; (ii) The ground state of two spherical macroions is ionized, and the degree of ionization (and therefore the attraction strength) grows with the *difference in surface charge density* between the two macroions. This behavior is highly reminiscent to the (molecular) ionic bonding where the *difference in electronegativity* between the two atoms governs its stability.

Moreover, I investigated the problem of adsorption for many model systems involving substrates and adsorbate that are both charged. In particular, polyelectrolyte adsorption, polyelectrolyte multilayering, and more recently polyampholyte adsorption have been addressed. The inclusion of image forces for spherical and planar substrates has shown that their effect are only vivid at short range distances of the order of the linear size of the microions[1] (counterions and/or charged monomers).

An important problem in soft matter that still lacks a deep understanding is the behavior of charged spherical colloids near an oppositely charged wall. Indeed a sound analytical solution for the adsorption/desorption transition is still missing. I think that some (analytical) work could be done in this direction by means of mean-field theories that should be suitable for marginally adsorbed colloids. On a more

[1] The behavior might be less clear for highly charged spherical macroions as adsorbate.

"material-oriented" level, I think that the polyelectrolyte multilayer structures could also be obtained by combining oppositely charged colloids. To confirm this idea, a considerable theoretical effort would be needed to identify the parameters window (such as salt concentration, charges of the colloids and the substrates, particle size etc.) allowing the onset of such structures without strong clustering.

Bibliography

[ADL98] E. Allahyarov, I. D'Amico, and H. Löwen. Attraction between like-charged spheres. *Phys. Rev. Lett.*, 81:1334–1336, 1998.

[ALHL03] E. Allahyarov, H. Löwen, J. P. Hansen, and A. A. Louis. Nonmonotonic variation with salt concentration of the second virial coefficient in protein solutions. *Phys. Rev. E*, 67:051404, 2003.

[ASL99] J. J. Arenzon, J. F. Stilck, and Y. Levin. Simple model for attraction between like-charged polyions. *Europ. J. Phys. B*, 12:79–82, 1999.

[BDHM04] M. C. Barbosa, M. Deserno, C. Holm, and R. Messina. Screening of spherical colloids beyond mean field: A local density functional approach. *Phys. Rev. E*, 69:051401, 2004.

[BJ96] J.-L. Barrat and J.-F. Joanny. Theory of polyelectrolyte solutions. *Adv. Chem. Phys.*, 94:1, 1996.

[BJW86] D. Bratko, B. Jönsson, and H. Wennerström. Electrical double layer interactions with image charges. *Chem. Phys. Lett.*, 128:449–454, 1986.

[BM77] L. Bonsall and A. A. Maradudin. Some static and dynamical properties of a two-dimensional Wigner crystal. *Phys. Rev. B*, 15:1959–1973, 1977.

[BS98] W. R. Bowen and A. O. Sharif. Long-range electrostatic attraction between like-charge spheres in a charged pore. *Nature*, 393:663–665, 1998.

[BSK+05] A. Barreira Fontecha, H. J. Schöpe, H. Köning, R. Messina T. Palberg, and H. Löwen. A comparative study on the phase behaviour of highly charged colloidal spheres in a confining wedge geometry. *J. Phys.: Condens. Matter*, 17:S2779–S2786, 2005.

[BVT06] W. Bu, D. Vaknin, and A. Travesset. How accurate is Poisson-Boltzmann theory for monovalent ions near highly charged interfaces? *Langmuir*, 22:5673–5681, 2006.

[CCM98] F. Caruso, R. A. Caruso, and H. Möhwald. Nanoengineering of inorganic and hybrid hollow spheres by collodal templating. *Science*, 282:1111–1114, 1998.

[CFA+98] F. Caruso, D. N. Furlong, K. Ariga, I. Ichinose, and T. Kunitake. Characterization of polyelectrolyte-protein multilayer films by atomic force microscopy, scanning electron microscopy, and Fourier transform infrared reflection-absorption spectroscopy. *Langmuir*, 14:4559–4565, 1998.

[Cha13] D. L. Chapman. A contribution to the theory of electrocapillarity. *Philos. Mag.*, 25:475–484, 1913.

[CJ00] M. Castelnovo and J. F. Joanny. Formation of polyelectrolyte multilayers. *Langmuir*, 16:7524–7532, 2000.

[Dec97] G. Decher. Fuzzy nanoassemblies: Towards layered polymeric multicomponents. *Science*, 277:1232–1237, 1997.

[dG79] P. G. de Gennes. *Scaling Concepts in Polymer Physics*. Cornell University Press, Ithaca, New York, 1979.

[DH23] P. Debye and E. Hückel. Zur theorie der Elektrolyte. I. Gefrierpunktserniedrigung und verwandte Erscheinungen. *Phys. Z*, 24:185–206, 1923.

[DHS92] G. Decher, J. D. Hong, and J. Schmitt. Buildup of ultrathin multilayer films by a self-assembly process. 3. Consecutively alternating adsorption of anionic and cationic polyelectrolytes on charged surfaces. *Thin Solid Films*, 210/211:831–835, 1992.

[DJAHLC01] M. Deserno, F. Jiménez-Ángeles, C. Holm, and M. Lozada-Cassou. Overcharging of DNA in the presence of salt: Theory and simulation. *J. Phys. Chem. B*, 105:10983–10991, 2001.

[DL41] B. V. Derjaguin and L. D. Landau. *Acta Physicochim. (USSR)*, 14:633–650, 1941.

[EML06] A. Esztermann, R. Messina, and H. Löwen. Localisation-delocalisation transition of electrolytes between micro-electrodes. *Europhys. Lett.*, 73:864–870, 2006.

[GC97] D. G. Grier and J. C. Crocker. Like-charge attractions in metastable colloidal crystallites. *Nature*, 385:230–355, 1997.

[GJBP98] N. Grønbech-Jensen, K. M. Beardmore, and P. Pincus. Interactions between charged spheres in divalent counterion solution. *Physica*, 261A:74–80, 1998.

[GJMBG97] N. Grønbech-Jensen, R. J. Mashl, R. F. Bruinsma, and W. M. Gelbart. Counterion-induced attraction between rigid polyelectrolytes. *Phys. Rev. Lett.*, 78:2477–2480, 1997.

[GNS02] A. Yu. Grosberg, T. T. Nguyen, and B. I. Shklovskii. The physics of charge inversion in chemical and biological systems. *Rev. Mod. Phys.*, 74:329–345, 2002.

[Gou10] G. L. Gouy. Sur la constitution de la charge électrique à la surface d'un électrolyte. *J. Phys. Radium*, 9:457–466, 1910.

[GP98] G. Goldoni and F. M. Peeters. Stability, dynamical properties, and melting of a classical bilayer Wigner crystal. *Phys. Rev. B*, 53:4591–4603, 1998.

[GTLCH85] E. González-Tovar, M. Lozada-Cassou, and D. Henderson. Hypernetted chain approximation for the distribution of ions around a cylindrical electrode. II. Numerical solution for a model cylindrical polyelectrolyte. *J. Chem. Phys.*, 83:361–370, 1985.

[HB00] J. J. Harris and M. L. Bruening. Electrochemical and in situ ellipsometric investigation of the permeability and stability of layered polyelectrolyte films. *Langmuir*, 16:2006–2013, 2000.

[HL97] B. Y. Ha and A. J. Liu. Counterion-mediated attraction between two like-charged rods. *Phys. Rev. Lett.*, 79:1289–1292, 1997.

[HM90] J. P. Hansen and I. McDonald. *Theory of Simple Liquids*. Academic, London, 1990.

[HSPP04] M. L. Henle, C. D. Santangelo, D. M. Patel, and P. A. Pincus. Distribution of counterions near discretely charged planes and rods. *Europhys. Lett.*, 66:284–290, 2004.

[Jac75] J. D. Jackson. *Classical Electrodynamics*. Wiley, New York, 1975.

[Joa01] J. F. Joanny. *Electrostatic Effects in Soft Matter and Biophysics*, volume 46, chapter Scaling description of charged polymers, page 149. Kluwer Academics Publishers, Netherlands, 2001.

[JWH80] B. Jönsson, H. Wennerstöm, and B. Halle. Ion distributions in lamellar liquid-crystals - A comparison between results from Monte-Carlo simulations and solution of the Poisson-Boltzmann equation. *J. Phys. Chem.*, 84:2179–2185, 1980.

[KL99] A. A. Kornyshev and S. Leikin. Electrostatic zipper motif for DNA aggregation. *Phys. Rev. Lett.*, 82:4138–4141, 1999.

[KM84] R. Kjellander and S. Marčelja. Correaltion and image charge effects in electric double layer. *Chem. Phys. Lett.*, 112:49–53, 1984.

[KM85] R. Kjellander and S. Marčelja. Inhomogeneous Coulomb fluids with image intercation between planar surfaces. I. *J. Chem. Phys.*, 82:2123–2135, 1985.

[LA02] Y. Levin and J. J. Arenzon. Why charges go to the surface: A generalized thompson problem. *Europhys. Lett.*, 63:415–418, 2002.

[Lev02] Y. Levin. Electrostatic correlations: from plasma to biology. *Rep. Prog. Phys.*, 65:1577–1632, 2002.

[LGB04] W. Lin, P. Galletto, and M. Borkovec. Charging and aggregation of latex particles by oppositely charged dendrimers. *Langmuir*, 20:7465–7473, 2004.

[Lin86] P. Linse. Image charge effects in spherical geometry with apllications to micellar systems. *J. Phys. Chem.*, 90:6821–6828, 1986.

[LL99] P. Linse and V. Lobaskin. Electrostatic attraction and phase separation in solutions of like-charged colloidal particles. *Phys. Rev. Lett.*, 83:4208–4211, 1999.

[LLP00] A. W. C. Lau, D. Levine, and P. Pincus. Novel electrostatic attraction from plasmon fluctuations. *Phys. Rev. Lett.*, 84:4116–4119, 2000.

[LMH$^+$05] H. Löwen, R. Messina, N. Hoffmann, C. N. Likos, C. Eisenmann, P. Keim, U. Gasser, G. Maret, R. Goldberg, and T. Palberg. Colloidal layers in magnetic fields and under shear flow. *J. Phys.: Condens. Matter*, 17:S3379–S3386, 2005.

[Löw01] H. Löwen. Colloidal soft matter under external control. *J. Phys.: Condens. Matter*, 13:R415–R432, 2001.

[LSLP02] D. B. Lukatsky, S. A. Safran, A. W. C. Lau, and P. Pincus. Enhanced counterion localization induced by surface charge modulation. *Europhys. Lett.*, 58:785–791, 2002.

[LSV+00] G. Ladam, P. Schaad, J. C. Voegel, P. Schaaf, G. Decher, and F. Cuisinier. In situ determination of the structural properties of initially deposited polyelectrolyte multilayers. *Langmuir*, 16:1249–1255, 2000.

[Mes02a] R. Messina. Image charges in spherical geometry: application to colloidal systems. *J. Chem. Phys.*, 117:11062–11074, 2002.

[Mes02b] R. Messina. Spherical colloids: effect of discrete macroion charge distribution and counterion valence. *Physica A*, 308:59–79, 2002.

[Mes03] R. Messina. Adsorption of oppositely charged polyelectrolytes onto a charged rod. *J. Chem. Phys.*, 119:8133–8139, 2003.

[Mes04a] R. Messina. Effect of image forces on polyelectrolyte adsorption at a charged surface. *Phys. Rev. E*, 70:051802, 2004.

[Mes04b] R. Messina. Polyelectrolyte multilayering on a charged planar surface. *Macromolecules*, 37:621–629, 2004.

[Mes06a] R. Messina. Behavior of rodlike polyelectrolytes near an oppositely charged surface. *J. Chem. Phys.*, 124:014705, 2006.

[Mes06b] R. Messina. Erratum: Effect of image forces on polyelectrolyte adsorption at a charged surface. *Phys. Rev. E*, 74:049906(E), 2006.

[MGLCH02] R. Messina, E. González-Tovar, M. Lozada-Cassou, and C. Holm. Overcharging: The crucial role of excluded volume. *Europhys. Lett.*, 60:383–389, 2002.

[MHK00a] R. Messina, C. Holm, and K. Kremer. Ground state of two unlike charged colloids: An anology with ionic bonding. *Europhys. Lett.*, 51:461–467, 2000.

[MHK00b] R. Messina, C. Holm, and K. Kremer. Strong attraction between charged spheres due to metastable ionized states. *Phys. Rev. Lett.*, 85:872–875, 2000.

[MHK01a] R. Messina, C. Holm, and K. Kremer. Effect of colloidal charge discretization in the primitive model. *Eur. Phys. J. E*, 4:363–370, 2001.

[MHK01b] R. Messina, C. Holm, and K. Kremer. Strong electrostatic interactions in spherical colloidal systems. *Phys. Rev. E*, 64:021405, 2001.

[MHK02a] R. Messina, C. Holm, and K. Kremer. Conformation of a polyelectrolyte complexed to a like-charged colloid. *Phys. Rev. E*, 65:041805, 2002.

[MHK02b] R. Messina, C. Holm, and K. Kremer. Like-charge colloid-polyelectrolyte complexation. *J. Chem. Phys.*, 117:2947–2960, 2002.

[MHK03] R. Messina, C. Holm, and K. Kremer. Polyelectrolyte multilayering on a charged sphere. *Langmuir*, 19:4473–4482, 2003.

[MHK04] R. Messina, C. Holm, and K. Kremer. Polyelectrolyte adsorption and multilayering on charged colloidal particles. *J. Polym. Science: Part B Polym. Phys.*, 42:3557–3570, 2004.

[MJCP03] J. L. Menchaca, B. Jachimska, F. Cuisinier, and E. Pérez. In situ surface structure study polyelectrolyte multilayers by liquid-cell AFM. *Colloids Surf. A*, 222:185–194, 2003.

[ML03] R. Messina and H. Löwen. Reentrant transitions in colloidal or dusty plasma bilayers. *Phys. Rev. Lett.*, 91:146101, 2003.

[ML06] R. Messina and H. Löwen. Confined colloidal bilayers under shear: Steady state and relaxation back to equilibrium. *Phys. Rev. E.*, 73:011405, 2006.

[MN02] A. G. Moreira and R. R. Netz. Counterions at charge-modulated substrates. *Europhys. Lett.*, 57:911–917, 2002.

[MSB03] A. Mukherjee, K. S. Schmitz, and L. B. Bhuiyan. Overcharging in macroions. effect of geometry/charge distribution. *Langmuir*, 19:9600–9612, 2003.

[MSW90] C. A. Murray, , W. O. Sprenger, and R. A. Wenk. Comparison of melting in three and two dimensions: Microscopy of colloidal spheres. *Phys. Rev. B*, 42:688–703, 1990.

[NAHN04] A. Naji, A. Arnold, C. Holm, and R. R. Netz. Attraction and unbinding of like-charged rods. *Europhys. Lett.*, 67:130–132, 2004.

[NBLP97] S. Neser, C. Bechinger, P. Leiderer, and T. Palberg. Finite-size effects on the closest packing of hard spheres. *Phys. Rev. Lett.*, 79–82:2348, 1997.

[Net99] R. R. Netz. Debye-Hückel theory for interfacial geometries. *Phys. Rev. E*, 60:3174–3182, 1999.

[NJ99] R. R. Netz and J. F. Joanny. Adsorption of semiflexible polyelectrolytes on charged planar surfaces: Charge compensation, charge reversal, and multilayer formation. *Macromolecules*, 32:9013–9025, 1999.

[NO99] R. R. Netz and H. Orland. Field theory for charged fluids and colloids. *Europhys. Lett.*, 45:726–732, 1999.

[OAK99] M. Onda, K. Ariga, and T. Kunitake. Activity and stability of glucose oxidase in molecular films assembled alternately with polyions. *Biosci. Bioeng.*, 87:69–75, 1999.

[OB83] C. W. Outhwaite and L. B. Bhuiyan. An improved Poisson-Boltzmann equation in electric double-layer theory. *J. Chem. Soc. Faraday Trans. II*, 79:707–718, 1983.

[OJLC06] G. Odriozola, F. Jiménez-Ángeles, and M. Lozada-Cassou. Effect of confinement on the interaction between two like-charged rods. *Phys. Rev. Lett.*, 97:018102, 2006.

[PPK03] M. Patra, M. Patriarca, and M. Karttunen. Stability of charge inversion, thomson problem, and application to electrophoresis. *Phys. Rev. E*, 67:031402, 2003.

[PSP83] P. Pieranski, L. Strzelecki, and B. Pansu. Thin colloidal crystals. *Phys. Rev. Lett.*, 50:900–903, 1983.

[QL05] K. Qamhieh and P. Linse. Effect of discrete macroion charge distributions in solutions of like-charged macroions. *J. Chem. Phys.*, 123:104901, 2005.

[RVMW00] M. Ruela Talingting, Ulrike Voigt, Petr Munk, and S. E. Webber. Observation of massive overcomepnsation in the complexation of sodium poly(styresulfonate) with cationivc polymer micelles. *Macromolecules*, 33:9612–9619, 2000.

[Sch03] H. Schiessel. The physics of chromatin. *J. Phys.: Condens. Matter*, 15:R699–R774, 2003.

[SdlC99] F. J. Solis and M. Olvera de la Cruz. Surface-induced layer formation in polyelectrolytes. *J. Chem. Phys.*, 110:11517–11522, 1999.

[Shk99a] B. I. Shklovskii. Screening of a macroion by multivalent ions: Correlation-induced inversion of charge. *Phys. Rev. E*, 60:5802–5810, 1999.

[Shk99b] B. I. Shklovskii. Wigner crystal model of counterion induced bundle formation of rodlike polyelectrolytes. *Phys. Rev. Lett.*, 82:3268–3271, 1999.

[SL96] M. Schmidt and H. Löwen. Freezing between two and three dimensions. *Phys. Rev. Lett.*, 76:4552–4555, 1996.

[SL97] M. Schmidt and H. Löwen. Phase diagram of hard spheres confined between two parallel plates. *Phys. Rev. E*, 55:7228–7241, 1997.

[SR90] M. J. Stevens and M. O. Robbins. Density functional theory of ionic screening: When do like charges attract? *Europhys. Lett.*, 12:81–86, 1990.

[SSP99a] I. V. Schweigert, V. A. Schweigert, and F. M. Peeters. Enhanced stability of the square lattice of a classical bilayer Wigner crystal. *Phys. Rev. B*, 60:14665–14674, 1999.

[SSP99b] I. V. Schweigert, V. A. Schweigert, and F. M. Peeters. Melting of the classical bilayer Wigner crystal: Influence of lattice symmetry. *Phys. Rev. Lett.*, 82:5293–5296, 1999.

[Tho04] J. J. Thomson. *Philos. Mag*, 7:237, 1904.

[TSYT05] P. Taboada-Serrano, S. Yiacoumi, and C. Tsouris. Behavior of mixtures of symmetric and asymmetric electrolytes near discretely charged planar surfaces: A monte carlo study. *J. Chem. Phys.*, 123:054703, 2005.

[TVO84] G. M Torrie, J. P. Valleau, and C. W. Outhwaite. Electrical double layers. VI. Image effects for divalent ions. *J. Chem. Phys.*, 81:6296–6300, 1984.

[TVP82] G. M Torrie, J. P. Valleau, and G. N. Patey. Electrical double layers. II. Monte Carlo and HNC studies of image effects. *J. Chem. Phys.*, 76:4615–4622, 1982.

[vGM00] H. H. von Grünberg and E. C. Mbamala. Colloidal suspensions at dielectric interfaces. *J. Phys. Condens. Matter*, 12:10349–10370, 2000.

[VO48] E. J. Verwey and J. T. G. Overbeek. *Theory of the stability of Lyophobic Colloids*. Elsevier, Amsterdam, 1948.

[WYLR99] A. Wu, D. Yoo, J. K. Lee, and M. F. Rubner. Solid-state light-emitting devices based on the tris-chelated ruthenium(ii) complex: 3. High efficiency devices via a layer-by-layer molecular-level blending approach. *J. Am. Chem. Soc.*, 121:4883–4891, 1999.

PART II:

PUBLICATIONS SELECTED FOR THE HABILITATION

A. R. Messina, C. Holm and K. Kremer
Strong attraction between charged spheres due to metastable ionized states
Phys. Rev. Lett. **85**, 872, (2000).

B. R. Messina, C. Holm and K. Kremer
Ground state of two unlike charged colloids: An analogy with ionic bonding
Europhys. Lett. **51**, 461, (2000).

C. R. Messina, C. Holm and K. Kremer
Strong electrostatic interactions in spherical colloidal systems
Phys. Rev. E **64**, 021405 (2001).

D. R. Messina, C. Holm and K. Kremer
Effect of colloidal charge discretization in the primitive model
Eur. Phys. J. E **4**, 363 (2001).

E. R. Messina
Spherical macroions: effect of discrete macroion charge distribution and counterion valence
Physica **A308**, 59 (2002).

F. R. Messina, E. G. Tovar, M. Lozada-Cassou, C. Holm
Overcharging: The crucial role of excluded volume
Europhys. Lett. **60**, 383 (2002).

G. R. Messina
Image charges in spherical geometry: Application to colloidal systems
J. Chem Phys. **117**, 11062 (2002).

H. R. Messina, C. Holm and K. Kremer
Polyelectrolyte adsorption and multilayering on charged colloidal particles
J. Pol. Sci. Part B Polym. Phys. **42** 3557 (2004).

I. R. Messina, C. Holm and K. Kremer
Like-charge colloid-polyelectrolyte complexation
J. Chem. Phys. **117** 2947 (2002).

J. R. Messina
Effect of image forces on polyelectrolyte adsorption at a charged surface
Phys. Rev. E **70** 051802 (2004); *ibid* Erratum **74** 049906(E) (2006).

K. R. Messina
Behavior of rodlike polyelectrolytes near an oppositely charged surface
J. Chem. Phys. **124** 014705 (2006).

L. R. Messina, C. Holm and K. Kremer
Polyelectrolyte multilayering on a charged sphere
Langmuir **19**, 4473 (2003).

M. R. Messina
Polyelectrolyte multilayering on a charged planar surface
Macromolecules **37** 621 (2004).

N. R. Messina and H. Löwen
Reentrant transitions in colloidal or dusty plasma bilayers
Phys. Rev. Lett. **91** 146101 (2003).

O. R. Messina and H. Löwen
Confined colloidal bilayers under shear: Steady state and relaxation back to equilibrium
Phys. Rev. E **73** 011405 (2006).

Appendix A

Strong attraction between charged spheres due to metastable ionized states

Strong Attraction between Charged Spheres due to Metastable Ionized States

René Messina, Christian Holm, and Kurt Kremer
Max-Planck-Institut für Polymerforschung, Ackermannweg 10, 55128, Mainz, Germany
(Received 12 January 2000)

We report a mechanism which can lead to long-range attractions between like-charged spherical macroions, stemming from the existence of metastable ionized states. We show that the ground state of a single highly charged colloid plus a few excess counterions is overcharged. For the case of two highly charged macroions in their neutralizing divalent counterion solution we demonstrate that, in the regime of strong Coulomb coupling, the counterion clouds are very likely to be unevenly distributed, leading to one overcharged and one undercharged macroion. This long-living metastable configuration in turn leads to a long-range Coulomb attraction.

PACS numbers: 82.70.Dd, 61.20.Ja

One of the great challenges in the theory of charged colloidal suspensions is the understanding of effective attractions between like-charged macroions that have recently been observed experimentally in confined systems [1,2], and for which no clear theoretical explanation is available. The usually employed mean field Derjaguin-Landau-Verwey-Overbeek theory [3,4] foresees purely repulsive electrostatic forces between like-charged macroions. However, with divalent counterions present, simulations (using a pair of macroions) find short-range attraction for a high macroion volume fraction in aqueous systems [5] or, at an extremely low dielectric constant, a Coulomb depletion force [6]. Recent simulations of similar systems in aqueous solutions also find attractive forces [7–9]. However all simulations have in common the fact that the observed attraction occurs only for very small distances away from the colloid surface (order of counterion size).

In this Letter we investigate highly charged macroions in *bulk* and present two important new results. The first concerns the ground state of an isolated macroion surrounded by excess counterions, where it is found that the first few overcharging counterions lower considerably the energy. As a second finding we demonstrate that, for two highly charged macroions separated by intermediate distances, thermal fluctuations are sufficient to distribute the counterions unevenly, leading to one overcharged and one undercharged macroion. This results in a long-range effective Coulomb attraction between the macroions.

Consider one or two spherical macroions of radius r_m and bare charge $Q = -Z_m e$ (where e is the elementary charge and $Z_m > 0$) within the framework of the primitive model [10] surrounded by an implicit solvent of relative dielectric permittivity ϵ_r. The small counterions with diameter σ and charge $+Z_c e$ are confined in a cubic box of length L, and the macroion(s) are held fixed. The colloid volume fraction f_m is defined as $N_m 4\pi r_m^3/3L^3$ (where N_m is the number of macroions). In the case of an isolated macroion, it is located at the center of the box, whereas, in the case of macroion pairs, they are placed symmetrically along the axis passing by the two centers of opposite faces.

The molecular dynamics method employed in this paper is similar to the one used by Kremer and Grest [11]. To simulate a constant temperature ensemble, the ions are coupled to a heat bath and their motion is governed by the Langevin equation: $m\frac{d^2}{dt^2}\vec{r}_i = -\vec{\nabla}V_{\text{tot}}(\vec{r}_i) - m\Gamma\frac{d}{dt}\vec{r}_i + \vec{f}_i(t)$, where m (chosen as unity) is the mass of the counterions, i is the ith counterion, V_{tot} is the total potential force made up of a Coulomb term and an excluded volume term, which are both pairwise additive, Γ is the friction coefficient, and $\vec{f}_i$ is a random force. These two last quantities are linked by the dissipation-fluctuation theorem $\langle \vec{f}_i(t) \cdot \vec{f}_j(t') \rangle = 6m\Gamma k_B T \delta_{ij}\delta(t - t')$. For the ground state simulations the random force was set to zero.

Excluded volume interactions are introduced via a pure short-range repulsive Lennard-Jones (LJ) potential given by $V_{\text{LJ}}(r) = 4\epsilon[(\frac{\sigma}{r-r_0})^{12} - (\frac{\sigma}{r-r_0})^6] + \epsilon$ for $r - r_0 < r_{\text{cut}}$, and 0 otherwise, where $r_0 = 0$ for the counterion-counterion interaction, $r_0 = 7\sigma$ for the macroion-counterion interaction, and r_{cut} $(= 2^{1/6}\sigma)$ is the cutoff radius. This leads to $r_m = 7.5\sigma$, whereas the closest center-center distance of the small ions to the macroion is therefore $a = 8\sigma$. The Coulomb potential between a Z_i and a Z_j valent ion at distance r, where i and j denote either macroion or counterion, is given by $V_{\text{Coul}}(r) = k_B T_0 l_B \frac{Z_i Z_j}{r}$, with the Bjerrum length $l_B = e^2/4\pi\epsilon_0\epsilon_r k_B T_0$, where ϵ_0 is the vacuum permittivity. To link this to experimental units and room temperature we denote $\epsilon = k_B T_0$ ($T_0 = 298$ K) and fix $\sigma = 3.57$ Å. We neglect hydrodynamical interactions and hydration effects. Being interested in strong Coulomb coupling we choose, for the rest of this paper, $\epsilon_r = 16$, corresponding to $l_B = 10\sigma$.

To study the possibility of overcharging a single macroion, we recall the Gillespie rule, also known as the valence-shell electron-pair repulsion theory [12]. From this, one knows that the ground state structure of two, three, and four electrons disposed on a hard sphere corresponds to simple geometrical situations, namely, a line (two electrons diametrically opposed), a triangle, and a tetrahedron, respectively. A straightforward calculation

 0031-9007/00/85(4)/872(4)$15.00

shows that, for a central charge of $+2e$, the maximally obtainable overcharging is $-2e$ (i.e., two electrons), being independent of macroion radius. The excess electrons gain more energy by assuming a topological favorable configuration than by escaping to infinity, by the simple reason of overcharge. We resort to simulations to elucidate this behavior for one colloid with a high central charge.

To quantify this phenomenon, we have considered three macroionic charge Z_m: 50, 90, and 180, corresponding to a surface charge density of one elementary charge per 180, 100, and 50 Å^2, respectively, and fixed $Z_c = 2$ for the rest of this Letter. We then add successively overcharging counterions (OC). The electrostatic energy as a function of the number of OC is displayed in Fig. 1. We note that the maximal (critical) acceptance of OC (4, 6, and 8) increases with the macroionic charge (50, 90, and 180, respectively). Furthermore, for a given number of OC, the gain in energy always increases with Z_m. Also, for a given macroionic charge, the gain in energy between two successive overcharged states decreases with the number of OC. Note that, at $T = 0$, the value ϵ_r acts only as a prefactor. It means that the *ground state structure* is dictated solely by topological rules (i.e., the counterions' arrangement around the sphere).

The resulting curve can be very simply explained by assuming that the energy ε per ion on the surface of a neutralized macroion depends linearly on the inverse distance between them, hence is proportional to $\sqrt{N}$ for fixed area, where N is the number of counterions on the surface. The energy gain $\Delta E_1 = (N + 1)\varepsilon(N + 1) - N\varepsilon(N)$ of the first OC is a pure surface correlation term. For the next OC, one needs to take into account the Coulomb repulsion $l_B Z_c^2/a$, leading to lowest order in $1/N$ for the energy gain of the nth OC:

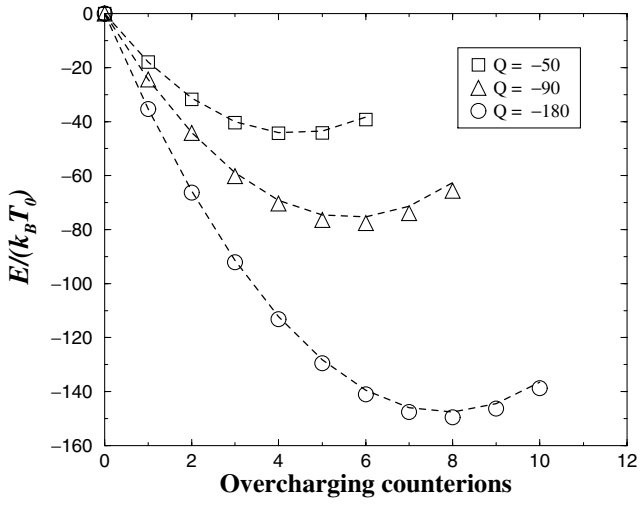

FIG. 1. Electrostatic energy (in units of $k_B T_0$) for *zero temperature* configurations of a single charged macroion of radius $r_m = 7.5\sigma$ as a function of the number of overcharging counterions for three different bare charges Q (in units of e). The neutral case was chosen as the potential energy origin, and the curves were produced using the theory of Eq. (2) (compare text).

$$\Delta E_n = n\epsilon(N)\left[\frac{3}{2} + \frac{3n}{8N}\right] + l_B Z_c^2 (k_B T_0)\,\frac{(n-1)n}{2a}. \tag{2}$$

Determining $\epsilon(N)$ from the measured value for ΔE_1, we obtain a curve that matches the simulation data almost perfectly (compare Fig. 1).

An energy per ion, which scales like $\sqrt{N}$, has been found for an ionic Wigner crystal (WC) on a planar surface, where each ion interacts with an oppositely charged background charge which is smeared out over its Wigner-Seitz cell. This energy per ion is given by $\varepsilon(c)/k_B T_0 = -\alpha c^{1/2} l_B Z_c^2$, with $\alpha = 1.96$, and c is the two-dimensional concentration of the crystallized counterions of valence Z_c [13]. This ansatz has been tried recently to explain strong ionic correlations observed in various soft matter systems [14,15]. In our simulation we find, for $\Delta E_1/(k_B T_0)$, -18.0, -24.4, and -35.3 for $Z_m = 50$, 90, and 180, respectively, whereas the Wigner crystal scenario predicts -21.0, -28.0, and -39.5, which is off by a decreasing rate of (17–12)%. This might be due to the assumption of a homogeneous background charge and the assumption of a planar geometry, neither of which are fully fulfilled; however, the error gets smaller for higher values of Z_m.

Using the Wigner crystal ionic energy and Eq. (2), the maximally obtainable number $n^*_{\max}$ of OC counterions is readily found to be

$$n^*_{\max} = \frac{1}{2} + \frac{9\alpha^2}{32\pi} + \frac{3\alpha}{4\sqrt{\pi}}\sqrt{N} + \left[\frac{3\alpha}{16\sqrt{\pi}} + \frac{27\alpha^3}{256\pi^{3/2}}\right]\frac{1}{\sqrt{N}} + \mathcal{O}(1/N). \tag{3}$$

This value depends only on the number of counterions N. It originates from the topological arrangement of the ions around a central charge, and is independent of the Bjerrum length or the radius of the macroion. For large Q it reduces to the form $Q^*_{\max}/e \approx \frac{3\alpha}{4\sqrt{\pi}} * \sqrt{Z_m Z_c}$ which was derived in Ref. [15] in a more elaborate fashion.

To obtain the interaction potential profile, we added one counterion coming from infinity towards a macroion of bare charge $Z_m = 180$ and computed the global electrostatic energy of the system (see Fig. 2). The first OC starts to gain correlational energy at a distance $r \approx 12\sigma$ from the center of the colloid, which is about 4σ from the surface. This fits only roughly with the distance $Z_c^2 l_B/4$ predicted from WC theory [14,15], and is more of the order $c^{-1/2}$. By adding more excess counterions, the Coulomb barrier increases, and for the ninth OC it exceeds the gain in correlational energy, when it is on the macroion surface. Thus the configuration becomes metastable. The curve for the *first* OC can be nicely fitted with an exponential fit of the form $E_1(r)/k_B T_0 = -35.3\exp[-7.1(r - a)/a]$. For the nth OC, simply the appropriate Coulomb monopole contribution $4l_B(n - 1)/r$ needs to be added (see Fig. 2). This exponential dependence is not predicted by the WC

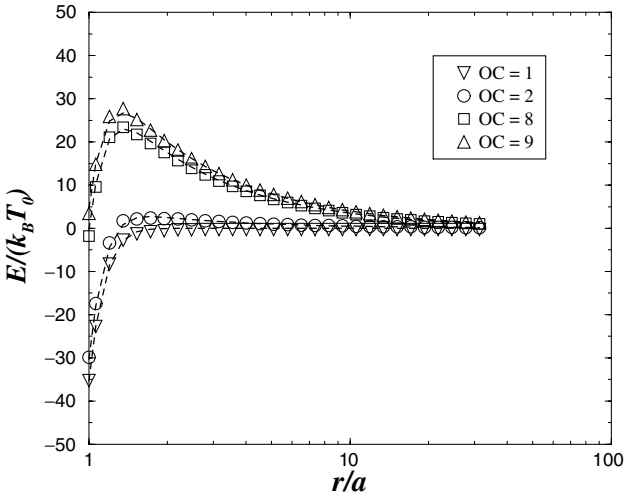

FIG. 2. Electrostatic energy (in units of k_BT_0) of a divalent counterion as a function of distance from the center of a macroion with radius $r_m = 7.5\sigma$ and charge $Q = -180$ (in units of e). The energy is normalized to zero at distance infinity. Data and fits are shown for the first, second, eighth, and ninth overcharging (OC) counterion.

theory, where a $1/r$ dependence should be seen due to the interaction of the removed ion with its correlation hole.

Next, we consider two spherical like-charged macroions at a colloidal volume fraction $f_m = 7 \times 10^{-3}$ at *room temperature* T_0, at fixed center-center separation R, in the presence of their divalent counterions (ensuring global charge neutrality). Initially the counterions are randomly generated. Figure 3 shows two macroions surrounded by their quasi-two-dimensional counterion layer. The striking peculiarity in this configuration is that it corresponds to an overcharged and an undercharged sphere. There is one counterion more on the left sphere and one less on the right sphere compared to the bare colloid charge. Such a configuration is referred to as an *ionized state*. In a total of ten typical runs, we observe this phenomenon five times. We have also carefully checked against a situation with periodic boundary conditions, yielding identical results. However, it is clear that such a state is in "pseudoequilibrium" because it is not the lowest energy state.

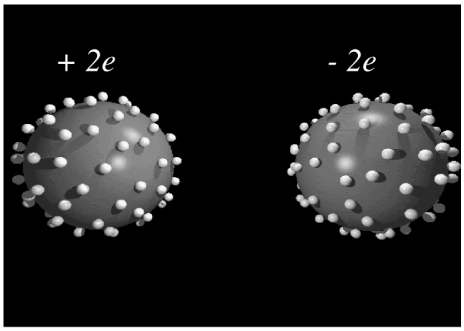

FIG. 3. Snapshot of a pseudoequilibrium configuration at room temperature T_0, where the counterion layers do not exactly compensate the macroions' charge. Here the deficiency charge is ± 1 counterion (or $\pm 2e$ as indicated above the macroions) and $R/a = 3.6$.

To estimate the energy barrier, electrostatic energy profiles at *zero temperature* were computed, where we move one counterion from the overcharged macroion to the undercharged macroion, restoring the neutral state (see Fig. 4). We have checked that the path leading to the lowest barrier of such a process corresponds to the line joining the two macroions' centers. One clearly observes a barrier, which increases linearly with the charge Z_m. The ground state corresponds, as expected, to the neutral state. The overcharged state is only slightly higher in energy, the difference being approximately the monopole contribution $E/k_BT_0 = l_B(4/8 - 4/12) \approx 1.67$. The physical origin of this barrier can be understood from the single macroion case, where we showed that a counterion gains high correlational energy near the surface. This gain is roughly equal for both macroion surfaces, and decreases rapidly with increasing distance from the surfaces, leading to the energy barrier with its maximum near the midpoint. For the single macroion case we showed that the correlational energy gain scales with $\sqrt{Z_m}$, whereas here we observe a linear behavior of the barrier height with Z_m. We attribute this effect to additional ionic correlations since both macroions are close enough for their surface ions to interact strongly. For large separations we find again that

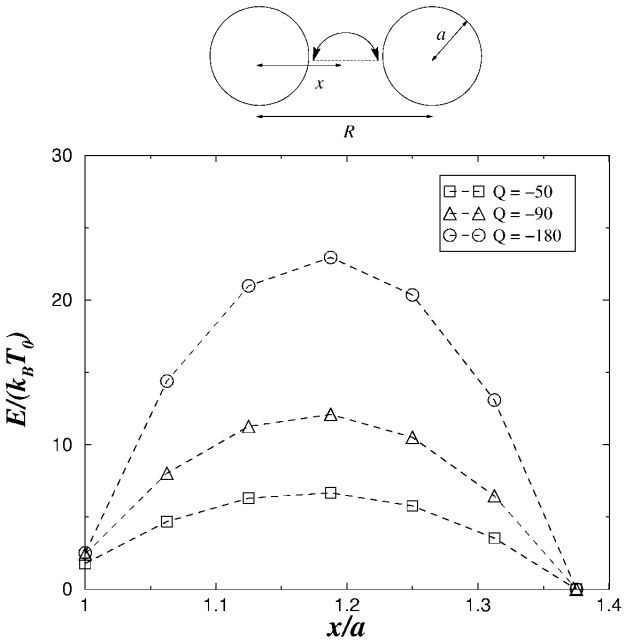

FIG. 4. Total electrostatic energy (in units of k_BT_0) of the system, for *zero temperature* configurations, of two macroions at a center-center separation of $R/a = 2.4$ as a function of one displaced counterion distance from the left macroion for three typical values Q (in units of e). The exact neutral state was chosen as the potential energy origin. The lines are guides to the eye. The inset indicates the path (dotted line) of the moved counterion. The ending arrows of the arc indicate the start position (left sphere) and final position (right sphere) of the moved counterion.

the barrier height increases with $\sqrt{Z_m}$, as expected. This Z_m dependence of the barrier also shows that at room temperature such ionized states can occur only for large Z_m. In our case, the ionized state was stable for all accessible computation times only for $Z_m = 180$. Unfortunately, it is not possible to get a satisfactory accuracy of the energy jumps at nonzero temperatures. Nevertheless, since we are interested in the strong Coulomb coupling regime, which is energy dominated, the zero temperature analysis is sufficient to capture the essential physics.

Results concerning the effective forces at *zero temperature* between the two macroions are now investigated in which the expression is given by

$$F_{\text{eff}}(R) = F_{mm}(R) + F_{\text{LJ}} + F_{mc}\,, \tag{4}$$

where $F_{mm}(R)$ is the direct Coulomb force between macroions, F_{LJ} is the excluded volume force between a given macroion and its surrounding counterions, and F_{mc} is the Coulomb force between a given macroion and all of the counterions. Because of symmetry, we focus on one macroion. To understand the extra-attraction effect of these ionizedlike states, we consider three cases: (i) $F_{\text{ion}} = F_{\text{eff}}$ in the ionized state, (ii) $F_{\text{neut}} = F_{\text{eff}}$ in the neutral case, and (iii) $F_{\text{mono}} = F_{\text{eff}}$ simply from the effective monopole contribution. Our results are displayed in Fig. 5 for $Z_m = 180$, where the ionized state was also observed at room temperature. The noncompensated case leads to a very important extra attraction. This becomes drastic for the charge asymmetry of ± 2 counterions at short separation $R/a \approx 2.5$, a situation which was also observed in our simulation at room temperature [16]. In contrast to previous studies [5,6], these attractions are long range. For a sufficiently large macroion separation (from 3.5) the effective force approaches in good approximation the monopole contribution.

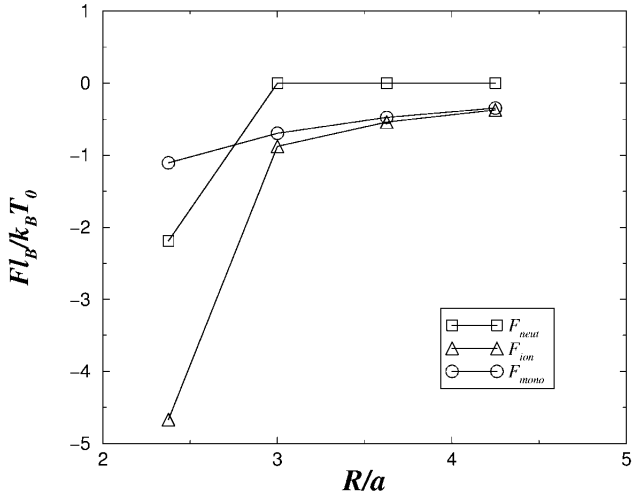

FIG. 5. Reduced effective force between the two spherical macroions at *zero temperature* for $Z_m = 180$ as a function of distance from the center. The different forces are explained in the text. The lines are guides to the eye.

In summary, we have shown that a sufficiently charged colloid can, in principle, be highly overcharged due to correlation effects of the counterions, and this effect is quantitatively well described by a Wigner crystal, i.e., Eqs. (2) and (3). In the strong Coulomb coupling regime, this energy gain can be of the order of many k_BT_0.

Furthermore, due to this energetically favorable overcharged state, it was found that for two like-charged macroions, an initially randomly placed counterion cloud of their neutralizing divalent counterions may not be equally distributed after relaxation, leading to two macroions of opposite net charges. The resulting configuration is metastable, however, and separated by an energy barrier of several k_BT_0 when the bare charge is sufficiently large. Such a configuration possesses a natural strong long-range attraction.

We acknowledge useful discussions with H. Löwen and M. Deserno. This work is supported by *Laboratoires Européens Associés* (LEA) and a computer time Grant hkf06 from NIC Jülich.

[1] G. M. Kepler and S. Fraden, Phys. Rev. Lett. **73**, 356 (1994).
[2] J. C. Crocker and D. G. Grier, Phys. Rev. Lett. **73**, 352 (1994); **77**, 1897 (1996); A. E. Larsen and D. G. Grier, Nature (London) **385**, 230 (1997).
[3] B. V. Derjaguin and L. D. Landau, Acta Physicochim. (USSR) **14**, 633 (1941).
[4] E. J. Verwey and J. T. G. Overbeek, *Theory of the Stability of Lyophobic Colloids* (Elsevier, Amsterdam, 1948).
[5] N. Grønbech-Jensen, K. M. Beardmore, and P. Pincus, Physica (Amsterdam) **261A**, 74 (1998).
[6] E. Allahyarov, I. D'Amico, and H. Löwen, Phys. Rev. Lett. **81**, 1334 (1998).
[7] E. Allahyarov, I. D'Amico, and H. Löwen, Phys. Rev. E **60**, 3199 (1999).
[8] J. Z. Wu, D. Bratko, H. W. Blanch, and J. M. Prausnitz, J. Chem. Phys. **111**, 7084 (1999).
[9] P. Linse and V. Lobaskin, Phys. Rev. Lett. **83**, 4208 (1999).
[10] T. L. Hill, *Statistical Mechanics* (Addison-Wesley, Reading, MA, 1960).
[11] K. Kremer and G. Grest, J. Chem. Phys. **92**, 5057 (1990).
[12] A theory that predicts molecular geometries by using the notion that valence electron pairs occupy sites around a central atom in such a way as to minimize electron-pair repulsion. See, for example, D. W. Oxtoby, H. P. Gillis, and N. H. Nachtrieb, *Principles of Modern Chemistry* (Saunders College Publishing, Fort Worth, TX, 1999), Chap. 3, p. 80.
[13] L. Bonsall and A. A. Maradudin, Phys. Rev. B **15**, 1959 (1977).
[14] I. Rouzina and V. A. Bloomfield, J. Phys. Chem. **100**, 9977 (1996); B. I. Shklovskii, Phys. Rev. Lett. **82**, 3268 (1999); V. I. Perel and B. I. Shklovskii, Physica (Amsterdam) **274A**, 446 (1999).
[15] B. I. Shklovskii, Phys. Rev. E **60**, 5802 (1999).
[16] R. Messina (unpublished).

Appendix B

Ground state of two unlike charged colloids: An analogy with ionic bonding

EUROPHYSICS LETTERS 15 August 2000

Europhys. Lett., **51** (4), pp. 461–467 (2000)

Ground state of two unlike charged colloids: An analogy with ionic bonding

R. Messina(*), C. Holm and K. Kremer

Max-Planck-Institut für Polymerforschung - Ackermannweg 10, 55128, Mainz, Germany

(received 4 April 2000; accepted in final form 22 June 2000)

PACS. 82.70.Dd – Colloids.
PACS. 61.20.Qg – Structure of associated liquids: electrolytes, molten salts, etc.
PACS. 41.20.-q – Applied classical electromagnetism.

Abstract. – In this letter, we study the ground state of two spherical macroions of identical radius, but asymmetric bare charge ($Q_A > Q_B$). Electroneutrality of the system is ensured by the presence of the surrounding divalent counterions. Using Molecular Dynamics simulations within the framework of the primitive model, we show that the ground state of such a system consists of an overcharged and an undercharged colloid. For a given macroion separation the stability of these ionized-like states is a function of the difference $(\sqrt{N_A} - \sqrt{N_B})$ of neutralizing counterions N_A and N_B. Furthermore the degree of ionization, or equivalently, the degree of overcharging, is also governed by the distance separation of the macroions. The natural analogy with ionic bonding is briefly discussed.

Charged colloids are found in a great variety of materials such as latex, clays, paints, and many biological systems, and thus have an important place in everyday life. To understand the complex interaction between charged colloids and their surrounding neutralizing counterions, a reasonable starting point is to study the elementary case of a pair of spherical macroions. From the theoretical side such a system is described by the Derjaguin-Landau-Verwey-Overbeek (DLVO) theory [1, 2] which leads to purely repulsive effective forces. More sophisticated modified Poisson-Boltzmann approaches based on density-functional theory [3] or inhomogeneous HNC techniques [4, 5] have been developed in order to incorporate the ion-ion correlations which are neglected in DLVO. Surprisingly recent experiments showed effective attractive forces between like-charged colloids [6–8] when they are confined near charged walls, and for which no clear theoretical explanation is available. This triggered reinvestigations of the pair-interactions in the bulk with computer simulations [9–13]. A common feature of all these studies is that they assume the two macroions identically charged. The results of refs. [9–12] show for high Coulomb coupling an attractive force in a range of the order of a few counterion radii. However, Messina *et al.* [13] have demonstrated that it is possible to get a strong long-range attraction between two like-charged colloids due to metastable ionized states. In particular it has been shown that the energy difference between the compensated bare charge case, where each colloid is exactly neutralized by the surrounding counterions, and the ionized state can be very small (less than 2 $k_{\mathrm{B}}T$).

(*) E-mail: messina@mpip-mainz-mpg.de

In this letter, we use molecular dynamics (MD) simulations to investigate the case where the colloidal radii are identical but the bare colloidal charges are different. It is found that in this asymmetric situation the ground state is no longer the intuitive bare charge compensated case, provided that the charge asymmetry is high enough and/or the colloid separation is not too large. We derive a simple formula valid for large separations which gives a sufficient condition for the bare charge asymmetry to produce a ground state consisting of an ionic pair leading to a natural long-range attractive force.

The system under consideration is made up of two spheres: i) macroions (A and B) of diameter d with bare charges $Q_A = -Z_A e$ (where e is the elementary charge and $Z_A = 180$ is *fixed*) for the highly charged sphere and $Q_B = -Z_B e$ (*variable*) for the less charged one and ii) a sufficient number of small counterions of diameter σ with charge $q = +Z_c e$ ($Z_c = 2$) to neutralize the whole system. The macroions center-center separation is given by R. The ions are confined in a cubic box of length L, and the two macroions are held fixed and disposed symmetrically along the axis passing by the two centers of opposite faces. The colloid volume fraction f_m is defined as $2 \cdot 4\pi(d/2)^3/3L^3$. For describing the charge asymmetry we define the quantity $\alpha = \sqrt{N_A} - \sqrt{N_B}$, where $N_A = -Q_A/q$, and $N_B = -Q_B/q$.

The motion of the counterions is coupled to a heat bath acting through a weak stochastic force $\boldsymbol{W}(t)$. The equation of motion of counterion i reads

$$m\frac{\mathrm{d}^2\boldsymbol{r}_i}{\mathrm{d}t^2} = -\nabla_i U - m\Gamma\frac{\mathrm{d}\boldsymbol{r}_i}{\mathrm{d}t} + \boldsymbol{W}_i(t)\,, \tag{1}$$

where m is the counterion mass, Γ is the friction coefficient, chosen here between 0.1 and 1.0, and U is the potential consisting of the Coulomb interaction and the excluded-volume interaction. Friction and stochastic force are linked by the fluctuation-dissipation theorem $\langle \boldsymbol{W}_i(t) \cdot \boldsymbol{W}_j(t')\rangle = 6m\Gamma k_\mathrm{B} T \delta_{ij}\delta(t-t')$. In the ground state $T = 0$ and thus the stochastic force vanishes.

Excluded-volume interactions are taken into account with a pure repulsive Lennard-Jones (LJ) potential given by

$$U_\mathrm{LJ}(r) = \begin{cases} 4\varepsilon\left[\left(\dfrac{\sigma}{r-r_0}\right)^{12} - \left(\dfrac{\sigma}{r-r_0}\right)^{6}\right] + \varepsilon\,, & \text{for} \quad r - r_0 < 2^{1/6}\sigma\,, \\ 0\,, & \text{for} \quad r - r_0 \geq 2^{1/6}\sigma\,, \end{cases} \tag{2}$$

where $r_0 = 0$ for the counterion-counterion interaction, $r_0 = 7\sigma$ for the macroion-counterion interaction, thus leading to a macroion diameter $d = 2r_0 + \sigma$ and electrostatically more important to a macroion-counterion distance of closest approach $a = 8\sigma$.

The pair electrostatic interaction between any pair ij, where i and j denote either a macroion or a counterion, reads

$$U_\mathrm{Coul}(r) = k_\mathrm{B} T_0 l_\mathrm{B} \frac{Z_i Z_j}{r}\,, \tag{3}$$

where $l_\mathrm{B} = e^2/4\pi\epsilon_0\epsilon_r k_\mathrm{B} T_0$ is the Bjerrum length describing the electrostatic strength. To link this to experimental units and room temperature, we denote $\varepsilon = k_\mathrm{B} T_0$ ($T_0 = 298\,\mathrm{K}$). Fixing $\sigma = 3.57$ Å would then lead to the Bjerrum length of water at room temperature (7.14 Å).

Being interested in the strong Coulomb coupling regime, we choose the relative permittivity $\epsilon_\mathrm{r} = 16$, corresponding to $l_\mathrm{B} = 10\sigma$.

The electrostatic energy of the system is investigated for different uncompensated bare charge cases [14] by simply summing up eq. (3) over all Coulomb pairs. Note that for the

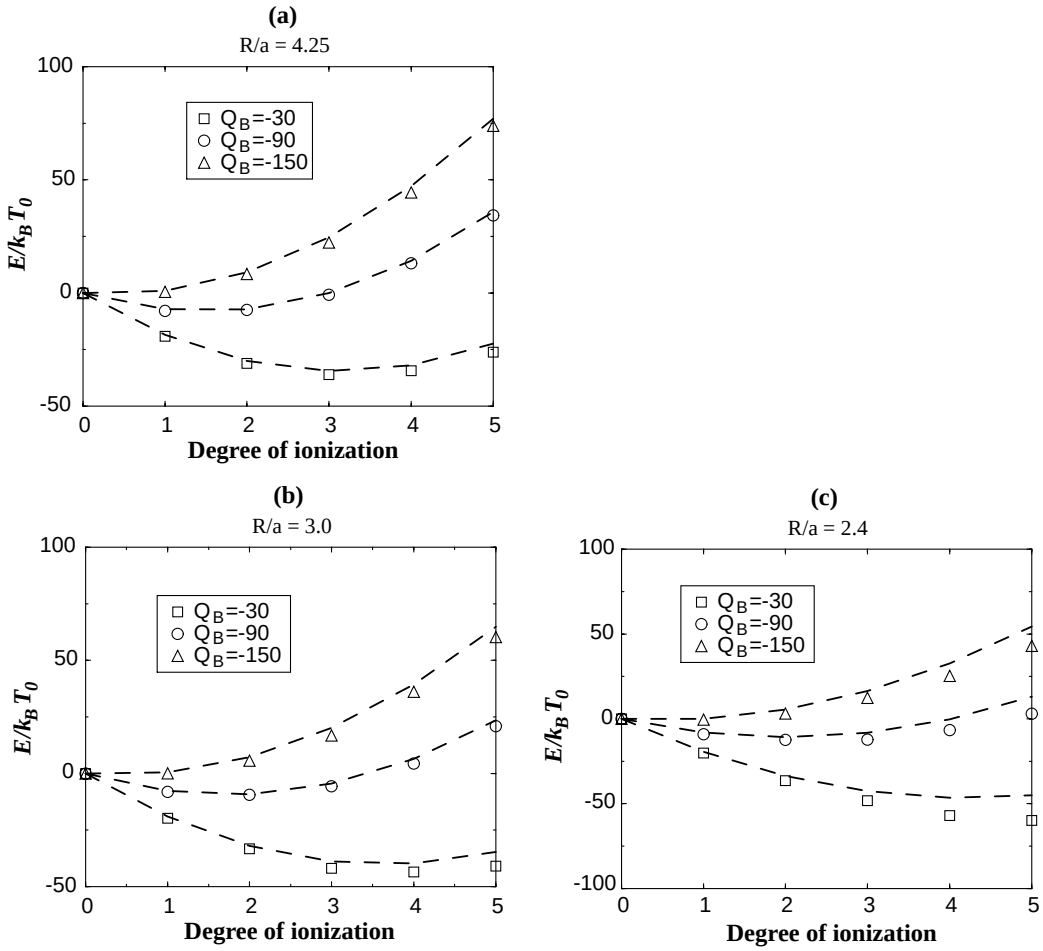

Fig. 1 – Total electrostatic energy as a function of the degree of ionization for zero-temperature configurations of two colloids (A and B), for three typical charges Q_B/e ($-30, -90$ and -150) for macroion B and for three given distance separations: a) $R/a = 4.25$, b) $R/a = 3.0$ and c) $R/a = 2.4$. Dashed lines are obtained using eq. (7).

zero-temperature ground-state study entropic effects are nonexistent. We define the *degree of ionization* (DI) as the number of counterions overcharging colloid A (or, equivalently, undercharging colloid B). The system is prepared in various DI and measure the respective energies. These states are separated by kinetic-energy barriers, as was demonstrated in ref. [13]. We consider three typical macroionic charges Z_B (30, 90 and 150) and separations R/a (2.4, 3.0 and 4.25). The main results are given in fig. 1. For the largest separation $R/a = 4.25$ and largest charge $Z_B = 150$ (see fig. 1a), one notices that the ground state corresponds to the classical compensated bare charge situation (referred to as the *neutral state*). Moreover the energy increases stronger than linear with the degree of ionization. If one diminishes the bare charge Z_B to 90 and 30, the *ground state* is actually the *ionized state* for a DI of 1 and 3, respectively. The ionized ground state is about 8 and 36 $k_{\mathrm{B}}T_0$, respectively, lower in energy compared to the neutral state. This shows that even for a relative large colloid separation, stable ionized states should exist for sufficient low temperatures and that their stability is conditioned by the structural charge asymmetry α.

For a shorter separation $R/a = 3.0$, ionized ground states are found (see fig. 1b) for the same charges Z_B as previously. Nevertheless, in the ground state the DI is now increased and it corresponds to 2 and 4 for $Z_B = 90$ and 30, respectively. The gain in energy is also

significantly enhanced. For the shortest separation under consideration $R/a = 2.4$, the ground state corresponds for *all* investigated values of Z_B to the ionized state, even for $Z_B = 150$. We conclude that decreasing the macroion separation R enhances the DI and the stability of the ionized state.

To understand this ionization phenomenon, it is sufficient to consider an *isolated* macroion surrounded by its neutralizing counterions. We have investigated the energies involved in the ionization (taking out counterions) and overcharging (adding counterions) processes. We show in ref. [13] how they can be separated into two parts: i) a pure correlational term ($\Delta E^{\rm cor}$) and ii) a monopole contribution ($\Delta E^{\rm mon}$), see also ref. [15] for the case of added salt. The main assumption is that the correlational energy per ion can be written as a pure surface term $\epsilon(N) = -\gamma\sqrt{N}$ (with $\gamma > 0$), as is predicted for example in a theory where the counterions on the surface of the colloids form a Wigner crystal (WC) [15, 16]. The gain in energy when adding the first counterion is simply a pure correlation term of the form

$$\Delta E_1^{\rm OC} = \Delta E_1^{\rm cor} = (N_A+1)\epsilon(N_A+1) - (N_A)\epsilon(N_A) = -\gamma\sqrt{N_A}\left[\frac{3}{2} + \frac{3}{8N_A} + \mathcal{O}(N_A^{-2})\right] . \quad (4)$$

Adding the summed up monopole contributions, one obtains the energy gained by adding the n-th counterion to leading order in $1/N_A$:

$$\Delta E_n^{\rm OC} = \Delta E^{\rm cor} + \Delta E^{\rm mon} = -n\gamma\sqrt{N_A}\left[\frac{3}{2} + \frac{3n}{8N_A}\right] + (k_{\rm B}T_0) l_{\rm B} Z_{\rm c}^2 \frac{(n-1)n}{2a} , \quad (5)$$

which has been verified to give a correct description when compared to simulations [13]. A derivation of the formula describing the ionization energy $\Delta E^{\rm ion}$ proceeds completely analogously and gives for the n-th degree of ionization

$$\Delta E_n^{\rm ion} = n\gamma\sqrt{N_B}\left[\frac{3}{2} - \frac{3n}{8N_B}\right] + (k_{\rm B}T_0) l_{\rm B} Z_{\rm c}^2 \frac{(n+1)n}{2a} . \quad (6)$$

In fig. 2 we compare the predictions of eqs. (5), (6) to our simulation data, which shows excellent agreement. Our numerical data for $\Delta E_1^{\rm ion}$ for $N_B = 15$, 45, and 75, the value of $\Delta E_1^{\rm OC}$ for $N_A = 90$, as well as the corresponding values for γ, which have been used for fig. 2 can be found in table I. They show that γ is almost independent of N. The value of γ can also be compared to the prediction of WC theory applied to an infinite plane which leads to the value $1.96 l_{\rm B} Z_{\rm c}^2 \sqrt{\frac{1}{F}} \approx 2.76$ [17], where F denotes the surface area of the colloid. The difference of 10% to WC theory is presumably related to the fact that we do not deal with purely planar correlations but have a finite spherical geometry.

TABLE I – *Measured value, for an* isolated *colloid, of the first ionization energy* $\Delta E_1^{\rm ion}$ *for* $N_B = 15, 45, 75$*, and the energy gain for the first overcharging counterion* $\Delta E_1^{\rm OC}$ *for* $N_A = 90$*. The value of* γ *can be compared to the prediction of WC theory for an infinite plane, which gives* 2.76*, compare text.*

Q/e	N	$\Delta E_1/k_{\rm B}T_0$	$\gamma/k_{\rm B}T_0$
− 30	15	17.9	2.26
− 90	45	29.2	2.42
−150	75	37.4	2.50
−180	90	−35.3	2.47

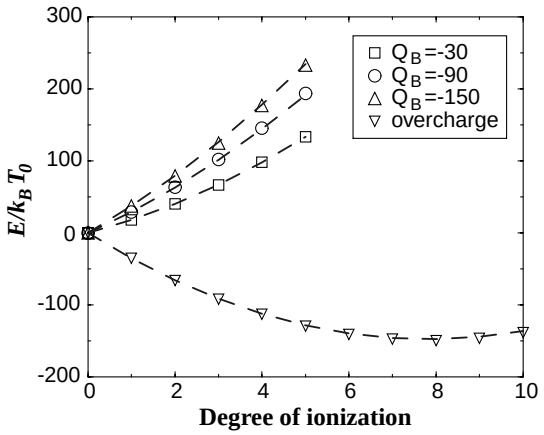

Fig. 2

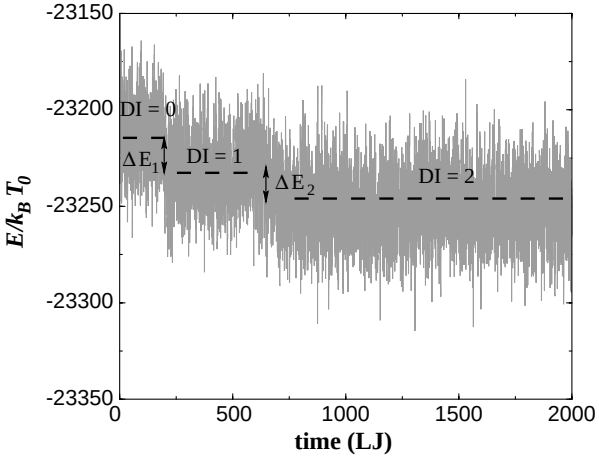

Fig. 3

Fig. 2 – Total electrostatic energy as a function of the degree of ionization for zero-temperature configurations of an *isolated* colloid. The three upper curves correspond to the ionization energy for the three typical charges Q_B/e ($-30, -90$ and -150). The lower curve corresponds to the energy gained by overcharging ($Q_A/e = -180$). Dashed lines were obtained using eqs. (5), (6) with the measured values for γ from table I.

Fig. 3 – Relaxation, at room temperature $T_0 = 298\,\mathrm{K}$, of an initial neutral state towards ionized state. Plotted is the total electrostatic energy *vs.* time (LJ units), for $Z_B = 30$ and $R/a = 2.4$. Dashed lines lines represent the mean energy for each DI state. Each jump in energy corresponds to a counterion transfer from the macroion B to macroion A leading to an ionized state (DI = 2) which is lower in energy than the neutral one. The two energy jumps $\Delta E_1/k_\mathrm{B}T_0 = -19.5$ and $\Delta E_2/k_\mathrm{B}T_0 = -17.4$ are in very good agreement with those of fig. 1c (-20.1 and -16.3).

With the help of eqs. (5), (6), one can try to predict the curves of fig. 1 for finite center-center separation R. Using for colloid A and B the measured values γ_A and γ_B, we obtain for the electrostatic energy difference at finite center-center separation R

$$\Delta E_n(R) \;=\; \Delta E_n^{\mathrm{ion}} + \Delta E_n^{\mathrm{OC}} = \frac{3}{2} n\gamma_B \sqrt{N_B}\left[1 - \frac{n}{4N_B}\right] - \\ -\frac{3}{2} n\gamma_A \sqrt{N_A}\left[1 + \frac{n}{4N_A}\right] + k_\mathrm{B}T_0 l_\mathrm{B} Z_\mathrm{c}^2 \frac{n^2}{a}\left(1 - \frac{a}{R}\right). \qquad (7)$$

The quality of the theoretical curves can be inspected in fig. 1. The prediction is very good for large separations, but the discrepancies become larger for smaller separations, and one observes that the actual simulated energies are lower. With the help of eq. (7), we can establish a simple criterion, valid for large macroionic separations, for the necessary charge asymmetry α to produce an ionized ground state of two unlike charged colloids with the same size:

$$\frac{3}{2}\gamma(\sqrt{N_A} - \sqrt{N_B}) > \frac{(k_\mathrm{B}T_0) l_\mathrm{B} Z_\mathrm{c}^2}{a}. \qquad (8)$$

The physical interpretation of this criterion is straightforward. The left term represents the difference in correlation energy and the right term the monopole penalty due to the ionization process. This means that the correlational energy gained by overcharging the highly charged colloid A must overcome the loss of correlation energy as well as the monopole contribution (*two* penalties) involved in the ionization of colloid B. If one uses the parameters of the present study one finds the requirement $N_B < 66$ to get a stable ionized state. This is consistent with

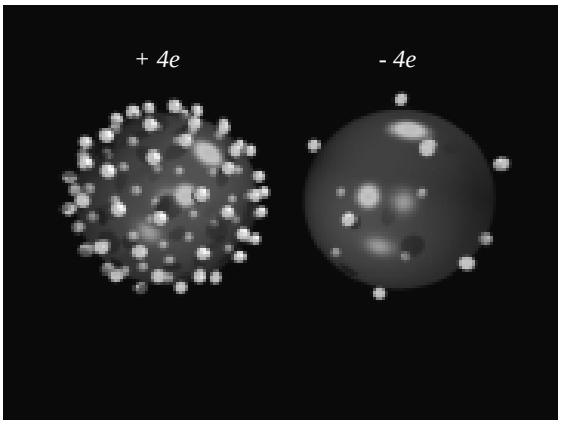

Fig. 4 – Snapshot of the ionized state (DI = 2) obtained in the relaxation process depicted in fig. 3, with the net charges $+4e$ and $-4e$ as indicated.

our findings where we show in fig. 1 that, for $N_B = 75$, and $R/a = 4.25$, no ionized ground state exists whereas for $N_B = 60$ we observed one even for infinite separation. The criterion eq. (8) is merely a sufficient condition, since we showed in fig. 1 that when the colloids are close enough this ionized state can appear even for smaller macroion charge asymmetry due to enhanced intercolloidal correlations. If the colloids have different radii this can be accounted for by simply replacing $N_i^{1/2}$ by the concentration of counterions $(N_i/F_i)^{1/2}$, and redefining γ in eq. (8).

At this stage, on looking at the results presented above, it appears natural and straightforward to establish an analogy with the concept of ionic bonding. It is well known in chemistry that the electro-negativity concept provides a simple yet powerful way to predict the nature of the chemical bonding [18]. If one refers to the original definition of the electro-negativity given by Pauling [18]: "the power of an atom in a molecule to attract electrons to itself", the role of the bare charge asymmetry becomes obvious. Indeed, it has an equivalent role at the mesoscopic scale as the electron affinity at the microscopic scale. Another interesting analogy is the influence of the colloidal separation on the stability of the ionized state. Like in diatomic molecules, the ionized state will be (very) stable only for sufficiently short colloid separations. Nevertheless, one should not push this analogy too far. Indeed, in many respects it breaks down, and these are in fact important and interesting points. One concerns the existence of an ionized ground state in colloidal system for *large* colloid separation, providing that α is large enough. In an atomistic system this is impossible since even for the most favorable thermodynamical case, namely CsCl, there is a cost in energy to transfer an electron from a cesium atom to a chlorine atom. Indeed, the smallest existing ionization energy (for Cs, 376 kJ mol^{-1}) is greater in magnitude than the largest existing electron affinity (for Cs, 349 kJ mol^{-1}). In other terms, for atoms separated by large distances in the gas phase, electron transfer to form ions is always energetically unfavorable.

As a last result, aimed at experimental verification, we show that an ionized state can also exist at *room temperature* T_0. Figure 3 shows the time evolution of the electrostatic energy of a system $Z_A = 180$ with $Z_B = 30$, $R/a = 2.4$ and $f_m = 7{\cdot}10^{-3}$, where the starting configuration is the neutral state (DI = 0). One clearly observes two jumps in energy, $\Delta E_1 = -19.5\, k_{\mathrm{B}}T_0$ and $\Delta E_2 = -17.4\, k_{\mathrm{B}}T_0$, which corresponds each to a counterion transfer from colloid B to colloid A. These values are consistent with the ones obtained for the ground state, which are$-20.1\, k_{\mathrm{B}}T_0$ and $-16.3\, k_{\mathrm{B}}T_0$, respectively. Note that this ionized state (DI = 2) is more stable than the neutral but is expected to be metastable, since it was shown previously that the most stable ground state corresponds to DI = 5. The other stable ionized states for higher

DI are not accessible with reasonable computer time because of the high-energy barrier made up of the correlational term and the monopole term which increases with DI [13]. In fig. 4 we display a typical snapshot of the ionized state (DI = 2) of this system at room temperature.

Obviously, these results are not expected by a DLVO theory even in the asymmetric case (see, *e.g.*, [19]). Previous simulations of asymmetric (charge and size) spherical macroions [20] were also far away to predict such a phenomenon since the Coulomb coupling was weak (water, monovalent counterions).

In summary, we have shown that the ground state of two unlike charged spherical macroions is mainly governed by two important parameters, namely the bare charge asymmetry α and the colloids separation R. If α is high enough, the ground state corresponds to the so-called ionized state, whatever the macroions separation R is. In return, the degree of ionization depends on R. Furthermore, for large R, we have established a criterion for α, allowing to predict when a stable ionized configuration can be expected. The bare charge difference α plays an analogous role to the electron affinity difference between two atoms forming a molecule with ionic bonding. We demonstrated that the results presented here for the ground state can lead to a stable ionic state even at room temperature providing that the Coulomb coupling and/or the charge asymmetry is sufficiently large. This is a possible mechanism which could lead to long-range attractions, even in bulk. Future work will treat the case where salt ions are present. Finally, it would be desirable to theoretically quantify the influence of intercolloidal correlations at short separations in a similar fashion as we have done for large separations.

* * *

This work is supported by *Laboratoires Européens Associés* (LEA). One of the authors (RM) thanks E. Allahyarov for fruitful discussions.

REFERENCES

[1] Derjaguin B. V. and Landau L. D., *Acta Physicochim. (USSR)*, **14** (1941) 633.
[2] Verwey E. J. and Overbeek J. T. G., *Theory of the Stability of Lyophobic Colloids* (Elsevier, Amsterdam) 1948.
[3] Groot R. D., *J. Chem. Phys.*, **95** (1991) 9191.
[4] Belloni L., *Chem. Phys.*, **99** (1985) 43.
[5] Sanchez-Sanchez J. E. and Lozada-Cassou M., *Chem. Phys. Lett.*, **190** (1992) 202.
[6] Kepler G. M. and Fraden S., *Phys. Rev. Lett.*, **73** (1994) 356.
[7] Crocker C. and Grier D. G., *Phys. Rev. Lett.*, **77** (1996) 1897.
[8] Larsen A. E. and Grier D. G., *Nature*, **385** (1997) 230.
[9] Grønbech-Jensen N., Beardmore K. M. and Pincus P., *Physica A*, **216** (1998) 74.
[10] Allahyarov E., D'Amico I. and Löwen H., *Phys. Rev. Lett.*, **81** (1998) 1334.
[11] Allahyarov E., D'Amico I. and Löwen H., *Phys. Rev. E*, **60** (1999) 3199.
[12] Wu J. Z., Bratko D., Blanch H. W. and Prausnitz J. M., *J. Chem. Phys.*, **111** (1999) 7084.
[13] Messina R., Holm C. and Kremer K., *Phys. Rev. Lett.*, **85** (2000) 872.
[14] Since we are using (MD) simulations, to avoid barrier energy problem the counterions were generated at the vicinity of the colloid surface.
[15] Shklovskii B. I., *Phys. Rev. E*, **60** (1999) 5802.
[16] Shklovskii B. I., *Phys. Rev. Lett.*, **82** (1999) 3268; Perel V. I. and Shklovskii B. I., *Physica A*, **274** (1999) 446.
[17] Bonsall L. and Maradudin A. A., *Phys. Rev. B*, **15** (1977) 1959.
[18] Pauling L., *The nature of the Chemical Bond* (Cornell University Press, New York) 1939.
[19] D'Aguanno B. and Klein R., *Phys. Rev. A*, **46** (1992) 7652.
[20] Allahyarov E., Löwen H. and Trigger S., *Phys. Rev. E*, **57** (1998) 5818.

Appendix C

Strong electrostatic interactions in spherical colloidal systems

PHYSICAL REVIEW E, VOLUME 64, 021405

Strong electrostatic interactions in spherical colloidal systems

René Messina,* Christian Holm,† and Kurt Kremer‡
Max-Planck-Institut für Polymerforschung, Ackermannweg 10, 55128 Mainz, Germany
(Received 17 January 2001; published 20 July 2001)

We investigate spherical macroions in the strong Coulomb coupling regime within the primitive model in salt-free environment. We first show that the ground state of an isolated colloid is naturally overcharged by simple electrostatic arguments illustrated by the Gillespie rule. We furthermore demonstrate that in the strong Coulomb coupling this mechanism leads to ionized states and thus to long range attractions between like-charged spheres. We use molecular dynamics simulations to study in detail the counterion distribution for one and two highly charged colloids for the ground state as well as for finite temperatures. We compare our results in terms of a simple version of a Wigner crystal theory and find excellent qualitative and quantitative agreement.

DOI: 10.1103/PhysRevE.64.021405 PACS number(s): 82.70.Dd, 61.20.Qg, 41.20.−q

I. INTRODUCTION

Charged colloidal suspensions are often encountered in the everyday life (technology, biology, medicine etc.) and have an important practical impact [1]. In numerous application-oriented situations, electrostatic repulsion among colloids (macroions) is desired in order to obtain a stabilized suspension. Consequently the understanding of the electrostatic interaction in such systems is motivated by practical as well as theoretical interests. There is recent experimental evidence that the effective interaction between two like-charged spherical colloids (in the presence of neutralizing salts) can be attractive in the presence of one or two glass walls [2–4]. This is in contrast with the classical work of Derjaguin, Landau, Verwey, and Overbeek (DLVO) based on a linearized Poisson Boltzmann theory [5,6], which foresees only repulsive effective Coulomb forces between two like-charged spheres even in confined geometry. There are some indications that this attraction might be explainable in terms of hydrodynamic effects induced by the walls [7].

Already in the bulk case there have been disputes for a long time about the existence of long range attractive forces, triggered mainly by the observation of voids in colloidal solutions [8–11]. There is no clear experimental and theoretical picture, either, and there have been speculations that the experiments observed phase coexistence. Recent theoretical [12–14] and simulation [15–18] investigations have shown the existence of *short range* attraction.

In two short communications [19,20], we demonstrated by molecular dynamics (MD) simulations, how a mechanism involving overcharged and undercharged spherical macroions could lead to a *strong long range* attraction between charged spheres. In this paper we give a more detailed account and elaborate on the physical mechanism responsible for *charge inversion* (overcharge). Why and how does a charged particle strongly ''bind'' electrostatically at its surface so many counterions that its net charge changes sign? We further will discuss the necessary ingredients to explain this phenomenon in terms of a simple Wigner crystal theory. Using this Ansatz we show that it is possible for a pair of colloids that are sufficiently different in charge density to have an ionized ground state. Both, the one and two colloid cases, are treated in terms of analytical predictions and verifications by simulation. Of special interest are the energy barriers necessary to cross from a neutral pair to an ionized pair state. We finally demonstrate by explicit simulations that the described features survive also at finite temperature.

The paper is organized as follows. In Sec. II a simple model based on the Gillespie rule is proposed to understand charge inversion. Section III contains details of our MD simulation model. Section IV is devoted to the study of a single highly charged colloid. In Sec. V we investigate the situation where two colloids are present. Finally, in Sec. VI we conclude with a summary of our results.

II. UNDERSTANDING OVERCHARGING VIA THE GILLESPIE RULE

Here we propose a simple model solely based on electrostatic energy considerations in order to understand the phenomenon of charge inversion for strongly coupled systems. Because of the analogy between a spherical macroion surrounded by counterions and an atom (i.e., nucleus + electrons), it turns out fruitful to use classical pictures of atomic physics in order to gain comprehension of certain phenomena occurring in mesoscopic colloidal systems [19,20]. To study the possibility of overcharging a single macroion, we recall the Gillespie rule also known as the valence-shell electron-pair repulsion theory [21,22] that is well known in chemistry to predict the molecular geometry in covalent compounds. Note that originally this model has nothing to do with overcharge. Applying simple electrostatics one can compute that the *ground state structure* of two, three, four, and five electrons disposed on a hard sphere corresponds to simple geometrical situations like those depicted in Fig. 1. The electrons try to maximize their mutual distances that leads, for example, in the case of three and four electrons to equilateral triangular and tetrahedral arrangements.

Now, we can apply this concept to a spherical colloid of

*Email address: messina@mpip-mainz.mpg.de
†Email address: holm@mpip-mainz.mpg.de
‡Email address: k.kremer@mpip-mainz.mpg.de

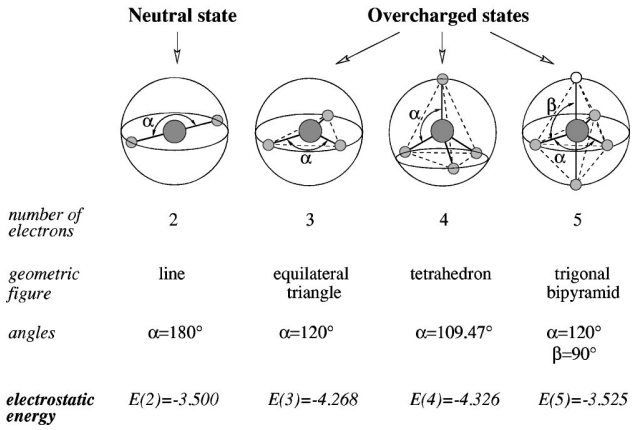

FIG. 1. Ground state configurations for two, three, four, and five counterions. The corresponding geometrical figures show the typical angles. The electrostatic energy (in units of k_BTl_B/a) is given for a central charge of $+2e$.

radius a, central charge $Z_m=+2e$, where e is the elementary charge, and N_c monovalent counterions. By referring to Fig. 1, the *neutral* system corresponds to the case where two counterions are present, and the three other cases (three, four, and five counterions) correspond to *non-neutral overcharged* states.

The total electrostatic energy $E(N_c)$ is merely made up of two terms: i) an attractive term $E_{att}(N_c)$ due to the attraction between the counterions and the central charge and (ii) a repulsive term $E_{rep}(N_c)$ due to the repulsion among the counterions. The final expression for the electrostatic energy as a function of the number of counter ions reads

$$E(N_c)=E_{att}(N_c)+E_{rep}(N_c)=k_BT\frac{l_B}{a}[-N_cZ_m+f(\theta)], \tag{1}$$

where $l_B=e^2/(4\pi\epsilon_0\epsilon_r k_BT)$ is the Bjerrum length and $f(\theta)$ is the repulsive energy part which is solely a function of the *topology* (relative angles between counterions, such as α and β appearing in Fig. 1, which also depend on N_c) of the ground state figure. For the specific cases reported in Fig. 1, the calculation of $E(N_c)$, with $2\leqslant N_c\leqslant 5$, is straightforward and the corresponding energy values are given in Fig. 1. One deduces that the maximally obtainable overcharging is $-2e$ (i.e., 100%) around the central charge. That is, the excess counterions gain more energy by assuming a topological favorable configuration than by escaping to infinity, the simple reason of overcharge. Note the arguments for overcharging are independent of the Bjerrum length and of the sphere radius, which enter only as prefactors in Eq. (1).

To safely use this above outlined model one has just to ensure that the counterion size is small enough to avoid excluded volume effects, which in practice is always true. The important message is that, from an energy point of view, a colloid *always* tends to be overcharged. Obviously, for high central charge, the direct computation of the electrostatic energy by using the exact equation (1) becomes extremely complicated. Therefore we resort to simulations for highly charged spheres.

III. SIMULATION MODEL

The system under consideration contains two types of spherical charges: (i) one or two macroion(s) with a bare central charge $Q=-Z_me$ (with $Z_m>0$) and (ii) small counterions of diameter σ with charge $q=+Z_ce$ (with $Z_c=2$) to neutralize the whole system. All these ions are confined in an impermeable cell and the macroion(s) is (are) held fixed.

The MD technique employed here is similar to the one used in previous studies [19,20]. In order to simulate a canonical ensemble, the motion of the counterions is coupled to a heat bath acting through a weak stochastic force $\mathbf{W}(t)$. The equation of motion of counterion i reads

$$m\frac{d^2\mathbf{r}_i}{dt^2}=-\boldsymbol{\nabla}_iU-m\gamma\frac{d\mathbf{r}_i}{dt}+\mathbf{W}_i(t), \tag{2}$$

where m is the counterion mass, U is the potential force having two contributions: the Coulomb interaction and the excluded volume interaction, and γ is the friction coefficient. Friction and stochastic force are linked by the dissipation-fluctuation theorem $\langle\mathbf{W}_i(t)\cdot\mathbf{W}_j(t')\rangle=6m\gamma k_BT\delta_{ij}\delta(t-t')$. For the ground state simulations the fluctuation force is set to zero.

Excluded volume interactions are taken into account with a purely repulsive Lennard-Jones potential given by

$$U_{LJ}(r)=\begin{cases}4\epsilon_{LJ}\left[\left(\dfrac{\sigma}{r-r_0}\right)^{12}-\left(\dfrac{\sigma}{r-r_0}\right)^{6}\right]+\epsilon_{LJ}, & \text{for } r-r_0<r_{cut},\\ 0, & \text{for } r-r_0\geqslant r_{cut},\end{cases} \tag{3}$$

where $r_0=0$ for the counterion-counterion interaction, $r_0=7\sigma$ for the macroion-counterion interaction, $r_{cut}(=2^{1/6}\sigma)$ is the cutoff radius. This leads to an *effective* macroion radius a $(a=r_0+\sigma=8\sigma)$ corresponding physically to the macroion-counterion distance of closest approach. Energy and length units in our simulations are defined as $\epsilon_{LJ}=k_BT_0$ (with $T_0=298$ K) and $\sigma=3.57$ Å, respectively. In the following we will set $k_BT_0=1$, so that all energies are measured in those units, suppressing thereby all factors of k_BT_0 in our equations.

The pair electrostatic interaction between any pair ij, where i and j denote either a macroion or a counterion, reads

TABLE I. Simulation parameters with some fixed values.

Parameters	
$\sigma = 3.57$ Å	Lennard Jones length units
$T_0 = 298$ K	Room temperature
$\epsilon_{LJ} = k_B T_0$	Lennard Jones energy units
Z_m	Macroion valence
$Z_c = 2$	Counterion valence
$l_B = 10\sigma$	Bjerrum length
f_m	Macroion volume fraction
$a = 8\sigma$	Macroion-counterion distance of closest approach

$$U_{coul}(r) = l_B \frac{Z_i Z_j}{r}, \tag{4}$$

where Z_i represents the valence of the ions (counterion or macroion). Being essentially interested in the strong Coulomb coupling regime we choose the relative permittivity $\epsilon_r = 16$, corresponding to a Bjerrum length of 10σ, for the remaining of this paper. To avoid image charges complications, the permittivity ϵ_r is supposed to be identical within whole the cell (including the macroion) as well as outside the cell. Typical simulation parameters are gathered in Table I.

IV. ONE-MACROION CASE

In this section, we focus on counterion distribution exclusively governed by *energy minimization*, i.e., $T = 0$ K. The single spherical macroion is fixed to the center of the large outer spherical simulation cell (i.e., both spheres are concentric) of radius $R = 40\sigma$. This leads to a colloid volume fraction $f_m = a^3/R^3 = 8 \times 10^{-3}$. In such a case correlations are maximal, and all the counterions lie on the surface of the spherical macroion. To avoid being trapped in metastable states, we systematically heated and cooled (10 cycles) the system and only kept the lowest energy state then obtained [23]. It turns out that for this type of repulsive potential (between counterions) no rough energy landscape appears and thus, the MD method is efficient to find the ground state. First, we checked that this method reproduces well the ground state energies and structures of the simple situations depicted in Fig. 1.

A. Counterion distribution

To characterize the counterion layer *structure*, we compute the counterion correlation function $g(r)$ on the surface of the sphere, defined as

$$c^2 g(r) = \sum_{i \neq j} \delta(r - r_i)\, \delta(r - r_j), \tag{5}$$

where $c = N/4\pi a^2$ is the surface counterion concentration (N being the number of counterions), r corresponds to the arc length on the sphere. Note that at zero temperature all equilibrium configurations are identical, thus only one is required to obtain $g(r)$. The pair distribution $g(r)$ is normalized as follows

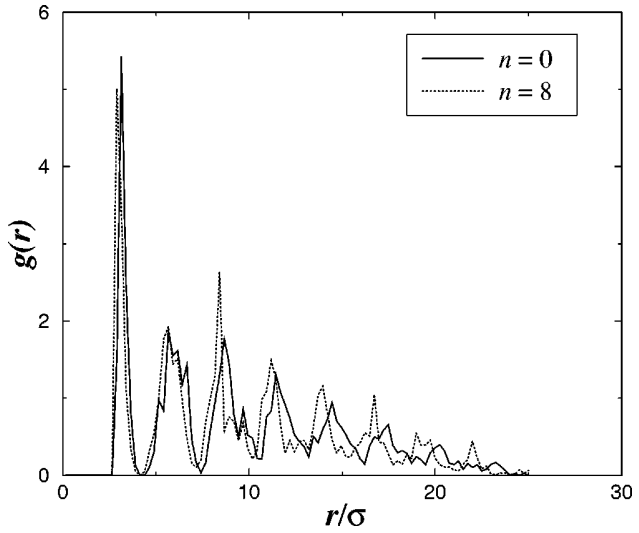

FIG. 2. Ground state surface counterion correlation functions for $Z_m = 180$ and two states of charge [neutral ($n = 0$) and overcharged ($n = 8$)].

$$c \int_0^{\pi a} 2\pi r g(r) dr = (N_c + n - 1), \tag{6}$$

where $N_c = Z_m / Z_c$ is the number of counterions in the neutral state and n is the number of overcharging counterions. Because of the *finite* size and the topology of the sphere, $g(r)$ has a cutoff at πa ($= 25.1\sigma$) and a *zero* value there. More precisely one cannot state that the uncorrelated case corresponds to $g(r) = 1$ for the present finite system. Therefore at ''large'' distance the correlation function differs from the one obtained with an infinite planar object. Furthermore the absolute value of $g(r)$ cannot be directly compared to the one obtained with an infinite plane.

Correlation functions for the structural charge $Z_m = 180$ and for two states of charge, neutral ($n = 0$) and overcharged ($n = 8$), can be inspected in Fig. 2. One remarks that both structures are very similar and highly ordered. A snapshot of the ground state structure of the neutral state ($n = 0$) is depicted in Fig. 3. A visual inspection gives an almost perfect *triangular* crystalline structure (see Fig. 3). A closer look at Fig. 2 reveals that the $g(r)$ of the overcharged state, containing eight more counterions than the neutral one, shows its first peak at some shorter distance compared to the $g(r)$ of the neutral state, as is expected for denser systems.

It is also interesting to know how the counterion-layer structure looks like when the system is brought to *room temperature* T_0. At non zero temperature, correlation functions are computed by averaging $\Sigma_{i \neq j} \delta(r - r_i)\, \delta(r - r_j)$ over 1000 independent equilibrium configurations that are statistically uncorrelated. Results are depicted in Fig. 4 for $Z_m = 180$ and $f_m = 8 \times 10^{-3}$. As expected the long-range counterion positional order is neatly weaker at room temperature than in the ground state case. Meanwhile, the structure remains very correlated and highly short-range ordered and therefore it is referred as a strongly correlated liquid [24]. In terms of Cou-

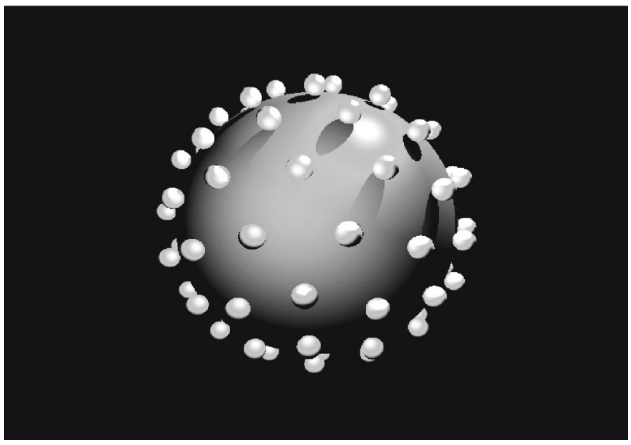

FIG. 3. Snapshot of the ground state structure of the neutral state ($n=0$) with a macroion charge $Z_m=180$ [see Fig. 2 for the corresponding $g(r)$].

lomb coupling parameter [24,25] $\Gamma=Z_c^2 l_B/a_{cc}$, where a_{cc} is the average distance between counterions, we have $\Gamma\approx 13$ for $Z_m=180$.

B. Energy analysis

As demonstrated in Sec. II, the spatial correlations are fundamental to obtain overcharge. Indeed, if we apply the same procedure and smear Z counterions onto the surface of the colloid of radius a, we obtain for the energy

$$E=l_B\left[\frac{1}{2}\frac{Z^2}{a}-\frac{Z_m Z}{a}\right]. \tag{7}$$

The minimum is reached for $Z=Z_m$, hence no overcharging occurs.

To generalize results of Sec. II to higher central charges we have considered three macroionic charge Z_m of values

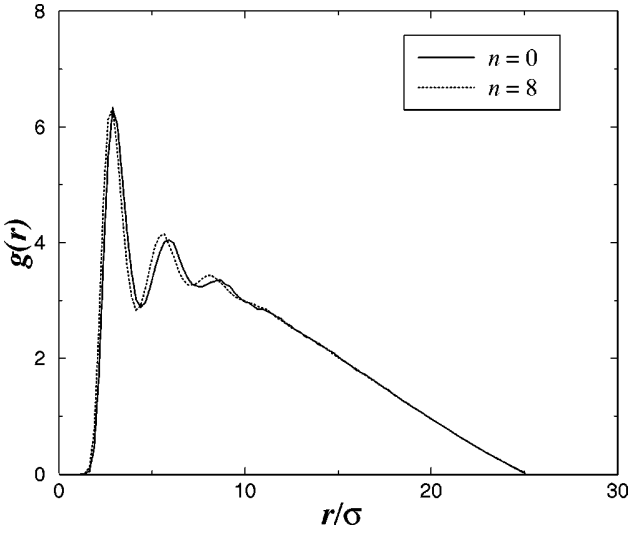

FIG. 4. Surface counterion correlation functions at *room temperature* T_0 for two states of charge [neutral (n=0) and overcharged ($n=8$)] with $Z_m=180$ and $f_m=6.6\times 10^{-3}$.

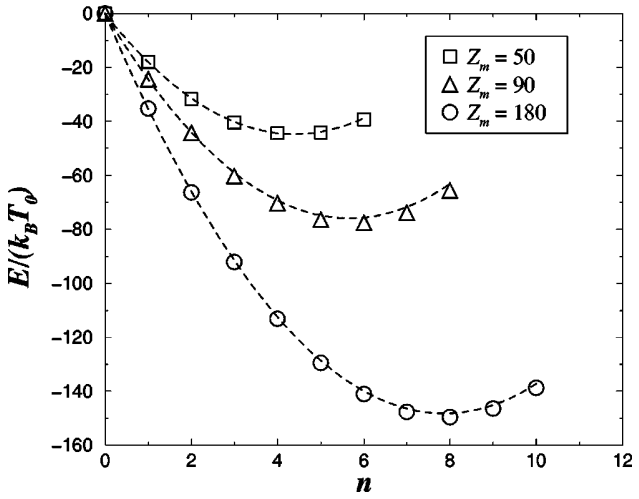

FIG. 5. Electrostatic energy (in units of k_BT_0) for *ground state* configurations of a single charged macroion of as a function of the number of *overcharging* counterions n for three different bare charges Z_m. The neutral case was chosen as the potential energy origin, and the curves were produced using the theory of Eq. (13), compare text.

50, 90, and 180 corresponding to a surface charge density of one elementary charge per 180, 100, and 50 Å ^{2}, respectively. For a given macroion, we always start by adding the exact number of counterions N_c to have an electroneutral system. Once equilibrium of this system is reached, we add the first overcharging counterion and let the new non-neutral system relax, and we repeat this operation a given number of times. The electrostatic energy is computed by summing up the pairwise interactions of Eq. (4) over all pairs.

The electrostatic energy as a function of the number of overcharging counterions n is displayed in Fig. 5. We note that the maximal (critical) acceptance of n (4, 6, and 8) increases with the macroionic charge Z_m (50, 90, and 180 respectively). Furthermore for fixed n, the gain in energy is always increasing with Z_m. Also, for a given macroionic charge, the gain in energy between two successive overcharged states is decreasing with n.

The results of Sec. IV A showed that in the ground state the counterions were highly ordered. Rouzina and Bloomfield [25] first stressed the special importance of these crystalline arrays for interactions of multivalent ions with DNA strands, and later Shklovskii ([12,24] and references therein) showed that the Wigner crystal (WC) theory can be applied to determine the interactions in strongly correlated systems. In two recent short contributions [19,20] we showed that the overcharging curves obtained by simulations of the ground state, like Fig. 5, can be simply explained by assuming that the energy ε per counterion on the surface of a macroion depends linearly on the inverse distance between them, hence is proportional to $\sqrt{N}$ for fixed macroion area, where N is the *total* number of counterions on the surface [19,20,26]. This can be justified by the WC theory. The idea is that the counterions form an ordered lattice on the surface of a homogeneously charged background of opposite charge, which is also called a one component plasma (OCP) [27]. Each ion

interacts in first approximation only with the oppositely charged background of its Wigner-Seitz (WS) cell [24], which can be approximated by a disk of radius h, which possesses the same area as the WS cell. Because we can assume the area of the WS cell to be evenly distributed among the N counterions on the sphere's surface $A=4\pi a^2$ we find

$$\pi h^2=\frac{A}{N}=c^{-1}. \tag{8}$$

The electrostatic interaction energy $\varepsilon^{(h)}$ of one counterion with the background of its WS cell can then be determined by

$$\epsilon^{(h)}=-l_B Z_c^2\int_0^h 2\pi r c\frac{1}{r}dr=-2\sqrt{\pi}l_B Z_c^2\sqrt{c}, \tag{9}$$

hence is proportional to $\sqrt{c}$, which proves our initial assumption. It is convenient to define $\ell=l_B Z_c^2$ and $\alpha^{(h)}=2\sqrt{\pi}\approx 3.54$. For fixed macroion area we can then rewrite Eq. (9) as

$$\varepsilon^{(h)}(N)=-\frac{\alpha^{(h)}\ell}{\sqrt{A}}\sqrt{N}. \tag{10}$$

If one computes this value for an infinite plane, where the counterions form an exact triangular lattice, and takes into account all interactions, one obtains the same form as in Eq. (9), but the prefactor $\alpha^{(h)}$ gets replaced by the numerical value $\alpha^{WC}=1.96$ [28]. Although the *value* is almost a factor of two smaller than the simple hole picture suggests, the *functional dependence* on the concentration is still the same.

Not knowing the precise value of α we can still use the simple scaling behavior with c to set up an equation to quantify the energy gain ΔE_1 by adding the first overcharging counterion to the colloid. To keep the OCP neutral we imagine adding a homogeneous surface charge density of opposite charge $(-Z_c e/A)$ to the colloid [29]. This ensures that the background still neutralizes the incoming overcharging counterion and we can apply Eq. (10). To cancel our surface charge addition we add another homogeneous surface charge density of opposite sign $Z_c e/A$. This surface charge does not interact with the now neutral OCP, but adds a self-energy term of magnitude $\ell/(2a)$, so that the total energy difference for the first overcharging counterion reads as

$$\Delta E_1=(N_c+1)\varepsilon(N_c+1)-N_c\varepsilon(N_c)+\frac{\ell}{2a}. \tag{11}$$

By using Eq. (10) this can be rewritten as

$$\Delta E_1=-\frac{\alpha\ell}{\sqrt{A}}[(N_c+1)^{3/2}-N_c^{3/2}]+\frac{\ell}{2a}. \tag{12}$$

Completely analogously one derives for the energy gain ΔE_n for n overcharging counterions [30]

$$\Delta E_n=-\frac{\alpha\ell}{\sqrt{A}}[(N_c+n)^{3/2}-N_c^{3/2}]+\frac{\ell}{a}\frac{n^2}{2}. \tag{13}$$

Equation (13) can be seen as an approximation of the exact general expression Eq. (1), where the topological term $f(\theta)$ is handled by assuming a perfect planar crystalline structure through Eqs. (11)–(13). Using Eq. (13), where we determined the unknown α from the simulation data for ΔE_1 via Eq. (12) we obtain a curve that matches the simulation data almost perfectly, compare Fig. 5. The second term in equation (13) also shows why the overcharging curves of Fig. 5 are shaped parabolically upwards for larger values of n.

Using the measured value of α we can simply determine the maximally obtainable number n_{max} of overcharging counterions by finding the stationary point of Eq. (13) with respect to n:

$$n_{max}=\frac{9\alpha^2}{32\pi}+\frac{3\alpha}{4\sqrt{\pi}}\sqrt{N_c}\left[1+\frac{9\alpha^2}{64\pi N_c}\right]^{1/2}. \tag{14}$$

The value of n_{max} depends only on the number of counterions N_c and α. For large N_c Eq. (14) reduces to $n_{max}\approx 3\alpha\sqrt{N_c}/4\sqrt{\pi}$ which was derived in Ref. [24] as the low temperature limit of a neutral system in the presence of salt. What we have shown is that the overcharging in this limit has a pure electrostatic origin, namely it originates from the topological favorable arrangement of the ions around a central charge. In the following we will investigate the behavior of α on the surface charge density and on the radius of the macroion.

We have performed simulations for various surface charge densities by keeping A fixed and changing $Z_m=2N_c$ in the range 2 up to 180. Results can be found in Table II and in Fig. 6. We observe that α is already for values of N_c as small as two, where one can use the Gillespie rule to calculate the energy exactly, close the planar value α^{WC}, and actually oscillates around this value. For $N_C>50$, one reaches a plateau of $\alpha=1.86\pm 0.05$.

This value is about 5% smaller then the one predicted by WC theory, and is presumably due to the finite curvature of the sphere. For large values of the radius a we expect α to reach the planar limit. To see the rate of convergence we varied[1] a at a fixed concentration c. The results can be found in Table III and Fig. 7. For our smallest value of $a=6\sigma$ we find $\alpha=1.91$. For small a, which is equivalent to a small number of N_c, we observe again a slight oscillatory behavior of α, whereas for our two largest values $a=80\sigma$ and 160σ we find up to numerical uncertainties the planar result $\alpha=\alpha^{WC}=1.96$. Again we stress that the numerical value of α enters only as a prefactor into the equations which govern the overcharging, it does not change the qualitative behavior.

One could wonder if the results presented above are still valid when the bare central charge of the colloid is replaced by small *discrete* ions lying on the macroion surface? In fact

[1]Note that this is the only part of the paper where $a\neq 8\sigma$.

TABLE II. Measured values for an *isolated* macroion, with fixed radius a, of the energy gain for the first overcharging counterion ΔE_1^{OC} for various macroion bare charge $Z_m=2N_c$. The value of α can be compared to the prediction of WC theory for an infinite plane, which gives 1.96, compare text. We also record the values of the fitting parameter τ of Eq. (15) for selected N_c corresponding to those of Fig. (9). The symbol $^{(i)}$ stands for the ionization process discussed in Sec. V B 1.

Z_m	N_c	$\Delta E_1/k_BT_0$	α	$\tau\sigma$
2	1	−2.5	1.94	0.12
4	2	−3.8	1.89	0.18
6	3	−5.3	1.97	0.19
8	4	−6.1	1.92	0.24
10	5	−7.5	2.02	0.24
20	10	−10.7	1.93	
$30^{(i)}$	15	+17.9	1.91	
32	16			0.41
50	25	−18.0	1.92	0.51
90	45	−24.4	1.88	0.68
$90^{(i)}$	45	+29.2	1.89	
128	64			0.79
$150^{(i)}$	75	+37.4	1.91	
180	90	−35.3	1.88	0.93
288	144			1.19
360	180	−50.0	1.86	

it has been shown that the energy of the overcharged state (Fig. 5) for *random* discrete colloidal charge distribution is more or less quantitatively affected [31,32] depending on the the valence of the counterions. More precisely it was shown that the overcharge still persists and has a similar (for monovalent counterions) or quasi-identical (for multivalent counterions) behavior to the one depicted in Fig. 5, and this, even if *ionic pairing* occurs between the counterions and the discrete colloidal charges [31,32], that is even when *no* counterion WC is formed.

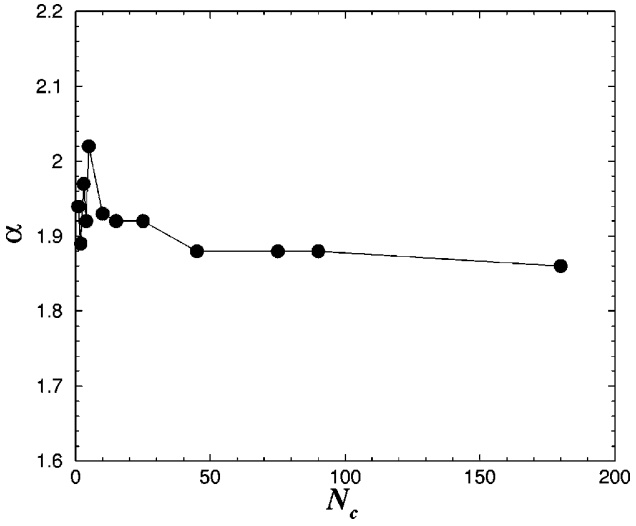

FIG. 6. Wigner crystal parameter α as a function of the number of counterions N_c for fixed colloid radius a.

TABLE III. Measured values of the energy gain ΔE_1^{OC} and fixed counterion concentration c, varying this time the macroion radius a and the number of counterions N_c.

a/σ	N_c	$\Delta E_1/k_BT_0$	α
6	9	−13.3	1.91
8	16	−14.4	1.97
10	25	−14.5	1.93
12	36	−14.7	1.92
14	49	−15.1	1.94
16	64	−15.1	1.92
20	100	−15.3	1.92
40	400	−15.9	1.94
80	1600	−16.4	1.97
160	6400	−16.5	1.96

C. Macroion-counterion interaction profile

In this part, we study the interaction potential profile at $T=0$ K between a *neutral effective* macroion (bare macroion + neutralizing counterions) and one excess overcharging counterion at a distance r from the colloid center. The profile is obtained by displacing adiabatically the excess overcharging counterion from infinity towards the macroion. We investigated the case of $Z_m=2$, 4, 6, 8, 10, 32, 50, 90, 128, 180, and 288. All curves can be nicely fitted with an exponential fit of the form

$$E_1(r)=\Delta E_1 e^{-\tau(r-a)}, \tag{15}$$

where ΔE_1 is the measured value for the first overcharging counterion, and τ is the only fit parameter (see Table II). Results for the two values $Z_m=50$ and 180 are depicted in Fig. 8. If one plots all our results for τ versus $\sqrt{N_c}$ we observe a linear dependence for a wide range of values for N_c,

$$\tau=m\sqrt{N_c}, \tag{16}$$

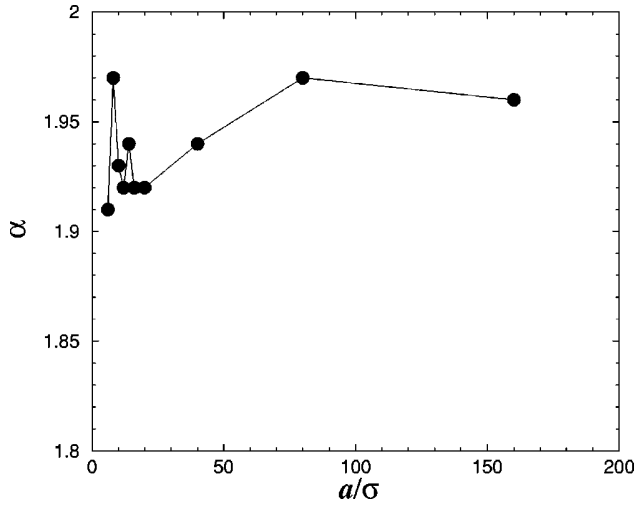

FIG. 7. Wigner crystal parameter α as a function of the colloid radius a for a fixed surface counterion concentration c.

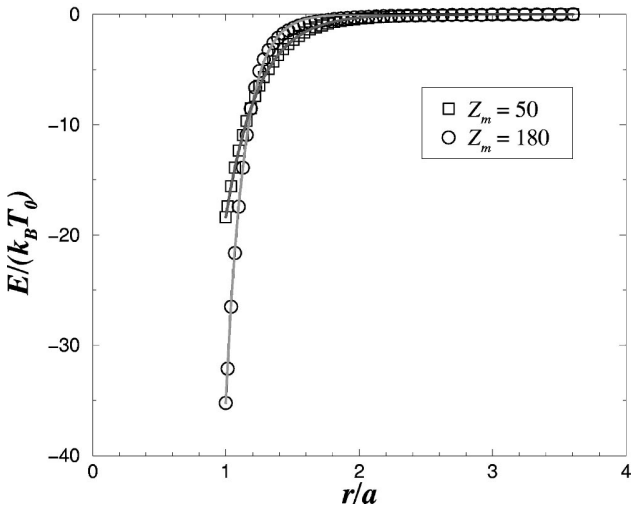

FIG. 8. Electrostatic interaction energy (in units of k_BT_0) of a divalent counterion with a neutral effective colloid (bare particle + surrounded counterions) as function of distance r/a from the center of a macroion for two different macroion bare charges Z_m. The energy is set to zero at distance infinity. Solid lines correspond to exponential fits [see Eq. (15)].

with $m\sigma \approx 0.1$, as can be inspected in Fig. 9.

This behavior can again be explained using a "WC hole" picture in the limiting situation where $x := r - a$ is small (i.e., the displaced counterion is close to the macroion surface). To this end we consider the classical electrostatic interaction $V_{disk}(x)$ between a uniformly charged disk (the WC hole—supposed planar) and a point ion (the displaced counterion) located on the axis of the disk at a distance x from its surface, which is given by

$$V_{disk}(x) = -2\pi\ell_c(\sqrt{h^2+x^2}-x). \tag{17}$$

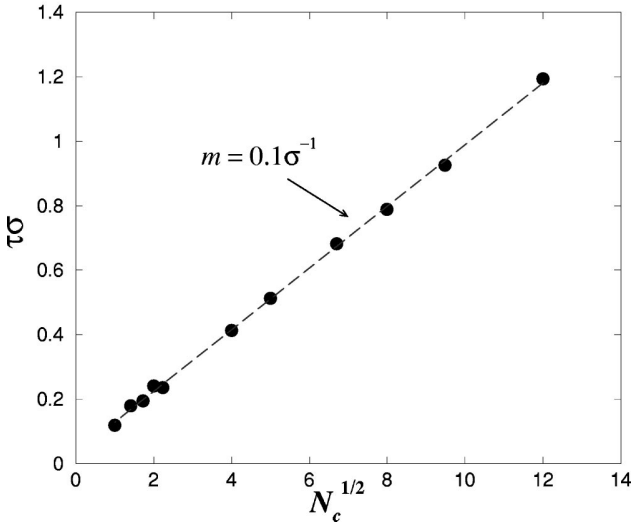

FIG. 9. Exponential fit parameter τ as a function of the square root of the number of counterions $\sqrt{N_c}$. The dashed line corresponds to a linear fit in $\sqrt{N_c}$.

As in Eq. (9), $h = (\pi c)^{-1/2}$ is the hole radius. For small distance x, we expand Eq. (17)

$$V_{disk}(x) = \varepsilon^{(h)}\left[1 - \frac{1}{h}x + \frac{1}{2h^2}x^2 + O\left(\frac{x^4}{h^4}\right)\right], \tag{18}$$

where the surface term $V_{disk}(x=0) = \varepsilon^{(h)}$ is given by Eq. (9). By expanding the exponential in Eq. (15) to 2nd order for small τx we obtain

$$E_1(x) = \Delta E_1\left[1 - \tau x + \frac{\tau^2}{2}x^2 + O(\tau^3 x^3)\right]. \tag{19}$$

A comparison between Eq. (19) and Eq. (18) shows that to this order we can identify

$$\tau = \frac{1}{h} = \sqrt{\pi c} = \frac{\sqrt{N_c}}{2a} \approx 0.06\sqrt{N_c}. \tag{20}$$

Comparing this to Eq. (16) we note that this simple illustration gives us already the correct scaling as well as the prefactor up to 30%. We neglected here the effect that the surface concentration changes when the ion is close to the macroion as well as the curvature of the macroion.

V. TWO-MACROION CASE

In this section we consider two fixed charged spheres of bare charge Q_A and Q_B separated by a center-center separation R and surrounded by their neutralizing counterions. All these ions making up the system are immersed in a cubic box of length $L = 80\sigma$, and the two macroions are held fixed and disposed symmetrically along the axis passing by the two centers of opposite faces. This leads to a colloid volume fraction $f_m = 2\frac{4}{3}\pi(a/L)^3 \approx 8.4\times10^{-3}$. For *finite* colloidal volume fraction f_m and temperature, we know from the study carried out above that in the strong Coulomb coupling regime all counterions are located in a spherical "monolayer" in contact with the macroion. Here, we investigate the mechanism of *strong long range* attraction stemming from *monopole* contributions: that is one colloid is overcharged and the other one undercharged.

A. Like charged colloids

1. Observation of metastable ionized states

In the present charge symmetrical situation we have $Q_A = Q_B = -Z_m e$. This system is brought at *room temperature* T_0. Initially the counterions are randomly generated inside the box. Figure 10 shows two macroions of bare charge $Z_m = 180$ surrounded by their quasi-two-dimensional counterions layer. The striking peculiarity in this configuration is that it corresponds to an overcharged and an undercharged sphere. There is one counterion more on the left sphere and one less on the right sphere compared to the bare colloid charge. Such a configuration is referred as *ionized state*. In a total of ten typical runs, we observe this phenomenon five times. We have also carefully checked against a situation with periodic boundary conditions, yielding identical results.

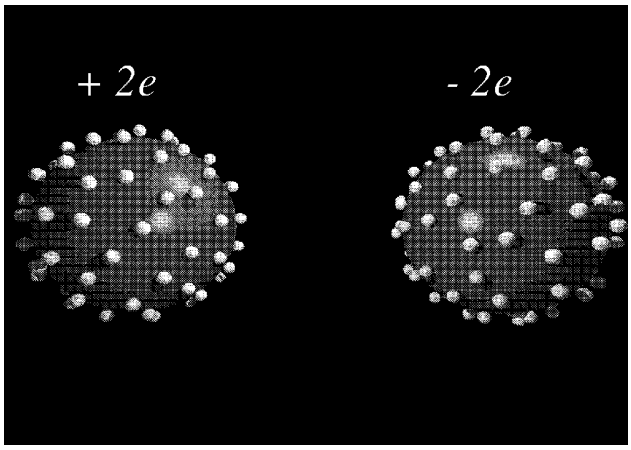

FIG. 10. Snapshot of a ''pseudoequilibrium'' configuration at room temperature T_0 where the counterion-layers do not exactly compensate the macroions charge. Here the deficiency charge is ± 1 counterion (or $\pm 2e$ as indicated above the macroions) and $R/a = 3.6$.

However it is clear that such a state is ''metastable'' because it is not the lowest energy state. Indeed, in this symmetrical situation the ground state should also be symmetrical so that both colloids should be exactly charge-compensated. Such arguments remain valid even at nonzero temperature as long as the system is strongly energy dominated, which is presently the case. Nevertheless the ionized states observed here seem to have a long life time since even after 10^8 MD time steps this state survives. In fact we could not observe within the actual computation power the recover of the stable neutral state. To understand this phenomenon we are going to estimate the energy barrier involved in such a process.

2. Energy barrier and metastability

To estimate the energy barrier, electrostatic energy profiles at *zero temperature* were computed, where we move one counterion from the overcharged macroion to the undercharged, restoring the neutral state [see drawing depicted in Fig. 11(a)]. We have checked that the path leading to the lowest barrier of such a process corresponds to the line joining the two macroions centers. The simulation data are sketched in Figs. 11(a–b) and were fitted using a similar technique to the single macroion-counterion interaction profile given by Eq. (15), which will be explicitly treated later. The resulting simulated energy barrier ΔE_{bar} is obtained by taking the difference between the highest energy value of the profile and the ionized state energy (start configuration). Values of ΔE_{bar} can be found in Table IV for the small macroion separation case $R/a = 2.4$. One clearly observes a barrier, which increases quasi linearly with the charge Z_m for the small colloids separation $R/a = 2.4$ [cf. Fig. 11(a) and Table IV]. The ground state corresponds as expected to the neutral state. Note that the ionized state and the neutral state are separated by only a small energy amount (less than 2.5), the difference being approximately of the order of the monopole contribution $E = l_B(4/8 - 4/11) \approx 1.36$. The physical origin of this barrier can be understood from the single macroion case where we showed that a counterion gains high correlational energy near the surface. This gain is roughly equal for both macroion surfaces and decreases rapidly with increasing distance from the surfaces, leading to the energy barrier with its maximum near the midpoint. For the single macroion case we showed that the correlational energy gain scales with $\sqrt{Z_m}$, whereas here we observe a linear behavior of the barrier height with Z_m. We attribute this effect to additional ionic correlations since both macroions are close enough for their surface ions to interact strongly. For large separations (here $R/a = 4.25$) we find again that the barrier height increases with $\sqrt{Z_m}$, as expected [see Fig. 11(b) and Table V]. Furthermore the energy barrier height naturally increases with larger colloidal separation. The Z_m dependence of the barrier also shows that at room temperature such ionized states only can occur for large Z_m. In our case only for $Z_m = 180$, the ionized state was stable for all accessible computation times. Unfortunately, it is not possible to get a satisfactory accuracy of the energy jumps at nonzero temperatures. Nevertheless, since we are interested in the strong Coulomb coupling regime, which is energy dominated, the zero temperature analysis is sufficient to capture the essential physics.

Simulation results presented in Fig. 11 can be again theoretically well described using the previously exponential profiles obtained for the macroion-displaced counterion in Sec. IV C for a *single* colloid. For the two macroions case, the general expression for the electrostatic interaction $E_{bar}(r,R)$ of the present process can be approximated as

$$E_{bar}(r,R) = \Delta E_1^* \exp[-\tau(r-a)] + \Delta E_1^* \exp[-\tau(R-r-a)] - \frac{\ell}{R-r}, \quad (21)$$

where ΔE_1^* is the ''effective'' *correlational* energy gained by the first OC at one macroion surface assumed identical for both colloids. The last term in Eq. (21) corresponds to the additional monopole attractive contribution of the displaced counterion with the undercharged colloid. Fitting parameters (ΔE_1^* and τ) for $R/a = 2.4$ and $R/a = 4.25$ can be found in Tables IV and V, respectively. Same values of τ were used here as those of the single macroion case (see Fig. 9 and Table II) . However for the small colloidal separation ($R/a = 2.4$), due to the extra intercolloidal surface counterions correlations, we used a slightly larger (absolute) value for ΔE_1^* compared to the one (ΔE_1) of an isolated colloid (compare Tables IV and V). This is compatible with the idea that between the two colloids (especially when both spheres come at contact), we have the formation of a ''superlayer'' that is more dense, thus leading to a smaller hole radius and a higher energy gain. An analysis of the counterions structure of the two macroions reveals that both WC counterion layers are interlocked, that is the projection along the axis passing through the colloid centers gives a superlattice structure (see Fig. 12).

For large colloidal separation ($R/a = 4.25$), the WC structure on one of the colloids is unperturbed by the presence of

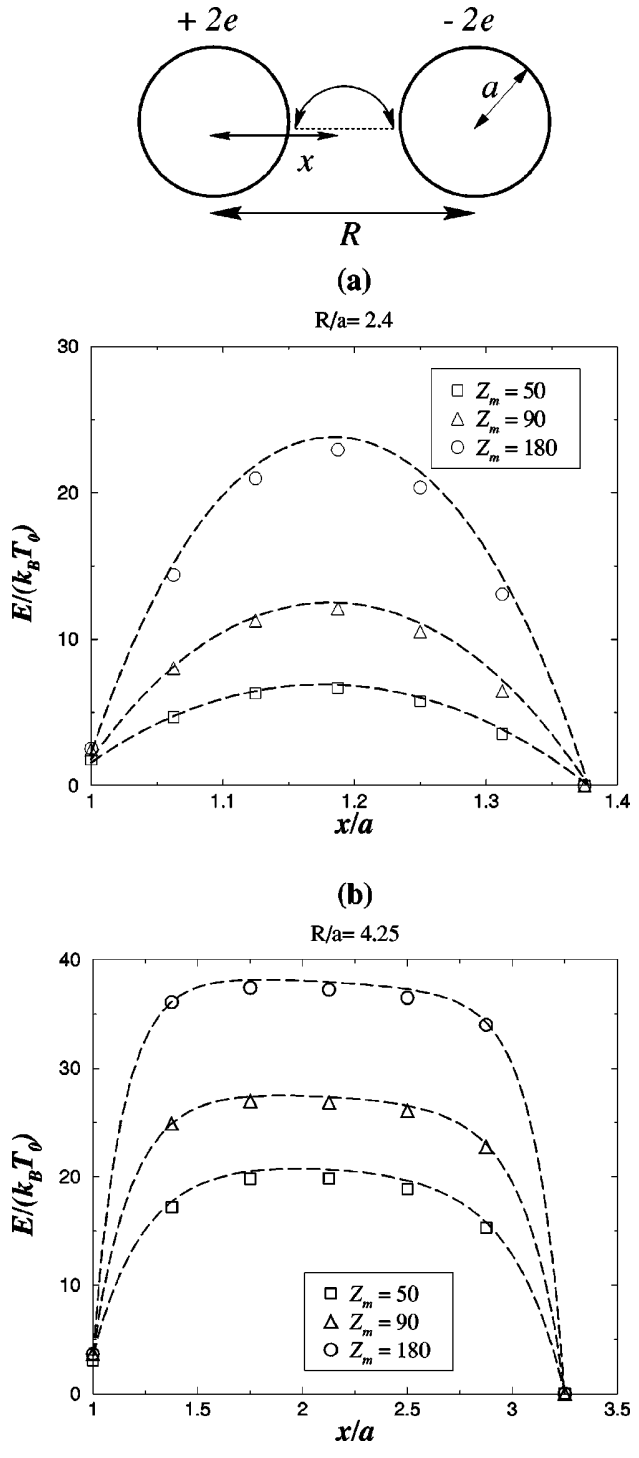

FIG. 11. Total electrostatic energy (in units of k_BT_0) of the system, for *zero temperature* configurations, of two macroions at a center-center separation of (a) $R/a=2.4$ (b) $R/a=4.25$ as a function of one displaced counterion distance from the left macroion for three typical values Z_m. The exact neutral state was chosen as the potential energy origin. The schematic drawing indicates the path (dotted line) of the moved counterion. The ending arrows of the arc indicate the start position (left sphere) and final position (right sphere) of the moved counterion. Dashed lines correspond to the fit using Eq. (21) of which parameters can be found in Tables IV and V.

TABLE IV. Measured value of the energy barrier and fit parameters of the electrostatic interaction process involved in Fig. 11(a) for $R/a=2.4$ and for for different macroion bare charges.

Z_m	$\Delta E_{bar}/k_BT_0$	$\Delta E_1^*/k_BT_0$	$\tau\sigma$
50	4.9	−20.4	0.51
90	9.6	−27.5	0.68
180	20.4	−39.4	0.92

the other, hence we can take $\Delta E_1^*=\Delta E_1$, and our simulation data can nicely be fitted by the parameters inferred from the single colloid system.

3. Effective forces

Results concerning the effective forces at *zero temperature* between the two macroions are now investigated which expression is given by

$$F_{eff}(R)=F_{mm}(R)+F_{LJ}+F_{mc}, \tag{22}$$

where $F_{mm}(R)$ is the direct Coulomb force between macroions, F_{LJ} is the excluded volume force between a given macroion and its surrounding counterions and F_{mc} is the Coulomb force between a given macroion and all the counterions. Because of symmetry, we focus on one macroion. To understand the extra-attraction effect of these ionizedlike states, we consider three cases: (i) $F_{ion}=F_{eff}$ in the ionized state with a charge asymmetry of $\pm$ 1 counterion (ii) $F_{neut}=F_{eff}$ in the neutral case (iii) $F_{mono}=F_{eff}$ simply from the effective monopole contribution. Our results are displayed in Fig. 13 for $Z_m=180$, where the ionized state was also observed at room temperature. The noncompensated case leads to a very important extra attraction. This becomes drastic for the charge asymmetry of ± 2 counterions at short separation $R/a=2.4$ leading to a reduced effective attractive force $Fl_B=-10.7$, a situation that was also observed in our simulation at room temperature. In contrast to previous studies [15,16], these attractions are long range. For a sufficiently large macroion separation (from $3.5a$), corresponding here roughly to a macroion surface-surface separation of one colloid diameter, the effective force approaches in good approximation the monopole contribution (see Fig. 13).

B. Asymmetrically charged colloids

In this section we investigate the case where the two colloids have different charge densities. We will keep the colloidal radii a fixed, but vary the bare colloidal charges. The

TABLE V. Measured value of the energy barrier and fit parameters of the electrostatic interaction process involved in Fig. 11(b) for $R/a=4.25$ and for different macroion bare charges.

Z_m	$\Delta E_{bar}/k_BT_0$	$\Delta E_1^*/k_BT_0$	$\tau\sigma$
50	16.8	−18.4	0.51
90	23.3	−24.4	0.68
180	33.8	−35.3	0.92

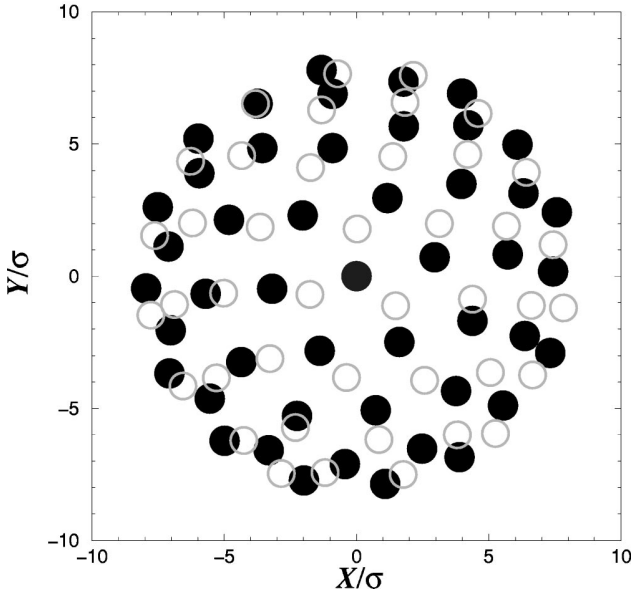

FIG. 12. Projection of the counterion positions, located on both inner (face to face) hemispheres, along the symmetrical axis passing through the macroion centers. Open (filled) circles are counterions belonging to macroion $A(B)$. One clearly sees the interlocking of the two ordered structures yielding locally to a superlattice.

charge on sphere A is *fixed* at $Z_A=180$, and sphere B carries *variable* charges with Z_B (where $Z_B<Z_A$) ranging from 30 up to 150. Global electroneutrality is ensured by adding N_A+N_B divalent counterions, with $N_A=Z_A/Z_c$, and $N_B=Z_B/Z_c$. In this way we vary the bare counterion concentrations $c_i=\sqrt{N_i/4\pi a^2}$, where i stands for A or B.

1. Ground state analysis

We start out again with studying the ground state of such a system. The electrostatic energy of the system is investigated for different uncompensated bare charge cases (ionized states) by simply summing up Eq. (4) over all Coulomb pairs. We define the *degree of ionization* (DI) as the number of counterions overcharging colloid A (or, equivalently, undercharging colloid B). The system is prepared at various DI and we measure the respective energies. These states are separated by kinetic energy barriers, as was demonstrated above. We consider three typical macroionic charges Z_B (30, 90, and 150) and separations R/a (2.4, 3.0, and 4.25). The main results of the present section are given in Fig. 14. For the largest separation $R/a=4.25$ and largest charge $Z_B=150$ [see Fig. 14(a)], one notices that the ground state corresponds to the classical compensated bare charge situation [referred as the *neutral state* (DI of 0)]. Moreover the energy increases stronger than linear with the degree of ionization. If one diminishes the bare charge Z_B to 90 and 30, the *ground state* is actually the ionized state for a DI of 1 and 3, respectively. The ionized ground state is about 8 and 36 , respectively, lower in energy compared to the neutral state. This shows that even for a relative large colloid separation, stable ionized states should exist for sufficient low temperatures and that their stability is a function of their charge asymmetry.

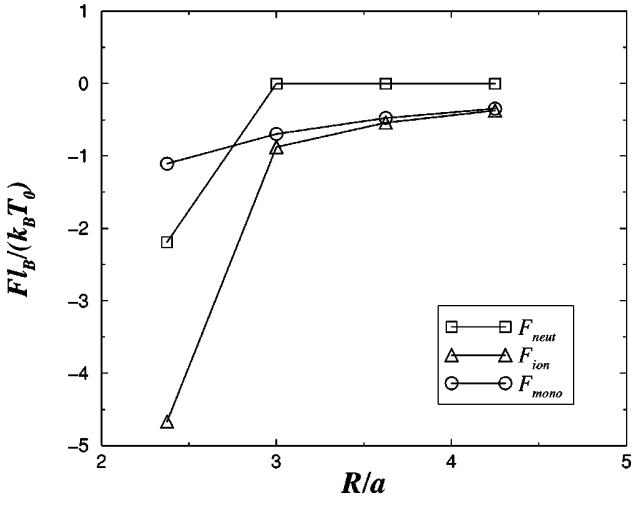

FIG. 13. Reduced effective force between the two spherical macroions at *zero temperature* for $Z_m=180$ as a function of distance from the center. The different forces are explained in the text. The lines are a guide to the eye.

For a shorter separation $R/a=3.0$, ionized ground states are found [see Fig. 14(b)] for the same charges Z_B as previously. Nevertheless, in the ground state the DI is now increased and it corresponds to 2 and 4 for $Z_B=90$ and 30, respectively. The gain in energy is also significantly enhanced. For the shortest separation under consideration $R/a=2.4$ [see Fig. 14(c)], the ground state corresponds for *all* investigated values of Z_B to the ionized state, even for $Z_B=150$. We conclude that decreasing the macroion separation R enhances the degree of ionization and the stability of the ionized state.

To understand this ionization phenomenon, it is sufficient to refer to an *isolated* macroion surrounded by its neutralizing counterions. We have investigated the energies involved in the ionization (taking out counterions). The complementary process of overcharging (adding counterions) has already been investigated (see Fig. 5). A derivation of the formula describing the ionization energy ΔE^{ion} proceeds completely analogously to the one carried out for the overcharging Eq. (13) and gives for the nth degree of ionization

$$\Delta E_n^{ion}=-\frac{\alpha^B\ell}{\sqrt{A}}[(N_B-n)^{3/2}-N_B^{3/2}]+\frac{\ell}{a}\frac{n^2}{2}, \qquad (23)$$

where $\alpha^{A,B}$ are the values of α belonging to colloid A and B, respectively. In Fig. 15 we compare the predictions of Eqs. (13) and (23) to our simulation data, which shows excellent agreement. Our numerical data for ΔE_1^{ion} for $N_B=15$, 45, and 75, the value of ΔE_1^{OC} for $N_A=90$ (overcharging process), as well as the corresponding values for α, which have been used for Fig. 15 can be found in Table II.

With the help of Eqs. (13) and (23), one can try to predict the curves of Fig. 14 for finite center-center separation R. Using for colloid A and B the measured values α^A and α^B, we obtain for the electrostatic energy difference at finite center-center separation R

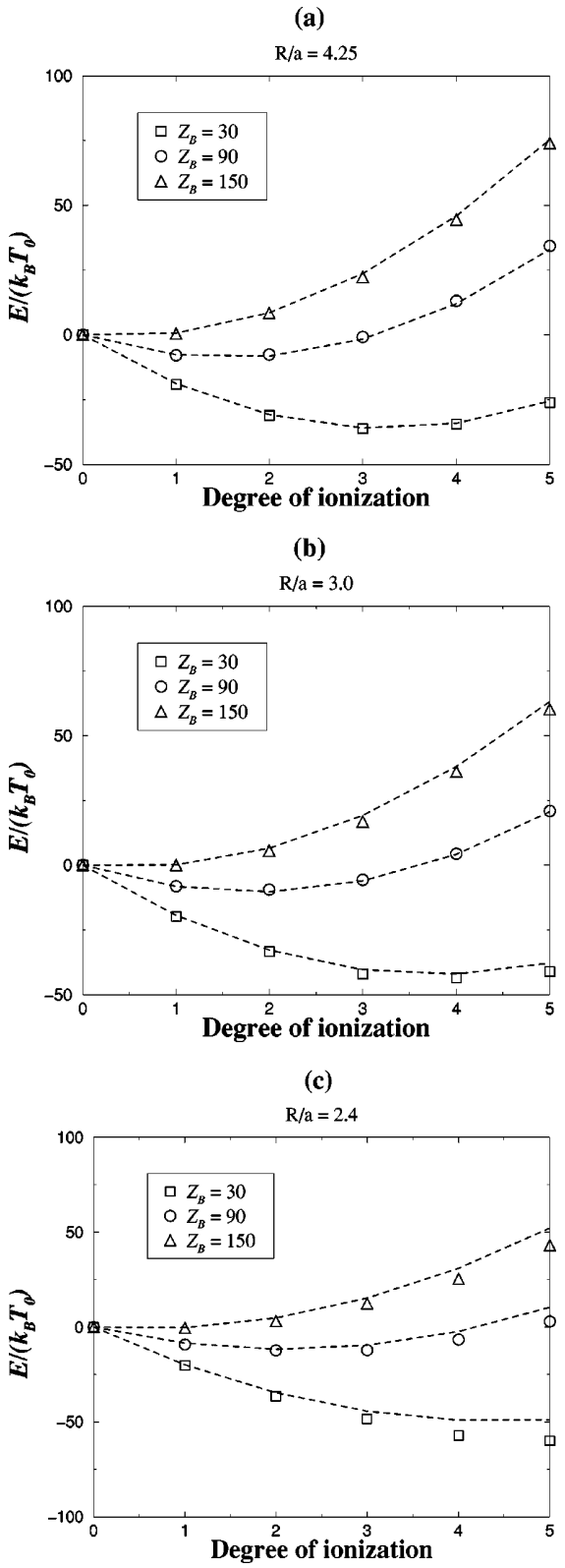

FIG. 14. Total electrostatic energy as a function of the degree of ionization for zero temperature configurations of two colloids (A and B), for three typical charges Z_B (30, 90, and 150) for macroion B and for three given distance separations: (a) $R/a=4.25$, (b) $R/a=3.0$ and (c) $R/a=2.4$. Dashed lines were obtained using Eq. (24).

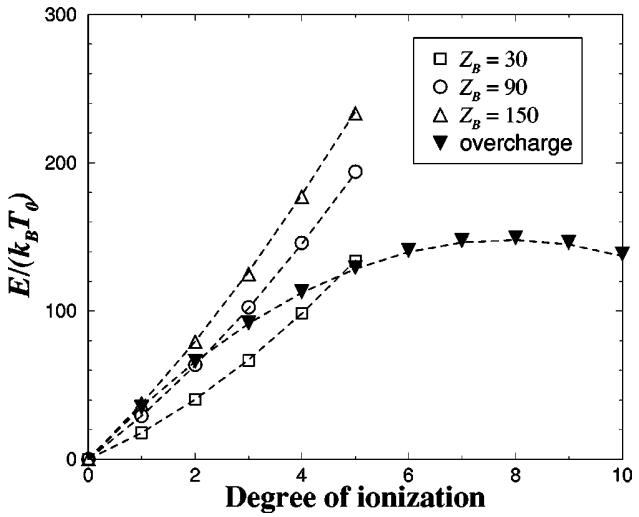

FIG. 15. Total electrostatic energy as a function of the degree of ionization for zero temperature configurations of an *isolated* colloid. The three upper curves correspond to the ionization energy for the three typical charges Z_B (30, 90, and 150). The lower curve corresponds to the energy gained (changed sign for commodity) by overcharging ($Z_A=180$). Dashed lines were obtained using Eqs. (13) and (23) with the measured values for α from Table II.

$$\begin{aligned}\Delta E_n(R) &= \Delta E_n^{ion} + \Delta E_n^{OC} \\ &= \frac{3n\alpha^B \ell}{2\sqrt{A}}\sqrt{N_B}\left[1-\frac{n}{4N_B}+\mathcal{O}\left(\frac{n^2}{N_B^2}\right)\right] \\ &\quad -\frac{3n\alpha^A \ell}{2\sqrt{A}}\sqrt{N_A}\left[1+\frac{n}{4N_A}+\mathcal{O}\left(\frac{n^2}{N_A^2}\right)\right] \\ &\quad +\frac{n^2\ell}{a}\left(1-\frac{a}{R}\right). \end{aligned} \tag{24}$$

The quality of the theoretical curves can be inspected in Fig. 14. The prediction is is very good for large separations, but the discrepancies become larger for smaller separations, and one observes that the actual simulated energies are lower. Improvements could be achieved by including polarization effects along the ideas leading to Eq. (21), by adjusting, for example, α^A and α^B. More important, the physical interpretation of Eq. (24) is straightforward. The left two terms represent the difference in correlation energy, and last term on the right the monopole penalty due to the ionization and overcharging process. This means that the correlational energy gained by overcharging the highly charged colloid A must overcome the loss of correlation energy as well as the monopole contribution (*two* penalties) involved in the ionization of colloid B. With the help of Eq. (24) we can establish a simple criterion (more specifically a sufficient condition), valid for large macroionic separations, for the charge asymmetry $\sqrt{N_A}-\sqrt{N_B}$ to produce an ionized ground state of two unlike charged colloids with the same size,

$$(\sqrt{N_A}-\sqrt{N_B}) > \frac{4\sqrt{\pi}}{3\alpha} \approx 1.2. \tag{25}$$

Referring to Fig. (15) this criterion is met when the overcharge curve (changed sign) is higher than the ionization curve.

If one uses the parameters of the present study one finds the requirement $N_B < 66$ to get a stable ionized state. This is consistent with our findings where we show in Fig. 14 that for $N_B = 75$, and $R/a = 4.25$, no ionized ground state exists whereas for $N_B = 60$ we observed one even for infinite separation (not reported here). The criterion Eq. (25) is merely a sufficient condition, since we showed in Fig. 14 that when the colloids are close enough, this ionized state can appear even for smaller macroion charge asymmetry due to enhanced intercolloidal correlations. At this stage, we would like to stress again, that the appearance of a stable ionized ground state is due merely to correlation. An analogous consideration with smeared out counterion distributions along the lines of Eq. (7) will again always lead to two colloids exactly neutralized by their counterions [33]. Our energetical arguments are quite different from the situation encountered at finite temperatures, because in this case even a Poisson-Boltzmann description would lead to an asymmetric counterion distribution. However, in the latter case this happens due to pure entropic reasons, namely, in the limit of high temperatures, the counterions want to be evenly distributed in space, leading to an effective charge asymmetry.

At this stage, on looking at the results presented above, it appears natural and straightforward to establish an analogy with the concept of ionic bonding. It is well known in chemistry that the electronegativity concept provides a simple yet powerful way to predict the nature of the chemical bonding [34]. If one refers to the original definition of the electronegativity given by Pauling [34]: ''the power of an atom in a molecule to attract electrons to itself,'' the role of the bare charge asymmetry becomes obvious. Indeed, it has an equivalent role at the mesoscopic scale as the electron affinity at the microscopic scale. Another interesting analogy is the influence of the colloidal separation on the stability of the ionized state. Like in diatomic molecules, the ionized state will be (very) stable only for sufficiently short colloid separations. Nevertheless, one should not push this analogy too far. One point where it breaks down concerns the existence of an ionized ground state in colloidal system for *large* colloid separation, providing that the difference in the counterion concentration on the surface is large enough. In an atomistic system this is impossible since even for the most favorable thermodynamical case, namely, CsCl, there is a cost in energy to transfer an electron from a cesium atom to a chlorine atom. Indeed, the smallest existing ionization energy (for Cs, 376 $\mathrm{kJ\,mol^{-1}}$) is greater in magnitude than the largest existing electron affinity (for Cs, 349 $\mathrm{kJ\,mol^{-1}}$). In other terms, for atoms separated by large distances in the gas phase, electron transfer to form ions is always energetically unfavorable.

2. Finite temperature analysis

As a last result, aimed at experimental verification, we show that an ionized state can also exist *spontaneously* at *room temperature* T_0. Figure 16 shows the time evolution of the electrostatic energy of a system $Z_A = 180$ with $Z_B = 30$,

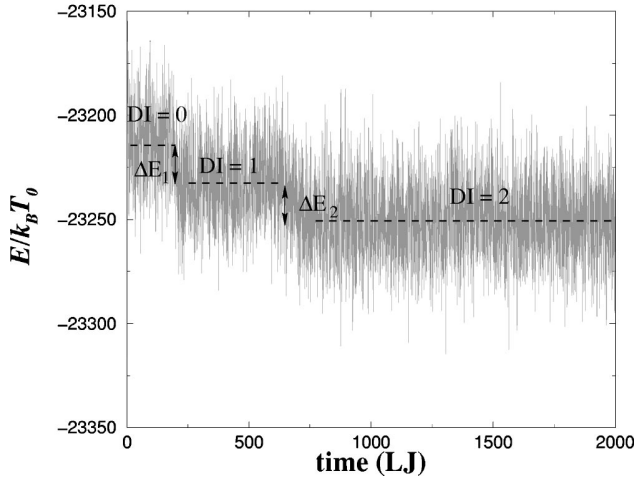

FIG. 16. Relaxation, at room temperature $T_0 = 298$ K, of an initial unstable neutral state towards ionized state. Plotted is the total electrostatic energy versus time (LJ units), for $Z_B = 30$ and $R/a = 2.4$. Dashed lines lines represent the mean energy for each DI state. Each jump in energy corresponds to a counterion transfer from the macroion *B* to macroion *A* leading to an ionized state (DI of 2) which is lower in energy than the neutral one. The two energy jumps $\Delta E_1/k_BT_0 = -19.5$ and $\Delta E_2/k_BT_0 = -17.4$ are in very good agreement with those of Fig. 14(c) (-20.1 and -16.3).

$R/a = 2.4$ and $f_m = 7 \times 10^{-3}$, where the starting configuration is the neutral state (DI of 0). One clearly observes two jumps in energy, $\Delta E_1 = -19.5$ and $\Delta E_2 = -17.4$, each of which corresponds to a counterion transfer from colloid *B* to colloid *A*. These values are consistent with the ones obtained for the ground state, which are -20.1 and -16.3, respectively. Note that this ionized state (DI of 2) is more stable than the neutral but is expected to be metastable, since it was shown previously that the most stable ground state corresponds to DI of 5. The other stable ionized states for higher DI are not accessible with reasonable computer time because of the high energy barrier made up of the correlational term and the monopole term that increases with DI. In Fig. 17 we display a typical snapshot of the ionized state (DI of 2) of this system at room temperature.

Obviously, these results are not expected by a DLVO theory even in the asymmetric case (see, e.g., [35]). Previous simulations of asymmetric (charge and size) spherical macroions [36] were also far away to predict such a phenomenon since the Coulomb coupling was weak (water, monovalent counterions).

VI. CONCLUDING REMARKS

In summary, we have shown that the ground state of a charged sphere in the presence of excess counterions is *always* overcharged. A sufficiently charged colloid can in principle be highly overcharged due to counterion mediated correlation effects, and this phenomenon is quantitatively well described by a simple version of Wigner crystal theory. In the strong Coulomb coupling regime, the energy gain of a single excess ion close to a counterion layer can be of the order of many tens of k_BT_0. Furthermore we demonstrated

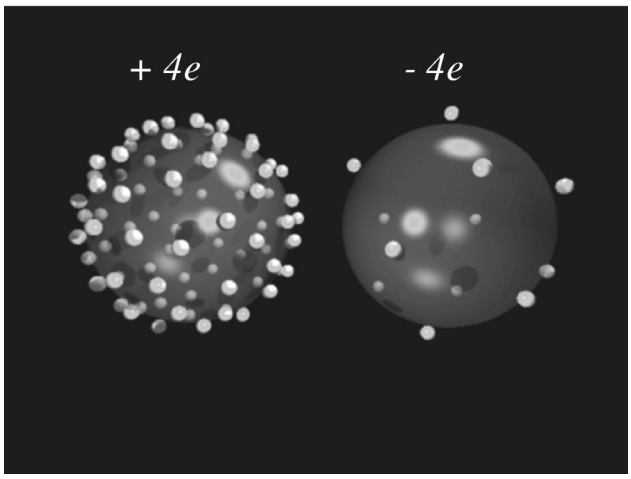

FIG. 17. Snapshot of the ionized state (DI of 2) obtained in the relaxation process depicted in Fig. 16, with the net charges $+4e$ and $-4e$ as indicated.

that the electrostatic interaction between a counterion and a macroion effectively neutralized by its counterions decays exponentially on a length scale which is equal to the Wigner crystal hole radius.

We further found that for two *like-charged* macroions (symmetric case), an initially randomly placed counterion cloud of their neutralizing divalent counterions may not be equally distributed after relaxation, leading to two macroions of opposite net charges. This is due to the short range WC attraction that leads to this energetically favorable overcharged state. The resulting configuration is metastable, however separated by an energy barrier of several $k_B T_0$ when the bare charge is sufficiently large, and can thus survive for long times. Such configuration possess a natural strong long range attraction.

In return, if the symmetry in the counterion concentration on the colloidal surface is sufficiently broken, the ionized state can be *stable*. The ground state of such a system is mainly governed by two important parameters, namely, the asymmetry in the counterion concentration determined by $\sqrt{c_A}-\sqrt{c_B}$, and the colloid separation R. If the counterion concentration difference is high enough, the ground state corresponds to an ionized state, whatever the macroions separation R is. However, the degree of ionization depends on R. Besides, for large R, we have established a criterion, allowing to predict when a stable ionized configuration can be expected. The counterion concentration difference plays an analogous role to the electron affinity between two atoms forming a molecule with ionic bonding. We demonstrated that the results presented here for the ground state can lead to a stable ionic state even at room temperature provided that the Coulomb coupling and/or the counterion concentration asymmetry is sufficiently large. This is also a possible mechanism that could lead to strong long range attractions, even in bulk. Future work will treat the case where salt ions are present.

ACKNOWLEDGMENTS

This work was supported by *Laboratoires Européens Associés* (LEA) and a computer time Grant No. hkf06 from NIC Jülich. We acknowledge helpful discussions with B. Jönsson, R. Kjellander, H. Schiessel, and B. Shklovskii.

[1] D. H. Everett, *Basic Principles of Colloidal Science* (Royal Society of Chemistry, London, 1988).
[2] G. M. Kepler and S. Fraden, Phys. Rev. Lett. **73**, 356 (1994).
[3] J. C. Crocker and D. G. Grier, Phys. Rev. Lett. **77**, 1897 (1996).
[4] A. E. Larsen and D. G. Grier, Nature (London) **385**, 230 (1997).
[5] B. V. Derjaguin and L. D. Landau, Acta Physicochim. URSS **14**, 633 (1941).
[6] E. J. Verwey and J. T. G. Overbeek, *Theory of the stability of Lyophobic Colloids* (Elsevier, Amsterdam, 1948).
[7] T. M. Squires and M. P. Brenner, Phys. Rev. Lett. **85**, 4976 (2000).
[8] N. Ise *et al.*, J. Chem. Phys. **78**, 536 (1983).
[9] K. Ito, H. Yoshida, and N. Ise, Science **263**, 66 (1994).
[10] B. V. R. Tata, E. Yamahara, P. V. Rajamani, and N. Ise, Phys. Rev. Lett. **78**, 2660 (1997).
[11] R. van Roij and J.-P. Hansen, Phys. Rev. Lett. **79**, 3082 (1997).
[12] B. I. Shklovskii, Phys. Rev. Lett. **82**, 3268 (1999).
[13] R. R. Netz and H. Orland, Europhys. Lett. **45**, 726 (1999).
[14] M. Tokuyama, Phys. Rev. E **59**, R2550 (1999).
[15] N. Grønbech-Jensen, K. M. Beardmore, and P. Pincus, Physica A **261**, 74 (1998).
[16] E. Allahyarov, I. D'Amico, and H. Löwen, Phys. Rev. Lett. **81**, 1334 (1998).
[17] J. Z. Wu, D. Bratko, H. W. Blanch, and J. M. Prausnitz, J. Chem. Phys. **111**, 7084 (1999).
[18] P. Linse and V. Lobaskin, Phys. Rev. Lett. **83**, 4208 (1999).
[19] R. Messina, C. Holm, and K. Kremer, Phys. Rev. Lett. **85**, 872 (2000).
[20] R. Messina, C. Holm, and K. Kremer, Europhys. Lett. **51**, 461 (2000).
[21] A theory that predicts molecular geometries using the notion that valence electron pairs occupy sites around a central atom in such a way as to minimize electron-pair repulsion. See for example, D. W. Oxtoby, H. P. Gillis, and N. H. Nachtrieb, *Principles of Modern Chemistry* (Saunders College Publishing, Fort Worth, TX, 1999), Chap. 3, p. 80.
[22] R. J. Gillespie, J. Chem. Educ. **40**, 295 (1963); Struct. Chem. **9**, 73 (1998).
[23] Since we are using MD simulations, to avoid barrier energy problem the counterions were generated in the vicinity of the colloidal surface.
[24] B. I. Shklovskii, Phys. Rev. E **60**, 5802 (1999).
[25] I. Rouzina and V. A. Bloomfield, J. Chem. Phys. **100**, 9977 (1996).

[26] This is certainly justified if the counterion-counterion distance is smaller than the curvature radius of the macroion.
[27] E. E. Salpeter, Ann. Phys. (N.Y.) **5**, 183 (1958); R. Abe, Prog. Theor. Phys. **22**, 213 (1959); M. Baus, J.-P. Hansen, Phys. Rep. **59**, 1 (1980).
[28] L. Bonsall and A. A. Maradudin, Phys. Rev. B **15**, 1959 (1977).
[29] T. T. Nguyen, A. Yu. Grosberg, and B. I. Shklovskii, *Electrostatic Effects in Soft Matter and Biophysics*, in Proceedings of the Les Houches School, edited by C. Holm, P. Kékicheff, and R. Podgornik (Kluwer, Dordrecht, 2001).
[30] Note that his expression differs slightly from the one used in Refs. [19,20].
[31] R. Messina, C. Holm, and K. Kremer, Eur. Phys. J. E **4**, 363 (2001).
[32] R. Messina, e-print cond-mat/0104076.
[33] H. Schiessel (private communication).
[34] L. Pauling, *The Nature of the Chemical Bond* (Cornell University Press, New York, 1939).
[35] B. D'Aguanno and R. Klein, Phys. Rev. A **46**, 7652 (1992).
[36] E. Allahyarov, H. Löwen, and S. Trigger, Phys. Rev. E **57**, 5818 (1998).

Appendix D

Effect of colloidal charge discretization in the primitive model

Eur. Phys. J. E **4**, 363–370 (2001)

THE EUROPEAN PHYSICAL JOURNAL E

EDP Sciences

Effect of colloidal charge discretization in the primitive model

R. Messina[a], C. Holm, and K. Kremer

Max-Planck-Institut für Polymerforschung, Ackermannweg 10, 55128, Mainz, Germany

Received 30 June 2000 and Received in final form 28 November 2000

Abstract. The effect of fixed discrete colloidal charges in the primitive model is investigated for spherical macroions. Instead of considering a central bare charge, as it is traditionally done, we distribute *discrete* charges randomly on the sphere. We use molecular dynamics simulations to study this effect on various properties such as overcharging, counterion distribution and diffusion. In the vicinity of the colloid surface the electrostatic potential may considerably differ from the one obtained with a central charge. In the strong Coulomb coupling, we showed that the colloidal charge discretization qualitatively influences the counterion distribution and leads to a strong colloidal charge-counterion pair association. However, we found that *charge inversion* still persists even if strong pair association is observed.

PACS. 82.70.Dd Disperse systems: Colloids – 61.20.Qg Structure of associated liquids: electrolytes, molten salts, etc. – 41.20.-q Applied classical electromagnetism

1 Introduction

The electrostatic interactions in charged colloidal systems play a crucial role in determining the physical properties of such materials [1,2]. The behavior of these systems is extremely complex due to the *long-range* Coulomb interactions. A first simplifying assumption is to treat the solvent as a dielectric medium solely characterized by its relative permittivity ϵ_{r}. A second widely used approximation consists in modeling the *short-range* ion-ion excluded-volume interaction by hard spheres. These two approximations are the basis of the so-called primitive model of electrolyte solutions. The system under consideration is an asymmetrical polyelectrolyte made up of highly charged macroions and small counterions in solution. A further simplification can be achieved by partitioning the system into subvolumes (cells), each containing one macroion together with its neutralizing counterions plus, if present, additional salt. This approximation has been called accordingly the cell model [3,4]. The cells assume the symmetry of the macroion, here spherical, and are electrostatically decoupled. In this way one has reduced a complicated many-body problem to an effective one-colloid problem. For spherical macroions the structural charge is normally modeled by a *central* charge, which, by Gauss theorem, is equivalent to considering a *uniform* surface charge density as far as the electric field *outside* the sphere is concerned.

Most analytical work as well as simulation approaches rely on the above assumptions. It is well known that in the strong Coulomb coupling regime ion-ion correlations become very important, and significant deviations from mean-field approaches are expected. One of the effects which a mean-field theory like the Poisson-Boltzmann one cannot explain is the phenomenon of overcharge, also called charge inversion. It consists of binding excess counterions to a charged particle (macroion) so that its net charge changes sign. This has recently attracted significant attention [5–14]. It may give rise to a possible mechanism for strong long-range attraction between like-sign charged colloids [12,13].

The purpose of this paper is to investigate if such a phenomenon (overcharge) depends on the way the structural charge is represented. The macroion is taken to be perfectly spherical, *i.e.* we neglect any surface roughness [15]. We introduce discrete charges on the macroion sphere instead of a central charge, and compare the results to those obtained with a central charge. We concentrate on the following properties in the strong Coulomb coupling: overcharging, counterion distribution and surface diffusion.

2 Simulation model

2.1 Macroion charge discretization

The macroion charge discretization is produced by using N_{m} identical microions of diameter σ, all identical to the counterions, distributed *randomly* on the surface of the macroion. Then the structural charge is $Q = -Z_{\mathrm{m}}e = -Z_{\mathrm{c}}N_{\mathrm{m}}e$, where $Z_{\mathrm{m}} > 0$, Z_{c} is the counterion valency and e is the positive elementary charge. The discrete colloidal charges (DCC) are *fixed* on the surface of the spherical macroion. In spherical coordinates the elementary surface

[a] e-mail: messina@mpip-mainz.mpg.de

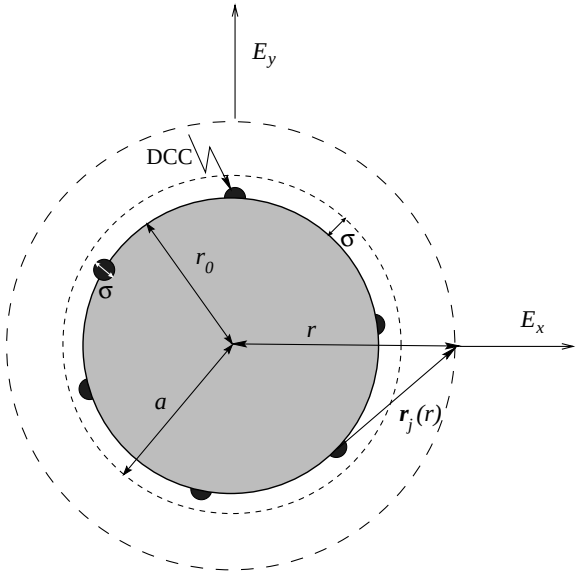

Fig. 1. Schematic view of the setup: the discrete colloidal charges (DCC) of diameter σ are in dark grey. The radial electrostatic field components E_x and E_y are represented. For a detailed meaning of the other symbols, see text. Note that this is a a two-dimensional representation of the three-dimensional system.

is given by

$$\mathrm{d}A = r_0^2 \sin\theta \mathrm{d}\theta \mathrm{d}\varphi = -r_0^2 \mathrm{d}(\cos\theta)\mathrm{d}\varphi \,, \tag{1}$$

and, to produce a random discrete charge distribution on the surface, we generated randomly the variables $\cos\theta$ and φ. Only configurations leading to an overlap of microions are rejected. Figure 1 shows a schematic view of the setup. Note that in real physical systems like sulfonated latex spheres, no large heterogeneities are expected in the charge distribution, provided that the colloid surface is relatively regular, therefore our choice is justified. Nevertheless, the experimental situation is more complicated since other phenomena such as surface chemical reactions [16], hydration, roughness [15] and many more may be present. Here, we restrict ourselves to a simple model in order to understand the effect of macroion charge discretization, and leave the other questions for future investigations.

2.2 Molecular dynamics procedure

We use molecular dynamics (MD) simulations to compute the motion of the counterions coupled to a heat bath acting through a weak stochastic force $\mathbf{W}(t)$. The equation of motion of counterion i reads

$$m\frac{\mathrm{d}^2\mathbf{r}_i}{\mathrm{d}t^2} = -\nabla_i U - m\Gamma\frac{\mathrm{d}\mathbf{r}_i}{\mathrm{d}t} + \mathbf{W}_i(t) \,, \tag{2}$$

where m is the counterion mass, U is the potential force having two contributions: the Coulomb interaction and the excluded-volume interaction and Γ is the friction coefficient. Friction and stochastic force are linked by the dissipation-fluctuation theorem $\langle \mathbf{W}_i(t) \cdot \mathbf{W}_j(t')\rangle = 6m\Gamma k_\mathrm{B}T\delta_{ij}\delta(t-t')$. For the ground state simulations the fluctuation force is set to zero.

Excluded-volume interactions are taken into account with a pure repulsive Lennard-Jones potential given by

$$U_\mathrm{LJ}(r) = \begin{cases} 4\epsilon\left[\left(\frac{\sigma}{r-r_0}\right)^{12} - \left(\frac{\sigma}{r-r_0}\right)^{6}\right] + \epsilon, \text{ for } r - r_0 < r_\mathrm{cut}, \\ \\ 0, \text{ for } r - r_0 \geq r_\mathrm{cut}, \end{cases} \tag{3}$$

where $r_0 = 0$ for the microion-microion interaction (the microion can be a counterion or a DCC), $r_0 = 7\sigma$ for the macroion-counterion interaction, and r_cut $(= 2^{1/6}\sigma)$ is the cut-off radius. This leads to a macroion-counterion distance of closest approach $a = 8\sigma$. Energy and length units in our simulations are defined as $\epsilon = k_\mathrm{B}T_0$ (with $T_0 =$ 298 K), and $\sigma = 3.57$ Å, respectively.

The pair electrostatic interaction between any pair ij, where i and j denote either a DCC or a counterion, reads

$$U_\mathrm{Coul}(r) = k_\mathrm{B}T_0 l_\mathrm{B}\frac{Z_i Z_j}{r} \,, \tag{4}$$

where $l_\mathrm{B} = e^2/4\pi\epsilon_0\epsilon_\mathrm{r}k_\mathrm{B}T_0$ is the Bjerrum length describing the electrostatic strength. Being essentially interested in the strong Coulomb coupling regime, we choose the relative permittivity $\epsilon_\mathrm{r} = 16$ $(l_\mathrm{B} = 10\sigma)$, *divalent* counterions $(Z_\mathrm{c} = 2)$ and *divalent* DCC for the remaining of this paper.

The macroion and the counterions are confined in a spherical impenetrable cell of radius R. The macroion is held fixed and is located at the center of the cell. The colloid volume fraction f_m is defined as r_m^3/R^3, where $r_\mathrm{m} = a - \sigma/2$ is the colloid radius. We have fixed $R = 40\sigma$ so that $f_\mathrm{m} = 6.6 \times 10^{-3}$. To avoid image charge complications, the permittivity ϵ_r is supposed to be identical within the whole cell (including the macroion) as well as outside the cell.

3 Macroion electric field

The first step to understand the effect of colloidal charge discretization consists of estimating the electric field, or equivalently, the electrostatic *potential* generated by such a sphere in the *absence* of counterions. A simple graphical visualization of the field lines is here not possible, since there is no perfect symmetry. Indeed, in the present case the electric field becomes very anisotropic and irregular close to the sphere, which is the most interesting region where correlations are expected to be large. To describe qualitatively the effect of charge discretization on the electrostatic potential, we compute for three perpendicular directions x, y, z the resulting *radial* potentials $V_x(r)$, $V_y(r)$, $V_z(r)$ for one given DCC random distribution as a function of the distance $r \geq a$ from the macroion center. The radial component of the electric field $E_i(r) = -\frac{\partial}{\partial r}V_i(r)$ has the important feature of representing the *attractive*

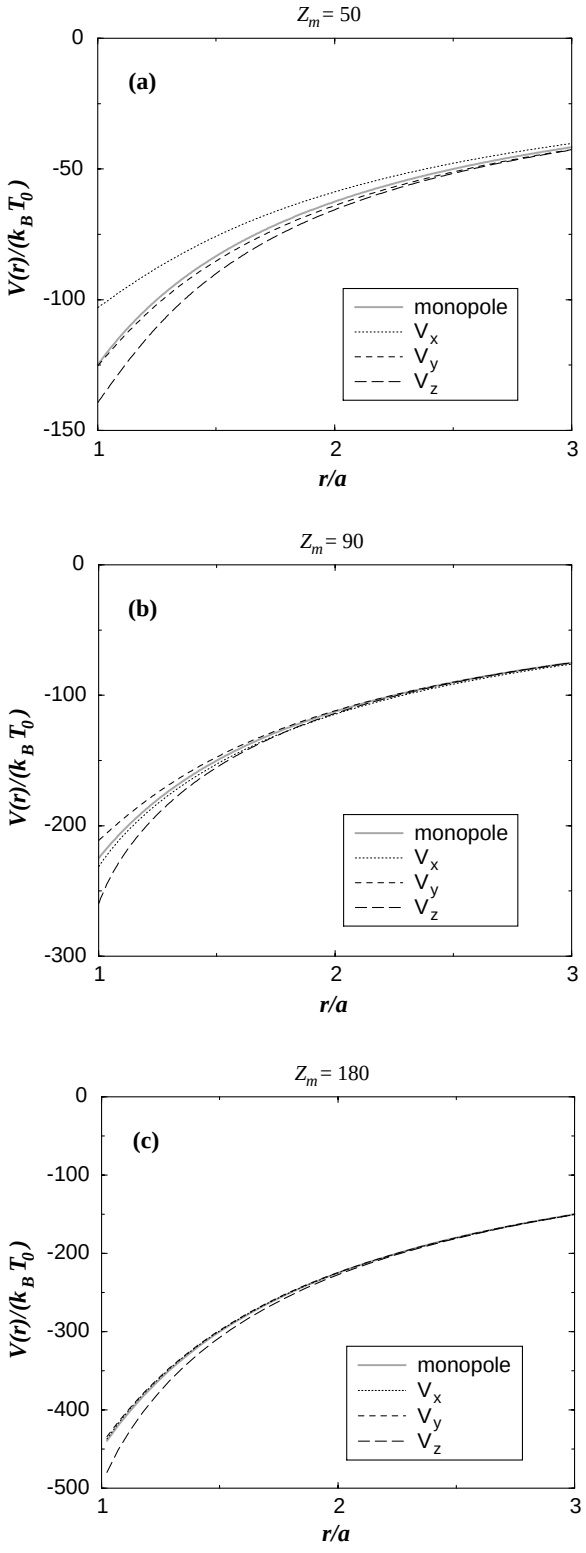

Fig. 2. Radial electrostatic potential as a function of the macroion center distance r produced by the fixed microscopic colloidal charges disposed on the sphere. These potentials have been measured in three perpendicular directions (x, y, z) (see Fig. 1). The isotropic case corresponds to the field obtained with a central charge (monopole). Three structural charges are considered: (a) $Z_{\rm m} = 50$, (b) $Z_{\rm m} = 90$, and (c) $Z_{\rm m} = 180$.

component towards the sphere. The normalized radial potential V_i in the i-th direction at a distance r from the colloid center is given by

$$V_i(r) = -k_{\rm B}T_0 l_{\rm B} Z_{\rm c}^2 \sum_{j=1}^{N_{\rm m}} \frac{1}{|\mathbf{r}_j(r)|}\,, \qquad (5)$$

where $\mathbf{r}_j(r)$ is the vector pointing from the microion j to the point where the electric potential is computed (see Fig. 1). Physically, $V(r)$ is the electrostatic potential interaction between a counterion and all the surface microscopic colloid charges. The monopole contribution is merely given by $V_{\rm mono}(r) = -k_{\rm B}T_0 l_{\rm B}\frac{Z_{\rm m}Z_{\rm c}}{r}$. In Figure 2 we show the electric potential for three typical bare charges, each corresponding to *one* given random macroion charge distribution. For all cases, one notes that in the vicinity of the surface the potential becomes very different from the one computed with a central charge. We carefully checked that similar results were obtained for other choices of x, y, z directions (by rotating the trihedron $(\mathbf{e}_x, \mathbf{e}_y, \mathbf{e}_z)$). However, if we observe the electric field sufficiently far away from the colloidal surface (about one macroion diameter), the field is almost exactly the same as the one produced by a central charge, which we term *isotropic* for the rest of this paper. A closer look at Figure 2 reveals that by increasing the bare charge $Z_{\rm m}$ the electric field starts to become isotropic at smaller distances from the sphere's surface. This last feature can be physically easily interpreted. In fact when one increases the bare charge, one also increases the absolute number of discrete charges which has the effect of approaching the uniform continuous charge density limit (corresponding to the isotropic case).

To capture the discretization effect on the *surface* electrostatic potential, we have measured the electrostatic potential along a circle of radius a concentric to the spherical macroion (see Fig. 1). We start from the top of a given DCC microion and move along a circle in a random direction and measure the electrostatic potential $V(s)$ as a function of the arc length separation s from the starting point. The same formula as equation (5) has been used here. The *constant* monopole contribution is merely given by $V_{\rm mono} = -k_{\rm B}T_0 l_{\rm B}\frac{Z_{\rm m}Z_{\rm c}}{a}$. Results are reported in Figure 3 for the same configurations as before. It clearly shows that the electrostatic potential is strongly fluctuating. More specifically, the higher the structural charge $Z_{\rm m}$, the larger the "oscillation frequency" of the potential fluctuations over the surface. This feature can be explained in terms of "*holes*". In the very vicinity of a given DCC the potential is increased (in absolute value) in average, and around a given DCC there is a hole (depletion of charges) which tends to decrease the potential (in absolute value). The average surface of this hole is increasing with decreasing bare charge $Z_{\rm m}$ (*i.e.* decreasing density of charged sites).

In the following sections we are going to study the effect of charge discretization on the counterions distribution in the strong Coulomb coupling. For all following results we used the same random charge distributions which gave the results of Figures 2 and 3.

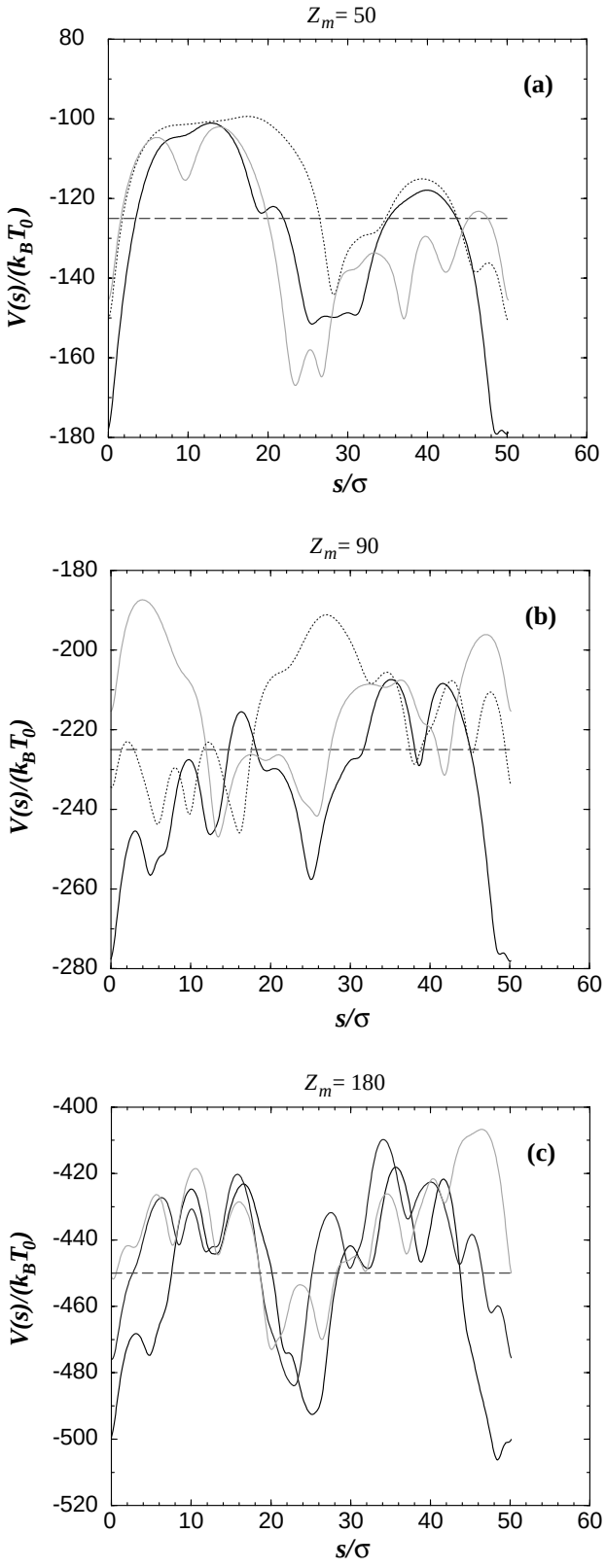

Fig. 3. Surface electrostatic potential as a function of the arc length s along a circle of radius a concentric to the the macroion for three different trajectories. The monopole contribution is represented by the dashed line. The same configurations as those of Figure 2(a-c) have been used.

4 Ground state analysis

In this section, we focus on counterion distribution exclusively governed by *energy minimization*, *i.e.* $T = 0$ K. In such a case correlations are maximal, and all the counterions lie on the surface of the spherical macroion. To avoid the trapping in metastable states, we systematically heat and cool (10 cycles) the system and retain the lowest energy state obtained in this way. Furthermore, we choose as the starting configuration the one where each DCC is exactly associated with one counterion, and each of these *dipoles* is radially oriented (each dipole vector and the macroion center lie on the same line). Preliminary, we checked that this method reproduces well the ground state energy and structure in simple situations where a central charge with two, three, four or five counterions is present. The structure of these systems is well known by the Gillespie rules [17]. It turns out that in these situations no rough energy landscape (even for $Z_{\rm m} = 180$ and 90 counterions) appears and therefore the MD simulation easily finds the global minimum. It is only in the case of DCC that several energy minima are observed.

4.1 Neutral case

First we consider the simple salt-free case where the system [macroion + counterions] is neutral. In order to characterize the counterion layer, we compute the counterion correlation function (denoted by CCF) $g(r)$ on the surface of the sphere, defined as

$$\rho_{\rm s}^2 g(r) = \sum_{i \neq j} \delta(r - r_i)\delta(r - r_j), \tag{6}$$

where $\rho_{\rm s} = N_{\rm c}/4\pi a^2$ is the surface counterion concentration ($N_{\rm c} = Z_{\rm m}/Z_{\rm c}$ being the number of counterions), r corresponds to the arc length on the sphere. Note that at zero temperature all equilibrium configurations are identical, thus only one is required to obtain the CCF. Similarly, one can also define a surface macroion correlation function (MCF) for the microions on the surface of the macroion. The CCF is normalized as follows:

$$\rho_{\rm s} \int_0^{\pi a} 2\pi r g(r) {\rm d}r = (N_{\rm c} - 1)\,. \tag{7}$$

Because of the *finite* size and the topology of the sphere, $g(r)$ has a cut-off at πa ($= 25.1\sigma$). Therefore at "large" distance the correlation function differs from the one obtained with an infinite planar object.

The CCF and MCF for two different structural charges $Z_{\rm m}$ (50 and 180) can be inspected in Figure 4. The CCF is computed for a system with a central charge (CC) and for the discrete colloid charges (DCC) case. One remarks that both CCF differ considerably following the nature of the colloidal charge, *i.e.*, discrete or central (see Fig. 4). For the isotropic case (central charge) a Wigner Crystal structure is observed as was already found in references [12,13, 18]. It turns out that when we have to deal with DCC the

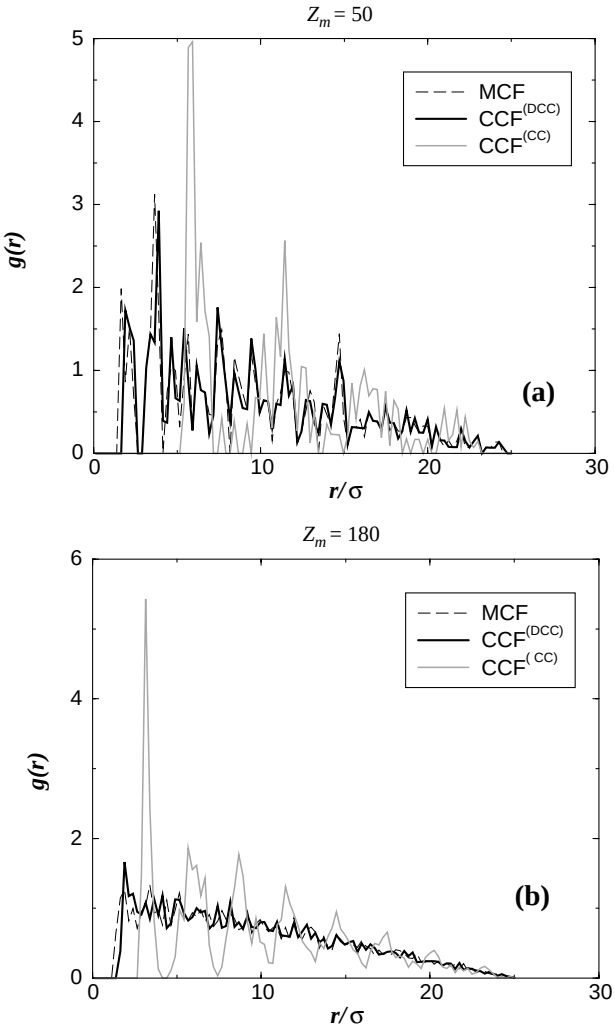

Fig. 4. Ground state surface correlation functions for two macroion bare charges: (a) $Z_{\rm m} = 50$ and (b) $Z_{\rm m} = 180$. The two counterion correlation functions (CCF) are obtained for discrete colloidal charges (DCC) and for the central charge (CC). To get the same distance range for CCF and the colloidal surface discrete microions correlation function (MCF), the MCF curve x-axis (r/σ) was rescaled by a factor a/r_0 (compare the setup of Fig. 1).

counterion distribution is strongly dictated by colloidal charge distribution (see Fig. 4). Ground state structures are depicted in Figure 5. It clearly shows the *ionic pairing*, between DCC and counterions. Also, it appears natural to call such a structure a *pinned* configuration. However, one can expect that the structure might become less pinned if the typical intra-dipole distance (here σ) and the typical mean inter-dipole distance become of the same order. This is a case which is not discussed in the present paper. It would correspond to extremely highly charged colloids that are rarely encountered in nature. Nevertheless, we checked that even for $Z_{\rm m} = 360$ the structure is still pinned, where the average inter-dipole distance is about 2σ.

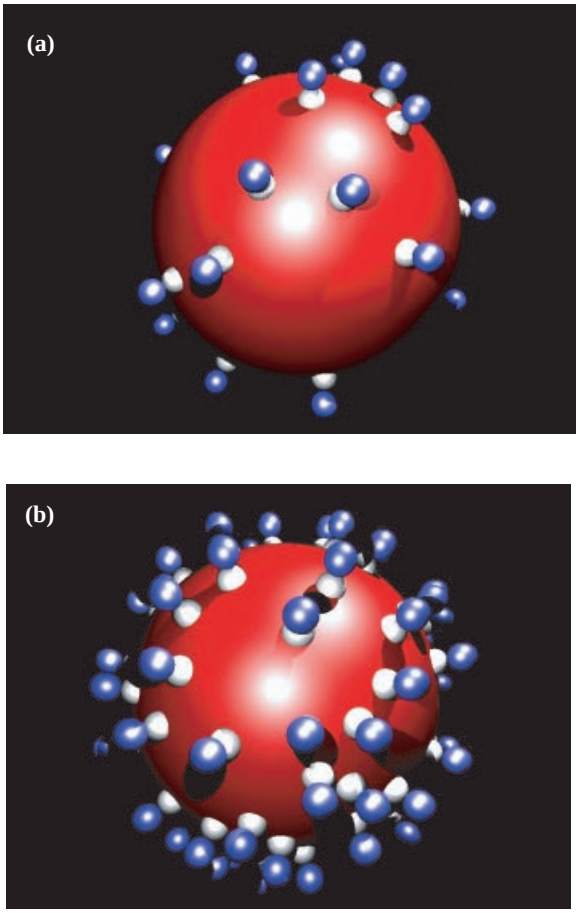

Fig. 5. Ground state structures for two values, (a) $Z_{\rm m} = 50$ and (b) $Z_{\rm m} = 180$, corresponding to the two cases of Figure 4. The colloidal surface microions are in white, and the counterions in blue. Full ionic pairing association occurs.

4.2 Overcharge

We now investigate the overcharge phenomenon. The starting configuration corresponds to neutral ground states as were previously obtained. The spirit of this study is very similar to the one undertaken in reference [12]. To produce overcharge, one adds successively overcharging counterions (OC) in the vicinity of the colloidal surface. Thus the resulting system is no longer neutral. By using Wigner crystal theory [6,19], we showed that the gain in electrostatic energy (compared to the neutral state) by overcharging a single *uniformly* charged colloid can be written in the following way [12,13,18]:

$$\Delta E_n^{\rm OC} = \Delta E^{\rm cor} + \Delta E^{\rm mon} = -n\gamma\sqrt{N_{\rm c}}\left[\frac{3}{2} + \frac{3n}{8N_{\rm c}}\right] + (k_{\rm B}T_0)l_{\rm B}Z_{\rm c}^2\frac{(n-1)n}{2a}\,, \qquad (8)$$

where $\Delta E^{\rm cor}$, which is equal to the first term of the right member, denotes the gain in energy due to ionic correlations for n OC. The functional form of this term can be derived from the WC theory [12,13,18]. The second term on the right-hand side, $\Delta E^{\rm mon}$, is the monopole repulsion, which sets in when the system is overcharged (with

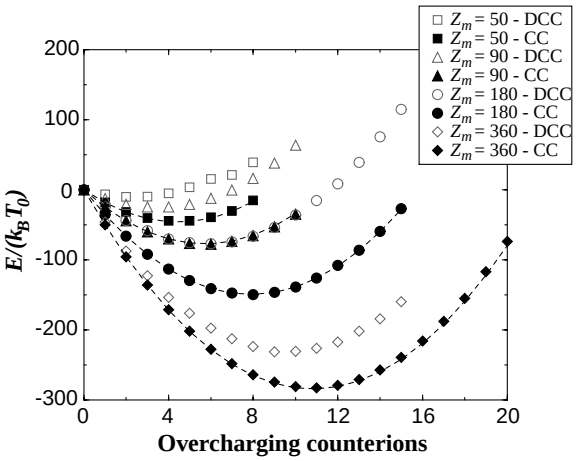

Fig. 6. Electrostatic energy (in units of $k_{\rm B}T_0$) for ground state configurations of a single charged macroion as a function of the number of *overcharging* counterions for three different bare charges $Z_{\rm m}$. CC stands for the central charge case. The neutral case was chosen as the potential energy origin. The dashed lines are produced by using equation (8).

$n > 1$). This term will, for sufficient high number n of OC, stop the process of overcharging. As before $N_{\rm c} = Z_{\rm m}/Z_{\rm c}$ is the number of counterions in the neutral state, and γ is a constant which was determined by using the measured value of $\Delta E_1^{\rm OC}$ of our simulations.

The total electrostatic energy of the system as a function of the number of OC is displayed Figure 6 for four bare charges $Z_{\rm m}$ (50, 90, 180 and 360). These energy curves corresponding to discrete systems were produced by averaging over five random DCC realizations. Again, the overcharging process is affected by the charge discretization and pinning, but it is still energetically *favorable*. The main effects of charge discretization are: i) the reduction of gain of energy and ii) the reduction of maximal (critical) acceptance of OC. Both points can be explained in terms of *ion-dipole* interaction. It is exactly this *attractive* ion-dipole correlation which is responsible of charge inversion for colloidal systems with discrete charges. When the first OC is present, it is normally located in between the pinning centers, and will essentially interact with its neighboring dipoles (DCC-counterion). This interaction increases with decreasing OC-dipole separation, *i.e.* increasing the colloid bare charge $Z_{\rm m}$. This explains why the energy gained increases with $Z_{\rm m}$ (see Fig. 6). On the other hand, the repulsion between the counterions is not fully minimized since they do not adopt the ideal Wigner crystal structure that is obtained with a central charge which in turn explains i). For a higher degree of overcharge, one has to take into account a repulsive monopolar contribution identical to $\Delta E^{\rm mon}$ appearing in equation (8). Again, since for DCC structures counterions are not perfectly ordered, the attractive correlational energy is smaller (in absolute value) than the one obtained with a central charge, which in turn explains ii). Note that for very high bare charge ($Z_{\rm m} = 360$) the overcharge curve obtained with DCC approaches the one from the continuous case as expected.

Common features of overcharging between isotropic and discrete systems are briefly given here. We note that the maximal (critical) acceptance of OC (4, 6 and 8 for a central charge and 2, 4 and 6 for DCC) increases with the macroionic charge $Z_{\rm m}$ (50, 90 and 180, respectively). Furthermore, for a given number of OC, the gain in energy is always increasing with $Z_{\rm m}$. Also, for a given macroionic charge, the gain in energy between two successive overcharged states is decreasing with the number of OC. Note that at $T = 0$, the value $\epsilon_{\rm r}$ acts only as a prefactor. All these features are captured by equation (8).

5 Finite temperature

In this part, the system is brought to room temperature T_0. We are interested in determining the counterions distribution as well as the counterion motion within the counterion layer. The radius R of cell is again fixed to 40σ so that the macroion volume fraction $f_{\rm m}$ has the *finite* value 6.6×10^{-3}. Under these conditions the system is still highly energy-dominated so that at equilibrium all counterions lie on the surface of the macroion (strong condensation).

5.1 Counterions distribution

Like in the ground state analysis, we characterize the counterion distribution via its surface correlation function. At non-zero temperature, correlation functions are computed by averaging $\sum_{i\neq j}\delta(r-r_i)\delta(r-r_j)$ over 1000 independent equilibrium configurations which are statistically uncorrelated. Results are depicted in Figure 7. For both bare charges $Z_{\rm m}$ (50 and 180) considered the counterions distributions are affected by charge discretization. The effect of temperature is to smooth the CCF. As expected, for the central charge case, the counterion positional order is much weaker at room temperature than in the ground state case.

5.2 Surface diffusion

The aim of this section is to answer the following question: do the counterions only oscillate around their equilibrium (ground state) position or do they have also a global translational motion over the sphere?

To answer to this question one introduces the following quantity:

$$\Delta x^2(t,t_0) = \frac{1}{t-t_0}\int_{t_0}^{t} {\rm d}t'[x(t') - x(t_0)]^2\,, \qquad (9)$$

which is referred to as the *mean-square displacement* (MSD), where $x(t_0)$ represents the position of a given counterion at time $t = t_0$ and $x(t,t_0)$ is its position at later time t. The root-mean-square displacement (RMSD)

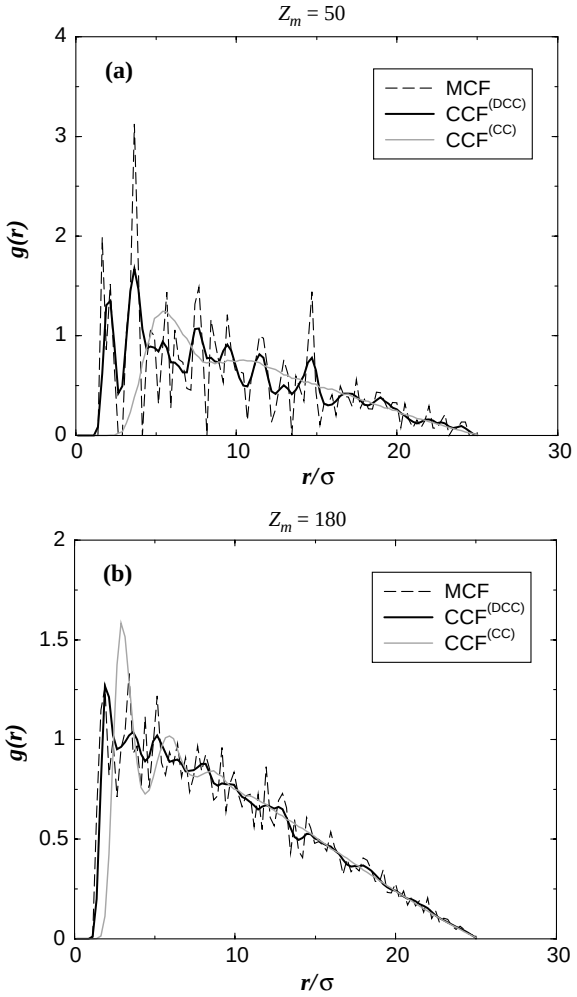

Fig. 7. Surface correlation functions at *room temperature*. The two CCF are obtained for discrete colloidal charges (DCC) and for the central charge (CC). (a) $Z_{\rm m} = 50$, (b) $Z_{\rm m} = 180$.

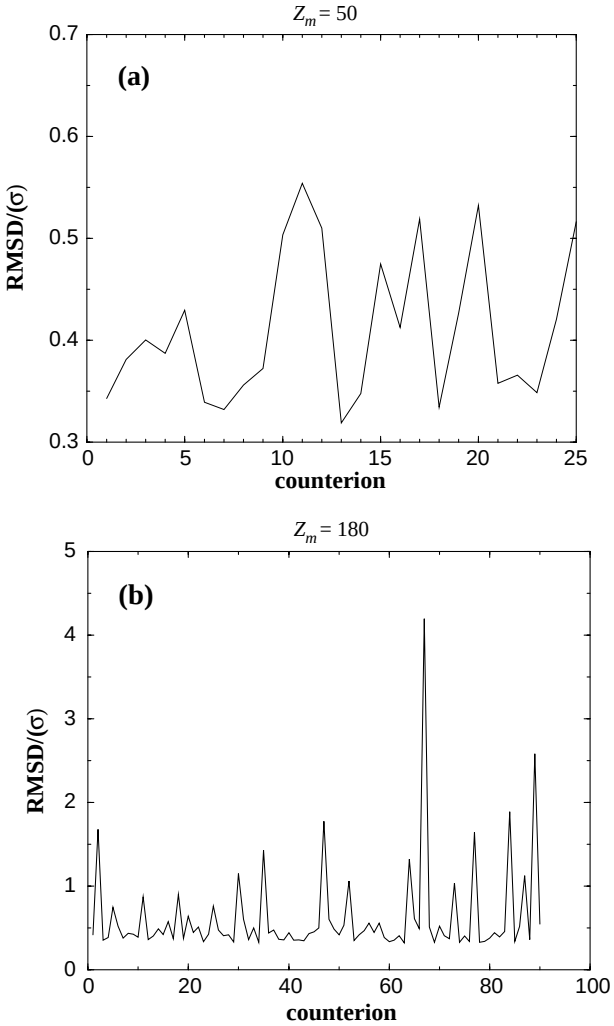

Fig. 8. Root mean square displacement (RMSD) for each counterion; (a) $Z_{\rm m} = 50$, (b) $Z_{\rm m} = 180$.

is defined as $\Delta x(t, t_0) = \sqrt{\Delta x^2(t, t_0)}$. Like for the surface correlation function, the MSD is measured on the spherical surface (arc length) and it has a natural upper limit $(\pi a)^2$. Results for the discrete case are depicted in Figure 8 for two macroion bare charges $Z_{\rm m}$ (50 and 180), where each counterion RMSD is given. In both cases, the RMSD is smaller than the typical mean inter-dipole separation, which is approximatively $(\rho_{\rm s})^{-1/2} \approx 6\sigma$ for $Z_{\rm m} = 50$ and $(\rho_{\rm s})^{-1/2} \approx 3\sigma$ for $Z_{\rm m} = 180$. This suggests that the motion of the counterion is *purely oscillatory* around its DCC pinning center. Figure 8 also shows that pinning is stronger for $Z_{\rm m} = 50$ than for $Z_{\rm m} = 180$. This is in agreement with our previous statement, where we point out that the inter-dipole distance has to be comparable (or smaller) to (than) the intra-dipole distance in order to reduce pinning effect. Thus the DCC sites do produce a noticeable energy well. One can get convinced on this point, by evaluating the electrostatic binding energy of an ionic pair $E_{\rm pin}$ which is

$$E_{\rm pin} = -k_{\rm B}T_0 l_{\rm B} Z_{\rm c}^2/\sigma = -40 k_{\rm B}T_0. \qquad (10)$$

However, for much higher temperatures a liquid-like behavior is to be expected. Also, of course, the strength of the pinning can be lowered by different parameters: larger ions, higher dielectric constant $\epsilon_{\rm r}$, monovalent ions as is captured by equation (10). For the isotropic case, we have checked that counterions have a large lateral motion and can move all over the sphere. This is obvious since in this situation there are no pinning centers.

6 Concluding remarks

We have carried out MD simulations within the framework of the primitive model to elucidate the effect of colloidal charge discretization. The main result of our study is that, in the strong Coulomb coupling, the charge inversion is still effective when the macroion structural charge is carried by discrete charges distributed randomly over its surface area. We have shown that the intrinsic electrostatic potential solely due to the surface colloidal microions varies strongly from point to point on the macroion

sphere. When counterions are present, it leads to a pinned structure where every counterion is associated with one colloidal charge site. Furthermore, we observed a pure phonon-like behavior (counterion vibration with small lateral motion) found at room temperature.

Future work will address the problem of valency asymmetry, that is when the colloidal charges are represented by monovalent counterions and the counterions are multivalent. This is a non-trivial situation since ionic pairing may be frustrated. Also, the case of the weak Coulomb coupling regime should be addressed.

We thank B. Shklovskii for helpful and constructive remarks. This work is supported by *Laboratoires Européens Associés* (LEA).

References

1. J. Israelachvili, *Intermolecular and Surface Forces* (Academic, London, 1992).
2. D.F. Evans, H. Wennerström, *The Colloidal Domain* (Wiley-VCH, New York, 1999).
3. T.L. Hill, *Statistical Mechanics* (Addison-Wesley, Reading, Mass., 1960).
4. H. Wennerström, B. Jönsson, P. Linse, J. Chem. Phys. **76**, 4665 (1982).
5. V. Perel, B. Shklovskii, Physica A **274**, 446 (1999).
6. B. Shklovskii, Phys. Rev. E **60**, 5802 (1999).
7. E.M. Mateescu, C. Jeppesen, P. Pincus, Europhys. Lett. **46**, 493 (1999).
8. J.F. Joanny, Eur. Phys. J. B **9**, 117 (1999).
9. E. Gurovitch, P. Sens, Phys. Rev. Lett. **82**, 339 (1999).
10. M. Lozada-Cassou, E. González-Tovar, W. Olivares, Phys. Rev. E **60**, R17 (1999).
11. M. Deserno, C. Holm, S. May, Macromolecules **33**, 199 (2000).
12. R. Messina, C. Holm, K. Kremer, Phys. Rev. Lett. **85**, 872 (2000).
13. R. Messina, C. Holm, K. Kremer, Europhys. Lett. **51**, 461 (2000).
14. T.T. Nguyen, A.Y. Grosberg, B.I. Shklovskii, J. Chem. Phys. **113**, 1110 (2000).
15. S. Bhattacharjee, C.H. Ko, M. Elimelech, Langmuir **14**, 3365 (1998).
16. O. Spalla, L. Belloni, J. Chem. Phys. **95**, 7689 (1991).
17. A theory that predicts molecular geometries using the notion that valence electron pairs occupy sites around a central atom in such a way as to minimize electron-pair repulsion. See, for example, D.W. Oxtoby, H.P. Gillis, N.H. Nachtrieb, *Principles of Modern Chemistry* (Saunders College Publishing, 1999), Chapt. 3, p. 80.
18. R. Messina, C. Holm, K. Kremer, submitted.
19. L. Bonsall, A.A. Maradudin, Phys. Rev. B **15**, 1959 (1977).

Appendix E

Spherical colloids: effect of discrete macroion charge distribution and counterion valence

ELSEVIER

Physica A 308 (2002) 59–79

PHYSICA A

www.elsevier.com/locate/physa

Spherical colloids: effect of discrete macroion charge distribution and counterion valence

René Messina*

Max-Planck-Institut für Polymerforschung, Ackermannweg 10, 55128 Mainz, Germany

Received 10 September 2001

Abstract

We report the coupled effects of macroion charge discretization and counterion valence in the primitive model for spherical colloids. Instead of considering a uniformly charged surface, as it is traditionally done, we consider a more realistic situation where *discrete monovalent microscopic charges* are randomly distributed over the sphere. Monovalent or multivalent counterions ensure global electroneutrality. We use molecular dynamics simulations to study these effects at the ground state and for finite temperature. The ground state analysis concerns the counterion structure and *charge inversion*. Results are discussed in terms of simple analytical models. For finite temperature, strong and weak Coulomb couplings are treated. In this situation of finite temperature, we considered and discussed the phenomena of ionic pairing (pinning) and unpairing (unpinning).

PACS: 82.70.Dd; 61.20.Qg; 64.60.Cn

Keywords: Charged colloids; Charge inversion; Order-disorder transformations; Molecular dynamics

1. Introduction

Charged colloidal suspensions are a subject of intense experimental and theoretical work not only because of their direct application in industrial or biological processes, but also because they represent model systems for atomistic systems. The electrostatic interactions involved in such systems have a fundamental role in determining their physico-chemical properties [1,2]. Theoretical description of highly charged colloidal solutions faces two challenges: (i) different typical length scales due to the presence of

* Tel.: +49-6131-379-148; fax: +49-6131-379-100.
E-mail address: messina@mpip-mainz.mpg.de (R. Messina).

0378-4371/02/$ - see front matter
PII: S0378-4371(02)00560-5

macroions (i.e., charged colloids of the size 10–1000 Å) and microscopic counterions and (ii) their *long-range* Coulomb interaction. A first simplifying assumption is to treat the solvent as a dielectric medium solely characterized by its relative permittivity ε_r. A second widely used approximation consists in modeling the *short range* ion–ion excluded volume interaction by hard spheres. These two approximations are the basis of the so-called primitive model of electrolyte solutions. The system under consideration is an asymmetrical electrolyte solution made up of highly charged macroions and small counterions. A further simplification motivated by this asymmetry can be made by partitioning the system into subvolumes (cells), each containing one macroion together with its neutralizing counterions plus (if present) additional salt. This approximation has been called accordingly the cell model [3,4]. The cells adopt the symmetry of the macroion, here spherical, and are electrostatically decoupled. It is within the cell model that we present our simulation results.

For spherical macroions the structural charge is usually modeled by a *central charge*, which by Gauss theorem is equivalent to a *uniform* surface charge density as far as the electric field (or potential) *outside* the spherical colloid is concerned.

Most analytical concepts as well as simulations rely on the above assumptions and especially on the central charge assumption. It is well known that in the strong Coulomb coupling regime ion–ion correlations become very important, and significant deviations from mean-field approaches are expected. A counter-intuitive effect which classical mean-field theories (like Poisson–Boltzmann model) cannot explain is the phenomenon of *overcharge*, also called charge inversion. That is, there are counterions in *excess* in the vicinity of the macroion surface so that its net charge changes sign. This has recently attracted significant attention [5–17]. In particular, we showed recently that this phenomenon may give rise to a strong long range attraction between like-sign charged colloids [12,13,17]. A natural question which comes up is: does overcharge and more generally ion–ion correlations strongly depend on the way the macroion structural charge is represented (i.e., uniformly charged or discrete charges on its surface)? In a recent paper [16], we studied such a situation in the strong Coulomb coupling regime where the macroion charge was carried by divalent microions in the presence of divalent counterions (*same* ionic valence). In Ref. [16] we reported the important result showing that overcharge is still possible under those conditions. Moreover we showed that the intrinsic electric field solely due to the macroion surface microions (without counterions) varies strongly from point to point on the colloidal sphere [16].

The goal of this paper is to study by means of molecular dynamics (MD) simulations the *coupled* effects of macroion charge discretization and counterion valence in the primitive model for spherical colloids. A systematic comparison with the uniform macroion charge distribution (i.e., central charge) is undertaken. The paper is organized as follows. In Section 2 we give some details on the macroion charge discretization as well as on the MD simulation model. Section 3 is devoted to the ground state analysis where surface counterion structure and overcharge are addressed. In Section 4 we investigate the finite temperature situation, where counterion structure is studied for strong and weak Coulomb couplings. Finally, in Section 5 we provide a summary of the results.

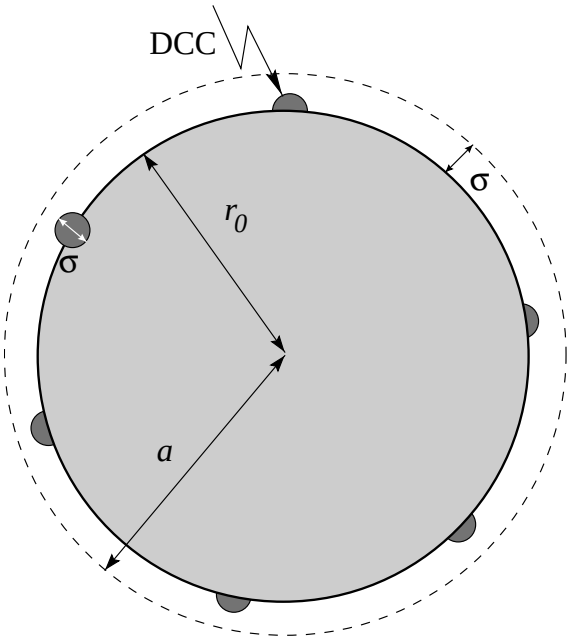

Fig. 1. Schematic view of the setup: the discrete colloidal charges (DCC) of diameter σ are in dark gray. For a detailed meaning of the other symbols see text. Note that this is a two-dimensional representation of the three-dimensional system.

2. Simulation model

2.1. Macroion charge discretization

The procedure is similar to the one used in a previous study [16]. The *discrete* macroion charge distribution is produced by using Z_m *monovalent* microions of diameter σ (same diameter as the counterions) distributed *randomly* on the surface of the macroion. Then the structural charge is $Q=-Z_m e=-Z_m Z_d e$, where $Z_m>0$, $Z_d=1$ is the valence of these discrete microions and e is the positive elementary charge. These discrete colloidal charges (DCC) are *fixed* on the surface of the spherical macroion. Fig. 1 shows a schematic view of the setup. The counterions (not shown in Fig. 1) have a charge $q=+Z_c e$, where $Z_c>0$ stands for the counterion valence. In spherical coordinates the elementary surface is given by

$$\mathrm{d}A = r_0^2 \sin\theta \,\mathrm{d}\theta \,\mathrm{d}\varphi = -r_0^2 \,\mathrm{d}(\cos\theta)\,\mathrm{d}\varphi\,, \tag{1}$$

where r_0 is the distance between the macroion center and the DCC center. Thus to produce a random discrete charge distribution on the surface we generated (uniformly) randomly the variables $\cos\theta$ and φ. Excluded volume is taken into account by rejecting configurations leading to an overlap of microions. Phenomena such as surface chemical reactions [18], hydration, roughness [19] are not considered. For commodity we introduce the notation $(-Z_d:+Z_c)$ to characterize the valence symmetry (asymmetry) for $Z_c=1$ ($Z_c>1$) of the ions (DCC and counterions) involved in discrete systems.

2.2. Molecular dynamics procedure

A MD simulation technique was used to compute the motion of the counterions coupled to a heat bath acting through a weak stochastic force $\mathbf{W}(t)$. The procedure is very similar to the one used in previous studies [12,16].

The motion of counterion i (DCC ions being *fixed*) obeys the Langevin equation

$$m\frac{\mathrm{d}^2\mathbf{r}_i}{\mathrm{d}t^2} = -\nabla_i U(\mathbf{r}_i) - m\gamma\frac{\mathrm{d}\mathbf{r}_i}{\mathrm{d}t} + \mathbf{W}_i(t)\,, \tag{2}$$

where m is the counterion mass, U is the potential force having two contributions: (i) the Coulomb interaction and (ii) the excluded volume interaction, and γ is the friction coefficient. Friction and stochastic force are linked by the dissipation-fluctuation theorem $\langle \mathbf{W}_i(t)\cdot\mathbf{W}_j(t')\rangle = 6m\gamma k_B T\delta_{ij}\delta(t-t')$. For the ground state simulations the stochastic force is set to zero.

Excluded volume interactions are taken into account with a pure repulsive Lennard–Jones potential given by

$$U_{LJ}(r) = \begin{cases} 4\varepsilon_{LJ}\left[\left(\dfrac{\sigma}{r-r_0}\right)^{12} - \left(\dfrac{\sigma}{r-r_0}\right)^{6}\right] + \varepsilon_{LJ}, & \text{for } r - r_0 < r_{cut}\,, \\ 0 & \text{for } r - r_0 \geqslant r_{cut}\,, \end{cases} \tag{3}$$

where $r_0 = 0$ for the microion–microion interaction (the microion being either a counterion or a DCC), $r_0 = 7\sigma$ for the macroion–counterion interaction and $r_{cut} = 2^{1/6}\sigma$ is the cutoff radius. This leads to a (center–center) macroion–counterion distance of closest approach $a = 8\sigma$ (see also Fig. 1). The macroion surface charge density σ_m is defined as

$$\sigma_m = \frac{Z_m}{4\pi a^2}\,. \tag{4}$$

Energy and length units in our simulations are related to experimental units by taking $\varepsilon_{LJ} = k_B T_0$ (with $T_0 = 298$ K) and $\sigma = 3.57$ Å, respectively.

The pair electrostatic interaction of any pair ij, where i and j denote either a DCC a counterion or the central charge (for the non-discrete case), reads

$$U_{coul}(r) = k_B T_0 l_B \frac{Z_i Z_j}{r}\,, \tag{5}$$

where $l_B = e^2/4\pi\varepsilon_0\varepsilon_r k_B T_0$ is the Bjerrum length describing the electrostatic strength. For the rest of this paper, electrostatic energy will always be expressed in units of $k_B T_0$. This also holds for the ground state analysis where the temperature is $T = 0$ K but $T_0 = 298$ K. From now on the pair electrostatic interaction will be written in reduced units so that Eq. (5) reads $U_{coul} = Z_i Z_j / r$.

The macroion and the counterions are confined in a spherical impenetrable cell of radius R. The macroion is held fixed and is located at the center of the cell. The colloid volume fraction f_m is defined as a^3/R^3. To avoid image charge complications,

Table 1
Simulation parameters with some fixed values

Parameters	
$\sigma = 3.57$ Å	Lennard–Jones length units
$T_0 = 298$ K	Room temperature
$\varepsilon_{LJ} = k_B T_0$	Lennard–Jones energy units
Z_m	Macroion valence
$Z_d = 1$	Discrete colloidal charge valence
Z_c	Counterion valence
l_B	Bjerrum length
$a = 8\sigma$	Macroion–counterion distance of closest approach
σ_m	Macroion surface charge density
$R = 40\sigma$	Simulation cell radius
$f_m = 8 \times 10^{-3}$	Macroion volume fraction

the permittivity ε_r is supposed to be identical within the whole cell (including the macroion) as well as outside the cell. Typical simulation parameters are gathered in Table 1.

3. Ground state analysis

In this section, we focus on counterion distribution exclusively governed by *energy minimization*, i.e., $T = 0$ K. In such a case correlations are maximal and all the counterions lie on the macroion surface. This situation has the advantage to enable accurate computation of energy variations in processes such as overcharging and also to provide a clear description of effects which are purely correlational in nature. The method employed here was successfully carried out in Refs. [12,13,16,17] and is explained in detail in Ref. [17]. The Bjerrum length l_B is set to 10σ. Note that in the ground state the value of l_B, or equivalently the value of the dielectric constant ε_r, does not influence the counterion structure at all. Only the electrostatic energy is rescaled accordingly.

3.1. Neutral case

First we consider the simple case where the system [macroion + counterions] is globally neutral. In order to characterize the two-dimensional counterion structure we compute the counterion correlation function (CCF) $g_c(r)$ on the surface of the sphere defined as

$$c^2 g_c(r = |r' - r''|) = \sum_{i \neq j} \delta(r' - r_i)\delta(r'' - r_j)\,, \tag{6}$$

where $c = N_c/4\pi a^2$ is the surface counterion concentration ($N_c = Z_m/Z_c$ being the number of counterions) and r corresponds to the arc length on the sphere. Note that at zero temperature all equilibrium configurations are identical (except for degenerate ground

state), thus only one is required to obtain $g_c(r)$. The counterion correlation function $g_c(r)$ is normalized as follows:

$$c\int_0^{\pi a} 2\pi r g_c(r)\,\mathrm{d}r = (N_c - 1)\,. \tag{7}$$

Because of the *finite* size and the topology of the sphere, $g(r)$ has a cut-off at $r_{gc} = \pi a = 25.1\sigma$ and $g(r_{gc}) = 0$. Furthermore the absolute value of $g(r)$ cannot be directly compared to the one obtained with an infinite plane.

Similarly, one can also define a surface macroion correlation function (MCF) $g_m(r)$ for the microions (representing the colloidal structural charge) on the surface of the macroion. The normalization of $g_m(r)$ is very similar to Eq. (7) and reads

$$\sigma_m\int_0^{\pi a} 2\pi r g_m(r)\,\mathrm{d}r = (Z_m - 1)\,, \tag{8}$$

where the arc length has been rescaled by a factor a/r_0 so that $g_c(r)$ and $g_m(r)$ are directly comparable (see also the setup Fig. 1) and are defined in the same r range.

3.1.1. Monovalent counterions

We first treat the systems where we have monovalent counterions, that is we have to deal with the symmetric discrete system $(-1:+1)$. The counterion correlation functions $g_c(r)$ are computed for a central macroion charge [denoted by $g_c^{(\mathrm{CC})}(r)$] and for discrete macroion charge distribution [denoted by $g_c^{(\mathrm{DCC})}(r)$]. Results for three structural charges $Z_m = 60$, 180 and 360 are given in Figs. 2(a), (b) and (c), respectively. For the continuous case (central charge) the counterion structure consists of a pseudo-Wigner crystal (WC) as was already found in Refs. [12,13,16,17]. Also the higher the absolute number of counterions N_c (i.e. the concentration c) the higher the order of counterion structure for the continuous case [compare Fig. 2(a) with Fig. 2(c)].

It turns out that in the case of discrete colloidal charges the counterion distribution is strongly dictated by the colloidal charge distribution and especially for low macroion surface charge density σ_m ($Z_m = 60$) [see Fig. 2(a)]. For $Z_m = 60$, $g_c^{(\mathrm{DCC})}(r)$ and $g_m(r)$ are almost identical. This indicates that each counterion is exactly associated with one DCC site. The ground state structure for $Z_m = 60$ is depicted in Fig. 3(a) where one clearly observes this ionic pairing.

This strong ionic pair association can be easily explained in terms of *local* correlations. Let us consider the picture sketched in Fig. 4 which holds for strong ionic pairing, where a given dipole A (ionic pair made up of a counterion and a DCC site) on the macroion surface essentially interacts with its first nearest surrounding dipoles B. Note that very similar lengths were also considered in a recent theoretical study [20] in the one-dimensional case (counterion adsorption on a linear polyelectrolyte). It is important to have in mind that such a local description is physically justified due to the strong screening generated by ionic pairing. Thereby local correlations are twofold: (i) the *attractive* interaction between the DCC site of dipole A with its paired counterion and the counterions of dipoles B, and (ii) the *repulsive* interaction between the counterion of dipole A and counterions of dipoles B. The

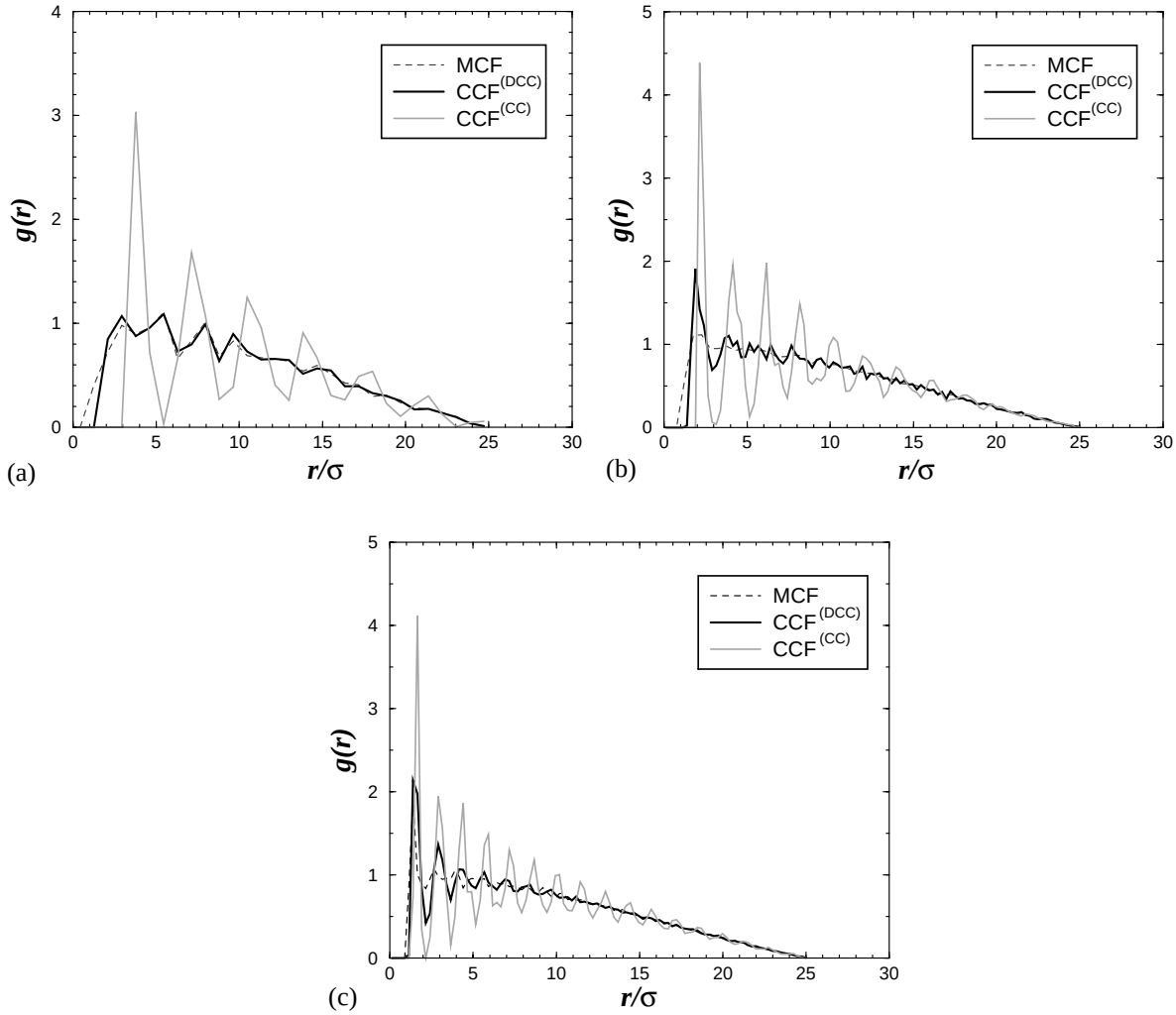

Fig. 2. Ground state surface correlation functions $g(r)$ for *monovalent* counterions ($Z_c = 1$) and for three macroion bare charges: (a) $Z_m = 60$ (b) $Z_m = 180$ and (c) $Z_m = 360$. The two counterion correlation functions (CCF) $g_c(r)$ are obtained for discrete colloidal charges [$g_c^{(\mathrm{DCC})}(r)$ denoted by $\mathrm{CCF}^{(\mathrm{DCC})}$] and for the central charge [$g_c^{(\mathrm{CC})}(r)$ denoted by $\mathrm{CCF}^{(\mathrm{CC})}$]. MCF stands for the discrete colloidal charges pair distribution $g_m(r)$.

correlations between DCC sites are not relevant since they are fixed. The intra-dipole attractive interaction E_{pin} between the DCC site and its "pinned" counterion can be written as

$$E_{pin} = -\frac{Z_d Z_c}{\sigma} \,. \tag{9}$$

For the elementary nearest inter-dipole (or inter-ionic pair) interactions, one can write for the attractive interaction E_{+-} between the DCC site of dipole A and the counterion of dipole B:

$$E_{+-} = -\frac{Z_d Z_c}{a_{dc}} \,. \tag{10}$$

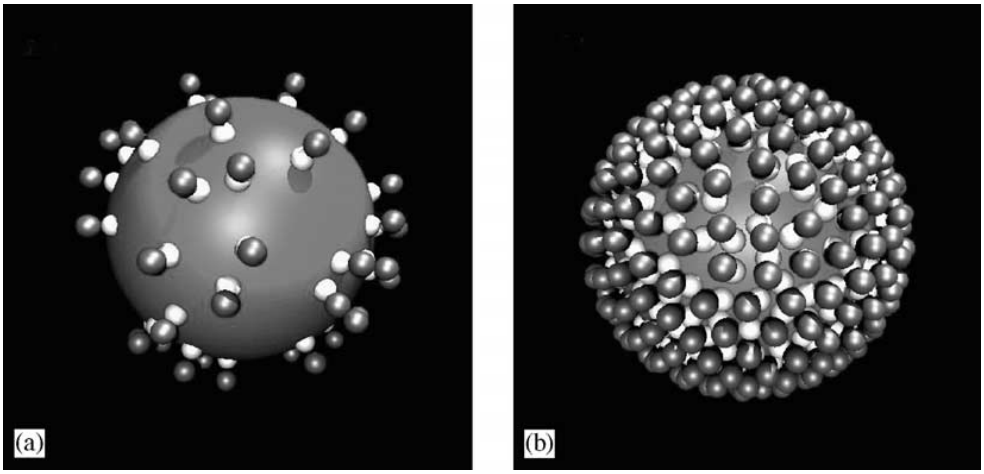

Fig. 3. Ground state structures for discrete monovalent systems $(-1:+1)$: (a) $Z_m = 60$ and (b) $Z_m = 360$. The discrete colloidal charges (DCC) are in white, and the counterions in blue. Full ionic pairing association occurs. The corresponding counterion correlation functions $g_c(r)$ can be found in Figs. 2(a) and (c).

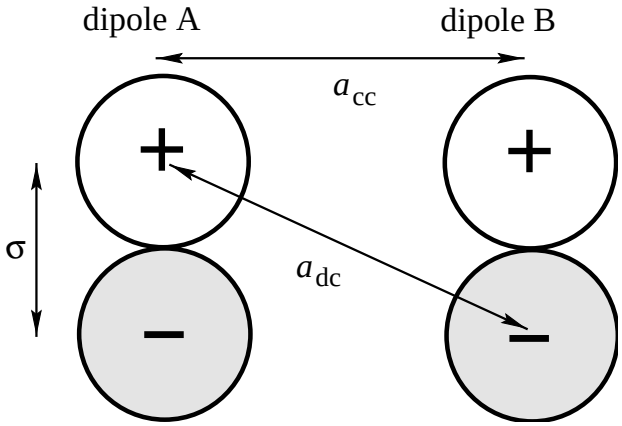

Fig. 4. Schematic view of the local electrostatic interactions and typical correlation lengths involved between nearest dipoles. The negatively charged DCC $(-)$ are in gray and the positively charged counterions $(+)$ in white.

A similar expression can be written for the repulsive inter-dipole interaction E_{++} involving counterions of dipole A and dipole B, which reads

$$E_{++} = \frac{Z_c^2}{a_{cc}} \,. \tag{11}$$

Note that the repulsive counterion–counterion term E_{++} alone, even if space *truncated*,[1] drives to the *long-range* ordered triangular WC structure. However at zero temperature the DCC sites represent pinning centers for the counterions where the electrostatic potential is considerably lowered (due to the term E_{pin}) compared to its direct "empty" neighborhood (charge hole), which in turn prevents the counterions

[1] This statement holds if the cutoff is larger than the lattice constant.

from adopting the ideal WC structure. This latter aspect was thoroughly discussed in Ref. [16]. Another important quantity characterizing discrete systems is the ratio

$$\rho_{pin} = \frac{\tilde{a}_{cc}}{d_{pin}} \tag{12}$$

between the mean inter-dipole separation $\tilde{a}_{cc}$ (more exactly the mean counterion–counterion separation) and intra-dipole separation d_{pin} of an ionic pair (in the present study $d_{pin} = \sigma$ as depicted in Fig. 4). The value of $\tilde{a}_{cc}$ can be obtained by taking the first peak position of $g_c^{(CC)}(r)$.

Obviously, for sufficiently low macroion surface charge density σ_m (i.e., large ρ_{pin}) the ionic pairing term E_{pin} will be dominant and strong ionic pairing occurs. More specifically, when the typical inter-dipole distance is large compared to the intra-dipole distance then dipole–dipole interactions are weak (i.e., $|E_{+-} - E_{++}| \ll |E_{pin}|$) and the DCC distribution dictates the counterion structure. This is what qualitatively explains our simulation findings for $Z_m = 60$ [see Figs. 2(a) and 3(a)].

When σ_m becomes sufficiently important the situation may become qualitatively different. In this case dipoles approach each other and because of excluded volume [2] a_{cc} becomes comparable to σ (see Fig. 4). [3] Thereby, the counterion–counterion repulsion term E_{++} (overcompensating E_{+-}) induces counterion ordering *compatible* with the local attractive pinning potential field generated by DCC centers. This effect can be inspected in Figs. 2(b) and (c) where one sees that upon increasing σ_m, $g_c^{(DCC)}(r)$ is gradually less correlated with $g_m(r)$ and more correlated with $g_c^{(CC)}(r)$. As a topological consequence, some counterions will be in contact with several (two or more) DCC attractors as can be seen in Fig. 3(b).

The quasi-triangular counterion arrangement for high σ_m ($Z_m = 360$) can be inspected in Fig. 3(b). For this symmetric system in size (same diameter for the counterions and the DCC ions) one expects that for a compact amorphous DCC layer the counterion structure should become perfectly ordered. This extreme limit which would correspond to unreachable experimental charge densities has not been addressed in our simulations.

In parallel, increasing σ_m induces by purely excluded volume effect a stronger local order within the DCC layer as can be checked on the $g_m(r)$ plots in Figs. 2(a)–(c). This is quite similar to what occurs in a system of hard spheres where the (dense) liquid phase is locally correlated and the (dilute) gaseous phase is uncorrelated.

In summary, the system depicted above is the siege of an *order–disorder* phase transition where upon increasing σ_m (i.e., decreasing ρ_{pin}) we pass from a disordered counterion structure (imposed by the DCC layer) to a *long-range* ordered one which is induced by *local* counterion–counterion correlations.

Although results presented above concern one given random distribution (for each Z_m), we carefully checked that similar results and conclusions could be drawn for different random realizations (systematically five). This also holds for the following section below where we deal with multivalent counterions.

---

[2] Note that in the present model no surface dipole flip is allowed which should also be the case experimentally.

[3] The limiting case is where the global structure is compact, i.e., touching spherical microions.

3.1.2. Multivalent counterions

We turn to the asymmetric discrete systems $(-1:+Z_c)$ where multivalent counterions are present ($Z_c > 1$). The correlation functions $g(r)$ for two macroion charges $Z_m = 60$ and 180 and various counterion valences Z_c can be found in Fig. 5. One remarks that upon decreasing the number of counterions N_c (i.e., increasing Z_c) for fixed Z_m, the first peak of $g_c(r)$ is gradually shifted to the right (compare also the monovalent case given in Fig. 2) whatever the nature of the macroion charge is (discrete or continuous). Furthermore, we observe for the discrete systems that upon increasing Z_c (for fixed Z_m) the correlation between $g_c^{(\mathrm{DCC})}(r)$ and $g_m(r)$ decreases and increases between $g_c^{(\mathrm{DCC})}(r)$ and $g_c^{(\mathrm{CC})}(r)$. This effect is clearly noticeable in Fig 2(b) and Fig. 5(c)–(e) corresponding to $Z_m = 180$. The very high counterion valence $Z_c = 10$ reported in Fig. 5(e) was undertaken in order to stress the counterion multivalence effect. These findings lead to the conclusion that the counterion valence has the effect of reducing the disorder in the counterion structure stemming from the randomness of the DCC distribution.

This related phenomenon can be theoretically explained with simple ideas. Basically, the mechanisms involved in this counterion valence induced ordering stem from two concomitant sources: (i) *topological* and (ii) correlational.

The topological aspect is due to the presence of $(Z_m - Z_m/Z_c)$ unbound DCC sites (free of associated counterion) ensuring global electroneutrality [cf. e.g. Figs. 3(a) and 6]. It is to say that here, compared to the monovalent case $(-1:+1)$, the counterions have all the more "freedom" to choose their pinning locations because Z_c is high. To be more precise, the number of topologically accessible "pinned" configurations is given[4] by

$$C_{Z_m}^{Z_m/Z_c} = \frac{Z_m!}{(Z_m - Z_m/Z_c)!(Z_m/Z_c)!} \tag{13}$$

which reduces to 1 for $Z_c = 1$. In the ground state, counterions will "decide" to choose among these various possible arrangements the one which minimizes the total energy of the system. It is clear that this topological feature by itself promotes counterion valence induced ordering.

Concomitantly, there is a purely counterion correlation induced ordering which is Z_c dependent. Indeed, using similar arguments as those previously employed for monovalent systems $(-1:+1)$ built on Eqs. (9)–(11), one can infer the role of Z_c. More specifically, by assuming an ordered WC structure[5] the term E_{++} given by Eq. (11) can be rewritten as

$$E_{++}^{WC} \sim \frac{Z_c^{3/2} Z_m^{1/2}}{a}\,, \tag{14}$$

[4] Rigorously, Eq. (13) holds when each counterion is associated with one and only one DCC site (case of low σ_m). For high σ_m, it remains a good approximation to capture the essential physics.

[5] From a topological point of view, it consists in replacing the current (random) Voronoi structure by the ordered WC structure.

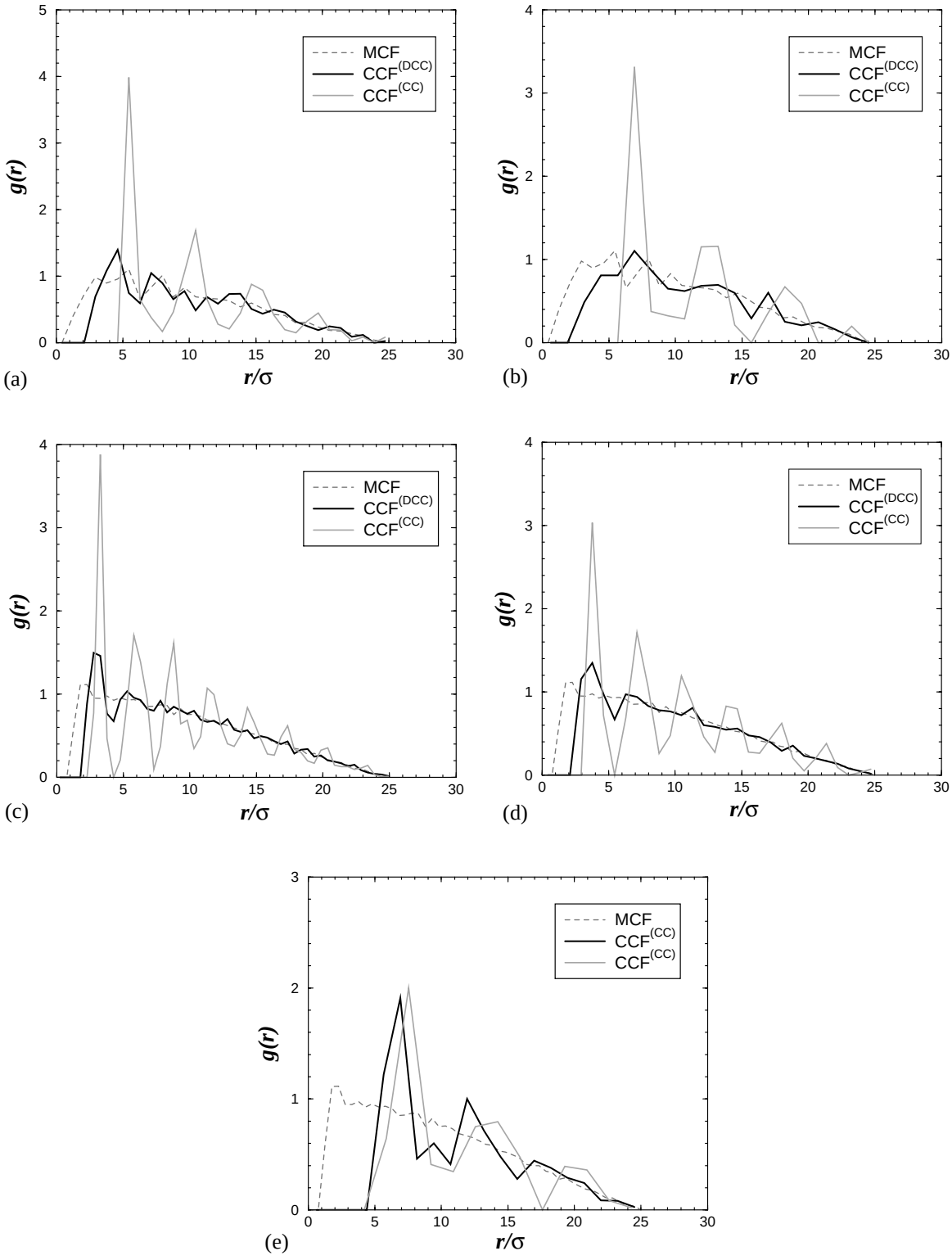

Fig. 5. Ground state surface correlation functions for different *multivalent* systems: (a) $Z_m = 60,\ Z_c = 2$; (b) $Z_m = 60,\ Z_c = 3$; (c) $Z_m = 180,\ Z_c = 2$; (d) $Z_m = 180,\ Z_c = 3$; (e) $Z_m = 180,\ Z_c = 10$. The two counterion correlation functions (CCF) are obtained for discrete colloidal charges (DCC) and for the central charge (CC). The $g_m(r)$ curves (denoted by MCF) are identical from (a) to (b) and from (c) to (e).

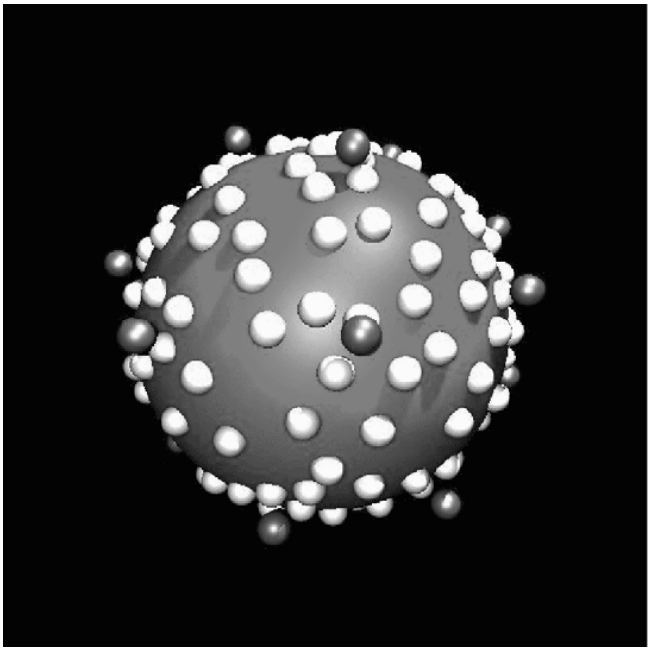

Fig. 6. Ground state structure for $(-1:+10)$ with $Z_m = 180$. The corresponding counterion correlation function $g_c(r)$ can be found in Fig. 5(e).

where a_{cc} in Eq. (11) is now given by

$$a_{cc} = \tilde{a}_{cc} \sim c^{-1/2} \sim \left(\frac{Z_m}{Z_c a^2}\right)^{-1/2} . \tag{15}$$

Eq. (14) shows that for fixed Z_m and a (i.e., fixed macroion charge density) $E_{++}^{WC} \sim Z_c^{3/2}$ whereas $E_{pin} \sim Z_c$ (recalling that $Z_d = 1$) and therefore for sufficiently high Z_c the term E_{++}^{WC} will be dominant. Thereby Z_c induces counterion ordering so as to minimize mutual counterion–counterion repulsion merely dictated by Eq. (14). As a topological consequence, some counterions which would be in contact with several DCC sites if they were monovalent can now be in contact with less DCC sites (see Fig. 6).

In summary, these discrete multivalent systems are again the siege of an order–disorder phase transition which is counterion valence controlled.

3.2. Overcharge

We now investigate the charge inversion (overcharge) phenomenon. The starting equilibrium configurations correspond to neutral ground states as were previously obtained. The method employed here is very similar to the one used in Refs. [12,16]. To produce a controlled overcharge, one adds successively overcharging counterions (OC) in the vicinity of the macroion surface. Thereby the resulting system is no longer neutral. Using Wigner crystal concepts [6,21], we showed that the gain in electrostatic energy (compared to the neutral state) by overcharging a single *uniformly* charged macroion (i.e., central charge) with n overcharging counterions can be written in the

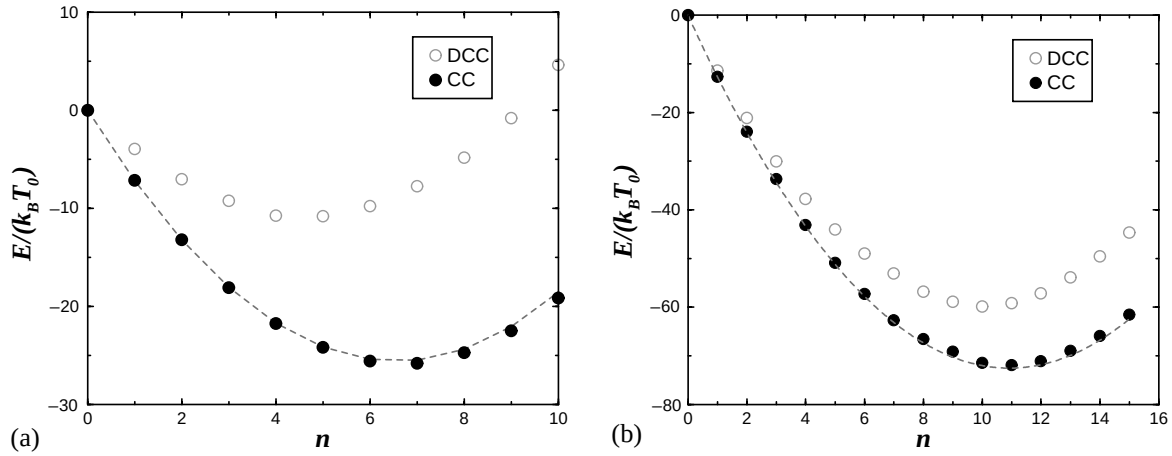

Fig. 7. Total electrostatic energy for *monovalent* counterions ground state configurations as a function of the number of *overcharging* counterions n: (a) $Z_m = 60$, $Z_c = 1$ (b) $Z_m = 180$, $Z_c = 1$. Overcharge curves were computed for discrete macroion charge distribution (DCC) and macroion central charge (CC). The neutral case was chosen as the potential energy origin. Dashed lines were produced by using Eq. (16). For discrete systems (DCC) error bars are smaller than symbols.

following way [12,13,17]:

$$\Delta E_n^{OC} = \Delta E_n^{cor} + \Delta E_n^{mon} = -\frac{\alpha Z_c^2}{\sqrt{A}}\left[(N_c + n)^{3/2} - N_c^{3/2}\right] + Z_c^2 \frac{n^2}{2a}\,. \tag{16}$$

As before $N_c = Z_m/Z_c$ is the number of counterions in the neutral state, A is the macroion area ($4\pi a^2$) and α is a positive constant which was determined by using simulation data for ΔE_1^{OC}. ΔE_n^{cor}, which is equal to the first term of the right member, denotes the gain in energy due to ionic correlations. The derivation of this term can be found in Refs. [12,13,17], and the basic idea is that each counterion interacts essentially with its neutralizing uniformly charged Wigner–Seitz cell. The second term on the right-hand side, ΔE_n^{mon}, is the self-energy of the excess of charge. This repulsive term stops the overcharging for sufficiently large n. Note that the WC concept for describing energy correlations is already excellent for highly short range ordered structures (strongly correlated liquids, see Ref. [6] for a detailed discussion). The total electrostatic energy of the system as a function of n is displayed Fig. 7 (for monovalent counterions) and Fig. 8 (for multivalent counterions) for two bare charges $Z_m = 60$ and 180. The energy curves corresponding to discrete systems were produced by systematically averaging over five random DCC realizations.

3.2.1. Monovalent counterions

Let us first focus on the monovalent symmetric case $(-1 : +1)$ where for the neutral state each DCC site is exactly associated with one counterion as was shown above. The results in Figs. 7(a) and (b) show that the overcharging process occurring with a discrete macroion charge distribution is quite different from the one obtained with an uniform surface charge distribution. Especially for the smallest bare charge $Z_m = 60$, the effect of disorder is very important in agreement with what was already found above for the neutral state in Section 3.1.1. The main effects of charge

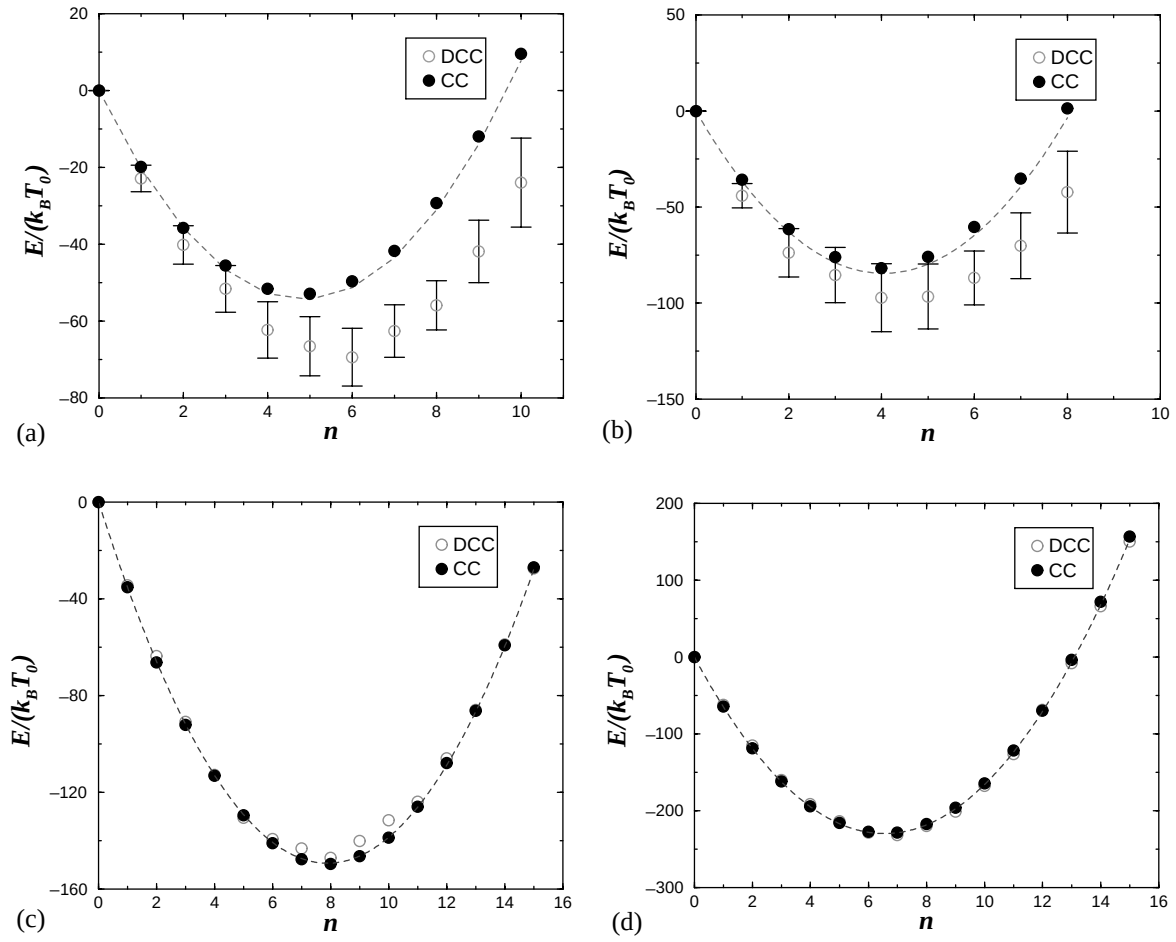

Fig. 8. Total electrostatic energy for *multivalent* counterions ground state configurations as a function of the number of *overcharging* counterions n: (a) $Z_m = 60$, $Z_c = 2$ (b) $Z_m = 60$, $Z_c = 3$ (c) $Z_m = 180$, $Z_c = 2$ (d) $Z_m = 180$, $Z_c = 3$. Overcharge curves were computed for discrete macroion charge distribution (DCC) and macroion central charge (CC). The neutral case was chosen as the potential energy origin. Dashed lines were produced by using Eq. (16). For discrete systems (DCC) error bars are only indicated when larger than symbols.

discretization are: (i) the reduction in gain of energy and (ii) the reduction of maximal (critical) number, n^*, of stabilizing overcharging counterions (corresponding to a minimum in the energy curve). Both points were thoroughly discussed elsewhere [16] for an equivalent symmetric discrete system $(-2:+2)$. It was shown that points (i) and (ii) can be explained in terms of *ion–dipole* interaction, which presently is the main driving force for overcharging. When the overcharging counterions are present, each of them will essentially interact (attractively) with its neighboring dipoles (ionic pairs). The attractive ion–dipole interaction increases with decreasing ion–dipole separation, i.e., increasing macroion charge density σ_m. This explains why the energy gain increases with Z_m [compare Figs. 7(a) and (b)]. On the other hand, the repulsion between the counterions is not fully minimized since they do not adopt the ideal WC structure that is obtained with a central charge which in turn explains (i) and (ii). However for high bare charge ($Z_m = 180$) the overcharge curve obtained with DCC [see Fig. 7(b)] approaches the one from the continuous case as expected for high counterion

concentration. This feature is fully consistent with what was already found in Section 3.1.1, where it was shown that the order of the counterion structure in the neutral state (for discrete systems) increases with σ_m. In other terms, the WC approach through Eq. (16) is a good approximation for describing discrete systems at high σ_m since stronger ordering exists.

Common features of overcharging between continuous and discrete systems are briefly given here. We note that n^* increases with the macroionic charge Z_m. Furthermore, for a given n, the gain in energy always increases with Z_m. Also, for a given macroionic charge Z_m, the gain in energy between two successive overcharged states is decreasing with n. Note that at $T=0$ K, the value of ε_r acts only as a prefactor. All these features are captured by Eq. (16).

3.2.2. *Multivalent counterions*

Now we are going to discuss the asymmetric discrete systems $(-1:+Z_c)$ where multivalent counterions are present ($Z_c > 1$). The results of Figs. 8(a)–(d) indicate that the energy gain in the overcharging process at fixed Z_m and n is higher the higher the counterion valence Z_c for both macroion charge distributions (discrete and continuous). For the continuous case this can be directly explained in terms of WC concepts [i.e., Eq. (16)]. Indeed the main leading term of the correlational energy ΔE_n^{cor} in Eq. (16) scales like

$$\Delta E_n^{cor} \sim -Z_c^{3/2} \tag{17}$$

for fixed n and fixed macroion charge Z_m, and recalling that $N_c=Z_m/Z_c$. Eq. (17) quantitatively (qualitatively) explains why overcharging is stronger with increasing counterion valence Z_c for the continuous (discrete) case.

As far as discrete systems are concerned, the overcharging mechanisms occurring with multivalent counterions differ from those occurring with symmetric monovalent systems $(-1:+1)$. This is again due to the presence of $(Z_m - Z_m/Z_c)$ unbound DCC sites in the neutral state as discussed in Section 3.1.2. When overcharging comes into play, each overcharging counterion becomes paired with some[6] of these free DCC sites. Fig. 8 shows that the overcharging with multivalent counterions (especially the higher Z_m) is significantly less affected by colloidal charge discretization than in the monovalent case (see Fig. 7).

For $Z_m = 60$, simulations show that overcharging in the discrete case can even be stronger than in the continuous case [see Figs. 8(a) and (b)]. This phenomenon can be qualitatively understood by referring to the very low macroion surface charge density limit, where the correlation term ΔE_n^{cor} in Eq. (16) becomes negligible compared to the ionic pairing term E_{pin} given by Eq. (9). In this limiting situation, the energy gain by overcharging is approximatively given by $-nZ_dZ_c/d_{pin}$ so that *full* overcharging occurs where each monovalent DCC site is paired with one multivalent counterion.

For $Z_m = 180$, the overcharging curves for discrete and continuous distributions are almost identical [see Figs. 8(c) and (d)]. This is consistent with what we already found

[6] It can be one or more depending on the valence, surface charged density and the local DCC site arrangement.

in Section 3.1.2 for the counterion structure in the neutral state, where we showed that $g_c^{(\mathrm{DCC})}(r)$ approaches $g_c^{(\mathrm{CC})}(r)$ with increasing Z_c. However, the agreement between discrete and continuous cases is even better for overcharging than for counterion structure [see the corresponding $g_c(r)$ given in Figs. 5(c) and (d)]. This is due to the fact that, as previously mentioned, the WC approach [Eq. (16)] quantifying the energy gain by overcharging is already excellent for highly short-ranged ordered systems. Generally speaking, all the ordering mechanisms related in Section 3.1 for neutral discrete systems hold for the overcharging features: *all causes leading to ordering enhance overcharging*.

4. Finite temperature

In this part, the system is globally *neutral* and is brought to room temperature T_0. We are interested in determining the counterion distribution as well as the counterion motion within the counterion layer. The cell radius R is fixed to 40σ so that the macroion volume fraction f_m has the *finite* value 8×10^{-3}.

4.1. Strong Coulomb coupling

The Bjerrum length l_B is set to 10σ as previously in the ground state study Section 3.1. In this section we consider two macroion bare charges Z_m (60 and 180) and three counterion valences Z_c (1, 2 and 3). A typical parameter for describing the Coulomb coupling strength is the so-called plasma parameter Γ [22] defined as $\Gamma = l_B Z_c^2/\tilde{a}_{cc}$. For our simulation parameters, Γ ranges from 2.6 (for $Z_m = 60$ and $Z_c = 1$) up to 23.1 (for $Z_m = 180$ and $Z_c = 3$). Under these conditions, systems are still highly energy dominated so that at equilibrium almost all (if not all depending on Z_m and Z_c) counterions lie in the vicinity of the macroion surface (strong condensation). Therefore for the strong Coulomb coupling regime it is suitable to focus on the counterion *surface* properties. In the following sections we are going to study surface counterion distribution and diffusion.

4.1.1. Counterion distribution

Like in the ground state analysis, we characterize the counterion distribution via its surface correlation function. At non-zero temperature, correlation functions are computed by averaging $\sum_{i \neq j} \delta(r' - r_i)\delta(r'' - r_j)$ over 1000 independent equilibrium configurations which are statistically uncorrelated.

The results for monovalent counterions are depicted in Figs. 9(a) and (b) for $Z_m = 60$ and 180, respectively. For both charges Z_m the counterion distributions are weakly affected by charge discretization and $g_c^{(\mathrm{DCC})}(r)$ and $g_c^{(\mathrm{CC})}(r)$ are almost identical. A closer look on Fig. 9 reveals that the agreement between discrete and continuous distributions is even better for high macroion charge density ($Z_m = 180$) as expected. In fact for monovalent systems the pinning term E_{pin} has its lowest magnitude so that, for sufficiently high σ_m, the *fluctuating* intra-dipole separation becomes comparable to the inter-dipole separation and discretization effects (i.e., pinning) are canceled. These

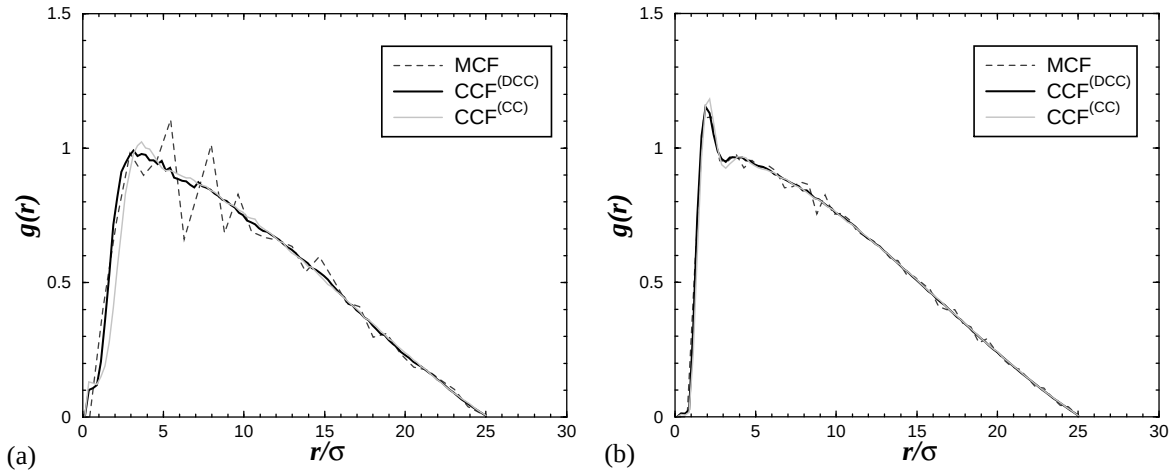

Fig. 9. Surface correlation functions at room temperature T_0 for *monovalent* counterions. The two counterion correlation functions (CCF) $g_c(r)$ are obtained for discrete colloidal charges (DCC) and for the central charge (CC): (a) $Z_m = 60$, $Z_c = 1$ (b) $Z_m = 180$, $Z_c = 1$. MCF stands for $g_m(r)$.

pinning and unpinning aspects will be addressed in more details in Section 4.1.2. As expected, the counterion positional order for discrete and continuous cases is much weaker at room temperature than in the ground state case (compare Figs. 9 and 2).

The results for multivalent counterions are depicted in Fig. 10. We now find that the counterion distributions are strongly affected by charge discretization, and especially the higher Z_c. This is in contrast with what was found in the ground state analysis (Section 3.1.2) where no counterion motion occurs. This effect is of course due to the pinning (inhibition of large counterion motion) which is proportional to Z_c.

Note that all the statements above hold for the particular finite temperature T_0. However the effect of finite temperature discussed here should hold, at least qualitatively, for a large temperature range. For very low temperature one should recover all ground state properties mentioned in Section 3.1.

4.1.2. Surface diffusion

This section is devoted to answer the following question: do the counterions only oscillate around the DCC sites or do they have also a large translational motion over the sphere?

To study this problem we introduce the following observable:

$$\Delta x^2(t, t_0) = \frac{1}{t - t_0} \int_{t_0}^{t} \mathrm{d}t' [x(t') - x(t_0)]^2 \,, \tag{18}$$

which is referred as the *mean square displacement* (MSD), where $x(t_0)$ represents the position of a given counterion at time $t = t_0$ (at equilibrium) and $x(t, t_0)$ is its position at later time t. All particles lying within a distance 9.2σ from the macroion center are radially projected on the macroion surface of radius $a = 8\sigma$ to give $x(t, t_0)$. The root mean square displacement (RMSD) $\Delta x(t, t_0)$ is defined as

$$\Delta x(t, t_0) = \sqrt{\Delta x^2(t, t_0)} \,. \tag{19}$$

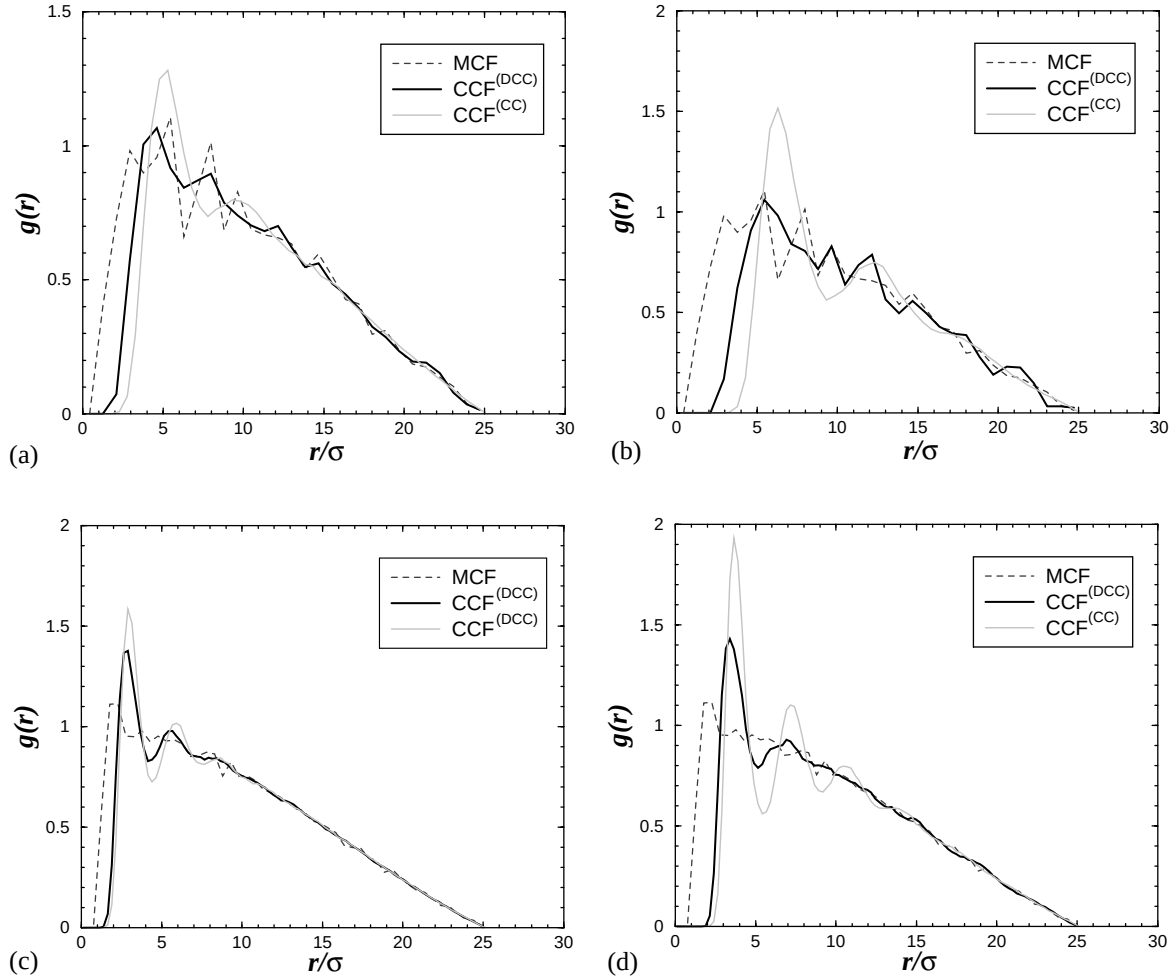

Fig. 10. Surface correlation functions at room temperature T_0 for *multivalent* counterions. The two counterion correlation functions (CCF) $g_c(r)$ are obtained for discrete colloidal charges (DCC) and for the central charge (CC): (a) $Z_m = 60$, $Z_c = 2$ (b) $Z_m = 60$, $Z_c = 3$ (c) $Z_m = 180$, $Z_c = 2$ (d) $Z_m = 180$, $Z_c = 3$. MCF stands for $g_m(r)$.

Like for the surface correlation function, the RMSD is measured on the spherical surface (arc length) and it has a natural upper limit πa. For the case of free counterions (i.e., macroion central charge without pinning) the RMSD Δx_{free} reads

$$\Delta x_{free} = a\sqrt{\frac{\pi^2 - 4}{2}} \approx 13.7\sigma \,. \tag{20}$$

This quantity Δx_{free} will be useful to refer to the "unpinned" state.

The results for discrete systems are sketched in Fig. 11 for $Z_m = 60$ and 180. Monovalent counterions are free to move over the macroion surface for both bare charges Z_m considered here. Moreover, our simulation data show that the counterions gradually become pinned with increasing Z_c. All these features are captured by the Z_c dependency of the pinning term E_{pin}. For multivalent counterions, the degree of pinning increases with decreasing Z_m. This is due to the fact that the discrete charges get closer from each other by increasing Z_m so that a counterion jump from site to site is energetically

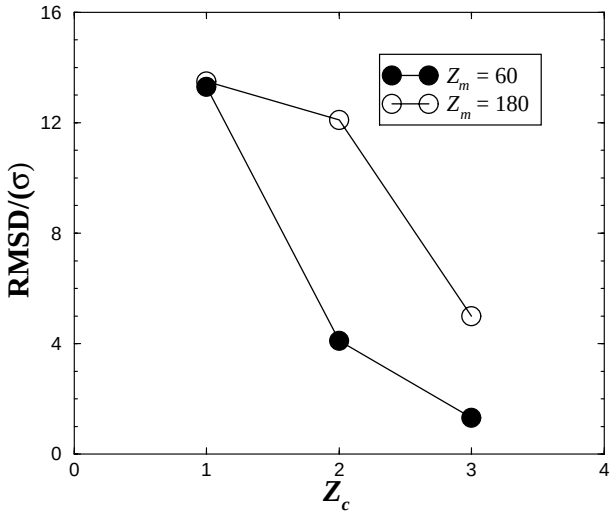

Fig. 11. Root mean square displacement (RMSD) as a function of counterion valence Z_c for $Z_m = 60$ and 180. Errors are smaller than symbols.

less demanding. For the continuous case, we have checked that for the same parameters counterions always have a large lateral motion and move all over the sphere.

4.2. Moderate Coulomb coupling

In this last part, the Bjerrum length corresponds to that of *water* at room temperature ($l_B = 2\sigma = 7.14$ Å). For this moderate Coulomb coupling counterions occupy *all* the cell volume. Clearly, the probability of finding counterions plainly outside the macroion surface is *no more* negligible (in contrast with the strong Coulomb coupling). The target quantity is the fraction $P(r)$ of counterions lying within a distance r from the macroion center and is defined as

$$P(r) = N(r)/N_c \tag{21}$$

with

$$N(r) = \int_{r_0}^{r} 4\pi r_i^2 c_v(r_i)\,\mathrm{d}r_i\,, \tag{22}$$

where $c_v(r)$ is the profile of the *volume* counterion concentration and $N(r)$ is the so-called integrated charge.

The results for $Z_m = 60$ and 12 are sketched in Figs. 12(a) and (b), respectively. For the highest charge, Fig. 12(a) shows that discretization effects are canceled for any counterion valence. On the other hand, for the small charge density case, Fig. 12(b) shows that discretization effects become important for multivalent counterions. In the present situation, the Coulomb coupling is five times less important than in the strong coupling case studied in Section 4.1. Therefore pinning effects can only be noticeable for sufficiently low σ_m (here $Z_m = 12$) and multivalent counterions.

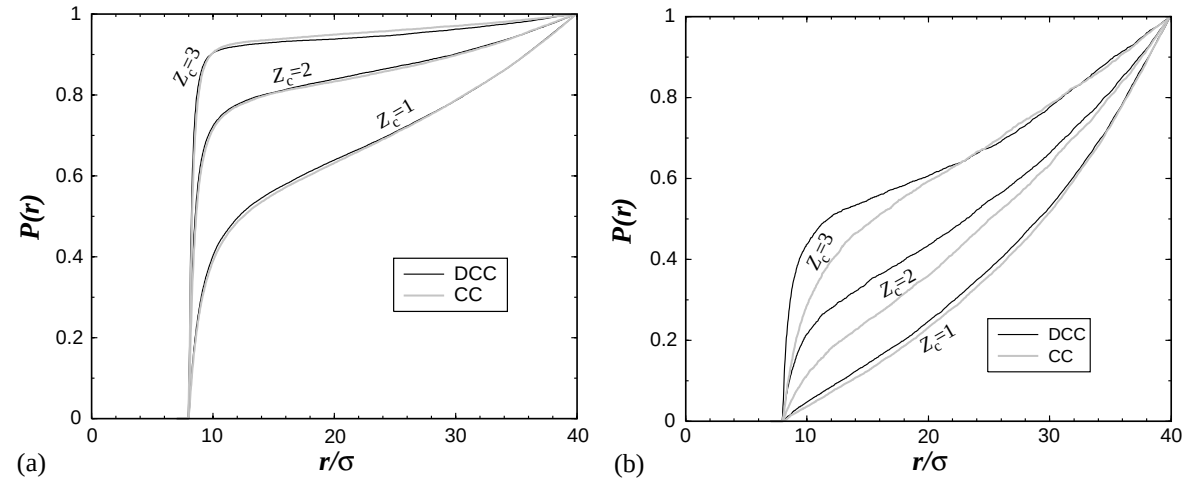

Fig. 12. Counterion fraction within a distance r from the macroion center for different counterion valence Z_c. (a) $Z_m = 60$ (b) $Z_m = 12$. Data were obtained for discrete macroion charge distribution (DCC) and macroion central charge (CC).

5. Conclusion

We have performed MD simulations within the framework of the primitive model to study the coupled effects of macroion charge discretization and counterion valence. The macroion bare charge is carried by monovalent microions randomly distributed over the colloidal surface. Different correlational regimes were considered: (i) ground state and (ii) finite temperature.

Concerning the ground state analysis, we were interested in the counterion structure in the neutral state and the overcharging phenomenon. We demonstrated that the order in the surface counterion structure (disorder in counterion structure induced by the discrete random macroion charge distribution) is increased (decreased) by increasing macroion surface charge density σ_m and/or counterion valence Z_c. For monovalent counterions, we showed that the ratio between the intra-ion pair (made up of a discrete colloidal surface ion and a counterion) distance and the mean distance between ion pairs is a fundamental quantity to describe counterion ordering. When overcharge comes into play similar effects occur. More precisely, for sufficiently high charge density σ_m the overcharging with monovalent as well as multivalent counterions is *quantitatively* the same as the one obtained in the continuous case. For low σ_m, the overcharging with multivalent counterions can even be stronger in the discrete case than in the continuous case counterions. In contrast, for monovalent counterions overcharging is always weaker than in the continuous case but approaches the latter with increasing σ_m.

In the finite temperature case, strong and moderate Coulomb couplings were addressed. In the strong Coulomb coupling, we showed that counterion pinning is very weak for monovalent counterions but it increases with increasing Z_c and decreasing σ_m. This involves an increasing disorder in the surface counterion structure with increasing Z_c and decreasing σ_m. In the moderate Coulomb coupling corresponding to an aqueous situation, the *volume* counterion distribution is only affected for low σ_m and multivalent counterions.

A future work will address the presence of added salts as well as the case of two interacting macroions.

Acknowledgements

I thank C. Holm, A. Johner, K. Kremer and B. Shklovskii for helpful discussions. This work is supported by *Laboratoires Européens Associés* (LEA).

References

[1] J. Israelachvili, Intermolecular and Surface Forces, Academic Press, London, 1992.
[2] D.F. Evans, H. Wennerström, The Colloidal Domain, Wiley-VCH, New York, 1999.
[3] T.L. Hill, Statistical Mechanics, Addison-Wesley, Reading, MA, 1960.
[4] H. Wennerström, B. Jönsson, P. Linse, J. Chem. Phys. 76 (1982) 4665.
[5] V. Perel, B. Shklovskii, Physica A 274 (1999) 446.
[6] B. Shklovskii, Phys. Rev. E 60 (1999) 5802.
[7] E.M. Mateescu, C. Jeppesen, P. Pincus, Europhys. Lett. 46 (1999) 493.
[8] J.F. Joanny, Eur. J. Phys. B 9 (1999) 117.
[9] E. Gurovitch, P. Sens, Phys. Rev. Lett. 82 (1999) 339.
[10] M. Lozada-Cassou, E. González-Tovar, W. Olivares, Phys. Rev. E 60 (1999) R17.
[11] M. Deserno, C. Holm, S. May, Macromolecules 33 (2000) 199.
[12] R. Messina, C. Holm, K. Kremer, Phys. Rev. Lett. 85 (2000) 872.
[13] R. Messina, C. Holm, K. Kremer, Europhys. Lett. 51 (2000) 461.
[14] T.T. Nguyen, A.Y. Grosberg, B.I. Shklovskii, Phys. Rev. Lett. 85 (2000) 1568.
[15] T.T. Nguyen, A.Y. Grosberg, B.I. Shklovskii, J. Chem. Phys. 113 (2000) 1110.
[16] R. Messina, C. Holm, K. Kremer, Eur. Phys. J. E 4 (2001) 363.
[17] R. Messina, C. Holm, K. Kremer, Phys. Rev. E 64 (2001) 021405.
[18] O. Spalla, L. Belloni, J. Chem. Phys. 95 (1991) 7689.
[19] S. Bhattacharjee, C.H. Ko, M. Elimelech, Langmuir 14 (1998) 3365.
[20] K.S. Schmitz, Langmuir 15 (1999) 2854.
[21] L. Bonsall, A.A. Maradudin, Phys. Rev. B 15 (1977) 1959.
[22] I. Rouzina, V.A. Bloomfield, J. Chem. Phys. 100 (1996) 9977.

Appendix F

Overcharging: The crucial role of excluded volume

EUROPHYSICS LETTERS 1 November 2002

Europhys. Lett., **60** (3), pp. 383–389 (2002)

Overcharging: The crucial role of excluded volume

R. Messina[1](*), E. González-Tovar[2,3,4](**), M. Lozada-Cassou[2,4](***) and C. Holm[1](*)

[1] *Max-Planck-Institut für Polymerforschung*
Ackermannweg 10, 55128 Mainz, Germany
[2] *Departamento de Física, Universidad Autónoma Metropolitana-Iztapalapa*
Apartado Postal 55-534, 09340 D.F., México
[3] *Instituto de Física, Universidad Autónoma de San Luis Potosí*
Álvara Obregón 64, 78000 San Luis Potosí, México
[4] *Programa de Ingeniería Molecular, Instituto Mexicano del Petróleo*
Lázaro Cardenas 152, 07730 D.F., México

(received 31 May 2002; accepted in final form 22 August 2002)

PACS. 61.20.Qg – Structure of associated liquids: electrolytes, molten salts, etc.
PACS. 82.70.Dd – Colloids.
PACS. 87.15.Aa – Theory and modeling; computer simulation.

Abstract. – In this letter we investigate the mechanism for the overcharging of a single spherical colloid in the presence of aqueous salts within the framework of the primitive model by molecular dynamics (MD) simulations as well as integral-equation theory. We find that the occurrence and strength of overcharging strongly depends on the salt-ion size, and the available volume in the fluid. To understand the role of the excluded volume of the microions, we first consider an uncharged system. For a fixed bulk concentration we find that upon increasing the fluid particle size one strongly increases the local concentration nearby the colloidal surface and that the particles become *laterally* ordered. For a charged system the first surface layer is built up predominantly by strongly correlated *counterions*. We argue that this is a key mechanism to produce overcharging with a low electrostatic coupling, and as a more practical consequence, to account for charge inversion with *monovalent* aqueous salt ions.

Overcharging, or charge inversion, is defined as the situation where a charged colloid (macroion) accumulates close to its surface more counterions than necessary to compensate its own bare charge. This effect was already discovered in the beginning of the '80s, both by computer simulations [1] and analytical studies [2, 3]. Based on *reversed* electrophoretic mobility, some experimental [4] and numerical (MD) [5] studies provide some hints for the manifestation of overcharging and its possible experimental relevance. More recently, it has regained a considerable attention on the theoretical side [6–16].

(*) E-mail: messina@mpip-mainz.mpg.de
(**) E-mail: henry@dec1.ifisica.uaslp.mx
(***) E-mail: marcelo@www.imp.mx
(*) E-mail: holm@mpip-mainz.mpg.de

Overcharging is rather well understood for counterions in *salt-free* or low-salt environment, when excluded-volume effects play no role. The underlying physics at zero temperature of such non-neutral systems can be quantitatively explained with Wigner crystal (WC) theory [6–8, 11]. The basic concept is that the counterions form a two-dimensional lattice on the macroion surface, and when overcharging counterions are present on this layer the energy of the system is lowered compared to the neutral case. This feature can be directly and *exactly* computed for a small number of counterions at zero temperature, and was illustrated in refs. [11]. This WC approach remains qualitatively correct for finite temperature as long as the Coulomb coupling is very high. The crystal then melts into a strongly correlated liquid, where the local order is still strong enough to lower the free energy for the overcharged state.

The situation becomes much more complicated for aqueous systems, where the coupling is weak and in addition salt is present. One-particle inhomogeneous integral equation theories can describe some of these situations fairly well [2, 3, 14, 16] but the computed correlation functions do not necessarily give direct insight into the physical mechanisms behind these effects. The presence of excluded-volume interactions can lead to layering effects near the macroion, which are known from simple fluid theories. Here, due to the presence of charge carriers of both signs, this can even lead to layers of oscillating charge inversions [3,14,17]. This overcharging was also observed (by integral-equation and simulation [3, 15]) for *monovalent* salt ions of large size. However, until today, the basic mechanism of charge inversion for dense salt solutions remains unclear.

The goal of this letter is i) to study in detail the role of the excluded-volume contribution for the overcharging of a colloidal macroion in the presence of salts and ii) to provide a qualitative insight into the mechanism behind these effects. We find that in the presence of salt the contribution of excluded volume can be so important that the size of the small ions dominates the occurrence of overcharging and the overcharging strength increases with increasing ionic size when the electrolyte concentration is fixed. Even for monovalent ions with high enough ionic size, we observe overcharging, which cannot be explained with a salt-free WC picture due to the low Coulomb coupling strength. In order to have the simplest system, we study only the cases where the coion and the counterions have the same size. This will reduce the effects of depletion forces which lead to nontrivial features already in neutral hard-sphere fluids.

Our proposed mechanism will rest on the following arguments: For a fixed salt concentration, the available volume in the fluid is a function of the electrolyte particle size. More precisely, the entropy of the solution is decreased by enlarging the size of the salt ions [18], which enhances inter-particle correlations. On the other hand, the interface provided by the macroion leads to an increase of microion density close to the macroion, and promotes there also *lateral* ordering, even in the absence of strong electrostatic coupling, similar to a pre-freezing phenomenon. However, entropy alone can never lead to overcharging, since in this limiting case coions and counterions have the same radial distribution. But ordering and weak electrostatic correlations can lead to overcharging, as we are going to prove in this letter.

In this work we carried out MD simulations and the HNC/MSA (hypernetted chain/mean spherical approximation) integral equation to study the overcharging in spherical colloidal systems within the primitive model. In particular, the solvent enters the model only by its dielectric constant and its discrete structure [19] is ignored. The system is made up of i) a large macroion with a bare central charge $Q = -Z_{\mathrm{m}}e$ (with $Z_{\mathrm{m}} > 0$) and ii) symmetric salt ions of diameter σ and valence Z_{c}. The system is globally electrically neutral.

For the simulation procedure, all these ions are confined in an impermeable cell of radius R and the macroion is held fixed at the cell center. In order to simulate a canonical ensemble, the Langevin thermostat has been used to predict the ions trajectory as has been done in refs. [11].

Table I – *Simulation run parameters for the charged fluid (A–F) and the neutral fluid (G–H).*

Parameters	Salt valence	$Z_{\rm m}$	$\sigma/l_{\rm B}$	f
run A	2:2	48	1	2.3×10^{-1}
run B	2:2	48	0.5	2.9×10^{-2}
run C	2:2	48	0.25	3.6×10^{-3}
run D	1:1	10	1	2.3×10^{-1}
run E	1:1	48	1	2.3×10^{-1}
run F	1:1	48	0.5	2.9×10^{-2}
run G	–	–	1	2.3×10^{-1}
run H	–	–	0.5	2.9×10^{-2}

Excluded-volume interactions are taken into account with a purely *repulsive* (6-12) Lennard-Jones (LJ) potential characterized by the standard (σ, ϵ) length and energy parameters, respectively, which is cut off at the minimum [20]. The macroion-counterion distance of closest approach is defined as a. Energy units in our simulations are fixed by $\epsilon = k_{\rm B}T$ (with $T = 298\,{\rm K}$).

The pair electrostatic interaction between any pair ij, where i and j denote either a macroion or a microion, reads $U_{\rm coul}(r) = k_{\rm B}T l_{\rm B} \frac{Z_i Z_j}{r}$, where $l_{\rm B} = e^2/(4\pi\epsilon_0\epsilon_{\rm r}k_{\rm B}T_0)$ is the Bjerrum length fixing the length unit. Being interested in aqueous solutions, we choose the relative permittivity $\epsilon_{\rm r} = 78.5$, corresponding to $l_{\rm B} = 7.14\,{\rm \AA}$. The time step is $\Delta t = 0.01\tau$ with $\tau = \Gamma^{-1}$, where Γ is the damping constant of the thermostat. Typical simulation runs consisted of $2\text{–}7 \times 10^6$ MD steps after equilibration.

In order to give prominence to the effect of ionic size, we choose to work at *fixed* distance of closest approach (between the centers of the macroion and the salt ion) $a = 2l_{\rm B} = 14.28\,{\rm \AA}$. In this way, the electrostatic correlation induced by the colloid remains the same (*i.e.* fixed macroion electric field at contact) no matter what the ionic size is. Thus by changing the ionic size σ one also changes the colloidal radius accordingly, so that a remains constant. The salt concentration ρ is given by N_-/V, where $V = \frac{4}{3}\pi R^3$ is the cell volume and N_- is the number of coions. We will restrict the present study to $\rho = 1\,{\rm M}$ salt concentration. The fluid volume fraction f is defined as $(N_+ + N_-)(\frac{\sigma}{2R})^3$, where N_+ is the number of counterions. To avoid size effects induced by the simulation cell, we choose a sufficiently large radius $R = 8.2l_{\rm B}$ yielding more than 1000 mobile charges. Simulation run parameters are gathered in table I. The HNC/MSA calculations were performed using the technique presented in [16] and references therein. Here it is assumed that the system size is infinite, and the bulk salt concentration is fixed. In practice, there should be no observable difference in the correlation functions (between HNC/MSA and MD) close to the macroions, because the wall effects die off sufficiently fast.

We first illustrate the excluded-volume correlations present for a *neutral* hard-sphere fluid (runs *G–H*) (identical to systems *A–B* and *E–F*, but uncharged (see table I)). Although these kinds of systems are "simple" fluids [21], it is fruitful to elucidate what exactly happens at this "low" fluid density upon varying the fluid particle size σ in the presence of a single large spherical particle. To characterize the fluid structure, we consider the pair distribution function $g(r)$ between the colloid and the fluid particle, which is just proportional to the local density $n(r)$: $n(r) = \rho g(r)$. Results are depicted in fig. 1. For the large value $\sigma = l_{\rm B}$, one clearly observes a relative high local concentration as well as a *short-range ordering* nearby the colloidal surface. When the particle size is reduced by a factor 2 (keeping a fixed), the behavior is qualitatively different and the system is basically uncorrelated. By increasing σ

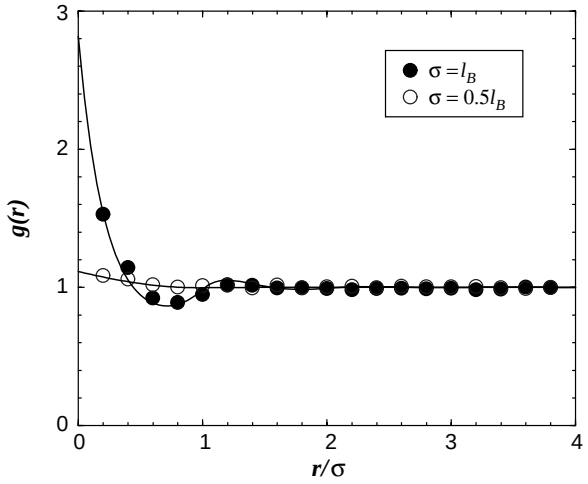

Fig. 1 – Pair distribution function $g(r)$ between the colloid and the fluid particle in the neutral state (runs *G*–*H*) for two particle sizes σ. The origin of the abscissa is taken at the distance of closest approach $a = 2l_{\mathrm{B}}$. Lines and symbols correspond to the HNC theory and simulation, respectively.

at fixed fluid density ρ, the mean surface-surface distance between particles is reduced, which in turn leads to higher collision probability and thus to higher correlations. In other words, by reducing the *available* volume, one promotes *ordering* [16, 22]. This seems to be trivial in the bulk, but the presence of the colloidal surface induces an even enhanced ordering and the system can prefreeze (order) close to the colloid. Note that the same effects are naturally present for a fluid close to a planar wall [21, 23].

To characterize the overcharging, we introduce the fluid integrated charge $Q(r)$ which corresponds to the total *net* charge in the fluid (omitting the macroion bare charge Z_{m}) within a distance r from the distance of closest approach a. Results are sketched in fig. 2(a) and (b) for divalent and monovalent salt ions, respectively. Theoretical and numerical analysis are in very good qualitative agreement.

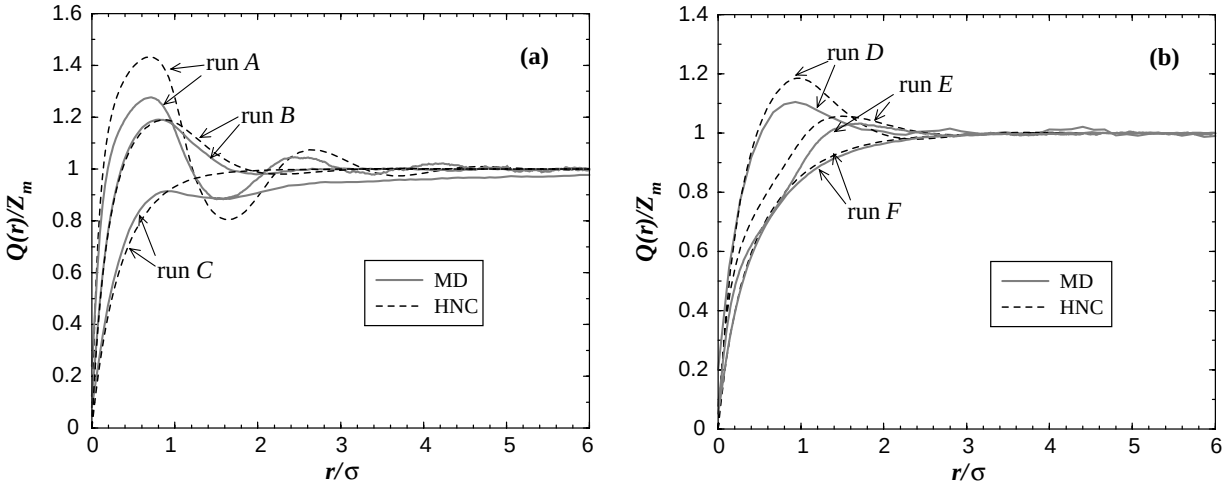

Fig. 2 – Reduced fluid integrated charge $Q(r)/Z_{\mathrm{m}}$ as a function of distance r for three different particle sizes σ. (a) Divalent salt ions (runs *A*–*C*), (b) monovalent salt ions (runs *D*–*F*). The origin of the abscissa is taken at the distance of closest approach $a = 2l_{\mathrm{B}}$.

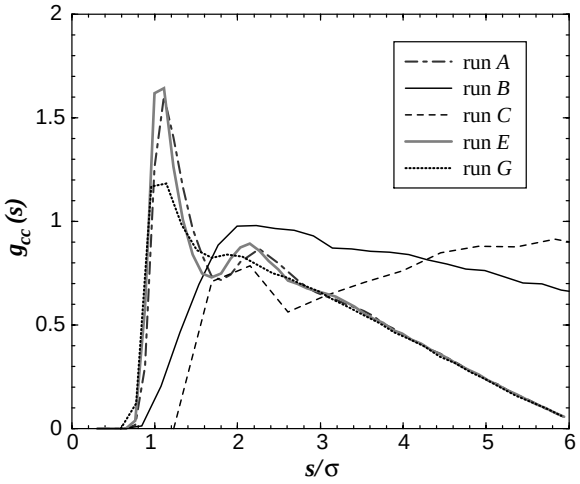

Fig. 3 – Two-dimensional surface counterion correlation functions $g_{cc}(s)$ for divalent salt (run A–C), monovalent salt (run E), and a neutral system (run G).

For the divalent electrolyte solutions (runs A–C), we observe that overcharging is strongly dictated by the ionic size σ (see fig. 2(a)). For small ions (run C) *no* overcharging occurs (*i.e.* $Q(r)/Z_m < 1$), which is a nontrivial effect probably related to the forming of ionic pairs (counterion-coion pairing) due to the strong pair interaction of $8k_BT$. This delicate point will be addressed in a future study, and was also observed in [15]. Upon increasing σ, the degree of overcharging increases. We carefully checked that the distance $r = r^*$, where $Q(r^*)$ assumes its maximal value, corresponds to a zone of coion depletion (in average there are less than 2 coions within r^*). This implies that also the absolute number of counterions at the vicinity of the macroion surface increases with increasing σ. This is qualitatively in agreement with what we observed above for neutral systems. However, we are going to show later that electrostatic correlations are also *concomitantly* responsible of this extra counterion population (increasing with σ) in the vicinity of the colloidal surface.

For the monovalent electrolyte solution (see fig. 2(b)) overcharging occurs for $\sigma = l_B$ (runs D and E). In respect to the salt-free WC picture this is rather unexpected since here the "plasma" parameter $\Gamma_{cc} = l_B Z_c^2/a_{cc}$, where $a_{cc} = (\pi c)^{-1/2}$ (c standing for the two-dimensional surface counterion concentration) is the mean distance between counterions on the surface, is small. More precisely for $Z_m = 10$ (run D) we find $\Gamma_{cc} \approx 0.8$, and for $Z_m = 48$ (run E) we have $\Gamma_{cc} < 1.0$ [24]. But following this salt-free approach, it is necessary to have at least $\Gamma_{cc} > 2$ to get overcharge [25]. Note that from run D ($Z_m = 10$) to run E ($Z_m = 48$) one increases the macroion surface-charge density leading (for $Z_m = 48$) to a higher *absolute* overcharging $Q(r^*)$ but a weaker ratio $Q(r^*)/Z_m$, which is qualitatively in accord with the WC picture, since the maximal overcharging is proportional to $\sqrt{c}$. A closer look at fig. 2(b) reveals that for $Z_m = 48$ (run E) r^*/σ is shifted to the right compared to the divalent case. This is merely a packing effect and it is due to the fact that for monovalent counterions the macroion charge (over)compensation involves twice more the number of counterions particles than in the divalent case. Therefore, for the macroion charge density under consideration ($Z_m = 48$), more than one counterion layer is needed to compensate for the macroion charge. Again, for a smaller ionic salt size $\sigma = 0.5l_B$ (run F) the overcharging effect is canceled.

Recently, a depletion of salt ions (*total* local density of co- and counter-ions) near the macroion surface was reported for bulk salt ion concentrations similar to ours but very *low* surface charge density [26]. For all of our investigated cases (runs A–F), however, we never

observe such a *depletion*. The reason is that such an effect vanishes as soon as the ionic size is sufficiently large and/or the surface-charge density is large enough, which is in agreement with our findings. Indeed, similarly to what happened with image charges, the self-image repulsion is only relevant for *low* charge density [27]. Note that the parameters leading to overcharging *cannot* give rise to an observation of salt ion depletion.

For the WC picture to be effective we need strong lateral correlations which cannot come from pure electrostatic effects. To see if such correlations are present, we consider the local two-dimensional surface counterion structure. We analyzed in our simulations the *two-dimensional* counterion pair distribution $g_{\rm cc}(s)$, where s is the arclength on the macroion sphere of radius a. All counterions lying at a distance $r < a + 0.5\sigma$ from the macroion center are radially projected to the contact sphere of radius a. Predominantly, counterions are present in the first layer. For the neutral system (run G) we analyzed the small neutral species. Results are given in fig. 3. We observe that all systems with an ion diameter $\sigma = l_{\rm B}$ show their first peak at roughly 1σ, and a weaker second peak at about 2σ, exhibiting long-range surface correlations. The second peak is very weak in the neutral system G, but clearly visible in system A and E. Due to the stronger electrostatic repulsion the second peak for the divalent system A is somewhat further apart than for the monovalent system E. The systems B and C with smaller ion diameters show a correlation hole of size $\approx 2\sigma$, which is of purely electrostatic origin. Therefore, lateral correlations can be produced either by pure entropy effects (run G) or pure electrostatic effects (run C), or we can have an enhanced lateral ordering due to the interplay of both (run A, E). Qualitatively, WC arguments are still applicable to monovalent systems (such as run E) if one considers an effective low local surface temperature stemming from the strong surface ordering.

In summary, the observed overcharging for low Coulomb coupling can be traced back to the complicated interplay of entropy and energy by the following two effects. First, by enlarging the excluded volume of the salt ions at fixed concentration, one lowers the accessible volume to the fluid particles. Second, the presence of the large macroion provides an interface near which the density of the fluid is increased as compared to the bulk, and the solution can prefreeze due to entropic effects, provided the available volume gets low enough. The closest layer to the interface possesses already strong lateral correlations, even for a neutral system. If the system is additionally charged, then even weak Coulomb correlations can lead to the formation of a strongly correlated liquid, where the overcharged state is energetically favorable, as shown in [7, 11, 12, 16]. The order of this counterion layer is however not created by electrostatic interactions as in the normal WC picture, but it is largely due to entropic effects. The observed overcharging effect might have implications for the stability of colloidal suspensions. Additions of monovalent salt will eventually make colloidal suspensions unstable due to the onset of the van-der-Waals attractions. Upon addition of even more monovalent salt, there is the possibility of salting the precipitate again in, as has been seen for polyelectrolyte systems [28]. The observation of such a re-entrant transition could be an important hint towards the existence of overcharging with monovalent salt ions.

* * *

The authors are grateful to K. Kremer for a critical reading of the manuscript, and RM thanks the LEA for financial support. EG-T acknowledges the support by PROMEP and FAI-UASLP.

REFERENCES

[1] van Megen W. and Snook I., *J. Chem. Phys.*, **73** (1980) 4656; Torrie G. M. and Valleau J. P., **73** (1980) 5807.
[2] Lozada-Cassou M., Saavedra-Barrera R. and Henderson H., *J. Chem. Phys.*, **77** (1982) 5150.
[3] Gonzales-Tovar E., Lozada-Cassou M. and Henderson D., *J. Chem. Phys.*, **83** (1985) 361.
[4] Galisteo F., de las Nieves López F. J., Cabrerizo M. and Hidalgo-Alvarez R., *Prog. Colloid Polym. Sci.*, **82** (1990) 313; Elimelech M. and O'Melia C. R., *Colloids Surf.*, **44** (1990) 165; Walker H. W. and Grant S. B., *Colloids Surf. A*, **119** (1996) 229; Götting N., Fritz H., Maier M., von Stamm J., Schoofs T. and Bayer E., *Colloid Polym. Sci.*, **277** (1999) 145.
[5] Tanaka M. and Grosberg A. Y., *Eur. Phys. J. E*, **7** (2002) 371.
[6] Shklovskii B. I., *Phys. Rev. Lett.*, **82** (1999) 3268.
[7] Shklovskii B. I., *Phys. Rev. E*, **60** (1999) 5802.
[8] Nguyen T. T., Grosberg A. Y. and Shklovskii B. I., *Phys. Rev. Lett.*, **85** (2000) 1568; *J. Chem. Phys.*, **113** (2000) 1110.
[9] Lozada-Cassou M., González-Tovar E. and Olivares W., *Phys. Rev. E*, **60** (1999) R17.
[10] Nguyen T. T. and Shklovskii B. I., *Phys. Rev. E*, **64** (2001) 041407.
[11] Messina R., Holm C. and Kremer K., *Phys. Rev. Lett.*, **85** (2000) 872; *Europhys. Lett.*, **51** (2000) 461; *Phys. Rev. E*, **64** (2001) 021405.
[12] Messina R., Holm C. and Kremer K., *Eur. Phys. J. E*, **4** (2001) 363; Messina R., *Physica A*, **308** (2002) 59.
[13] Tanaka M. and Grosberg A. Y., *J. Chem. Phys.*, **115** (2001) 567.
[14] Greberg H. and Kjellander R., *J. Chem. Phys.*, **108** (1998) 2940.
[15] Deserno M., Jiménez-Ángeles F., Holm C. and Lozada-Cassou M., *J. Phys. Chem. B*, **105** (2001) 10983.
[16] Lozada-Cassou M. and Jiménez-Ángeles F., arXiv:physics/0105043 v2 (2001).
[17] Deserno M., May S. and Holm C., *Macromolecules*, **33** (2000) 199.
[18] This argument holds far enough from the solid-liquid transition as in the present study (*i.e.* the highest fluid volume fraction f we consider is 0.23). Indeed entropy alone can drive crystallization as in hard-sphere systems.
[19] Allahyarov E. and Löwen H., *J. Phys. Condens. Matter*, **13** (2001) L277; *Phys. Rev. E*, **63** (2001) 041403.
[20] The LJ potential is, rigorously speaking, not a hard-core one, but can be considered in practice as such.
[21] Hansen J.-P. and McDonald I., *Theory of Simple Liquids* (Academic, London) 1990.
[22] This feature holds only if the fixed particle (here the colloid) is larger than the fluid particles.
[23] Courtemanche D. J. and van Swol F., *Phys. Rev. Lett.*, **69** (1992) 2078; Götzelmann B., Haase A. and Dietrich S., *Phys. Rev. E*, **53** (1996) 3456; Kegel W. K., *J. Chem. Phys.*, **115** (2001) 6538.
[24] This is due to a packing effect which imposes that a_{cc} cannot be smaller than σ.
[25] Rouzina I. and Bloomfield V., *J. Chem. Phys.*, **100** (1996) 9977.
[26] Allahyarov E., Löwen H., Louis A. A. and Hansen J. P., *Europhys. Lett.*, **57** (2002) 731.
[27] Messina R., *Image charges in spherical geometry: Application to colloidal systems*, e-print:cond-mat/0204550.
[28] Eisenberg H. and Mohan G. R., *J. Phys. Chem.*, **63** (1959) 671; Eisenberg H. and Casassa E. F., *J. Polym. Sci.*, **47** (1960) 29.

Appendix G

Image charges in spherical geometry: application to colloidal systems

ARTICLES

Image charges in spherical geometry: Application to colloidal systems

René Messina[a)]
Max-Planck-Institut für Polymerforschung, Ackermannweg 10, 55128 Mainz, Germany

(Received 9 May 2002; accepted 24 September 2002)

The effects of image charges (i.e., induced surface charges of polarization) in spherical geometry and their implication for charged colloidal systems are investigated. We study analytically and exactly a single microion interacting with a dielectric sphere and discuss the similarities and discrepancies with the case of a planar interface. By means of extensive Monte Carlo simulations, we study within the framework of the primitive model the effects of image charges on the structure of the electrical double layer. Salt-free environment as well as salty solutions are considered. A remarkable finding of this study is that the position of the maximum in the counterion density (appearing at moderately surface charge density) remains quasi-identical, regardless of the counterion valence and the salt content, to that obtained within the *single*-counterion system. [DOI: 10.1063/1.1521935]

I. INTRODUCTION

In charged colloidal systems electrostatic effects, and especially the structure of the electrical double layer, often play a determinant role for their physico-chemical properties. It is well known that charged colloids (i.e., macroions) have typically a low dielectric constant ($\varepsilon_r \approx 2-5$) which is much smaller than that of the surrounding solvent (e.g., for water $\varepsilon_r \approx 80$). In most of the theoretical works, this dielectric discontinuity is ignored.

Nevertheless, a few studies have addressed the effects of image charges (i.e., image forces stemming from the dielectric discontinuity) on the counterion distribution for planar geometry which is closely related to our problem. An electrolyte close to a charged wall[1,2] or confined between two charged plates[3] had been the subject of MC simulations. Similar systems have also been investigated by integral-equation[4–6] and mean field theories.[7–9]

As far as the spherical geometry is concerned, much less literature is available. Counterion distributions with image forces in salt-free environment were investigated by MC simulations.[10] There some approximations for the treatment of the image forces were used that are not always fully controlled. The main conclusions however remain qualitatively correct.

The aim of this paper is to provide a detailed analysis of the image forces in spherical geometry and their effects on the structure of the electrical double layer. The remainder of this article is set out as follows. Section II corresponds to the analytical part of the paper. We first briefly present the general theoretical background of the concept of image charges in spherical geometry. Then we apply it to colloidal systems to compute (exactly) some relevant observables and discuss our results. Section III is devoted to the computational details of our MC simulations. In Sec. IV, we present our simulation results for salt-free environment as well as salty solutions where image forces are explicitly taken into account with no approximation. Finally, Sec. V contains brief concluding remarks.

II. THEORY

In this part we mainly study the interaction of a *single excess* charge with a dielectric sphere. We briefly present the formalism of the dielectric model for spherical interfaces and discuss some important electrostatic properties. Such a system captures the underlying physics of image forces in spherical geometry. Moreover a systematic quantitative comparison with the planar geometry is undertaken.

A. Poisson equation with azimuthal symmetry

The model system is sketched in Fig. 1. Consider an *uncharged* dielectric sphere of radius a and dielectric constant (relative permittivity) ε_2 embedded in an infinite dielectric medium (region 1) characterized by ε_1. A single excess charge of magnitude q is located outside the dielectric sphere at a distance $b=|\mathbf{b}|$ from its center.

The central problem is to determine the electrostatic potential $\Phi(\mathbf{r})$ at any point in the space. This is achieved by solving the Poisson equation which reads

$$\Delta\Phi(\mathbf{r}) = -\frac{\rho(\mathbf{r})}{\varepsilon}, \tag{1}$$

where $\rho(\mathbf{r})$ is the volume charge density and $\varepsilon=\varepsilon_0\varepsilon_i$ with ε_0 being the vacuum permittivity and $i=1,2$. Since here $\rho(\mathbf{r})=q\,\delta(\mathbf{r}-\mathbf{b})$ and taking into account the azimuthal symmetry, Eq. (1) reduces (for $\mathbf{r}\neq\mathbf{b}$) to the Laplace equation

a)Electronic address: messina@thphy.uni-duesseldorf.de; Permanent address: Institut für theoretische Physik II, Heinrich-Heine-Universität Düsseldorf, Universitätsstrasse 1, 40225 Düsseldorf, Germany.

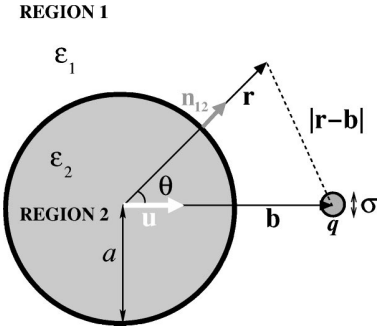

FIG. 1. Model for a dielectric sphere (colloid) of dielectric constant ε_2 embedded in an infinite medium characterized by a different dielectric constant ε_1. An excess charge (q) is located near the boundary outside the spherical particle. This is a two-dimensional representation of the three-dimensional system.

$$\Delta\Phi(r,\theta)=\frac{1}{r^2}\frac{\partial}{\partial r}\left(r^2\frac{\partial\Phi}{\partial r}\right)+\frac{1}{r^2}\frac{1}{\sin\theta}\frac{\partial}{\partial\theta}\left(\sin\theta\frac{\partial\Phi}{\partial\theta}\right)=0, \tag{2}$$

where θ is the angle between $\mathbf{r}$ and $\mathbf{b}$ (see Fig. 1) and $r=|\mathbf{r}|$. The general solution of the Laplace equation with azimuthal symmetry is given by[12–14]

$$\Phi(r,\theta)=\sum_{l=0}^{\infty}\left[M_l r^l+N_l\frac{1}{r^{l+1}}\right]P_l(\cos\theta), \tag{3}$$

where $P_l(\cos\theta)$ is the associated Legendre polynomial of order l.

Inside the dielectric sphere (region 2) the electrostatic potential $\Phi_2(\mathbf{r})$ must be finite at $r=0$ so that $N_l=0$ in Eq. (3), and hence

$$\Phi_2(r,\theta)=\sum_{l=0}^{\infty}A_l r^l P_l(\cos\theta). \tag{4}$$

Concerning the electrostatic potential outside the dielectric sphere (region 1) we know that without dielectric discontinuity (at $r=a$) the potential would simply be given by $q/4\pi\varepsilon_0\varepsilon_1|\mathbf{r}-\mathbf{b}|$. Making use of the following identity

$$\frac{1}{|\mathbf{r}-\mathbf{b}|}=\sum_{l=0}^{\infty}\frac{r_<^l}{r_>^{l+1}}P_l(\cos\theta), \tag{5}$$

where $r_<$ ($r_>$) is the smaller (larger) of r and b, the electrostatic potential $\Phi_1(\mathbf{r})$ in region 1 reads[11]

$$\Phi_1(r,\theta)=\sum_{l=0}^{\infty}\left[C_l\frac{1}{r^{l+1}}+\frac{q}{4\pi\varepsilon_0\varepsilon_1}\frac{r_<^l}{r_>^{l+1}}\right]P_l(\cos\theta), \tag{6}$$

recalling that $\Phi_1(\mathbf{r})$ must be finite at $r\to\infty$ so that $M_l=0$ in Eq. (3).

B. Boundary conditions

The electrostatic potentials given by Eqs. (4) and (6) will be univocally determined by applying the proper boundary conditions that will fix A_l and C_l. The boundary conditions are derived from the full set of Maxwell equations. The results are that the normal components of the displacement $\mathbf{D}$ and the tangential components of $\mathbf{E}$ on either side of the spherical interface at $r=a$ satisfy

$$\begin{aligned}(\mathbf{D}_1-\mathbf{D}_2)\cdot\mathbf{n}_{12}&=0\\(\mathbf{E}_1-\mathbf{E}_2)\times\mathbf{n}_{12}&=0,\end{aligned} \tag{7}$$

where $\mathbf{n}_{12}=\mathbf{r}/r$ is a unit normal vector to the surface directed from region 2 to region 1 (see Fig. 1). Within the framework of the linear response theory we have $\mathbf{D}=\varepsilon\mathbf{E}$. Combining Eqs. (4) and (6) with Eq. (7) and noting that $\mathbf{E}=-\nabla\Phi$, it follows that

$$\begin{aligned}\varepsilon_2 A_l l a^{l-1}&=\varepsilon_1\left[-C_l\frac{l+1}{a^{l+2}}+\frac{q}{4\pi\varepsilon_0\varepsilon_1}\frac{la^{l-1}}{b^{l+1}}\right]\\A_l a^l&=C_l\frac{1}{a^{l+1}}+\frac{q}{4\pi\varepsilon_0\varepsilon_1}\frac{a^l}{b^{l+1}}.\end{aligned} \tag{8}$$

This set of two equations [Eq. (8)] can be readily solved to yield the Legendre coefficients A_l and C_l:

$$\begin{aligned}A_l&=\frac{q}{4\pi\varepsilon_0\varepsilon_1}\frac{1}{b^{l+1}}\frac{\varepsilon_1(2l+1)}{\varepsilon_1(l+1)+\varepsilon_2 l}\\C_l&=\frac{q}{4\pi\varepsilon_0\varepsilon_1}\frac{a^{2l+1}}{b^{l+1}}\frac{(\varepsilon_1-\varepsilon_2)l}{\varepsilon_1(l+1)+\varepsilon_2 l}\end{aligned} \tag{9}$$

and hence

$$\Phi_1(r,\theta)=\frac{q}{4\pi\varepsilon_0\varepsilon_1}\left[\frac{1}{|\mathbf{r}-\mathbf{b}|}+\sum_{l=1}^{\infty}\frac{a^{2l+1}}{b^{l+1}}\frac{(\varepsilon_1-\varepsilon_2)l}{\varepsilon_1(l+1)+\varepsilon_2 l}\frac{1}{r^{l+1}}P_l(\cos\theta)\right]. \tag{10}$$

The physical interpretation of Eq. (10) is straightforward. The first term represents the usual electrostatic potential (without image forces) generated by q and the second term can be referred to as the electrostatic potential due to ''image charges'' stemming from the dielectric discontinuity. As expected, the strength of the image force is strongly governed by the jump $\Delta\varepsilon$ in the dielectric constant defined as

$$\Delta\varepsilon=\varepsilon_1-\varepsilon_2. \tag{11}$$

In particular, one can anticipate and state that the interaction between the microion q and the dielectric particle (i.e., the *self-image interaction*) is *repulsive* for $\Delta\varepsilon>0$ (i.e., $\varepsilon_1>\varepsilon_2$) and *attractive* for $\Delta\varepsilon<0$ (i.e., $\varepsilon_1<\varepsilon_2$) as it is also the case in planar geometry.

One can show that Eq. (10) can also be written as follows (see, e.g., Ref. 15 and references therein)

$$\Phi_1(r,\theta)=\frac{q}{4\pi\varepsilon_0\varepsilon_1}\left\{\frac{1}{|\mathbf{r}-\mathbf{b}|}+\frac{\varepsilon_1-\varepsilon_2}{\varepsilon_1+\varepsilon_2}\frac{1}{a}\left[\frac{u}{|\mathbf{r}-\mathbf{u}|}-\frac{\varepsilon_1}{\varepsilon_1+\varepsilon_2}\int_0^u\frac{(u/x)^{\varepsilon_2/(\varepsilon_1+\varepsilon_2)}}{|\mathbf{r}-\mathbf{x}|}dx\right]\right\}, \tag{12}$$

where $\mathbf{u}=\mathbf{b}a^2/b^2$ (see Fig. 1).[16] In this formalism the geometrical structure of the image charges is transparent and it is specified by the second main term (between brackets) of Eq. (12). More precisely, one has to deal with an *infinite manifold* of image charges distributed along the oriented segment $\mathbf{u}$ that electrically compensates the image point-charge q_{im} located at $\mathbf{u}$ and whose magnitude is given by

$$q_{im}=q\frac{\varepsilon_1-\varepsilon_2}{\varepsilon_1+\varepsilon_2}\frac{a}{b}. \tag{13}$$

C. Polarization charge

It is important to know the surface distribution of the induced charge on the spherical interface. In the bulk (i. e., in region 1 or 2) we have a zero volume density of polarization charge (ρ_{pol}) since $\rho_{pol}=\varepsilon_0\nabla\cdot\mathbf{E}=-\nabla\cdot\mathbf{P}=0$ (except at $\mathbf{r}=\mathbf{b}$). At the interface ($r=a$) the surface density of polarization charge $\sigma_{pol}^{(sph)}$ is given by

$$\sigma_{pol}^{(sph)}=-(\mathbf{P}_1-\mathbf{P}_2)\cdot\mathbf{n}_{12}, \tag{14}$$

where

$$\begin{aligned}\mathbf{P}_1&=\varepsilon_0(\varepsilon_1-1)\mathbf{E}_1=-\varepsilon_0(\varepsilon_1-1)\nabla\Phi_1\\ \mathbf{P}_2&=\varepsilon_0(\varepsilon_2-1)\mathbf{E}_2=-\varepsilon_0(\varepsilon_2-1)\nabla\Phi_2\end{aligned} \tag{15}$$

are the polarizations in region 1 and 2, respectively. Using Eqs. (4), (6), (9), (14) and (15), the final expression of $\sigma_{pol}^{(sph)}$ reads

$$\sigma_{pol}^{(sph)}(\cos\theta)=\frac{q}{4\pi\varepsilon_1 b^2}\sum_{l=1}^{\infty}\left(\frac{a}{b}\right)^{l-1}(2l+1)l \times\frac{\varepsilon_1-\varepsilon_2}{\varepsilon_1(l+1)+\varepsilon_2 l}P_l(\cos\theta). \tag{16}$$

The net charge of polarization $Q_{pol}^{(sph)}=\int_{-1}^{1}2\pi a^2\sigma_{pol}^{(sph)}(\cos\theta)d(\cos\theta)$ is zero,[17] meaning that there is *no monopole* contribution as it should be.

The critical angle θ^* where $\sigma_{pol}^{(sph)}$ changes sign is given by the geometrical condition

$$\begin{aligned}\mathbf{E}_1(r=a,\theta^*)&\perp\mathbf{n}_{12}\\ \mathbf{E}_2(r=a,\theta^*)&\perp\mathbf{n}_{12}\end{aligned} \tag{17}$$

which is the orthogonality condition at the interface between the (inner and outer) electric field and $\mathbf{n}_{12}$. In terms of Legendre polynomials, Eq. (17) can be equivalently written as

$$\sum_{l=1}^{\infty}\left(\frac{a}{b}\right)^{l-1}\frac{(2l+1)l}{\varepsilon_1(l+1)+\varepsilon_2 l}P_l(\cos\theta^*)=0, \tag{18}$$

where Eq. (16) was used. Two limiting cases can be easily described: (i) for $b/a\gg 1$ we have $\theta^*\to\pi/2$ [recalling that $P_1(\cos\theta)=\cos\theta$] and (ii) for $b/a\to 1$ we have $\theta^*\to 0$. In general, θ^* increases with b and it is a complicated function of b/a, ε_1 and ε_2.

For a *planar* interface, the surface density of polarization charge $\sigma_{pol}^{(plan)}(d)$ is given by[14]

$$\sigma_{pol}^{(plan)}(d)=\frac{q}{2\pi\varepsilon_1}\frac{\varepsilon_1-\varepsilon_2}{\varepsilon_1+\varepsilon_2}\frac{b-a}{[(b-a)^2+d^2)]^{3/2}}, \tag{19}$$

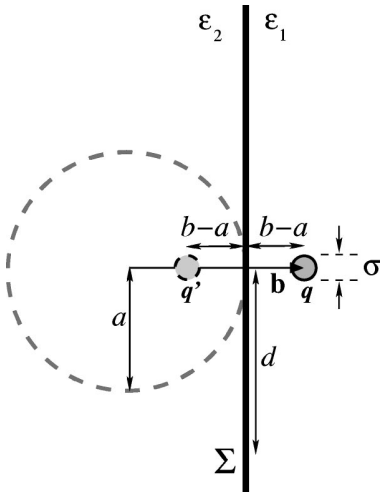

FIG. 2. Model for a microion (q) near a planar interface (Σ) separating the two semi-infinite media characterized by ε_1 and ε_2. The imaginary spherical dielectric of radius a is shown for geometrical comparison with the setup of Fig. 1. This is a two-dimensional representation of the three-dimensional system.

where $d=\sqrt{x^2+y^2}$ is the radial distance (in cylindrical coordinates system) belonging to the planar interface (see Fig. 2). Equation (19) demonstrates that $\sigma_{pol}^{(plan)}(d)$ *never* changes sign [as can also be deduced from simple geometrical considerations—Eq. (17)] in contrast with the spherical interface. The total charge of polarization $Q_{pol}^{(plan)}$ is obtained by direct integration of $\sigma_{pol}^{(plan)}(d)$ and its expression is given by

$$Q_{pol}^{(plan)}=\frac{q'}{\varepsilon_1}, \tag{20}$$

where

$$q'=q\frac{\varepsilon_1-\varepsilon_2}{\varepsilon_1+\varepsilon_2} \tag{21}$$

is the *unique* image charge located at the mirror position of q (see Fig. 2). This *nonzero* monopolar contribution for the planar interface involves a *stronger* and *longer ranged* self-image interaction.

D. Application to colloidal systems

So far we treat in a rather general manner the physics of a point charge near a spherical dielectric interface. We now would like to apply the above theory to colloidal systems. In the remaining of this paper we suppose that region 1 corresponds to water, so that we take $\varepsilon_1=80$ corresponding to the water dielectric constant at room temperature. To characterize the low permittivity of the colloid we consider here $\varepsilon_2=2$ so that $\Delta\varepsilon=78$. The little ion carries a charge $q=Ze$ where e stands for the elementary charge and Z for its valence, and has a diameter σ. An important quantity is

$$r_0=a+\frac{\sigma}{2} \tag{22}$$

being the center–center distance of closest approach between the colloid and the microion q.

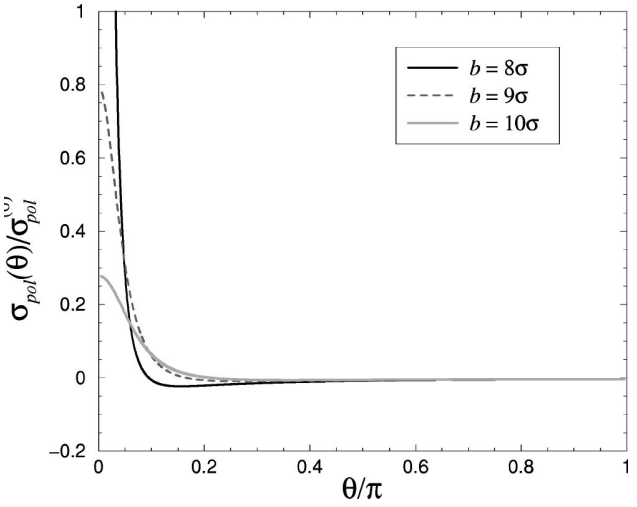

FIG. 3. Polar profile of the surface density of polarization charge $\sigma_{pol}^{(sph)}(\theta)$ in units of $\sigma_{pol}^{(0)}=(q/4\pi\varepsilon_1\sigma^2)$ for different radial distances b of the excess charge q with $\varepsilon_1=80$, $\varepsilon_2=2$ and $a=7.5\sigma$.

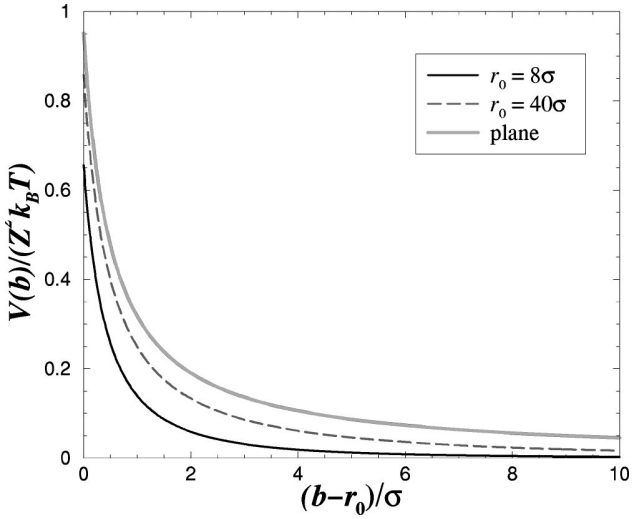

FIG. 4. Potential of self-image interaction for a microion ($q=Ze$) in spherical and planar geometries with $\varepsilon_1=80$ and $\varepsilon_2=2$.

1. Induced surface charge

It is helpful to have a precise representation of the polar profile of $\sigma_{pol}^{(sph)}(\theta)$ in order to get a clear understanding of the source of the image forces. Although at first glance such a study should belong to standard electrostatics we are not aware of any data in the literature that treats this relevant aspect.

The numerical computation of Eq. (16) was performed using a cutoff $l_{max}=300$ in the Legendre space leading to high accuracy.[18] The plot of $\sigma_{pol}^{(sph)}(\theta)$ for $a=7.5\sigma$ and $b/\sigma=8$, 9 and 10 can be found in Fig. 3. One can clearly observe that $\sigma_{pol}^{(sph)}(\theta)$ is strongly *inhomogeneous*. For small θ, $\sigma_{pol}^{(sph)}(\theta)$ is highly positive (i.e., it carries the same charge sign as q) and decreases abruptly. The angle θ^* [given by Eq. (18)] where $\sigma_{pol}^{(sph)}(\theta)$ changes sign is 16.9°, 29.5° and 37.4° for $b/\sigma=8$, 9 and 10, respectively. In parallel, by increasing b one drastically decreases the magnitude as well as the inhomogeneity of $\sigma_{pol}^{(sph)}(\theta)$. Recall that for $b/a\gg 1$ we have $\sigma_{pol}^{(sph)}(\theta)\sim\cos\theta$.

It is insightful to compare $\sigma_{pol}^{(sph)}(\theta=0)$ with $\sigma_{pol}^{(plan)}(d=0)$ [computed from Eq. (19)] since both quantities give the maximum of $\sigma_{pol}^{(sph)}(\theta)$ and $\sigma_{pol}^{(plan)}(d)$, respectively. The corresponding numerical values are gathered in Table I. The values found at finite curvature are very similar to those of zero one. The fact that $\sigma_{pol}^{(sph)}(\theta=0)$ is systematically smaller than $\sigma_{pol}^{(plan)}(d=0)$ is consistent with the idea that in spherical geometry we have the presence of opposite image charges. Nevertheless, for sufficiently large a one should recover the planar case.

TABLE I. Numerical values of $\sigma_{pol}^{(sph)}(\theta=0)$ and $\sigma_{pol}^{(plan)}(d=0)$ in units of $q/4\pi\varepsilon_1\sigma^2$ as a function of b. The corresponding profiles of $\sigma_{pol}^{(sph)}(\theta)$ can be found in Fig. 3.

b/σ	$\sigma_{pol}^{(sph)}(\theta=0)$	$\sigma_{pol}^{(plan)}(d=0)$
8	7.41	7.61
9	0.794	0.846
10	0.278	0.304

2. Self-image interaction

We now compute the potential of interaction between the microion q and the dielectric particle or, in terms of image forces, the potential of self-image interaction. This is the work done in bringing the microion from infinity to its position **b**, and it is equal to the *half*-product of q and the second term of $\Phi_1(r=b)$ given by Eq. (10). In that case we have $\mathbf{r}=\mathbf{b}$ (see Fig. 1), so that $\theta=0$ and therefore $P_l[\cos(\theta=0)]=1$. In order to normalize the energy with k_BT we introduce the Bjerrum length $l_B=e^2/(4\pi\varepsilon_0\varepsilon_1 k_BT)$ which is 7.14 Å for water at $T=298$ K. By choosing $\sigma=3.57$ Å we have $l_B=2\sigma$. The potential of self-image interaction $V_{self}^{(sph)}(b)$ is then given by

$$V_{self}^{(sph)}(b)=\frac{1}{2}k_BTl_B\frac{Z^2}{b}\sum_{l=1}^{\infty}\left(\frac{a}{b}\right)^{2l+1}\frac{(\varepsilon_1-\varepsilon_2)l}{\varepsilon_1(l+1)+\varepsilon_2 l}. \tag{23}$$

Equation (23) shows that the typical interaction range scales like $1/b^4$ and therefore it is *short-ranged*.[19] Note that it is fully equivalent to compute $V_{self}^{(sph)}(b)$ from the surface polarization charges as follows

$$V_{self}^{(sph)}(b)=\frac{1}{2}\frac{1}{4\pi\varepsilon_0}\int_{-1}^{1}2\pi a^2 q\frac{\sigma_{pol}^{(sph)}(\cos\theta)}{|\mathbf{r}_a-\mathbf{b}|}d(\cos\theta), \tag{24}$$

where $\mathbf{r}_a$ is the radial vector of magnitude $|\mathbf{r}_a|=a$ and $\sigma_{pol}^{(sph)}(\cos\theta)$ is given by Eq. (16).

It is insightful to compare the potential of self-image interaction obtained in spherical geometry with that, $V_{self}^{(plan)}(b-a)$, obtained in planar geometry. The setup for a planar interface is sketched in Fig. 2. In this situation the analytical expression of $V_{self}^{(plan)}(b-a)$ is simply given by

$$V_{self}^{(plan)}(b-a)=\frac{1}{2}k_BTl_BZ^2\frac{\varepsilon_1-\varepsilon_2}{\varepsilon_1+\varepsilon_2}\frac{1}{2(b-a)}. \tag{25}$$

Profiles of $V_{self}^{(sph)}(b)$ (for two colloidal radii) and $V_{self}^{(plan)}(r)$ are reported in Fig. 4. Since in both (planar and spherical) cases the potential of interaction diverges at the interface, we only show results from $r>r_0$ as it is the case in experimental systems. The numerical computation of Eq. (23) was performed using the formalism of Eq. (12) allowing an arbitrary precision.[20]

Figure 4 clearly shows that the self-image interaction is weaker (the higher the curvature) with a spherical interface than with a planar one. In particular, at contact we have $V_{self}^{(sph)}(r_0=8\sigma)=0.66Z^2k_BT$ and $V_{self}^{(sph)}(r_0=40\sigma)=0.86Z^2k_BT$ for the spherical interface and $V_{self}^{(plan)}(\sigma/2)=0.95Z^2k_BT$ for the planar one. These features can be physically explained in terms of polarization charges. In the contact region (i.e., for small θ—see Fig. 2) we know that the surface polarization charge is quasi-identical on both spherical and planar interfaces. However, for *finite* curvature we also know that $\sigma_{pol}^{(sph)}$ changes sign above θ^* and in the present case $\sigma_{pol}^{(sph)}$ gets *oppositely* charged to q. This latter effect is the main cause that leads to a weaker self-image interaction for spherical interfaces. Nevertheless, by increasing a (i.e., reducing the curvature) one approaches the planar case as expected (see Fig. 4). Physically, this means that the contribution of the negative polarization charges (lying at $\theta>\theta^*$) to the self-image interaction [Eq. (24)] becomes negligible for sufficiently large colloidal radius.

3. Effect of curvature on the contact potential

It is clear that for sufficiently low curvature one should recover the planar case as far as the self-image interaction is concerned. Thus, a natural question that arises is: for which typical colloidal size are curvature effects relevant?

A suitable observable for this problem is provided by the contact potential $V_{self}^{(sph)}(b=a+\sigma/2)$. This quantity is of special interest since it will correspond to the highest repulsive part of the global interaction between a macroion (i.e., *charged* macro-particle) and an oppositely charged counterion. In order to investigate the effect of finite curvature we are going to compare $V_{self}^{(sph)}(a+\sigma/2)$ to the contact potential $V_{self}^{(plan)}(b-a=\sigma/2)$ obtained with a planar interface.

The plot of the normalized contact potential $V_0^*(a)$ defined as

$$V_0^*(a)=\frac{V_{self}^{(sph)}\left(a+\frac{\sigma}{2}\right)}{V_{self}^{(plan)}\left(\frac{\sigma}{2}\right)} \tag{26}$$

can be found in Fig. 5. For the sake of numerical stability we used the formalism of Eq. (12) allowing an arbitrary precision. Figure 5 shows that for a/σ larger than about 100 the contact potential is close to that of the planar interface (less than 5% difference). This length scale typically corresponds to "true" colloidal systems ($\sim$100 nm). Therefore, in the dilute regime where the self-image interaction is dominant (i.e., lateral microion–microion correlations are negligible), large-sized colloidal particles can be reasonably approximated by planar interfaces as far as the modeling of the self-image interaction is concerned. On the other hand, for

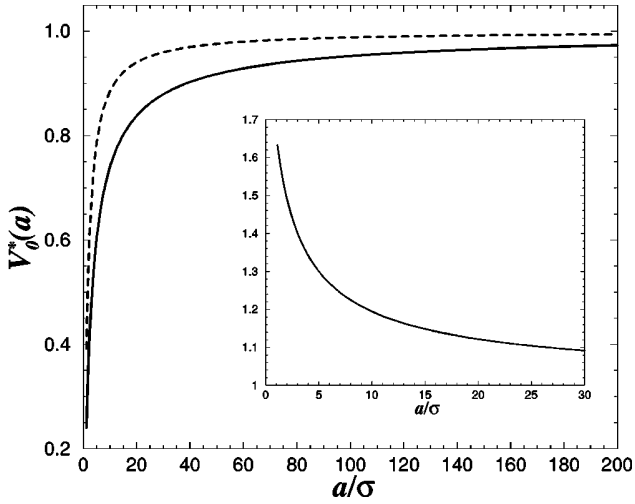

FIG. 5. Reduced contact potential $V_0^*(a)$ as a function of the colloidal radius a with $\varepsilon_1=80$, $\varepsilon_2=2$. The limit value of unity corresponds to the planar interface. The solid line is the exact contact potential $V_0^*(a)$ and the dashed one is the contact potential $\tilde{V}_0^*(a)$ obtained with the two-image charge approximation used by Linse (Ref. 10). The insert shows the ratio $\tilde{V}_0^*(a)/V_0^*(a)$.

a/σ smaller than about 20 the contact potential varies rapidly and therefore it is strongly dependent on the curvature. This length scale typically corresponds to micellar systems ($\sim$ 10 nm).

Some years ago, Linse[10] used an approximation where he replaced the (exact) infinite manifold of image charges [entering Eq. (12)] of total charge $-q_{im}$ by a single image point-charge $-q_{im}$ [given by Eq. (13)] located at the center of the sphere.[21] Although this ansatz was motivated by the study of many counterions (where the degree of spherical symmetry can be enhanced compared to the single-counterion system), it is instructive to see what this approximation involves for the self-image interaction. Doing so, the setup of image charges consists of a (two point-charge) dipole $\mathbf{p}_{im}=q_{im}\mathbf{u}$, and the corresponding contact potential $\tilde{V}_{self}^{(sph)}(r_0)$ reads

$$\tilde{V}_{self}^{(sph)}(b=r_0)=k_BTl_B\frac{Z^2}{2}\frac{\varepsilon_1-\varepsilon_2}{\varepsilon_1+\varepsilon_2}\frac{a}{r_0}\left[\frac{1}{r_0-u}-\frac{1}{r_0}\right]. \tag{27}$$

The plot of

$$\tilde{V}_0^*(a)=\frac{\tilde{V}_0^{(sph)}\left(a+\frac{\sigma}{2}\right)}{V_{self}^{(plan)}\left(\frac{\sigma}{2}\right)} \tag{28}$$

can also be found in Fig. 5. It shows that the two-image charge approximation used by Linse is only valid for very low curvature (i.e., close to the planar case) and may strongly overestimate the self-image repulsion as expected by its inherent construction.[22] Using MC simulations, Linse[10] investigated micelles of radius 12−18 Å (i.e., $a/\sigma\sim3.5-5$) leading to errors as large as 40% (see insert of Fig. 5). This proves that this ansatz is unsuitable to determine the self-image interaction in this regime, which is the source of

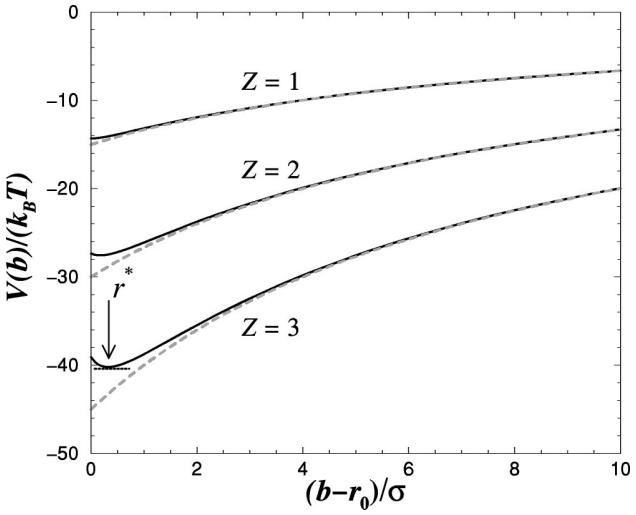

FIG. 6. Global macroion-counterion potential of interaction (solid lines) with $Z_m=60$, $r_0=8\sigma$, $\varepsilon_1=80$ and $\varepsilon_2=2$. The values of the corresponding minima r^* can be found in Table II. The dashed lines correspond to the usual electrostatic potential of interaction without image forces (i.e., $\Delta\varepsilon=0$).

the image forces. Even in a many-counterion system, this approximation is too strong when the self-image interaction is dominant.[23] However, in the limit of high spherical symmetry (with many counterions) this approximation becomes precise, but then the effects of image forces are negligible.

4. Charged colloid

As a last theoretical result, we consider the interaction between (a single counterion) q and a negatively *charged* dielectric sphere. The procedure is completely similar to the neutral colloid case, and we now apply the principle of superposition to take into account the additional potential due to a central charge $Q_m=-Z_me$. The (global) macroion-counterion potential of interaction $V_m(b)$ reads

$$V_m(b)=-k_BTl_B\frac{Z_mZ}{b}+V_{self}^{(sph)}(b), \tag{29}$$

where $V_{self}^{(sph)}(b)$ is given by Eq. (23), and hence

$$V_m(b)=k_BT\frac{l_B}{b}Z^2\left[-\frac{Z_m}{Z}+\frac{1}{2}\times\sum_{l=1}^{\infty}\left(\frac{a}{b}\right)^{2l+1}\frac{(\varepsilon_1-\varepsilon_2)l}{\varepsilon_1(l+1)+\varepsilon_2 l}\right]. \tag{30}$$

Profiles of $V_m(b)$ for $Z_m=60$, $r_0=8\sigma$, $\varepsilon_2=2$ and $Z=1$, 2 and 3 are reported in Fig. 6. An important result is the occurrence of a *minimum* in $V_m(b)$ whose depth and position r^* increase with increasing Z. This is due to the purely *repulsive* self-image interaction which scales like Z^2, whereas the direct *attractive* Coulomb macroion-microion interaction scales like Z (at fixed Z_m). Nevertheless the occurrence of a minimum is strongly dictated by the ratio Z_m/Z [see Eq. (30)]. For high value of Z_m/Z, $|V_m(b)|$ is maximal for $b=r_0$ (only *attraction* occurs) and for small Z_m/Z one recovers the neutral colloid case where only *repulsion* occurs. Of course the same qualitatively happens for charged plates.[24] The values of r^* minimizing $V_m(b)$ (with $b>r_0$) are given in Table II. The quantity r^* will be useful to discuss our simulation results that concern *many* counterions and where we also have the same macroion bare charge ($Z_m=60$).

TABLE II. Theoretical values of r^* minimizing the macroion-counterion potential of interaction (with $Z_m=60$, $\varepsilon_1=80$, $\varepsilon_2=2$ and $r_0=8\sigma$). The corresponding profiles can be found in Fig. 6.

ε_2	$\Delta\varepsilon$	Z	$(r^*-r_0)/\sigma$
2	78	1	0
2	78	2	0.17
2	78	3	0.32

Keep in mind that all our results above concern a single microion. When *many* counterions come into play, other important effects might appear in principle. In particular, when the number of counterions near the macroion surface is very large the image forces are practically canceled by symmetry reason.[10,25] Clearly, by approaching the (perfect) spherical symmetry one asymptotically cancels the polarization charges everywhere on the macroion surface. This point shows that the discrete nature of the counterions is crucial for the existence of image charges in spherical geometry.[26–28] In planar geometry the situation is radically different, where one gets an amplified image force upon increasing the number of ''surface'' counterions.

III. MONTE CARLO SIMULATION

Standard canonical MC simulations following the Metropolis scheme were used.[29,30] The system we consider is similar to those studied in previous works.[31,32] It is made up of two types of charged hard spheres: (i) a macroion of radius a with a bare charge $Q_m=-Z_me$ (with $Z_m>0$) and (ii) small microions (counterions and coions) of diameter σ with charge $q=\pm Ze$ to ensure the electroneutrality of the system. All these ions are confined in an impermeable cell of radius R and the macroion is held fixed at the center of the cell.

The dielectric media are modeled as in Sec II. It is to mention that we suppose, for the sake of simplicity, that the dielectric discontinuity coincides with the macroion radius. One must note that the effects of image forces can be significantly reduced when the location of the dielectric boundary is somewhat (a few Angströms) beneath the macroion surface.[10] On the other hand, the outer region of the simulation cell is assumed to have the same dielectric constant ε_1 as the solvent in order to avoid the appearance of artificial image forces.

The work done in bringing the (real) ions together from infinite separation gives the interaction energy of the system. The corresponding Hamiltonian, U_{tot}, can be expressed as

$$U_{tot}=\sum_i\left[U_i^{(m)}+\sum_{j>i}U_{ij}^{(bare)}\right]+\sum_i\left[U_i^{(self)}+\sum_{j>i}U_{ij}^{(im)}\right]. \tag{31}$$

The first two terms in Eq. (31) correspond to the traditional electrostatic interactions between real charges. More explicitly,

$$U_i^{(m)}(r_i)=\begin{cases}\pm l_B k_B T\dfrac{Z_m Z}{r_i}, & \text{for } r_i \geqslant a+\dfrac{\sigma}{2},\\ \infty, & \text{for } r_i < a+\dfrac{\sigma}{2},\end{cases} \tag{32}$$

represents the macroion-microion interaction, where (+) applies to coions and (-) to counterions, and

$$U_{ij}^{(bare)}(r_{ij})=\begin{cases}\pm l_B k_B T\dfrac{Z^2}{r_{ij}}, & \text{for } r_{ij} \geqslant \sigma,\\ \infty, & \text{for } r_{ij} < \sigma,\end{cases} \tag{33}$$

the pair interaction between microions j and i where (+) applies to microions of the same type and (−) otherwise.

The two last terms in Eq. (31) account for the interaction between images and microions. The *repulsive* self-image interaction is given by

$$U_i^{(self)}(r_i)=\begin{cases}\dfrac{1}{2}k_B T l_B \dfrac{Z^2}{r_i}\displaystyle\sum_{l=1}^{l_{max}}\left(\frac{a}{r_i}\right)^{2l+1}\frac{(\varepsilon_1-\varepsilon_2)l}{\varepsilon_1(l+1)+\varepsilon_2 l}, & \text{for } r_i \geqslant a+\dfrac{\sigma}{2},\\ \infty, & \text{for } r_i < a+\dfrac{\sigma}{2},\end{cases} \tag{34}$$

where l_{max} is the cutoff in the Legendre space, and

$$U_{ij}^{(im)}(\mathbf{r}_i,\mathbf{r}_j)=\begin{cases}\pm l_B k_B T Z^2\displaystyle\sum_{l=1}^{l_{max}}\frac{a^{2l+1}}{r_j^{l+1}}\frac{(\varepsilon_1-\varepsilon_2)l}{\varepsilon_1(l+1)+\varepsilon_2 l}\frac{1}{r_i^{l+1}}P_l(\cos\theta), & \text{for } r_i \geqslant a+\dfrac{\sigma}{2},\\ \infty, & \text{for } r_i < a+\dfrac{\sigma}{2},\end{cases} \tag{35}$$

represents the interaction between microion i and the image (surface charge induced by) of microion j, where (+) applies to charges of the same sign [and (−) otherwise] and θ is the angle between $\mathbf{r}_i$ and $\mathbf{r}_j$. It is this term that generates *lateral* image-counterion correlations. Due to the symmetry of $U_{ij}^{(im)}$ upon exchanging ij with ji there is an implicit factor 1/2 in Eq. (35).

Convergence of the Legendre sums with a relative error of 10^{-6} is obtained with the employed value of $l_{max}=100$.[33] For the sake of computational efficiency and without loss of accuracy, we computed the image-ion interactions on a (very) fine $(r,\cos\theta)$ grid where the coordinates of the microions were extrapolated. The radial distances r_i are discretized over logarithmically equidistant nodes so that close to the macroion surface the radial resolution is 0.01σ and near the simulation wall 0.1σ. The polar discretization consists of 2000 equidistant $\cos\theta$-nodes leading to even smaller lateral resolutions. The corresponding values of $U_i^{(self)}(r_i)$ and $U_{ij}^{(im)}(r_i,r_j,\cos\theta)$ were then initially stored into tables. Note that in principle one could also have used the formalism of Eq. (12) to compute the image-ion interactions. However, at identical numerical accuracy, this method involving a numerical integration is too time and resource consuming.

Typical simulation parameters are gathered in Table III. The case $\varepsilon_2=80$ corresponds to the situation where there is *no* dielectric discontinuity ($\Delta\varepsilon=0$). Measurements were performed over 10^6 MC steps per particle.

TABLE III. Model simulation parameters with some fixed values. Apart from the charge sign, counterions and coions have the same parameters.

Parameters	
$T=298$ K	room temperature
$\varepsilon_1=80$	water solvent dielectric constant
$\varepsilon_2=2$	colloidal dielectric constant
$\Delta\varepsilon=\varepsilon_1-\varepsilon_2=78$	strength of dielectric discontinuity
Z_m	macroion valence
Z	counterion valence
$\sigma=3.57$ Å	counterion diameter
$l_B=2\sigma=7.14$ Å	Bjerrum length
$a=7.5\sigma$	macroion radius
$r_0=a+\dfrac{\sigma}{2}=8\sigma$	macroion-counterion distance of closest approach
R	radius of the outer simulation cell

IV. SIMULATION RESULTS

Here we present our MC simulation results in salt-free environment as well as in the presence of multivalent salt-ions. We essentially study in detail the radial microion distributions $n_i(r)$ around the macroion, which are normalized as follows

$$\int_{r_0}^{R}4\pi r^2 n_+(r)dr=N_+$$
$$\int_{r_0}^{R}4\pi r^2 n_-(r)dr=N_-, \tag{36}$$

TABLE IV. System parameters.

System	*A*	*B*	*C*	*D*	*E*	*F*	*G*	*H*	*I*	*J*
Z_m	60	60	60	60	60	60	60	60	180	180
Z	1	1	2	2	3	3	2	2	2	2
N_+	60	60	30	30	20	20	430	430	445	445
N_-	-	-	-	-	-	-	400	400	400	400
ε_2	2	80	2	80	2	80	2	80	2	80
$\Delta\varepsilon$	78	0	78	0	78	0	78	0	78	0
R/σ	40	40	40	40	40	40	20	20	20	20

where r is the distance separation from the macroion center, $+(-)$ stands for counterion (coion) species and N_+ (N_-) is the total number of counterions (coions) contained in the simulation cell.

Another quantity of special interest is the integrated (or cumulative) fluid net charge $Q(r)$ defined as

$$Q(r)=\int_{r_0}^{r} 4\pi u^2 Z[n_+(u)-n_-(u)]du, \tag{37}$$

where we chose $e=1$. $Q(r)$ corresponds to the total fluid charge (omitting the macroion bare charge Z_m) within a distance r from the macroion center, and at the cell wall $Q(r=R)=Z_m$. Up to a factor proportional to $1/r^2$, $[Q(r)-Z_m]$ gives (by simple application of the Gauss theorem) the mean electric field at r. Therefore $Q(r)$ can measure the strength of the macroion charge screening by salt-ions. In salt-free environment systems we have $n_-(r)=0$ and $N_+=Z_m/Z$.

The simulation run parameters can be found in Table IV. For all these simulation systems, the ion densities $n_i(r)$ were computed with the same radial resolution Δr.[34] The discretization of the radial distance r in $n_i(r)$ is realized over logarithmically equidistant points so that close to the macroion surface ($r-r_0<\sigma$) we have $\Delta r<0.04\sigma$. It is important to obtain such an accuracy (and the required statistics) if one wants to describe quantitatively the effects of image forces which are short-ranged at strong curvature.

A. Salt-free environment

Salt-free systems $A-F$ (see Table IV) were investigated for a moderately charged macroion $Z_m=60$ corresponding to a surface charge density $\sigma_0=0.11\ \mathrm{Cm}^{-2}$.

1. Monovalent counterions

The profiles of $n_+(r)$ and $Q(r)$ are depicted in Figs. 7(a) and 7(b), respectively for the monovalent counterion systems *A* and *B*.

Figure 7(a) shows that the counterion density at contact ($r=r_0$) is somewhat smaller with $\Delta\varepsilon=78$ as a direct consequence of the self-image repulsion. However there is no maximum appearing in $n_+(r)$ with $\Delta\varepsilon=78$, in agreement with the study of the single-counterion system (see Fig. 6 and Table II). For $r-r_0>\sim 0.6\sigma$ (corresponding roughly to three half ionic sizes from the interface), the effects of image forces are negligible and all $n_+(r)$ curves are nearly identical.

To gain further insight into the effects of *lateral* image-counterion correlations, we have considered the same system

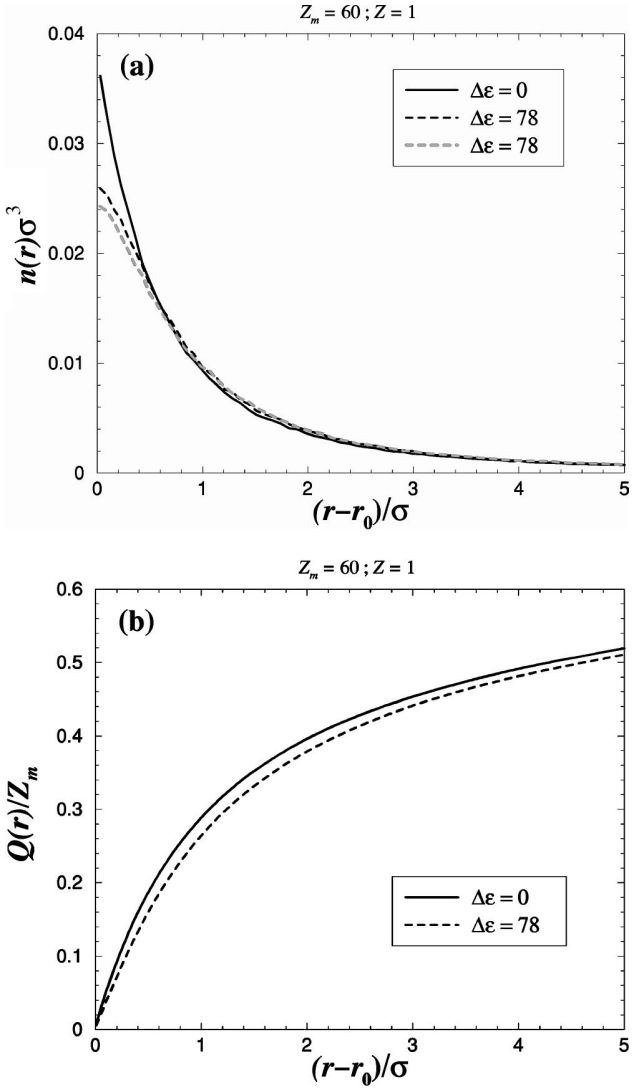

FIG. 7. Monovalent counterion distributions (systems *A* and *B*): (a) Density $n_+(r)$. The dashed line in gray corresponds to the counterion density $n_+^{(self)}(r)$ obtained in the same system *A* ($\Delta\varepsilon=78$) but where the (lateral) image-counterion correlational term $U_{ij}^{(im)}$ [Eq. (35)] has been omitted in the total Hamiltonian U_{tot} [Eq. (31)]. (b) Fluid charge.

A ($\Delta\varepsilon=78$) but omitted the correlational term $U_{ij}^{(im)}$ [Eq. (35)] in the total Hamiltonian U_{tot} [Eq. (31)]. Physically, this means that, on the level of the image force, each counterion sees uniquely its self-image interaction. Thereby, Fig. 7(a) shows that (i) the corresponding counterion density $n_+^{(self)}(r)$ is nearly identical to $n_+(r)$, and (ii) in the vicinity of the interface $n_+^{(self)}(r)$ is slightly smaller than $n_+(r)$. These findings (i) and (ii) lead to the two important conclusions:

•For monovalent counterions and moderately charged macroions, the *effective* image force is basically identical to the self-image force.[35]

•The crucial effect of lateral image-counterion correlations is to *screen* the self-image repulsion.

This latter feature is generally true for any *finite* curvature at identical fixed macroion charge density. Finding (i) is also consistent with the fact that, close to the interface (say r

$-r_0<0.2\sigma$), the average number of (surface) counterions $\overline{N}$ is (very) small ($\overline{N}<5$) as can be deduced from the fraction of counterions $Q(r)/Z_m$ [Fig. 7(b)].

Figure 7(b) shows that the fluid charge $Q(r)$ decreases when image forces are present, meaning that they lower the macroion charge screening by counterions. At the distance $r-r_0=\sigma$ (corresponding to a 2σ-layer thickness), the macroion is 29% electrically compensated [i.e., $Q(r-r_0=\sigma)/Z_m=0.29$] with $\Delta\varepsilon=0$ against 26% with $\Delta\varepsilon=78$. At the distance $r-r_0=4\sigma$, the relative difference $\Delta Q/Q$ between the $Q(r)$ obtained with $\Delta\varepsilon=0$ and $\Delta\varepsilon=78$ drops to 2% (against 10% at $r-r_0=\sigma$) where the bare macroion charge is nearly half-compensated.

2. Multivalent counterions

a. Divalent counterions. The profiles of $n_+(r)$ and $Q(r)$ are depicted in Figs. 8(a) and 8(b), respectively for the divalent counterion systems *C* and *D*.

Figure 8(a) shows that the counterion density at contact becomes strongly reduced with $\Delta\varepsilon=78$ due to the Z^2-dependence of the self-image repulsion [compare the case $Z=1$ in Fig. 7(a)]. This sufficiently strong (short-ranged) repulsion leads to a maximum in $n_+(r)$ close to the macroion surface. The corresponding radial position r^* maximizing $n_+(r)$ is $r^*=r_0+0.22\sigma$, in very good agreement (within Δr) with the *one-counterion* theoretical value $r_0+0.17\sigma$ (see Table II). This shows that for divalent counterions many-body effects do nearly not affect r^*. This nontrivial finding is the result of the competition between two driving forces that control r^* in *many*-counterion systems:

- F_{im}: the screening of the self-image *repulsion* by the (extra) negative polarization charges tends to *decrease* the r^* obtained in the one-counterion system.
- F_{mc}: the screening of the macroion-counterion *attraction* by the (extra) surface counterions tends to *increase* the r^* obtained in the one-counterion system.

It is precisely a balance of these two driving forces that leads to a nearly unchanged r^* (compared to the one-counterion system) in many-counterion systems. Whereas for monovalent counterions both driving forces F_{im} and F_{mc} are weak, those become relevant for multivalent counterions.

We stress the fact that this is specific to the spherical geometry, and that for a planar interface (at identical surface charge density) one should get a higher r^* (compared to that of the one-counterion system), since there we have no screening driving force F_{im}. We are not aware of any previous studies for the planar interface that address this issue.[36]

To gain even further insight into the effect of Z on the lateral image-counterion correlations, we have ignored the term $U_{ij}^{(im)}$ in U_{tot} in the same system *D* ($\Delta\varepsilon=78$) as done previously with system *A*. Figure 8(a) shows a qualitatively different $n_+^{(self)}(r)$ where $r^*=r_0+0.26\sigma$ is now somewhat larger, proving that with divalent counterions the screening of the self-image repulsion by lateral image-counterion correlations is appreciable. This is in contrast to what was observed with $Z=1$.

At the distance $r-r_0=\sigma$, Fig. 8(b) shows that the macroion is 62% electrically compensated for $\Delta\varepsilon=0$ against 53% for $\Delta\varepsilon=78$ [compare the case $Z=1$ in Fig. 7(b)].

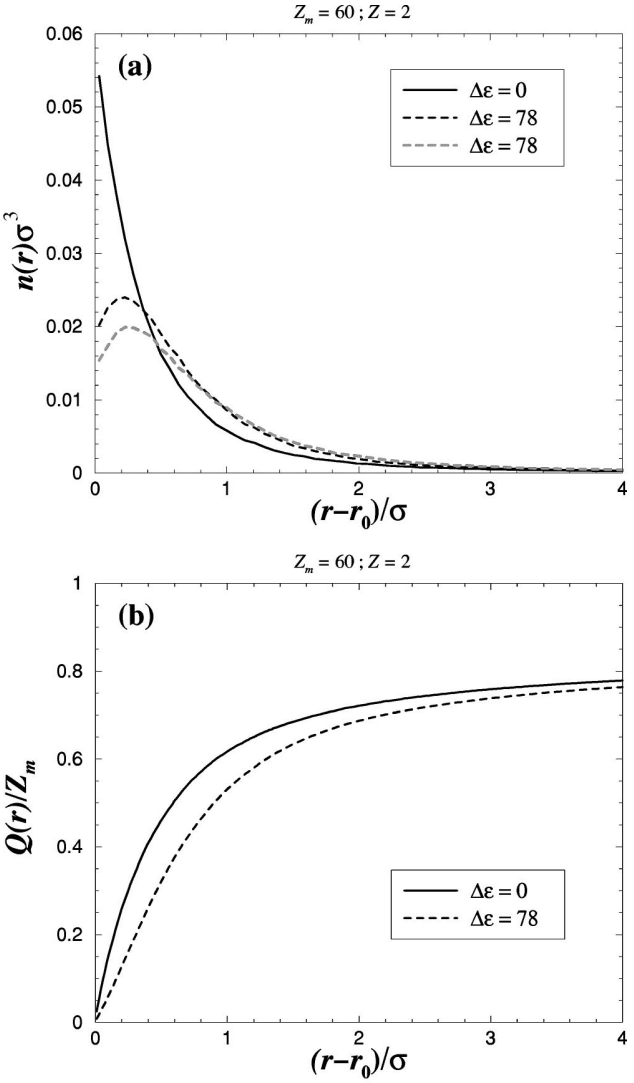

FIG. 8. Divalent counterion distributions (systems *C* and *D*): (a) Density $n_+(r)$. The dashed line in gray corresponds to the counterion density $n_+^{(self)}(r)$ obtained in the same system *C* ($\Delta\varepsilon=78$) but where the (lateral) image-counterion correlational term $U_{ij}^{(im)}$ [Eq. (35)] has been omitted in the total Hamiltonian U_{tot} [Eq. (31)]. (b) Fluid charge.

b. Trivalent counterions. The profiles of $n_+(r)$ and $Q(r)$ are depicted in Figs. 9(a) and 9(b), respectively for trivalent counterion systems *E* and *F*.

Figure 9(a) shows that the counterion density at contact is drastically reduced with $\Delta\varepsilon=78$, as expected for high Z (compare the previous cases). At $\Delta\varepsilon=78$, we have $r^*=r_0+0.36\sigma$, in quantitative agreement with the *one-counterion* theoretical value $r_0+0.32\sigma$ (see Table II). This shows again that even for trivalent counterions many-body effects do (practically) not affect r^* (compared to that obtained in the single-counterion system) due to a balance of the driving forces F_{im} and F_{mc}.

By neglecting the lateral image-counterion correlations in the same system *E* ($\Delta\varepsilon=78$), Fig. 9(a) indicates that the position r^* of the maximum in $n_+^{(self)}(r)$ gets considerably

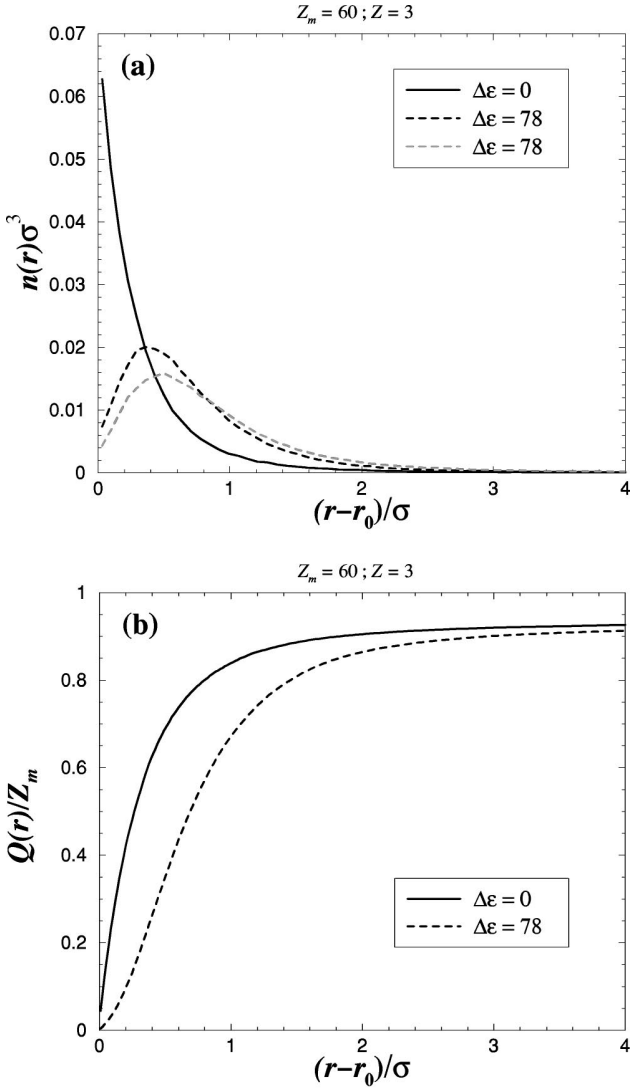

FIG. 9. Trivalent counterion distribution (systems E and F): (a) Density $n_+(r)$. The dashed line in gray corresponds to the counterion density $n_+^{(self)}(r)$ obtained in the same system E ($\Delta\varepsilon=78$) but where the (lateral) image-counterion correlational term $U_{ij}^{(im)}$ [Eq. (35)] has been omitted in the total Hamiltonian U_{tot} [Eq. (31)]. (b) Fluid charge.

larger ($r^*=r_0+0.50\sigma$). This relatively strong shift confirms the Z-enhancing of the screening of the self-image repulsion by lateral image-counterion correlations.

At the distance $r-r_0=\sigma$, the macroion is 84% electrically compensated for $\Delta\varepsilon=0$ against only 67% for $\Delta\varepsilon=78$ [see Fig. 9(b) and compare previous systems]. Snapshots of typical equilibrium configurations for $\Delta\varepsilon=0$ and $\Delta\varepsilon=78$ can be visualized in Figs. 10 (a) and 10(b), respectively.

B. Salty solutions

We focus on the case of divalent salt-ions. This choice is motivated by two reasons: (i) effects of image charges are clearly observable for multivalent counterions and (ii) such systems must be experimentally reachable. To study the effect of added salt we have considered two macroion charges $Z_m=60$ (as previously) and $Z_m=180$ corresponding to a

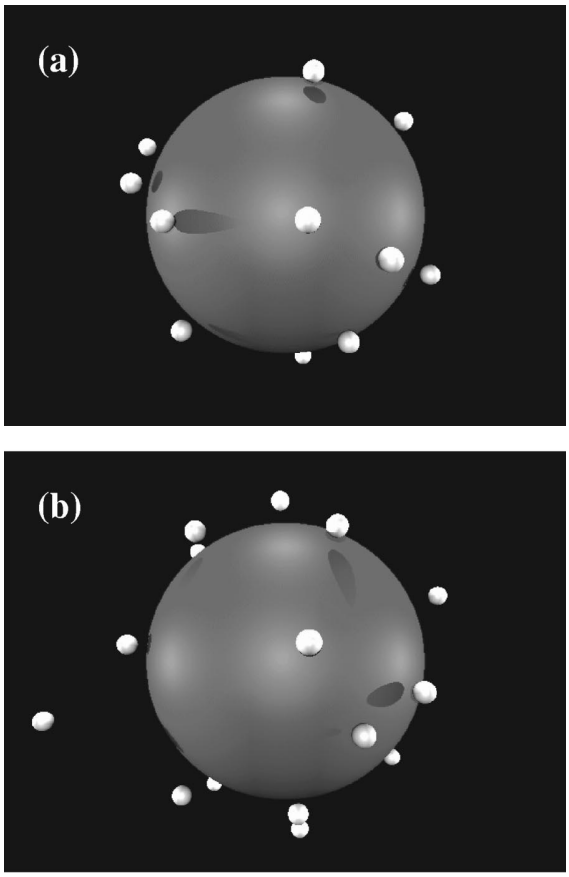

FIG. 10. Snapshots of typical equilibrium configurations for trivalent counterions (systems E and F). (a) $\Delta\varepsilon=0$ (b) $\Delta\varepsilon=78$. One can clearly observe the larger mean radial counterion distance for $\Delta\varepsilon=78$ stemming from the self-image repulsion.

charge density $\sigma_0=0.32$ Cm^{-2}. The salt concentration defined as ($N_-/\frac{4}{3}\pi R^3$) is 0.44 M for all salty systems $G-J$ (see Table IV). The simulation cell radius $R=20\sigma$ of these systems is still very large compared to any screening lengths so that finite size effects are negligible.

1. Moderately charged macroion

Profiles of $n_\pm(r)$ and $Q(r)$ are depicted in Figs. 11(a) and 11(b), respectively for the salty systems G and H with $Z_m=60$.

The coion density $n_-(r)$ with $\Delta\varepsilon=78$ is basically shifted to the right of about 0.15σ (compared to that with $\Delta\varepsilon=0$) due to the repulsive coion' self-image interaction. Near the colloidal surface, the counterion densities $n_+(r)$ are considerably higher than those obtained with no added salt (systems C and D) as it should be [compare Fig. 8(a)].

A rather surprising result here is that, despite the presence of a considerable amount of added salt, we still have $r^*=r_0+0.22\sigma$ remaining unchanged. This is a nontrivial finding since one should have an (extra) *attractive* contribution to the macroion-counterion potential of mean force stemming from the (localized) *negative* polarization charges induced by the coions, which in turn could lead to a shorter r^*. However there are two concomitant sources that lead to

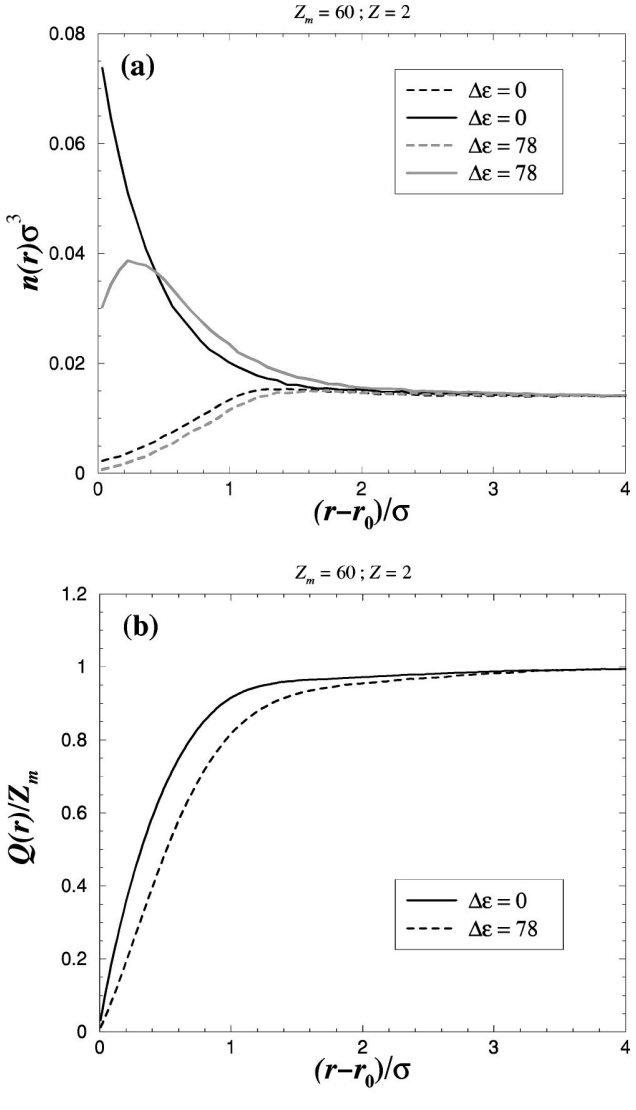

FIG. 11. Divalent salt-ion distribution (systems *G* and *H*) with $Z_m = 60$: (a) The solid and dashed lines correspond to counterion and coion densities, respectively. (b) Net fluid charge.

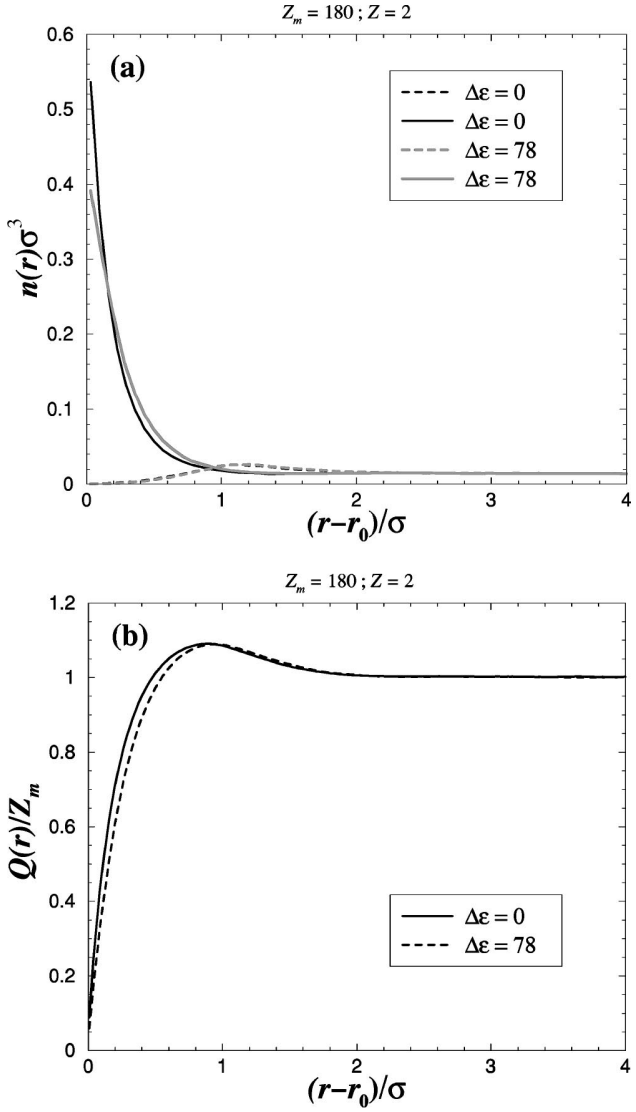

FIG. 12. Divalent salt-ion distribution (systems *I* and *J*) with $Z_m = 180$: (a) The solid and dashed lines correspond to counterion and coion densities, respectively. (b) Net fluid charge.

a marginal screening of the counterion' self-image repulsion by the negative coion-induced polarization charges: (i) there is a strong coion depletion close to the interface [see Fig. 11(a)] due to the large direct Coulomb macroion-coion repulsion and (ii) $|\sigma_{pol}^{(sph)}|$ decreases abruptly with the radial distance of the microion as discussed in Sec. II D 1 (see also Fig. 3). Of course the role of the *excluded volume* is crucial here.

As expected the macroion charge screening is weaker when image forces come into play as can be deduced from the profile of $Q(r)$ plotted in Fig. 11(b).

2. Highly charged macroion

Profiles of $n_{\pm}(r)$ and $Q(r)$ are depicted in Figs. 12(a) and 12(b), respectively for the salty systems *I* and *J* with $Z_m = 180$.

Figure 12(a) shows that the effects of image forces are considerably reduced. The relatively small difference between the $n_+(r)$ obtained with $\Delta\varepsilon = 0$ and that obtained with $\Delta\varepsilon = 78$ decreases drastically in the vicinity of the interface, and already for $r - r_0 > \sim 0.2\sigma$ the two profiles of $n_+(r)$ are nearly identical. Besides, near the interface *no* effective macroion-counterion repulsion occurs at $\Delta\varepsilon = 78$. This absence of a maximum in $n_+(r)$ is due to two main concomitant effects:

•For such a highly charged macroion, there is a very large number of counterions close to the interface [compare Fig. 12(b) and Fig. 11(b)]. In this limit, one can use Wigner crystal concepts and say that, on the level of the force stemming from the bare charges (i.e., ignoring the image forces), each surface counterion essentially interacts with the oppositely charged background of its Wigner-Seitz (WS) cell. At sufficiently high macroion charge density (i.e., small WS hole radius), this attractive interaction becomes very important and it always overcomes the self-image repulsion.

•The second (concomitant) mechanism is specific to the closed spherical topology: at high number of surface counte-

rions, the image forces are reduced because of the enhanced degree of spherical symmetry as already mentioned in Sec. II D 4.

The coion densities $n_-(r)$ are basically identical for both dielectric discontinuities $\Delta\varepsilon$, in contrast to what happened with $Z_m=60$ (systems *J* and *K*). This phenomenon can be explained as the enhanced screening of the coion' self-image repulsion by the positive polarization charges induced by the other coions present in the electrical double layer (EDL). Indeed, because of the macroion charge *reversal* that occurs at $Z_m=180$ [i.e., $Q(r)/Z_m>1$—see Fig. 12(b)], there is also a larger number of coions (at fixed salt concentration) in the EDL [compare Fig. 12(a) and Fig. 11(a)]. Therefore, since the magnitude and the inhomogeneity of $-\sigma_{pol}^{(sph)}(\theta)$ induced by a coion strongly decreases with its radial distance [see Eq. (16) and Fig. 3], the screening of the coion' self-image repulsion gets highly sensitive to an increase in number of coions in the EDL.

Concerning the net fluid charge $Q(r)$, we see that both profiles obtained with $\Delta\varepsilon=78$ and $\Delta\varepsilon=0$ are nearly identical, as expected from those of $n_\pm(r)$. The net fluid charge $Q(r)$ reaches its maximum at $r_Q^*-r_0=0.90\sigma$ and 0.94σ for $\Delta\varepsilon_2=0$ and 78, respectively. In both cases we have a macroion charge reversal of 9% [more explicitly $Q(r_Q^*)/Z_m=1.09$]. This proves the important result that, for typical systems (with high macroion charge density) leading to overcharging,[27,28,32,37,38] image forces do *not* affect the strength of the macroion charge reversal.

V. CONCLUDING REMARKS

We have presented fundamental results about the effects of image forces on the counterion distribution around a spherical macroion.

Exact analytical results have been provided for the case of a single microion interacting with a dielectric sphere. Within this framework, the self-image interaction and the surface charge of polarization have been studied and also compared to those obtained with a planar interface. Besides we also estimated the position r^* where the macroion-counterion potential of interaction is minimized. We demonstrated that the effects of image forces due to a spherical interface are qualitatively different from those occurring with a planar interface, especially when the colloidal curvature is large. We showed that the *self-screening* of the polarization charges (i.e., the screening of the positive surface charges of polarization by the negative ones) is decisive to explain the weaker and the shorter range of the self-image interaction in spherical geometry. This self-screening increases with the colloidal curvature.

Many-counterion systems have been investigated by means of extensive MC simulations where image forces were properly taken into account.

In salt-free environment and for moderately charged macroions, a maximum in the counterion density (near the spherical interface) appears for sufficiently large dielectric discontinuity $\Delta\varepsilon$. An important result is that the corresponding position r^* is basically identical, regardless of the counterion valence *Z*, to that obtained within the *one*-counterion system. This feature is specific to the spherical geometry and can not take place with planar interfaces where there is *no* self-screening of the polarization charges. For monovalent counterions we showed that the (effective) image force is basically equal to that of the self-image interaction, and the *lateral* image -counterion correlations are (very) weak. However for multivalent counterions the lateral image-counterion correlations affect significantly the counterion density, and as major effect they *screen* the self-image repulsion. Nevertheless, the combined effects of (i) the macroion charge screening by counterions and (ii) the screening of the self-image repulsion lead to a nearly unchanged r^* (compared to that obtained in the single-counterion system) for multivalent many-counterion systems. Furthermore, we showed that the counterion density at contact decreases drastically with *Z* (as also found in Ref. 10), and that r^* also increases with *Z* as expected. These latter results have important implications for the stabilization of charged colloidal suspensions where a component of the pair-force is proportional to the ion density at contact.

By adding salt, it was found for moderately charged macroions that the strength of the image forces induced by the *coions* is very small compared to that resulting from the counterions. This is due to the coupled effects of (i) the coion depletion in the vicinity of the colloidal interface due to the strong direct Coulomb macroion-coion repulsion and (ii) the (highly) short range of the image forces in spherical geometry. Consequently the position r^* remains identical to that obtained in salt free environment and a fortiori to that obtained within the one-counterion system. For *highly* charged macroions the effects of image charges are significantly reduced since (i) the attractive counterion-hole interaction dominates the repulsive counterion' self-image interaction and (ii) the screening of the counterion' self-image repulsion gets enhanced by symmetry reason. In this situation *no* maximum appears in the counterion density and it was found that *overcharging* is nearly unaffected by image forces.

Although our MC analysis was carried at given macroion size, all the above reasonings that concern *many* counterions remain unchanged (for symmetry reason) for any *finite* curvature by a rescaling at fixed macroion charge density.

Finally, this contribution should constitute a solid basis to understand and predict the effects of image charges in other similar systems (e.g., polyelectrolyte adsorption onto spherical charged colloids).

ACKNOWLEDGMENTS

The author thanks C. Holm, K. Kremer and H. Schiessel for valuable discussions. This work was supported by the *Laboratoires Européens Associés* (LEA).

[1] G. M. Torrie, J. P. Valleau, and G. N. Patey, J. Chem. Phys. **76**, 4615 (1982).
[2] G. M. Torrie, J. P. Valleau, and C. W. Outhwaite, J. Chem. Phys. **81**, 6296 (1984).
[3] D. Bratko, B. Jönsson, and H. Wennerström, Chem. Phys. Lett. **128**, 449 (1986).
[4] T. Croxton *et al.*, Can. J. Chem. **59**, 1998 (1981).
[5] R. Kjellander and S. Marčelja, Chem. Phys. Lett. **112**, 49 (1984).
[6] R. Kjellander and S. Marčelja, J. Chem. Phys. **82**, 2122 (1985).

[7] C. W. Outhwaite and L. B. Bhuiyan, J. Chem. Soc., Faraday Trans. 2 **79**, 707 (1983).
[8] R. R. Netz, Phys. Rev. E **60**, 3174 (1999).
[9] H. H. von Grünberg and E. C. Mbamala, J. Phys.: Condens. Matter **12**, 10349 (2000).
[10] P. Linse, J. Phys. Chem. **90**, 6821 (1986).
[11] Equation (5) is also of the form of Eq. (3).
[12] J. G. Kirkwood, J. Chem. Phys. **2**, 351 (1934).
[13] M. R. Spiegel, *Fourier Analysis with Applications to Boundary Value Problems* (McGraw-Hill, New York, 1974).
[14] J. D. Jackson, *Classical Electrodynamics* (Wiley, New York, 1975).
[15] G. Iversen, Y. I. Kharkats, and J. Ulstrup, Mol. Phys. **94**, 297 (1998).
[16] Note that for $\varepsilon_2 \to \infty$ in Eq. 12 one recovers the case of a metallic *conducting* sphere where there is a *single* image point-charge $q_{im} = -qa/b$ located at **u**.
[17] Mathematically, this is a direct consequence of the orthogonality of the Legendre polynomials. Indeed, we have $\int_{-1}^{1} P_l(x) P_0(x) dx = 0$ and since $P_0(x) = 1$ it results from this that $\int_{-1}^{1} P_l(x) dx = 0$.
[18] It turns out that the convergence of the Legendre sum in Eq. (16) is extremely slow. With $l_{max} = 300$ we have a relative error of 10^{-6} in the most severe case where $b = 8\sigma$.
[19] This holds when the microion q is sufficiently far away from the interface so that only the dipolar term matters (i.e., $l = 1$). However close to the colloidal surface one has to take all higher multipolar contributions to get the exact potential of interaction.
[20] We have carefully checked that both methods [i.e., Eq. (10) and Eq. (12)] are numerically identical. However, at large a (typically $a > 30\sigma$) the Legendre sum in Eq. (23) becomes numerically unstable.
[21] Originally, Linse[10] made some manipulations in the Legendre expansion and drops all l components after having approximated $(1/\varepsilon_1 + \varepsilon_2 l/(l+1)) \approx (1/\varepsilon_1 + \varepsilon_2)$. This operation equivalents to replace the (exact) infinite manifold of image charges [entering Eq. (12)] by a single image point-charge $-q_{im}$ located at the center of the sphere.
[22] Note that the two-image charge approximation also holds when the charge q is very far from the interface (i.e., $b/a \gg 1$). Unfortunately, all the relevant effects of image forces in spherical geometry occur within the opposite limit $b/a \to 1$.
[23] Our simulations will show that, especially for micellar systems, the image forces in many-counterion systems become only relevant when the self-image interaction is dominant.
[24] In the case of a charged plate, to be consistent, one has to think either of a large finite plate in the presence of a single microion, or equivalently of an infinite plate in the presence of a very dilute dispersion of microions.
[25] C. Holm (private communication).
[26] This problem is very similar, in spirit, to that of the discretization of the macroion surface charge whose effect is (asymptotically) canceled for small separations between microions (Refs. 27, 28).
[27] R. Messina, C. Holm, and K. Kremer, Eur. Phys. J. E **4**, 363 (2001).
[28] R. Messina, Physica A **308**, 59 (2002).
[29] N. Metropolis *et al.*, J. Chem. Phys. **21**, 1087 (1953).
[30] M. P. Allen and D. J. Tidelsey, *Computer Simulations of Liquids* (Clarendon, Oxford, 1987).
[31] H. Wennerström, B. Jönnson, and P. Linse, J. Chem. Phys. **76**, 4665 (1982).
[32] R. Messina, C. Holm, and K. Kremer, Phys. Rev. E **64**, 021405 (2001).
[33] Here, the convergence of the Legendre sum in Eqs. (34) and (35) is much faster, in contrast to what happened with the computation of $\sigma_{pol}^{(sph)}(\theta)$ [Eq. (16)]. The most sensitive region is the one where $r \to r_0$. There, for $r_0 = 8\sigma$ we have a relative error of 10^{-6} with $l_{max} = 100$.
[34] For the net fluid charge $Q(r)$ one has an arbitrary resolution Δr.
[35] This feature also shows how important it is to treat precisely the self-image interaction as done in the present study with a Legendre sum.
[36] Using MC simulations, Torrie *et al.* (Ref. 1) also reported in the planar case the appearance of a maximum in the counterion density for low surface charge density and fairly small salt content. However, they did not make any comparison between the position of this maximum and the position of a single counterion (per simulation box) minimizing the plate-counterion potential of interaction.
[37] R. Messina, C. Holm, and K. Kremer, Phys. Rev. Lett. **85**, 872 (2000).
[38] R. Messina, C. Holm, and K. Kremer, Europhys. Lett. **51**, 461 (2000).

Appendix H

Polyelectrolyte adsorption and multilayering on charged colloidal particles

Polyelectrolyte Adsorption and Multilayering on Charged Colloidal Particles

RENÉ MESSINA,[1] CHRISTIAN HOLM,[2] KURT KREMER[2]

[1]Institut für Theoretische Physik II, Heinrich-Heine-Universität Düsseldorf, Universitätsstrasse 1, D-40225 Düsseldorf, Germany and Max-Planck-Institut für Polymerforschung, Ackermannweg 10, 55128 Mainz, Germany

[2]Max-Planck-Institut für Polymerforschung, Ackermannweg 10, 55128 Mainz, Germany

Received 10 November 2003; revised 20 February 2004; accepted 1 March 2004
DOI: 10.1002/polb.20203
Published online in Wiley InterScience (www.interscience.wiley.com).

ABSTRACT: In this article we review the complexation behavior of charged polymers adsorbed onto charged substrates. In the first part we summarize the results obtained on the adsorption properties of a single polyelectrolyte chain with one or several oppositely charged spherical colloids. The results of various simulational studies are compared with theoretical predictions. After that, we show that under strong electrostatic coupling conditions one can also obtain complexations, where chain and colloid carry the *same* charge (like-charge complexation). This effect is due to counterion correlation effects. Finally, we investigate the case of polyelectrolyte multilayers structures, which are composed of alternating polycations and polyanions on various substrate geometries. This structure, normally obtained by a so-called layer-by-lay deposition, is very stable experimentally, but only poorly understood in terms of theoretical approaches. Our simulation results suggest that short range attractive interactions (e.g., van der Waals) are important for obtaining a stable sequence of multilayers.
 J Polym Sci Part B: Polym Phys 42: 3557–3570, 2004

INTRODUCTION

Polyelectrolytes (PEs) are polymers that possess ionizable groups that can dissociate charges in polar solvents, resulting in charged polymers and small counterions. Both charged species can be influenced by external electric fields, or additional charged bodies, like charged membranes, charged colloids, or other charged polymers. Because the interactions are long ranged in low-salt or salt-free solutions, and due to the complicated interactions, various complexes, and even hierarchical nanostructures, can emerge. On the other hand, charged species are notoriously difficult to describe with analytical theories.[1,2] This is one reason that theoretical insight of very complex charged systems had to go hand in hand with more and more involved computer simulations of such systems. With the increase in speed of modern computers on the one hand, and with the development of advanced simulation methods for the treatment of time consuming electrostatics routines[3] on the other hand, more and more insight could be gained by computer simulations.

In this article we present three different circumstances under which PE adsorption were studied by numerical simulations. The first one deals with the usual adsorption of PEs onto an *oppositely* charged spherical particle. This case has been experimentally extensively studied[4–7] because it can be observed in many soft matter

Correspondence to: C. Holm (E-mail: holm@mpip-mainz.mpg.de)

systems like surfactant–polyelectrolyte systems, protein–DNA complexes, or even chromatin fibers that are built out of DNA–histone complexes in a very complicated fashion.[8] Various authors have investigated this phenomenon theoretically[9–17] and by Monte Carlo simulations,[18–22] and we will put the different findings into relation with each other. The second part deals with the much less investigated case of the complexation of a charged sphere with a *like-charged* PE. It is only very recently that we reported such a phenomenon in the strong Coulomb coupling regime.[23,24] From a theoretical point of view, the long-range Coulomb interactions of these systems represents a formidable challenge, and especially the understanding of effective attraction of like-charged bodies has attracted recent attention.[25] There, we will elaborate on the complexation between a sphere and a long flexible PE *both negatively charged.* Although complexation in the strong coupling limit due to counterion correlations is expected, we report new and rather unexpected chain conformations. We present MD simulation results without added salt but taking into account the counterions explicitly. We will explain the mechanisms accounting for the different encountered complex structures. The last part of this article deals with thin PE multilayer films made up of alternating layers of polycations (PCs) and polyanions (PAs). The so-called layer-by-layer method, first introduced in *planar* geometry by Decher, consists in a successive adsorption of the polyions onto a charged surface, and has proven to be extremely efficient.[26,27] Due to the many potential technological applications such as biosensing,[28] catalysis,[29] optical devices,[30] and more, this process is today widely used. Another very interesting application is provided by the PE coating of *spherical* metallic nanoparticles.[7,31] This process can modify in a well-controlled way the physicochemical surface properties of the colloidal particle.

Some experiments (see, e.g., ref. 32) were devoted to the basic mechanisms governing PE multilayering on planar mica surfaces where, especially, the role of surface charge overcompensation was pointed out. Nevertheless, despite the huge amount of experimental works, the detailed understanding of the multilayering process is still rather unclear.[33] Hence, the study of PE multilayering is motivated by both experimental and theoretical interests. We will discuss our recently obtained results on substrates of various geometries, and stress the importance of nonelectrostatic short-range interactions for a smooth layering structure.

ADSORPTION OF A SINGLE POLYELECTROLYTE

Case of an Oppositely Charged Sphere

We first briefly review the works related to the adsorption of a long PE onto an *oppositely* charged sphere. The situation where a single PE chain wraps around a spherical macroion is often encountered in practical situations. For instance, the case of chromatin corresponding to the complexation between DNA and histone is one of the most well-known examples, and was thoroughly reviewed by Schiessel.[8] Many analytical works were devoted to understand the role of electrostatic interactions coming into play within those structures.[10–16,34] The most common result is the overcharging of the spherical macroion by the long PE chain and a strong wrapping, see Figure 1 for an example.

On the simulation side, there is today a considerable amount of available contributions where various authors have analyzed the PE–macroion complexation by means of MC simulations.[19–22,35–40] We briefly review here the main results.

Effect of Chain Stiffness

The effect of *chain flexibility* (at prescribed chain length) was first systematically investigated by Wallin and Linse[19] and then recently further investigated by Stoll and Chodanowski[37] and Akinchina and Linse.[38] In these first simulations, with explicit counterions in a salt-free environment, Wallin and Linse[19] showed that the degree of PE adsorption, and concomitantly that of overcharging, decreases with the stiffness of the chain as expected. Using Debye-Hückel pair interactions in their MC simulations, Stoll and Chodanowski[37] could include the effect of added salt beside of that of the chain flexibility. In that work,[37] the PE carries the same absolute charge as that of the spherical macroion, so that *no* PE-induced overcharging could occur. Within this framework, Stoll and Chodanowski[37] showed that by increasing the chain stiffness, solenoid conformations are progressively achieved at the particle surfaces, as also analytically predicted by Nguyen and Shklovskii[16] for semiflexible chains. At high salt concentration, full PE desorption is always predicted.[37] It is interesting to mention that the

large values of PE stiffness (characterized there by k_{ang} considered at zero-salt concentration in ref. 19 and ref. 37 differ in *many* orders of magnitude. This explains the qualitatively different PE conformations observed at large k_{ang} (compare Fig. 6 in ref. 19 with Table 3 in ref. 37). Unfortunately, Stoll and Chodanowski[37] did not comment this point, nor did they compare their results with those of the earlier work of Wallin and Linse.[19]

Effect of Chain Length

Some systematical studies about the effects of chain length (or more precisely, the ratio $\alpha_L = L/d$ between the chain contour length L and the colloid diameter d) on the micro structural properties of the PE–colloid complexation were carried out by Wallin and Linse,[21] Chodanowski and Stoll,[35,36] and Akinchina and Linse.[38] At (very) high α_L Chodanowski and Stoll[35,36] found, for fully flexible chains, that only a marginal portion of the PE is adsorbed to the colloid, and extended tails in solution are formed. At "intermediate" α_L, again for fully flexible chains, the PE always collapses (at low salt concentration) to a so-called "tennis-ball" like conformations.[35,36] At sufficiently small α_L, one basically recovers the planar case (i.e., zero curvature), where the PE conformations look very similar.[36] Akinchina and Linse[38] also investigated the effect of chain stiffness in addition to α_L. They find a rich phase diagram (see Fig. 1 in ref. 38) comprising "tennis ball"-like, solenoid, multiloop (also called "rosette"[34]), single loop, as well as "U" conformations. The rosette conformation had already been predicted theoretically for short-range attractive sphere–polymer interactions[17] that could correspond to a high-salt concentration regime. Nonetheless, Schiessel also confirms theoretically this type of structure for screened Coulomb interactions (involving charged species) for *low* salt concentration (see Fig. 2 of ref. 17) and a (very) good qualitative agreement is reached with the MC findings (at a salt-free environment) of Akinchina and Linse.[38]

Other Relevant Effects

Recently, Carlsson et al.[41] considered the effect of the discrete nature of the protein charge distribution on protein–polyelectrolyte complexation. Still, in the primitive model, instead of considering a uniform surface-charge density (see also Ref. 42 for a more detailed discussion), they distribute little ions (each of valence $Z = -1$, 0 or $+1$) so that the net charge of the protein could be either positive or negative.[41] The motivation of such a protein charge model[41] stems from the experimental situation (lyzozymes) where the protein net charge, as prescribed by the number of ionized amino groups, is pH-dependent. Besides electrostatic correlations, short-range attractions (typically scaling like $-1/r^6$) were also considered so as to allow a more realistic comparison with experimental data.[41] Within that framework, Carlsson et al.[41] showed the following interesting results:

1. Complexation can be stronger with a discrete protein-charge distribution. This latter result is fully consistent with the finding of Messina concerning counterion distribution (see Fig. 12b in ref. 44).
2. Concomitantly, their analysis also reveals that the negative beads tends to be localized around the positive discrete positive surface ions, as expected.

For the completeness of the model, image charges should have been taken into account, as recently analyzed by one of us.[43]

The "polarizability" of PE–colloid complexes (i.e., the derivative $\alpha = dP/dE$ of the complex-polarization P with respect to the external applied electric field E) has also been recently inves-

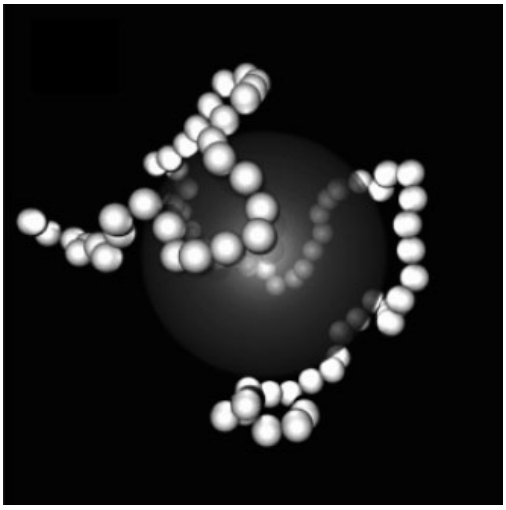

Figure 1. An example of PE–colloid complexation (tennis ball-like conformation). Here all 80 monomers are positively charged (1e/bead) with a diameter σ, and the oppositely charged colloid carries a bare charge of $-40e$ and has a diameter of 9σ.[40]

tigated by Dzubiella et al. (see Sec. III in Ref. 39). Notice that, strictly speaking, in a presence of a *uniform* external electric field the true equilibrium state corresponds to a colloid and a PE chain that are infinitely separated from each other. In practice, however, one can say that the energy barrier of "decomplexation" is so high that the complex state is apparently very stable (but still metastable). The authors restrict their MC study to the case where the PE chain and the spherical macroion have the same charge in absolute value, so that there is no monopole contribution.[39] Moreover, image forces[43] were not taken into account, which might be a crude approximation for short chains. Within this framework, Dzubiella et al.[39] showed that two length scales are relevant:

1. For small chains and small E, α is strong and reaches its maximal value for chain length comparable to the circumference of the colloid. This regime can be theoretically well described in terms of thermally fluctuating dipoles with an effective length that depends on the chain length.
2. For chains longer than circumference of the colloid, the magnitude of the polarizability α is of the order of that of a classical conducting sphere of radius of the complex size.

Multisphere Complexation

The complexation between a single PE and many spherical colloids were investigated by Jonsson and Linse[45,46] by means of MC simulations. In these works, electroneutrality is ensured by the explicit presence of little monovalent counterions (anions and cations), and no salt-ions were added. The effect of charge density, chain length, and macroion charge was discussed in ref. 45, whereas the effect of chain flexibility was discussed in ref. 46. Jonsson and Linse introduced two dimensionless charge-parameters:[45,46]

$$\beta \equiv \left| \frac{N_M Z_M}{N_m Z_m} \right|, \tag{1}$$

and

$$\beta^c \equiv \left| \frac{N_M^c Z_M}{N_m Z_m} \right|, \tag{2}$$

where N_M is the total number of macroions, Z_M is the negative valence of the macroions, N_m is the number of monomers, Z_m is the positive valence of the monomers, and N_M^c is the number of macroions in molecular contact to the PE defining the degree of complexation. We briefly review and discuss the main results of those two articles.[45,46]

Effect of Charge Density, Chain Length, and Macroion Charge[45]

In this study, the PE is modeled as charged hard spheres connected by harmonic bonds, so that here the chain is fully flexible (i.e., $k_{ang} = 0$). The main relevant findings can be summarized as follows:

1. For undercharged complexes (i.e., $\beta^c \leq 1$), the degree of complexation [i.e., $\beta^c = \beta^c(\beta)$] is first linear in β at low β, and in the overcharging regime (i.e., $\beta^c > 1$) β^c exhibits a plateau that is the signature of an overcharging saturation.
2. An increase of the linear charge density and/or of the colloidal surface-charge density leads to a stronger complexation or equivalently to a stronger overcharging (i.e., higher values of β^c), as expected.
3. At fixed PE linear charge density, an increase of the chain length leads also to a stronger complexation.

From an overcharging viewpoint, one can say that those results are in qualitative agreement with the theoretical predictions of Nguyen and Shklovskii[16,47] and Schiessel et al.[48]

Effect of Chain Flexibility[46]

In a subsequent work,[46] Jonsson and Linse considered the effect of chain flexibility ($k_{ang} > 0$). The latter is taken into account by a harmonic angular potential. The main relevant findings can be summarized as follows:

1. In the undercharging regime ($\beta^c \leq 1$), the binding isotherms [$\beta^c = \beta^c(\beta)$] is also linear and identical to that found for flexible chains.
2. The complexation structure, however, strongly depends on the chain flexibility. As the latter is decreased, the macroion arrangement gets gradually more linear and ordered along the chain.

LIKE-CHARGE COLLOID–POLYELECTROLYTE COMPLEXATION

The complexation of a highly charged colloid with a long flexible PE, *both negatively charged,* was recently investigated by ourself [23,24] by means of molecular dynamics (MD) simulations. Electroneutrality is ensured by multivalent counterions, whose presence is crucial for the occurrence of that rather counterintuitive like-charge complexation. In this MD simulation model,[23,24] the counterions of the colloid and the PE are supposed to be identical. Below, we review some important aspects of those new studies that concern the strong Coulomb coupling[23] and the weak Coulomb coupling,[24] the latter corresponding to aqueous solutions. We would like to mention here that there is no particular advantage to use MD simulations rather than MC ones. These two methods are fully equivalent as long as *equilibrium* properties are concerned. It is only for "historical" reasons that MD simulations were employed here in the present context.

Strong Coulomb Coupling

The colloid carries a negative bare charge of $-180e$ and has a diameter $d = 15\sigma$ with $\sigma = 3.57$ Å being the diameter of the positive divalent counterions. The long polymer chain contains about $N_m = 256$ monomers, and $1/f$ monomer is negatively charged ($-2e$). The strong Coulomb coupling is ensured by taking a Bjerrum length of $l_B = 10\sigma = 35.7$ Å.

Typical equilibrium microstructures of the colloid–polyelectrolyte complex can be found in Figure 2. In all reported cases complexation occurs and the PE is completely adsorbed onto the colloidal surface. This renders the conformation quasi-*two-dimensional,* in contrast to the bulk case (i.e., in the absence of the macroion but with the presence of the PE counterions — see also Fig. 3 in ref. 24. Nevertheless, the structure of these resulting complexes depends strongly on the value of f. For the fully charged PE case [$f = 1$, see Fig. 2(a)] the monomers are closely packed forming a two-dimensional compact Hamiltonian-walk with the condensed counterions on the PE. Upon reducing f [see Figs 2(b) and (c)], the complex structures are qualitatively different. For $f = 1/2$ [see Fig. 2(b)], the monomers spread more over the particle surface and the polymer partially wraps around the sphere exhibiting a quasi-two-dimensional pearl necklace structure. For $f = 1/3$ [see Fig. 2(c)], the monomers spread entirely over the particle surface, and the chain wraps the colloidal particle leading to an almost isotropic distribution of the monomers around the spherical macroion.

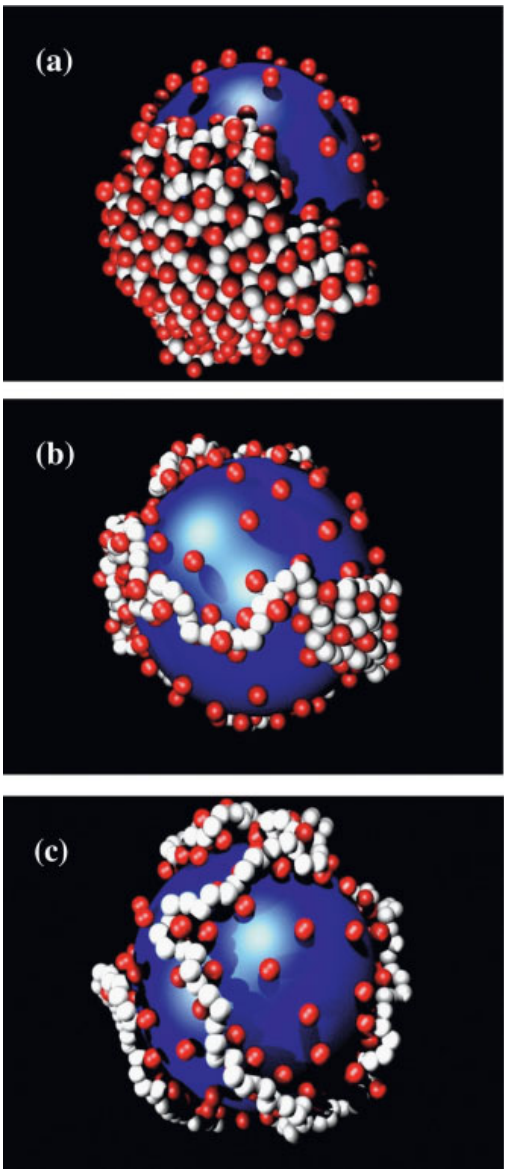

Figure 2. Typical equilibrium configurations of the *like-charge* colloid–polyelectrolyte complex in strong Coulomb coupling for (a) $f = 1$, (b) $f = 1/2$, and (c) $f = 1/3$. Monomers are in white and counterions in red.

Within this strong Coulomb coupling regime, we were able to quantify the chain conformation with simple theoretical concepts.[23,24] More pre-

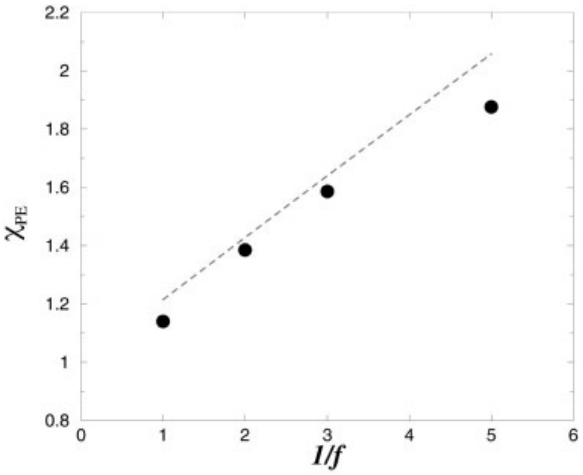

Figure 3. Degree of PE overcharging χPE as a function of 1/*f*. The dashed line corresponds to the theoretical prediction (eq 4).[23]

cisely, it was shown that the concept of polyelectrolyte overcharging is relevant to rationalize those observed PE conformations. The degree of PE overcharging χ_{PE} is defined as follows

$$\chi_{PE} = \frac{N_{cd}}{N_{cm}}, \tag{3}$$

where N_{cd} is the number of "condensed" counterions onto the PE chain (i.e., counterions that are within a prescribed distance from the PE chain) and N_{cm} stands for the total number of charged monomers. Hence, the PE is (locally) overcharged when $\chi_{PE} > 1$. The plot of χ_{PE} as a function of 1/*f* can be found in Figure 3. It is seen that χ_{PE} is a decreasing function of *f*. This result can also be obtained analytically (see also Fig. 3) by assuming that the counterion distribution of the colloid (that are responsible of the PE overcharging) is nearly unperturbed by the presence of the PE chain with its stuck counterions. This latter feature was carefully checked by our MD simulations in refs. 23 and 24. Thereby, the theoretical degree of PE overcharging is given by:

$$\chi_{PE} \approx 1 + C/f, \tag{4}$$

where *C* is a constant that depends on the chosen system parameters (see eqs 4 and 5 in ref. 23). Because the renormalized charge q^*_m of a monomer can be given by

$$q^*_m = -(\chi_{PE} - 1)q_m, \tag{5}$$

where q_m is the bare monomers charge, we can state that q^*_m increases with 1/*f* as deduced from Figure 3. This PE overcharging leads to an effective local monomer–monomer repulsion that is controlled by q^*_m, and therefore, to a bond stiffening that is *f*-dependent. The latter in turn explains why the PE expands with increasing 1/*f*. Concomitantly, by increasing 1/*f*, one reduces the number of available dipoles (i.e., ion pairs made up of monomers and counterions), which also disfavors the compaction of the chain.

Weak Coulomb Coupling

The case of a weak Coulomb coupling, involving monovalent monomers and the Bjerrum length of water l_B = 7.14 Å (i.e., aqueous solvent), was also investigated by us.[24] Interestingly, it was found that even in that situation like-charge complexation can occur for trivalent counterions.

Typical colloid–PE complex microstructures are depicted in Figure 4. In all cases (here, $1/3 \leq f \leq 1$), we have adsorption of the PE onto the like-charged colloid. Compared to the (very) strong Coulomb coupling, the PE adsorption is much weaker due to the reduced counterion correlations in the weak Coulomb coupling. More specifically, for $f = 1$ [see Fig. 4(a)] the PE conformation consists of dense globules (which are mainly counterion induced and at least extend entropically mediated) separated by strings, reminiscent of the pearl necklaces found in studies of polyampholytes.[49] Upon reducing *f*, the PE adsorption is weakened due to the reduced available dipoles leading to the formation of chain *loops* [see Fig. 4(b) and (c)].

MULTILAYERING

PE multilayer thin films are made of alternating layers of polycations (PCs) and polyanions (PAs), supposing that the substrate is negatively charged. It was only recently that the study of PE multilayering by means of numerical simulations was reported.[40,50,51] The presence of oppositely and highly charged PEs renders the understanding of PE multilayers extremely difficult, and a robust analytical theory will be difficult to construct.[14,52,53] We briefly review some important

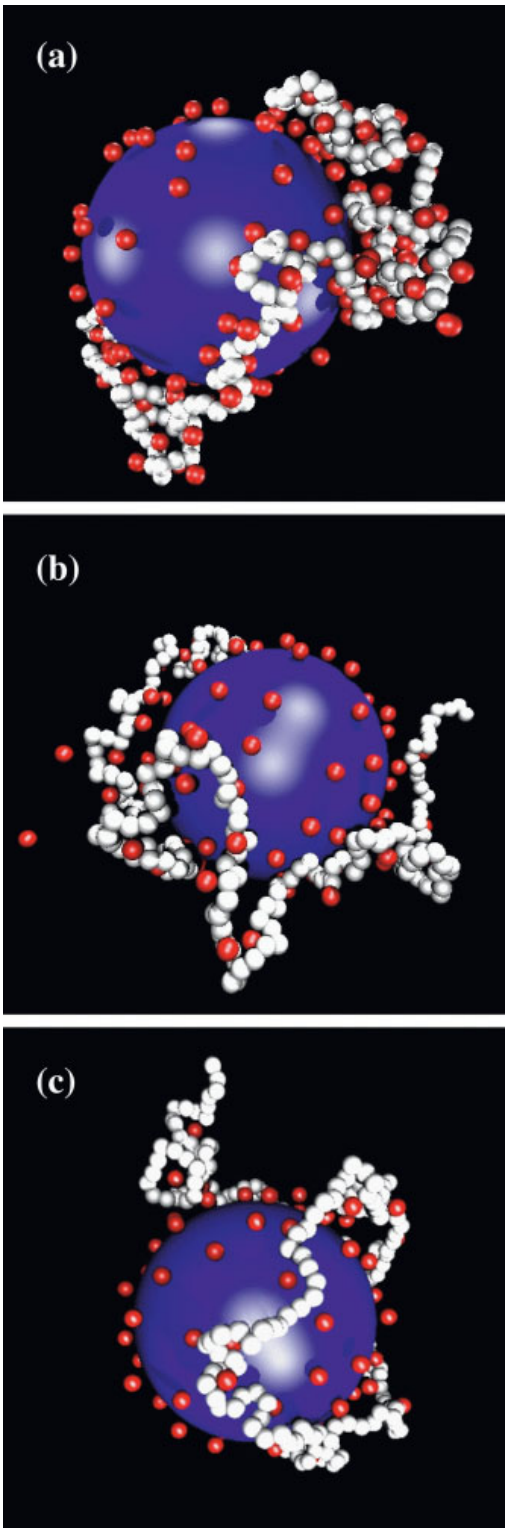

aspects of PE multilayering for spherical,[40] planar,[50] and cylindrical substrates.[51]

In all these studies,[40,50,51] the influence of an additional nonelectrostatic short-range attraction between the PC monomers and the substrate was considered. The strength of this "sticky" potential is characterized by a value for the attractive energy χ_{vdw} that corresponds to the PC monomer energy (in units of k_BT) at contact. The PEs are always fully charged ($f = 1$), and the PAs and PCs have the same length and carry the same charge in absolute value.

Spherical Substrate

The formation of PE multilayers on charged spheres was investigated by MC simulations in ref. 40. The colloid is characterized by a radius $a = 4.5\sigma$, with $\sigma = 4.25$ Å being the microion (monomer and counterion) radius, and a negative charge of $-40e$. Counterions were explicitly taken into account, ensuring the overall electroneutrality of the system.

A highly interesting situation is already provided by the study of PE *bilayering*. Equilibrium configurations of two oppositely charged PEs (with $N_m = 80$) adsorbed onto the negatively charged colloid can be found in Figure 5. One can clearly see that at sufficiently low χ_{vdw} (in particular at $\chi_{vdw} = 0$ corresponding to purely electrostatic regime) the oppositely charged PEs build up a rather compact complex (i.e., a *globule*), reminiscent of the classical PE collapse. In return for $\chi_{vdw} \geq 2$ the PE complex gets *flatter* and wraps around the colloidal particle, indicating the importance of nonelectrostatic contribution in the bilayering process. The two main mechanisms controlling the structure and the PE bilayer can be summarized as follows:

1. The PC–PA globalization driving force tends to produce one or more neutral globules and results thus in a weaker and more diffuse PE adsorption.
2. The attractive PC monomer–colloid short-range interaction increases the PE adsorption. True bilayering (involving flat layers)

Figure 4. Typical equilibrium configurations of the *like-charge* colloid–polyelectrolyte complex in "weak" Coulomb coupling for (a) $f = 1$, (b) $f = 1/2$, and (c) $f = 1/3$. Monomers are in white and counterions in red.

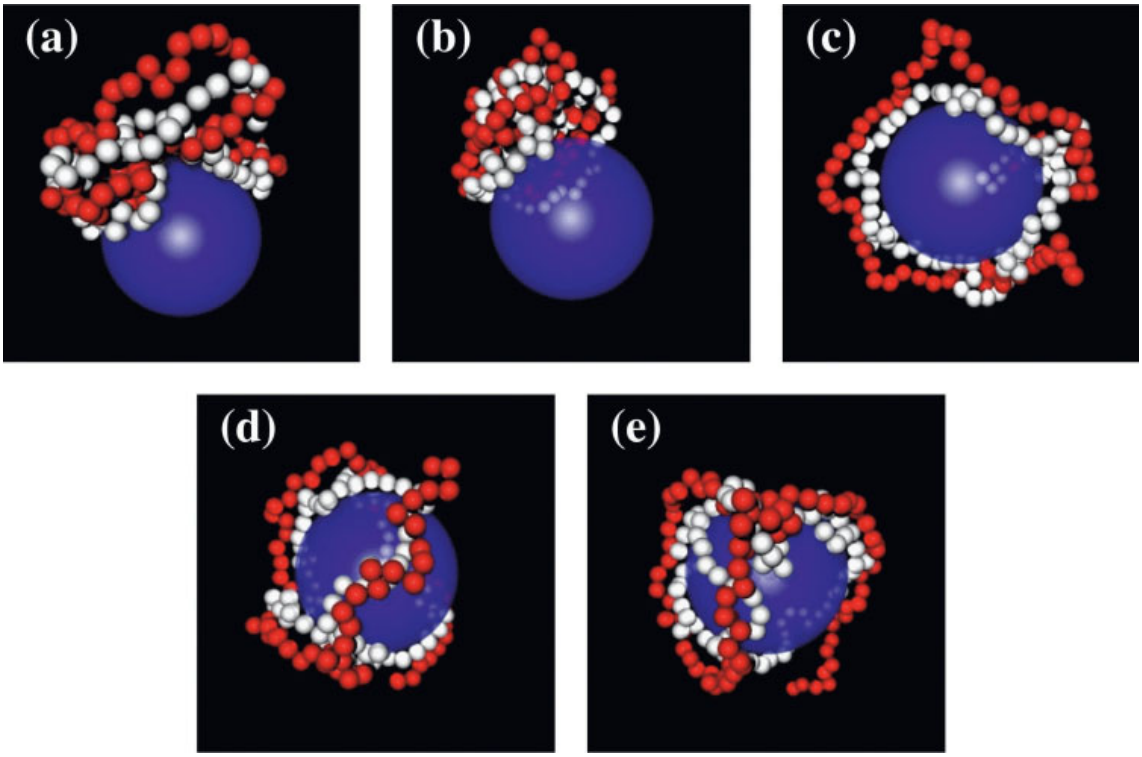

Figure 5. Typical equilibrium configurations for one PC (in white) and one PA (in red) adsorbed onto the negatively charged colloid at different χ_{vdw} couplings. The little counterions (anions and cations) are omitted for clarity. (a) $\chi_{vdw} = 0$ (b) $\chi_{vdw} = 1$ (c) $\chi_{vdw} = 2$ (d) $\chi_{vdw} = 3$ (e) $\chi_{vdw} = 5$.

requires a minimal χ_{vdw}, and hence, flat layers cannot be obtained within a purely electrostatic regime.

For a detailed analysis of the monomer and the net fluid charge distributions, the reader is invited to look at Secs. IV and V of ref. 40.

Now that PE bilayering is rather well understood, the much more complicated case of PE multilayering (beyond bilayering) can be addressed. The adsorption of 12 PEs (6 PCs and 6 PAs) onto the negatively charged colloid is sketched in Figure 6. Even for such a high number of adsorbed PE chains (always with $N_m = 80$), MC simulations show that in a purely electrostatic regime [$\chi_{vdw} = 0$; see Fig. 6(a)] that the formation of globular PC–PA complexes is still strong, leading to a nonhomogeneous monomer coverage of the colloidal surface. In particular, large "holes" are present at $\chi_{vdw} = 0$ due to this PC–PA globalization driving force. On the other hand, at $\chi_{vdw} = 3$ [see Fig. 6(b)], the monomer coverage gets much more homogeneous, where the colloidal surface is nearly uniformly recovered by the PC and PA monomers. This feature indicates again the important role of nonelectrostatic interaction in PE multilayering (even at a relatively high degree of layering).

The influence of chain length was also investigated by considering the adsorption of short PE chains with $N_m = 10$ (see Sec. VII of ref. 40). Typical equilibrium configurations are sketched in Figure 7. In the purely electrostatic regime ($\chi_{vdw} = 0$), the PE adsorption is weak and it significantly increases with χ_{vdw}. Nevertheless, at finite χ_{vdw} only PE bilayering is found to be stable in contrast to previous systems containing long chains (for a more quantitative analysis, compare also Fig 13 with Fig. 10 of ref. 40). Moreover, several globally neutral PC–PA complexes are detected in the bulk, whose number decrease with χ_{vdw} (see Fig. 7). This feature is inhibited for long chains (here $N_m = 80$) due to the strong PC–PA binding energy that keeps all chains near the colloidal surface. Those results concerning short chains, indicate that PE multilayering must also

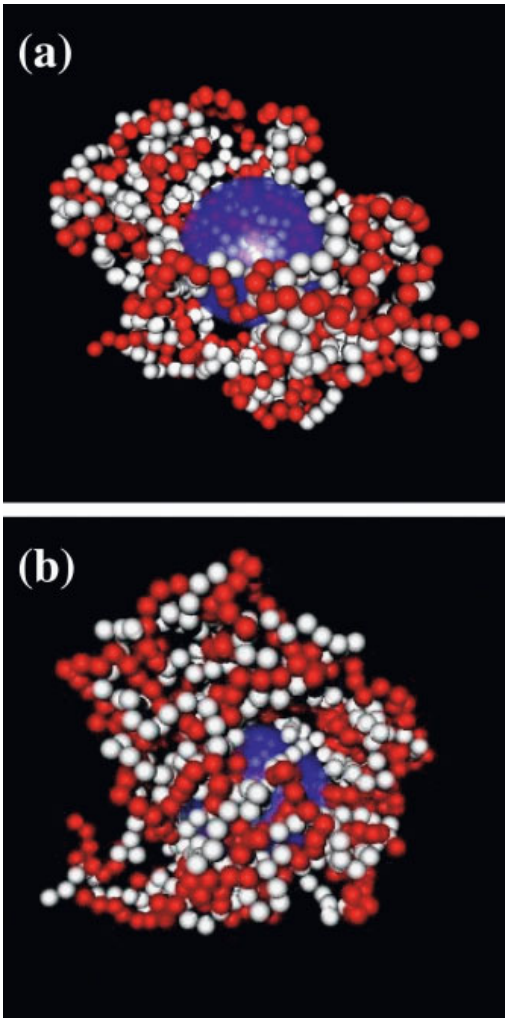

Figure 6. Typical equilibrium configurations for 12 PEs (6 PCs in white and 6 PAs in red) adsorbed onto the negatively charged colloid at different χ_{vdw} couplings. The little counterions (anions and cations) are omitted for clarity. (a) $\chi_{vdw} = 0$ (b) $\chi_{vdw} = 3$.

involve specific PC–PA interactions and/or non-equilibrium effects that are not captured by our model.

Comparison with Other Substrate Geometries

More insight can be gained by comparing the process of PE multilayering just studied above for a spherical substrate with those involving different charged substrate geometries. For instance, the case of a planar substrate has the property of being curvature-independent (where no wrapping can occur), and hence, it corresponds to a more universal situation. On the other hand, the case of a cylindrical substrate presents a very low dimensionality.

Planar Substrate

The study of PE multilayering onto charged planar surfaces was investigated by one of us (see Sec. VI of ref 50 for the present discussion). The monomer density profiles $n_{\pm}(z)$ are depicted in Figure 8 (at fixed total number of monomers of 800 where the number of PC and PA chain is the same) and the corresponding microstructures can be found in Figure 9. Even at $\chi_{vdw} = 0$ with $N_m = 10$, a nonnegligible second peak in $n_+(z)$ can be detected [see Fig. 8(b)], which is the signature of a third layer. This finding strongly contrasts with what was just reported above at spherical substrates for short chains (also with a similar macroion surface charge density), where not even a stable PE bilayer could build up. This behavior can be accounted by geometrical arguments. Indeed, the electrostatic potential in spherical geometry goes like $1/r$ against z in the planar case. Hence, at sufficiently high curvature (as it was the case in ref. 40 where $N_m\sigma/a > 1$), qualitative differences from the planar case are then expected. Always at $\chi_{vdw} = 0$, but with longer chains ($N_m = 20$), Figure 8(a) shows that the degree of layering is higher as expected. This feature is well illustrated by Figure 9(b), where the PA monomers are visibly more attracted to the planar macroion surface. At $\chi_{vdw} = 5$, the adsorption of monomers is drastically increased due to the enhanced stability of the first PC layer that, in turn, induces a larger adsorption of the subsequent PAs and PCs. Compared to $\chi_{vdw} = 0$, all the peaks in $n_{\pm}(z)$ are shifted to smaller z, indicating a higher compaction. These higher ordering and compaction at $\chi_{vdw} = 5$ can be visually checked in Figure 9(c) and (d).

Cylindrical Substrate

The adsorption of oppositely charged PEs onto a charged rod was recently investigated by on of us in ref. 51. Typical equilibrium configurations ($N_m = 20$) can be visualized in Figure 10(a)–(f). The main relevant conclusions of this work can be summarized as follows:

1. As far as the PC adsorption is concerned (in the absence of PAs), it was demonstrated that huge macroion charge reversal occurs even at $\chi_{vdw} = 0$ (see Fig. 3 in ref.

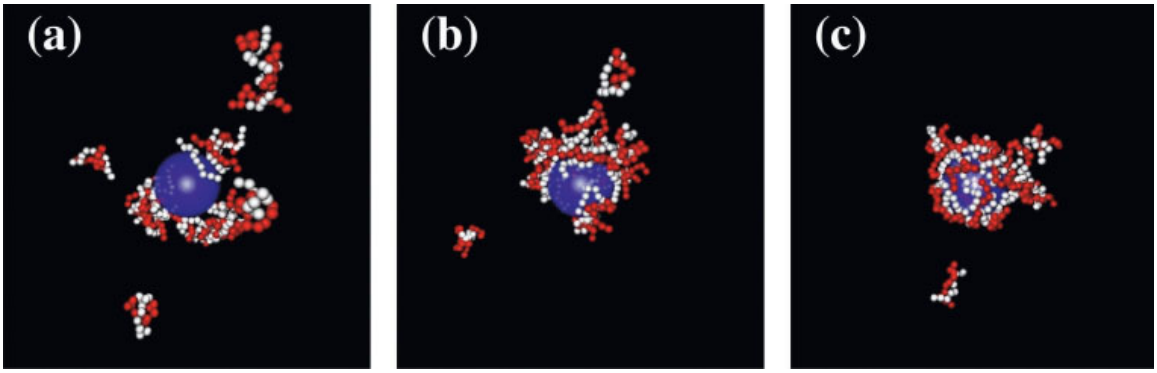

Figure 7. Typical equilibrium configurations for short PC (in white) and PA (in red) chains adsorbed onto the negatively charged colloid at different χ_{vdw} couplings. The little counterions (anions and cations) are omitted for clarity. (a) $\chi_{vdw} = 0$ (b) $\chi_{vdw} = 3$ (c) $\chi_{vdw} = 5$.

51). By adding exactly the same amount of PAs, only a (relatively) marginal overcharging is surprisingly observed [see Fig. 10(a)], which is due to (a) PC–PA clustering and (b) above all to *entropic* effects.

2. At higher number of PEs, MC simulation data show that true bilayering (i.e., flat and dense PE layers) can only occur at finite χ_{vdw}, in contrast to what was found with planar substrates,[50] but similar to the spherical case. Even at finite χ_{vdw}, stable multilayering (beyond bilayering) is hard to reach at large macroion rod curvature [see Figs. 10(b), (d), and (f), and Fig. 5 in ref. 51 for a detailed radial monomer distribution] due to the *high entropy* loss there. This latter, in turn, inhibits the appearance of charge *oscillations*.

CONCLUDING REMARKS

In this article we have reviewed various ways how polyelectrolytes adsorb onto other charged objects. This can happen with oppositely charged colloids, like-charged colloids, or with polyanions and polycations which form multilayers on

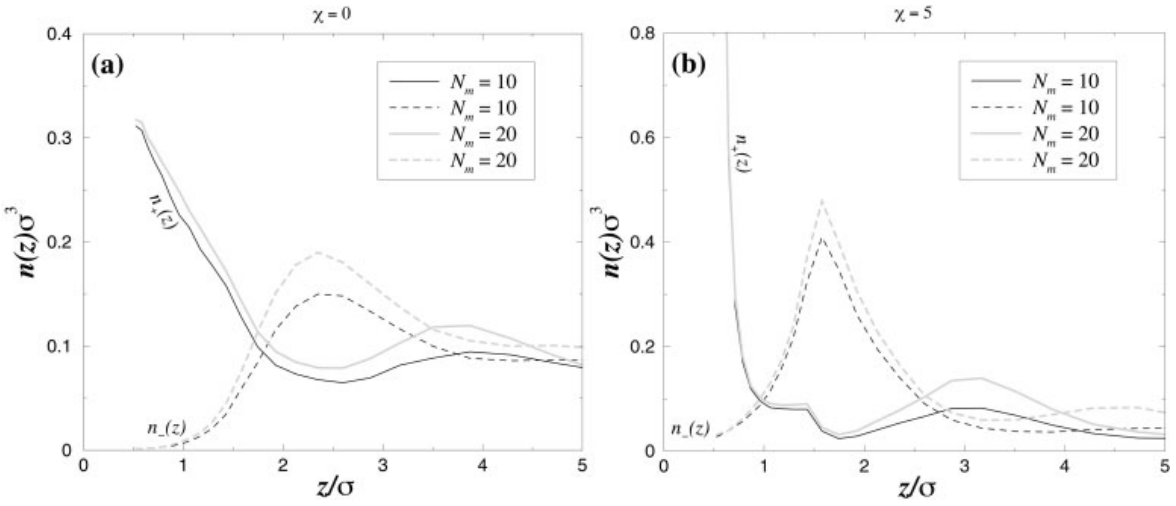

Figure 8. Profiles of monomer density $n \pm (z)$ for oppositely charged PEs adsorbed onto a negatively charged planar substrate. χ_{vdw} couplings. (a) $\chi_{vdw} = 0$ (b) $\chi_{vdw} = 5$.

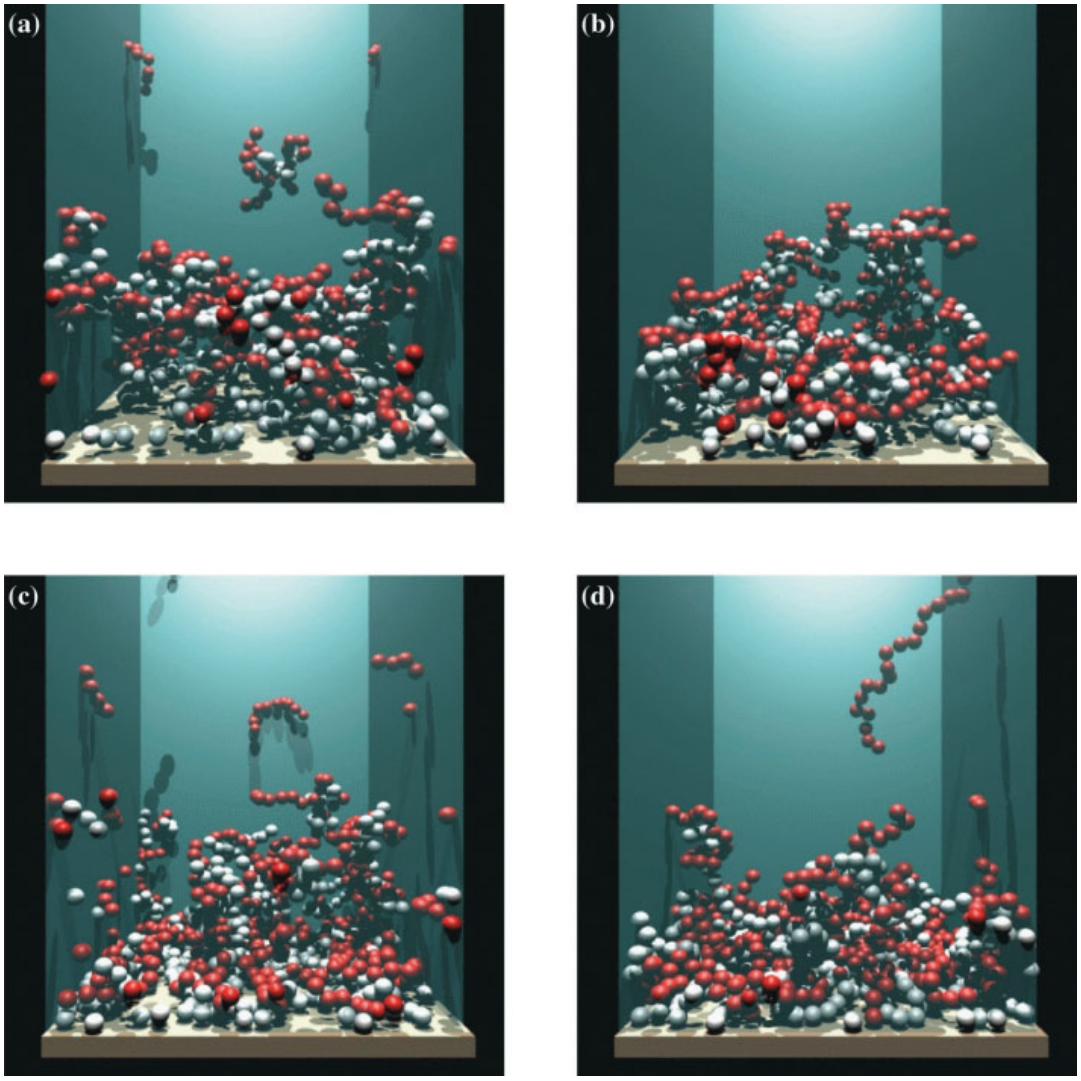

Figure 9. Corresponding microstructures of systems involved in Figure 8, with PCs in white and PAs in red. The little counterions (anions and cations) are omitted for clarity. (a) $\chi_{vdw} = 0, N_m = 10$ (b) $\chi_{vdw} = 0, N_m = 20$ (c) $\chi_{vdw} = 5, N_m = 10$ (d) $\chi_{vdw} = 5, N_m = 20$.

charged surfaces with varying substrate geometries.

At this point we would like to remark that the analytical theories have been developed best for the polyelectrolyte complexes with oppositely charged bodies. The discussed case of like-charged complexations is based on strong charge correlations, and requires thus a strong Coulomb interaction. This is certainly out of the validity of mean-field theories, and needs alternative theoretical approaches, like Wigner crystal theories or theories based on strong coupling expansions. For the last discussed case of polyelectrolyte multilayers it is not even known if the experimentally observed PE multilayers are equilibrium structures or meta-stable states. At least for our choice of short range χ_{vdw} and of the electrostatic coupling parameter, which is based on chain interactions in the bulk state, we do not observe a slow relaxation dynamics of the layers. The chains can reorient in the layers quite freely. This is different from observations in experiments,[33] under slightly different conditions. It is too early to compare quantitatively

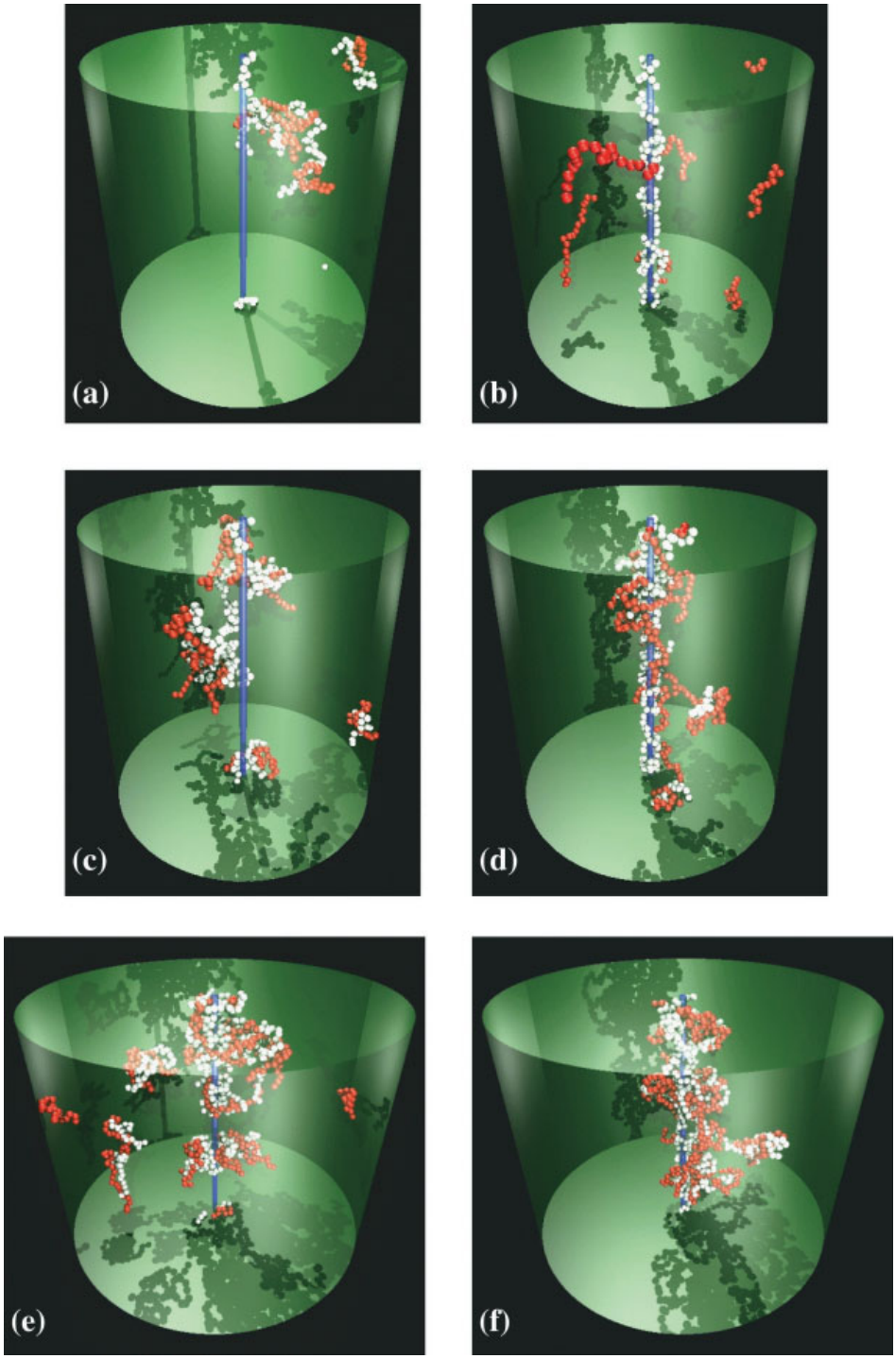

Figure 10. Typical equilibrium configurations for the adsorption of oppositely charged PE chains (at different total number N_{PE} of PEs) onto a cylindrical macroion. The polycations are in white and the polyanions in red. The little ions are omitted for clarity. The outer green cylinder is a guide for the eye. (a) $\chi_{vdw} = 0$, $N_{PE} = 12$ (b) $\chi_{vdw} = 5$, $N_{PE} = 12$ (c) $\chi_{vdw} = 0$, $N_{PE} = 24$ (d) $\chi_{vdw} = 5$, $N_{PE} = 24$ (e) $\chi_{vdw} = 0$, $N_{PE} = 48$ (f) $\chi_{vdw} = 5$, $N_{PE} = 48$.

the outcome of our simulations with experiments, because we dealt only with a considerably small number of chains that also were rather short. However, our results suggest that also nonelectrostatic interactions quite strongly influence the layer morphology. Certainly, more careful experiments and simulations are needed to elaborate on this point.

In basically all cases the observed PE conformations depend highly on the exact parameters of the systems like stiffness, salt content, charge strength, counterion type, and others. The mutual dependencies of these parameters on the observed complexes lead to a highly nontrivial behavior. Although we are far from understanding all the details, we made great progress in understanding at least the qualitative behavior of these systems. Nevertheless, there are still many more questions to be resolved in the future, which partially explains why this field has attracted that much interest in the last few years.

R.M. thanks F. Caruso, H. Löwen, S.K. Mayya, and E. Pérez for helpful discussions. This work was supported in part by the SFB TR6, the SFB 625, and the "Zentrum für Multifunktionelle Werkstoffe und Miniaturisierte Funktionseinheiten," grant BMBF 03N 6500.

REFERENCES AND NOTES

1. Barrat, J.-L.; Joanny, J.-F. Ad Chem Phys 1996, 94, 1.
2. Holm, C.; Kékicheff, P.; Podgornik, R. Eds.; Electrostatic Effects in Soft Matter and Biophysics. NATO Science Series II — Mathematics, Physics and Chemistry; Kluwer Academic Publishers: Dordrecht, 2001; Vol. 46
3. Holm, C.; Kremer K. In Electrostatic Effects in Soft Matter and Biophysics; Holm, C.; Kékicheff, P.; Podgornik, R.; Eds.; Kluwer Academic Publishers: Dordrecht, 2001.
4. van Holde, K. E. Chromatin; Springer: New York, 1989.
5. McQuigg, D. W.; Kaplan, J. I.; Dublin, P. L. J Phys Chem 1992, 96, 1973.
6. Grunstein, M. Nature 1997, 389, 349.
7. Caruso, F.; Caruso, R. A.; Möhwald, H. Science 1998, 282, 1111.
8. Schiessel, H. J Phys Condens Matter 2003, 15, R699.
9. Marky, N. L.; Manning, G. S. J Mol Biol 1995, 255, 50.
10. von Goeler, F.; Muthukumar, M. J Chem Phys 1994, 100, 7796.
11. Gurovitch, E.; Sens, P. Phys Rev Lett 1999, 82, 339.
12. Mateescu, E. M.; Jeppesen, C.; Pincus, P. Europhys Lett 1999, 46, 493.
13. Park, S. Y.; Bruinsma, R. F.; Gelbart, W. M. Europhys Lett 1999, 46, 454.
14. Netz, R. R.; Joanny, J. F. Macromolecules 1999, 32, 9026.
15. Kunze, K.-K.; Netz, R. R. Phys Rev Lett 2000, 85, 4389.
16. Nguyen, T. T.; Shklovskii, B. I. Physica A 2001, 293, 324.
17. Schiessel, H.; Rudnick, J.; Bruisma, R.; Gelbart, W. M. Europhys Lett 2000, 51, 237.
18. Jonsson, M.; Linse, P. J Chem Phys 2001, 115, 3406.
19. Wallin, T.; Linse, P. Langmuir 1996, 12, 305.
20. Wallin, T.; Linse, P. J Phys Chem 1996, 100, 17873.
21. Wallin, T.; Linse, P. J Phys Chem B 1997, 101, 5506.
22. Kong, C. Y.; Muthukumar, M. J Chem Phys 1998, 109, 1522.
23. Messina, R.; Holm, C.; Kremer, K. Phys Rev E 2002, 65, 041805.
24. Messina, R.; Holm, C.; Kremer, K. J Chem Phys 2002, 117, 2947.
25. Gelbart, W. M.; Bruinsma, R. F.; Pincus, P. A.; Parsegian, V. A. Phys Today 2000, 53, 38.
26. Schmitt, J.; Decher, G.; Hong, G. Thin Solid Films 1992, 210/211, 831.
27. Decher, G. Science 1997, 277, 1232.
28. Caruso, F.; Furlong, D. N.; Ariga, K.; Ichinose, I.; Kunitake, T. Langmuir 1997, 14, 4559.
29. Onda, M.; Ariga, K.; Kunitake, T. Biosci Bioeng 1999, 87, 69.
30. Wu, A.; Yoo, D.; Lee, J. K.; Rubner, M. F. J Am Chem Soc 1999, 121, 4883.
31. Gittins, D. I.; Caruso, F. J Phys Chem B 2001, 105, 6846.
32. Lowack, K.; Helm, C. A. Macromolecules 1998, 31, 823.
33. Kovacevic, D.; van der Burgh, S.; Cohen-Stuart, M. A. Langmuir 2002, 18, 5607.
34. Schiessel, H. Macromolecules 2003, 36, 3424.
35. Chodanowski, P.; Stoll, S. Macromolecules 2001, 34, 2320.
36. Chodanowski, P.; Stoll, S. J Chem Phys 2001, 115, 4951.
37. Chodanowski, P.; Stoll, S. Macromolecules 2002, 35, 9556.
38. Akinchina, A.; Linse, P. Macromolecules 2002, 35, 5183.
39. Dzubiella, J.; Moreira, A. G.; Pincus, P. A. Macromolecules 2003, 36, 1741.
40. Messina, R.; Holm, C.; Kremer, K. Langmuir 2003, 19, 4473.
41. Carlsson, F.; Linse, P.; Malmsten, M. J Phys Chem B 2001, 105, 9040.

42. Messina, R.; Holm, C.; Kremer, K. Eur Phys 2001, 4, 363.
43. Messina, R. J Chem Phys 2002, 117, 11062.
44. Messina, R. Physica A 2002, 308, 59.
45. Jonsson, M.; Linse, P. J Chem Phys 2001, 115, 3406.
46. Jonsson, M.; Linse, P. J Chem Phys 2001, 115, 10975.
47. Nguyen, T. T.; Shklovskii, B. I. J Chem Phys 2001, 114, 5905.
48. Schiessel, H.; Bruinsma, R. F.; Gelbart, W. M. J Chem Phys 2001, 115, 7245.
49. Kantor, Y.; Kadar, M. Europhys Lett 1994, 27, 643.
50. Messina, R. Macromolecules 2004, 37, 621.
51. Messina, R. J Chem Phys 2003, 119, 8133.
52. Solis, F. J.; Olvera de la Cruz, M. J Chem Phys 1999, 110, 11517.
53. Castelnovo, M.; Joanny, J. F. Langmuir 2000, 16, 7524.

Appendix I

Like-charge colloid-polyelectrolyte complexation

Like-charge colloid–polyelectrolyte complexation

René Messina,[a] Christian Holm,[b] and Kurt Kremer[c]
Max-Planck-Institut für Polymerforschung, Ackermannweg 10, 55128 Mainz, Germany

(Received 6 February 2002; accepted 10 May 2002)

We investigate the complexation of a highly charged sphere with a long flexible polyelectrolyte, *both negatively charged* in a salt-free environment. Electroneutrality is insured by the presence of divalent counterions. Using molecular dynamics within the framework of the primitive model, we consider different Coulomb coupling regimes. At strong Coulomb coupling we find that the adsorbed chain is always confined to the colloidal surface but forms different conformations that depend on the linear charge density of the chain. A mechanism involving the polyelectrolyte *overcharging* is proposed to explain these structures. At intermediate Coulomb coupling, the chain conformation starts to become three-dimensional, and we observe multilayering of the highly charged chain while for lower charge density the chain wraps around the colloid. At weak Coulomb coupling, corresponding to an aqueous solvent, we still find like-charge complexation. In this latter case the chain conformation exhibits loops. © *2002 American Institute of Physics.*
[DOI: 10.1063/1.1490595]

I. INTRODUCTION

The adsorption of polyelectrolytes onto an *oppositely* charged spherical particle has been experimentally extensively studied recently.[1–4] Various authors have investigated this phenomenon theoretically[5–13] and by Monte Carlo simulations.[14–18] Nonetheless, much less is known concerning the complexation of a charged sphere with a like-charged polyelectrolyte. It is only very recently that we reported in a short communication such a phenomenon in the strong Coulomb coupling regime.[19] From a theoretical point of view, the long range Coulomb interactions of these systems represents a formidable challenge, and especially the understanding of effective attraction of like charged bodies has attracted recent attention.

In this paper, we elaborate on the complexation between a sphere and a long flexible polyelectrolyte *both negatively charged*. While complexation in the strong coupling limit it is expected, we report new and rather unexpected chain conformations. We present MD simulation results without added salt but taking into account the counterions explicitly. Various Coulomb couplings as well as different polyelectrolyte linear charge densities are investigated. A detailed study of the ions (monomer and counterion) distribution is reported and mechanisms accounting for the different encountered complex structures are proposed.

The paper is organized as follows: Section II contains details of our MD simulation model. Section III is devoted to the strong Coulomb coupling regime. Section IV is devoted to the intermediate Coulomb coupling regime. In Sec. V, we consider the like-charge complexation in the weak Coulomb coupling regime corresponding to the water solvent.

[a]Electronic mail: messina@mpip-mainz.mpg.de
[b]Electronic mail: holm@mpip-mainz.mpg.de
[c]Electronic mail: k.kremer@mpip-mainz.mpg.de

II. SIMULATION METHOD

The MD method employed here is based on the Langevin equation and is similar to that employed in previous studies.[20] Consider within the framework of the primitive model one spherical macroion characterized by a diameter d and a bare charge $Q_M=-Z_M e$ (where e is the elementary charge and $Z_M>0$) surrounded by an implicit solvent of relative dielectric permittivity ϵ_r. The polymer chain is made up of N_m monomers of diameter σ. Both ends of the chain are always charged and each $1/f$ monomer is charged so that the chain contains $N_{cm}=(N_m-1)f+1$ *charged* monomers. The monomer charge is $q_m=-Z_m e$ (with $Z_m>0$). The small counterions, assumed all are identical, ensure global electroneutrality and have a diameter σ and charge $+Z_c e$ (with $Z_c>0$). All these particles making up the system are confined in an impermeable spherical cell of radius R, and the spherical macroion is held *fixed* at the center of the cell.

The equation of motion of any mobile particle (counterion or monomer) i reads

$$m\frac{d^2\mathbf{r}_i}{dt^2}=-\nabla_i U(\mathbf{r}_i)-m\gamma\frac{d\mathbf{r}_i}{dt}+\mathbf{W}_i(t), \tag{1}$$

where m is the mass particle (supposed identical for all mobile species), U is the *total* potential force, and γ is the friction coefficient. Friction and stochastic force are linked by the dissipation-fluctuation theorem $\langle \mathbf{W}_i(t)\cdot\mathbf{W}_j(t')\rangle = 6m\gamma k_B T\delta_{ij}\delta(t-t')$.

Excluded volume interactions are introduced via a pure short range repulsive Lennard-Jones (LJ) potential given by

$$U_{\mathrm{LJ}}(r)=\begin{cases} 4\epsilon\left[\left(\dfrac{\sigma}{r-r_0}\right)^{12}-\left(\dfrac{\sigma}{r-r_0}\right)^{6}\right]+\epsilon, \\ \quad \text{for } r-r_0<r_{\mathrm{cut}}, \\ 0, \quad \text{for } r-r_0\geqslant r_{\mathrm{cut}}, \end{cases} \tag{2}$$

TABLE I. General data of the simulation model. Note that the temperature is used as energy scale for the simulations.

Parameters	
$\sigma=3.57$ Å	Lennard-Jones length units
$T=298$ K	room temperature
$\epsilon=k_BT$	Lennard-Jones energy units
$Z_M=180$	macroion valence
Z_m	monomer valence
Z_c	counterion valence
N_c	total number of counterions
l_B	Bjerrum length
$a=8\sigma$	macroion–counterion distance of closest approach
$R=40\sigma$	simulation cell radius
$f_M=8\times10^{-3}$	macroion volume fraction
$\kappa=1000kT/\sigma12$	FENE spring constant
$R_0=1.5\sigma$	FENE cutoff
$l=0.8\sigma$	average bond length
N_m	total number of monomers
N_{cm}	number of charged monomers
f	monomer charge fraction
$\lambda_{PE}=Z_mef/l$	polyelectrolyte linear charge density

where $r_0=0$ for the microion–microion interaction, $r_0=7\sigma$ for the macroion–microion interaction, and $r_{\text{cut}}=2^{1/6}\sigma$ is the cutoff radius. This leads to $d=2r_0+\sigma=15\sigma$, whereas the closest center–center distance of the microions to the spherical macroion is $a=r_0+\sigma=8\sigma$. The macroion volume fraction is defined as $f_M=(a/R)^3$ and is fixed to 8×10^{-3} with $R=40\sigma$.

The pair electrostatic interaction between any pair ij, where i and j denote either a macroion or a charged microion (counterion or charged monomer), reads

$$\frac{U_{\text{coul}}(r)}{k_BT}=l_B\frac{Z_iZ_j}{r}, \tag{3}$$

where $l_B=e^2/4\pi\epsilon_0\epsilon_rk_BT$ is the Bjerrum length. Energies are measured in units of $\epsilon=k_BT$ with $T=298$ K. Choosing $\sigma=3.57$ Å requires that the Bjerrum length of water at room temperature equals 2σ (7.14 Å). In this work the macroion charge is fixed at $Z_M=180$.

The polyelectrolyte chain connectivity is modeled by using a standard finitely extensible nonlinear elastic (FENE) potential in good solvent (see for example Ref. 20), which reads

$$U_{\text{FENE}}(r)=\begin{cases}-\frac{1}{2}\kappa R_0^2\ln\left[1-\frac{r^2}{R_0^2}\right], & \text{for } r<R_0,\\ \infty, & \text{for } r\geqslant R_0,\end{cases} \tag{4}$$

where κ is the spring constantlike chosen as $1000k_BT/\sigma^2$ and $R_0=1.5\sigma$. These values lead to an equilibrium bond length $l=0.8\sigma$.

Typical simulation parameters are summarized in Table I. The simulation runs are reported in Table II. The time step is $\Delta t=0.002\tau$ with $\tau=\gamma^{-1}$. Each simulation run requires about 10^7 MD steps, and equilibrium is typically reached after 5×10^5 up to 3×10^6 steps. We normally performed between 5×10^6 and 10^7 MD steps to take measurements. We cover the whole range of strength of Coulomb electrostatic interaction from the strong coupling limit, which is more theoretical interest, to the weak coupling limit, which corresponds to an aqueous solvent.

III. STRONG COULOMB COUPLING

First we look at the like-charge complexation in the strong Coulomb coupling regime. We choose the relative permittivity $\epsilon_r=16$, corresponding to $l_B=10\sigma$, and divalent microions ($Z_m=Z_c=2$). Such a set of parameters is of special theoretical interest to study the influence of strong electrostatic correlations.

A. Single charged object

In this section we first study *separately* (i) the spherical macroion and (ii) the flexible polyelectrolyte in the presence of their surrounding neutralizing divalent counterions. This provides the reference states for the more complicated situation, where both of these two objects interact.

TABLE II. Specification of the simulated systems. The chain radii of gyration $R_g^{(\text{bulk})}$ and $R_g^{(\text{comp})}$ are given for an isolated chain (i.e., in the absence of the colloid) and for the complexed case (i.e., in the presence of the colloid), respectively.

Parameter	$1/f$	N_m	N_{cm}	N_c	Z_m	Z_c	l_B/σ	$R_g^{(\text{bulk})}/\sigma$	$R_g^{(\text{comp})}/\sigma$
run A	1	256	256	346	2	2	10	3.81	6.42
run B	2	257	129	219	2	2	10	3.90	8.69
run C	3	256	86	176	2	2	10	3.95	8.75
run D	5	256	52	142	2	2	10	4.49	8.86
run E	1	256	256	346	2	2	4	4.40	4.8
run F	2	257	129	219	2	2	4	4.8	9.4
run G	3	256	86	176	2	2	4	5.4	9.3
run H	1	256	256	346	2	2	2	6.6	6.1
run I	2	257	129	219	2	2	2	12	13
run J	3	256	86	176	2	2	2	⋯	21
run K	1	252	252	144	1	3	2	⋯	8.4
run L	2	251	126	102	1	3	2	⋯	9.8
run M	3	250	84	88	1	3	2	⋯	10.4
run N	1	256	256	436	1	1	2	⋯	⋯

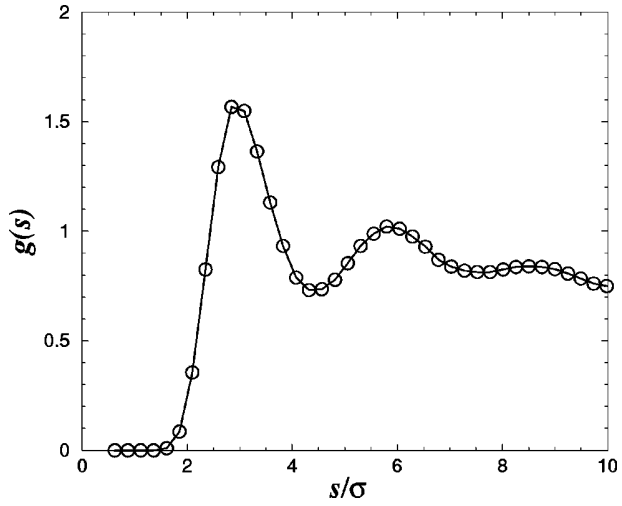

FIG. 1. Counterion *surface* correlation function $g(s)$ for 90 divalent counterions ($Z_M=180$) in the case of an *isolated* macroion in strong Coulomb coupling ($l_B=10\sigma$). See Fig. 2 for a typical equilibrium snapshot.

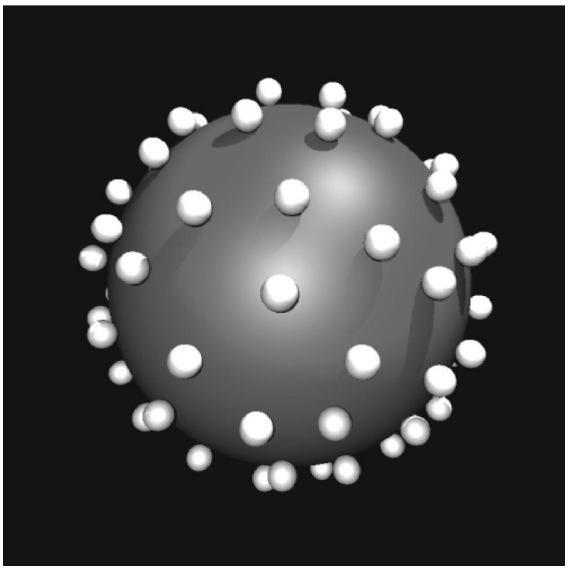

FIG. 2. Snapshot of the equilibrium counterion structure of an *isolated* macroion with a bare charge $Z_M=180$ [see Fig. 1 for the corresponding $g(s)$].

1. Spherical macroion

Consider an isolated macroion with its surrounding divalent counterions. A pertinent parameter to describe the Coulomb coupling for such highly asymmetric electrolyte solution (macroion and counterions) is the so-called "plasma" parameter $\Gamma=Z_c^2 l_B/a_{cc}$, where a_{cc} (which will be determined below) is the average distance (triangular lattice parameter in the ground state) between counterions lying on the macroion surface.[21] For the strong Coulomb coupling considered we find $\Gamma\approx 13$ (with $Z_M=180$), and for finite macroion volume fraction (here $f_M=8\times 10^{-3}$), all counterions lie in the vicinity of the macroion surface.[22–25]

To characterize the counterion layer *structure*, we compute the counterion correlation function $g(s)$ on the surface of the sphere,[23,25] defined as

$$c^2 g(s)=\left\langle \sum_{i\neq j} \delta(s'-s_i)\,\delta(s''-s_j)\right\rangle, \tag{5}$$

where $c=N_c/4\pi a^2$ is the surface counterion concentration ($N_c=Z_M/Z_c$ being the number of counterions), and $s=|s'-s''|$ corresponds to the *arc length* on the sphere of radius a (center-distance of closest approach of macroion and counterion). Each counterion (located in the vicinity of the surface) is radially projected on the ("contact") shell around the macroion center of radius $a=8\sigma$. Correlation functions are computed by averaging $g(s)$ over 1000 independent equilibrium configurations which are statistically uncorrelated. The pair distribution $g(s)$ is normalized as follows:

$$c\int_0^{\pi a} 2\pi s g(s)\,ds=(N_c-1). \tag{6}$$

Because of the *finite* size and the topology of the sphere, $g(s)$ has a cutoff at πa $(=25.1\sigma)$ and a *zero* value there. Therefore, at large values of s, $g(s)$ cannot directly be compared to the correlation function in an infinite plane.

Results are depicted in Fig. 1 for $Z_M=180$. The first peak[26] appears at about $s=a_{cc}\approx 3\sigma$, whereas the second peak about $s\approx 6\sigma$ and finally the third small peak around $s\approx 9\sigma$. This structure, which is highly correlated, is referred to as a strongly correlated liquid (SCL),[23,27] but not yet a Wigner crystal. A typical equilibrium configuration is depicted in Fig. 2, where one can see the local arrangement close to a triangular lattice.

2. Polyelectrolyte chain

Now we investigate an isolated polyelectrolyte chain together with its surrounding divalent counterions in bulk confined to the same spherical cell of radius $R=40\sigma$. We consider four monomer charge fractions (i.e., four linear charge densities) $f=1$, 1/2, 1/3, and 1/5. The chain is made up of $N_m=256$ monomers ($N_m=257$ for $f=1/2$), while $Z_m=Z_c=2$. The polymer chain parameters are identical to those of the complexation case (see Table II). The chain extension is characterized by its radius of gyration R_g given by

$$R_g^2=\frac{1}{N_m}\left\langle \sum_{i=1}^{N_m} (\mathbf{r}_i-\mathbf{r}_{\mathrm{CM}})^2\right\rangle, \tag{7}$$

where $\mathbf{r}_{\mathrm{CM}}$ is the center-of-mass position of the chain.

The corresponding values of R_g can be found in Table II [see $R_g^{(\mathrm{bulk})}$ for runs A–D]. The chain extension varies little with f and is roughly given by $R_g\approx 4\sigma$. For this strong Coulomb coupling, *all* counterions are "condensed" into the polyelectrolyte globule for all three linear charge densities considered. The strong counterion condensation induces a collapse of the chain, which is by now well understood.[28–32] A typical equilibrium chain conformation is shown in Fig. 3 for $f=1$. As expected the structure is very compact and highly ordered. Very similar structures are obtained for $f=1/2$, 1/3, and 1/5.

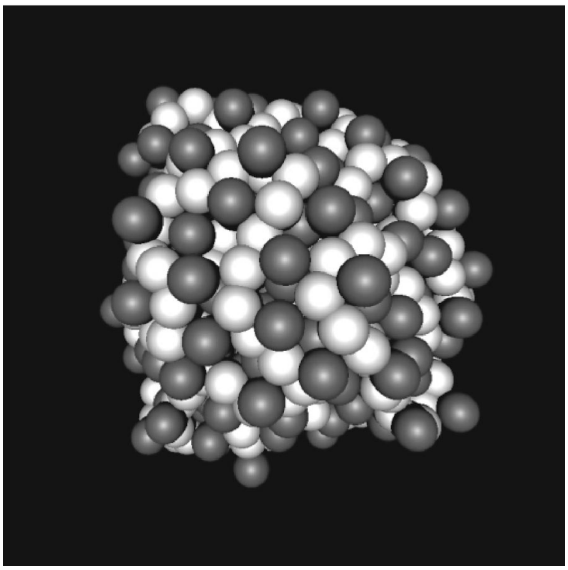

FIG. 3. Snapshot of the equilibrium conformation of an *isolated* polyelectrolyte chain made up of 256 monomers where all monomers are charged ($f=1$). Monomers are in white and counterions in dark gray.

B. Complexation

We now investigate the complexation of a highly charged colloid with a long flexible polyelectrolyte, both negatively charged. Four different parameter combinations, denoted by run A, B, C, and D, were investigated which are summarized in Table II. Going from run A to D the polyelectrolyte charge fraction f decreases from 1 to 1/5. The contour length of the chain is much larger ($N_m l/d \approx 14$ times) than the colloidal particle diameter.

Due to the high coupling energies involved for $f=1$ (run A), we carefully examined the final results, to avoid metastable states. We started with several initial configuration where each monomer is close to the macroion surface, and ensured that we ended up each time in the same final (lowest energy) equilibrium state. By starting from a chain that is far from the colloid we found a ''long globule'' adsorbed on the macroion surface with a much higher energy ($\Delta E \approx 80 k_B T$), which we therefore discarded. For all other investigated parameters, we found the same final equilibrium configuration, irrespectively of the starting configuration.

1. Observation of the complexation

Figure 4 shows typical equilibrium configurations of the colloid–polyelectrolyte complex. We notice that in all reported cases complexation occurs and the polyelectrolyte is completely adsorbed onto the colloidal surface, that is, in presence of a highly charged colloid, the polyelectrolyte conformation becomes quasi-*two-dimensional* in contrast to the bulk case (compare Fig. 4 with Fig. 3). However the struc-

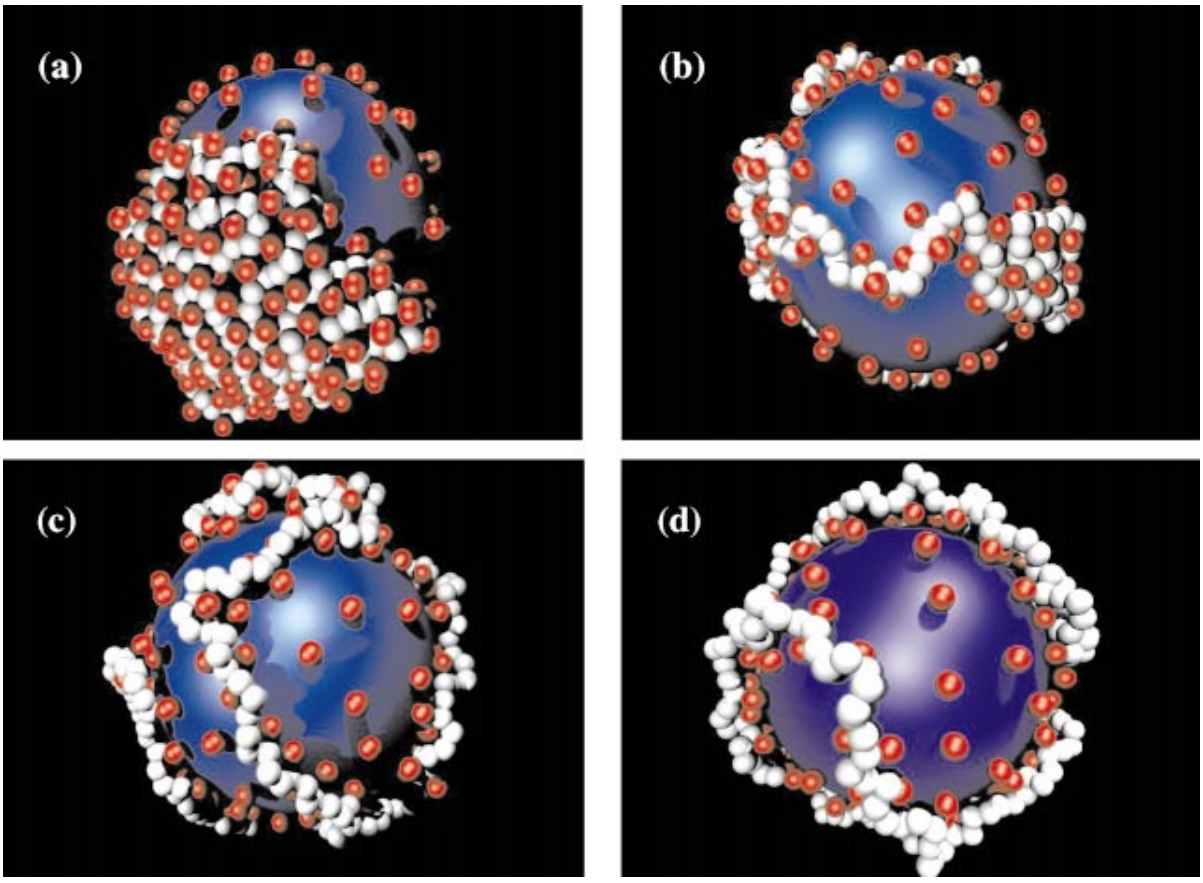

FIG. 4. (Color) Typical equilibrium configurations of the colloid–polyelectrolyte complex in strong Coulomb coupling ($l_B = 10\sigma$) for (a) run A ($f=1$), (b) run B ($f=1/2$), (c) run C ($f=1/3$), and (d) run D ($f=1/5$). Monomers are in white and counterions in red.

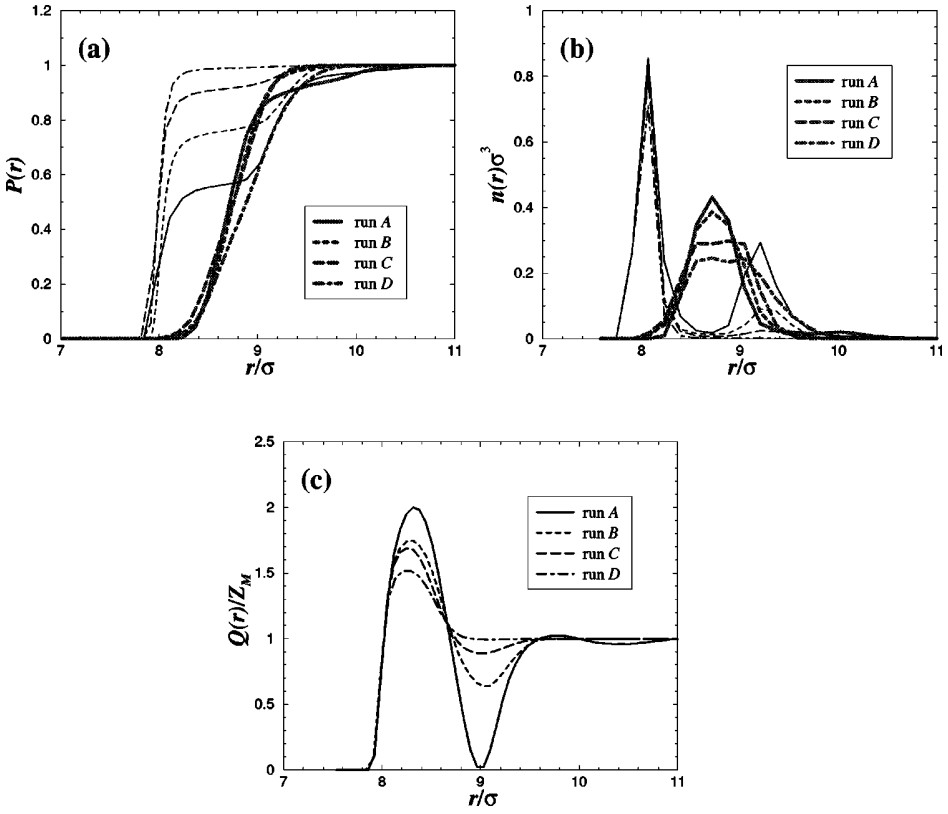

FIG. 5. Ion adsorption profiles (runs A–D) as a function of the distance r from the macroion center. (a) Fraction $P(r)$ and (b) radial density $n(r)$ of counterions (thin lines) and monomers (thick lines); (c) reduced net fluid charge $Q(r)/Z_M$.

ture of these resulting complexes depends strongly on the value of f. For the fully charged polyelectrolyte case [run A with $f=1$, see Fig. 4(a)] the monomers are closely packed forming a *two-dimensional* compact Hamiltonian-walk with the condensed counterions on the polyelectrolyte. This structure consists of closed packed lines made from either counterions or monomers. When the linear change density is reduced [see Figs. 4(b)–4(d)], the complex structures are qualitatively different. In these cases the monomers are no longer closely packed. For run B [$f=1/2$, Fig. 4(b)], the monomers spread more over the particle surface and the polymer partially wraps around the sphere exhibiting a quasi-two-dimensional surface pearl-necklace structure. For run C [$f=1/3$, Fig. 4(c)] and run D [$f=1/5$, Fig. 4(d)], the monomers spread entirely over the particle surface, and the chain wraps the colloidal particle leading to an almost isotropic distribution of the monomers around the spherical macroion.

The like-charge complex formation is due to the strong counterion mediated correlations which are known to induce attractions in the strong Coulomb coupling regime. Basically, the charged species will try to order locally in a way which is compatible with the chain connectivity and the macroion surface constraints. We now quantify those observations and propose a simple mechanism to explain the observed conformations.

2. Adsorption profile

To quantify the adsorption of the monomers and counterions on the macroion particle surface, we analyze three quantities: (i) the ion radial distribution function $n_i(r)$, (ii) the ion fraction $P_i(r)$, and (iii) the net fluid charge $Q_i(r)$ (omitting the macroion bare charge Z_M), where r is the distance from the spherical macroion center. The radial ion distribution function $n_i(r)$ is normalized as follows:

$$\int_{r_0}^{R} n_i(r) 4\pi r^2 dr = N_i \quad \text{with} \quad i=c,m, \tag{8}$$

where N_i is the total number of ions, and the subscripts c and m stand for counterion and monomer, respectively. The reduced integrated ion radial density $P_i(r)$ is linked to $n_i(r)$ via

$$P_i(r) = \frac{\int_{r_0}^{r} n_i(r') 4\pi r^2 dr'}{N_i} \quad \text{with} \quad i=c,m. \tag{9}$$

Note that for $f<1$, neutral and charged monomers are all included in the quantities $n_m(r)$ and $P_m(r)$. The net fluid charge $Q(r)$ is given by

$$Q(r) = \int_{r_0}^{r} [Z_c n_c(r') - Z_m n_m(r')] 4\pi r^2 dr', \tag{10}$$

where we choose $e=1$.

Integrated distribution $P(r)$, radial distribution $n(r)$, and fluid net charge $Q(r)$ profiles are depicted in Figs. 5(a)–5(c), respectively. Figure 5(a) shows that all ions for all runs are condensed within a distance of about 10σ from the colloid center and more than 80% of the monomers and counterions are within a distance of 9.3σ from the colloid center corresponding roughly to two atomic layers [see also the radial distribution in Fig. 5(b)]. Due to strong electrostatic attraction between the sphere and the counterions and strong

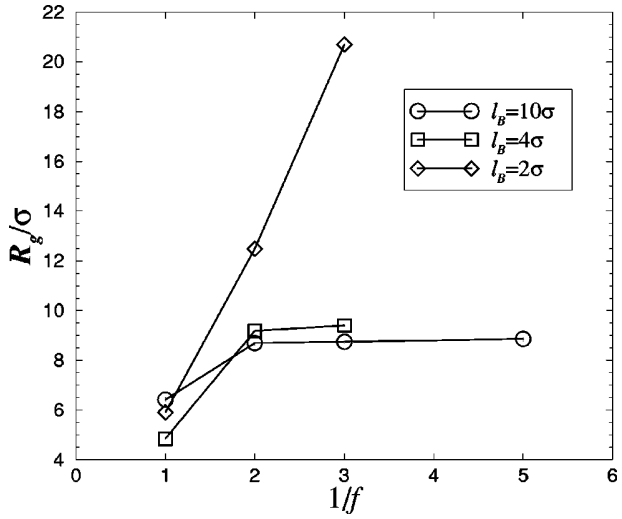

FIG. 6. Radius of gyration of the polymer as a function of the polyelectrolyte charge fraction f for $l_B=10\sigma$ (runs A–D), $l_B=4\sigma$ (runs E–G), and $l_B=2\sigma$ (runs H–J).

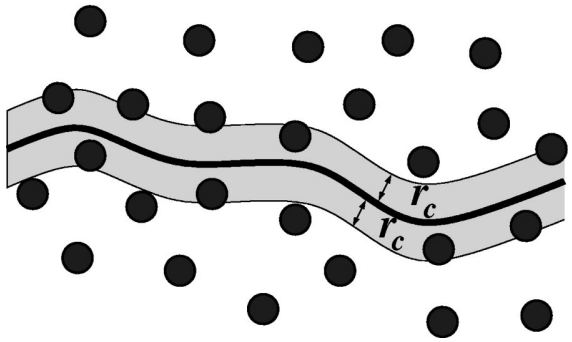

FIG. 7. Schematic view of the chain intercepting counterions within a distance r_c.

electrostatic repulsion between the sphere and the charged monomers the first layer ($r\sim a=8\sigma$) is exclusively made up of counterions [see Figs. 5(a) and 5(b)]. Note that the monomer depletion in this first counterion layer also concerns *neutral* monomers (runs B–D) and this effect is attributed to the chain connectivity. This means that the repulsion stemming from the *charged* monomers impose the polymer structure as long as f and the Coulomb coupling are sufficiently high, which is the case in the present study. The height of the first peak in the counterion $n_c(r)$ profile is almost independent on f. The second ion layer is mixed of monomers and counterions, however with a majority of monomers [see Figs. 5(a) and 5(b)]. Indeed the first monomer peak in the $n_m(r)$ profile (located at $r\approx 8.7\sigma$) and the second counterion peak in the $n_c(r)$ profile (located at $r\approx 9.2\sigma$) are only separated by roughly $\Delta r\approx 0.5\sigma$ [see Fig. 5(b)]. This leads to a medium position located at $r\approx 9\sigma$ corresponding to a bilayer thickness. The height of the second peak in the counterion $n_c(r)$ profile increases with increasing f [see Fig. 5(b)].

For $f=1$ (run A), we observe a massive macroion *charge inversion* of more than 100% [i.e., $Q(r)/Z_M>2$] in the first layer as well as a strong charge oscillation [see Fig. 5(c)]. Upon reducing f (runs B–D) the macroion charge overcompensation decreases as well as the charge oscillation amplitude [see Fig. 5(c)]. This is due to the fact that upon reducing f less counterions are present and their correlations change.

3. Polyelectrolyte chain radius of gyration

Next, we investigate the radius of gyration R_g of the chain, i.e., Eq. (7), in order to gain insight of the spreading of the monomers over the sphere. The results reported in Fig. 6 (for $l_B=10\sigma$) show that R_g increases with decreasing f which demonstrates that the spreading of the monomers over the macroion surface is enhanced by decreasing the polyelectrolyte charge density. The jump in R_g is particularly large between $f=1$ and $f<1$. This is in agreement with the visual inspection of the chain conformations presented in Fig. 4. Moreover, the isotropic case (monomers fully spread over the particle) corresponding to $R_g\approx 8.7\sigma$ (Ref. 33) is already reached for $f=1/2$ (run B).

4. Surface counterion correlation function

In this section we are interested in determining the structure of the ''free'' counterions which are *not condensed* onto the polyelectrolyte chain. Counterions are called ''condensed'' on the polyelectrolyte chain when they lie within a distance $r_c=1.2\sigma$ perpendicular to the chain (Fig. 7). All other counterions are called ''free,'' although they are still adsorbed onto the colloidal surface. To characterize the structure of the free counterions we proceed in the same way as in Sec. III A 1. The surface free counterion correlation function $g_{\text{free}}(s)$ is now given by

$$c_{\text{free}}^2 g_{\text{free}}(s)=\left\langle \sum_{i\neq j} \delta(s'-s_i)\,\delta(s''-s_j)\right\rangle, \tag{11}$$

where the sum in Eq. (11) is restricted to the free counterions, and $c_{\text{free}}=N_{\text{free}}/4\pi a^2$ is the surface free counterion concentration, with N_{free} being the average number of free counterions. The normalization is obtained as follows:

$$c_{\text{free}}\int_0^{\pi a} 2\pi s g_{\text{free}}(s)\,ds=(N_{\text{free}}-1). \tag{12}$$

Results are depicted in Fig. 8 for runs A–D. The important result is that the first peak of $g_{\text{free}}(r)$ is located at the same position ($s\approx 3\sigma$) as in the ''unperturbed'' case of an isolated macroion (without polyelectrolyte) studied in Sec. III A 1 (see Fig. 1). Although the second peak of $g_{\text{free}}(s)$ is less pronounced than in the ''unperturbed'' case (compare Fig. 8 with Fig. 1), the local order of the free counterion structure is still high as can be visually inspected on the snapshots sketched in Fig. 4. Thus the adsorbed chain only affects the counterion distribution significantly in its immediate neighborhood.

5. Polyelectrolyte overcharging

We now show that the concept of polyelectrolyte *overcharging* can be used to explain the observed complex struc-

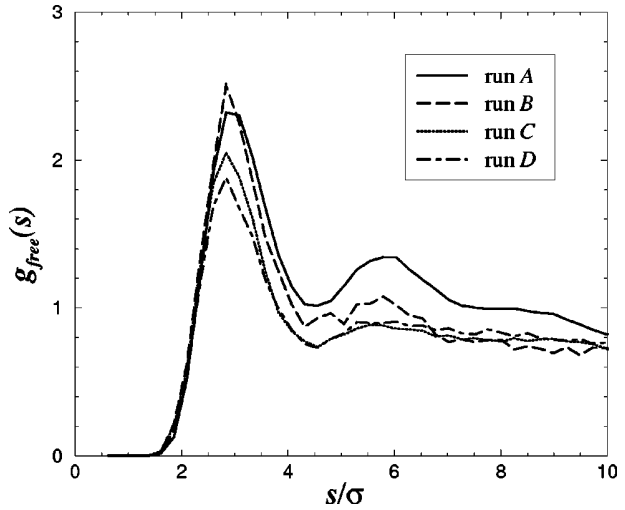

FIG. 8. Free counterion (unbounded to the polyelectrolyte) surface correlation function $g_{\text{free}}(s)$ for runs A–D.

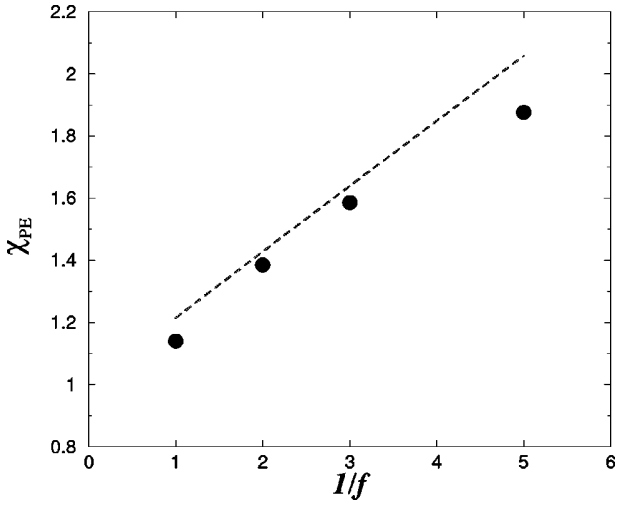

FIG. 9. Polyelectrolyte overcharge as a function of f (runs A–D). The dashed line corresponds to the theoretical prediction where Eq. (14) was used.

tures. Let N_{cd} be the number of counterions we consider as condensed onto the polyelectrolyte. Then the overcharging ratio χ_{PE} is defined as

$$\chi_{PE}=\frac{N_{cd}}{N_{cm}}, \tag{13}$$

which is merely the ratio between the amount of the *total* condensed counterion charge and the polyelectrolyte *bare* charge.

This ''overcharging'' can also be analytically predicted by the simple assumption that the presence of the polyelectrolyte (with its counterions) does not affect the free counterion distribution.[34] Let us consider the bare charged chain plus its own neutralizing counterions as an uncharged object that gets overcharged by intercepting all counterions (of the macroion) whose center lie within a ribbon of width $2r_c$ and area $A_{\text{rib}}=2r_cN_ml$ (Fig. 7). If c is the counterion (of the macroion) concentration, then the theoretical overcharging ratio χ_{th} is merely given by

$$\chi_{\text{th}}=1+\frac{A_{\text{rib}}c}{N_{cm}}=1+\frac{2r_cN_mlZ_M}{N_{cm}Z_c4\pi a^2}, \tag{14}$$

and since the number of charged monomers N_{cm} is given by $N_{cm}=(N_m-1)f+1$, Eq. (14) reduces for $N_m\gg 1$ to

$$\chi_{\text{th}}\sim 1+C/f, \tag{15}$$

with $C=2r_clZ_M/Z_c4\pi a^2$.

Results are presented in Fig. 9 and the corresponding values can be found in Table III. It indicates that in all cases overcharging occurs (i.e., $\chi_{PE}>1$), and that it increases with decreasing polyelectrolyte charge density. We have excellent agreement (less than 10% difference) between simulation results and our toy model [Eq. (14)]. In turn it explains why χ_{PE} varies almost linearly with $1/f$ in our simulations.

The f-dependency of the complexation structure can be explained through the overcharging. For this we consider the overcharged polyelectrolyte as a *dressed* (or *renormalized*) chain [bare chain+counterions] with an *effective* (or *renormalized*) linear charge density $\lambda^*_{PE}=-(\chi_{PE}-1)\lambda_{PE}$ that obviously has the opposite sign of λ_{PE}.[35] Similarly one can define the *renormalized* charge of a monomer as

$$q^*_m=-(\chi_{PE}-1)q_m. \tag{16}$$

Using Eq. (16) and the results of Fig. 9 this shows that q^*_m increases with increasing $1/f$. The overcharging leads to an effective local repulsion of the monomers, and subsequently to a bond stiffening of the chain. This in turn explains why the chain expands with increasing $1/f$ (see Figs. 4 and 6 for the corresponding structures).[36]

IV. INTERMEDIATE COULOMB COUPLING

In this section we are dealing with a higher dielectric constant ($\epsilon_r=40$), meaning that we consider weaker Coulomb coupling ($l_B=4\sigma$). Experimentally this could correspond to using alcohol as a solvent. We consider a set of three runs E–G with $l_B=4\sigma$ (see Table II). Thus these systems are, up to a shorter Bjerrum length l_B, identical to runs A–C. It will be helpful to start the discussion with the description of the observed complex microstructures.

A. Complex microstructure

Typical equilibrium macroion–polyelectrolyte complex structures are sketched in Fig. 10. When the polyelectrolyte is fully charged ($f=1$, run E), Fig. 10(a) shows again a strongly compact chain conformation. But in the present situation the chain does not spread on the macroion surface as it was the case in the strong Coulomb coupling [compare Fig.

TABLE III. Polyelectrolyte overcharge χ_{PE} values as a function of f.

Run	$1/f$	χ_{PE} (MD)	χ_{PE} (Theory)
A	1	1.140 ± 0.002	1.21
B	2	1.39 ± 0.02	1.43
C	3	1.59 ± 0.02	1.64
D	5	1.88 ± 0.03	2.06

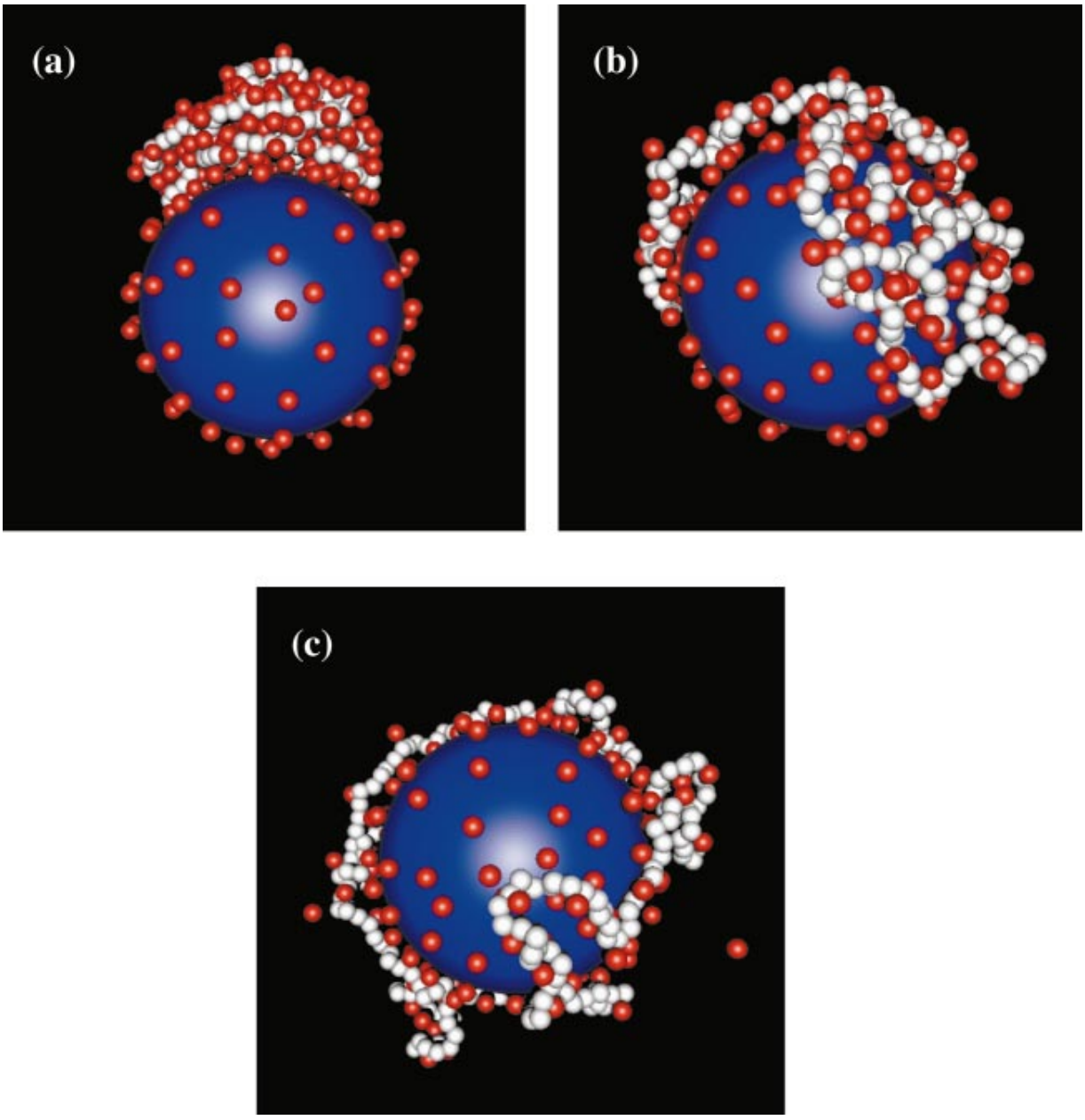

FIG. 10. (Color) Typical equilibrium configurations of the colloid-polyelectrolyte complex in moderate Coulomb coupling ($l_B=4\sigma$) for (a) run E ($f=1$), (b) run F ($f=1/2$), and (c) run G ($f=1/3$). Monomers are in white and counterions in red.

10(a) with Fig. 4(a)]. In fact the conformation of the charged chain in the presence of the macroion is very similar to the bulk conformation [compare Fig. 10(a) with Fig. 3].

By reducing the monomer charge fraction, Figs. 10(b) and 10(c) show that the complex microstructure for runs F, G is again qualitatively different from the fully charged case (run E). For these smaller polyelectrolyte linear charge densities ($f=1/2$ and $f=1/3$), the chain conformation is again almost wrapping around the colloid. For $f=1/2$ (run F) the pearl-necklace structure observed in the strong Coulomb coupling [see Fig. 4(b)] does not appear here, instead small loops appear [see Fig. 10(b)]. For the smallest monomer charge fraction ($f=1/3$, run G) the monomers fully spread over the macroion surface and the conformation is not compact, and also small loops appear [see Fig. 10(c)]. Again it is observed that upon reducing the polymer charge density the chain expands, but this time it expands also into the radial direction away from the macroion.

The forthcoming sections are devoted to study in more detail the monomer and counterion distributions.

B. Adsorption profile

Integrated distribution $P(r)$, radial distribution $n(r)$, and fluid net charge $Q(r)$ profiles are given in Figs. 11(a)–11(c), respectively. In a general manner, the fraction of monomers and counterions in the vicinity of the macroion surface is clearly smaller than the one obtained in the strong

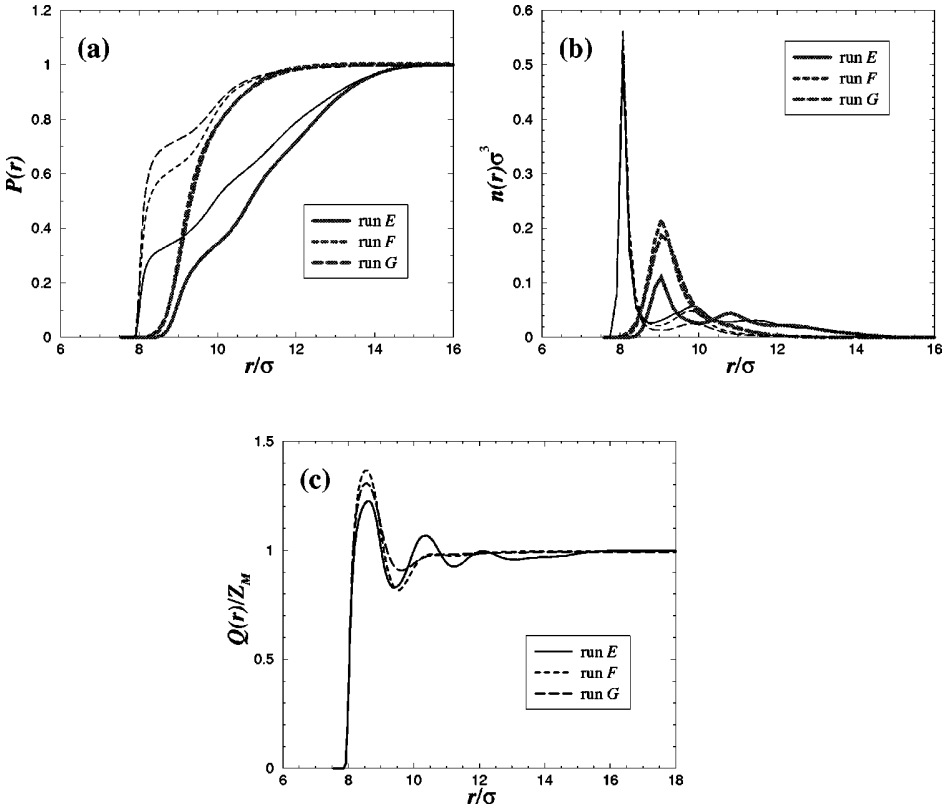

FIG. 11. Ion adsorption profiles (runs E–G) as a function of the distance r from the macroion center. (a) Fraction $P(r)$ and (b) radial density $n(r)$ of counterions (thin lines) and monomers (thick lines); (c) reduced net fluid charge $Q(r)/Z_M$.

Coulomb coupling as expected [compare Fig. 11(a) with Fig. 5(a)]. Also the width in the $P(r)$ profile of adsorbed ions is enlarged with decreasing Coulomb coupling [compare Fig. 11(a) with Fig. 5(a)]. These features show that the monomer adsorption is more diffuse (in the normal direction to the macroion sphere) as expected for a weaker Coulomb coupling. Concerning the ion density $n(r)$ profile [see Fig. 11(b)], it is interesting to note that the height of the *first* peak in the monomer density $n_m(r)$ profile is twice smaller for $f=1$ than for $f<1$, whereas the one from the counterion density profile is almost independent on f. In parallel, the macroion charge overcompensation as well as charge oscillation amplitudes are clearly reduced compared to the strong Coulomb regime [compare Fig. 11(c) with Fig. 5(c)].

For the fully charged polyelectrolyte case ($f=1$, run E) the $n_m(r)$ profile in Fig. 11(b) shows a strong second monomer peak and a weaker third one in agreement with the snapshot of Fig. 10(a). The radial monomer ordering naturally goes along with a counterion ordering in antiphase. In other words, multilayering of different chain segments occurs, but without strong adsorption of the macroion [compare Fig. 10(a) with Fig. 4(a)]. Therefore we find three charge oscillations [see Fig. 11(c)] against only two in the strong Coulomb coupling [see Fig. 5(c)].

For smaller linear charge density, Figs. 11(a) and 11(b) indicate that for runs F ($f=1/2$) and G ($f=1/3$) the chain is almost fully adsorbed to the macroion surface without monomer chain multilayering [i.e., no appearance of monomer second peak in the $n_m(r)$ profile, see Fig. 11(b)]. However, the conformation is a little bit swollen probably due to the onset of loop formation, compare the snapshots in Fig. 10. As in the strong Coulomb coupling case, we find here only one charge oscillation for $f=1/2$ and $f=1/3$, and the amplitude of the reduced net fluid charge decreases with decreasing f.

C. Polyelectrolyte chain radius of gyration

Results for the radius of gyration R_g of the polymer chain are reported in Fig. 6 (for $l_B=4\sigma$). As for the high Coulomb coupling case with $l_B=10\sigma$, R_g increases with decreasing f. However, for $f=1$, here we obtain $R_g\approx 4.8\sigma$ which is clearly smaller than the value $R_g\approx 6.4\sigma$ obtained in run A (see Fig. 6). This proves that for $l_B=4\sigma$ the chain conformation stays as a globule, since we already found that for the same chain length and with $l_B=10\sigma$ the chain conformation was compact and two-dimensional. In the case under consideration ($f=1, l_B=4\sigma$), the value of $R_g\approx 4.8\sigma$ is almost identical to the one obtained in the bulk where $R_g=4.4\sigma$ (see Table II).

Upon reducing f (runs F and G), the chain is much more expanded and it is found that $R_g\approx 9.4\sigma$. Taking into account the fact the chain is still adsorbed for both systems (runs F and G) as was found in the analysis of the adsorption profile

TABLE IV. Polyelectrolyte overcharge χ_{PE} values as a function of f (runs E–G).

Run	$1/f$	χ_{PE}
E	1	1.043 ± 0.002
F	2	1.089 ± 0.003
G	3	1.065 ± 0.006

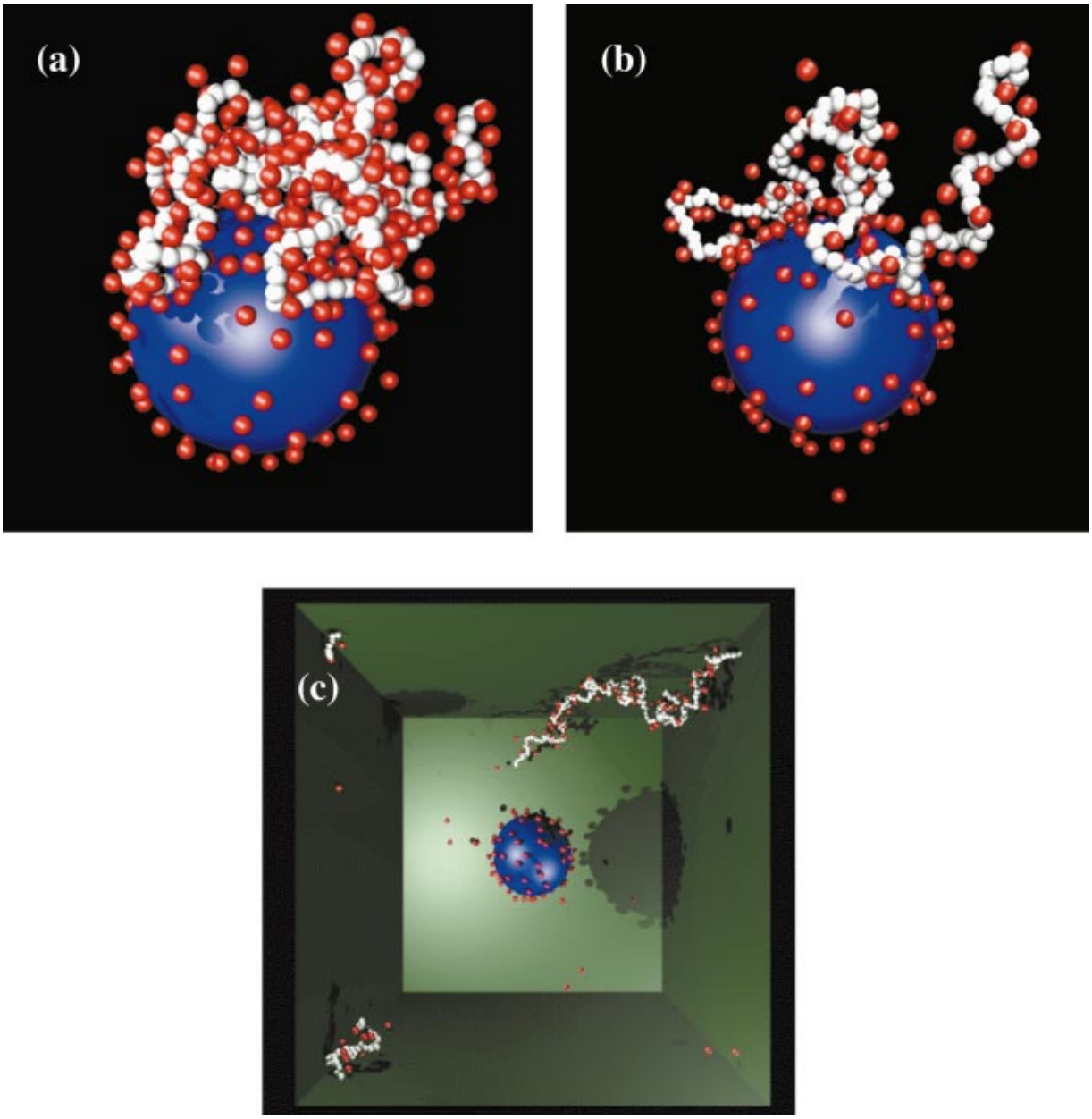

FIG. 12. (Color) Typical equilibrium configurations of the colloid-polyelectrolyte complex in weak Coulomb coupling ($l_B=2\sigma$) for (a) run H ($f=1$), (b) run I ($f=1/2$), and (c) run J ($f=1/3$). Monomers are in white and counterions in red. Snapshot (c) was obtained with periodic boundary conditions.

(see Fig. 11), one deduces that the spreading of the monomers is very important as soon as $f<1$. A comparison with the strong Coulomb coupling shows that values of R_g for $l_B=4\sigma$ are systematically larger than those of R_g with $l_B=10\sigma$ (see Fig. 6 and Table II), indicating again that the chain fluctuates more in the outward macroion radial direction at weaker Coulomb coupling.

D. Polyelectrolyte overcharging

In order to check if the local polyelectrolyte overcharge is responsible for the expansion of the chain upon reducing f as was demonstrated in the strong Coulomb coupling for $l_B=10\sigma$ in Sec. III B 5, we again consider the overcharging ratio χ_{PE} defined by Eq. (13) with the same condensation distance $r_c=1.2\sigma$ as was done for $l_B=10\sigma$ in Sec. III B 5.

Numerical values of χ_{PE} can be found in Table IV. It clearly shows that polyelectrolyte overcharge is negligible (i.e., $\chi_{PE}\approx 1$) for the present Coulomb coupling regime whatever the value of f. Consequently one cannot explain the expansion of the chain with increasing $1/f$ with a polyelectrolyte overcharge mechanism. We will give clear and qualitative arguments in Sec. VI that account for these conformations.

V. WEAK COULOMB COUPLING

This part is devoted to aqueous solutions where the Bjerrum length is $l_B=2\sigma=7.14$ Å corresponding to the dielec-

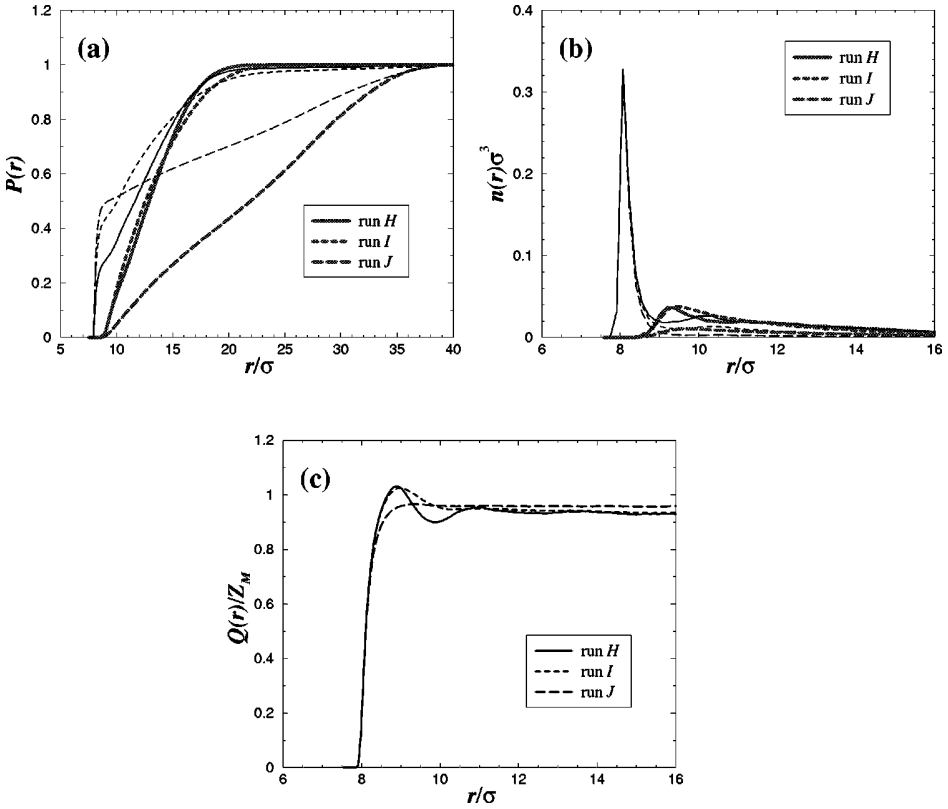

FIG. 13. Ion adsorption profiles (runs H–J) as a function of the distance r from the macroion center. (a) Fraction $P(r)$ and (b) radial density $n(r)$ of counterions (thin lines) and monomers (thick lines) adsorbed on the spherical macroion; (c) reduced net fluid charge $Q(r)/Z_M$.

tric constant $\epsilon_r \approx 80$ of *water*. Such systems will be referred to as the weak Coulomb coupling regime. We have considered the set of runs H–N (see Table II). Runs H–J are identical to the previous ones but with a shorter Bjerrum length $l_B = 2\sigma$. Runs K–M, that will be investigated in Sec. V D, correspond to systems where each charged monomer is monovalent ($Z_m = 1$) and counterions are trivalent ($Z_c = 3$). This latter choice (runs K–M) is motivated by the fact that such systems should be easily accessible by experiments. Run N has both, counterions and monomers, monovalent.

A. Complex microstructure

Typical equilibrium macroion–polyelectrolyte complex structures for runs H–J can be found in Fig. 12. In all cases, one finds that the polymer *never* adopts a ''two-dimensional'' conformation. A comparison of the bulk value of R_g and the R_g of the chain in the complexed situation (compare Table II) reveals that the chain conformation is only weakly affected by the macroion. For the fully charged polymer ($f = 1$, run H), the conformation is again rather compact but without exhibiting a strong monomer-counterion ordering (within the polymeric aggregate) as it was the case for higher Coulomb coupling regimes [compare Fig. 12(a) with Figs. 4(a) and 10(a)]. However we do have an effective macroion–polyelectrolyte attraction, and the dense monomer–counterion aggregate is adsorbed onto the colloidal surface.

For $f = 1/2$ (run I), the chain conformation is more expanded than for $f = 1$ [compare Fig. 12(b) with Fig. 12(a)]. Nevertheless we do have polymer adsorption with the formation of chain loops. Therefore even for couplings which are typical of aqueous systems, our simulations show that like-charge complexation can occur for $f = 1$ and $f = 1/2$ with divalent ions ($Z_m = Z_c = 2$).

For even lower linear charge density ($f = 1/3$, run J), Fig. 12(c) shows polymer desorption from $f = 1/2$ to $f = 1/3$. In the same time there is a certain ''*counterion release*'' for $f = 1/3$, meaning that not all counterions are in the vicinity of the highly charged objects (macroion and polyelectrolyte). We carefully checked that, with periodic boundary conditions, the same features qualitatively appear, namely, chain desorption from $f = 1/2$ to $f = 1/3$.

B. Adsorption profile

Integrated distribution $P(r)$, radial distribution $n(r)$ and fluid net charge $Q(r)$ profiles for runs H–J are depicted in Figs. 13(a)–13(c), respectively. The ion fraction $P(r)$ profiles show that for $f = 1$ (run H) and $f = 1/2$ (run I) almost all particles lie within a distance $a < r < 20\sigma$ [i.e., $P(r = 20\sigma) \approx 1$], corresponding to roughly one macroion diameter away from the colloidal surface [see Fig. 13(a)]. This is in contrast to what was previously found (with $f = 1$ and $f = 1/2$) at stronger Coulomb coupling regimes where almost all ions lie within a distance of a few monomer sizes from the macroion surface [compare Fig. 13(a) with Figs. 5(a) and 11(a)]. For $f = 1/3$ (run J) only a very small fraction of monomers [$P_m(r = 10\sigma) < 5\%$] lie in the vicinity of the macroion surface. In this latter situation, the counterion $P_c(r)$ profile indicates that a larger fraction of counterions float in the solution. Because the R_g of the chain is very large and some chain monomers might be interacting with the cell boundary we performed for this situation a simulation where we em-

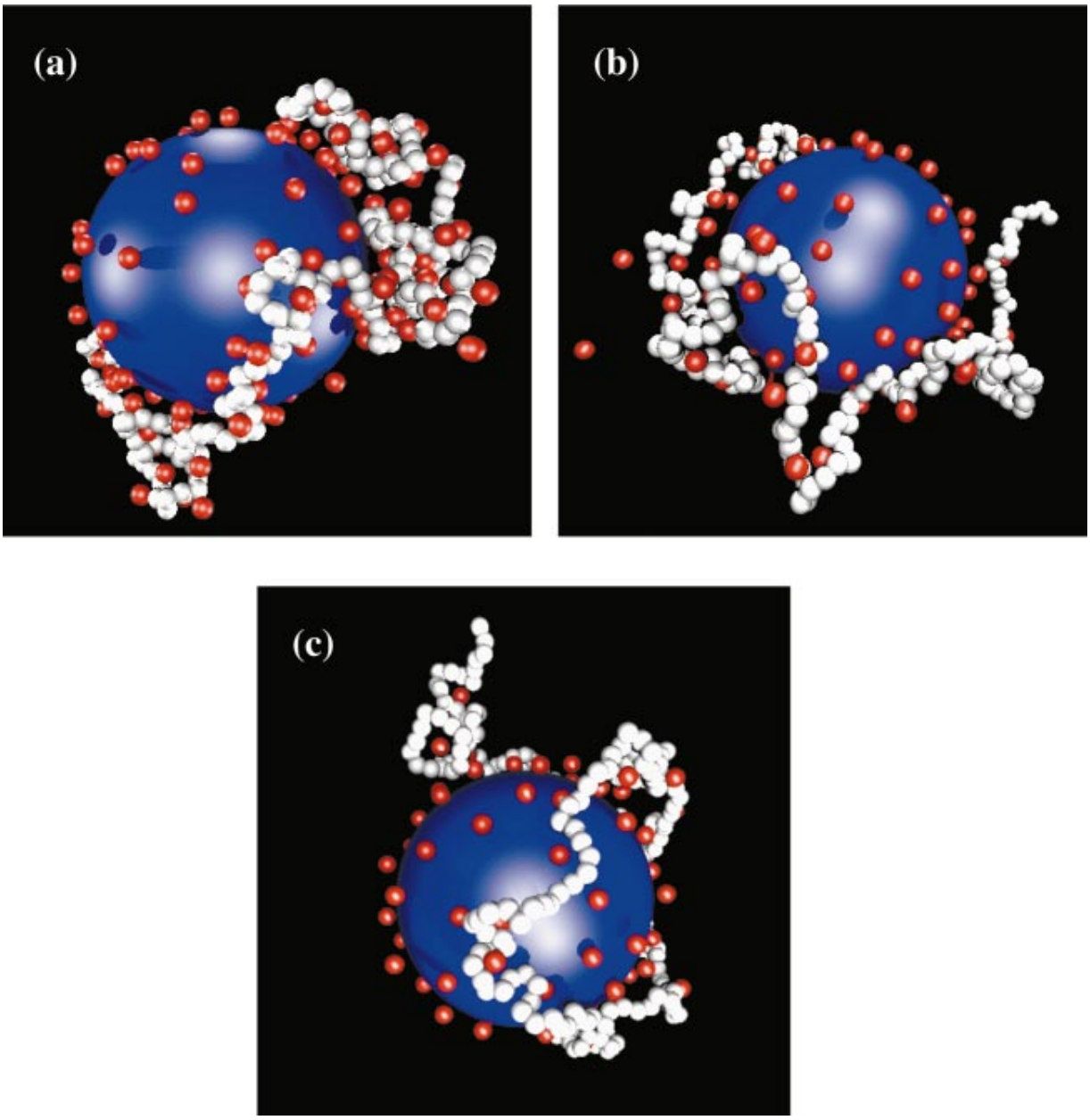

FIG. 14. (Color) Typical equilibrium configurations of the colloid–polyelectrolyte complex in weak Coulomb coupling ($l_B=2\sigma$, $Z_m=1$, and $Z_c=3$) for (a) run K ($f=1$), (b) run L ($f=1/2$), and (c) run M ($f=1/3$). Monomers are in white and counterions in red.

ployed periodic boundary condition, and where the interactions were computed using the P3M algorithm.[37] With this run we found no chain monomers in the vicinity of the colloid surface, hence unambiguously found monomer desorption from the colloidal surface.

Concerning the intrachain monomer ordering for $f=1$, Fig. 13(b) shows that, although the chain conformation is relatively dense, there is only one main peak in the monomer $n_m(r)$ profile (the second peak is marginal). This proves that there is no strong intrachain monomer ordering (in the normal direction to the macroion sphere) in this weak Coulomb coupling in contrast with our observations at $l_B=4\sigma$ [compare with Fig. 11(b)]. Nevertheless a second counterion layer (third monomer layer) is built. The height h_m of the monomer peak is identical (within the statistical uncertainty) for $f=1$ and $f=1/2$ and corresponds to $h_m\approx 0.038/\sigma^3$, whereas for $f=1/3$ we have $h_m\approx 0.01/\sigma^3$.

C. Polyelectrolyte chain radius of gyration

As far as the net fluid charge $Q(r)$ is concerned, Fig. 13(c) shows that for $f=1$ a weak charge oscillation appears with a marginal macroion overcharge compensation of 3%. For $f=1/2$, the same marginal macroion overcharging occurs but without exhibiting charge oscillation. Finally, for $f=1/3$ no overcharging appears and the net charge increases monotonically.

In Fig. 6 (for $l_B=2\sigma$) the chain radius of gyration R_g as function of f is plotted for runs H–J. It is found that R_g increases almost linearly with $1/f$. This result fits well with

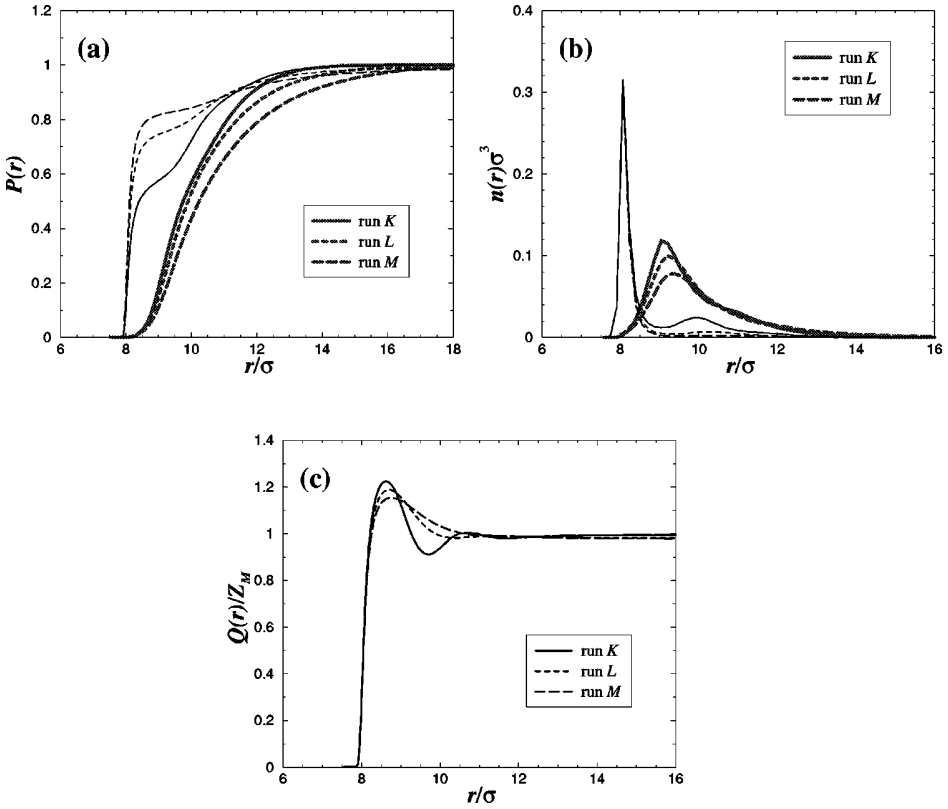

FIG. 15. Ion adsorption profiles (runs K–M) as a function of the distance r from the macroion center. (a) Fraction $P(r)$ and (b) radial density $n(r)$ of counterions (thin lines) and monomers (thick lines) adsorbed on the spherical macroion; (c) reduced net fluid charge $Q(r)/Z_M$.

the scaling theory in this regime from Ref. 38, where it is found that the chain extension shrinks proportionally with l_B, and we can assume for our purposes $f \propto l_B$. Because the electrostatic interactions are weaker in the present case ($l_B = 2\sigma$), the ion pair (monomer-condensed counterion) attractions are weaker which results in a higher R_g value (at fixed f) than in the strong Coulomb coupling regime.

D. Moderately charged polyelectrolyte

Typical macroion-polyelectrolyte complex microstructures for runs K–M are depicted in Fig. 14. In all cases we have adsorption of the polyelectrolyte onto the like-charged sphere. Similar features as with systems H–J (i.e., $Z_m = Z_c = 2$) happen here. In particular, for the highest linear charge density [$f = 1$, run K, Fig. 14(a)] the polyelectrolyte consists of dense globules separated by strings, reminiscent of the pearl-necklaces found in studies of polyampholytes.[39] Also for run K, we have a stronger polymer adsorption compared to run H due to the stronger counterion mediated correlations. By decreasing f [see Figs. 14(b) and 14(c)], we observe the formation of loops as for run I.

Integrated distribution $P(r)$, radial distribution $n(r)$, and fluid net charge $Q(r)$ profiles are depicted in Figs. 15(a)–15(c), respectively. Figure 15(a) shows that within $r \approx 10\sigma$, corresponding to a three-layer thickness, most of the counterions are adsorbed [i.e., $P_c(r \approx 10\sigma) \approx 80\%$]. Moreover, the fraction $P_m(r)$ of adsorbed monomers is significantly higher than that with systems H–J [compare Fig. 13(a)]. As in the previous runs H–J, the height of the first peak in the counterion density $n_c(r)$ is nearly independent of f [compare Figs. 13(b) and 15(b)]. The monomer density $n_m(r)$ is now significantly higher than for runs H–J and h_m increases with f as was observed on the snapshots in Fig. 14.

The expansion of the chain as a function of f can be deduced from R_g. The corresponding values are gathered in Table II and show that the chain expands with decreasing f as observed in the previous runs.

The net fluid charge is similar to that of runs H–J [compare Figs. 13(c) and 15(c)]. Due to the stronger counterion induced correlations that occur with $Z_c = 3$, we find a stronger macroion overcharging and amplified charge oscillations.

Finally, we checked that for $Z_c = Z_m = 1$ and $f = 1$, corresponding to run N (see Table II), we have a strong macroion–polyelectrolyte repulsion that does not allow like-charge complexation.

VI. CONCLUDING REMARKS

We have carried out MD simulations to study the complexation of a charged colloid with a charged polyelectrolyte of the same charge for various Coulomb couplings l_B and varying monomer charge fraction f.

For high Coulomb coupling ($l_B = 10\sigma$) we gave a reasoning for the observed conformation in terms of overcharging of the single chain. However this argument only worked for the largest coupling parameter.

A complementary view of the observed conformations is to regard both macroions as being neutralized by their counterions. The isolated chain would then collapse into a globule, and the colloid would be regularly covered by its counterions. By changing the Bjerrum length l_B we change the correlations between the charges which lead in a first ap-

proximation to attractions of dipolar origin, and the attraction is roughly proportional to l_B. On the other hand, by varying f we change the number of counterions of the chain, hence the number of available dipoles.

For $f=1$ we can regard the colloidal particle as exerting only a perturbation of the chain complex (which has a higher density of dipoles). For $l_B=10\sigma$ the strong attraction results in a flat disk, whereas for smaller l_B the disk swells back into the bulk structure, the globule.

By reducing f, the number of counterions of the polyelectrolyte and the colloid become comparable in number, and both macroions can equally compete for the counterions leading to a greater freedom of both macroions to ''move'' in their common counterion cloud. For the largest value of l_B we have again the strongest dipolar attractions leading to a purely 2D conformation, where the chain is wrapped around the colloid. For smaller values of l_B the conformations become more and more 3D-like, but the chain is still wrapping around the colloid.

Of special interest here is the fact that even for a coupling strength which is typically for an aqueous solvent ($l_B=2\sigma=7.1$ Å) we find that like-charge complexation still occurs provided that the linear charge density is sufficiently large or the counterion valence Z_c high enough. However the adsorption of the polymer chain onto the colloid is weaker than in the larger Coulomb coupling regimes. For divalent chain-monomers (i.e., $Z_m=2$) and $f=1/2$, we observe formation of large loops. For $Z_m=2$ and $f=1/3$ we find no complex, but end with two single macroions together with their counterion cloud which interact mainly with their bare charge, i.e., repulsively. In the case of monavalent chain-monomers ($Z_m=1$) and trivalent counterions ($Z_c=3$), we find for all $f\geqslant 1/3$ like-charge complexation where the chain wraps around the colloid. Again, for $f=1$ the conformation is more compact and expands with decreasing f, showing loops for all f.

Our parameters concerning aqueous solutions should be experimentally accessible, typically for small highly charged colloids (micelles and relatively short polyelectrolyte chains). The other cases corresponding to lower dielectric constants might also be relevant for organic solutions.

ACKNOWLEDGMENT

This work is supported by Laboratoires Européens Associés (LEA).

[1] K. E. van Holde, *Chromatin* (Springer, New York, 1989).
[2] D. W. McQuigg, J. I. Kaplan, and P. L. Dublin, J. Phys. Chem. **96**, 1973 (1992).
[3] M. Grunstein, Nature (London) **389**, 349 (1997).
[4] F. Caruso, R. A. Caruso, and H. Möhwald, Science **282**, 1111 (1998).
[5] F. von Goeler and M. Muthukumar, J. Chem. Phys. **100**, 7796 (1994).
[6] N. L. Marky and G. S. Manning, J. Mol. Biol. **255**, 50 (1995).
[7] E. Gurovitch and P. Sens, Phys. Rev. Lett. **82**, 339 (1999).
[8] E. M. Mateescu, C. Jeppesen, and P. Pincus, Europhys. Lett. **46**, 493 (1999).
[9] S. Y. Park, R. F. Bruinsma, and W. M. Gelbart, Europhys. Lett. **46**, 454 (1999).
[10] R. R. Netz and J. F. Joanny, Macromolecules **32**, 9026 (1999).
[11] H. Schiessel, J. Rudnick, R. Bruisma, and W. M. Gelbart, Europhys. Lett. **51**, 237 (2000).
[12] K.-K. Kunze and R. R. Netz, Phys. Rev. Lett. **85**, 4389 (2000).
[13] T. T. Nguyen and B. I. Shklovskii, Physica A **293**, 324 (2001).
[14] T. Wallin and P. Linse, Langmuir **12**, 305 (1996).
[15] T. Wallin and P. Linse, J. Phys. Chem. **100**, 17873 (1996).
[16] T. Wallin and P. Linse, J. Phys. Chem. B **101**, 5506 (1997).
[17] C. Y. Kong and M. Muthukumar, J. Chem. Phys. **109**, 1522 (1998).
[18] M. Jonsson and P. Linse, J. Chem. Phys. **115**, 3406 (2001).
[19] R. Messina, C. Holm, and K. Kremer, Phys. Rev. E **65**, 041805 (2002).
[20] K. Kremer and G. Grest, J. Chem. Phys. **92**, 5057 (1990).
[21] I. Rouzina and V. A. Bloomfield, J. Phys. Chem. **100**, 9977 (1996).
[22] R. Messina, C. Holm, and K. Kremer, Phys. Rev. Lett. **85**, 872 (2000).
[23] R. Messina, C. Holm, and K. Kremer, Phys. Rev. E **64**, 021405 (2001).
[24] R. Messina, C. Holm, and K. Kremer, Europhys. Lett. **51**, 461 (2000).
[25] R. Messina, C. Holm, and K. Kremer, Eur. Phys. J. E **4**, 363 (2001); R. Messina, Physica A **308**, 59 (2002).
[26] It is this value $a_{cc}\approx 3\sigma$ which gives $\Gamma\approx 13$.
[27] B. Shklovskii, Phys. Rev. E **60**, 5802 (1999).
[28] M. J. Stevens and K. Kremer, Phys. Rev. Lett. **71**, 2228 (1993).
[29] M. J. Stevens and K. Kremer, J. Chem. Phys. **103**, 1669 (1995).
[30] R. G. Winkler, M. Gold, and P. Reineker, Phys. Rev. Lett. **80**, 3731 (1997).
[31] R. Golestanian, M. Kardar, and T. B. Liverpool, Phys. Rev. Lett. **82**, 4456 (1999).
[32] N. V. Brilliantov, D. V. Kuznetsov, and R. Klein, Phys. Rev. Lett. **81**, 1433 (1998).
[33] This value corresponds to the first monomer peak position in the $n_m(r)$ profile [see Fig. 5(b)].
[34] This mainly holds for the first correlational peak which is the most important for the present discussion, as we showed in the previous Sec. III B 4.
[35] This argument assumes that the ions (charged monomers+condensed counterions) distribution along the chain is uniform. This should be relatively well satisfied since the bare charged monomers are already uniformly distributed.
[36] This reasoning holds in the strong Coulomb coupling regime where the polymer structure is essentially dictated by the charged (effective) monomers.
[37] M. Deserno and C. Holm, J. Chem. Phys. **109**, 7678 (1998).
[38] H. Schiessel and P. Pincus, Macromolecules **31**, 7953 (1998).
[39] Y. Kantor and M. Kardar, Europhys. Lett. **27**, 643 (1994).

Appendix J

Effect of Image Forces on Polyelectrolyte Adsorption at a Charged Surface

Effect of image forces on polyelectrolyte adsorption at a charged surface

René Messina*
Institut für Theoretische Physik II, Heinrich-Heine-Universität Düsseldorf, Universitätsstrasse 1, D-40225 Düsseldorf, Germany
(Received 3 June 2004; published 9 November 2004)

The adsorption of flexible and highly charged polyelectrolytes onto oppositely charged planar surfaces is investigated by means of Monte Carlo simulations. The effect of image forces stemming from the dielectric discontinuity at the substrate interface is analyzed. The influence, at fixed polyelectrolyte volume fraction, of chain length and surface-charge density is also considered. A detailed structural study, including monomer and fluid charge distributions, is provided. It is demonstrated that image forces can considerably reduce the degree of polyelectrolyte adsorption and, as a major consequence, inhibit the charge inversion of the substrate by the polyelectrolytes.

DOI: 10.1103/PhysRevE.70.051802 PACS number(s): 82.35.Gh, 82.35.Rs, 61.20.Qg, 61.20.Ja

I. INTRODUCTION

The adsorption of charged polymers [polyelectrolytes (PEs)] on charged surfaces is an important phenomenon in industrial and biological processes. Well controlled model experiments [1,2] were devoted to characterize PE adsorption. The understanding of PE adsorption remains an outstanding problem because of the many different typical interactions involved there: strong electrostatic substrate-PE binding, monomer-monomer (PE-PE) repulsion, chain entropy, excluded volume, etc. Another complication arises from the *dielectric discontinuity* between the solvent and the substrate generating surface-polarization charges. In most practical cases, water plays the role of the solvent for PEs, whereas the substrate corresponds to an unpolar dielectric medium leading to considerable polarization (image) forces.

On the theoretical side, PE adsorption on planar charged surfaces has been intensively studied by several authors [3–24] on the level of mean--field theories. The case of PE adsorption on heterogeneously charged surfaces was recently theoretically addressed by de Vries *et al.* [21]. A remarkable common feature of some of these studies is the charge reversal (*overcharging*) of the substrate by the adsorbed PEs (see, e.g., Refs. [12,13,15,16,19,25]). The problem of PE adsorption onto *similarly* charged substrates was recently investigated by Dobrynin and Rubinstein [19] and Cheng and Lai [23,24]. In the latter situation, the PE adsorption is then driven either by *nonelectrostatic short-range* forces [19] or *attractive image forces* [23,24] stemming from a high-dielectric surface. The problem of *repulsive* image forces stemming from a low-dielectric surface was studied by Borisov *et al.* [9] and Netz and Joanny [16] on the level of the Debye-Hückel approximation.

As far as computer simulations are concerned, there exist few Monte Carlo (MC) studies about PE adsorption on planar charged substrates [23,26–30]. The first MC study on PE adsorption was that of Beltán *et al.* [26], where a lattice model was employed. Yamakov *et al.* [28] performed extensive MC simulations and found excellent agreement with the scaling predictions of Borisov *et al.* [9], where different regimes of adsorption are identified. Ellis *et al.* [29] considered the interesting case of heterogeneously charged surfaces (made of positively and negatively charged surface sites) and demonstrated that a PE carrying the same sign of charge as that of the net charge of the substrate can adsorb. Cheng *et al.* [23] also investigated the effect of image charges on a high-dielectric constant substrate. It is important to mention that all these MC simulations [23,26–29] use the Debye-Hückel approximation. The problem of PE multilayering was very recently studied by Messina [30], where the full unscreened long-range electrostatic interactions were considered but without image forces.

In this paper, we investigate multichain adsorption in the dilute regime at fixed PE volume fraction in a salt-free environment but where counterions from the substrate and the PEs are explicitly taken into account. In order to clearly identify the effect of image forces on PE adsorption, we systematically compare situations *with* and *without* image forces, which was not properly done in the literature (see, e.g., Refs. [9,16,24]). The influence of chain length (for short chains) and substrate-charge density is also considered. Our paper is organized as follows. The model and simulation technique are detailed in Sec. II. Our results are presented in Sec. III, and Sec. IV provides concluding remarks.

II. MODEL AND PARAMETERS

A. Simulation model

The setup of the system under consideration is similar to that recently investigated with a planar substrate (without image forces) [30]. Within the framework of the primitive model, we consider a PE solution near a charged hard wall with an implicit solvent (water at $z>0$) of relative dielectric permittivity $\epsilon_{\mathrm{solv}}\approx 80$. The substrate located at $z<0$ is characterized by a relative dielectric permittivity ϵ_{subs} which leads to a dielectric jump Δ_ϵ (when $\epsilon_{\mathrm{solv}}\neq\epsilon_{\mathrm{subs}}$) at the interface defined as

$$\Delta_\epsilon=\frac{\epsilon_{\mathrm{solv}}-\epsilon_{\mathrm{subs}}}{\epsilon_{\mathrm{solv}}+\epsilon_{\mathrm{subs}}}\geqslant 0. \tag{1}$$

*Electronic address: messina@thphy.uni-duesseldorf.de

The *negative* bare surface-charge density of the substrate is $-\sigma_0 e$, where e is the (positive) elementary charge and $\sigma_0 > 0$ is the number of charges per unit area. Electroneutrality is always ensured by the presence of explicit monovalent ($Z_c = 1$) substrate counterions (i.e., monovalent cations) of diameter a. PE chains are made up of N_m *monovalent* positively charged monomers ($Z_m = 1$) of diameter a. Each monomer is charged so that the fraction of charged monomers is unity. Their counterions (monovalent anions) are also explicitly taken into account with the same parameters up to the charge sign as the monomers. Hence, all microions are monovalent: $Z = Z_c = Z_m = 1$ with the same diameter size a.

All these particles making up the system are immersed in a rectangular $L \times L \times \tau$ box. Periodic boundary conditions are applied in the (x,y) directions, whereas hard walls are present at $z = 0$ (location of the charged interface) and $z = \tau$ (location of an *uncharged* wall).

The total energy of interaction of the system can be written as

$$U_{\text{tot}} = \sum_i [U_{\text{hs}}^{(\text{plate})}(z_i) + U_{\text{Coul}}^{(\text{plate})}(z_i)] + \sum_{i,i<j} [U_{\text{hs}}(r_{ij}) + U_{\text{Coul}}(\mathbf{r}_i, \mathbf{r}_j) + U_{\text{FENE}}(r_{ij}) + U_{\text{LJ}}(r_{ij})], \quad (2)$$

where the first (single) sum stems from the interaction between an ion i (located at $z = z_i$) and the charged plate, and the second (double) sum stems from the pair interaction between ions i and j with $r_{ij} = |\mathbf{r}_i - \mathbf{r}_j|$. All these contributions to U_{tot} in Eq. (2) are described in detail below.

Excluded volume interactions are modeled via a hardcore potential [31] defined as follows:

$$U_{\text{hs}}(r_{ij}) = \begin{cases} 0 & \text{for } r_{ij} \geqslant a \\ \infty & \text{for } r_{ij} < a \end{cases} \quad (3)$$

for the microion-microion one, and

$$U_{\text{hs}}^{(\text{plate})}(z_i) = \begin{cases} 0 & \text{for } a/2 \leqslant z_i \leqslant \tau - a/2 \\ \infty & \text{otherwise} \end{cases} \quad (4)$$

for the plate-microion one. For clarity, we recall that a microion stands either for a (charged) monomer or a counterion.

The electrostatic energy of interaction between two microions i and j reads

$$\beta U_{\text{Coul}}(\mathbf{r}_i, \mathbf{r}_j) = \pm l_B \left[\frac{1}{r_{ij}} + \frac{\Delta_\epsilon}{\sqrt{x_{ij}^2 + y_{ij}^2 + (z_i + z_j)^2}} \right], \quad (5)$$

where $+$ $(-)$ applies to microions of the same (opposite) sign, $l_B = \beta e^2 / 4\pi\epsilon_0\epsilon_{\text{solv}}$ is the Bjerrum length corresponding to the distance at which two protonic charges interact with $1/\beta = k_B T$, and Δ_ϵ is given by Eq. (1). The first term in Eq. (5) corresponds to the direct Coulomb interaction between real ions, whereas the second term represents the interaction between the real ion i and the image of ion j. By symmetry, the latter also describes the interaction between the real ion j and the image of ion i yielding an implicit factor $1/2$. The electrostatic energy of interaction between an ion i and the (uniformly) charged plate reads

TABLE I. List of key parameters with some fixed values.

Parameters	
$T = 298$ K	room temperature
$\sigma_0 L^2$	charge number of the substrate
$\Delta_\epsilon = 0$ or 0.951	dielectric discontinuity
$Z = 1$	microion valence
$a = 4.25$ Å	microion diameter
$l_B = 1.68a = 7.14$ Å	Bjerrum length
$L = 25a$	(x,y)-box length
$\tau = 75a$	z-box length
N_{PE}	number of PEs
N_m	number of monomers per chain

$$\beta U_{\text{Coul}}^{(\text{plate})}(z_i) = l_B \left[\pm 2\pi\sigma_0 z_i + \frac{\Delta_\epsilon}{4z_i} \right], \quad (6)$$

where, for the first term, $+$ $(-)$ applies to positively (negatively) charged ions. The second term in Eq. (6) stands for the *self-image* interaction, i.e., the interaction between the ion i and its own image. An appropriate and efficient modified Lekner sum was utilized to compute the electrostatic interactions with periodicity in *two* directions [32]. To link our simulation parameters to experimental units and room temperature ($T = 298$ K), we choose $a = 4.25$ Å leading to the Bjerrum length of water $l_B = 1.68a = 7.14$ Å. In order to investigate the effect of image forces, we take a value of $\epsilon_{\text{subs}} = 2$ for the dielectric constant of the charged substrate (which is a typical value for silica or mica substrates [33]) and $\epsilon_{\text{solv}} = 80$ for that of the aqueous solvent yielding $\Delta_\varepsilon = (80-2)/(80+2) \approx 0.951$. The case of identical dielectric constants $\epsilon_{\text{solv}} = \epsilon_{\text{subs}}$ $(\Delta_\epsilon = 0)$ corresponds to the situation where there are no image charges.

The PE chain connectivity is modeled by employing a standard finite extension nonlinear elastic (FENE) potential for good solvent, which reads

$$U_{\text{FENE}}(r) = \begin{cases} -\frac{1}{2}\kappa R_0^2 \ln\left[1 - \frac{r^2}{R_0^2}\right] & \text{for } r < R_0 \\ \infty & \text{for } r \geqslant R_0 \end{cases} \quad (7)$$

with $\kappa = 27 k_B T / a^2$ and $R_0 = 1.5a$. The excluded volume interaction between chain monomers is taken into account via a shifted and truncated Lennard-Jones (LJ) potential given by

$$U_{\text{LJ}}(r) = \begin{cases} 4\epsilon\left[\left(\frac{a}{r}\right)^{12} - \left(\frac{a}{r}\right)^{6}\right] + \epsilon & \text{for } r \leqslant 2^{1/6}a \\ 0 & \text{for } r > 2^{1/6}a \end{cases}, \quad (8)$$

where $\epsilon = k_B T$. These parameter values lead to an equilibrium bond length $l = 0.98a$.

All the simulation parameters are gathered in Table I. The set of simulated systems can be found in Table II. The equilibrium properties of our model system were obtained by using standard canonical MC simulations following the Metropolis scheme [34,35]. Single-particle moves were considered with an acceptance ratio of 30% for the monomers and

TABLE II. Simulated systems' parameters. The number of counterions (cations and anions) ensuring the overall electroneutrality of the system is not indicated.

System	N_{PE}	N_m	$\sigma_0 L^2$
A	96	2	64
B	48	4	64
C	24	8	64
D	12	16	64
E	6	32	64
F	12	16	32
G	12	16	128
H	12	16	192

50% for the counterions. Depending on the parameters, the length of a simulation run ranges from 2×10^6 up to 7×10^6 MC steps per particle. Typically, about 3×10^5 to 2.5×10^6 MC steps were required for equilibration, and $(1-4)\times10^6$ subsequent MC steps were used to perform measurements.

B. Measured quantities

We briefly describe the different observables that are going to be measured. In order to study the PE adsorption, we compute the monomer density $n(z)$ that is normalized as follows:

$$\int_{a/2}^{\tau-a/2} n(z)L^2dz = N_{\mathrm{PE}}N_m. \tag{9}$$

To further characterize the PE adsorption, we also compute the total number of accumulated monomers $\overline{N}(z)$ within a distance z from the planar charged plate that is given by

$$\overline{N}(z) = \int_{a/2}^{z} n(z')L^2dz'. \tag{10}$$

It is useful to introduce the fraction of adsorbed monomers, $N^*(z)$, which is defined as follows:

$$N^*(z) = \frac{\overline{N}(z)}{N_{\mathrm{PE}}N_m}. \tag{11}$$

Another relevant quantity is the global *net fluid charge* $\sigma(z)$, which is defined as follows:

$$\sigma(z) = \int_{a/2}^{z} [n_+(z') - n_-(z')]dz', \tag{12}$$

where n_+ and n_- stand for the density of all the positive microions (i.e., monomers and plate's counterions) and negative microions (i.e., PEs' counterions), respectively. It is useful to introduce the reduced surface charge density $\sigma^*(z)$ defined as follows:

$$\sigma^*(z) = \frac{\sigma(z)}{\sigma_0}. \tag{13}$$

Thereby, $\sigma^*(z)$ corresponds, up to a prefactor $\sigma_0 e$, to the net fluid charge per unit area (omitting the surface charge density $-\sigma_0 e$ of the substrate) within a distance z from the charged wall. At the uncharged wall, electroneutrality imposes $\sigma^*(z=\tau-a/2)=1$. By simple application of Gauss' law, $[\sigma^*(z)-1]$ is directly proportional to the mean electric field at z. Therefore, $\sigma^*(z)$ can measure the *screening* strength of the substrate by the neighboring solute charged species.

III. RESULTS AND DISCUSSION

From previous studies [9,16,36,37], it is well understood that effects of image charges become especially relevant at sufficiently low surface charge density of the interface. It is also clear that the self-image interaction (*repulsive* for $\Delta_\epsilon>0$, as is presently the case) is higher the higher the charge of the ions (polyions) since it scales like Z^2. In the present situation where we have to deal with PEs, the length of the chain (N_m) is a key parameter that can be seen as the valence of a polyion. Hence, we are going to study (i) the influence of chain length (Sec. III A) and (ii) that of surface charge density (Sec. III B). For the sake of consistency, we fixed the total number of monomers to $N_{\mathrm{PE}}N_m=192$, meaning that the monomer concentration is *fixed* (see also Table II): The PE volume fraction

$$\phi = \frac{4\pi}{3}\frac{N_{\mathrm{PE}}N_m(a/2)^3}{L^2\tau} \approx 2.14\times10^{-3}$$

is fixed.

A. Influence of chain length

In this part, we consider the influence of chain length N_m at fixed surface charge density parameter $\sigma_0L^2=64$. The latter corresponds experimentally to a moderate [2] surface charge density with $-\sigma_0 e\approx-0.091$ C/m^2. The chain length is varied from $N_m=2$ up to $N_m=32$ (systems $A-E$, see Table II). We have ensured that, for the longest chain with $N_m=32$, size effects are still negligible since the mean end-to-end distance is about $14a$, which is significantly smaller than $L=25a$ or $\tau=75a$.

The profiles of the monomer distribution $n(z)$ can be found in Fig. 1 and the corresponding microstructures are sketched in Fig. 2. Let us first comment on the more simple case where no image charges are present [$\Delta_\epsilon=0$—see Fig. 1(a)]. For (very) short chains (here $N_m\leqslant4$), Fig. 1(a) shows that the density profiles exhibit a monotonic behavior even near contact. Within this regime of chain length, the monomer density near the charged wall increases with increasing N_m. This feature is fully consistent with the idea that stronger *lateral* correlations, the latter scaling like $Z^{3/2}$ for spherical counterions at fixed σ_0 [38,39], induce a higher polyion adsorption. In other words, at (very) low N_m, *conformational entropic* effects are not dominant and the short-chains systems can be qualitatively understood with the picture provided by spherical (or pointlike) ions. The scenario becomes

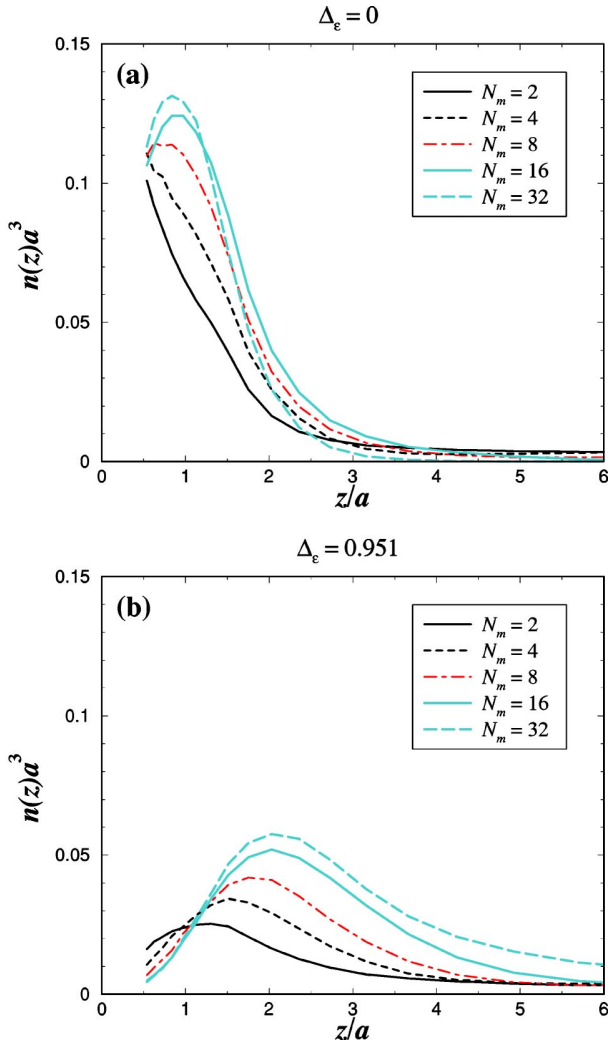

FIG. 1. Profiles of the monomer density $n(z)$ for different chain length N_m with $\sigma_0 L^2=64$ (systems $A-E$). (a) $\Delta_\epsilon=0$. (b) $\Delta_\epsilon=0.951$.

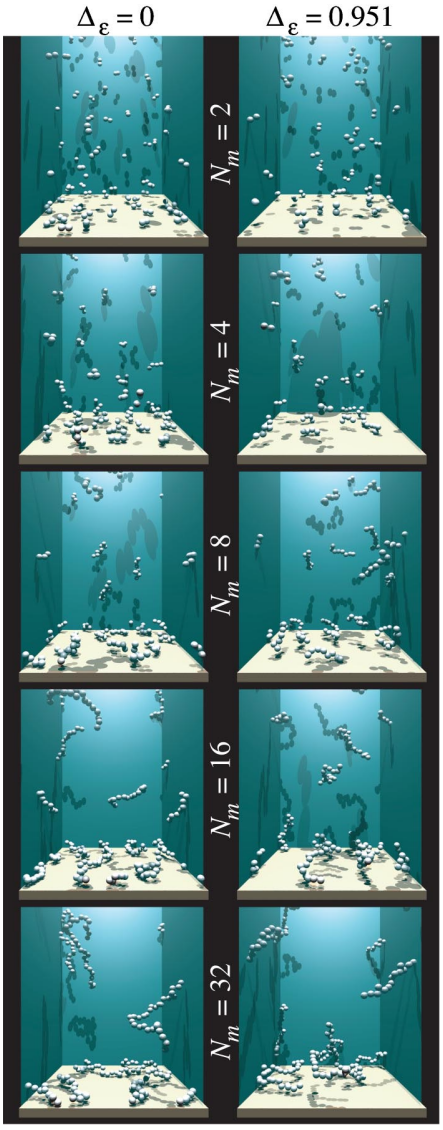

FIG. 2. Typical equilibrium microstructures of systems $A-E$. The little counterions are omitted for clarity.

qualitatively different at higher chain length [here $N_m \geqslant 8$—see Fig. 1(a)], where $n(z)$ presents a maximum near contact which is the signature of a *short-range repulsion* that was also theoretically predicted [10]. This nontrivial feature can be explained in terms of entropy: Near the surface of the substrate, the number of available PE conformations is considerably reduced, yielding to an entropic repulsion that can be detected if the driving force of PE adsorption (crucially controlled by σ_0) is not strong enough. This latter statement will be properly examined and confirmed in Sec. III B, where the influence of σ_0 is addressed. Nonetheless, the highest value of $n(z;N_m)$ increases with N_m, as it should be. All these mentioned features can be visualized on the microstructures depicted in Fig. 2. One can summarize those relevant findings, valid for small enough σ_0 and $\Delta_\epsilon=0$, as follows: (i) For very short chains, the PE adsorption is similar to that occurring with spherical electrolytes; (ii) PE chains experience a short-range repulsion near the substrate due to conformational entropic effects. Now, at *true* contact (i.e., $z=0.5a$) it seems that the monomer density $n(z \to a/2)$ [40] seems to be nearly independent of N_m for the parameters under consideration. In fact, for a (one-component) electrolyte, the density at contact can be *exactly* obtained [41] via the relation $n(z=a/2)-n(z=\tau-a/2)=2\pi l_B \sigma_0^2$ yielding $n(z=a/2)\approx 0.11a^{-3}$ [where basically $n(z=\tau-a/2)\approx 0$], which is in remarkable agreement with the value found in Fig. 1(a). One can wonder why such a simple theorem is "equally" well satisfied for PE systems that significantly deviate from simple structureless spherical ions. In fact, this is a nontrivial finding since already for *rodlike* PEs a fully different behavior is observed. Certainly more data are needed to clarify this point.

We now turn to the more complicated situation where image forces are present [$\Delta_\epsilon=0.951$—see Fig. 1(b)]. An immediate remark that can be drawn from a comparison with the $\Delta_\epsilon=0$ case is that the PE adsorption is much weaker due to the repulsive image-polyion interactions. At all N_m, $n(z)$ presents a maximum at $z=z^*$ that is gradually shifted to larger z with increasing N_m. In other words, the *thickness* of

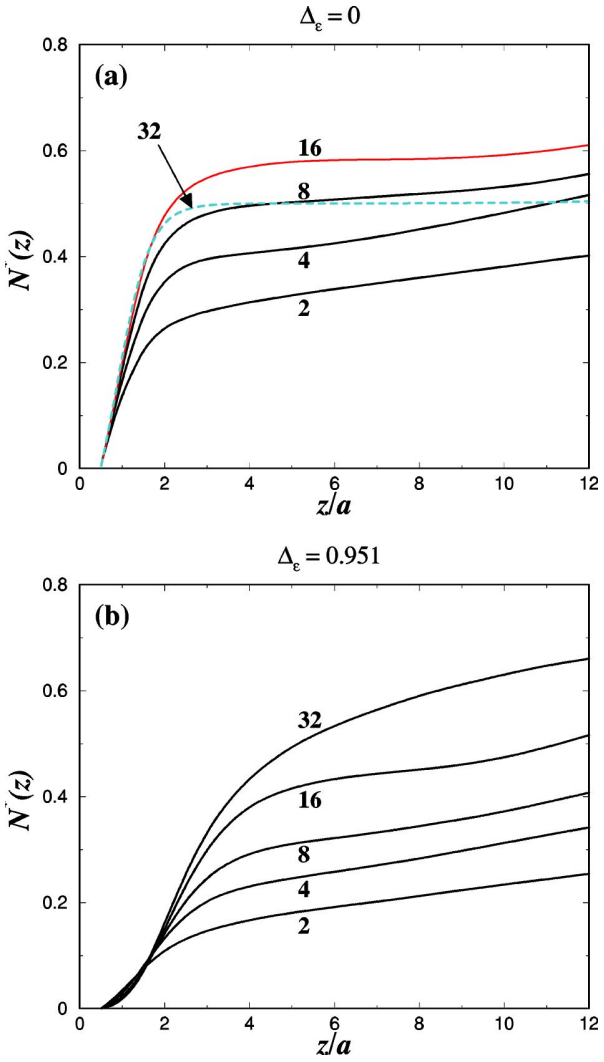

FIG. 3. Profiles of the fraction of adsorbed monomers $N^*(z)$ for different chain length N_m (as indicated by its numerical value) with $\sigma_0 L^2=64$ (systems $A-E$). (a) $\Delta_\epsilon=0$. (b) $\Delta_\epsilon=0.951$.

the adsorbed PE layer as determined by z^* increases with N_m. This phenomenon is of course due to the fact that the image-polyion repulsion increases with N_m, similarly to what happens with multivalent (pointlike or spherical) counterions [36,37]. On the other hand, interestingly, the monomer density at contact *decreases* with increasing N_m. This is the result of a *combined* effect of (i) conformational entropy as explained above and (ii) the N_m-induced image-polyion repulsion. All those features are well illustrated on the microstructures of Fig. 2.

To gain further insight into the properties of PE adsorption, we have plotted the fraction of adsorbed monomers $N^*(z)$ [Eq. (11)] in Fig. 3. At $\Delta_\epsilon=0$ [see Fig. 3(a)], it is observed in the immediate vicinity of the wall (roughly for $z \lesssim 1.5a$) that $N^*(z;N_m)$ increases monotonically with N_m, as expected. However, further away from the wall, a nontrivial effect is found where $N^*(z;N_m)$ surprisingly exhibits a nonmonotonic behavior with respect to N_m. More explicitly, in the regime of large N_m we have $N^*(z;N_m=32)$, which is clearly smaller than $N^*(z;N_m=16)$ and even smaller than $N^*(z;N_m=8)$ when one is sufficiently far from the wall. This remarkable phenomenon is going to be explained later by advocating the role of overcharging. Upon switching the image forces on [$\Delta_\epsilon=0.951$—see Fig. 3(b)], $N^*(z;N_m)$ shows a qualitatively different behavior from that found at $\Delta_\epsilon=0$, in accordance with our study concerning $n(z)$. More precisely, (i) very close to the wall, $N^*(z;N_m)$ *decreases* with N_m, while (ii) sufficiently far away from the wall, $N^*(z;N_m)$ *increases* with N_m. This behavior is fully consistent with our mechanisms previously discussed for $n(z)$. Below, we are going to show that the reduced net fluid charge $\sigma^*(z)$ is a key observable to account for those reported properties of $N^*(z;N_m)$.

A deeper understanding of the physical mechanisms involved in PE adsorption can be gained by considering the net fluid charge parameter $\sigma^*(z)$ [Eq. (13)] that describes the screening of the charged interface. The profiles of $\sigma^*(z)$ for different N_m can be found in Fig. 4. At $\Delta_\epsilon=0$ [see Fig. 4(a)], it is shown that for long enough chains (here $N_m \geqslant 4$) the substrate gets locally *overcharged*, as signaled by $\sigma^*(z)>1$. Physically, this means that the global local charge of the adsorbed monomers [42] is larger in absolute value than that of the interface. In other words, the charged wall is *overscreened* by the adsorbed PE chains. Figure 4(a) indicates that the degree of overcharging increases with N_m, as expected from the behavior of multivalent counterions, and seems to saturate at high N_m. This enhanced N_m overcharging leads to a sufficiently strong effective repulsion between the substrate and the PEs in the solution, which in turn prevents further adsorption. It is precisely this mechanism that explains the apparent anomaly found in Fig. 3(a), where, sufficiently away from the surface, it was reported a significantly lower monomer fraction $N^*(z;N_m)$ at $N_m=32$ than at $N_m=16$ or $N_m=8$. That is to say, although the amount of overcharging is essentially the same for $N_m=32$ and $N_m=16$, the *effective repulsive* interaction between the wall (covered by the adsorbed PEs) and the nonadsorbed PEs increases with N_m, leading to a stronger PE depletion above the PE layer at large enough N_m. This spectacular effect (due to electrostatic correlations) is well illustrated in Fig. 2 (with $N_m=32$), where above the (strongly bound) adsorbed PEs there is a depletion zone.

Upon inducing polarization charges [$\Delta_\epsilon=0.951$—see Fig. 4(b)], overscreening is canceled. This, in turn, accounts for the absence of plateau in $N^*(z;N_m)$ at $\Delta_\epsilon=0.951$. That striking disappearance of overcharging can be rationalized by establishing again an analogy with multivalent spherical ions, as follows.

For the sake of simplicity, let us assume that the PE can be electrostatically envisioned as a spherical polyion of valence N_m with a radius corresponding roughly to the radius of gyration of the chain. Thereby, the image-polyion *repulsive* interactions [including the self-image repulsion as well as the lateral image-ion correlations as given by the second term of Eq. (5)] scale like N_m^2, whereas the *attractive* driving force of polyion adsorption due to Wigner crystal ordering scales like $N_m^{3/2}$ [37]. The latter driving force corresponds to the highest possible attraction between the substrate and the polyion, and

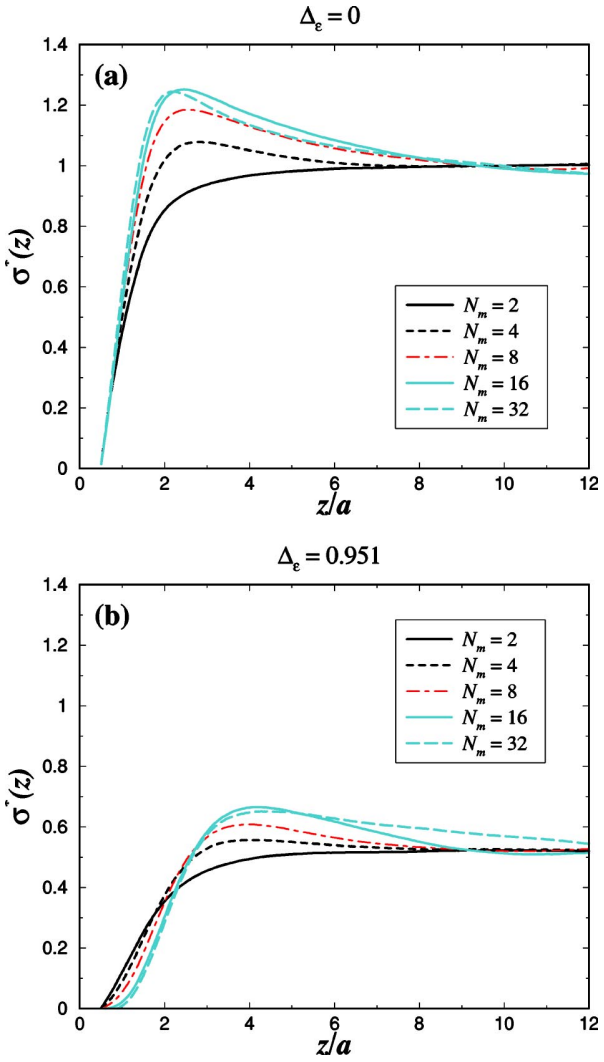

FIG. 4. Profiles of the reduced net fluid charge $\sigma^*(z)$ for different chain length N_m with $\sigma_0 L^2=64$ (systems $A-E$). (a) $\Delta_\epsilon=0$. (b) $\Delta_\epsilon=0.951$.

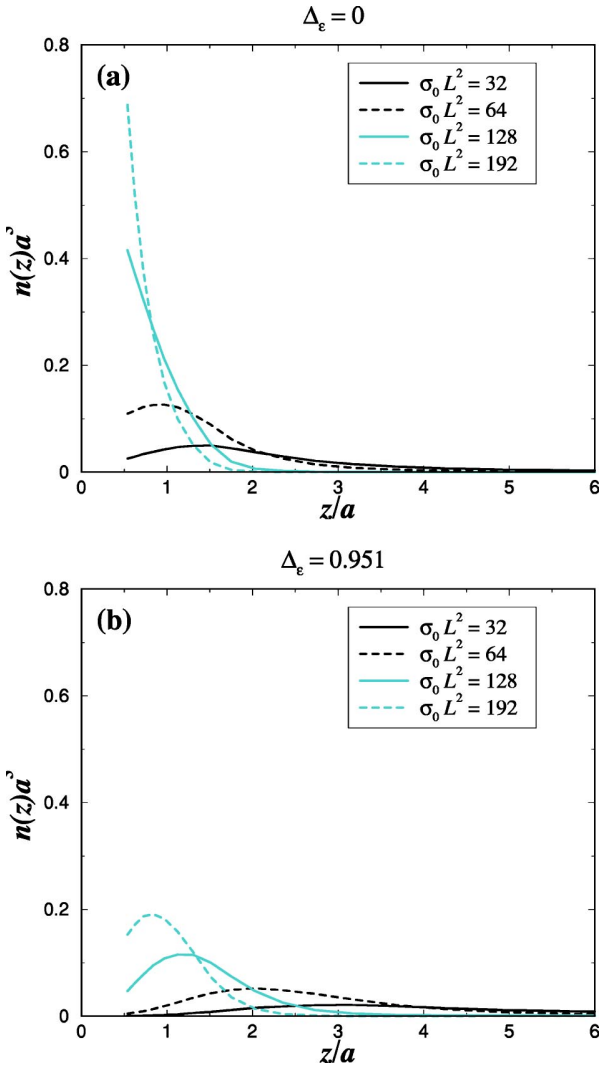

FIG. 5. Profiles of the monomer density $n(z)$ for different parameters of surface charge density $\sigma_0 L^2$ with $N_m=16$ (systems $D, F-H$). The case $\sigma_0 L^2=64$ (system D) from Fig. 1 is reported here again for easier comparison. (a) $\Delta_\epsilon=0$. (b) $\Delta_\epsilon=0.951$.

is therefore a good candidate for the present discussion. Consequently, at large enough N_m, image forces are dominant and inhibit overcharging.

This behavior strongly contrasts with the case of *spherical* substrates, where image forces do not affect the occurrence of overcharging [37].

B. Influence of substrate surface-charge density

To complete our investigation, we would like to address the influence of the substrate charge density on the PE adsorption in the presence of image forces. In this respect, we consider (at fixed $N_m=16$) three additional values of the charge density: $\sigma_0 L^2=32$, 128, 192 corresponding to the systems F, G, H, respectively (see Table II).

The plots of the monomer density $n(z)$ at various values of $\sigma_0 L^2$ can be found in Fig. 5. Microstructures of systems F and H are presented in Fig. 6. At $\Delta_\epsilon=0$ [see Fig. 5(a)], the monomer density at contact increases with σ_0 as it should be. Interestingly, the local maximum in $n(z)$ [present at small σ_0 (here $\sigma_0 L^2 \leqslant 64$)] *vanishes at large* σ_0 [see Fig. 5(a)]. This feature is the result of a σ_0-enhanced driving force of adsorption that overcomes entropic effects at large enough σ_0. The strong adsorption at $\sigma_0 L^2=192$ leads to a *flat* PE layer as well, illustrated in Fig. 6.

By polarizing the substrate surface ($\Delta_\epsilon=0.951$), it can be seen from Fig. 5(b) and the snapshot of Fig. 6 that there is a strong monomer depletion near contact at $\sigma_0 L^2=32$. This feature is due to the combined effects of (i) conformational entropy, (ii) image-monomer repulsion, and (iii) a lower electrostatic wall-monomer attraction. Upon increasing σ_0, the monomer density near contact becomes larger, and concomitantly, the maximum in $n(z)$ is systematically shifted to smaller z. That is to say, the thickness of the adsorbed PE layer decreases with σ_0.

The profiles of $N^*(z)$ are provided in Fig. 7, from which further characterization of PE adsorption can be obtained. At

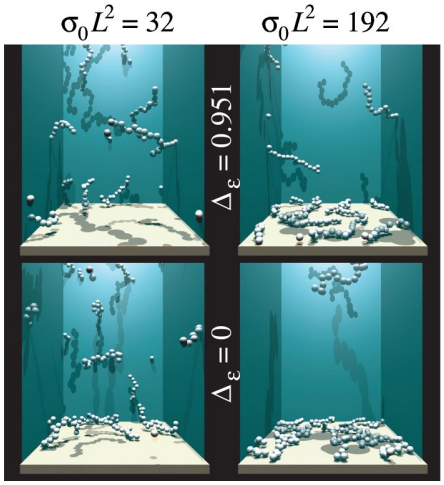

FIG. 6. Typical equilibrium microstructures of systems *F* and *H*. The little counterions are omitted for clarity.

$\Delta_\epsilon=0$, Fig. 7(a) indicates that $N^*(z;\sigma_0)$ increases with σ_0 but saturates at high σ_0. This latter saturation effect should only be relevant for a regime of charge where $\eta \equiv N_{\mathrm{PE}}N_m/\sigma_0 L^2$ is about unity. Indeed, in a typical experimental situation at finite monomer concentration (even in the dilute regime), we have $\eta \gg > 1$ so that overcharging is always possible at large σ_0 and thereby $N^*(z;\sigma_0)$ should always significantly increase with σ_0 as long as packing effects (as generated by the excluded volume of the monomers) are not vivid. In parallel, the plateau reported at $\sigma_0 L^2=128$ and $\sigma_0 L^2=192$ in Fig. 7(a) is the signature of a monomer depletion above the adsorbed PE layer (see also Fig. 6) due to a strong screening of the surface charge by the latter. At $\Delta_\epsilon=0.951$, Fig. 7(b) shows that $N^*(z)$ is considerably smaller than at $\Delta_\epsilon=0$ even for high σ_0, in accordance with the behavior of $n(z)$ from Fig. 5. The Δ_ϵ-induced desorption is especially strong at $\sigma_0 L^2=32$, where the image-monomer repulsion clearly counterbalances the electrostatic wall-monomer attraction. More quantitatively, at $z=3a$ (a z distance corresponding roughly to the radius of gyration of the chain with $N_m=16$), about 30% [i.e., $N^*(z)=0.3$] of the monomers are adsorbed with $\Delta_\epsilon=0$ against only 10% with $\Delta_\epsilon=0.951$ [see Fig. 7(b)].

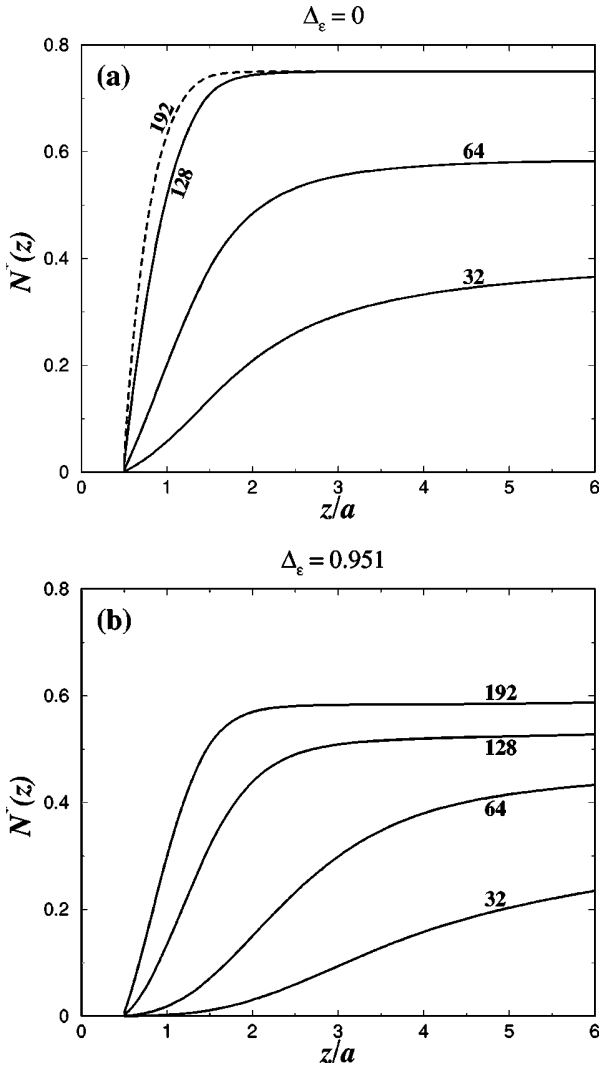

FIG. 7. Profiles of the fraction of adsorbed monomers $N^*(z)$ for different parameters of surface charge density $\sigma_0 L^2$ (as indicated by its numerical value) with $N_m=16$ (systems *D*,*F*-*H*). The case $\sigma_0 L^2=64$ (system *D*) from Fig. 3 is reported here again for easier comparison. (a) $\Delta_\epsilon=0$. (b) $\Delta_\epsilon=0.951$.

IV. CONCLUDING REMARKS

We first would like to make some final remarks about the presented results. As far as the charge surface distribution on the substrate's surface is concerned, we have assumed a *smeared-out* one in contrast to a real experimental situation where it is *discrete*. Previous numerical studies [43–45] have shown that the counterion distribution at inhomogeneously charged substrates may deviate from that obtained at smeared-out ones at strong Coulomb coupling (i.e., multivalent counterions and/or high Bjerrum length) or strong substrate charge modulations. Nonetheless, at standard Bjerrum length (i.e., $l_B=7.1$ Å for water at room temperature, as is presently the case) and with discrete monovalent ions generating the substrate's surface charge, it has been demonstrated that the counterion distribution is marginally modified [43] even for trivalent counterions. Hence, we think that our results will not qualitatively differ from the more realistic situation of non-smeared-out substrate charges consisting of discrete monovalent ions.

Another approximation in our model is the location of the dielectric discontinuity. More precisely, it was implicitly assumed that the latter coincides with the charged interface (considered here as a hard wall). In fact, experimentally, it is not clear where the dielectric discontinuity is located and the transition is rather gradual and spreads out over several angstroms [46], so that in a continuum description the dielectric discontinuity might be located somewhat below the *hard* interface. In this respect, our model tends to slightly overestimate the effect of image forces and namely, with $\Delta_\epsilon>0$, the self-image *repulsion*. Furthermore, in the presence of *short-range* attractive interactions between the substrate and the

PEs (for instance, stemming from some specific chemical properties of the chains and the substrate, i.e., chemisorption), the effect of image charges might also be reduced [19]. This means that the substrate-charge *undercompensation* by PEs induced by repulsive image forces as reported in Fig. 4(b) is dependent on the relative strength of that short-range attractive interaction, which is not taken into account in our model. Nevertheless, we are confident that our results provide a reliable fingerprint for the understanding of the effect of image forces on PE adsorption in a salt-free environment.

It is not a straightforward task to access experimentally these effects stemming from image forces. One major difficulty arises from the fact that by changing the dielectric constant of the solvent, ϵ_{solv}, one changes the degree of ionization of the PEs. However, there is the experimental possibility to tune Δ_ϵ by using *organic* solvents (i.e., with a low ϵ_{solv} but still polar) with a mixture of large colloidal particles [e.g., latex particles with weak curvature and (low) dielectric constant ϵ_{subs} such that $\epsilon_{\mathrm{subs}} \leqslant \epsilon_{\mathrm{solv}}$] and PEs. In this experimental context, one should be able to verify the trends of our current findings.

To conclude, we have performed MC simulations to address the effect of image forces on PE adsorption at oppositely charged planar substrates. The influence of chain length and surface-charge density was also considered. We have considered a finite monomer concentration in the dilute regime for relatively short chains. Our main findings can be summarized as follows.

(i) For very short chains (here $N_m \leqslant 4$) and with no image forces (i.e., $\Delta_\epsilon = 0$), the PE adsorption is similar to that occurring with little (spherical) multivalent counterions. For longer chains (here $N_m \geqslant 8$), the PEs experience (even at $\Delta_\epsilon = 0$) a short-range repulsion near the substrate due to chain entropy effects. This latter feature is especially relevant at low substrate charge σ_0.

(ii) At fixed σ_0 and in the presence of repulsive *image forces* (here $\Delta_\epsilon = 0.951$), it was demonstrated that the monomer depletion in the vicinity of the substrate as well as the thickness of the PE layer grow with chain length N_m. Concomitantly, and as a major result, the *charge reversal* of the substrate by the adsorbed PEs *vanishes*. This latter point was in fact overlooked in the literature (see, e.g., Refs. [9,15,16,24]).

(iii) Upon varying σ_0 at fixed N_m, it was shown at $\Delta_\epsilon = 0$ that the net substrate-PE force becomes purely attractive at sufficiently high σ_0, where chain-entropy effects are overcompensated. When image forces are present, the PE *depletion* near the substrate as well as the thickness of the adsorbed PE layer decrease with σ_0.

A future work will address the adsorption of stiff *rodlike* PEs. This situation was recently theoretically examined by Cheng and de la Cruz [22]. Nonetheless, simulation data would be of great help to further characterize the arrangement of the rodlike charged particles near the interface as well as to elucidate the influence of image forces on the latter.

ACKNOWLEDGMENTS

The author thanks H. Löwen for enlightening discussions. The SFB TR6 is acknowledged for financial support.

[1] N. Hansupalak and M. M. Santore, Langmuir **19**, 7423 (2003).
[2] A. Tulpar and W. A. Ducker, J. Phys. Chem. B **108**, 1667 (2004).
[3] F. W. Wiegel, J. Phys. A **10**, 299 (1977).
[4] H. A. Van der Schee and J. Lyklema, J. Phys. Chem. **88**, 6621 (1984).
[5] M. Muthukumar, J. Chem. Phys. **86**, 7230 (1987).
[6] M. R. Böhmer, O. A. Evers, and J. M. H. M. Scheutjens, Macromolecules **23**, 2288 (1990).
[7] R. Varoqui, A. Johner, and A. Elaissari, J. Chem. Phys. **94**, 6873 (1991).
[8] R. Varoqui, J. Phys. II **3**, 1097 (1993).
[9] O. V. Borisov, E. B. Zhulina, and T. M. Birshtein, J. Phys. II **4**, 913 (1994).
[10] I. Borukhov, D. Andelman, and H. Orland, Europhys. Lett. **32**, 499 (1995).
[11] X. Châtellier and J.-F. Joanny, J. Phys. II **6**, 1669 (1996).
[12] P. Linse, Macromolecules **29**, 326 (1996).
[13] V. Shubin and P. Linse, Macromolecules **30**, 5944 (1997).
[14] I. Borukhov, D. Andelman, and H. Orland, Macromolecules **31**, 1665 (1998).
[15] J. F. Joanny, Eur. Phys. J. B **9**, 117 (1999).
[16] R. R. Netz and J. F. Joanny, Macromolecules **32**, 9013 (1999).
[17] A. V. Dobrynin, A. Deshkovski, and M. Rubinstein, Phys. Rev. Lett. **84**, 3101 (2000).
[18] A. V. Dobrynin, A. Deshkovski, and M. Rubinstein, Macromolecules **34**, 3421 (2001).
[19] A. V. Dobrynin and M. Rubinstein, J. Phys. Chem. B **107**, 8260 (2003).
[20] A. Shafir, D. Andelman, and R. R. Netz, J. Chem. Phys. **119**, 2355 (2003).
[21] R. de Vries, F. Weinbreck, and C. G. de Kruif, J. Chem. Phys. **118**, 4649 (2003).
[22] H. Cheng and O. de la Cruz, J. Chem. Phys. **119**, 12 635 (2003).
[23] C.-H. Cheng and P.-Y. Lai, e-print cond-mat/0312315.
[24] C.-H. Cheng, and P.-Y. Lai, e-print cond-mat/0403722.
[25] A. Y. Grosberg, T. T. Nguyen, and B. I. Shklovskii, Rev. Mod. Phys. **74**, 329 (2002).
[26] S. Beltrán, H. H. Hooper, H. W. Blanch, and J. M. Prausnitz, Macromolecules **24**, 3178 (1991).
[27] C. Y. Kong and M. Muthukumar, J. Chem. Phys. **109**, 1522 (1998).
[28] V. Yamakov, A. Milchev, O. Borisov, and B. Dunweg, J. Phys.: Condens. Matter **11**, 9907 (1999).
[29] M. Ellis, C. Y. Kong, and M. Muthukumar, J. Chem. Phys. **112**, 8723 (2000).
[30] R. Messina, Macromolecules **37**, 621 (2004).
[31] Only the monomer-monomer excluded volume interaction was

not modeled by a hard-sphere potential. There, a purely repulsive Lennard-Jones potential was used.
[32] A. Grzybowsky and A. Brodka, Mol. Phys. **100**, 1017 (2002).
[33] M. D. Malinsky, K. L. Kelly, G. C. Schatz, and R. P. van Duyne, J. Phys. Chem. B **105**, 2343 (2001).
[34] N. Metropolis *et al.*, J. Chem. Phys. **21**, 1087 (1953).
[35] M. P. Allen and D. J. Tildesley, *Computer Simulations of Liquids* (Clarendon Press, Oxford, 1987).
[36] G. M. Torrie, J. P. Valleau, and G. N. Patey, J. Chem. Phys. **76**, 4615 (1982).
[37] R. Messina, J. Chem. Phys. **117**, 11062 (2002).
[38] B. Shklovskii, Phys. Rev. E **60**, 5802 (1999).
[39] R. Messina, C. Holm, and K. Kremer, Phys. Rev. E **64**, 021405 (2001).
[40] Note that in a simulation, the density at contact $n(z \to a/2)$ can only be obtained by extrapolation.
[41] See, for instance, H. Wennerström, B. Jönsson, and P. Linse, J. Chem. Phys. **76**, 4665 (1982).
[42] Near the wall, the presence of the counterions at $\Delta_\epsilon = 0$ is marginal so that the fluid charge is quasiexclusively provided by the charges of the adsorbed monomers. This becomes especially vivid when $N_m \geqslant 4$, where overcharging occurs.
[43] R. Messina, Physica A **308**, 59 (2002).
[44] E. Allahyarov, H. Löwen, A. A. Louis, and J.-P. Hansen, Europhys. Lett. **57**, 731 (2002).
[45] A. G. Moreira and R. R. Netz, Europhys. Lett. **57**, 911 (2002).
[46] P. Linse, J. Phys. Chem. **90**, 6821 (1986).

Erratum: Effect of image forces on polyelectrolyte adsorption at a charged surface [Phys. Rev. E. 70, 051802 (2004)]

René Messina*

(Received 22 August 2006; published 13 October 2006)

DOI: 10.1103/PhysRevE.74.049906 PACS number(s): 82.35.Gh, 82.35.Rs, 61.20.Qg, 61.20.Ja, 99.10.Cd

Equation (6) is erroneous and leads to an overestimation of the effect of image forces. The correct form of that equation containing the dielectric term discontinuity Δ_ϵ reads

$$\beta U_{\mathrm{Coul}}^{(\mathrm{plate})}(z_i) = l_B\left[\pm 2\pi\sigma_0(1+\Delta_\epsilon)z_i + \frac{\Delta_\epsilon}{4z_i}\right]. \tag{6}$$

It is precisely the term $(1+\Delta_\epsilon)$ that was missing in the original paper, which physically represents the image charge contribution stemming from the charged interface itself. A simple derivation can be obtained as follows: Assume that a charged surface characterized by a surface charge density σ is located at $z=\delta>0$ ($z=0$ being the dielectric interface position), then its image is located at $z=-\delta<0$ with a charge $\Delta_\epsilon\sigma$. Taking the limit $\delta\to 0$, the effective surface charge density of the interface becomes $(1+\Delta_\epsilon)\sigma$ [1]. Doing so the total image charge of the electroneutral system (charged interface+counterions) remains also zero. Despite the error in Eq. (6) most of our conclusions remain qualitatively correct. The only conclusion that is truly affected concerns the overcharging. With our data based on the corrected Eq. (6), it is found that *overcharging is robust against image forces*. Furthermore, all our results obtained in the absence of image charges (i.e., $\Delta_\epsilon=0$) in the original paper are evidently unaffected by this mistake.

We now briefly discuss the impact of our corrections by providing some representative corrected data. The profiles of the monomer distribution $n(z)$ can be found in Fig. 1 that corresponds to our earlier Fig. 1(b). From Fig. 1, it can be seen that the same qualitative behavior is found as that sketched in Fig. 1(b) from the original paper. The height of the peaks in Fig. 1 are roughly twice as large as those found in Fig. 1(b) in the original paper. Some data from Fig. 1 were also published elsewhere [see Fig. 3(b) in Ref. [2]].

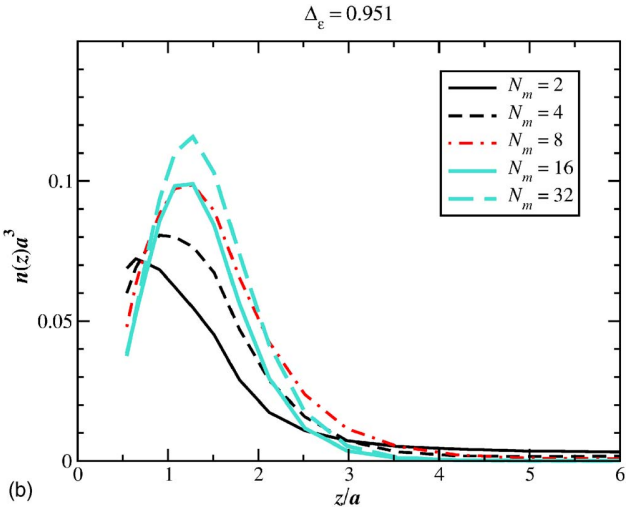

FIG. 1. (Color online) Profiles of the monomer density $n(z)$ for different chain length N_m with $\sigma_0 L^2=64$ and $\Delta_\epsilon=0.951$.

*Electronic address: messina@thphy.uni-duesseldorf.de

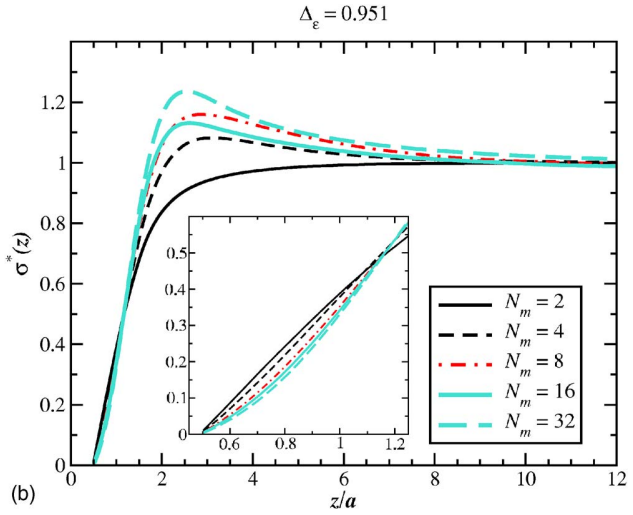

FIG. 4. (Color online) Profiles of the reduced net fluid charge $\sigma^*(z)$ for different chain length N_m with $\sigma_0 L^2=64$ and $\Delta_\epsilon=0.951$. The inset is a magnification of the region near contact.

An important change concerns Fig. 4(b) in the original paper where an erroneous cancellation of overcharging was reported. The corrected data are now depicted in Fig. 4. The strength of the overcharging is presently nearly identical to that obtained without image forces at $\Delta_\epsilon=0$ (compare with Fig. 4 in the original paper). Near contact ($z \lesssim 1.2a$) it is found that the fraction of charge $\sigma^*(z)$ (see Fig. 4), that is, essentially due to the adsorbed monomers, decreases with growing N_m. This feature was already reported in Fig. 4(b) from the original paper.

[1] Note that one obtains exactly the same effective surface charge density if we start from a charged surface located at $z=-\delta<0$ and then take the limit $\delta \to 0$.

[2] R. Messina, J. Chem. Phys. **124**, 014705 (2006).

Appendix K

Behavior of rodlike polyelectrolytes near an oppositely charged surface

Behavior of rodlike polyelectrolytes near an oppositely charged surface

René Messina[a)]
Institut für Theoretische Physik II, Heinrich-Heine-Universität Düsseldorf, Universitätsstrasse 1, D-40225 Düsseldorf, Germany

(Received 2 August 2005; accepted 1 November 2005; published online 4 January 2006)

The behavior of highly charged short rodlike polyelectrolytes near oppositely charged planar surfaces is investigated by means of Monte Carlo simulations. A detailed microstructural study, including monomer and fluid charge distributions and chain orientation, is provided. The influence of chain length, substrate's surface-charge density, and image forces is considered. Due to the lower chain entropy (compared to flexible chains), our simulation data show that rodlike polyelectrolytes can, in general, better adsorb than flexible ones do. Nonetheless, at low substrate-dielectric constant, it is found that repulsive image forces tend to significantly reduce this discrepancy. © *2006 American Institute of Physics*. [DOI: 10.1063/1.2140692]

I. INTRODUCTION

Polyelectrolyte (PE) (i.e., charged polymer) adsorption on charged surfaces is a versatile process having industrial as well as biological applications. In particular, the case of rodlike (stiff) PEs, which corresponds to the situation of short DNA fragments or other similar biomaterials, has some relevance for biological processes such as gene therapy[1] or biotechnology.[2–4]

From a theoretical viewpoint, the behavior of stiff PEs near an oppositely charged surface has been studied by various authors on a mean-field level.[5–11] Menes *et al.*[5] considered the interaction between two infinitely long charged rods near a salty surface in the framework of the Debye-Hückel theory. Due to the low dimensionality of the system, they reported an algebraic decay for the effective interaction that was confirmed by their Brownian dynamics simulations.[5] The more simple and fundamental situation of a *single* and *infinitely long* charged rod in the vicinity of a charged surface was investigated by several authors.[6–8] The problem of the so-called counterion release (i.e., "Manning decondensation") from a rigid PE approaching an oppositely charged was examined by Sens and Joanny[7] and by Fleck and von Grünberg[8] using the Poisson-Boltzmann theory. In a similar spirit, Menes *et al.*[6] found that the screening of the adsorbed charged rod's field, due to counterions and mobile surface charges, is highly sensitive to the degree of membrane's surface charging. The adsorption of *short* rodlike PEs was also considered by some researchers.[9,10] Recently, Cheng and Olvera de la Cruz[9] investigated the adsorption/desorption transition including lateral correlations by assuming a regular flat lattice for the adsorbed charged rods. This latter assumption is only valid when the electrostatic rod-surface binding is strong enough. Closely related to our problem, Hoagland[10] analyzed the monomer concentration profile as well as the chain orientation with respect to the charged substrate's surface for a single short rodlike PE. The notorious complication of image forces stemming from the dielectric discontinuity between the substrate and the solvent was also addressed by some authors.[7,11,12] More specifically, for low dielectric constant (i.e., repulsive image forces) and fixed surface ions of the substrate, (i) Sens and Joanny[7] showed that the condensed counterions are not always released as the stiff PE approaches the substrate and (ii) Netz[11] showed an extra decrease of the charge dissociation of the stiff PE (i.e., charge regulation in salty solution nearby an uncharged polarized interface).

Since those studies[7,10,11] were realized in the framework of the the Poisson-Boltzmann theory and for a single chain, the relevant phenomenon of *charge reversal* of the substrate's surface charge by the adsorbed PEs cannot be captured.

In this paper, we propose to elucidate the microstructural behavior of (very) short rodlike PEs near an oppositely charged surface by using Monte Carlo (MC) computer simulations. The effect of image forces is also systematically investigated. To better understand the effect of chain entropy, a comparison with the previous work of Messina[13] concerning fully flexible PEs is carried out. Our article is organized as follows: The simulation model is detailed in Sec. II. Our results are presented in Sec. III, and concluding remarks are provided in Sec. IV.

II. MODEL AND PARAMETERS

A. Simulation model

The model system under consideration is similar to that recently investigated for the adsorption of flexible chains.[13,14] Within the framework of the primitive model, we consider a PE solution near a charged hard wall with an implicit solvent of relative permittivity $\epsilon_{\text{solv}} \approx 80$ (i.e., water at $z>0$). The substrate located at $z<0$ is characterized by a relative permittivity ϵ_{subs} which leads to a dielectric jump Δ_ϵ (when $\epsilon_{\text{solv}} \neq \epsilon_{\text{subs}}$) at the interface (positioned at $z=0$) defined as

$$\Delta_\epsilon = \frac{\epsilon_{\text{solv}} - \epsilon_{\text{subs}}}{\epsilon_{\text{solv}} + \epsilon_{\text{subs}}}. \tag{1}$$

a)Electronic mail: messina@thphy.uni-duesseldorf.de

The *negative* bare surface-charge density of the substrate's interface is $-\sigma_0 e$, where e is the (positive) elementary charge and $\sigma_0 > 0$ is the number of charges per unit area. The latter is always electrically compensated by its accompanying monovalent counterions of charge $Z_+ e$ (i.e., monovalent cations with $Z_+ = +1$) of diameter a. Rodlike PE chains are made up of N_m *monovalent* positively charged monomers ($Z_m = Z_+ = +1$) of diameter a. The bond length l is also set to $l = a$ so that the length $L_{\rm rod}$ of a rodlike PE is $L_{\rm rod} = N_m l = N_m a$. The counterions (monovalent anions: $Z_- = -1$) of the PEs are also explicitly taken into account with the same parameters, up to the charge sign, as the substrate's counterions. Hence, all the constitutive microions are monovalent ($Z = Z_+ = Z_m = -Z_- = 1$) and monosized with diameter a. All these particles are immersed in a rectangular $L \times L \times \tau$ box. Periodic boundary conditions are applied in the (x,y) directions, whereas hard walls are present at $z = 0$ (location of the charged interface) and $z = \tau$ (location of an *uncharged* wall). It is to say that we work in the framework of the cell model.

The total energy of interaction of the system can be written as

$$U_{\rm tot} = \sum_i \left[U_{\rm hs}^{\rm (intf)}(z_i) + U_{\rm Coul}^{\rm (intf)}(z_i) \right] + \sum_{i,i<j} \left[U_{\rm hs}^{\rm (mic)}(r_{ij}) + U_{\rm Coul}^{\rm (mic)}(\mathbf{r}_i, \mathbf{r}_j) \right], \quad (2)$$

where the first (single) sum stems from the interaction between a microion i [located at $z = z_i$ with $i = (+,-,m)$] and the charged interface, and the second (double) sum stems from the pair interaction between microions i and j with $r_{ij} = |\mathbf{r}_i - \mathbf{r}_j|$. All these contributions to $U_{\rm tot}$ in Eq. (2) are described in detail below.

Excluded volume interactions are modeled via a hard-core potential defined as follows:

$$U_{\rm hs}^{\rm (mic)}(r_{ij}) = \begin{cases} 0 & \text{for } r_{ij} \geqslant a \\ \infty & \text{for } r_{ij} < a \end{cases} \quad (3)$$

for the microion-microion one and

$$U_{\rm hs}^{\rm (intf)}(z_i) = \begin{cases} 0 & \text{for } a/2 \leqslant z_i \leqslant \tau - a/2 \\ \infty & \text{otherwise} \end{cases} \quad (4)$$

for the interface-microion one.

The electrostatic energy of interaction between two microions i and j reads

$$\beta U_{\rm Coul}^{\rm (mic)}(\mathbf{r}_i, \mathbf{r}_j) = Z_i Z_j l_B \left[\frac{1}{r_{ij}} + \frac{\Delta_\epsilon}{\sqrt{x_{ij}^2 + y_{ij}^2 + (z_i + z_j)^2}} \right], \quad (5)$$

where $l_B = \beta e^2/(4\pi\epsilon_0\epsilon_{\rm solv})$ is the Bjerrum length corresponding to the distance at which two protonic charges interact with $1/\beta = k_B T$, and Δ_ϵ is given by Eq. (1). The first term in Eq. (5) corresponds to the direct Coulomb interaction between real microions, whereas the second term represents the interaction between the real microion i and the image of microion j. By symmetry, the latter also describes the interaction between the real microion j and the image of microion i, yielding an implicit prefactor of $1/2$ in Eq. (5). The electrostatic energy of interaction between a microion i and the (uniformly) charged interface reads

$$\beta U_{\rm Coul}^{\rm (intf)}(z_i) = l_B \left[2\pi Z_i (1 + \Delta_\epsilon) \sigma_0 z_i + \frac{Z_i^2 \Delta_\epsilon}{4 z_i} \right]. \quad (6)$$

The second term in Eq. (6) stands for the *self-image* interaction, i.e., the interaction between the microion i and its own image. An appropriate and efficient modified Lekner sum was utilized to compute the electrostatic interactions with periodicity in *two* directions.[15] This latter technique was already successfully applied to the case of PE multilayering[14] and polycation adsorption.[13] To link our simulation parameters to experimental units and room temperature ($T = 298$ K), we choose $a = 4.25$ Å leading to the Bjerrum length of water $l_B = 1.68a = 7.14$ Å. In order to investigate the effect of image forces, we take a value of $\epsilon_{\rm subs} = 2$ for the dielectric constant of the charged substrate (which is a typical value for silica or mica substrates[16]) and $\epsilon_{\rm solv} = 80$ for that of the aqueous solvent yielding $\Delta_\epsilon = (80-2)/(80+2) \approx 0.951$. The case of identical dielectric constants $\epsilon_{\rm subs} = \epsilon_{\rm solv}$ ($\Delta_\epsilon = 0$) corresponds to the situation where there are no image charges.

All the simulation parameters are gathered in Table I. The set of simulated systems can be found in Table II. The equilibrium properties of our model system were obtained by using standard canonical MC simulations following the Metropolis scheme.[17,18] In detail, single-particle (translational) moves were applied to the counterions (i.e., anions and cations) with an acceptance ratio of 50%. As far as trial moves for the rodlike PEs are concerned and given the anisotropy of

TABLE I. List of key parameters with some fixed values.

Parameters	
$T = 298$ K	Room temperature
$\sigma_0 L^2$	Charge number of the substrate
$\Delta_\epsilon = 0$ or 0.951	Dielectric discontinuity
$Z = 1$	Microion valence
$a = 4.25$ Å	Microion diameter
$l_B = 1.68a = 7.14$ Å	Bjerrum length
$L = 25a$	(x,y) box length
$\tau = 75a$	z box length
$N_{\rm rod}$	Number of rodlike PEs
$N_{\rm m}$	Number of monomers per rodlike chain

TABLE II. Simulated systems' parameters. The number of counterions (cations and anions) ensuring the overall electroneutrality of the system is not indicated.

System	$N_{\rm rod}$	N_m	$\sigma_0 L^2$
A	96	2	64
B	48	4	64
C	32	6	64
D	24	8	64
E	16	12	64
F	24	8	32
G	24	8	128

these objects, random translational moves as well as *rotational* ones were performed at the same frequency.[19] Random rotational moves were achieved by choosing randomly new orientation vectors of the rodlike particles. This method is (i) computationally not too demanding, (ii) leads to an efficient configurational space sampling, and (iii) fulfills the rules of detailed balance. The acceptance ratio was also set to 50%.

The total length of a simulation run is set to 3×10^6 MC steps per particle. Typically, about 10^5 MC steps were required for equilibration, and 2.5×10^6 MC steps were used to perform measurements.

B. Measured quantities

We briefly describe the different observables that are going to be measured. In order to study the PE adsorption, we compute the monomer density $n(z)$ that is normalized as follows:

$$\int_{a/2}^{\tau-a/2} n(z)L^2dz = N_{\mathrm{rod}}N_m. \tag{7}$$

To further characterize the PE adsorption, we also compute the total number of accumulated monomers $\bar{N}(z)$ within a distance z from the charged interface that is given by

$$\bar{N}(z) = \int_{a/2}^{z} n(z')L^2dz'. \tag{8}$$

It is useful to introduce the fraction of adsorbed monomers $N^*(z)$, which is defined as follows:

$$N^*(z) = \frac{\bar{N}(z)}{N_{\mathrm{rod}}N_m}. \tag{9}$$

The *orientation* of the rodlike PEs can be best monitored by the angle θ formed between the z axis and the PE axis.[10] A convenient quantity is provided by its second-order Legendre polynomial:

$$P_2[\cos\theta(z)] = \tfrac{1}{2}[3\cos^2\theta(z) - 1], \tag{10}$$

where z corresponds to the smallest wall-monomer distance for a given PE. Thereby

$$S(z) \equiv \langle P_2[\cos\theta(z)]\rangle \tag{11}$$

takes the values $-\frac{1}{2}$, 0, and +1 for PEs that are perpendicular, randomly oriented, and parallel to the z axis, respectively.

Another relevant quantity is the global *net fluid charge* $\sigma(z)$ which reads

$$\sigma(z) = \int_{a/2}^{z} [n_+(z') - n_-(z')]dz', \tag{12}$$

where n_+ and n_- stand for the density of all the positive microions (i.e., monomers and substrate's counterions) and negative microions (i.e., PEs' counterions), respectively. The corresponding reduced surface-charge density $\sigma^*(z)$ is given by

$$\sigma^*(z) = \frac{\sigma(z)}{\sigma_0}. \tag{13}$$

Thereby, $\sigma^*(z)$ corresponds, up to a prefactor $\sigma_0 e$, to the net fluid charge per unit area (omitting the surface-charge density $-\sigma_0 e$ of the substrate) within a distance z from the charged wall. At the uncharged wall, electroneutrality imposes $\sigma^*(z=\tau-a/2)=1$. By simple application of the Gauss law, $[\sigma^*(z)-1]$ is directly proportional to the mean electric field at z. Therefore $\sigma^*(z)$ can measure the *screening* strength of the substrate by the neighboring solute charged species.

III. RESULTS AND DISCUSSION

It is well known that the effects of image forces become especially relevant at low surface-charge density of the interface.[21,22] Furthermore, it is also clear that the self-image interaction (*repulsive* for $\Delta_\epsilon>0$, as is presently the case) is higher the higher the charge of the ions (polyions). Hence, we are going to study (i) the influence of chain length (Sec. III A) and (ii) that of surface-charge density (Sec. III B). For the sake of consistency, we set the total number of monomers to $N_{\mathrm{rod}}N_m=192$, meaning that the monomer concentration is *fixed* leading to a PE volume fraction $\phi=(4\pi/3)\times[N_{\mathrm{rod}}N_m(a/2)^3/L^2\tau]\approx2.14\times10^{-3}$ (see also Table II).

A. Influence of chain length

In this part, we consider the influence of chain length N_m at fixed surface-charge-density parameter $\sigma_0L^2=64$. The latter would experimentally correspond to a moderate[20] surface-charge density with $-\sigma_0 e\approx-0.091$ C/m^2. The chain length is varied from $N_m=2$ up to $N_m=12$ (systems $A-E$, see Table II). We have ensured that, for the longest chains with $N_m=12$, finite-size effects are not important since there $L_{\mathrm{rod}}=12a$ which is significantly smaller than $L=25a$ or $\tau=75a$.

1. Monomer distribution

The profiles of the monomer distribution $n(z)$ can be found in Fig. 1, and the corresponding microstructures are sketched in Fig. 2. When no image charges are present [$\Delta_\epsilon=0$, Fig. 1(a)], the monomer-density profile $n(z)$ exhibits a monotonic behavior for very short rigid chains (here $N_m=2$). For longer chains there exists a small monomer depletion near the charged wall for an *intermediate* regime of N_m (here $4\leqslant N_m\leqslant8$). At high enough N_m (here $N_m=12$) our simulation data reveal again a monotonic behavior of $n(z)$. This interesting behavior is the result of two antagonistic driving forces, namely, (i) chain entropy and (ii) the electrostatic wall-monomer attraction. More precisely, the mechanisms responsible for this N_m-induced reentrant behavior at $\Delta_\epsilon=0$ are as follows.

- For very short chains (here $N_m=2$) chain-entropy effects are negligible so that one gets a similar behavior to that of pointlike counterions with the usual monotonic decaying $n(z)$ profile.

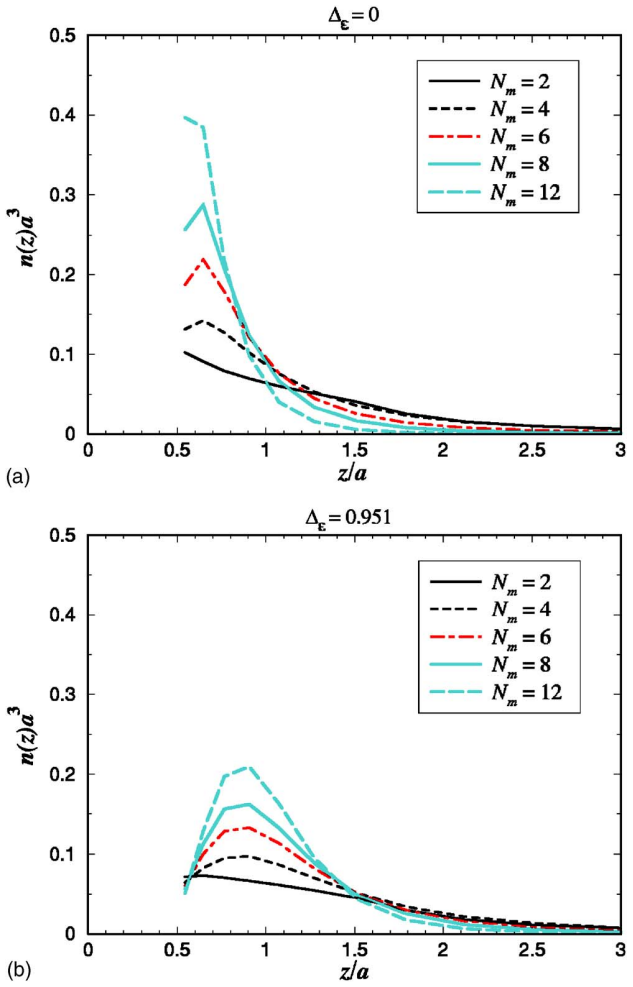

FIG. 1. Profiles of the monomer density $n(z)$ for different chain length N_m with $\sigma_0 L^2=64$ (systems $A-E$). (a) $\Delta_\epsilon=0$. (b) $\Delta_\epsilon=0.951$.

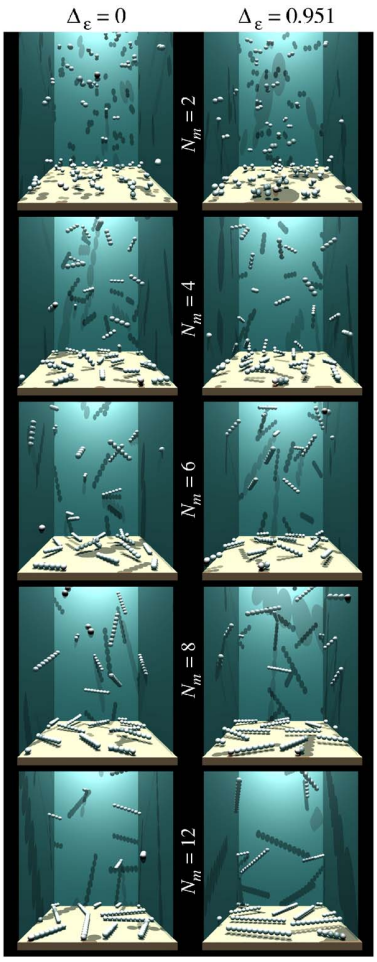

FIG. 2. Typical equilibrium microstructures of systems $A-E$. The little counterions are omitted for clarity.

- The chain-entropy loss (per chain) by adsorption should typically scale like $\ln N_m$, whereas the electrostatic wall-chain attraction scales like N_m, explaining why at high enough N_m a purely *effective* attractive wall-monomer interaction is recovered.

Upon polarizing the charged interface [$\Delta_\epsilon=0.951$, Fig. 1(b)], the PE adsorption becomes weaker and the $n(z)$ profile more broadened due to the repulsive image-polyion interaction. For $N_m \leqslant 4$, $n(z)$ presents a maximum at $z=z^* \approx 0.9a$ that can be seen as the *thickness* of the adsorbed PE layer. Interestingly, the monomer density at contact *decreases* with increasing N_m. This is the result of a *combined* effect of (i) chain-entropy loss near the interface and (ii) the N_m-induced image-polyion repulsion. All those features are well illustrated on the microstructures of Fig. 2.

It is instructive to compare the above findings with those obtained for *fully flexible* chains. To do so, we use existing MC data for flexible chains from our previous work[13] where all the parameters, up to the chain flexibility, are identical with those presently employed for rodlike PEs. The comparison is provided in Fig. 3. At $\Delta_\epsilon=0$ [see Fig. 3(a)], the $n(z)$ profiles for flexible and rigid PEs are quasi-identical for $N_m=2$, as it should be. For longer chains ($N_m=8$), we clearly see at $\Delta_\epsilon=0$ that the degree of adsorption as indicated by the value of $n(z)$ near contact is considerably stronger for rigid chains. This feature is due to entropy and electrostatic effects. Indeed, in the bulk and at given degree of polymerization N_m, the chain entropy associated to rigid PEs is much lower than that associated to flexible chains, so that chain-entropy loss upon adsorption is reduced for rigid chains. Secondly and concomitantly, the wall-PE attraction is more efficient for rigid chains than for flexible chains because in the latter case the z *fluctuations* of the charged monomers are more important.

As far as the monomer density at true contact is concerned [i.e., $n(z \to a/2)$], it seems that, for flexible PEs, its value is nearly independent of N_m as already reported in Ref. 13. For a single ionic species of *spherical* shape, a variant of the contact theorem provides the exact relation, $n(a/2) - n(\tau - a/2) = 2\pi\sigma_0^2 l_B$, yielding to $n(a/2) \approx 0.11a^{-3}$, which is surprisingly in remarkable agreement with the value reported in Fig. 3(a) for flexible PE (and rigid ones for $N_m \leqslant 4$). Nonetheless, Fig. 3(a) shows, already with $N_m=8$, a strong deviation from the contact theorem (which in principle only holds for structureless spherical ions) for rigid PEs, as expected.

The scenario becomes qualitatively different when $\Delta_\epsilon=0.951$ [see Fig. 3(b)], where the $n(z)$ profiles for flexible

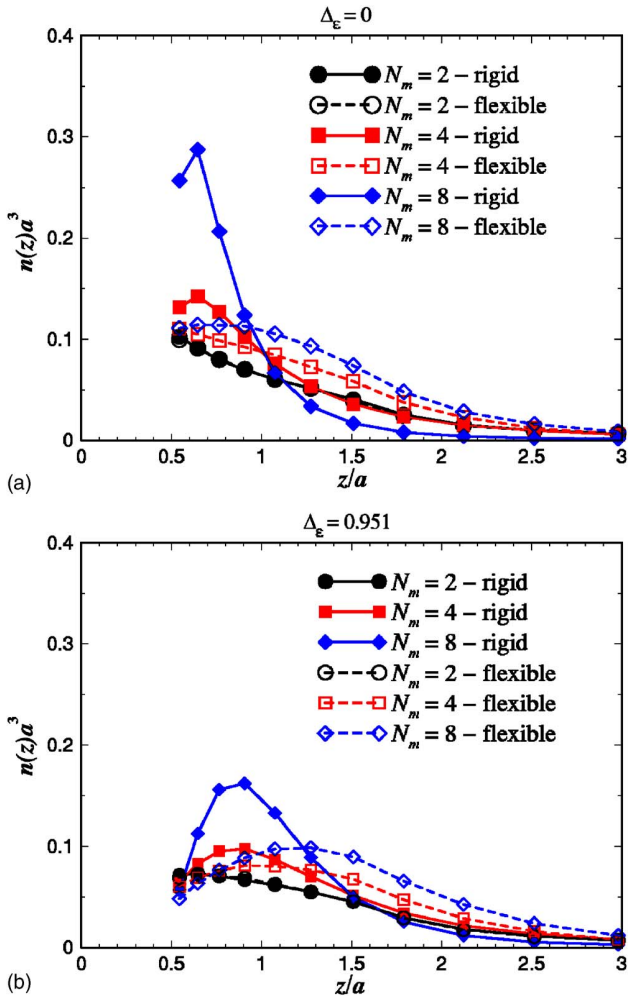

FIG. 3. Comparison between *flexible* and rodlike (rigid) PEs for the profiles of the monomer density $n(z)$ at different chain length N_m. (a) $\Delta_\epsilon=0$. (b) $\Delta_\epsilon=0.951$.

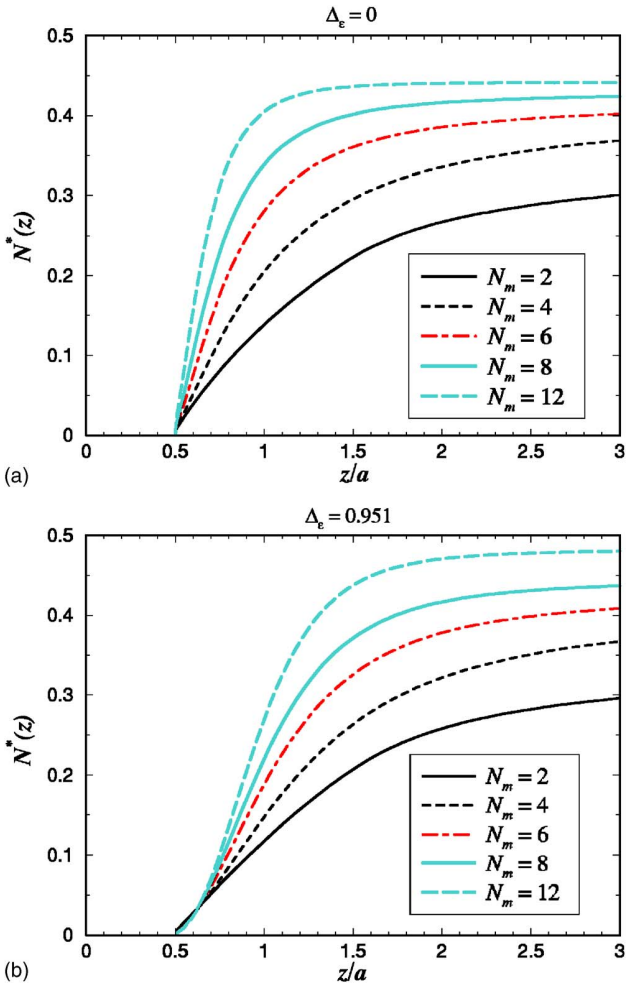

FIG. 4. Profiles of the fraction of adsorbed monomers $N^*(z)$ for different chain length N_m with $\sigma_0 L^2=64$ (systems $A-E$). (a) $\Delta_\epsilon=0$. (b) $\Delta_\epsilon=0.951$. The inset is merely a magnification near contact.

and rigid PEs become more similar. It is to say that the image-polyion repulsion tends to cancel chain-entropy effects. A closer look at Fig. 3(b) reveals, however, that, at given N_m, the degree of PE adsorption is systematically larger for rigid PEs than for flexible ones, as expected. Those relevant findings can be summarized as follows.

- Without dielectric discontinuity ($\Delta_\epsilon=0$) rigid PE chains can much better adsorb than flexible ones at oppositely charged surfaces essentially because of their significant lower chain entropy.
- In the presence of polarization charges ($\Delta_\epsilon=0.951$) the degree of PE adsorption becomes significantly less sensitive to the chain stiffness.

In order to quantify the amount of adsorbed monomers as a function of the distance z from the charged wall, we have also studied $N^*(z)$ as defined by Eq. (9). Our results are reported in Fig. 4. At $\Delta_\epsilon=0$ [see Fig. 4(a)] the fraction of adsorbed monomers $N^*(z)$ is always larger with growing N_m even near the interface. On the other hand, at $\Delta_\epsilon=0.951$ [see Fig. 4(b)], (i) $N^*(z)$ gets smaller with growing N_m near the interface (roughly for $z/a\lesssim 0.65$) and (ii) $N^*(z)$ is considerably reduced compared to the $\Delta_\epsilon=0$ case. For instance (with $N_m=12$), at $z/a=0.9$ (corresponding to a layer thickness at $\Delta_\epsilon=0.951$), $N^*(z)$ can be as large as 0.4 for $\Delta_\epsilon=0$ against only 0.2 for $\Delta_\epsilon=0.951$.

2. PE orientation

To gain further insight into the properties of rodlike PE adsorption, we have plotted $S(z)$ as given by Eq. (11) in Fig. 5 so as to characterize the PE orientation with respect to the charged interface. At $\Delta_\epsilon=0$, Fig. 5(a) shows that in the vicinity of the interface (roughly for $z\lesssim a$), the rodlike PEs tend to be parallel to the interface plane with growing N_m, i.e., $S(z)\to -1/2$ (see also Fig. 2). This effect is obviously due to the electrostatic wall-PE binding whose strength increases linearly with N_m. For the longest chains ($N_m=12$) non-negligible *positive* $S(z)$ values are reported at intermediate distance from the wall (roughly for $2\lesssim z/a\lesssim 6$), signaling a nontrivial orientation correlation with respect to the interface plane that will be properly discussed later. Sufficiently away from the wall, the rodlike PEs are randomly oriented [i.e., $S(z)\to 0$], as it should be.

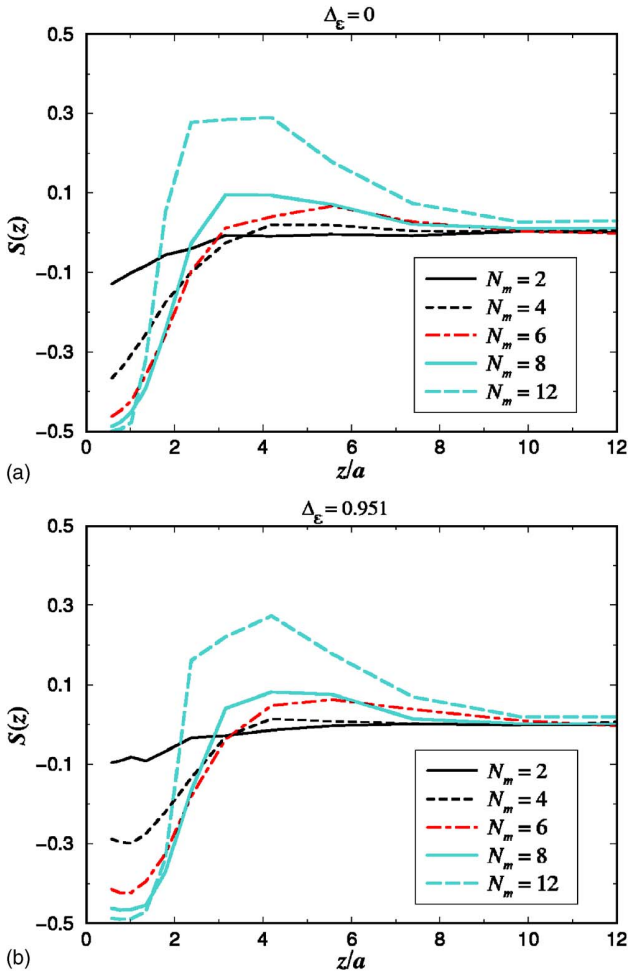

FIG. 5. Profiles of $S(z)$ for different chain length N_m with $\sigma_0 L^2=64$ (systems $A-E$). (a) $\Delta_\epsilon=0$. (b) $\Delta_\epsilon=0.951$.

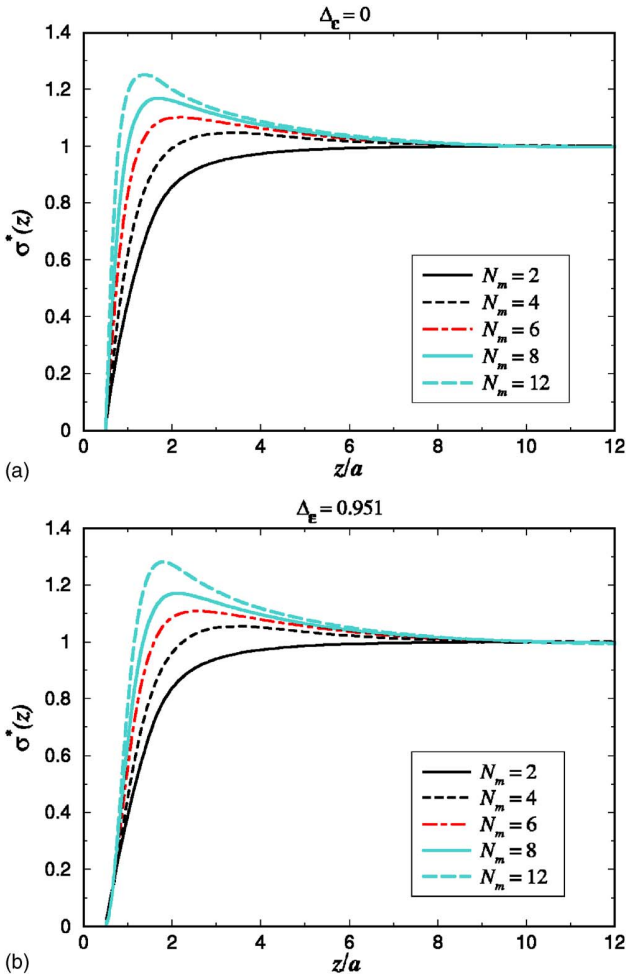

FIG. 6. Profiles of the reduced net fluid charge $\sigma^*(z)$ for different chain length N_m with $\sigma_0 L^2=64$ (systems $A-E$). (a) $\Delta_\epsilon=0$. (b) $\Delta_\epsilon=0.951$.

In the presence of image forces [$\Delta_\epsilon=0.951$, see Fig. 5(b)] the $S(z)$ behavior is more complex. A comparison with Fig. 5(a) corresponding to $\Delta_\epsilon=0$ immediately shows that repulsive image forces tend to inhibit the alignment of the rodlike PEs with respect to the interface plane near contact. This effect will be especially vivid at lower surface-charge density σ_0, as we are going to show later.

The nonmonotonic behavior of $S(z)$ near contact at $\Delta_\epsilon=0.951$, similar to that reported for $n(z)$ in Fig. 1(b), is the result of two antagonistic forces: (i) the repulsive image driving force that scales like $1/z$ and (ii) the attractive wall-monomer one that scales like z. As in the case with $\Delta_\epsilon=0$, (i) the degree of PE-wall parallelism increases with growing N_m near contact and (ii) far enough from the wall the PEs are randomly oriented.

3. Fluid charge

Another interesting property is provided by the net fluid charge parameter $\sigma^*(z)$ [Eq. (13)] that describes the screening of the charged interface. The profiles of $\sigma^*(z)$ for different N_m can be found in Fig. 6. At $\Delta_\epsilon=0$ [see Fig. 6(a)], it is shown that for long enough chains (here $N_m \geqslant 4$) the substrate gets locally *overcharged* as signaled by $\sigma^*(z)>1$. Physically, this means that the (integrated) local charge of the adsorbed monomers[23] is larger in absolute value than that of the substrate's surface charge. In other words, the plate is *overscreened* by the adsorbed PE chains. Fig. 6(a) indicates that the degree of overcharging increases with N_m as expected form the behavior of multivalent counterions. Upon inducing polarization charges [$\Delta_\epsilon=0.951$, see Fig. 6(b)] overscreening is *maintained* and weakly disturbed, proving that the latter is robust against repulsive image forces.

B. Influence of substrate's surface-charge density

To complete our investigation, we would like to address the influence of the substrate-charge density on the PE adsorption. In this respect, we consider (at fixed $N_m=8$) two additional values for the surface-charge density: $\sigma_0 L^2=32$ and 128, corresponding to the systems F and G, respectively (see Table II).

1. Monomer distribution

The plots of the monomer density $n(z)$ for various values of $\sigma_0 L^2$ can be found in Fig. 7. Typical microstructures of systems F and G are sketched in Fig. 8. At $\Delta_\epsilon=0$ [see Fig. 7(a)], the monomer density at contact increases with σ_0, as it should be. Interestingly, the local maximum in $n(z)$, present

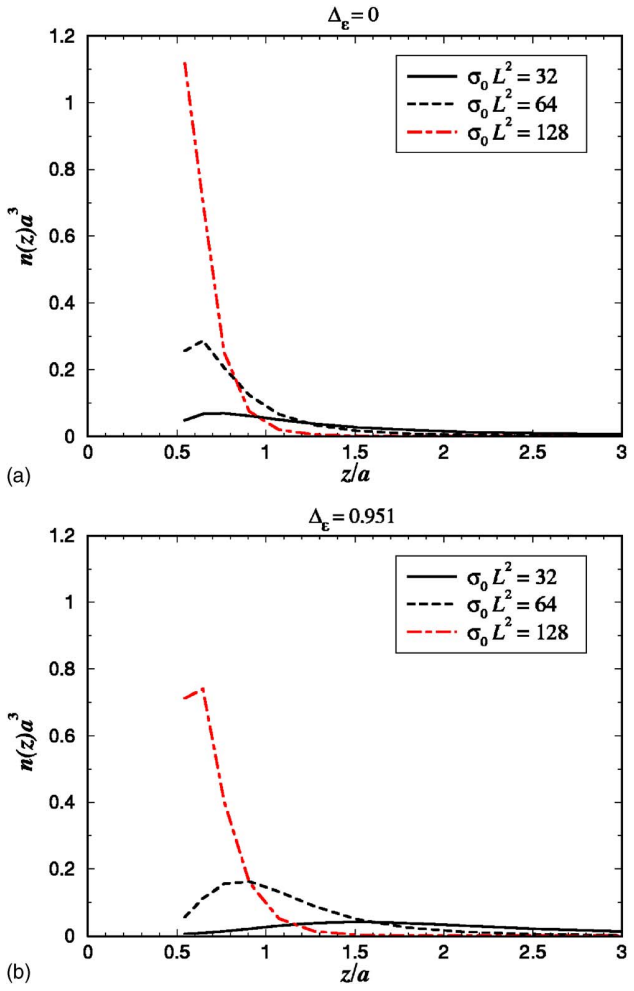

FIG. 7. Profiles of the monomer density $n(z)$ for different parameters of surface-charge density $\sigma_0 L^2$ with $N_m=8$ (systems *D*, *F*, and *G*). The case $\sigma_0 L^2=64$ (system *D*) from Fig. 1 is reported here again for easier comparison. (a) $\Delta_\epsilon=0$. (b) $\Delta_\epsilon=0.951$.

at small σ_0 (here $\sigma_0 L^2 \leqslant 64$), *vanishes at large* σ_0 [see Fig. 7(a)]. This feature is the result of a σ_0-enhanced driving force of adsorption that overcomes chain-entropy effects at large enough σ_0. The strong adsorption at $\sigma_0 L^2=128$ leads to a *flat* PE layer, as well illustrated in Fig. 8.

By polarizing the interface ($\Delta_\epsilon=0.951$), it can be seen from Fig. 7(b) and the snapshot from Fig. 8 that there is a strong monomer depletion near the interface for $\sigma_0 L^2=32$. This feature is due to the combined effects of (i) image-PE repulsion and (ii) a lower electrostatic wall-PE attraction. Upon increasing σ_0 the monomer density near contact becomes larger, and concomitantly, the location of the maximum in $n(z)$ is systematically shifted to smaller z. It is to say that the thickness of the adsorbed PE layer decreases with σ_0. We also expect that, at very large σ_0 (not reported here), this maximum vanishes leading to a purely attractive effective wall-PE interaction.

2. PE orientation

At $\Delta_\epsilon=0$, Fig. 9(a) shows that near the charged interface (when $z \lesssim a$), the degree of parallelism between the rodlike PE and the interface increases with growing σ_0, as indicated

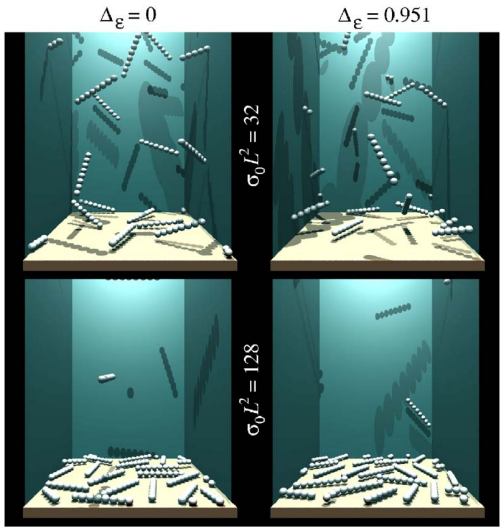

FIG. 8. Typical equilibrium microstructures of systems *F* and *G*. The little counterions are omitted for clarity.

by $S(z)\to -1/2$. This observation is merely due to the electrostatic wall-PE binding whose strength scales like σ_0 at fixed N_m.

In the presence of image forces ($\Delta_\epsilon=0.951$), Fig. 9(b) demonstrates again for $\sigma_0 L^2=32$ [see also Fig. 5(b) for comparison] a strongly nonmonotonic behavior of $S(z)$ near the interface. This feature is fully consistent with the ideas that (i) image forces become especially strong at low σ_0 and (ii) repulsive image forces induce orientational disorder, as previously established. This finding leads to the important general statement: Repulsive image forces at low surface-charge density induce *orientational disorder* near the interface.

3. Fluid charge

The profiles of $\sigma^*(z)$ for different $\sigma_0 L^2$ can be found in Fig. 10. At $\Delta_\epsilon=0$ [see Fig. 10(a)], it is found that the planar interface gets always locally overcharged as signaled by $\sigma^*(z)>1$. The location of the maximum in $\sigma^*(z)$ is shifted to lower z with increasing σ_0.

Upon inducing polarization charges [$\Delta_\epsilon=0.951$, see Fig. 10(b)], overscreening is still there. However, at $\sigma_0 L^2=64$, there is a non-negligible shift of the maximum of about $0.5a$. The distance at which the substrate is compensated [i.e., where $\sigma^*(z)=1$] corresponds to $1.72a$ ($2.54a$) for $\Delta_\epsilon=0$ ($\Delta_\epsilon=0.951$), leading to a neutralization z shift of $0.72a$.

IV. SUMMARY

To conclude, we have performed MC simulations to address the behavior of rodlike polyelectrolytes at oppositely charged planar surfaces. The influence of image forces stemming from the dielectric discontinuity at the charged interface was also analyzed. We have considered a finite and *fixed* monomer concentration in the dilute regime for relatively short chains.

In the absence of image forces ($\Delta_\epsilon=0$), our main findings can be summarized as follows.

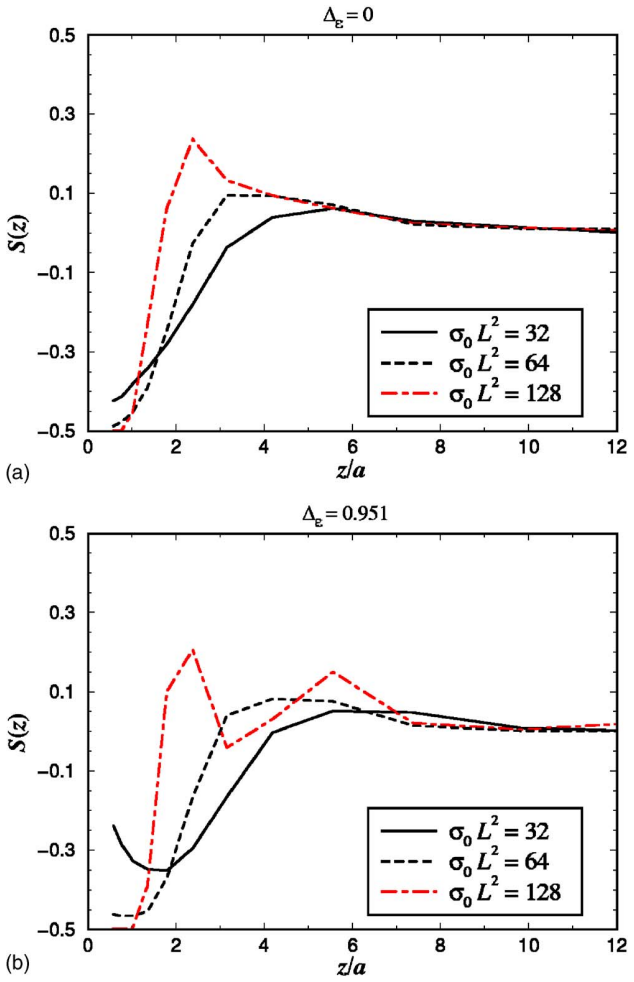

FIG. 9. Same as Fig. 7 but for $S(z)$.

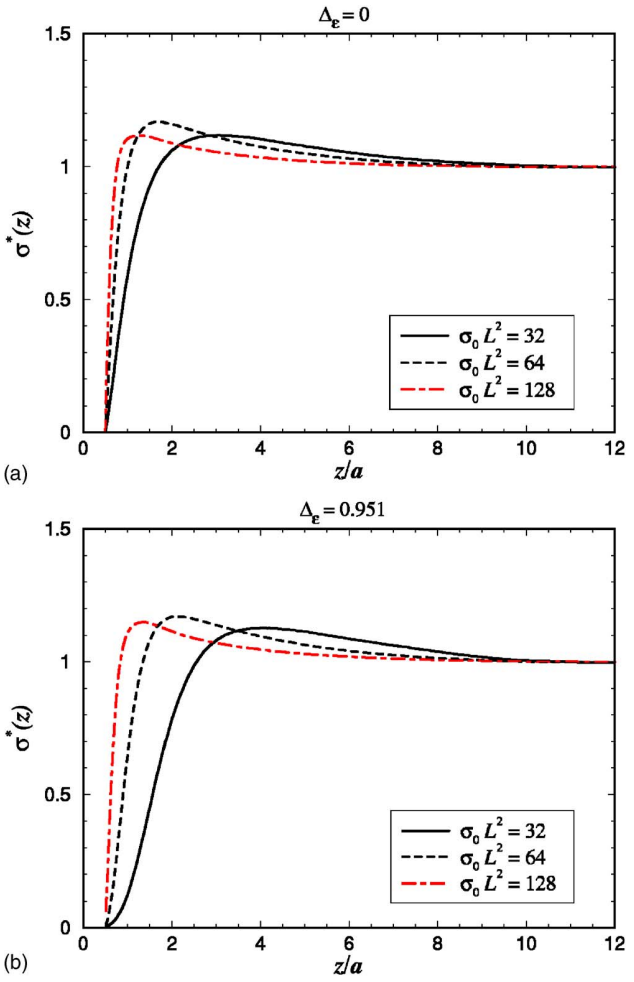

FIG. 10. Same as Fig. 7 but for $\sigma^*(z)$.

- At moderately charged interfaces, only (*very*) short rodlike PEs (here $2 < N_m \leqslant 8$) experience a short-ranged repulsion near the interface. For longer rodlike PEs the effective wall-PE interaction becomes purely attractive. This behavior is in contrast to that occurring with *flexible* PEs, where the chain entropy is larger leading to stronger entropy-driven depletion.
- Near the charged interface, the rodlike PEs get more and more parallel to the interface plane when the chain length N_m is increased. Concomitantly, the strength of the substrate-charge reversal is N_m enhanced.
- Upon increasing the substrate-surface-charge density σ_0 it was demonstrated that: (i) The monomer adsorption is enlarged and the wall-PE effective interaction becomes purely attractive for high enough σ_0. (ii) The degree of parallelism (near the interface) between the interface plane and the rodlike PE is enhanced.

The main effects stemming from repulsive image forces as revealed by this study are as follows.

- The monomer adsorption is reduced at finite Δ_ϵ and the $n(z)$ profiles become similar to those obtained with flexible chains, in contrast to what was reported at $\Delta_\epsilon = 0$.
- Repulsive image forces induce PE orientational disorder near the interface.
- The substrate-charge reversal is robust against repulsive image forces.

ACKNOWLEDGMENTS

The author thanks H. Löwen and R. Blaak for fruitful discussions. Financial support from DFG via LO418/12 and SFB TR6 is also acknowledged.

[1] J. O. Rädler, I. Koltover, T. Salditt, and C. R. Safinya, Science **275**, 810 (1997).
[2] S. P. A. Fodor, Science **277**, 393 (1997).
[3] T. Pfohl, J. H. Kim, M. Yasa *et al.*, Langmuir **17**, 5343 (2001).
[4] T. Pfohl, F. Mugele, R. Seemann, and S. Herminghaus, ChemPhysChem **4**, 1291 (2003).
[5] R. Menes, N. Grønbech-Jensen, and P. A. Pincus, Eur. Phys. J. E **1**, 345 (2000).
[6] R. Menes, P. Pincus, R. Pittman, and N. Dan, Europhys. Lett. **44**, 393 (1998).
[7] P. Sens and J.-F. Joanny, Phys. Rev. Lett. **84**, 4862 (2000).
[8] C. Fleck and H. H. von Grünberg, Phys. Rev. E **63**, 061804 (2001).
[9] H. Cheng and M. Olvera de la Cruz, J. Chem. Phys. **119**, 12635 (2003).
[10] D. A. Hoagland, Macromolecules **23**, 2781 (1990).

[11] R. R. Netz, J. Phys.: Condens. Matter **15**, S239 (2003).
[12] R. R. Netz and J.-F. Joanny, Macromolecules **32**, 9013 (1999).
[13] R. Messina, Phys. Rev. E **70**, 051802 (2004).
[14] R. Messina, Macromolecules **37**, 621 (2004).
[15] A. Grzybowsky and A. Brodka, Mol. Phys. **100**, 1017 (2002).
[16] M. D. Malinsky, K. L. Kelly, G. C. Schatz, and R. P. van Duyne, J. Phys. Chem. B **105**, 2343 (2001).
[17] N. Metropolis, A. W. Rosenbluth, M. N. Rosenbluth, A. H. Teller, and E. Teller, J. Chem. Phys. **21**, 1087 (1953).
[18] M. P. Allen and D. J. Tildesley, *Computer Simulations of Liquids* (Clarendon, Oxford, 1987).
[19] R. Blaak, D. Frenkel, and B. M. Mulder, J. Chem. Phys. **110**, 11652 (1999).
[20] A. Tulpar and W. A. Ducker, J. Phys. Chem. B **108**, 1667 (2004).
[21] G. M. Torrie, J. P. Valleau, and G. N. Patey, J. Chem. Phys. **76**, 4615 (1982).
[22] R. Messina, J. Chem. Phys. **117**, 11062 (2002).
[23] Near the charged wall, the presence of the counterions at $\Delta_\epsilon=0$ is marginal so that the fluid charge is quasiexclusively provided by the charges of the adsorbed monomers. This becomes especially vivid when $N_m \geqslant 4$, where overcharging occurs.

Appendix L

Polyelectrolyte Multilayering on a Charged Sphere

Polyelectrolyte Multilayering on a Charged Sphere

René Messina,* Christian Holm,† and Kurt Kremer‡

Max-Planck-Institut für Polymerforschung, Ackermannweg 10, 55128 Mainz, Germany

Received December 12, 2002. In Final Form: February 24, 2003

The adsorption of highly *oppositely* charged flexible polyelectrolytes on a charged sphere is investigated by means of Monte Carlo simulations in a fashion which resembles the layer-by-layer deposition technique introduced by Decher. Electroneutrality is ensured at each step by the presence of monovalent counterions (anions and cations). We study in detail the structure of the *equilibrium* complex. Our investigations of the first few layer formations strongly suggest that multilayering on a charged colloidal sphere is not possible as an equilibrium process with purely electrostatic interactions. We especially focus on the influence of specific (nonelectrostatic) short-range attractive interactions (e.g., van der Waals) on the stability of the multilayers.

I. Introduction

Polyelectrolyte multilayer thin films are made of alternating layers of polycations (PCs) and polyanions (PAs). The so-called layer by layer method, first introduced in *planar* geometry by Decher, consists of a successive adsorption of the polyions onto a charged surface and has proved to be extremely efficient.[1,2] Due to the many potential technological applications such as biosensing,[3] catalysis,[4] optical devices,[5] etc., this process is nowadays widely used. Various techniques are employed to control the polymer multilayer buildup such as optical[6,7] and neutron[8,9] reflectometry, AFM,[10] UV spectroscopy,[11] NMR techniques,[12] and others. Some experiments (see, e.g., ref 13) were devoted to the basic mechanisms governing polyelectrolyte multilayering on planar mica surfaces where, in particular, the role of surface charge overcompensation was pointed out.

Another very interesting application is provided by the polyelectrolyte coating of *spherical* metallic nanoparticles.[14,15] This process can modify in a well-controlled way the physicochemical surface properties of the colloidal particle. Despite of the huge amount of experimental works, the detailed understanding of the multilayering process is still rather unclear, especially for a charged colloidal sphere. Hence, the study of polyelectrolyte multilayering is motivated by both experimental and theoretical interests.

On the theoretical side, the literature on this subject is rather poor. Based on Debye−Hückel approximations for the electrostatic interactions and including lateral correlations by considering different typical semiflexible polyelectrolyte-layer structures, Netz and Joanny[16] found a remarkable stability of the periodic structure of the multilayers in planar geometry. For weakly charged flexible polyelectrolytes at high ionic strength, qualitative agreements between theory,[17] based on scaling laws, and experimental observations,[9,18] have been provided. The driving force of all these multilayering processes is of electrostatic origin, and it is based on an overcharging mechanism, where the first layer overcharges the macroion and the subsequent layers overcharge the layers underneath. However, the role of nonelectrostatic interactions, though pointed out in refs 17 and 19, is not clear. In particular, it is still open whether the layer buildup is an equilibrium or out of equilibrium process, which resembles more a succession of dynamically trapped states. Therefore, we do not know whether the complex polyelectrolyte is in *thermodynamical equilibrium*. This point has also been emphasized in a recent experimental work on planar multilayers[7] where considerable kinetic effects were reported. So far, there are neither analytical results nor simulation data for multilayering formation onto charged spheres.

The goal of this paper is to study the underlying physics involved in the polyelectrolyte multilayering onto a charged colloidal sphere by means of MC simulations. The paper is organized as follows: section II is devoted to the description of our MC simulation method. The relevant target quantities are specified in section III. The single chain adsorption is studied in section IV, and the polyelectrolyte bilayering in section V. Then the multi-

* Corresponding author. E-mail: messina@thphy.uni-duesseldorf.de. Permanent address: Institut für theoretische Physik II, Heinrich-Heine-Universität Düsseldorf, Universitätsstrasse 1, D-40225 Düsseldorf, Germany.

† E-mail: holm@mpip-mainz.mpg.de.

‡ E-mail: kremer@mpip-mainz.mpg.de.

(1) Schmitt, J.; Decher, G.; Hong, G. *Thin Solid Films* **1992**, *210/211*, 831.
(2) Decher, G. *Science* **1997**, *277*, 1232−1237.
(3) Caruso, F.; Furlong, D. N.; Ariga, K.; Ichinose, I.; Kunitake, T. *Langmuir* **1997**, *14*, 4559−4565.
(4) Onda, M.; Ariga, K.; Kunitake, T. *Biosci. Bioeng.* **1999**, *87*, 69−75.
(5) Wu, A.; Yoo, D.; Lee, J. K.; Rubner, M. F. *J. Am. Chem. Soc.* **1999**, *121*, 4883−4891.
(6) Dijt, J. C.; Cohen-Stuart, M. A.; Fleer, G. J. *J. Adv. Colloid Interface Sci.* **1994**, *50*, 79−101.
(7) Kovacevic, D.; van der Burgh, S.; Cohen-Stuart, M. A. *Langmuir* **2002**, *18*, 5607−5612.
(8) Schmitt, J.; Grünewald, T.; Decher, G.; Pershan, PS.; Kjaer, K.; Lösche, M. *Macromol.* **1993**, *26*, 7058−7063.
(9) Lösche, M.; Schmitt, J.; Decher, G.; Bouwman, W. G.; Kjaer, K. *Macromolecules* **1998**, *31*, 8893−8906.
(10) McAloney, R. A.; Sinyor, M.; Dudnik, V.; Goh, M. C. *Langmuir* **2001**, *17*, 6655−6663.
(11) Schoeler, B.; Kumaraswamy, G.; Caruso, F. *Macromolecules* **2002**, *35*, 889−897.
(12) McCormick, M.; Smith, R.; Graf, R.; Barrett C. J.; Reven, L.; Spiess, H. W. Preprint.
(13) Lowack, K.; Helm, C. A. *Macromolecules* **1998**, *31*, 823−833.
(14) Caruso, F.; Carsuo, R. A.; Möhlwald, H. *Science* **1998**, *282*, 1111−1114.
(15) Gittins, D. I.; Caruso, F. *J. Phys. Chem. B* **2001**, *105*, 6846−6852.
(16) Netz, R. R.; Joanny, J. F. *Macromolecules* **1999**, *32*, 9013−9025.
(17) Castelnovo, M.; Joanny, J. F. *Langmuir* **2000**, *16*, 7524−7532.
(18) Farhat, T.; Yassin, G.; Dubas, S. T.; Schlenoff, J. B. *Langmuir* **1999**, *15*, 6621−6623.
(19) Joanny, J. F. *Eur. Phys. J. B* **1999**, *9*, 117−122.

10.1021/la026988n CCC: $25.00
Published on Web 04/12/2003

layering process is investigated in section VI. The case of short polyelectrolyte chains is considered in section VII. Finally, section VIII contains some brief concluding remarks.

II. Simulation Method

The setup of the system under consideration is very similar to those recently investigated by means of molecular dynamics simulations.[20,21] Within the framework of the primitive model we consider one charged colloidal sphere characterized by a radius a (=4.5σ) and a bare charge $Q_M = -Z_M e$ (where e is the elementary charge and $Z_M = 40$) surrounded by Z_M neutralizing monovalent ($Z_c = 1$) counterions and an implicit solvent (water) of relative dielectric permittivity $\epsilon_r \approx 80$. In the remainder of the paper, we will refer to the term *macroion* as the charged colloidal sphere. Polyelectrolyte chains (N_+ PCs and N_- PAs) are made up of N_m *monovalent* monomers ($Z_m = 1$) of diameter σ. For the sake of simplicity, we only consider here symmetrical complexes where PC and PA chains have the same length and carry the same charge in absolute value. To each charged PC or PA we also add N_m small *monovalent* ($Z_c = 1$) counterions (anions and cations countering the charge of the polyelectrolytes) of diameter σ; hence, always a charge neutral entity was added. Thereby all the microions have the same valence $Z = Z_c = Z_m = 1$ as well as the same diameter σ. Added salt of course would even weaken the effects observed and would be especially important for the case of an adsorption interaction between macroion and polyelectrolyte.

All these particles making up the system are confined in an impermeable spherical cell of radius $R = 60\sigma$. The spherical macroion is held fixed and located at the center of the cell. To avoid the appearance of image charges,[22] we assume that the macroion has the same dielectric constant as the solvent.

Standard canonical MC simulations following the Metropolis scheme were used.[23,24]

The total energy of interaction of the system can be written as

$$U_{tot} = \sum_{i,i<j} U_{hs} + U_{coul} + U_{FENE} + U_{LJ} + U_{vdw} \quad (1)$$

where all the contributions of the pair potentials in eq 1 are described in detail below.

Excluded volume interactions are modeled via a hard sphere potential U_{hs}[25] defined as follows

$$U_{hs}(r) = \begin{cases} \infty, & \text{for } r < r_{cut} \\ 0, & \text{for } r \geq r_{cut} \end{cases} \quad (2)$$

where $r_{cut} = \sigma$ for the microion−microion excluded volume interaction, and $r_{cut} = a + \sigma/2$ for the macroion−microion excluded volume interaction. Hence the center−center distance of closest approach between the macroion and a microion is $r_0 = a + \sigma/2 = 5\sigma$.

The pair electrostatic interaction between two ions i and j (where i and j can be either a microion or the macroion) reads

$$U_{coul}(r_{ij}) = \pm k_B T l_B \frac{Z_i Z_j}{r_{ij}} \quad (3)$$

where +(−) applies to charges of the same (opposite) sign and $l_B = e^2/4\pi\epsilon_0\epsilon_r k_B T$ is the Bjerrum length corresponding to the distance at which two elementary charges interact with $k_B T$. To link our simulation parameters to experimental units and room temperature ($T = 298$ K), we choose $\sigma = 4.25$ Å, leading to the Bjerrum length of water $l_B = 1.68\sigma = 7.14$ Å and to a macroion surface charge density of 0.14 Cm^{-2}.

The polyelectrolyte chain connectivity is modeled by using a standard FENE potential in good solvent (see, e.g., ref 26), which reads

$$U_{FENE}(r) = \begin{cases} -\frac{1}{2}\kappa R_0^2 \ln\left[1 - \frac{r^2}{R_0^2}\right], & \text{for } r < R_0 \\ \infty, & \text{for } r \geq R_0 \end{cases} \quad (4)$$

where we chose $\kappa = 27 k_B T/\sigma^2$ and $R_0 = 1.5\sigma$. The excluded volume interaction between chain monomers is taken into account via a purely repulsive Lennard-Jones (LJ) potential given by

$$U_{LJ}(r) = \begin{cases} 4\epsilon\left[\left(\frac{\sigma}{r}\right)^{12} - \left(\frac{\sigma}{r}\right)^{6}\right] + \epsilon, & \text{for } r \leq 2^{1/6}\sigma \\ 0, & \text{for } r > 2^{1/6}\sigma \end{cases} \quad (5)$$

where $\epsilon = k_B T$. These parameters lead to an equilibrium bond length $l = 0.98\sigma$.

An important interaction in the multilayering process addressed in this study is the *non*-electrostatic *short ranged attraction*, U_{vdw}, between the macroion and the PC chain. To account for this kind of interaction, we choose without loss of generality a van der Waals (VDW) potential of interaction between the macroion and a PC monomer that is given by

$$U_{vdw}(r) = -\epsilon\chi_{vdw}\left(\frac{\sigma}{r - r_0 + \sigma}\right)^6, \quad \text{for } r \geq r_0 \quad (6)$$

where χ_{vdw} is a positive dimensionless parameter describing the strength of the attraction. Thereby, at contact (i.e., $r = r_0$), the magnitude of the attraction is $\chi_{vdw}\epsilon = \chi_{vdw} k_B T$, and for $\chi_{vdw} = 1$, one recovers the standard attractive component of the LJ-potential (see eq 5). Since it is not straightforward to link this strength of adsorption directly to experimental values, we therefore investigated different possible strengths of attraction, which are known to be realistic for soft matter systems.

All the simulation parameters are gathered in Table 1. The set of simulated systems can be found in Table 2. Single-particle moves were considered with an acceptance ratio of 20−30% for the monomers and 50% for the counterions. At equilibrium, the (average) length of the trial moves Δr are about 30σ for the counterions and 0.1σ for the monomers. About 10^5−10^6 MC steps per particle were required for equilibration, and about 2×10^6 subsequent MC steps were used to perform measurements.

III. Target Quantities

Before presenting the results, we briefly describe the different observables that are going to be measured. Of

(20) Messina, R.; Holm, C.; Kremer, K. *Phys. Rev. E* **2002**, *65*, 041805.
(21) Messina, R.; Holm, C.; Kremer, K. *J. Chem. Phys.* **2002**, *117*, 2947−2960.
(22) Messina, R. *J. Chem. Phys.* **2002**, *117*, 11062−11074.
(23) Metropolis, N.; Rosenbluth, A. W.; Rosenbluth, M. N.; Teller, A. N.; Teller, E. *J. Chem. Phys.* **1953**, *21*, 1087.
(24) Allen, M. P.; Tidelsey, D. J. *Computer Simulations of Liquids*; Clarendon Press: Oxford, England, 1987.
(25) Only the monomer−monomer excluded volume interaction was not modeled by a hard-sphere potential. There, a purely repulsive Lennard-Jones potential was used.
(26) Kremer, K. *Computer Simulation in Chemical Physics*; Kluwer Academic Publishers: Amsterdam, 1993.

Table 1. Model Simulation Parameters with Some Fixed Values

parameters	
$T = 298$ K	room temp
$Z_M = 40$	macroion valence
$Z = 1$	microion valence
$\sigma = 4.25$ Å	microion diameter
$l_B = 1.68\sigma = 7.14$ Å	Bjerrum length
$a = 4.5\sigma$	macroion radius
$r_0 = a + \sigma/2 = 5\sigma$	macroion−microion dist of closest approach
$R = 60\sigma$	radius of the outer simulation cell
N_+	no. of PCs
N_-	no. of PAs
$N_{PE} = N_+ + N_-$	total no. of polyelectrolyte chains
N_m	no. of monomers per chain
χ_{vdw}	strength of the specific van der Waals attraction

Table 2. System Parameters

system	N_{PE}	N_+	N_-	N_m
A	1	1	0	80
B	2	1	1	80
C	3	2	1	80
D	4	2	2	80
E	5	3	2	80
F	6	3	3	80
G	12	6	6	80
H	40	20	20	10

[a] The number of counterions (cations and anions) ensuring the overall electroneutrality of the system is not indicated.

first importance, we compute the radial density of monomers $n_\pm(r)$ around the spherical macroion normalized as follows

$$\int_{r_0}^{R} 4\pi r^2 n_\pm(r)\, dr = N_\pm N_m \tag{7}$$

where (+)− applies to PCs (PAs). This quantity is of special interest to characterize the degree of ordering in the vicinity of the macroion surface.

The total number of accumulated monomers $\bar{N}_\pm(r)$ within a distance r from the macroion center is then given by

$$\bar{N}_\pm(r) = \int_{r_0}^{r} 4\pi r'^2 n_\pm(r')\, dr' \tag{8}$$

where (+)− applies to PCs (PAs). This observable will be used for the study of the adsorption of (i) a single PC chain (section IV) and (ii) two oppositely charged polyelectrolytes (section V).

Another quantity of special interest is the global *net fluid charge* $Q(r)$ which is defined as follows

$$Q(r) = \int_{r_0}^{r} 4\pi r'^2 Z[\tilde{n}_+(r') - \tilde{n}_-(r')]\, dr' \tag{9}$$

where $\tilde{n}_+$ ($\tilde{n}_-$) include the density of all the positive (negative) microions. Thus, $Q(r)$ corresponds to the total fluid charge (omitting the macroion bare charge Z_M) within a distance r from the macroion center, and at the cell wall $Q(r = R) = Z_M$. Up to a factor proportional to $1/r^2$, $[Q(r) - Z_M]$ gives (by simple application of the Gauss theorem) the mean electric field at r. Therefore, $Q(r)$ can measure the strength of the macroion charge screening by the charged species present in its surrounding solution.

IV. Single Chain Adsorption

In this part, we study the adsorption of a single long PC chain (system A) for different couplings χ_{vdw}. Experimentally, this would correspond to the process of the *first* polyelectrolyte layer formation.

The monomer density $n_+(r)$ and fraction $\bar{N}_+(r)/N_m$ are depicted in Figure 1, parts a and b, respectively. The density $n_+(r)$ near contact ($r \sim r_0$) increases considerably with χ_{vdw} as expected. At a radial distance of 1.5σ from the macroion surface (i.e., $r = r_0 + \sigma$), more than 97% of the monomers are adsorbed for sufficiently large χ_{vdw} (here $\chi_{vdw} > 3$) against only 78% for $\chi_{vdw} = 0$.

The net fluid charge $Q(r)$ is reported in Figure 2. In all cases, we observe a macroion charge reversal (i.e., $Q(r)/Z_M > 1$), as expected from previous studies[27,28] addressing only $\chi_{vdw} = 0$. The position $r = r^*$ at which $Q(r^*)$ gets its maximal value decreases with χ_{vdw}, due to the χ_{vdw}-enhanced adsorption of the chain. This *overcharging* increases with χ_{vdw}, since the gain in energy by macroion-monomer VDW interactions can better overcome (the higher χ_{vdw}) the cost of the self-energy stemming from the adsorbed excess charge. Note that the maximal value of charge reversal of 100% allowed by the total PC charge (i.e., $Q(r^*)/Z_M = 2$) cannot be reached due to a slight accumulation of microanions.

Typical equilibrium configurations can be found in Figure 3. For all χ_{vdw} values, there is a wrapping of the chain around the macroion. In parallel, one can clearly see that the formation of chain loops is gradually inhibited by increasing χ_{vdw}.

Although all the obtained results are intuitively easy to understand, they will turn out to be helpful in order to have a quantitative analysis of the effect of an extra short-range attraction already on the level of a single chain adsorption.

V. Adsorption of Two Oppositely Charged Polyelectrolytes

We now consider the case where we have additionally a PA chain (system B), so that we have a neutral polyelectrolyte complex (i.e., one PC and one PA). Experimentally this would correspond to the process of the *second* polyelectrolyte layer formation (with system A as the initial state). We stress the fact that this process is fully reversible for the parameters investigated in our present study. In particular, we checked that the same final *equilibrium* configuration is obtained either by (i) starting from system A and then adding a PA or (ii) starting with no chains and then adding the two oppositely charged polyelectrolytes, together with their counterions, simultaneously.

The monomer density $n_\pm(r)$ and fraction $\bar{N}_\pm(r)/N_m$ are depicted in Figure 4. parts a and b, respectively. The corresponding microstructures are sketched in Figure 5. The density of PC monomers $n_+(r)$ near contact ($r \sim r_0$) increases considerably with χ_{vdw} as expected. However, a comparison with system A (see Figure 1) indicates that the adsorption of PC monomers (at given χ_{vdw}) is weaker when an additional PA is present. This is consistent with the idea that the PC chain tends to build up a globular state by getting complexed to the PA chain. This feature is well illustrated in Figure 5. More precisely, for sufficiently small $\chi_{vdw} \lesssim 1$, the polyelectrolyte globular state is highly favorable compared to the "flat" bilayer state (see also Figure 5). Nevertheless, at sufficiently large $\chi_{vdw} \gtrsim 2$, the first layer made up of PC monomers is sufficiently stable to produce a second layer made up of PA monomers. Thereby, the two chains wrap around the macroion. As far as the PA monomer adsorption is concerned, Figure

(27) Wallin, T.; Linse, P. *Langmuir* **1996**, *12*, 305−314.
(28) Wallin, T.; Linse, P. *J. Phys. Chem.* **1996**, *100*, 17873−17880.

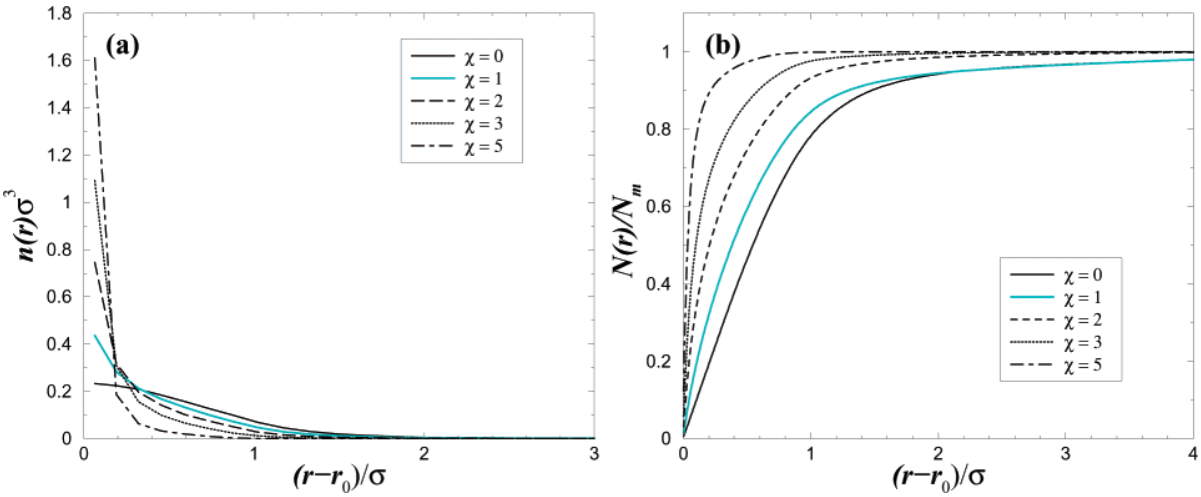

Figure 1. Monomer adsorption profiles of a single PC-chain (system A) at different χ_{vdw} couplings: (a) radial density $n_+(r)$; (b) fraction of monomers $\bar{N}_+(r)/N_m$.

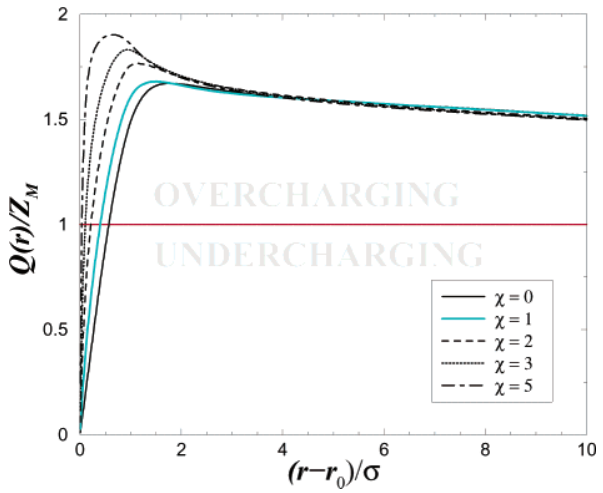

Figure 2. Net fluid charge $Q(r)$ for system A at different χ_{vdw} couplings. The horizontal line corresponds to the isoelectric point.

4 shows that $n_-(r)$ always increases with χ_{vdw}. For $\chi_{vdw} = 0$, the polyelectrolyte complex is very close to the globular polyelectrolyte *bulk* state (i.e., in the absence of the macroion). This a nontrivial result, since naively one would expect a "true" multilayering for any χ_{vdw}. It is only for large $\chi_{vdw} \gtrsim 3$ that one gets a true bilayer formation, where there is a pronounced peak in $n_-(r)$ around $r - r_0 \approx \sigma$.

It is useful to introduce the following dimensionless interaction parameters $\Gamma_M = Z_M Z(l_B/r_0)$, which measures the strength of the macroion−PC electrostatic attraction, and $\Gamma_m = Z^2(l_B/\sigma)$ which controls the PC−PA complex interaction. For large values of Γ_m the bulk complex will always be in a globular state, since then the Coulomb interaction will give rise to a chain collapse, similar to those seen in polyelectrolyte systems. Thus, for a sufficiently large value of Γ_m/Γ_M at given χ_{vdw}, the globular state will always be favorable and no bilayering can occur. In this case *unwrapping* occurs, similar to the microstructures depicted in Figure 5, parts a and b. On the other hand, we find at fixed parameters Γ_m and Γ_M, that one needs a sufficiently large value χ^*_{vdw}, to achieve bilayering.

One can summarize these important results as follows:

•The equilibrium *bilayering* process on a spherical charged colloid with long polyelectrolyte chains requires a sufficiently strong extra short-ranged macroion−PC attraction.

A closer look at Figure 4b reveals a further nontrivial behavior in the profiles of $\bar{N}_\pm(r)$ at high χ_{vdw}. Very close to the macroion surface we always have a monotonic behavior of the fraction of adsorbed PC $[\bar{N}_+(r; \chi_{vdw})]$ and PA monomers $[\bar{N}_-(r; \chi_{vdw})]$ with respect to χ_{vdw} as it should be. However, for a certain distance away from the surface we observe an unexpected behavior where $\bar{N}_+(r; \chi_{vdw} = 3) > \bar{N}_+(r; \chi_{vdw} = 5)$ as well as $\bar{N}_-(r; \chi_{vdw} = 3) > \bar{N}_-(r; \chi_{vdw} = 5)$. One can qualitatively explain this effect by the onset of the formation of one (or several) polyelectrolyte microglobule(s), i.e., small cluster(s) of oppositely charged monomers (see Figure 5, parts d and e). This is indeed possible because at high χ_{vdw} in principle more PC (and consequently also PA) monomers want to get close to the macroion surface. Already for neutral chains a two-dimensional flat adsorbed chain needs a high (surface) binding energy. Compared to bulk conformations the chain entropy is roughly reduced by $k_B T N \ln(q_{d=2}/q_{d=3})$. Here q is the effective number of conformational degrees of freedom of a bond, giving that $\ln(q_{d=2}/q_{d=3}) = O(1)$. Thus, local microglobules that induce a small local desorption, are entropically much more favorable. Also, on the level of the energy, an increase of q concomitantly favors the PC−PA microglobule.

The net fluid charge $Q(r)$ is reported in Figure 6. For $\chi_{vdw} \gtrsim 2$, the macroion gets even overcharged and undercharged as one gets away from its surface, whereas for low χ_{vdw} no *local* overcharging occurs. Again, at high χ_{vdw} the strength of the charge oscillation is not a monotonic function of χ_{vdw} where we observe a higher local overcharging (and undercharging) with $\chi_{vdw} = 3$ than with $\chi_{vdw} = 5$. This latter feature is fully consistent with the profiles of $\bar{N}_\pm(r)$ (see Figure 4b) previously discussed.[29] However this onset of local (surface) microglobules (for $\chi_{vdw} = 5$) is not strong enough to produce a nonmonotonic behavior of r^* with respect to χ_{vdw}.

VI. Multilayering

We now turn to the case where there are many polyelectrolytes (with $N_{PE} \geq 3$) in the system. We recall

(29) Here we assume the presence of little counterions to be negligible in the vicinity of the macroion surface, which is a very good approximation.

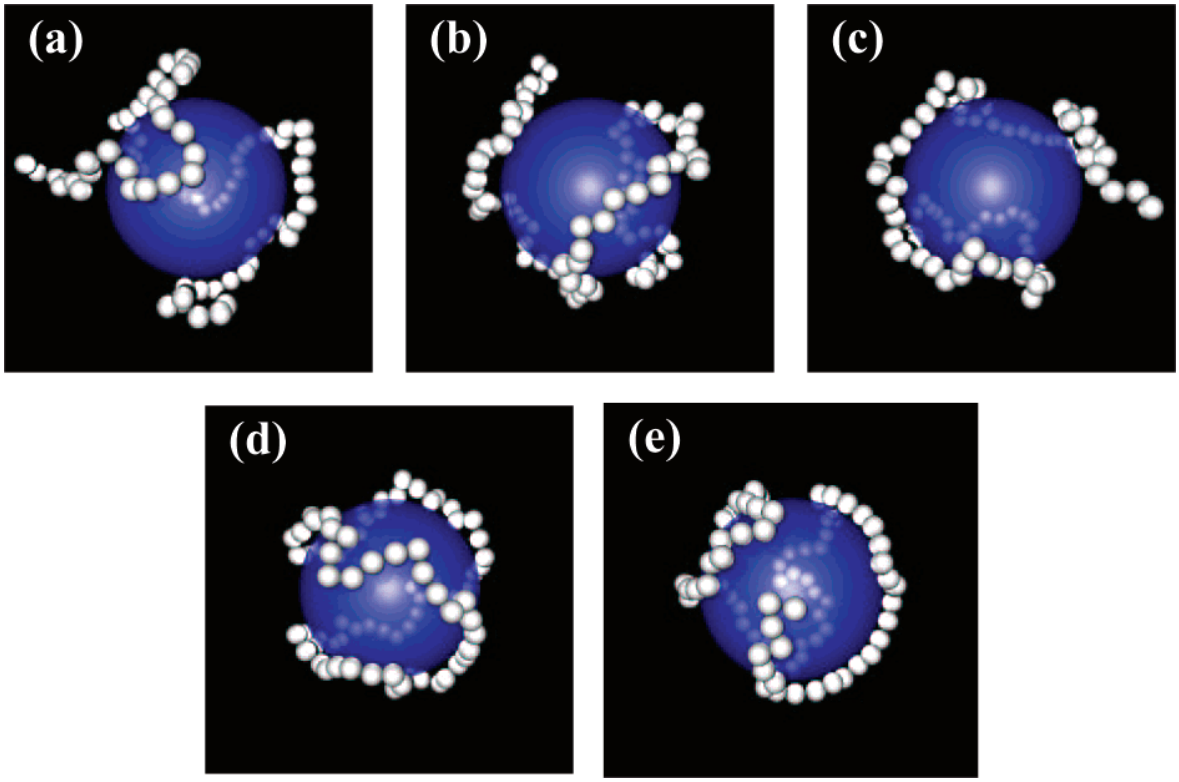

Figure 3. Typical equilibrium configurations for a single PC adsorbed onto an oppositely charged macroion (system A). The little ions are omitted for clarity. (a) $\chi_{vdw} = 0$ (b) $\chi_{vdw} = 1$ (c) $\chi_{vdw} = 2$ (d) $\chi_{vdw} = 3$ (e) $\chi_{vdw} = 5$.

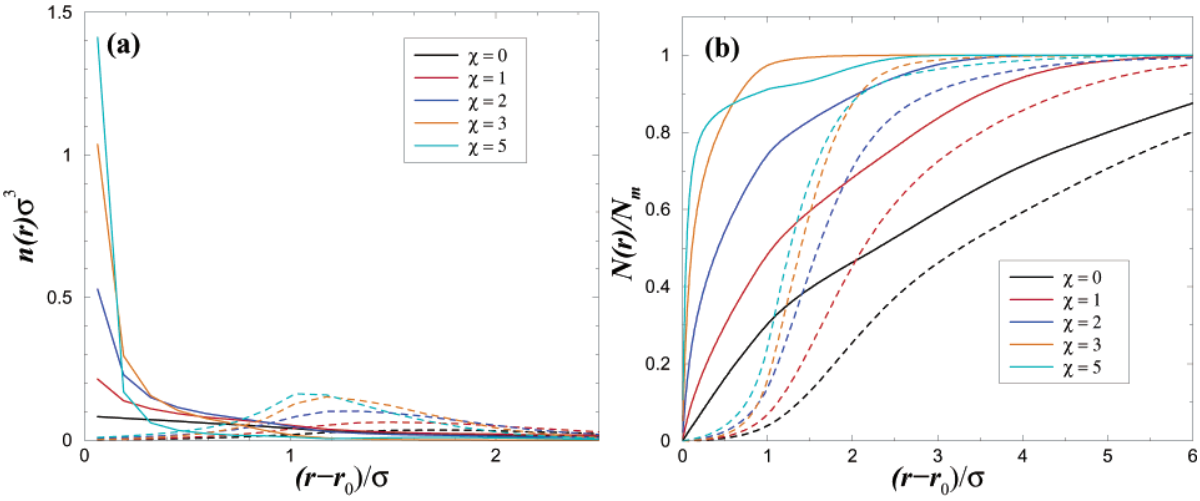

Figure 4. Monomer adsorption profiles of two polyelectrolyte chains (system B) at different χ_{vdw} couplings. The solid and dashed lines correspond to PC and PA monomers, respectively. Key: (a) radial density $n_{\pm}(r)$; (b) fraction of monomers $N_{\pm}(r)/N_m$.

that when $\chi_{vdw} \neq 0$, the VDW interaction concern monomers of all PCs lying within the range of interaction. To keep the number of plots manageable, we will present our results obtained for $\chi_{vdw} = 0$ and $\chi_{vdw} = 3$. The case $\chi_{vdw} = 0$ is (conceptually) important since it corresponds to the situation where only purely electrostatic interactions are present. The other case $\chi_{vdw} = 3$ seems to be a reasonable choice, since we found a "true" bilayering for that value. Moreover, such a strength should be easily accessible experimentally.

A. Adsorption with $\chi_{vdw} = 0$. The density profiles of $n_{\pm}(r)$ for the systems A−G (with $\chi_{vdw} = 0$) are reported in Figure 7, and the corresponding microstructures are sketched in Figure 8.

Figure 7 shows that when the total polyelectrolyte charge

$$Q_{PE} \equiv (N_+ - N_-)N_m e \qquad (10)$$

is zero, the density of PC monomers $n_+(r)$ near contact is lower than when charge $Q_{PE} = N_m e$ (recalling that our systems are such that $Q_{PE} = 0$ or $N_m e$). This tendency [lower $n_+(r)$ near contact with $Q_{PE} = 0$] gradually decreases as the total number N_{PE} of polyelectrolytes is increased. In particular, for system G, where $N_{PE} = 12$ and $Q_{PE} = 0$, the density $n_+(r)$ near contact is nearly identical to that of systems A, C, and E where $Q_{PE} = N_m e$. On the other hand, when $Q_{PE} = N_m e$, then $n_+(r)$ near contact is nearly

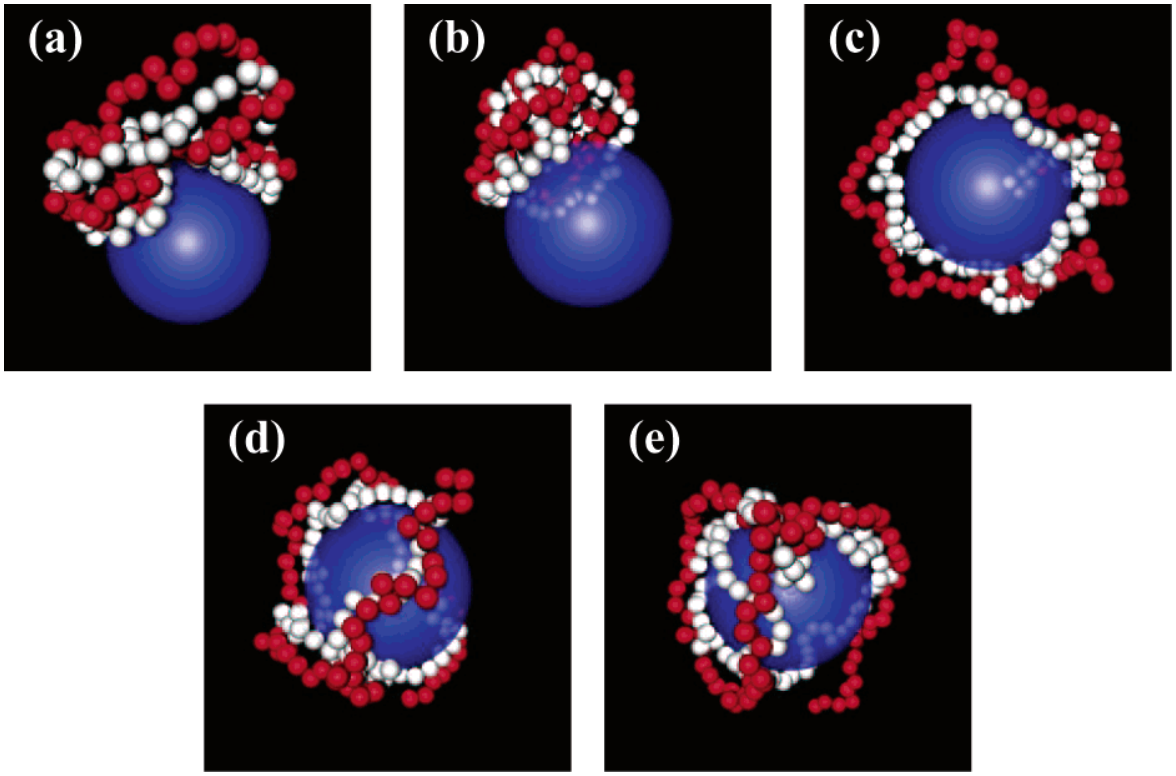

Figure 5. Typical equilibrium configurations for one PC (in white) and one PA (in red) adsorbed onto the charged macroion (system B). The little ions are omitted for clarity. (a) $\chi_{vdw} = 0$ (b) $\chi_{vdw} = 1$ (c) $\chi_{vdw} = 2$ (d) $\chi_{vdw} = 3$ (e) $\chi_{vdw} = 5$.

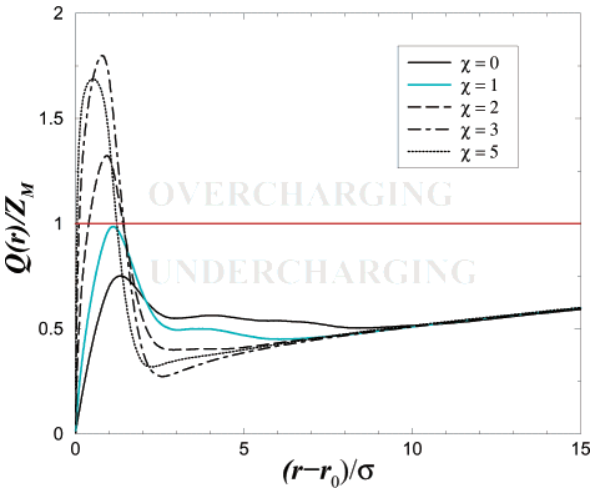

Figure 6. Net fluid charge $Q(r)$ for system B at different χ_{vdw} couplings. The horizontal line corresponds to the isoelectric point.

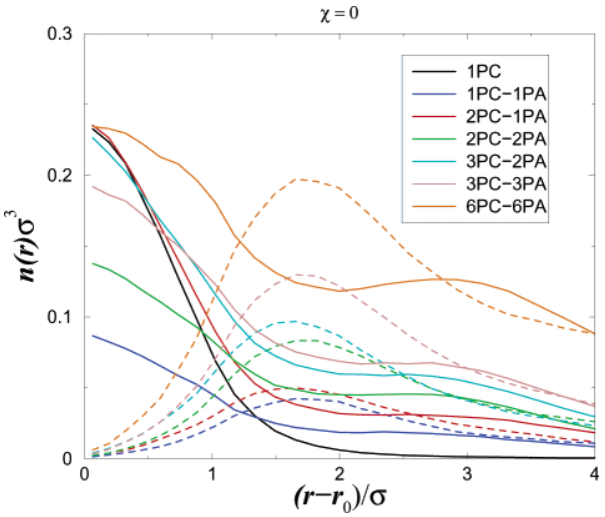

Figure 7. Radial monomer density for the systems A−G with $\chi_{vdw} = 0$. The solid and dashed lines correspond to $n_+(r)$ and $n_-(r)$, respectively. The number of PC and PA chains is indicated. The plots of $n_\pm(r)$ for the systems A (1PC) and B (1PC-1PA) are again reported here for direct comparison.

independent of N_{PE}. The height of the peak in the PA monomer density $n_-(r)$ *increases monotonically* with N_{PE}. Concomitantly, a *third* layer made of PC monomers builds up for high enough N_{PE}. This multilayering is especially remarkable for $N_{PE} = 12$ (system G).

All these features concerning the *first* layer structure can be rationalized with simple ideas. When $Q_{PE} = 0$, then the resulting global attraction between the macroion and the polyelectrolyte complex is much weaker than when $Q_{PE} = N_m e$. In this latter situation, where $Q_{PE} = N_m e$, this excess charge carried by a PC chain leads to a relatively strong PC adsorption near the surface. The equilibrium configurations sketched in Figure 8 suggest a wrapping from the PC monomers when $Q_{PE} = N_m e$ (see Figure 8, parts a and c) and a (partial) *unwrapping* when $Q_{PE} = 0$ [see Figure 8, parts b and d). Even for high $N_{PE} = 12$ (see Figure 8e), we can see this tendency of unwrapping leading to a polyelectrolyte complex globular state. However, for symmetry reasons, when the total number of monomers is large enough as it is the case with $N_{PE} = 12$, the distribution of the polyelectrolyte complex gets more isotropic leading to a weaker unwrapping at $Q_{PE} = 0$.

The collapse into a globular polyelectrolyte complex becomes even more spectacular when σ is reduced (i.e., larger Γ_m).[30] In that case (not reported here), we found a

(30) Messina, R. Unpublished data.

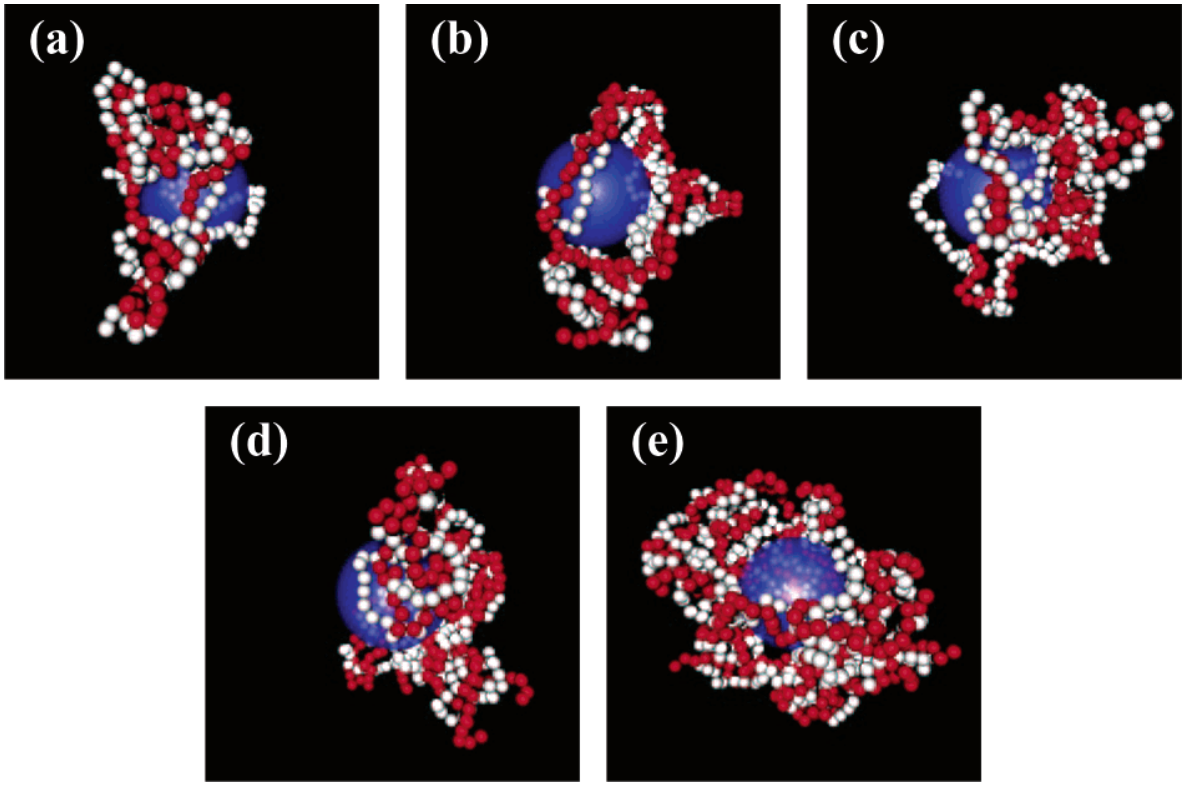

Figure 8. Typical equilibrium configurations for *many* polyelectrolyte chains adsorbed onto the charged macroion with $\chi_{vdw} = 0$. The PC monomers are in white and PA ones in red. The little ions are omitted for clarity. (a) 2PC-1PA (system C) (b) 2PC-2PA (system D) (c) 3PC-2PA (system E) (d) 3PC-3PA (system F) (e) 6PC-6PA (system G).

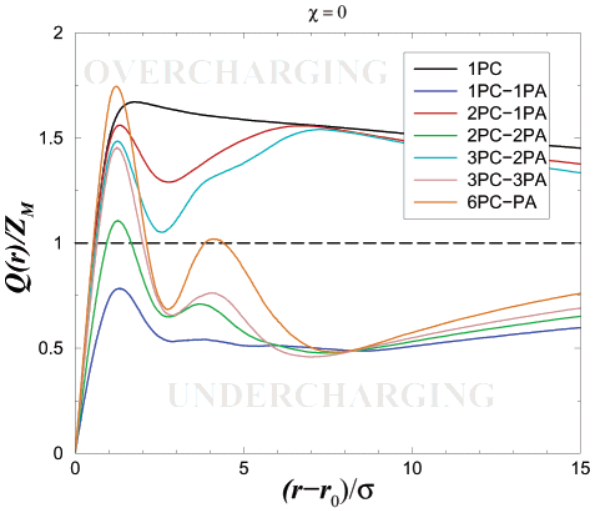

Figure 9. Net fluid charge $Q(r)$ for the systems A−G with $\chi_{vdw} = 0$. The number of PC and PA chains is indicated. The plots for the systems A (1PC) and B (1PC-1PA) are again reported here for direct comparison. The horizontal line corresponds to the isoelectric point.

wrapping (for $Q_{PE} = N_m e$) similar to that depicted in Figure 8, parts a and c, and a *strong* unwrapping (for $Q_{PE} = 0$) where the compact neutral polyelectrolyte complex is adsorbed onto a small area of the colloid.

The net fluid charge $Q(r)$ is reported in Figure 9. As expected one detects an overcharging and undercharging for $Q_{PE} = N_m e$ and $Q_{PE} = 0$, respectively. For $Q_{PE} = 0$, the macroion is also locally overcharged very close to the macroion surface and its strength increases with N_{PE}. On the other hand, the strength of the undercharging (occurring at the largest radial position r^* of the extrema) at $Q_{PE} = 0$ is nearly independent of N_{PE}. In parallel, the strength of the overcharging (occurring at the largest radial position r^* of the extrema) measured at $Q_{PE} = N_m e$ is also nearly independent of N_{PE} (systems C and E). Moreover, our simulations show that for $N_{PE} \geq 2$ the strength of the overcharging (with $Q_{PE} = N_m e$) and undercharging (with $Q_{PE} = 0$) have nearly the same amplitude, in qualitative agreement with experimental data.

B. Adsorption with $\chi_{vdw} \neq 0$. In this part, we consider the additional attractive VDW macroion−PC monomer interaction with $\chi_{vdw} = 3$. The same investigation as with $\chi_{vdw} = 0$ is carried out here.

The density profiles of $n_{\pm}(r)$ for the systems A−G (with $\chi_{vdw} = 3$) are reported in Figure 10, and the corresponding microstructures are sketched in Figure 11.

Figure 10 shows that the density $n_+(r)$ near contact (for a given system) is about six times larger than that obtained at $\chi_{vdw} = 0$ (compare Figure 7). When $Q_{PE} = N_m e$, the density $n_+(r)$ at contact (slightly) increases monotonically with N_{PE} in contrast to what happened at $\chi_{vdw} = 0$ where it was nearly independent of N_{PE}. When $Q_{PE} = 0$, we remark that the density $n_+(r)$ near contact is nearly independent of N_{PE} (for $N_{PE} \geq 2$) in contrast to what happened at $\chi_{vdw} = 0$.

As far as the PA density $n_-(r)$ is concerned, the height of the first peak (for a given system) is about twice larger than that obtained at $\chi_{vdw} = 0$. This height is a monotonic function of N_{PE} *within* a given regime of Q_{PE} (here, either 0 or $N_m e$). Nevertheless, in general this height exhibits a nontrivial dependence on N_{PE}, in contrast to our results with $\chi_{vdw} = 0$. For the systems B and C both containing a single PA chain ($N_- = 1$), the height of the first peak in $n_-(r)$ is smaller with $N_+ = 2$ (system C) than with $N_+ = 1$ (system B). This is again due to the formation of clusters of oppositely charged monomers that takes place *above*

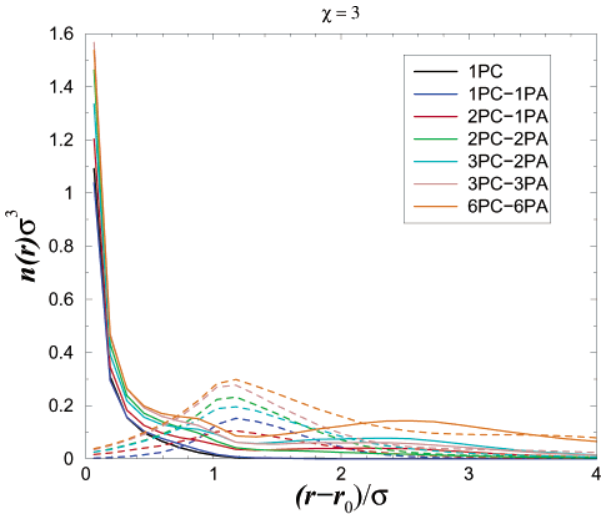

Figure 10. Same as Figure 7 but with $\chi_{vdw} = 3$.

the first layer. This effect is more pronounced when the amount of PC monomers (at given N_-) is larger (system C), leading to a local desorption of PA monomer. Those features are remarkable by a comparison of the snapshots of the systems B and C depicted in Figure 5d and Figure 11a, respectively. Similar arguments can be used for the systems D and E, where the same effect is found. At large N_{PE}, the height of the first peak in $n_-(r)$ saturates as expected.

For $3 \leq N_{PE} \leq 6$, our simulation shows that the formation of the *third* layer [i.e., the second peak in $n_+(r)$ at $r - r_0 \approx 2.6\sigma$] is enhanced when $Q_{PE} = N_m e$ at fixed N_+. This effect can again be explained in terms of polyelectrolyte (micro)globules formation. Indeed, above the *second* layer, the formation of clusters made up of oppositely charged monomers is enhanced when the polyelectrolyte complex (seen by the underneath bilayer) is uncharged which corresponds to a state of charge $Q_{PE} = 0$.

It is interesting to see that with $N_{PE} = 12$ one even gets a second peak (and not a shoulder) in $n_-(r)$, which is the signature of a *fourth* layer. This qualitatively contrasts with our findings at $\chi_{vdw} = 0$. Therefore, we conclude that the effect of an extra short-ranged macroion−PC attraction is crucial for the multilayering process.

On a more qualitative level, it is very insightful to compare the microstructures obtained with purely electrostatic interactions ($\chi_{vdw} = 0$) sketched in Figure 8 with those obtained with a short-ranged VDW macroion−PC interaction ($\chi_{vdw} = 3$) sketched in Figure 11. From such a visual inspection, it is clear that in all cases the adsorbed polyelectrolyte complex is flatter at $\chi_{vdw} = 3$ than at $\chi_{vdw} = 0$. An other important qualitative difference, is that the *unwrapping* occurring at $\chi_{vdw} = 0$ with $Q_{PE} = 0$ [see Figure 8b and (d)] is no longer effective when $\chi_{vdw} = 3$ (see Figure 11, parts b and d). In the same spirit, for a large number of chains ($N_{PE} = 12$), the macroion surface is only partially covered by the PC monomers where some (large) holes appear (see Figure 8e), in contrast to what occurs at $\chi_{vdw} = 3$, where all the macroion surface is covered (see Figure 11e).

The net fluid charge $Q(r)$ is reported in Figure 12. As expected one finds an overcharging and undercharging for $Q_{PE} = N_m e$ and $Q_{PE} = 0$, respectively. Now one can get a local overcharging larger than 100% (i.e., $Q(r)/Z_M > 2$) due to the VDW attraction that can lead to a first layer with *many* PC chains. For systems C and E, we see that the overcharging at the third layer is around 50% and nearly independent of N_{PE}.

On the other hand, the strength of the undercharging (occurring at the largest radial position r^* of the extrema) at $Q_{PE} = 0$ decreases with increasing N_{PE}, providing a

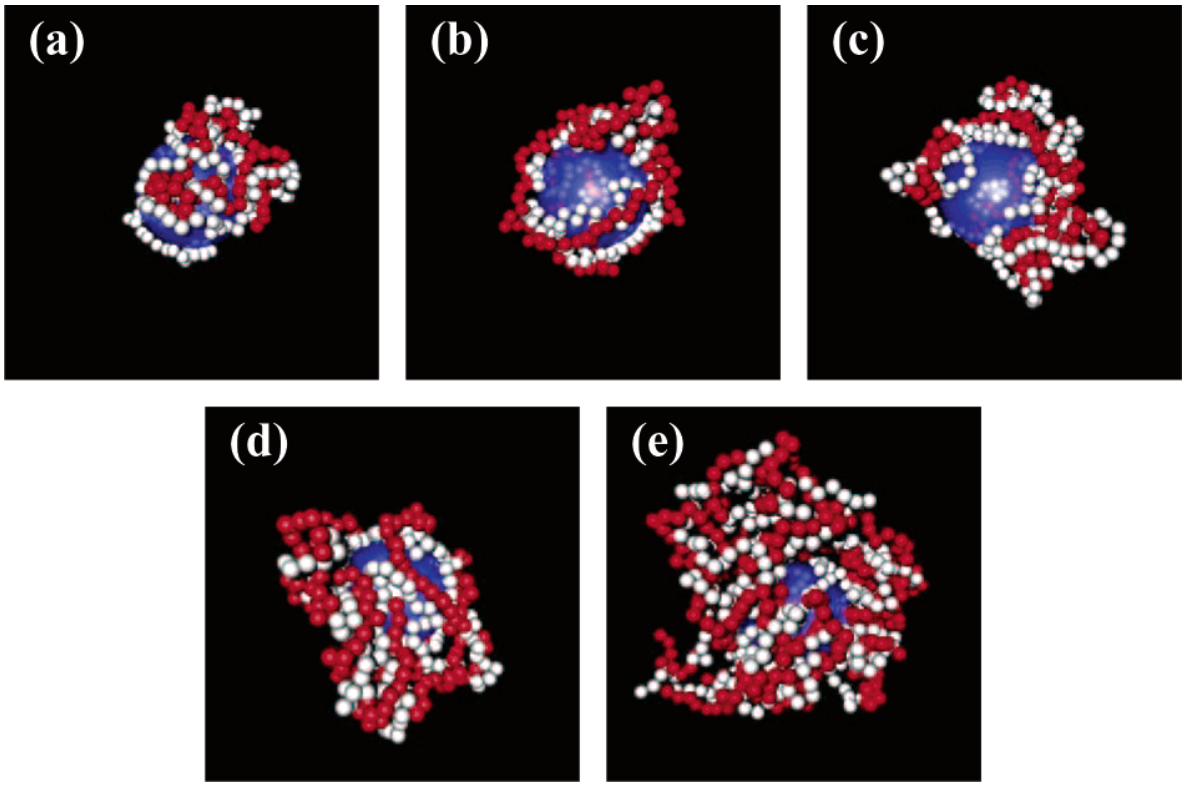

Figure 11. Same as Figure 8 but with $\chi_{vdw} = 3$. (a) 2PC-1PA (system C) (b) 2PC-2PA (system D) (c) 3PC-2PA (system E) (d) 3PC-3PA (system F) (e) 6PC-6PA (system G).

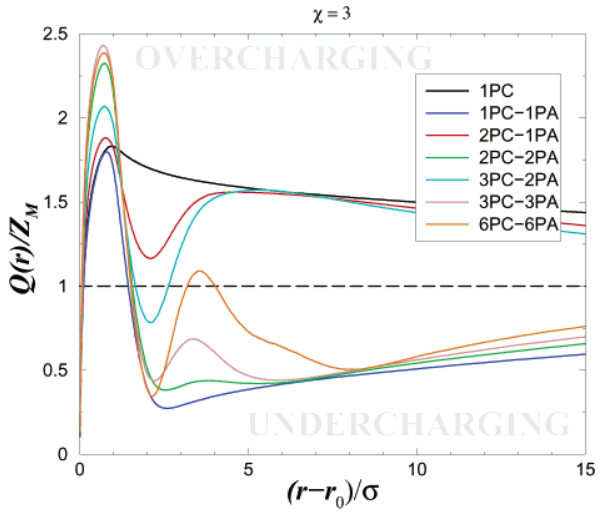

Figure 12. Same as Figure 9 but with $\chi_{vdw} = 3$.

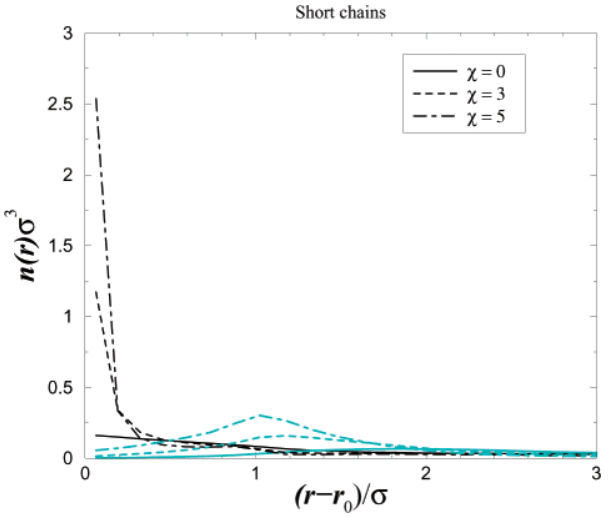

Figure 13. Radial monomer density for short polyelectrolyte chains (system H) at different χ_{vdw} couplings. The black and gray lines correspond to PC and PA monomers, respectively.

gradually weaker driving force for the subsequent adsorption of the PC chain. On the basis of our results with $\chi_{vdw} = 0$, we expect that the strength of the undercharging at $\chi_{vdw} = 3$ (for larger N_{PE}) should stabilize around 50%. So it appears that the oscillations of under- and overcharging are not 100% but instead close to 50%. This is probably sensitive to the specific model parameters chosen. What can be stated from our data is that there is no reason to find a generally applicable overcharging fraction. In particular, for the case of relatively small colloids, the results will strongly depend on the specific system parameters, which are both of electrostatic and of nonelectrostatic natures.

VII. Case of Short Chains

We now investigate the effect of chain length dependence. In this case, the adsorption of a single chain does not necessarily produce an overcharging since the chain length ($N_m = 10$, system H) is too short. The density profiles of $n_{\pm}(r)$ are reported in Figure 13 for various χ_{vdw}, and the corresponding microstructures are sketched in Figure 14.

In the purely electrostatic regime ($\chi_{vdw} = 0$), the polyelectrolyte adsorption is weak and it significantly increases with χ_{vdw}. However, for all reported cases, we only observe a bilayering in contrast with previous long chain systems (compare Figure 13 with Figures 7 and 10) where thereby a true multilayering was reported.

In addition we observe several globally neutral polyelectrolyte complexes in the bulk, whose number decreases with χ_{vdw} (see Figure 14). This feature was inhibited for long chains due to the strong PC−PA binding energy that keeps all the chains near the macroion surface. At sufficiently strong χ_{vdw} (see Figure 14c with $\chi_{vdw} = 5$), the macroion area gets largely (and *uniformly*) covered by the PC chains, leading to a strong bilayering. Nevertheless, due to the weak PC−PA binding energy, the formation of additional layer seems to be prohibited in contrasts to what was observed at $\chi_{vdw} = 3$ with systems D and E that contain a similar number of monomers. Those observations lead us to the relevant conclusion that multilayering with short chains (if experimentally observed on a charged colloidal sphere) must involve additional nontrivial driving forces like specific PC monomer−PA monomer interactions that are not captured by our model. This again seems to be in agreement with the arguments presented in ref 7 which argue against a stable thermodynamic equilibrium complex when there is excess polyelectrolytes present.

The net fluid charge plotted in Figure 15 indicates that only one charge oscillation (around the isoelectric point) is obtained in contrast to what can happen with longer chains. Again, here the driving force for the bilayer formation is the overcharging that increases with χ_{vdw}.

VIII. Concluding Remarks

We have carried out MC simulations to study the basic mechanisms involved in forming equilibrium polyelectrolyte complexes on a charged colloidal sphere. This work

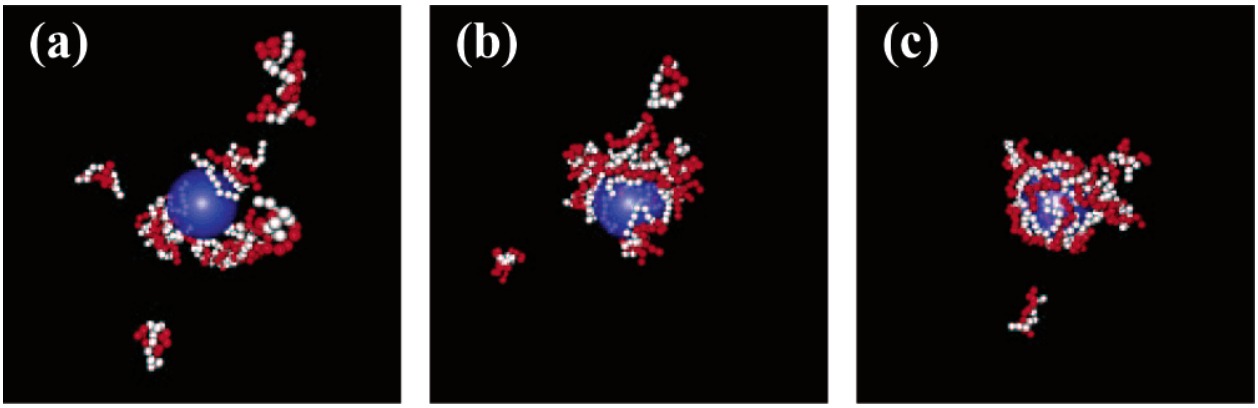

Figure 14. Typical equilibrium configurations for short PC (in white) and PA (in red) chains adsorbed onto the charged macroion (system H). The little ions are omitted for clarity. (a) $\chi_{vdw} = 0$ (b) $\chi_{vdw} = 3$ (c) $\chi_{vdw} = 5$.

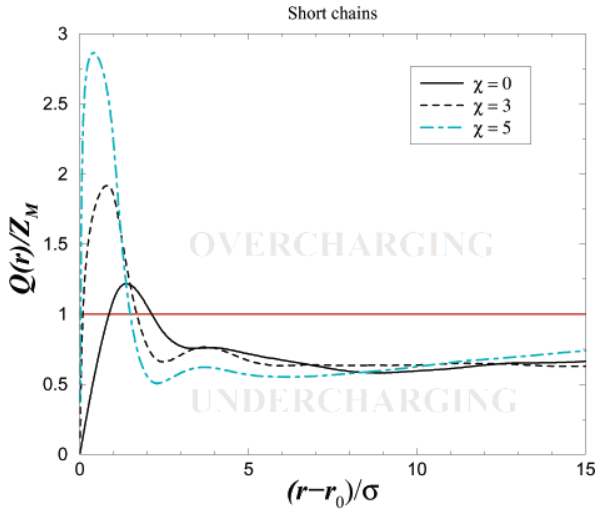

Figure 15. Net fluid charge $Q(r)$ for system H at different χ_{vdw} couplings. The horizontal line corresponds to the isoelectric point.

emphasizes the role of the short-range van der Waals-like attraction (characterized here by χ_{vdw}) between the spherical macroion surface and the oppositely charged adsorbed chain(s).

It was demonstrated that, for the bilayering process involving two long oppositely charged chains at fixed Γ_m and Γ_M, it is necessary to have a sufficiently high χ_{vdw}. In particular, below a certain value of $\chi_{vdw} = \chi^*_{vdw}$, a dense adsorbed polyelectrolyte globule is obtained, whereas above χ^*_{vdw} a flat bilayer builds up.

The same qualitatively applies to the case of many (more than two) long polyelectrolytes. In a purely electrostatic regime (i.e., $\chi_{vdw} = 0$) one can never obtain a true (uniform) multilayering. However, by increasing χ_{vdw}, one gradually increases the polyelectrolyte (polycation and polyanion) chain adsorption ultimately leading to a true multilayering where the macroion is uniformly covered. Nonetheless, at given χ_{vdw} and especially for small χ_{vdw}, the polyelectrolyte globular state is always favored when its net charge is zero.

As far as the short chain case is concerned, it was shown that even bilayering cannot be reached within the pure electrostatic regime. Only at higher χ_{vdw} (higher than those coming into play with long chains), one recovers a bilayer formation. However, multilayering (beyond bilayering) with very short chains seems to be very unlikely within our model. The large complex would not be thermodynamically stable and dissolve into smaller charge neutral polyelectrolyte complexes, consistent with the ideas presented in ref 7.

As an overall conclusion, our results clearly demonstrated that besides an overcharging driving force [i.e., successive macroion (effective) charge reversal by successive polymer layering], the stability of the polyelectrolyte multilayer is strongly influenced by the specific macroion-polyelectrolyte short-range attraction. This statement should at least hold for the investigated cases of equilibrium structures.

A future study should include other important effects, such as chain flexibility, specific interchain monomer−monomer interaction, microion valency, etc. Nevertheless, our present findings hopefully will generate some further systematic studies to explore the effects of nonelectrostatic effects for the layer-by-layer deposition technique.

Acknowledgment. R.M. thanks F. Caruso and S. K. Mayya for helpful and stimulating discussions. This work was supported by Laboratoires Européens Associés (LEA) and the SFB 625.

LA026988N

Appendix M

Polyelectrolyte Multilayering on a Charged Planar Surface

Polyelectrolyte Multilayering on a Charged Planar Surface

René Messina†

Institut für Theoretische Physik II, Heinrich-Heine-Universität Düsseldorf, Universitätsstrasse 1, D-40225 Düsseldorf, Germany

Received May 23, 2003; Revised Manuscript Received October 22, 2003

ABSTRACT: The adsorption of highly *oppositely* charged flexible polyelectrolytes (PEs) on a charged planar substrate is investigated by means of Monte Carlo (MC) simulations. We study in detail the equilibrium structure of the first few PE layers. The influence of the chain length and of a (extra) nonelectrostatic short range attraction between the polycations and the negatively charged substrate is considered. We show that the stability as well as the microstructure of the PE layers are especially sensitive to the strength of this latter interaction. Qualitative agreement is reached with some recent experiments.

I. Introduction

PE multilayer structures are often obtained in a so-called layer-by-layer method by alternating exposure of a charged substrate to solutions of polycations (PCs) and polyanions (PAs). This widely used technique was first introduced by Decher and co-workers,[1,2] and its simplicity and versatility have triggered a large interest in the engineering community. As examples of technological applications, one can mention biosensing,[3] catalysis,[4] nonlinear optical devices,[5] nanoparticles coating,[6−7] etc.

On the theoretical side, there exist a few analytical works about PE multilayers on charged planar surfaces based on different levels of approximation.[8−10] Solis and Olvera de la Cruz considered the conditions under which the spontaneous formation of polyelectrolyte layered structures can be induced by a charged wall.[8] On the basis of Debye−Hückel approximations for the electrostatic interactions, including some lateral correlations by the consideration of given adsorbed PE structures, Netz and Joanny[9] found a remarkable stability of the (semiflexible) PE multilayers supported by scaling laws. For weakly charged flexible polyelectrolytes at high ionic strength qualitative agreements between theory,[10] also based on scaling laws, and experimental observations[11] (such as the predicted thickness and net charge of the PE multilayer) have been provided.

The important driving force for all these PE multilayering processes is of electrostatic origin. More precisely, it is based on an overcharging mechanism, where the first layer overcharges the substrate and, along the PE multilayering process, the top layer overcharges the adsorbed PE layers underneath. Nevertheless, the strong correlations existing between oppositely charged polyions, especially for highly charged PEs, provide a formidable challenge for the understanding of the PE multilayer microstructures. In this respect, numerical simulations are of great help. It is only recently, that MC simulations were carried out to study such PE structures built up on *spherical* charged surfaces.[12]

In this paper, we provide a detailed study of the PE multilayer structure adsorbed on a charged planar surface and discuss the basic mechanisms that are involved there by means of MC simulations. Our paper is organized as follows: section II is devoted to the description of our MC simulation technique. The measured quantities are specified in section III. The PE monolayering is studied in section IV, and the PE bilayering is studied in section V. Then the PE multilayering process is addressed in section VI. Finally, section VII contains some brief concluding remarks.

† E-mail: messina@thphy.uni-duesseldorf.de.

II. Simulation Details

The setup of the system under consideration is similar to that recently investigated with a spherical substrate.[12] Within the framework of the primitive model, we consider a PE solution near a charged hard wall with an implicit solvent (water) of relative dielectric permittivity $\epsilon_r \approx 80$. This charged substrate located at $z = 0$ is characterized by a negative surface bare charge density $-\sigma_0 e$, where e is the (positive) elementary charge and $\sigma_0 > 0$ is the number of charges per unit area. Electroneutrality is always ensured by the presence of explicit monovalent ($Z_c = 1$) plate's counterions of diameter a. PE chains (N_+ PCs and N_- PAs) are made up of N_m *monovalent* monomers ($Z_m = 1$) of diameter a. Hence, all microions are monovalent: $Z = Z_c = Z_m = 1$. For the sake of simplicity, we only consider here symmetrical complexes where PC and PA chains have the same length and carry the same charge in absolute value.

All these particles making up the system are confined in a $L \times L \times \tau$ box. Periodic boundary conditions are applied in the (x, y) directions, whereas hard walls are present at $z = 0$ (location of the charged plate) and $z = \tau$ (location of an *uncharged* wall). To avoid the appearance of image charges,[13,14] we assume that on both parts of the charged plate (at $z = 0$) the dielectric constants are the same.

The total energy of interaction of the system can be written as

$$U_{\text{tot.}} = \sum_i [U_{\text{hs}}^{(\text{plate})}(z_i) + U_{\text{coul}}^{(\text{plate})}(z_i) + U_{\text{vdw}}^{(\text{plate})}(z_i)] + \sum_{i,i<j} [U_{\text{hs}}(r_{ij}) + U_{\text{coul}}(r_{ij}) + U_{\text{FENE}}(r_{ij}) + U_{\text{LJ}}(r_{ij})] \quad (1)$$

where the first (single) sum stems from the interaction between an ion i (located at $z = z_i$) and the charged plate, and the second (double) sum stems from the pair

10.1021/ma034689e CCC: $27.50
Published on Web 12/16/2003

interaction between ions i and j with $r_{ij} = |\mathbf{r}_i - \mathbf{r}_j|$. All these contributions to $U_{\text{tot.}}$ in eq 1 are described in detail below.

Excluded volume interactions are modeled via a hardcore potential defined as follows

$$U_{\text{hs}}(r_{ij}) = \begin{cases} \infty, & \text{for } r_{ij} < a \\ 0, & \text{for } r_{ij} \geq a \end{cases} \quad (2)$$

for the microion−microion one, except for the monomer−monomer one,[15] and

$$U_{\text{hs}}^{(\text{plate})}(z_i) = \begin{cases} \infty, & \text{for } z_i < a/2 \\ \infty, & \text{for } z_i > \tau - a/2 \\ 0, & \text{for } a/2 \leq z_i \leq \tau - a/2 \end{cases} \quad (3)$$

for the plate−microion one.

The electrostatic energy of interaction between two ions i and j reads

$$\frac{U_{\text{coul}}(r_{ij})}{k_{\text{B}}T} = \pm \frac{l_{\text{B}}}{r_{ij}} \quad (4)$$

where +(−) applies to charges of the same (opposite) sign, and $l_{\text{B}} = e^2/4\pi\epsilon_0\epsilon_{\text{r}}k_{\text{B}}T$ is the Bjerrum length corresponding to the distance at which two monovalent ions interact with $k_{\text{B}}T$. The electrostatic energy of interaction between an ion i and the (uniformly) charged plate reads

$$\frac{U_{\text{coul}}^{(\text{plate})}(z_i)}{k_{\text{B}}T} = \pm 2\pi l_{\text{B}}\sigma_0 z_i \quad (5)$$

where +(−) applies to positively (negatively) charged ions. An appropriate and efficient modified Lekner sum was utilized to compute the electrostatic interactions with periodicity in *two* directions.[16,17] To link our simulation parameters to experimental units and room temperature ($T = 298$ K), we choose $a = 4.25$ Å, leading to the Bjerrum length of water $l_{\text{B}} = 1.68a = 7.14$ Å. The surface charge density of the planar macroion was chosen as $-\sigma_0 e \approx -0.165$ C/m^2.

The polyelectrolyte chain connectivity is modeled by employing a standard FENE potential in good solvent (see, e.g., ref 18), which reads

$$U_{\text{FENE}}(r) = \begin{cases} -\frac{1}{2}\kappa {R_0}^2 \ln\left[1 - \frac{r^2}{{R_0}^2}\right], & \text{for } r < R_0 \\ \infty, & \text{for } r \geq R_0 \end{cases} \quad (6)$$

with $\kappa = 27k_{\text{B}}T/a^2$ and $R_0 = 1.5a$. The excluded volume interaction between chain monomers is taken into account via a purely repulsive Lennard-Jones (LJ) potential given by

$$U_{\text{LJ}}(r) = \begin{cases} 4\epsilon\left[\left(\frac{a}{r}\right)^{12} - \left(\frac{a}{r}\right)^{6}\right] + \epsilon, & \text{for } r \leq 2^{1/6}a \\ 0, & \text{for } r > 2^{1/6}a \end{cases} \quad (7)$$

where $\epsilon = k_{\text{B}}T$. These parameter values lead to an equilibrium bond length $l = 0.98a$.

An important interaction in PE multilayering is the *non*electrostatic *short ranged attraction*, $U_{\text{vdw}}^{(\text{plate})}$, between the planar macroion and the PC chain. To include this kind of interaction, we choose without loss of generality a (microscopic) van der Waals (VDW) potential of interaction between the planar macroion and a PC monomer that is given by

$$U_{\text{vdw}}^{(\text{plate})}(z) = -\epsilon\chi_{\text{vdw}}\left(\frac{a}{z + a/2}\right)^6, \quad \text{for } z \geq a/2 \quad (8)$$

where χ_{vdw} is a positive dimensionless parameter describing the strength of this attraction. Thereby, at contact (i.e., $z = a/2$), the magnitude of the attraction is $\chi_{\text{vdw}}\epsilon = \chi_{\text{vdw}}k_{\text{B}}T$ which is, in fact, the relevant characteristic of this potential. Since it is not straightforward to directly link this strength of adsorption to experimental values, we chose $\chi_{\text{vdw}} = 5$ (also considered among other values in the case of a spherical macroion[12]), so as to mimic good "anchoring" properties to the planar substrate.

Table 1. Model Simulation Parameters with Some Fixed Values

parameters	
$T = 298$ K	room temp
$\sigma_0 = 90/L^2$	macroion surface charge
$Z = 1$	microion valence
$a = 4.25$ Å	microion diameter
$l_{\text{B}} = 1.68a = 7.14$ Å	Bjerrum length
$L = 22a$	(x, y)-box length
$\tau = 75a$	z-box length
N_+	no. of PCs
N_-	no. of PAs
$N_{\text{PE}} = N_+ + N_-$	total no. of PEs
N_{m}	no. of monomers per chain
χ_{vdw}	strength of the specific VDW attraction

Table 2. System Parameters[a]

system	N_{PE}	N_+	N_-	N_{m}
A	20	20	0	10
B	10	10	0	20
C	40	20	20	10
D	20	10	10	20
E	80	40	40	10
F	40	20	20	20

[a] The number of counterions (cations and anions) ensuring the overall electroneutrality of the system is not indicated.

All the simulation parameters are gathered in Table 1. The set of simulated systems can be found in Table 2. The equilibrium properties of our model system were obtained by using standard canonical MC simulations following the Metropolis scheme.[19,20] Single-particle moves were considered with an acceptance ratio of 30% for the monomers and 50% for the counterions. Typically, about 5×10^4 to 10^6 MC steps per particle were required for equilibration, and about $5 \times 10^5 - 10^6$ subsequent MC steps were used to perform measurements. To improve the computational efficiency, we omitted the presence of PE counterions when $N_+ = N_-$ so that the system is still globally electroneutral. We have systematically checked for $N_+ = N_- = 20$ (system C) that the (average) PE configurations (especially the monomer distribution) are indistinguishable, within the statistical uncertainty, from those where PE counterions are explicitly taken into account, as it should be.

III. Measured Quantities

We briefly describe the different observables that are going to be measured. To characterize the PE adsorption, we compute the monomer density $n_\pm(z)$ that is normalized as follows

$$\int_{a/2}^{\tau - a/2} n_\pm(z) L^2 \, \mathrm{d}z = N_\pm N_m \quad (9)$$

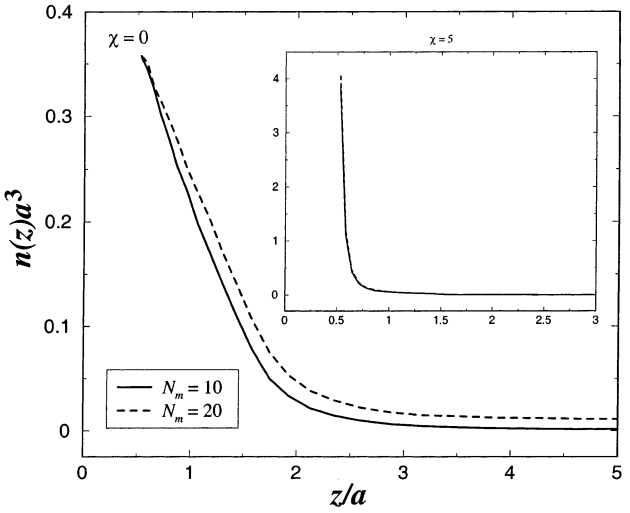

Figure 1. Profiles of PC monomer-density $n_+(z)$ at different χ_{vdw} couplings (systems A and B). The inset corresponds to $\chi_{vdw} = 5$ where the two curves ($N_m = 10$ and 20) are nearly indistinguishable.

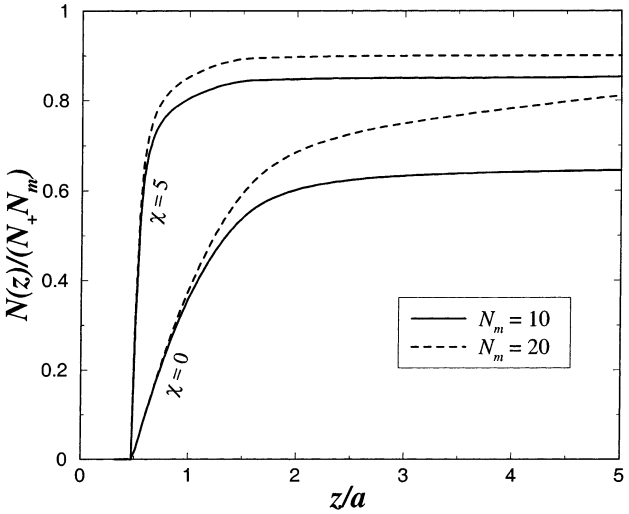

Figure 2. Fraction $\bar{N}_+(z)/(N_+N_m)$ of adsorbed PC monomers at different χ_{vdw} couplings (systems A and B).

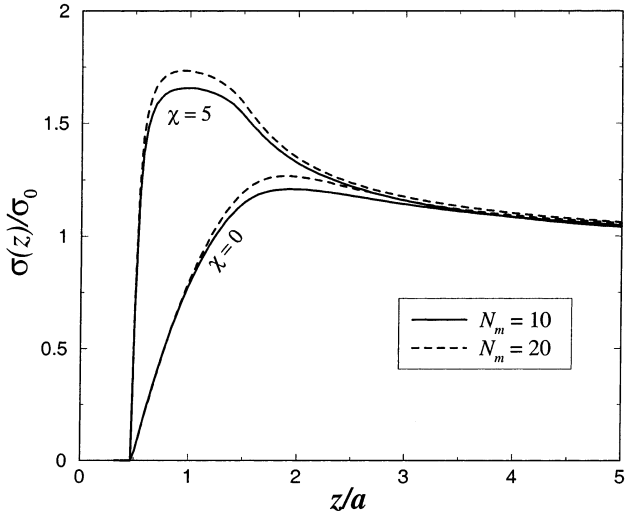

Figure 3. Net fluid charge $\sigma(z)$ at different χ_{vdw} couplings (systems A and B).

where + (−) applies to PCs (PAs). This quantity is of special interest to characterize the degree of ordering in the vicinity of the planar macroion surface.

The total number of accumulated monomers $\bar{N}_\pm(r)$ within a distance z from the planar macroion is given by

$$\bar{N}_\pm(z) = \int_{a/2}^{z} n_\pm(z')L^2\,dz' \qquad (10)$$

where + (−) applies to PCs (PAs). This observable will be addressed in the study of PE monolayer (section 4) and PE bilayer (section 5).

Another relevant quantity is the global *net fluid charge* $\sigma(z)$, which is defined as follows

$$\sigma(z) = \int_{a/2}^{z} [\tilde{n}_+(z') - \tilde{n}_-(z')]\,dz' \qquad (11)$$

where $\tilde{n}_+$ ($\tilde{n}_-$) stands for the density of all the positive (negative) microions (i.e., monomers and counterions). Thus, $\sigma(z)$ corresponds to the net fluid charge per unit area (omitting the bare macroion surface charge $-\sigma_0$) within a distance z from the charged wall. At the uncharged wall, electroneutrality imposes $\sigma(z = \tau - a/2) = \sigma_0$. By simple application of the Gauss' law, $[\sigma(z) - \sigma_0]$ is directly proportional to the mean electric field at z. Therefore, $\sigma(z)$ can measure the *screening* strength of the macroion-plate charge by the neighboring solute charged species.

IV. Monolayer

In this part, we study the adsorption of PC chains for two chain lengths $N_m = 10$ (system A) and $N_m = 20$ (system B), and for two different couplings $\chi_{vdw} = 0$ and $\chi_{vdw} = 5$. Experimentally, this would correspond to the formation of the *first* polyelectrolyte layer. This is a decisive step to elucidate the even more complex PE multilayer structures where additionally PAs are also present.

Here, where $N_- = 0$ (i.e., no polyanions), global electroneutrality is ensured by the presence of explicit PC's counterions (i.e., monovalent anions) and the macroion-plate's counterions (i.e., monovalent cations). Also, we recall that the total number of monomers, $N_+N_m = 200$, is identical for both systems A and B under consideration (see Table 2). Hence, the total monomer charge is the same for systems A and B.

The profiles of the monomer density $n_+(z)$ are depicted in Figure 1. At $\chi_{vdw} = 0$, the density $n_+(z)$ near contact ($z \sim a/2$) is basically independent of the chain size N_m. However, away from the surface, the density of monomers is slightly higher for larger N_m. This is a combined effect of (i) entropy and (ii) electrostatic correlations. These underlying mechanisms at $\chi_{vdw} = 0$ can be explained with simple ideas as follows:

- At fixed number of total monomers, entropic effects are larger the shorter the chains, and in the limiting case of $N_m = 1$ (i.e., the electrolyte limit) entropy effects are maximal leading to the highest monomer "release". It is to say that the chain connectivity lowers the entropy of the system.

- In parallel, electrostatic correlations[21−23] are also higher the higher the valence of the adsorbed particles. In our case N_m plays the role of the polyion valence.

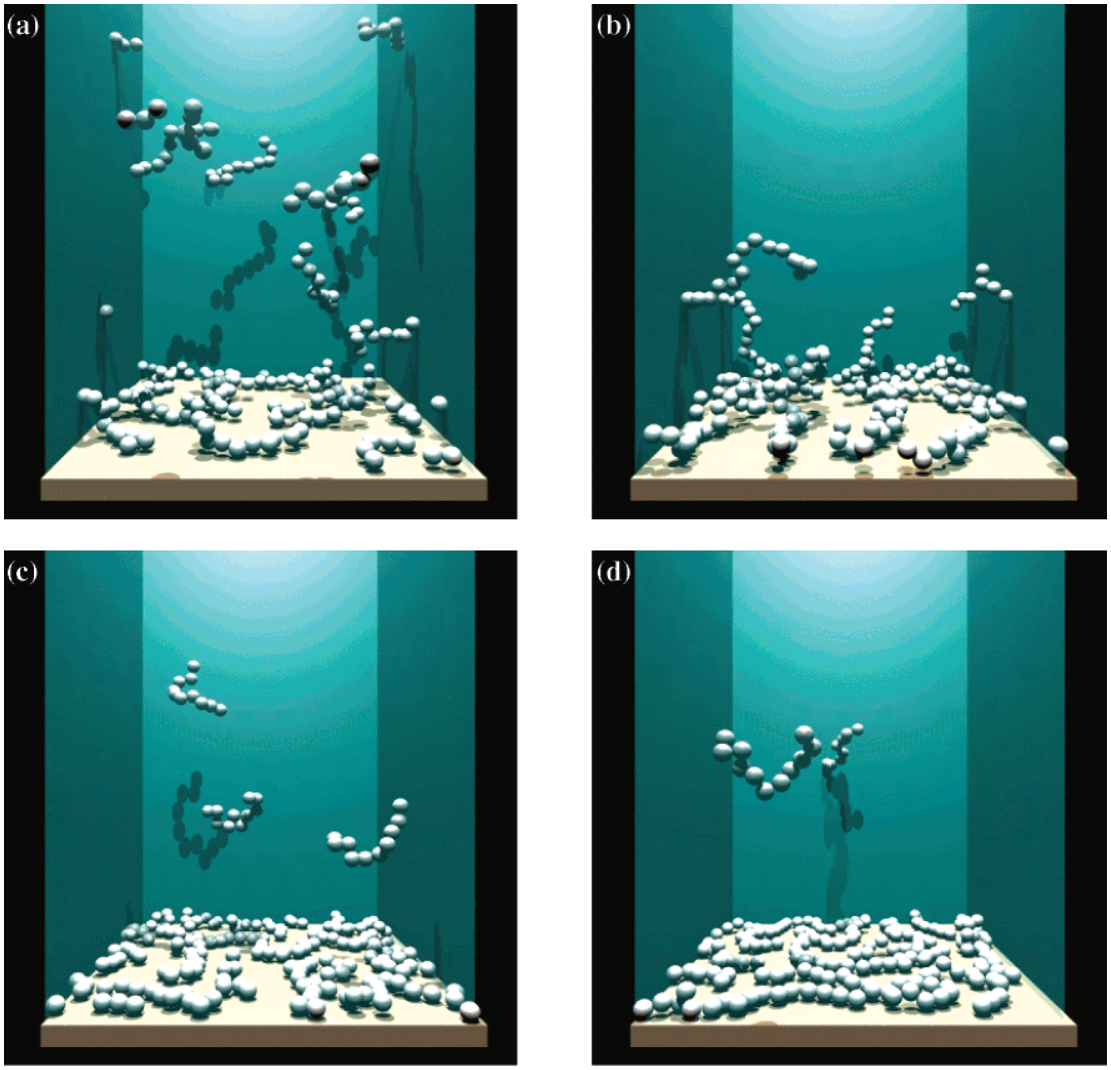

Figure 4. Typical equilibrium configurations for PC chains adsorbed onto an oppositely charged planar macroion (systems A and B). The little counterions are omitted for clarity. Key: (a) $\chi_{vdw} = 0$, $N_m = 10$; (b) $\chi_{vdw} = 0$, $N_m = 20$; (c) $\chi_{vdw} = 5$, $N_m = 10$; (d) $\chi_{vdw} = 5$, $N_m = 20$.

The density $n_+(z)$ near contact increases considerably with χ_{vdw} (here about 1 order of magnitude) as expected. It turns out that with $\chi_{vdw} = 5$, the $n_+(z)$-profiles are basically identical for $N_m = 10$ and $N_m = 20$. This is due to the sufficiently strong nonelectrostatic attractive force that can overcompensate the antagonistic entropic effects that were more efficient at $\chi_{vdw} = 0$.

The fraction $\bar{N}_+(z)/(N_+N_m)$ of adsorbed monomers can be found in Figure 2. At a z-distance of $1.5a$ from the planar macroion surface (corresponding to a width of two monomers), about 90% of the monomers are adsorbed for $\chi_{vdw} = 5$ against only ~50% for $\chi_{vdw} = 0$. Again, at given χ_{vdw}, $\bar{N}_+(z)/(N_+N_m)$ is larger for longer chains due to the same coupled effects of entropy and electrostatic correlations explained above.

The (global) net fluid charge $\sigma(z)$ is reported in Figure 3. In all cases, we observe a macroion-surface charge reversal (i.e., $\sigma(z)/\sigma_0 > 1$). The position $z = z^*$ at which $\sigma(z^*)$ gets its maximal value decreases with χ_{vdw}, due to the χ_{vdw}-enhanced adsorption of the PCs. Concomitantly, this *overcharging* increases with χ_{vdw}, since the (extra) gain in energy by macroion-monomer VDW interactions can better overcome (the higher χ_{vdw}) the cost of the self-energy stemming from the adsorbed excess charge.[12] More quantitatively, we have $\sigma(z^*)/\sigma_0 \approx 1.7$ at $\chi_{vdw} = 5$ against only $\sigma(z^*)/\sigma_0 \approx 1.25$ at $\chi_{vdw} = 0$. Note that the maximal value of charge reversal of $(200-90)/90 = 122\%$ (i.e., $\sigma(z^*)/\sigma_0 = 2.22$) allowed by the total charge of PCs cannot be reached due to a slight accumulation of microanions. In agreement with the profiles of $n_+(z)$ and $\bar{N}_+(z)$ (see Figure 1 and Figure 2), at given χ_{vdw}, the overcharging gets higher the higher the chain length. Those (locally) overcharged states should be the driving force for the building of subsequent PE bilayers when PA chains are added.

Typical equilibrium configurations can be found in Figure 4. The qualitative difference between $\chi_{vdw} = 0$ (Figure 4, parts a and b) and $\chi_{vdw} = 5$ (Figure 4, parts c and d) is rather spectacular. Without additional VDW attraction ($\chi_{vdw} = 0$) the adsorption is much weaker than at $\chi_{vdw} = 5$, where in the latter situation the z-fluctuation is very weak within the adsorbed layer. Basically the first layer is glued at $\chi_{vdw} = 5$, and the excess PC chains float in the solution. It is typically this type of configurations for the first layer that is wanted in experimental situations.

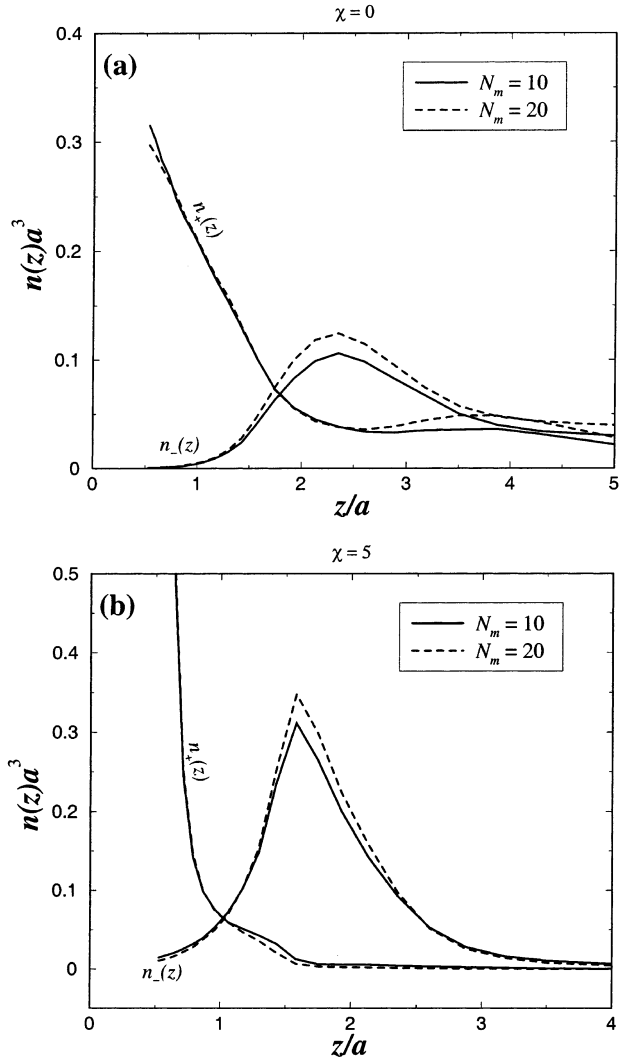

Figure 5. Profiles of monomer density $n_{\pm}(z)$ for oppositely charged polyelectrolytes (systems C and D). Key: (a) $\chi_{vdw} = 0$; (b) $\chi_{vdw} = 5$.

The next section (section 5), which concerns bilayering, will show that the (enhanced) stability of this first layer is decisive for the onset of multilayers.

V. Bilayer

We now consider the case where additionally PA chains are present (systems C and D), so that we have a neutral polyelectrolyte complex (i.e., $N_+N_m = N_-N_m = 200$). Global electroneutrality is ensured by the counterions of the planar macroion as usual. For such parameters, the final equilibrium structure consists essentially of bilayers with sometimes the onset of a weakly stable third layer. Experimentally this would correspond to the process of the *second* polyelectrolyte layer formation (with system A or B as the initial state). We stress the fact that this process is fully reversible for the parameters investigated in our present study. In particular, we checked that the same final *equilibrium* configuration is obtained either by (i) starting from system A or B and then adding PAs or (ii) starting directly with the mixture of oppositely charged polyelectrolytes.

The profiles of the monomer density $n_{\pm}(z)$ at $\chi_{vdw} = 0$ and $\chi_{vdw} = 5$ are depicted in Figure 5, parts a and b, respectively. The corresponding microstructures are sketched in Figure 6. The density of PC monomers $n_+(r)$ near contact increases considerably with χ_{vdw} as expected. Interestingly, at $\chi_{vdw} = 0$, a comparison with systems A and B (see Figure 1) indicates that the adsorption of PC monomers is weaker when additional PAs are present. This effect was already observed with spherical substrates,[12] and the same mechanisms apply here to planar surfaces. More explicitly, the PC chain tends to build up a globular state (reminiscent of the classical *bulk* PE collapse[24]) by getting complexed to the PA chain, as well illustrated in Figure 6, parts a and b. Thereby, the mean monomer coordination number (or the mean number of monomer neighbors) gets higher which is *both* (i) entropically and (ii) energetically (at least from the PE complex viewpoint) favorable. This PC desorption is only appreciable at sufficiently low χ_{vdw} where the energy loss stemming from the PC desorption is well balanced (or even overcompensated depending generally on the parameters) by the energy gained in building a PC−PA globular structure. This "auto-globalization" is also enhanced by increasing N_m as it should be (compare Figure 6, part a and part b). Note also that there is a small second peak in $n_+(z)$ at $z \approx 3.8a$ (see Figure 5a), which is rather the signature of a strong PC−PA globalization than a third PE layer. Besides, the peak in the PA density $n_-(z)$ located at $z = z^* \approx 2.3a$ (see Figure 5a), which is relatively far from that of a compact bilayer where $z^* = 1.5a$, indicates the diffuse character of the bilayer at $\chi_{vdw} = 0$.

At $\chi_{vdw} = 5$, the $n_+(z)$-profiles are basically identical for $N_m = 10$ and $N_m = 20$. In contrast to $\chi_{vdw} = 0$, $n_+(z)$ near contact is somewhat larger at $\chi_{vdw} = 5$, and it is going to be explained later in the discussion of $\bar{N}_+(z)$. As far as the PA density $n_-(z)$ is concerned, we see that the peak is roughly 2−3 times higher (depending on N_m) with $\chi_{vdw} = 5$ than with $\chi_{vdw} = 0$. Also, its position ($z^* \approx 1.5a$) corresponds to that of a compact bilayer. A visual inspection of Figure 6, parts c and d, confirms this feature. This again shows how important is the role of extra nonelectrostatic attractive force for the stability of bilayers.

An intermediate conclusion can be drawn from the above findings and especially from the microstructures depicted in Figure 6:

• True bilayering (i.e., flat and dense layers) can only occur at *nonzero* χ_{vdw}, as already reported for spherical charged substrates[12] with large curvature.

An interesting common characteristic of the microstructures at $\chi_{vdw} = 0$ and $\chi_{vdw} = 5$ is the formation of *small islands* (along the substrate) made up of more or less flat (depending on χ_{vdw}) PC−PA complexes, easily identifiable at $N_m = 20$ (see Figure 6, parts b and d).

The fraction $\bar{N}_+(z)/(N_+N_m)$ of adsorbed monomers at $\chi_{vdw} = 0$ and $\chi_{vdw} = 5$ can be found in Figure 7, parts a and b, respectively. A close look at Figure 7a reveals a smaller PC monomer accumulation (at $\chi_{vdw} = 0$) up to $z \approx 3a$ (independently of N_m) than in the case where PA chains were absent (compare with Figure 2). This is fully consistent with the formation of PC−PA globules (relevant at $\chi_{vdw} = 0$) leading to the effective PC desorption already discussed above. In parallel, this PC−PA globalization tends to cancel the effect of chain length N_m on $\bar{N}_+(z)$. On the other hand, at $\chi_{vdw} = 5$, the situation is qualitatively different where the presence of PAs now induces an *increase* of $\bar{N}_+(z)$ (compare Figure 7b and Figure 2). This phenomenon can be explained by electrostatic correlation effects. Indeed, at $\chi_{vdw} = 5$, the highly stable PC layer attracts more PA monomers than at $\chi_{vdw} = 0$, and thereby, "super" dipoles made of

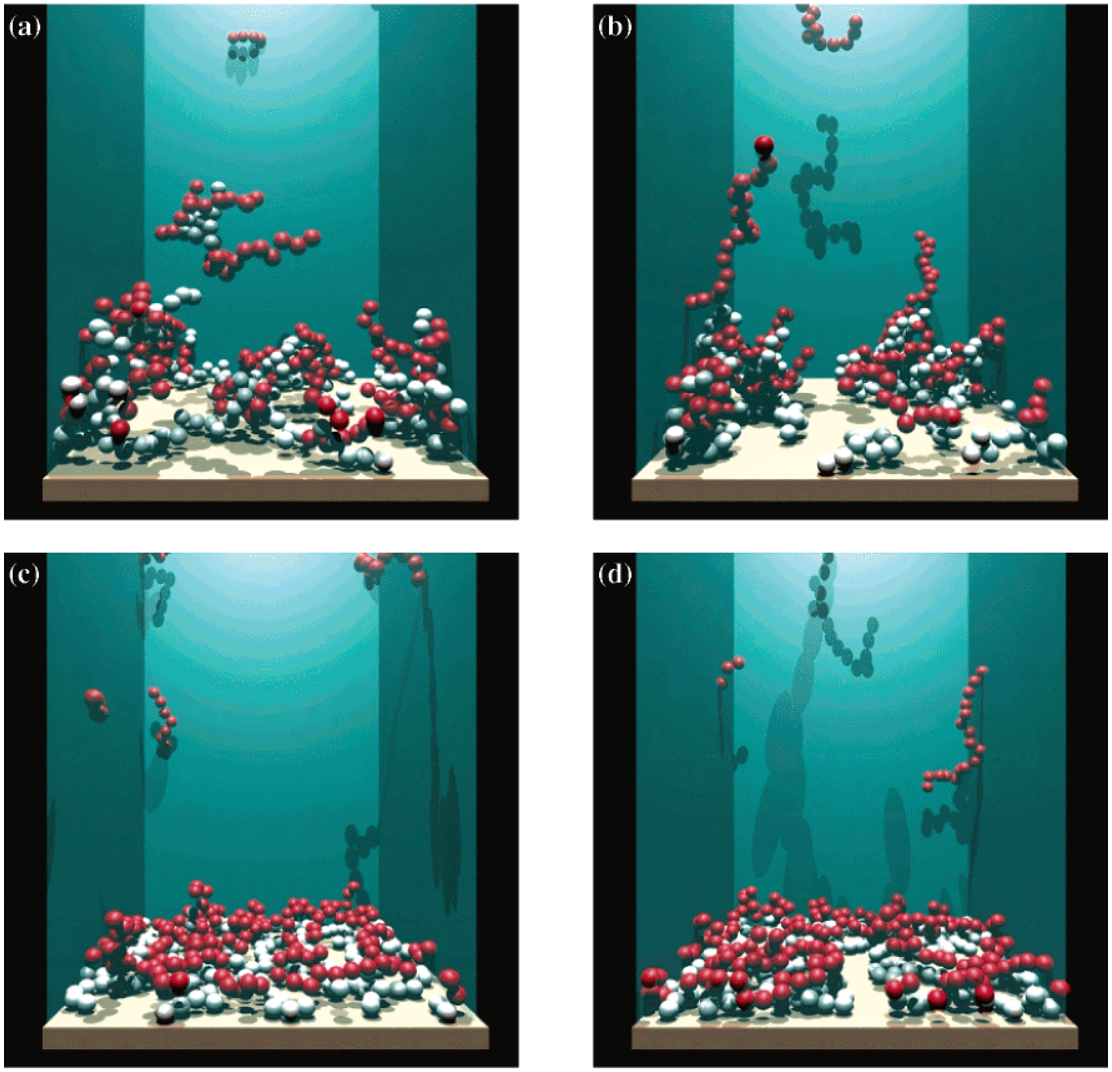

Figure 6. Typical equilibrium configurations for the adsorption of oppositely charged PE chains (systems C and D) onto a planar macroion. The polycations are in white and the polyanions in red. The little ions are omitted for clarity. Key: (a) $\chi_{vdw} = 0$, $N_m = 10$; (b) $\chi_{vdw} = 0$, $N_m = 20$; (c) $\chi_{vdw} = 5$, $N_m = 10$; (d) $\chi_{vdw} = 5$, $N_m = 20$.

PC−PA monomer pairs build up, that are perceptible in Figure 6, parts c and d. This leads to a strong attractive correlation interaction between the plate and those dipoles. In other terms the effect of finite χ_{vdw} is to (strongly) *polarize* the adsorbed charged chains. Note also that at $\chi_{vdw} = 5$ the PC−PA globalization is much less favorable than at $\chi_{vdw} = 0$ due to the higher cost of PC desorption energy in the former case. As a net effect there can be more adsorbed PC monomers compared to $\chi_{vdw} = 0$. In that case of $\chi_{vdw} = 5$, it is precisely this mechanism that tends to cancel the effect of N_m on $\bar{N}_+(z)$. As far as the PA monomer fraction $\bar{N}_-(z)$ is concerned, Figure 7 shows that the adsorption of monomers is much weaker and more diffuse at $\chi_{vdw} = 0$ than at $\chi_{vdw} = 5$, as expected from Figures 5 and 6.

The net fluid charge $\sigma(z)$ is reported in Figure 8. In all cases, the planar macroion gets overcharged and undercharged as one gets away from its surface. That is we have to deal with charge *oscillations*. Our results clearly show that the amplitude of those oscillations is systematically larger at high N_m, as also observed without PAs (see Figure 3). This is consistent with the idea that lateral electrostatic correlations are enhanced by increasing the valence of the polyions (here N_m). Nevertheless, as soon as *oppositely charged polyions* can interact, there is a subtle interplay between clustering and the lateral correlations of polyions that governs the degree of overcharging near the planar macroion. At $\chi_{vdw} = 5$, we observe a significantly higher overcharging than without PAs (compare with Figure 3). This is in agreement with the profiles of $N_+(z)$ discussed previously. However, the positions of the first peak ($z^* \approx a$ for $\chi_{vdw} = 5$ and $z^* \approx 1.8a$ for $\chi_{vdw} = 0$) in $\sigma(z)$ remain nearly unchanged by the presence of PAs (compare Figure 8 with Figure 3).

VI. Multilayer

Presently, we consider the case where there are enough polyelectrolytes ($N_+N_m = N_-N_m = 400$) in the system to produce *multilayers* (systems E and F). Hence, compared to systems C and D, we have now doubled the polyelectrolyte concentration. Global electroneutrality is ensured by the counterions of the planar macroion as usual.

The density profiles of $n_\pm(r)$ for $\chi_{vdw} = 0$ and $\chi_{vdw} = 5$ are depicted in Figure 9, parts a and b, respectively. The corresponding microstructures are sketched in

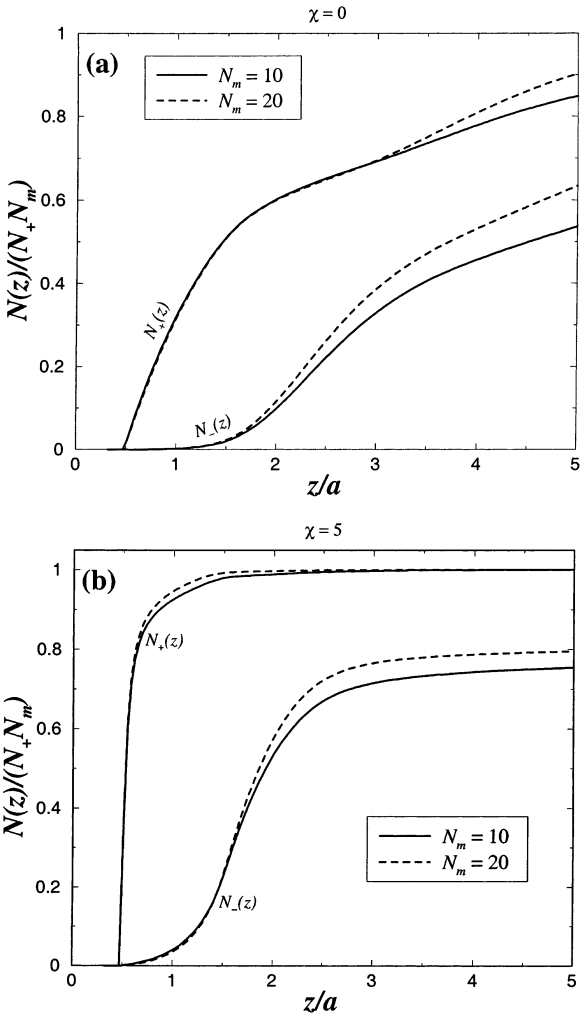

Figure 7. Fraction of adsorbed monomers $\bar{N}_{\pm}(z)$ for oppositely charged polyelectrolytes (systems C and D). Key: (a) $\chi_{vdw} = 0$; (b) $\chi_{vdw} = 5$.

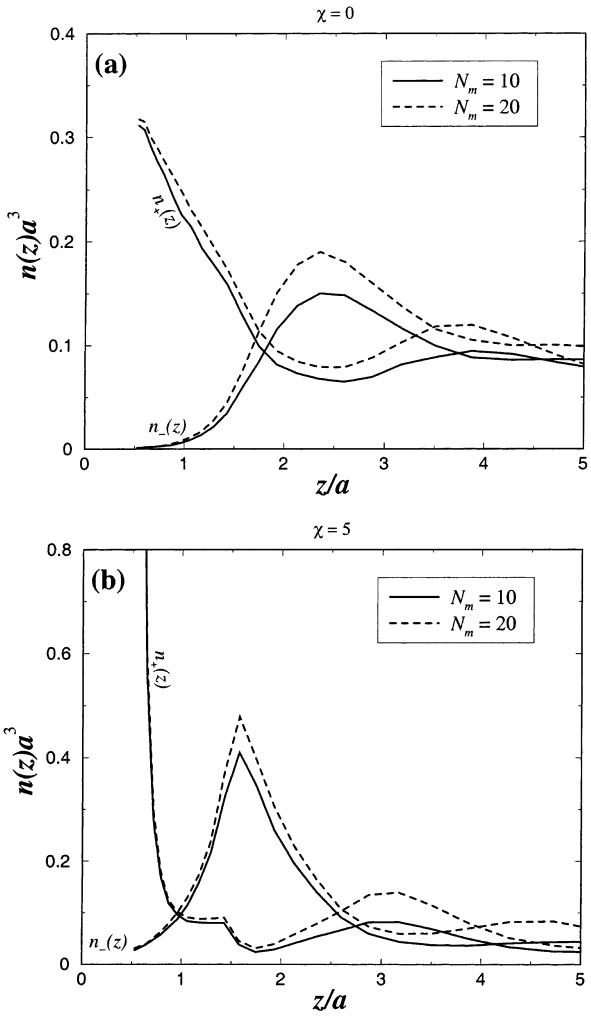

Figure 9. Profiles of monomer density $n_{\pm}(z)$ for oppositely charged polyelectrolytes (systems E and F). Key: (a) $\chi_{vdw} = 0$; (b) $\chi_{vdw} = 5$.

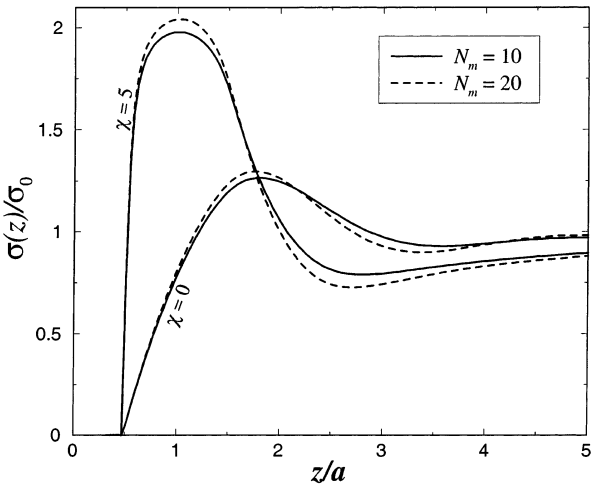

Figure 8. Net fluid charge $\sigma(z)$ at different χ_{vdw} couplings (systems C and D).

Figure 10. In general, the densities of PC and PA monomers are systematically larger than those found for systems C and D corresponding to a lower PE concentration. This effect is due to the fact that, at higher concentration of oppositely charged chains, the number of dipoles (i.e., PC−PA monomer pairs) are also larger, and from this it gives larger plate−dipole correlations.

Even at $\chi_{vdw} = 0$ with $N_m = 10$, we can observe a nonnegligible second peak in $n_+(z)$ (located at $z \approx 3.8a$) which is the signature of a third layer. This finding contrasts with what was observed at spherical substrates[12] (also with $\chi_{vdw} = 0$, $N_m = 10$, and with a similar macroion surface charge density), where not even a stable bilayer could build up. This radically different behavior can be accounted by geometrical arguments. Indeed, the potential of electrostatic interaction scales like $1/r$ in spherical geometry against z in planar one. Hence, at sufficiently high curvature (as it was the case in ref 12 where $N_m a/r_0 > 1$[25] with r_0 being the radius of the spherical macroion), qualitative differences from the planar case are then expected. However, the corresponding microstructure (see Figure 10a) suggests a relatively large formation of PC−PA globules leading to a diffuse and porous multilayer. Always at $\chi_{vdw} = 0$, but with longer chains ($N_m = 20$), Figure 9a shows that the degree of layering is higher as expected. This feature is well illustrated by Figure 10b, where the PA monomers are visibly more attracted to the planar macroion surface.

At $\chi_{vdw} = 5$, the adsorption of monomers is drastically increased due to the enhanced stability of the first PC

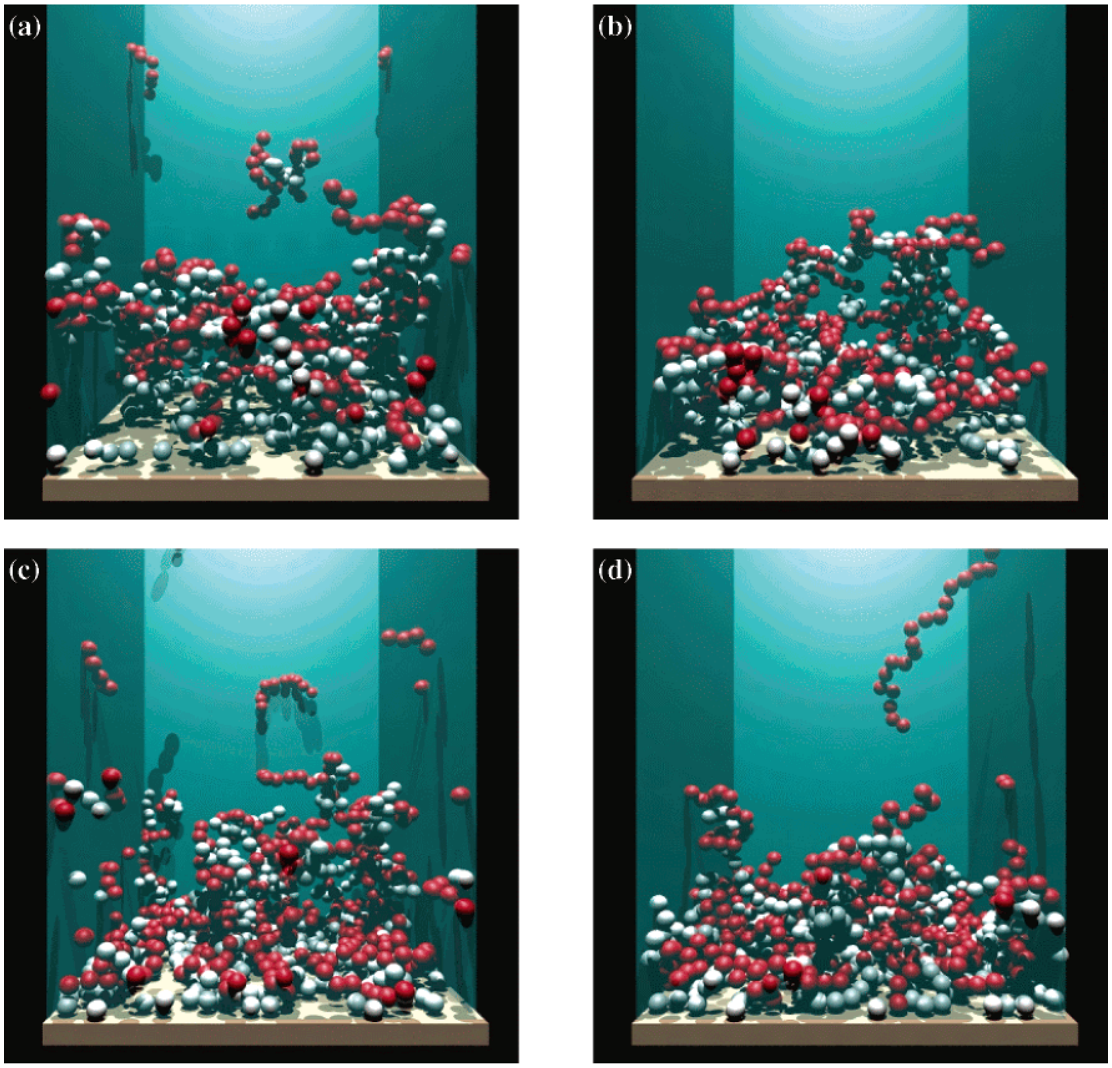

Figure 10. Typical equilibrium configurations for the adsorption of oppositely charged PE chains (systems E and F) onto a planar macroion. The polycations are in white and the polyanions in red. The little ions are omitted for clarity. Key: (a) $\chi_{vdw} = 0$, $N_m = 10$; (b) $\chi_{vdw} = 0$, $N_m = 20$; (c) $\chi_{vdw} = 5$, $N_m = 10$; (d) $\chi_{vdw} = 5$, $N_m = 20$.

layer that, in turn, induces a larger adsorption of the subsequent PAs and PCs. Compared to $\chi_{vdw} = 0$, all the peaks in $n_{\pm}(z)$ are shifted to smaller z, indicating a higher compaction. These higher ordering and compaction at $\chi_{vdw} = 5$ can be visually checked in Figure 10, parts c and d.

The net fluid charge $\sigma(z)$ is reported in Figure 11. As expected charge oscillations are detected. However in all cases, the corresponding amplitude is *decaying* (as also found in ref 12 for spherical geometry). Compared to the bilayer situation (see Figure 8), one remarks that the charge oscillations are now larger due to the enhanced "plate−dipole" correlations occurring at higher chain concentrations (as discussed above). On the other hand, the positions of the extrema in the charge oscillations remain quasi unchanged.

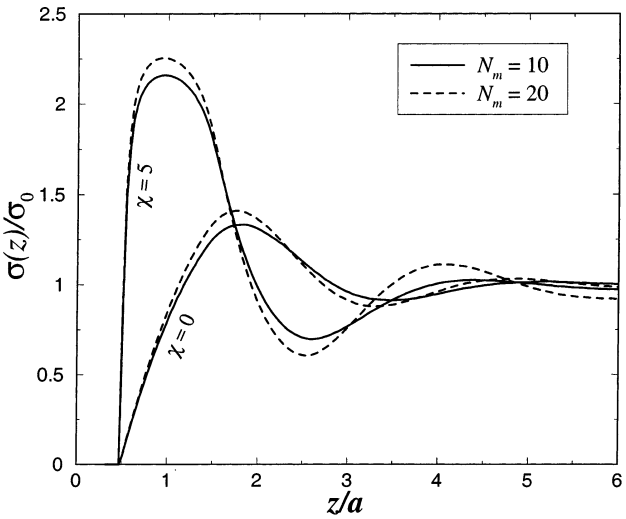

Figure 11. Net fluid charge $\sigma(z)$ at different χ_{vdw} couplings (systems E and F).

VII. Concluding Remarks

We first would like to briefly discuss our findings with some experimental examples.Our results concerning the first layer (i.e., single PC layer) show that an additional nonelectrostatic force is needed to enhance its stability. Experimentally, this is achieved by choosing PCs with good "anchoring" properties to a given substrate. In our model this was done by taking $\chi_{vdw} = 5$. This being said, the case $\chi_{vdw} = 0$ is from a fundamental point of view

interesting, since it corresponds to a purely electrostatic regime.

Recently, Menchaca et al. found, by means of "liquid-cell AFM", that PE-complex grains appear at the first PE-layers.[26] This kind of structure (that we referred to as small islands—see Figure 6) are confirmed by our simulations. Concomitantly, a significant roughness of the deposited bilayer was also detected in this experiment, which is directly linked to the presence of those grains. This microstructure seems also to be (indirectly) reported in other experiments using ellipsometry,[27] where it is found that the structure of the two first bilayers are more porous than that of later bilayers. This is also in qualitative agreement with our microstructures depicted in Figures 6 and 10. However, more simulation data are needed to understand the PE structure beyond two bilayers.

The degree of charge inversion of the substrate can be indirectly obtained by measuring the ζ-potential via electrophoresis.[11] In their experiment, Ladam et al.[11] observed that, *after a few deposited PE layers*,[28] the ζ-potential profile is symmetrically oscillating. This reveals a "stationary" regime where successively, polycations and polyanions are adsorbed with the same strength. Unfortunately, it is not possible for us to investigate numerically this regime due to the highly prohibitive computation time required there. However, the charge oscillations observed in our $\sigma(z)$ profiles indicate that by increasing the amount of layers, one first increases the amplitude of these oscillations. This confirms at least the general experimental evidence of the nonstationary regime a the *early stage* of PE multilayering.

We also would like to mention the possible effect of image charges stemming from the dielectric discontinuity between the substrate (typically $\epsilon_r \approx 2-5$) and the solvent (here $\epsilon_r \approx 80$), as is the case under experimental conditions. It is expected that image forces become especially relevant for PE monolayering (i.e., when PCs solely are present).[29] Indeed for multivalent ions, a strong self-image repulsion occurs and leads to a shifted density-profile $n_+(z)$ with a maximum located somewhat further than the contact region.[13,14] However for *PE multilayering*, due to the presence of oppositely charged PEs, the effect of image forces may be considerably reduced (especially sufficiently away from the wall) due to the (self-)screening of the image charges.

In summary, we have investigated by means of extensive MC simulations the equilibrium buildup of the few first layers adsorbed on a charged planar substrate. Two parameters were considered: (i) the chain length N_m and (ii) the extra nonelectrostatic short-range attraction (characterized here by χ_{vdw}) between the planar macroion surface and the polycation chains.

For the bilayering, it was demonstrated that, within the electrostatic regime (i.e., $\chi_{vdw} = 0$), significant PC−PA globules build up leading to a very "porous" and diffuse bilayer structure. The PC−PA globalization is enhanced with N_m. At sufficiently large χ_{vdw} (here $\chi_{vdw} = 5$), the bilayer is much less diffuse and the oppositely charged chains are more polarized, leading to a high stability of the structure.

The same qualitatively applies to the case of the two-bilayer (i.e., four PE layers) adsorption. Within this regime of layering as investigated here (up to four layers), we also found a nonlinear regime, where for instance the separation of the peaks in the monomer densities are not identical. This is in qualitative agreement with the finding of Ladam et al.[11] where they reported a nonlinear regime in the so-called "region I" corresponding to the PE multilayer-region close to the buffer.[28] The effect of N_m is to globally enhance the stability of the multilayer structure due to the higher electrostatic correlations and also due to entropic effects.

A future study should take into account the rigidity of the chain, which can drastically change the multilayer structure depending the stiffness. The formation of PE multilayers on *cylindrical* substrates seems also to be a promising research area, and to our knowledge it has never been investigated so far.[30]

Acknowledgment. The author thanks F. Caruso, H. Löwen, S. K. Mayya, and E. Pérez for helpful and stimulating discussions.

References and Notes

(1) Schmitt, J.; Decher, G.; Hong, G. *Thin Solid Films* **1992**, *210/211*, 831.
(2) Decher, G. *Science* **1997**, *277*, 1232.
(3) Caruso, F.; Furlong, D. N.; Ariga, K.; Ichinose, I.; Kunitake, T. *Langmuir* **1998**, *14*, 4559.
(4) Onda, M.; Ariga, K.; Kunitake, T. *Biosci. Bioeng.* **1999**, *87*, 69.
(5) Wu, A.; Yoo, D.; Lee, J. K.; Rubner, M. F. *J. Am. Chem. Soc.* **1999**, *121*, 4883.
(6) Caruso, F.; Caruso, R. A.; Möhwald, H. *Science* **1998**, *282*, 1111.
(7) Gittins, D. I.; Caruso, F. *J. Phys. Chem. B* **2001**, *105*, 6846.
(8) Solis, F. J.; de la Cruz, M. O. *J. Chem. Phys.* **1999**, *110*, 11517.
(9) Netz, R. R.; Joanny, J. F. *Macromolecules* **1999**, *32*, 9013.
(10) Castelnovo, M.; Joanny, J. F. *Langmuir* **2000**, *16*, 7524.
(11) Ladam, G.; Schaad, P.; Voegel, J. C.; Schaaf, P.; Decher, G.; Cuisinier, F. *Langmuir* **2000**, *16*, 1249.
(12) Messina, R.; Holm, C.; Kremer, K. *Langmuir* **2003**, *19*, 4473.
(13) Messina, R. *J. Chem. Phys.* **2002**, *117*, 11062.
(14) Torrie, G. M.; Valleau, J. P.; Patey, G. N. *J. Chem. Phys.* **1982**, *76*, 4615.
(15) Only the monomer−monomer excluded volume interaction was not modeled by a hard-sphere potential. There, a purely (truncated and shifted) repulsive Lennard-Jones potential was used (see eq 7) so as to be compatible with the FENE potential employed to generate the chain connectivity.
(16) Grzybowsky, A.; Brodka, A. *Mol. Phys.* **2002**, *100*, 1017.
(17) To further improve the computational efficiency, the corresponding electrostatic energies were initially stored into tables. Bear in mind, that such simulations (despite of this initial storage) involving Lekner sums are extremely time-consuming. As an example, the equilibration of system F with a satisfactory statistical accuracy requires about one month CPU time with a Pentium 4 processor of 2.0 Ghz.
(18) Kremer, K. *Computer Simulation in Chemical Physics*; Kluwer Academic Publishers: Amsterdam, 1993.
(19) Metropolis, N.; Rosenbluth, A. W.; Rosenbluth, M. N.; Teller, A. N.; Teller, E. *J. Chem. Phys.* **1953**, *21*, 1087.
(20) Allen, M. P.; Tildesley, D. J. *Computer Simulations of Liquids*; Clarendon Press: Oxford, England, 1987.
(21) Shklovskii, B. *Phys. Rev. E* **1999**, *60*, 5802.
(22) Messina, R.; Holm, C.; Kremer, K. *Phys. Rev. E* **2001**, *64*, 021405.
(23) Levin, Y. *Rep. Prog. Phys.* **2002**, *65*, 1577.
(24) Hayashi, Y.; Ullner, M.; Linse, P. *J. Chem. Phys.* **2002**, *116*, 6836.
(25) Note that in the opposite limit of low curvature where $N_m a/r_0 \ll 1$, the spherical case can be well approximated by a planar interface.
(26) Menchaca, J. L.; Jachimska, B.; Cuisinier, F.; Pérez, E. *Colloids Surf. A* **2003**, *222*, 185.
(27) Harris, J. J.; Bruening, M. L. *Langmuir* **2000**, *16*, 2006.
(28) Experimentally, Ladam et al.[11] reported a linear regime for the PE multilayer thickness as a function of the number of PE layers after the deposition of *six* PE layers (see also Figure 4 of ref 11). After a similar number of deposited PE layers, the ζ-potential alternates nearly symmetrically keeping the same absolute value (see Figure 3 of ref 11).
(29) Messina, R. Manuscript in preparation.
(30) Messina, R. *J. Chem. Phys.* **2003**, *119*, 8133.

MA034689E

Appendix N

Reentrant transitions in colloidal or dusty plasma bilayers

Reentrant Transitions in Colloidal or Dusty Plasma Bilayers

René Messina* and Hartmut Löwen†

Institut für Theoretische Physik II, Heinrich-Heine-Universität Düsseldorf, Universitätsstrasse 1, D-40225 Düsseldorf, Germany

(Received 18 February 2003; published 30 September 2003)

The phase diagram of crystalline bilayers of particles interacting via a Yukawa potential is calculated for arbitrary screening lengths and particle densities. Staggered rectangular, square, rhombic, and triangular structures are found to be stable including a first-order transition between two different rhombic structures. For varied screening length at fixed density, one of these rhombic phases exhibits both a single and even a double reentrant transition. Our predictions can be verified experimentally in strongly confined charged colloidal suspensions or dusty plasma bilayers.

DOI: 10.1103/PhysRevLett.91.146101 PACS numbers: 68.65.Ac, 52.27.Lw, 82.70.Dd

Confined systems exhibit structural and dynamical behavior very much different from the corresponding bulk state [1,2]. In particular, freezing is strongly affected by the presence of a planar wall. In equilibrium, solidification near walls can occur at thermodynamic conditions where the bulk is still fluid (so-called "prefreezing") [3,4]. In nonequilibrium, the wall may act as a center of heterogeneous nucleation [5] in order to initiate crystal growth [6]. A system confined between two parallel planar walls exhibits various layered crystalline states at low temperature if the plate distance gets comparable to the mean interparticle distance. For hard spheres between hard plates, geometric packing considerations lead to the stability of different crystalline lattices including multiple square and hexagonal layers [7] as well as buckled [8], rhombic [8,9], and prism superlattices [10]. On the other hand, for pure Coulombic systems such as (classical) electrons in quantum wells [11] or trapped ions [12], several crystalline bilayer structures were reported [13].

Most of our experimental knowledge of freezing in confining slitlike geometry is based on real-space measurements of mesoscopic model systems such as charged colloidal suspensions between glass plates [7,10] or of multilayers of highly charged dusty plasmas [14]. The actual interaction between these mesoscopic "macroions" is neither hard-sphere-like nor pure Coulombic but is described by an intermediate screened Coulomb or Yukawa pair potential [15,16] due to the screening via additional microions in the system. The screening length can be tailored by changing the microion concentration: For charged colloids, salt ions are conveniently added to the aqueous suspensions; the complex plasma, on the other hand, consists of electrons and impurity ions.

In the present Letter, we study the stability of different crystal lattices in bilayers of Yukawa particles as motivated by the experimental model systems. The zero-temperature phase diagram is calculated for arbitrary screening lengths and particle densities [17]. We find a variety of different staggered solid lattices to be stable which are separated by either first- or second-order phase transitions. The two known extreme limits of zero or infinite screening length corresponding to hard spheres [9] and the plasma [13,18] are recovered. For intermediate screening lengths, the phase behavior is strikingly different from a simple interpolation between these two limits. First, there is a first-order coexistence between two different staggered rhombic lattices differing in their relative shift of the two unit cells. Second, one of these staggered rhombic phases exhibits a novel reentrant effect for fixed density and varied screening length. Depending on the density, the reentrant transition can proceed via a staggered square or a staggered triangular solid including even a double reentrant transition of the rhombic phase. All of our theoretical predictions can, in principle, be verified in real-space studies of confined charged suspensions or dusty plasmas.

In detail, our system consists of two layers containing in total N particles in the (x, y) plane. The total area density of the two layers is $\rho = N/A$ with A denoting the system area in the (x, y) plane. The distance D between the layers in the z direction is prescribed by the external potential confining the system. The particles are interacting via the Yukawa pair potential,

$$V(r) = V_0 \frac{\exp(-\kappa r)}{\kappa r}, \tag{1}$$

where r is the central separation. The inverse screening length κ which governs the range of the interaction is given in terms of the microion concentration by Debye-Hückel screening theory. The energy amplitude $V_0 = Z^2 \exp(2\kappa R)\kappa/\epsilon(1 + \kappa R)^2$ scales with the square of the charges Z of the particles of physical hard core radius R [19] reduced by the dielectric ϵ permittivity of the solvent ($\epsilon = 1$ for the dusty plasma). Typically, Z is of the order of 100–100 000 elementary charges such that $V(r)$ at typical interparticle distances can be much larger than the thermal energy $k_B T$ at room temperature justifying formally zero-temperature calculations. Then the energy scale is set by V_0 alone and phase transitions in large bilayer systems are completely determined by two

dimensionless parameters, namely, the reduced layer density $\eta = \rho D^2/2$ and the relative screening strength $\lambda = \kappa D$. For zero temperature, the stable state is solid but different crystalline structures of the bilayers are conceivable. As possible candidate structures, we assume that the two two-dimensional periodic lattices in the bilayers are the same, have a simple unit cell, and are shifted relative to each other in the lateral direction by a displacement vector $\mathbf{c}$. If the two layers are labeled with A and B, the particle positions in the (x, y) plane of the two layers are given by

$$\mathbf{R}_A(m, n) = m\mathbf{a}_1 + n\mathbf{a}_2, \qquad \mathbf{R}_B(m, n) = m\mathbf{a}_1 + n\mathbf{a}_2 + \mathbf{c}, \tag{2}$$

where $\mathbf{a}_1$ and $\mathbf{a}_2$ are the primitive vectors of the two-dimensional lattice and m, n are integers. The total internal energy U is obtained by the double lattice sum,

$$U = \frac{1}{2}\sum_{\mathbf{R}_A \neq \mathbf{R}'_A} V(|\mathbf{R}_A - \mathbf{R}'_A|) + \frac{1}{2}\sum_{\mathbf{R}_B \neq \mathbf{R}'_B} V(|\mathbf{R}_B - \mathbf{R}'_B|) + \sum_{\mathbf{R}_A, \mathbf{R}_B} V([|\mathbf{R}_A - \mathbf{R}_B|^2 + D^2]^{1/2}). \tag{3}$$

In the limit $N \to \infty$, the stable crystalline structure minimizes the total internal energy per particle U/N.

We have minimized U/N with respect to $\mathbf{a}_1$, $\mathbf{a}_2$, and $\mathbf{c}$ under the constraint of prescribed density η for given λ mapping out the phase diagram in the $(\eta\lambda)$ plane. As a result, five typical staggered lattice structures turn out to minimize U/N for different η. Adopting the notation developed for plasma bilayers [18], we label them by I, II, III, IV, and V. As summarized in Table I, phase I is the staggered rectangular crystal with a fixed aspect ratio a_2/a_1 of $\sqrt{3}$; phase II is also staggered rectangular but with a different aspect ratio γ interpolating continuously between phase I and the staggered-square phase III where $a_2/a_1 = 1$. The staggered rhombic phase IV has two nonorthogonal lattice unit vectors ($\mathbf{a}_1$ and $\mathbf{a}_2$) forming an angle θ and contains a general lateral shift $\mathbf{c} = \alpha(\mathbf{a}_1 + \mathbf{a}_2)$ between the two rhombic lattices. In fact, we find two possibilities for α defining two variants of stable rhombic phases which we call IVA and IVB. For IVA, $\alpha = 1/2$ while $\alpha < 1/2$ for IVB. Finally, phase V is a staggered triangular crystal. Both phases III and V can be considered as special cases of the rhombic phase IV; the former has $\theta = \pi/2$ and $\alpha = 1/2$ while the latter is characterized by $\theta = \pi/3$ and $\alpha = 1/3$.

TABLE I. Structure and parameters of the different staggered bilayer crystals. $\mathbf{a}_1$ is set to $(a_1, 0)$, where a_1 is the nearest intralayer distance between particles. For phase II, $\gamma = a_2/a_1$ is the aspect ratio. For phase IV, θ is the angle between $\mathbf{a}_1$ and $\mathbf{a}_2$, and α is a free parameter characterizing the relative lateral interlattice shift $\mathbf{c}$.

Phase	$\mathbf{a}_2/a_1$	$\mathbf{c}$	$\rho a_1^2/2$
I. Rectangular	$(0, \sqrt{3})$	$(\mathbf{a}_1 + \mathbf{a}_2)/2$	$1/\sqrt{3}$
II. Rectangular	$(0, \gamma)$	$(\mathbf{a}_1 + \mathbf{a}_2)/2$	γ
III. Square	(0,1)	$(\mathbf{a}_1 + \mathbf{a}_2)/2$	1
IV. Rhombic	$(\cos\theta, \sin\theta)$	$(\mathbf{a}_1 + \mathbf{a}_2)\alpha$	$1/\sin\theta$
V. Triangular	$(1/2, \sqrt{3}/2)$	$(\mathbf{a}_1 + \mathbf{a}_2)/3$	$2/\sqrt{3}$

The result for the phase diagram for a wide range of screening strengths ($0 \leq \lambda \leq 100$; $\lambda \to \infty$) and densities ($0 \leq \eta \leq 0.8$) is shown in Fig. 1. At very low screening λ, we recover the known plasma limit [18], with our labeling of the phases being in line with their sequence

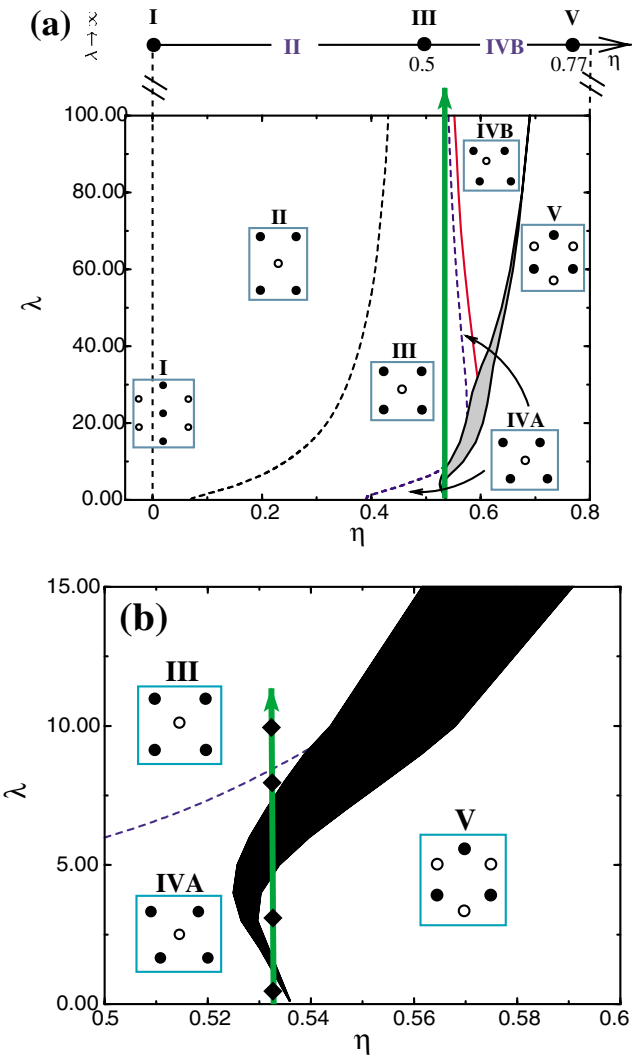

FIG. 1 (color online). Phase diagram of the Yukawa bilayer in the (η, λ) plane. (a) The hard sphere limit $\lambda \to \infty$ is sketched on top. The dashed (solid) lines denote continuous (discontinuous) transitions. The filled region corresponds to the coexistence domain of phases IV and V. The vertical arrow indicates the double reentrant behavior of phase IVA. The insets show the lattice geometries, where the filled (open) circles correspond to the lower (upper) layer. (b) Magnification of (a) showing a reentrant behavior of phase IVA occurring at moderate λ. The four diamonds along the arrow indicate state points which were investigated by computer simulation at finite temperatures.

for increasing density η. Phase I has a finite but extremely small density region of stability up to $\eta = 3.6 \times 10^{-5}$ at $\lambda = 0$ [18]. For finite λ, the I $\rightarrow$ II transition stays second order and occurs at even smaller densities which decrease monotonically to zero as a function of λ until the hard-sphere limit $\lambda \rightarrow \infty$ is reached. In this latter case, a_1 is playing the role of an effective particle diameter. This is sketched by the vertical line in Fig. 1. The II $\rightarrow$ III transition is second order and the transition densities increase drastically with growing λ and interpolating monotonically between the plasma and hard-sphere limit. More details of the I $\rightarrow$ II $\rightarrow$ III transition scenario are depicted in Fig. 2 where the aspect ratio γ of phase II is shown versus η for different λ. Phases I and III correspond to $\gamma = \sqrt{3}$ and $\gamma = 1$, respectively. As can be clearly deduced from Fig. 2, the aspect ratio γ interpolates continuously as a function of η between $\sqrt{3}$ and 1 for any λ such that both the I $\rightarrow$ II and the II $\rightarrow$ III transitions are second order. In the hard-sphere limit, γ approaches $\gamma_{\rm hs} = -2\eta + \sqrt{4\eta^2 + 3}$ continuously which is also shown in Fig. 2.

Novel effects are observed for the III $\rightarrow$ IV $\rightarrow$ V transitions. First, for small λ, the III $\rightarrow$ V transition proceeds via a IVA phase, the former being second order, and the latter first order. For $\lambda \approx 8$, however, there is a strong first-order transition directly from III to V with a large density jump as determined by Maxwell's construction [20]. For even higher screening, $\lambda \gtrsim 30$, the III $\rightarrow$ V transition happens via the cascade III $\rightarrow$ VIA $\rightarrow$ IVB $\rightarrow$ V. The stability range of the IVA phase becomes smaller for increasing λ shrinking to zero in the hard-sphere limit. Details of the III $\rightarrow$ V transition scenario can be detected via the order parameters $\sin\theta$ and α of the lattice minimizing the total potential energy at prescribed density η. Plotting $\sin\theta$ and α versus η reveals the order of the transitions (see Fig. 3): A cusp, which is found for the III $\rightarrow$ IVA transformation, implies a second-order transition. All other transitions are first order as signaled by discontinuous jumps in at least one of these order parameters. The corresponding coexistence density gap is not shown in Fig. 3 but included in Fig. 1(a). Across the IVA $\rightarrow$ IVB transition, the order parameter jump is small yielding a tiny density gap which cannot be resolved in Fig. 1(a).

Our most striking result is reentrant behavior of the IVA phase at fixed density upon varying λ as indicated in Fig. 1 by the vertical arrow. For $0.5 < \eta < 0.525$, there is reentrance of the VIA phase via the III phase. The full sequence over the whole range of λ is IVA $\rightarrow$ III $\rightarrow$ IVA $\rightarrow$ IVB. For $0.530 < \eta < 0.536$, there is even a double reentrant behavior of the VIA phase via the

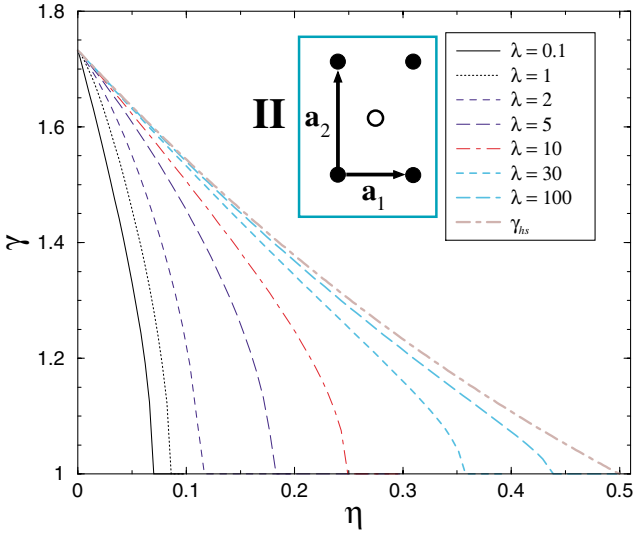

FIG. 2 (color online). Aspect ratio $\gamma = a_2/a_1$ for phase II versus density η for different screening strengths λ. The hard sphere case $\gamma_{\rm hs}$ is also shown. The lattice geometry is shown as an inset, where the filled (open) circles correspond to the lower (upper) layer.

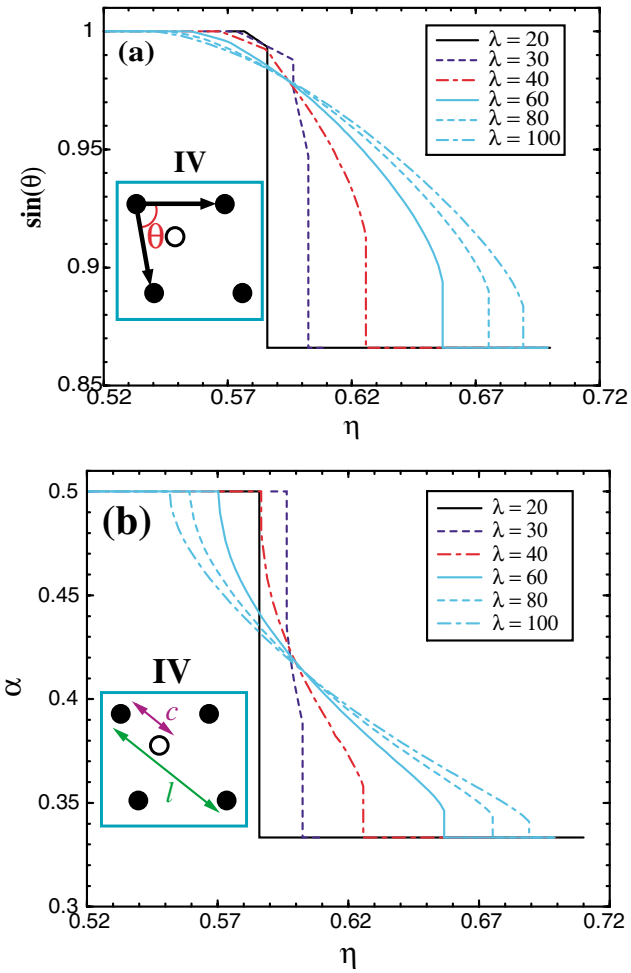

FIG. 3 (color online). (a) Sine of the angle θ and (b) the relative shift parameter $\alpha = c/\ell$ (with $\ell = |\mathbf{a}_1 + \mathbf{a}_2|$) versus density regarding the III $\rightarrow$ IV $\rightarrow$ V transition scenario for different λ. The insets show the lattice geometry of phase IV.

sequence IVA → V → IVA → III → IVA → IVB. This rich scenario is due to a subtle interplay of the range of the interaction in conjunction with the different bilayer lattice structures. Finally, at finite temperatures T, we performed extensive Monte Carlo computer simulations with 800 particles in a rectangular-shaped box periodically repeated in the x and y directions and with hard walls of distance D in the z direction allowing fluctuating z positions of the particles ("buckling"). For fixed $\eta = 0.533$, we investigated four states at $\lambda = 0.5, 3.0, 8.2, 10$ [see the four diamonds along the arrow in Fig. 1(b)] for different T up to melting. The melting point is detected via a modified Lindemann-type criterion involving differences of mean-square displacements of nearest neighbors [13]. We confirm that the reentrant behavior is stable with respect to increasing T up to melting.

In summary, we have calculated the full phase diagram for a Yukawa bilayer at zero temperature by lattice sum minimizations. A competition between three length scales, namely, the bilayer distance D, the averaged particle distance $\rho^{-1/2}$, and the range $1/\kappa$ of the interaction, induces a rich phase behavior which is different from a simple interpolation of the extreme limits of the confined plasma and the hard-sphere system. We predict a coexistence of two different rhombic phases at finite screening and a single and double reentrant scenario for one of the rhombic phases for varied "softness" of the interaction. These effects are in principle detectable in real-space experiments of charged colloidal suspensions confined between plates and in layers of dusty plasmas by tuning the screening strength via the microion concentration. The reentrant effect as obtained here in equilibrium should also manifest itself as an interesting fingerprint in nonequilibrium situations. For example, bilayer crystal nucleation and growth could be greatly stimulated via structures which are energetically close to the stable ones [21]. Soft particle interactions different from the Yukawa type of Eq. (1), as, e.g., inverse power potentials where $V(r) \propto r^{-n}$, will lead to similar reentrant effects as long as the softness of the potential (e.g., the exponent n) is varied. Different realizations of soft interactions occur in sterically stabilized colloids, in spherical block-copolymer micelles, and in star polymers and dendrimers, where the softness of the effective interaction can be tuned by the length and grafting density of the polymer chains or the solvent quality [22]. Hence, the reentrant scenario should also occur in foam films containing polymer bilayers [23]. Finally, for a general external potential confining the particles to layers, the bilayer distance D is not prescribed but the system will minimize its total energy realizing an optimal D. In this case, second-order phase transitions will still be described in terms of scaled parameters. This implies a universal behavior of our bilayer phase diagram. In a general external potential, however, the system has the additional possibility to split into tri- and higher-order multilayers. This can happen either discontinuously or continuously via merging prism phases. Details have to be explored in future studies.

We thank C. N. Likos and M. Schmidt for helpful discussions, and the DFG (SFB TR6) for financial support.

*Electronic address: messina@thphy.uni-duesseldorf.de
†Electronic address: hlowen@thphy.uni-duesseldorf.de

[1] K. Binder, J. Non-Equilib. Thermodyn. **23**, 1 (1998).
[2] C. Bechinger and E. Frey, J. Phys. Condens. Matter **13**, R321 (2001).
[3] J. E. Hug, F. van Swol, and C. F. Zukoski, Langmuir **11**, 111 (1995).
[4] M. Heni and H. Löwen, Phys. Rev. Lett. **85**, 3668 (2000).
[5] M. Würth *et al.*, Phys. Rev. E **52**, 6415 (1995).
[6] K. P. Velikov *et al.*, Science **296**, 106 (2002).
[7] C. A. Murray, W. O. Sprenger, and R. A. Wenk, Phys. Rev. B **42**, 688 (1990).
[8] P. Pieranski and L. Strzelecki, Phys. Rev. Lett. **50**, 331 (1983).
[9] M. Schmidt and H. Löwen, Phys. Rev. Lett. **76**, 4552 (1996); Phys. Rev. E **55**, 7228 (1997).
[10] S. Neser *et al.*, Phys. Rev. Lett. **79**, 2348 (1997).
[11] G. J. Kalman, Z. Donko, and K. I. Golden, Contrib. Plasma Phys. **41**, 191 (2001).
[12] M. G. Raizen *et al.*, Phys. Rev. A **45**, 6493 (1992).
[13] I. V. Schweigert, V. A. Schweigert, and F. M. Peeters, Phys. Rev. Lett. **82**, 5293 (1999); Phys. Rev. B **60**, 14 665 (1999).
[14] M. Zuzic *et al.*, Phys. Rev. Lett. **85**, 4064 (2000).
[15] A recent justification for the Yukawa interaction in dusty plasmas can be found in S. Nunomura *et al.*, Phys. Rev. Lett. **89**, 035001 (2002).
[16] M. O. Robbins, K. Kremer, and G. S. Grest, J. Chem. Phys. **88**, 3286 (1988).
[17] For moderate screening strength λ, the bilayer phase diagram (obtained by Monte Carlo simulations) was already reported in Ref. [13] but without the reentrance effect, the density jump across first-order transitions, and the stable IVB phase.
[18] G. Goldoni and F. M. Peeters, Phys. Rev. B **53**, 4591 (1996).
[19] We neglect the nonoverlap condition $r > 2R$ in Eq. (1) since charged particles are typically not at contact.
[20] Strictly speaking, volume terms of the microions will also contribute to the density jumps, but these terms are relevant only for strongly deionized systems: see R. van Roij and J.-P. Hansen, Phys. Rev. Lett. **79**, 3082 (1998). For high salinity, these terms will shrink the density jumps: see H. Graf and H. Löwen, Phys. Rev. E **57**, 5744 (1998).
[21] T. Palberg, J. Phys. Condens. Matter **11**, R323 (1999).
[22] C. N. Likos *et al.*, Phys. Rev. Lett. **80**, 4450 (1998).
[23] B. Kolaric, W. Jaeger, and R. von Klitzing, J. Phys. Chem. B **104**, 5096 (2000).

Appendix O

Confined colloidal bilayers under shear: Steady state and relaxation back to equilibrium

Confined colloidal bilayers under shear: Steady state and relaxation back to equilibrium

René Messina and Hartmut Löwen
Institut für Theoretische Physik II, Heinrich-Heine-Universität Düsseldorf, Universitätsstrasse 1, D-40225 Düsseldorf, Germany
(Received 24 June 2005; revised manuscript received 17 October 2005; published 18 January 2006)

Crystalline bilayers of charged colloidal suspensions which are confined between two parallel plates and sheared via a relative motion of the two plates are studied by extensive Brownian dynamics computer simulations. The charge-stabilized suspension is modeled by a Yukawa pair potential. The unsheared equilibrium configuration is two crystalline layers with a nested quadratic in-plane structure. For increasing shear rates $\dot{\gamma}$, we find the following steady states: First, up to a threshold of the shear rate, there is a static solid which is elastically sheared. Above the threshold, there are two crystalline layers sliding on top of each other with a registration procedure. Higher shear rates melt the crystalline bilayers and even higher shear rates lead to a reentrant solid stratified in the shear direction. This qualitative scenario is similar to that found in previous bulk simulations. We have then studied the relaxation of the sheared steady state back to equilibrium after an instantaneous cessation of shear and found a nonmonotonic behavior of the typical relaxation time as a function of the shear rate $\dot{\gamma}$. In particular, application of high shear rates accelerates the relaxation back to equilibrium since shear-ordering facilitates the growth of the equilibrium crystal. This mechanism can be used to grow defect-free colloidal crystals from strongly sheared suspensions. Our theoretical predictions can be verified in real-space experiments of strongly confined charged suspensions.

DOI: 10.1103/PhysRevE.73.011405 PACS number(s): 82.70.Dd, 83.10.Mj, 61.20.Ja

I. INTRODUCTION

A fundamental understanding of the different processes governing the relaxation of metastable phases back to equilibrium is critical for many basic questions in condensed matter physics and material science. Also, relaxational processes are omnipresent in industrial applications. Colloidal suspensions represent excellent model systems where such questions can be studied directly in real space as the length scales are conveniently accessed experimentally, the (variable) interactions can be described theoretically in a simple way, and the microscopic processes are rather slow as compared to molecular materials. This has been extensively exploited in previous studies of interaction-dependent equilibrium properties and dynamics [1–4]. One important example for a nonequilibrium steady state is a *sheared* colloidal suspension. It is known that application of shear may destroy the underlying equilibrium crystalline structure of the unsheared suspension [5] and can also lead to a reentrance ordering for high shear rates [6]. After cessation of shear the system will relax back to equilibrium from the sheared steady state. The microscopic details of this relaxation process are far from being resolved.

If an additional confinement between two parallel plates is considered [7], various experiments [8–14] reveal a rich and subtle influence of shear on the structure. Accordingly the relaxation back to equilibrium after cessation of shear is a fascinating but complex process which is a competition between wetting effects near the walls and bulk relaxation. In experiments on strongly confined suspensions, for instance, a complex pathway of the relaxation back to equilibrium was obtained [15]: a bilayer bcc crystal was shear-molten to recrystallize as a buckled single-layer triangular lattice which subsequently underwent a martensitic transition back to the equilibrium phase.

Most of the theoretical studies on colloidal suspensions have addressed the influence of linear shear flow on the bulk structure via nonequilibrium Brownian dynamics (NEBD) computer simulations [16] where hydrodynamic interactions [17] are neglected and involve charged colloidal particles modeled by a Yukawa pair interaction [18–27]. Shear-induced melting of colloidal bulk crystals and subsequent reentrant ordering at higher shear rates are confirmed by simulation. More recent works addressing a wall acting on a sheared suspension include a NEBD simulation in a channel [28] and theoretical investigations for a single colloidal particle [29,30].

In the present paper we address the relaxation of shear-induced structures after cessation of shear. We use the standard Yukawa model for confined systems and employ NEBD simulations. Here we focus on the simple and transparent situation of colloidal bilayers which are confined between two parallel plates and sheared via a relative motion of the two plates. The reasons to do so are threefold: First, the equilibrium phase diagram for confined crystalline bilayers interacting via a Yukawa pair potential is known from recent lattice-sum techniques at low temperatures [31]. The phase diagram is drastically influenced by the presence of the walls and differs from its bulk limit. This phase diagram was recently confirmed in experiments on charged suspensions strongly confined between two glass plates [32]. Second, the structure and the defects in a crystalline bilayer are easier to classify than in a multilayer. Last but not least, there are experimental studies for strongly confined situations which are not completely understood and are a challenge for a theoretical treatment [15]. Recent simulation studies of Das and co-workers [33,34] have addressed similar questions regarding sliding bilayers. The model employed in the studies of Das *et al.*, however, is simpler than ours: it does not possess a spatial dimension z perpendicular to the plates and hopping

processes between the layers are ignored. Furthermore, the relaxation back to equilibrium is not investigated in Refs. [33,34].

In order to be specific, we chose the unsheared equilibrium configuration to be two crystalline layers with a nested quadratic in-plane structure. This is the same starting configuration as used in the experiments [15]. For increasing shear rates $\dot{\gamma}$, we find the following scenario of steady states: first, there is a static solid which is elastically sheared until a shear-rate threshold is reached. Then there are two crystalline layers sliding on top of each other with a lock-in registration procedure similar to that observed in recent experiments by Palberg and Biehl [35,36]. Higher shear rates melt the crystalline bilayers and even higher shear rates lead to a reentrant solid stratified in the shear direction. This qualitative scenario is similar to that found in previous bulk simulations [18,20,23]. The shear-induced ordering at high shear rates is reminiscent of the transition towards lane formation in oppositely driven particles [37]. We have then studied the relaxation of the sheared steady state back to equilibrium after an instantaneous cessation of shear and found a nonmonotonic behavior of the typical relaxation time as a function of the shear rate $\dot{\gamma}$. In particular, application of high shear rates accelerates the relaxation back to equilibrium via shear ordering in the steady state. This mechanism can be used to grow defect-free colloidal crystals from strongly sheared suspensions as was proposed by Clark and co-workers [38,39]. Our theoretical predictions can be verified in experiments of confined charged suspensions [15,35,36].

The paper is organized as follows: In Sec. II, we introduce the ground state model for crystalline bilayers. The nonequilibrium Brownian dynamics simulation technique is explained in Sec. III. Results are presented in Sec. IV. Finally we conclude in Sec. V.

II. THE MODEL

In this part, we define our model. This is basically a generalization towards finite temperature of the ground state model used in Ref. [31] concerning the *equilibrium* (i.e., without external applied shear flow) phase diagram of crystalline colloidal bilayers interacting via a Yukawa potential. In detail, our system consists of two layers containing in total N particles in the (x,y) plane. The total area density of the two layers is $\rho=N/A$ with A denoting the layer area in the (x,y) plane. The distance D between the layers in the z direction is prescribed by the external potential confining the system. The particles are interacting via the Yukawa pair potential

$$V_{yuk}^{(part)}(r) = V_0 \frac{\exp(-\kappa r)}{\kappa r}, \tag{1}$$

where r is the center-center separation. The inverse screening length κ which governs the range of the interaction is given in terms of the micro-ion concentration by Debye-Hückel screening theory. The energy amplitude $V_0 = Z^2 \exp(2\kappa R)\kappa/\epsilon(1+\kappa R)^2$ scales with the square of the charges Z of the particles of physical hard core radius R reduced by the dielectric ϵ permittivity of the solvent ($\epsilon=1$ for the dusty plasma). Typically, Z is of the order of 100–100 000 elementary charges such that $V_{yuk}(r)$ at typical interparticle distances can be much larger than the thermal energy k_BT at room temperature, justifying formally zero-temperature calculations. Then the energy scale is set by V_0 alone and phase transitions in large bilayer systems are completely determined by two dimensionless parameters, namely the reduced layer density,

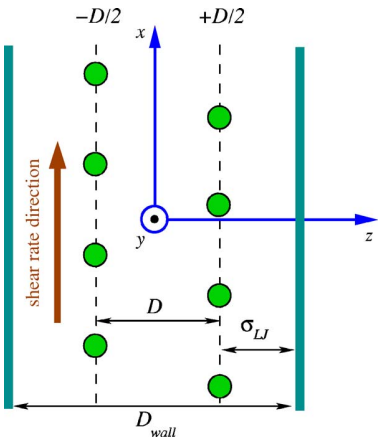

FIG. 1. (Color online) View in the (x,z) plane of the setup of the colloidal bilayer confined between two walls.

$$\eta = \rho D^2/2, \tag{2}$$

and the reduced screening strength,

$$\lambda = \kappa D. \tag{3}$$

For zero temperature, the stable state is solid but different crystalline structures of the bilayers are conceivable. The result for the phase diagram in a (η,λ)-map can be found in Ref. [31]. Here, we explore the same model for finite temperature by computer simulation.

III. THE NONEQUILIBRIUM BROWNIAN DYNAMICS COMPUTER SIMULATION

A. Simulation method

Here, we provide a detailed description of our Brownian dynamics method that was used to investigate *nonequilibrium* sheared colloidal bilayers (at finite temperature). A schematic setup of the system in the (x,z) plane is depicted in Fig. 1. The integration scheme for our model system in the presence of an external steady shear rate $\dot{\gamma}$ reads

$$\mathbf{r}_i(t+\delta t) = \mathbf{r}_i(t) + \frac{D_0}{k_BT}\mathbf{F}_i(t)\delta t + \delta\mathbf{W}_i + \dot{\gamma} z_i(t)\delta t \mathbf{e}_x. \tag{4}$$

Thereby $\mathbf{r}_i(t)=[x_i(t),y_i(t),z_i(t)]$ is the position of the ith colloidal particle at time t and D_0 denotes its free diffusion constant. By imposing a linear velocity profile, the

possibility of solvent shear-banding is excluded. All the contributions to the equation of motion (4) are explained below.

Within a small time interval δt, that particle moves under the influence of the sum of conservative forces $\mathbf{F}_i(t)$ stemming from (i) the pair interaction V_{yuk} [see Eq. (1)] between particle i and the neighboring ones and (ii) the repulsive interaction with the (soft) wall(s) whose potential of interaction, V_{wall}, is modeled as follows:

$$V_{wall}^{(LJ)}(z) = \begin{cases} \alpha\epsilon_{LJ}\left[\left(\dfrac{\sigma_{LJ}}{\dfrac{D_{wall}}{2}-|z|}\right)^{10}-\left(\dfrac{\sigma_{LJ}}{\dfrac{D_{wall}}{2}-|z|}\right)^{4}\right]+\epsilon_{LJ}, & \text{for } \dfrac{\dfrac{D_{wall}}{2}-|z|}{\sigma_{LJ}} \geqslant \left(\dfrac{5}{2}\right)^{1/6}, \\ 0, & \text{for } \dfrac{\dfrac{D_{wall}}{2}-|z|}{\sigma_{LJ}} < \left(\dfrac{5}{2}\right)^{1/6}, \end{cases} \tag{5}$$

where

$$\alpha = -\left[\left(\frac{1}{z_{min}}\right)^{10}-\left(\frac{1}{z_{min}}\right)^{4}\right]^{-1} = 3.070\,02...$$

[with $z_{min}=(5/2)^{1/6}\sigma_{LJ}$ minimizing V_{wall} in Eq. (5)] so that $V_{wall}(\sigma_{LJ})=\epsilon_{LJ}$. This (truncated and shifted) 10−4 Lennard-Jones potential given by Eq. (5) assumes that we have thin soft walls. Note that the use of a 9−3 Lennard-Jones potential corresponding to *semi-infinite* walls would not qualitatively change the results. Also the use of charged hard walls would not affect our main results. To check this latter statement, we have also considered charged walls leading to the following external interaction potential,

$$V_{wall}^{(ch)}(z) = W_0[\cosh(\kappa z) - 1], \tag{6}$$

where the amplitude W_0 is governed by the surface charge density of the plates.

Furthermore, due to the presence of the solvent, the particles experience (i) a friction whose constant is given by k_BT/D_0 and (ii) random displacements, $\delta\mathbf{W}_i$. Those latter are sampled from a Gaussian distribution with zero mean and variance $2D_0\delta t$ (for each Cartesian component). The last term in Eq. (4) represents the applied shear in the x direction and imposes an explicit linear flow field. The zero velocity plane of the imposed shear lies at the midplane between the plates.

B. Parameters

The colloidal particles are confined in a rectangular $L\times L\times D_{wall}$ box where periodic boundary conditions are applied in the (x,y) directions. The system is made up of $N=800$ particles (i.e., 400 particles per layer). The units are set as follows: $k_BT=1/\beta$ sets the energy scale, the (typical average) interlayer separation $D=D_{wall}-2\sigma_{LJ}$ (see also Fig. 1) sets the length scale, and $\tau=D^2/D_0$ sets the time scale. For the screened Coulomb wall-particle interaction [see Eq. (6)] we use $\beta W_0=30$. For the Yukawa interparticle interaction [see Eq. (1)] we choose $\beta V_0=6000$, whereas for the wall-particle interaction [see Eq. (5)] we choose $\beta\epsilon_{LJ}=1$ and $\sigma_{LJ}=0.1D$. The time step was set to $\delta t=10^{-5}\tau$. The reduced colloidal particle density is set to $\eta=ND^2/2L^2=0.24$ (so that $L=40.82D$) and the reduced screening is $\lambda=\kappa D=2.5$. Those latter parameters lead to the staggered square phase in the ground state (or at very low temperature) as can be seen on the phase diagram from Ref. [31].

A time interval of 1.5×10^5 BD time steps (i.e., 1.5τ) was sufficient to obtain the equilibrium (i.e., $\dot\gamma=0$) properties of our model system. The corresponding in-plane (x,y) pair distribution function $g(r)$ is shown in Fig. 2. It clearly shows a high degree of ordering as characterized by the pronounced peaks and the deep minima. The snapshot also provided in Fig. 2 confirms the square lattice structure expected for those parameters. Moreover, the structural properties are insensitive to the kind of particle-wall potential [here Eq. (5) versus Eq. (6)] as expected.

To quantify the layer extension in the z direction we have also plotted the particle density $n(z)$ that can be found in Fig. 3. The mean interlayer separation is then given by $2\int_0^{D_{wall}/2} z n(z) L^2 dz \approx 0.99D$, so that (in practice) D corresponds indeed to the interlayer separation. This latter result was identically obtained by employing either Eq. (5) or (6). In the forthcoming, where $\dot\gamma\neq0$, we will only show results for the LJ potential [Eq. (5)]. We have carefully checked that the results are qualitatively the same as those obtained with charged walls [Eq. (6)]. In particular, the general scenario for increasing shear rates does not change.

IV. RESULTS

A. Effect of shear flow

Starting from the equilibrium configuration described in the previous section, an external shear is applied during a

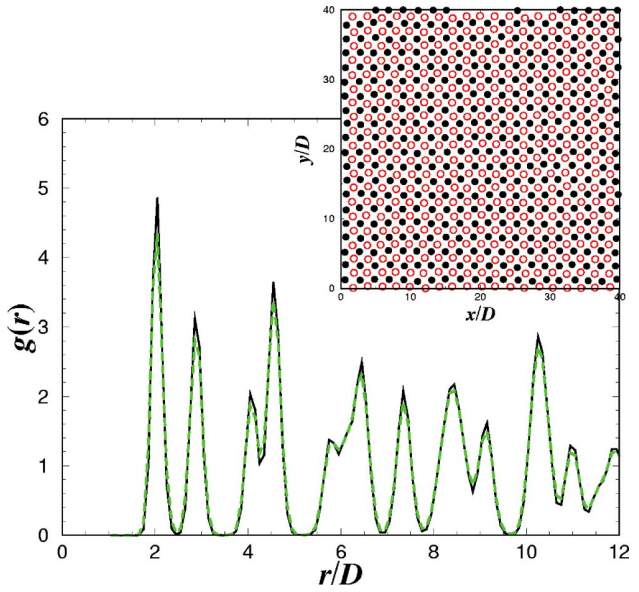

FIG. 2. (Color online) Intralayer (x,y) pair distribution function $g(r=\sqrt{x^2+y^2})$ at equilibrium $(\dot{\gamma}=0)$. The solid and dashed lines correspond to the use of Eqs. (5) and (6) (for the wall-particle potential of interaction), respectively. The inset shows a simulation snapshot where the filled (open) circles represent particles belonging to the upper (lower) layer.

period of 4×10^6 BD steps (i.e., 40τ). A steady state is reached after typically 10τ, and subsequent measurements are performed over a typical period of 20τ.

It is instructive to start our study by analyzing the microstructures reported in Fig. 4 corresponding to different $\dot{\gamma}$. From a structural point of view one can (qualitatively) identify three regimes:

• At sufficiently low shear rates (here $\dot{\gamma}=20/\tau$ and $\dot{\gamma}=50/\tau$), it can be seen that the crystalline structure (namely square) as well as the degree of ordering are conserved compared to the equilibrium situation (i.e., $\dot{\gamma}=0$, see Fig. 2). Consequently, we are in an elastic regime.

• For intermediate shear rates (here $\dot{\gamma}=60/\tau$ and $\dot{\gamma}=80/\tau$), there is a (relatively) strong disorder and the structure can therefore be qualified as liquid. In other words we have to deal with a *shear induced melting*.

• At high shear rates (here $\dot{\gamma}=100/\tau$ and $\dot{\gamma}=200/\tau$), the system gets *ordered again* (especially for the highest shear rate $\dot{\gamma}=200/\tau$) but exhibits a different (intralayer) crystalline symmetry (namely a triangular lattice) than the equilibrium one. Consequently, we have a reentrant behavior concerning the *intralayer*-ordering upon shearing.

In order to obtain a more quantitative description of these $\dot{\gamma}$-dependent structural properties, we have also computed the (azimuthally averaged) interlayer- and intralayer-pair-distribution functions $g(r=\sqrt{x^2+y^2})$ for different $\dot{\gamma}$. The results are presented in Fig. 5.

The elastic behavior can be best understood by considering the interlayer and intralayer $g(r)$. From Fig. 5, we see that at weak shearing (here $\dot{\gamma}=20/\tau$), the intralayer crystalline structure as well as the interlayer-lattice-correlation remains unchanged compared to the $\dot{\gamma}=0$ case (the latter is not reported in Fig. 5). At larger shear rate (here $\dot{\gamma}=50/\tau$) the degree of interlayer-lattice-correlation gets weaker than that of the intralayer one. A closer look at Fig. 5(a) reveals that, for $\dot{\gamma}=50/\tau$, the first peak is (asymmetrically) split into two neighboring peaks. This is the signature of a small relative displacement of the two square layer lattices. Upon further increasing the shear rate (now at $\dot{\gamma}=60/\tau$), the bilayer becomes a liquid, demonstrating that there is a critical shear rate $\dot{\gamma}_0$ (below which an elastic behavior is recovered) whose value is such that $50/\tau<\dot{\gamma}_0<60/\tau$.

Above $\dot{\gamma}_0$, the intralayer $g(r)$ exhibits a nontrivial behavior with respect to $\dot{\gamma}$ [see Fig. 5(b)], in agreement with our previous discussion on the microstructures depicted in Fig. 4. More precisely, at intermediate $\dot{\gamma}$ (here $60/\tau$ and $80/\tau$), the intralayer layer structure corresponds to a liquid one. Nonetheless and interestingly, at first neighbor separations, the square structure locally persists, but in coexistence with a triangular structure, as indicated by the broadened (splitted) first peak. This feature can also be nicely visualized on the snapshots from Fig. 4. At high shear rates (here $100/\tau$ and $200/\tau$), there is a strong short-ranged (*re*)ordering into a triangular lattice as indicated by the shifted first pronounced peak (especially for $\dot{\gamma}=200/\tau$). However, the degree of ordering reported for those highly sheared structures is not as high as that observed below $\dot{\gamma}_0$.

In order to quantify the degree of ordering in the x shear direction, we have also investigated the (intralayer) *one-dimensional* pair distribution function $g(|x|)$. For the computation of $g(|x|)$ we consider pairs of particles (of a given layer) that lie within a width $\Delta y/D=0.25$. The results are shown in Fig. 5(c): Below $\dot{\gamma}_0$ and for $\dot{\gamma}=200/\tau$ a crystalline state is found, whereas for the intermediate values of $\dot{\gamma}$ a liquid one is reported. A special case is achieved for $\dot{\gamma}_{max}=100/\tau$ [thick solid line in Figs. 5(b) and 5(c)]: Here there is liquid-like ordering in the shear flow direction [see Fig.

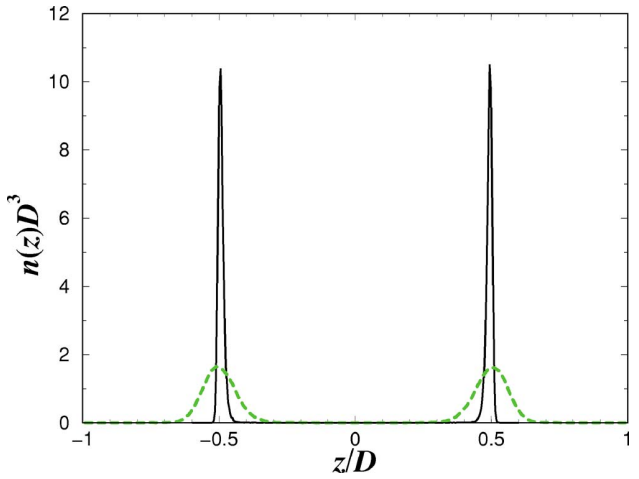

FIG. 3. (Color online) Laterally averaged inhomogeneous particle density $n(z)$ at equilibrium $(\dot{\gamma}=0)$. The solid and dashed lines correspond to the use of Eqs. (5) and (6) (for the wall-particle potential of interaction), respectively.

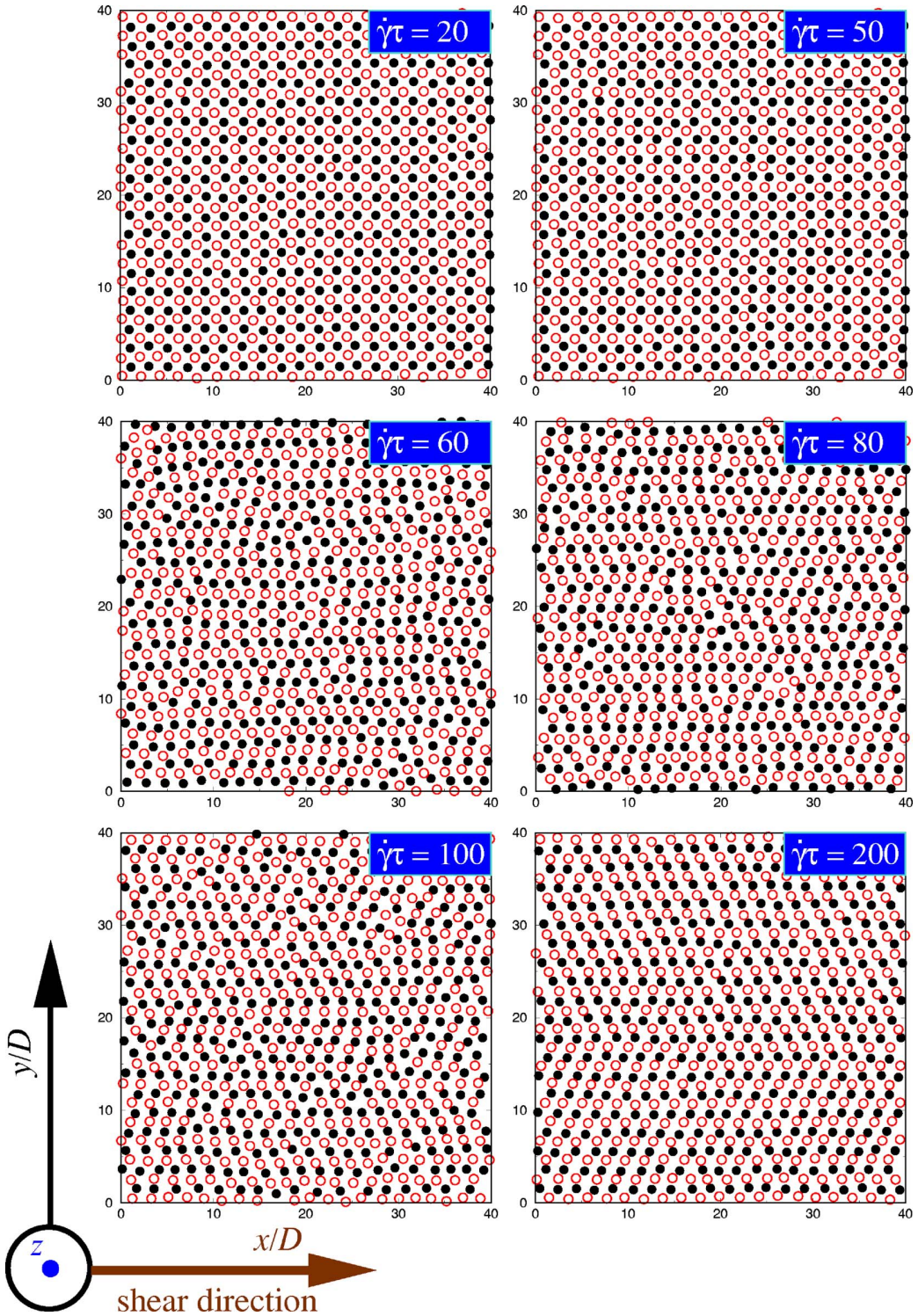

FIG. 4. (Color online) Simulation snapshots for different values of the shear rate $\dot{\gamma}$ (as indicated) where the filled (open) circles represent particles belonging to the upper (lower) layer.

5(c)], but long-ranged solid-like ordering in the radial $g(r)$ [see Fig. 5(b)]. This immediately implies that there is solid-like ordering in the vorticity direction. Hence, this structure can be classified as a liquid crystalline columnar phase.

To further quantify the behavior of highly sheared colloidal bilayers and also to provide a dynamical information, we are going to examine the (dimensionless) modified Lindemann parameter, $\Gamma_L(t)$, that is defined as follows,

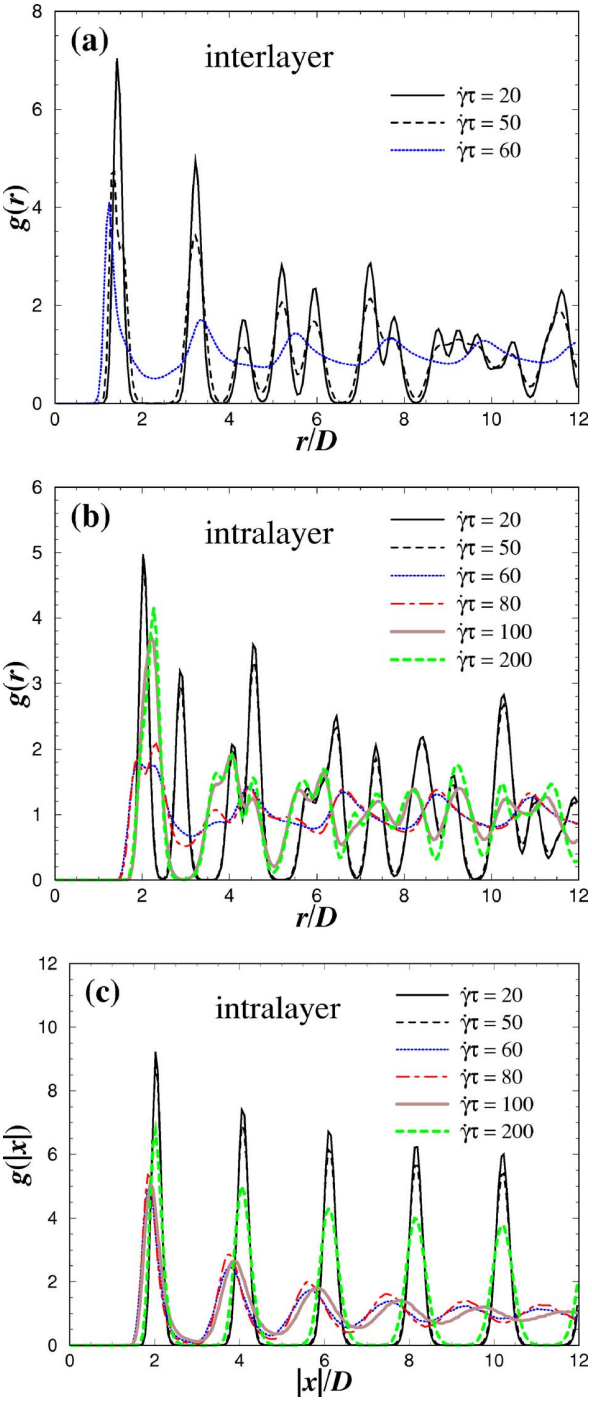

FIG. 5. (Color online) (a) Interlayer (x,y) pair distribution function $g(r=\sqrt{x^2+y^2})$ for small values of $\dot\gamma$ (as indicated in the legend). (b) Intralayer (x,y) pair distribution function $g(r=\sqrt{x^2+y^2})$ and (c) $g(|x|)$ for different values of $\dot\gamma$ (as indicated in the legend). The corresponding simulation snapshots are displayed in Fig. 4.

$$\Gamma_L(t) = \frac{\langle u^2(t)\rangle}{D^2}, \tag{7}$$

where $\langle u^2(t)\rangle$ corresponds to the difference in the mean square displacement of neighboring particles from their initial sites $\mathbf{r}_0=\mathbf{r}(t=t_0)$. More explicitly, $\langle u^2(t)\rangle$ can be written as

$$\langle u^2(t)\rangle = \left\langle \frac{1}{N}\sum_{i=1}^{N}\frac{1}{N_b}\sum_{j=1}^{N_b}\{[\mathbf{r}_i(t)-\mathbf{r}_i(t_0)]-[\mathbf{r}_j(t)-\mathbf{r}_j(t_0)]\}^2\right\rangle, \tag{8}$$

where $\mathbf{r}_i(t)=[x_i(t),y_i(t)]$, $\langle\cdots\rangle$ denotes an averaging over BD steps and the index j stands for the N_b nearest neighbors of particle i lying in the same upper or lower layers. Typically, for a (local) triangular lattice environment $N_b=6$ while for a rectangular one $N_b=4$. Besides, we also average over several reference times t_0 to improve the statistics. Due to the finite size of the simulation box, one is typically limited to observation times Δt_{obs} of the order of $\Delta t_{obs}\approx L/\dot\gamma_{max}D\approx 0.2\tau$ (by taking here $\dot\gamma_{max}=200/\tau$).

Our results are presented in Fig. 6. In the elastic regime (small $\dot\gamma$), the Lindemann parameter $\Gamma(t)$ exhibits a plateau at

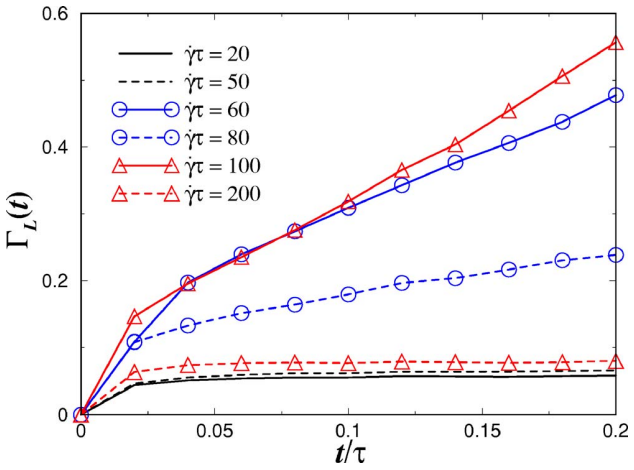

FIG. 6. (Color online) Modified Lindemann parameter $\Gamma_L(t)$ for different values of $\dot\gamma$ (as reported in the legend).

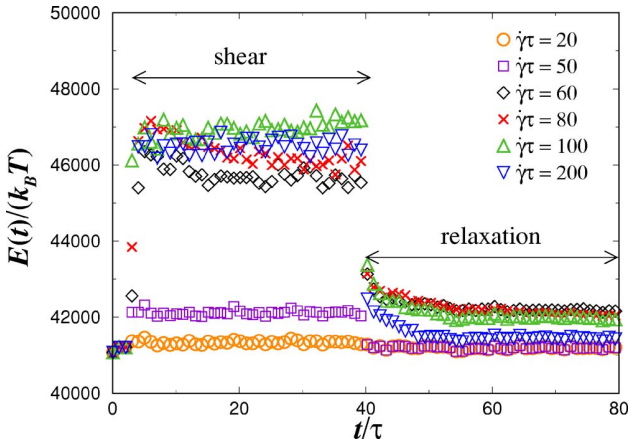

FIG. 7. (Color online) Time evolution of the total potential energy of interaction $E(t)$: before, during, and after shear. The values of $\dot\gamma$, considered during the shear process, are reported in the legend.

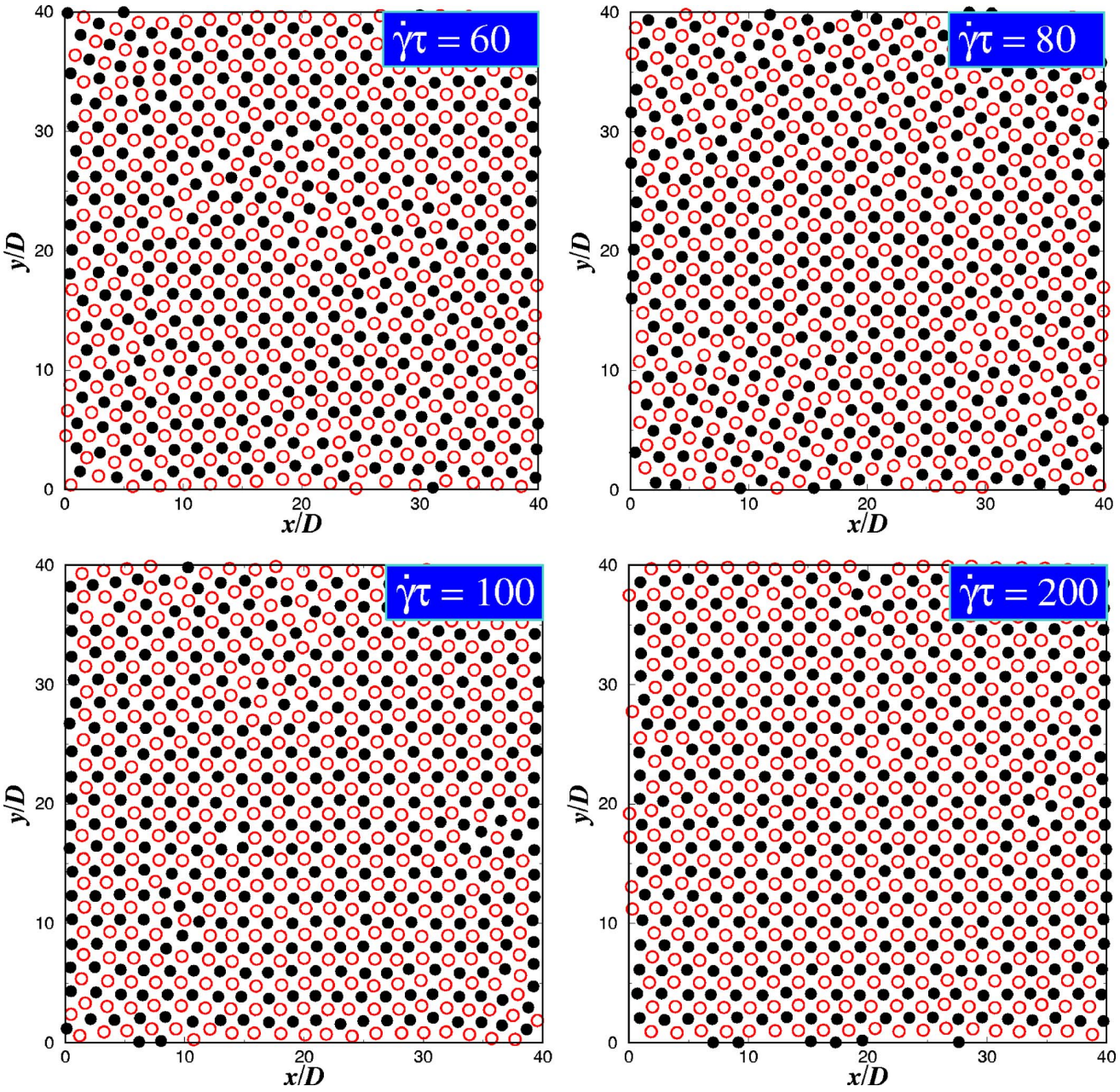

FIG. 8. (Color online) Simulation snapshots of relaxed systems taken at $t=80\tau$ for different values of the prior applied shear rates $\dot{\gamma}$ (as indicated).

"long" times, confirming the crystalline intralayer structure. At higher $\dot{\gamma}$ (i.e., $\dot{\gamma} \geqslant 60/\tau$) the situation gets more complicated. For $60/\tau \leqslant \dot{\gamma} \leqslant 100/\tau$, $\Gamma_L(t)$ diverges, proving a liquid behavior, in agreement with our static analysis of $g(|x|)$ [see Fig. 5(c)]. It is therefore only at very high shear rate (i.e., $\dot{\gamma} \geqslant 200/\tau$) that *true* intralayer crystalline reordering is recovered, as indicated by the existence of the plateau in $\Gamma_L(t)$ whose value is comparable to that obtained in the elastic regime.

B. Relaxation after cessation of shear

We now investigate how the system gets back to equilibrium after cessation of shear. A suitable and simple way to study a relaxation process is to monitor the evolution in time of the total potential energy of interaction $E(t)=V_{yuk}+V_{wall}$. In our simulations, the cessation of shear occurs at $t=40\tau$. Profiles of $E(t)$ for different shear rates $\dot{\gamma}$ applied *prior* relaxation are plotted in Fig. 7. The corresponding microstructures at long time $t=80\tau$ for $60/\tau \leqslant \dot{\gamma} \leqslant 200/\tau$ are sketched in Fig. 8. For low $\dot{\gamma}$ (here $\dot{\gamma} \leqslant 50/\tau$), the relaxation process is very fast as it should be. Note that the equilibrium energy value is not exactly recovered because of the existence of some long-living defects.

The relaxation process gets qualitatively different for more highly sheared systems (here $\dot{\gamma} \geqslant 60/\tau$). For the samples that have undergone a shear-induced melting as de-

duced from our criterion based on $\Gamma_L(t)$ [see Fig. 6 with $\dot{\gamma}\tau=60,80,100$], we remark that they all exhibit a similar relaxation behavior [see Fig. 7 with $\dot{\gamma}\tau=60,80,100$]. In particular the relaxation is thereby much slower, partly due to the existence of *many* long-living defects. Those latter also explain the high energy reported in the long time scale. There are several defects such as dislocations, (low angle) grain boundaries (especially for $\dot{\gamma}\tau=60,80$), and vacancies that are easily identifiable in the snapshots of Fig. 8.

On the other hand, at large enough $\dot{\gamma}$ (here $\dot{\gamma}=200/\tau$), the relaxation is faster as indicated by the faster earlier occurrence of an $E(t)$ plateau (which is also deeper). Nonetheless, the energy of this (nearly) relaxed system remains higher than those that were weakly sheared ($\dot{\gamma}<\dot{\gamma}_0$). Again the existence of some vacancies (see Fig. 8 with $\dot{\gamma}=200/\tau$) increases the energy system as well as the time of *full* relaxation.

By fitting $E(t)$ with an exponential decay, we were able to extract a typical relaxation time, τ_R, for the early stage ($40.5<t/\tau<60$) of the relaxation process: $\tau_R/\tau=5.3(\pm0.1),9.3(\pm0.1),4.7(\pm0.1),4.3(\pm0.1)$ for $\dot{\gamma}\tau=60,80,100,200$, respectively. Those data confirm at least the general trend that very highly sheared samples having strong ordering (prior cessation of shear) relax faster than those moderately sheared having weak ordering.

V. CONCLUSIONS

To conclude we perform Brownian dynamics computer simulations to study crystalline bilayers of charged colloidal suspensions which are confined between two parallel plates and sheared via a relative motion of the two plates. For the parameters under consideration, the unsheared equilibrium configuration is two crystalline layers with a nested quadratic in-plane structure. For increasing shear rates $\dot{\gamma}$, we find the following steady states: first, there is a static solid which is elastically sheared until a shear-rate threshold is reached. Higher shear rates melt the crystalline bilayers and even higher shear rates lead to a reentrant solid stratified in the shear direction. We have then studied the relaxation of the sheared steady state back to equilibrium after an instantaneous cessation of shear and found a nonmonotonic behavior of the typical relaxation time as a function of the shear rate $\dot{\gamma}$. In particular, application of (very) high shear rates accelerates the (post-)relaxation back to equilibrium since shear ordering facilitates the growth of the equilibrium crystal. The steady-state structure may be drastically altered by shearing topographically structured walls (e.g., atomic structures, roughness, chemical patterns, etc.). Hydrodynamic flow effects of the solvent are also expected to have significant influence at high shear rate. These questions will be addressed in future work. We finally point out that similar effects might be present in sheared granular sheets [40].

ACKNOWLEDGMENTS

We thank T. Palberg and C. Wagner for helpful comments. This work was supported by the DFG within the Transregio SFB TR6 (project section D1).

[1] For a review, see P. N. Pusey, in *Liquids, Freezing and the Glass Transition*, edited by J. P. Hansen, D. Levesque, and J. Zinn-Justin (North Holland, Amsterdam, 1991).
[2] W. van Megen, T. C. Mortensen, S. R. Williams, and J. Müller, Phys. Rev. E **58**, 6073 (1998).
[3] H. Löwen, Phys. Rep. **237**, 249 (1994).
[4] H. Löwen, J. Phys.: Condens. Matter **13**, R415 (2001).
[5] B. J. Ackerson and N. A. Clark, Phys. Rev. Lett. **46**, 123 (1981).
[6] B. J. Ackerson and N. A. Clark, Phys. Rev. A **30**, 906 (1984); B. J. Ackerson and P. N. Pusey, Phys. Rev. Lett. **61**, 1033 (1988); B. J. Ackerson, Physica A **174**, 15 (1991); S. E. Paulin, B. J. Ackerson, and M. S. Wolfe, J. Colloid Interface Sci. **178**, 251 (1996).
[7] D. G. Grier and C. A. Murray, J. Chem. Phys. **100**, 9088 (1994).
[8] M. Würth, J. Schwarz, F. Culis, P. Leiderer, and T. Palberg, Phys. Rev. E **52**, 6415 (1995).
[9] A. Heymann *et al.*, J. Colloid Interface Sci. **207**, 119 (1998).
[10] T. Palberg and M. Würth, J. Phys. I **6**, 237 (1996).
[11] M. D. Haw, W. C. K. Poon, and P. N. Pusey, Phys. Rev. E **57**, 6859 (1998).
[12] C. Dux and H. Versmold, Phys. Rev. Lett. **78**, 1811 (1997).
[13] M. R. Maaroufi, A. Stipp, and T. Palberg, Prog. Colloid Polym. Sci. **108**, 83 (1998).
[14] I. Cohen, T. G. Mason, and D. A. Weitz, Phys. Rev. Lett. **93**, 046001 (2004).
[15] J. Weiss, D. W. Oxtoby, D. G. Grier, and C. A. Murray, J. Chem. Phys. **103**, 1180 (1995).
[16] A recent overview about nonequilibrium computer simulations has been given by S. Hess, in *Advances in the Computer Simulation of Liquid Crystals*, edited by P. Parisi and C. Zannoni (Kluwer, Dordrecht, 2000), pp. 189–233.
[17] E. R. Dufresne, T. M. Squires, M. P. Brenner, and D. G. Grier, Phys. Rev. Lett. **85**, 3317 (2000).
[18] W. Xue and G. S. Grest, Phys. Rev. Lett. **64**, 419 (1990).
[19] M. J. Stevens, M. O. Robbins, and J. F. Belak, Phys. Rev. Lett. **66**, 3004 (1991).
[20] M. J. Stevens and M. O. Robbins, Phys. Rev. E **48**, 3778 (1993).
[21] J. Chakrabarti, A. K. Sood, and H. R. Krishnamurthy, Phys. Rev. E **50**, R3326 (1994).
[22] S. Butler and P. Harrowell, J. Chem. Phys. **103**, 4653 (1995).
[23] S. R. Rastogi, N. Wagner, and S. R. Lustig, J. Chem. Phys. **104**, 9234 (1996).
[24] N. Olivi-Tran, R. Botet, and B. Cabane, Phys. Rev. E **57**, 1997 (1998).
[25] S. R. Rastogi, N. Wagner, and S. R. Lustig, J. Chem. Phys. **104**, 9249 (1996).
[26] R. Blaak, S. Auer, D. Frenkel, and H. Löwen, Phys. Rev. Lett.

93, 068303 (2004).
[27] R. Blaak, S. Auer, D. Frenkel, and H. Löwen, J. Phys.: Condens. Matter **16**, S3873 (2004).
[28] M. A. Valdez and O. Manero, J. Colloid Interface Sci. **190**, 81 (1997).
[29] S. G. Bike and D. C. Prieve, J. Colloid Interface Sci. **175**, 422 (1995).
[30] P. Warszynski, X. Wu, and T. G. M. van de Ven, Colloids Surf., A **140**, 183 (1998).
[31] R. Messina and H. Löwen, Phys. Rev. Lett. **91**, 146101 (2003).
[32] A. B. Fontecha, H. J. Schope, H. König, T. Palberg, R. Messina, H. Löwen, 17, S2779 (2005).
[33] M. Das, S. Ramaswamy, and G. Ananthakrishna, Europhys. Lett. **60**, 636 (2002).
[34] M. Das, G. Ananthakrishna, and S. Ramaswamy, Phys. Rev. E **68**, 061402 (2003).
[35] T. Palberg and R. Biehl, Faraday Discuss. **123**, 133 (2003).
[36] R. Biehl and T. Palberg, Europhys. Lett. **66**, 291 (2004).
[37] J. Dzubiella, G. P. Hoffmann, and H. Löwen, Phys. Rev. E **65**, 021402 (2002).
[38] N. A. Clark, A. J. Hurd, and B. J. Ackerson, Nature (London) **281**, 57 (1979).
[39] A. J. Hurd, N. A. Clark, R. C. Mockler, and W. J. Sullivan, Phys. Rev. A **26**, 2869 (1982).
[40] J.-C. Tsai and J. P. Gollub, Phys. Rev. E **70**, 031303 (2004).